Oxidative Medicine and Cellular Longevity

Mechanisms and Oxidative Stress in Neuroinflammation

Lead Guest Editor: Luzia Kalyne Almeida Moreira Leal
Guest Editors: Francisco Rios and Silvânia Maria Mendes Vasconcelos

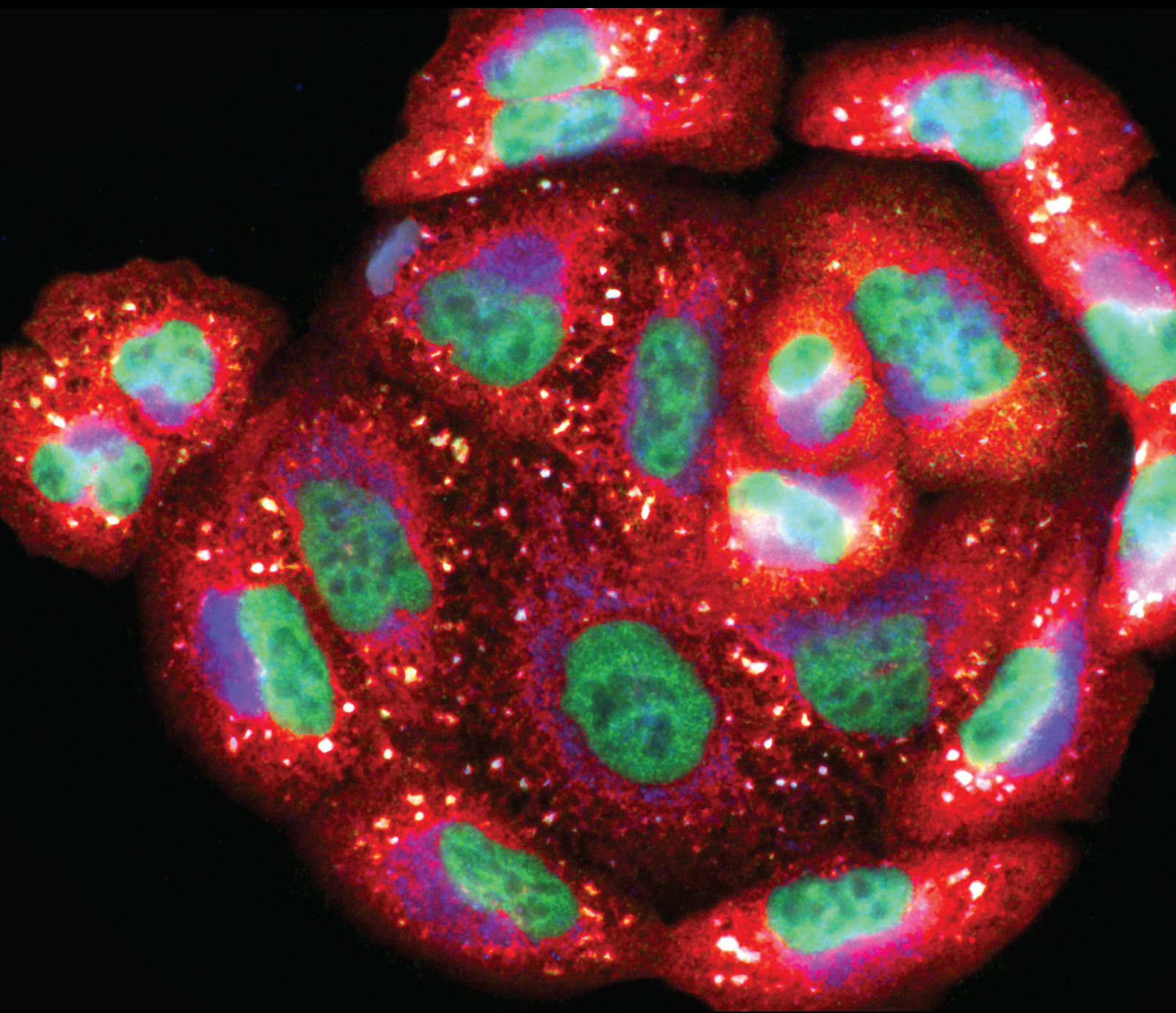

Mechanisms and Oxidative Stress in Neuroinflammation

Oxidative Medicine and Cellular Longevity

Mechanisms and Oxidative Stress in Neuroinflammation

Lead Guest Editor: Luzia Kalyne Almeida Moreira Leal
Guest Editors: Francisco Rios and Silvânia Maria Mendes Vasconcelos

Contents

Epiisopiloturine, an Alkaloid from *Pilocarpus microphyllus*, Attenuates LPS-Induced Neuroinflammation by Interfering in the TLR4/NF-κB-MAPK Signaling Pathway in Microglial Cells
João Antônio Costa de Sousa, Francisco Vinícius Clemente Serra Azul, Ana Bruna de Araújo, Rebeca Colares Tomé, Francisca Raysse Mesquita Silva, Silvânia Maria Mendes de Vasconcelos, Francisco José Rios, and Luzia Kalyne Almeida Moreira Leal
Research Article (11 pages), Article ID 4752502, Volume 2023 (2023)

Role of Oxidative Stress in Retinal Disease and the Early Intervention Strategies: A Review
Jun Wang, Mengling Li, Ziyue Geng, Saadullah Khattak, Xinying Ji, Dongdong Wu, and Yalong Dang
Review Article (13 pages), Article ID 7836828, Volume 2022 (2022)

Isorhamnetin Attenuated the Release of Interleukin-6 from β-Amyloid-Activated Microglia and Mitigated Interleukin-6-Mediated Neurotoxicity
Pei-Cih Wei, Guey-Jen Lee-Chen, Chiung-Mei Chen, Ying Chen, Yen-Shi Lo, and Kuo-Hsuan Chang
Research Article (15 pages), Article ID 3652402, Volume 2022 (2022)

Anxiolytic Effect of Carvedilol in Chronic Unpredictable Stress Model
Caren Nádia Soares de Sousa, Ingridy da Silva Medeiros, Germana Silva Vasconcelos, Gabriel Ângelo de Aquino, Francisco Maurício Sales Cysne Filho, Jamily Cunha de Almeida, Ana Paula Negreiros Nunes Alves, Danielle S. Macêdo, Luzia Kalyne Almeida Moreira Leal, and Silvânia Maria Mendes Vasconcelos
Research Article (14 pages), Article ID 6906722, Volume 2022 (2022)

Activation of LRP1 Ameliorates Cerebral Ischemia/Reperfusion Injury and Cognitive Decline by Suppressing Neuroinflammation and Oxidative Stress through TXNIP/NLRP3 Signaling Pathway in Mice
Cheng-Jie Yang, Xin Li, Xiao-Qing Feng, Ye Chen, Jian-Guo Feng, Jing Jia, Ji-Cheng Wei, and Jun Zhou
Research Article (23 pages), Article ID 8729398, Volume 2022 (2022)

Preventing Axonal Sodium Overload or Mitochondrial Calcium Uptake Protects Axonal Mitochondria from Oxidative Stress-Induced Alterations
Rebecca Ulshöfer, Helena Bros, Anja Erika Hauser, Raluca Aura Niesner, Friedemann Paul, Bimala Malla, and Carmen Infante-Duarte
Research Article (13 pages), Article ID 6125711, Volume 2022 (2022)

Effect of Ethyl Acetate Fraction from *Eucommia ulmoides* Leaves on $PM_{2.5}$-Induced Inflammation and Cognitive Dysfunction
Min Ji Kim, Jin Yong Kang, Jong Min Kim, Jong Hyun Moon, Hyo Lim Lee, Hye Rin Jeong, Min Ji Go, Uk Lee, and Ho Jin Heo
Research Article (26 pages), Article ID 7157444, Volume 2022 (2022)

MicroRNA-299a-5p Protects against Spinal Cord Injury through Activating AMPK Pathway
Zong-Ze Zhang, Shu-Yue Xian, Chong Bao, and Feng Chen
Research Article (13 pages), Article ID 8659587, Volume 2022 (2022)

URB597 and Andrographolide Improve Brain Microvascular Endothelial Cell Permeability and Apoptosis by Reducing Oxidative Stress and Inflammation Associated with Activation of Nrf2 Signaling in Oxygen-Glucose Deprivation
Da-Peng Wang, Kai Kang, Jun Sun, Qi Lin, Qiao-Li Lv, and Jian Hai
Research Article (23 pages), Article ID 4139330, Volume 2022 (2022)

Thioredoxin-Interacting Protein (TXNIP) Knockdown Protects against Sepsis-Induced Brain Injury and Cognitive Decline in Mice by Suppressing Oxidative Stress and Neuroinflammation
Yu Zhang, Cheng-Jun Xing, Xiao Liu, Ya-Hong Li, Jing Jia, Jian-Guo Feng, Cheng-Jie Yang, Ye Chen, and Jun Zhou
Research Article (23 pages), Article ID 8645714, Volume 2022 (2022)

Antineuroinflammatory Effect of *Amburana cearensis* and Its Molecules Coumarin and Amburoside A by Inhibiting the MAPK Signaling Pathway in LPS-Activated BV-2 Microglial Cells
Ana Bruna de Araújo, Francisco Vinícius Clemente Serra Azul, Francisca Raysse Mesquita Silva, Talysson Silva de Almeida, João Victor Nunes Oliveira, Antônia Torres Ávila Pimenta, Antônio Marcos Esmeraldo Bezerra, Nuno J. Machado, and Luzia Kalyne Almeida Moreira Leal
Research Article (14 pages), Article ID 6304087, Volume 2022 (2022)

Evaluation of Antiarthritic and Antinociceptive Effects of Cedrol in a Rat Model of Arthritis
Fatemeh Forouzanfar, Ali Mohammad Pourbagher-Shahri, and Hamed Ghazavi
Research Article (10 pages), Article ID 4943965, Volume 2022 (2022)

Glycyrrhizin Attenuates Hypoxic-Ischemic Brain Damage by Inhibiting Ferroptosis and Neuroinflammation in Neonatal Rats via the HMGB1/GPX4 Pathway
Kaiyi Zhu, Xing Zhu, Shiqi Liu, Jie Yu, Songwei Wu, and Mingyan Hei
Research Article (18 pages), Article ID 8438528, Volume 2022 (2022)

The Polysaccharides from the Aerial Parts of *Bupleurum chinense* DC Attenuate Epilepsy-Like Behavior through Oxidative Stress Signaling Pathways
Xiaomao Li, Yan Liu, Siyi Wang, Yikai Jiang, Adnan Mohammed Algradi, Yuanyuan Zhou, Wei Guan, Juan Pan, Haixue Kuang, and Bingyou Yang
Research Article (17 pages), Article ID 7907814, Volume 2022 (2022)

Ferroptosis Mediated by Lipid Reactive Oxygen Species: A Possible Causal Link of Neuroinflammation to Neurological Disorders
Ying Cheng, Yiting Song, Huan Chen, Qianqian Li, Yuan Gao, Guanchao Lu, and Chengliang Luo
Review Article (13 pages), Article ID 5005136, Volume 2021 (2021)

Hindawi
Oxidative Medicine and Cellular Longevity
Volume 2023, Article ID 4752502, 11 pages
https://doi.org/10.1155/2023/4752502

Research Article

Epiisopiloturine, an Alkaloid from *Pilocarpus microphyllus*, Attenuates LPS-Induced Neuroinflammation by Interfering in the TLR4/NF-κB-MAPK Signaling Pathway in Microglial Cells

João Antônio Costa de Sousa,[1] **Francisco Vinícius Clemente Serra Azul**,[1] **Ana Bruna de Araújo**,[1] **Rebeca Colares Tomé**,[1] **Francisca Raysse Mesquita Silva**,[1] **Silvânia Maria Mendes de Vasconcelos**,[2] **Francisco José Rios**,[3] **and Luzia Kalyne Almeida Moreira Leal**[1]

[1]*Center of Cosmetics and Pharmaceutical Studies, CEFAC, Faculty of Pharmacy, Odontology, and Nursing, Department of Pharmacy, Federal University of Ceará, CEFAC, Fortaleza, CE, Brazil*
[2]*Neuropharmacology Laboratory, Department of Physiology and Pharmacology, NPDM, Federal University of Ceará, Fortaleza, CE, Brazil*
[3]*Institute of Cardiovascular and Medical Sciences, University of Glasgow, 126 University Place, Glasgow G12 8TA, UK*

Correspondence should be addressed to Luzia Kalyne Almeida Moreira Leal; kalyne@ufc.br

Received 23 May 2022; Accepted 18 March 2023; Published 28 April 2023

Academic Editor: Anwen Shao

Neuroinflammation is present in the pathophysiological mechanisms of several diseases that affect the central nervous system (CNS). Microglia have a prominent role in initiating and sustaining the inflammatory process. Epiisopiloturine (EPI) is an imidazole alkaloid obtained as a by-product of pilocarpine extracted from *Pilocarpus microphyllus* (jaborandi) and has shown promising anti-inflammatory and antinociceptive properties. In the present study, we investigated the effects of EPI on the inflammatory response in microglial cells (BV-2 cells) induced by lipopolysaccharide (LPS) and explored putative underlying molecular mechanisms. Cell viability was not affected by EPI (1-100 μg/mL) as assessed by both LDH activity and the MTT test. Pretreatment with EPI (25, 50, and 100 μg/mL) significantly reduced the proinflammatory response induced by LPS, as observed by a decrease in nitrite oxide production and iNOS protein expression. EPI (25 μg/mL) reduced IL-6 and TNF-α production, by 40% and 34%, respectively. However, no changes were observed in the anti-inflammatory IL-10 production. Mechanistically, EPI inhibited the TLR4 expression and phosphorylation of NF-κB p65 and MAPKs (JNK and ERK1/2) induced by LPS, but no changes were observed in TREM2 receptor expression in LPS-stimulated cells. In conclusion, our data demonstrated the potent anti-inflammatory properties of EPI in microglial cells. These effects are associated with the reduction of TLR4 expression and inhibition of intracellular signaling cascades, including NF-κB and MAPKs (JNK and ERK1/2).

1. Introduction

Inflammatory response plays a crucial role in the development and progression of many neurodegenerative diseases (ND) that are closely related to aging, such as Parkinson's disease (PD) and Alzheimer's disease (AD), which are progressive chronic illnesses and result in patient death [1–3]. However, the current pharmacotherapy approved by the Food and Drug Administration is mostly symptomatic and has limitations. Hence, it is of high priority to investigate new drugs to prevent or improve the treatment of these diseases [4].

The microglial cells are considered "Central Nervous System (CNS) macrophages," constituting 5–10% of total brain cells, and interact with almost all cell types in the brain (e.g., astrocytes, oligodendrocytes, and neurons) contributing to

brain development, plasticity, and maintaining of the homeostasis [5]. Microglial cells modulate neuronal activity, and in return, neurons may also interfere with microglial functions. Under stress conditions, microglia might acquire different activation phenotypes that vary according to the microenvironment including (i) classically activated M1 phenotype characterized by the production of proinflammatory mediators, including IL-1β, TNF-α, and IL-6, and increased expression of inducible nitric oxide synthase (iNOS) and surface markers, CD16/32, CD86, and CD40), and (ii) alternatively activated M2 phenotype, which is associated with phagocytosis of apoptotic cells and release of anti-inflammatory mediators (IL-10, TGFβ, and galectin-3) [6–8]. In ND, there is an imbalance of M1/M2 favoring M1.

In the CNS, microglia interact with damage-associated molecular patterns (DAMPS) (cell debris, modified proteins, including Aβ species and alpha-synuclein, and oxidized lipids) or pathogen-associated molecular patterns (PAMPs) such as LPS, a component of the outer membrane of Gram-negative bacteria. This PAMP acts by activating the innate immune receptor Toll-like 4 (TLR4) which is highly expressed in microglia. The LPS activates intracellular signaling pathways associated with transcription factors such as NF-κB dimer (p50 and p65) and mitogen-activated protein kinases (MAPKs), producing inflammatory mediators. In contrast, the triggering receptors expressed on myeloid cells 2 (TREM 2) and expressed in microglial cells have opposite effects by downregulating the production of proinflammatory mediators, such as TNF-α [9–11].

The activation of NF-κB by LPS-TLR4 and subsequent translocation of this transcription factor from the cytoplasm to the nucleus leads to transcription of genes involved in the production of inflammatory enzymes (e.g., iNOS), TNF-α, IL-1β, IL-6, and other chemical mediators, while the activation of MAPK family members such as JNK, ERK1/2, and p-38 results in the activation of activator protein 1 (AP-1) family transcription factors which regulate the expression of various inflammatory proteins [9, 12–15]. Thus, several studies have been assessing the modulation of microglial functions as a strategy to treat ND. The therapeutic approach is associated with microglial activation, by targeting innate immune receptors and intracellular signaling pathways including TLR, MAPKs, and transcription factors that are directly involved in the production of neuroinflammatory mediators and oxidant species (e.g., nitric oxide and reactive oxygen species) associated to ND [16–18]. Of importance, various plant-derived alkaloids, such as berberine and caffeine, have shown neuroprotective effects by reducing neuroinflammation and regulating microglial cell functions [19].

Epiisopiloturine (EPI) (see Figure 1) is an imidazole alkaloid obtained as a by-product of pilocarpine extracted from *Pilocarpus microphyllus*. Recently, we demonstrated that EPI reduces the inflammatory response in human neutrophils by suppressing NF-κB activation, TNFα, IL-6, and ROS production [20]. We also demonstrated an antinociceptive effect of this alkaloid in carrageenan-induced acute inflammatory pain models in rodents [20, 21]. Additional pharmacological activities have been described for EPI including antibacterial, antiproliferative, anti-inflammatory, and antinociceptive in mice [22–24]. In the current study, we investigated the effects of EPI on the inflammatory response induced by LPS on the microglia cell line. In particular, we focused on cytokine production and phosphorylation of MAPK and NF-κB pathways.

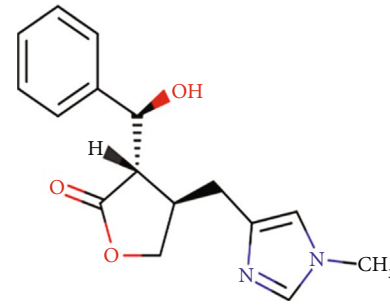

Figure 1: Chemical structure of epiisopiloturine (EPI) from *Pilocarpus microphyllus*.

2. Materials and Methods

2.1. Alkaloid Epiisopiloturine. The epiisopiloturine alkaloid (EPI) (99.7% purity) was obtained as a by-product of pilocarpine extracted from *P. microphyllus*, and a voucher specimen (HDELTA2869) was deposited in the herbarium Delta do Parnaíba, Federal University of Piauí. EPI was dissolved in dimethyl sulfoxide (DMSO) 0.1% in water.

2.2. Chemicals and Biological Materials. N-(1-Naphthyl)ethylenediamine dihydrochloride (NEED) (Sigma-Aldrich, EUA), bovine serum albumin (BSA) (Sigma-Aldrich, EUA), absolute ethyl alcohol (Dinâmica, Brazil), 3-(4,5-dimethylthiazol-2-yl)-2,5-diphenyltetrazolium bromide (MTT) (Sigma-Aldrich, EUA), sodium chloride (Dinâmica, Brazil), potassium chloride (Dinâmica, Brazil), DMSO (Sigma-Aldrich, EUA), sodium dodecyl sulfate (SDS) (Biorad, EUA), sodium deoxycholate (Bio-Rad, EUA), monobasic sodium phosphate (Dinâmica, Brazil), dibasic sodium phosphate (Dinâmica, Brazil), glycerol (Dinâmica, Brazil), lipopolysaccharide (LPS) (Sigma-Aldrich, EUA), methanol (Dinâmica, Brazil), Roswell Park Memorial Institute (RPMI) (Gibco by Life Technologies, EUA), fetal bovine serum (FBS) (Gibco by Life Technologies, EUA), sulfanilamide (Dinâmica, Brazil), Tris-HCl (Dinâmica, Brazil), Triton x-100 (Sigma-Aldrich, EUA).

Fetal bovine serum (FBS) and cell culture medium RPMI-1640 were purchased from Gibco, USA. Murine microglial cells (BV-2 cell line) were acquired from Cell Biobank, Rio de Janeiro, Brazil. Anti-TLR4 and anti-TREM2 were obtained from Invitrogen, Carlsbad, CA, USA. Anti-p-P65 NF-κB, anti-p-NF-κB total, anti-p-JNK, anti-p-total JNK, and anti-p-ERK1/2 were obtained from Cell Signaling Technology®, Danvers, MA, USA. Anti-ERK1/2 total was obtained from Abcam®, Cambridge, and anti-mouse secondary antibody was obtained from Bio-Rad Laboratories, CA, USA, or anti-rabbit was obtained from Sigma-Aldrich, New York, USA.

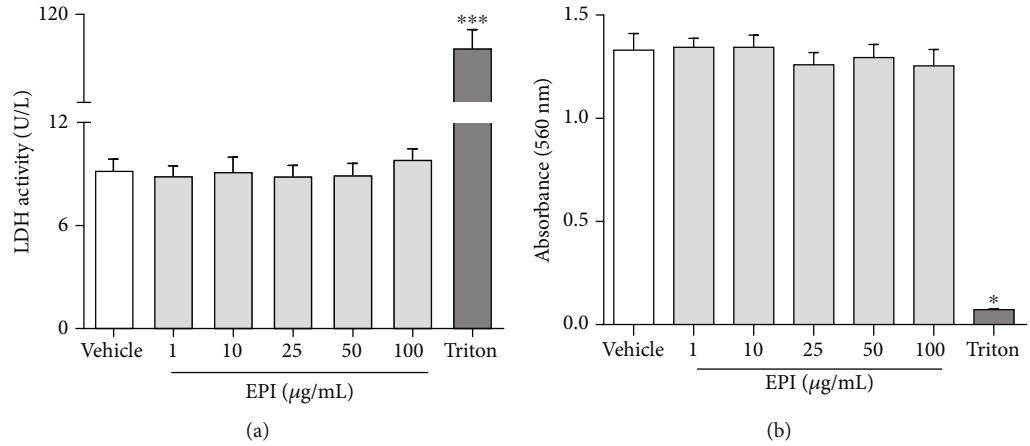

Figure 2: Effect of EPI on cell viability. LDH activity (a) and MTT test (b) were assessed in microglial BV-2 cells treated with different concentrations of EPI. Results are expressed as mean ± S.E.M. * vs. vehicle/RPMI ($p < 0.05$—one-way ANOVA and Bonferroni test), n = 4/group.

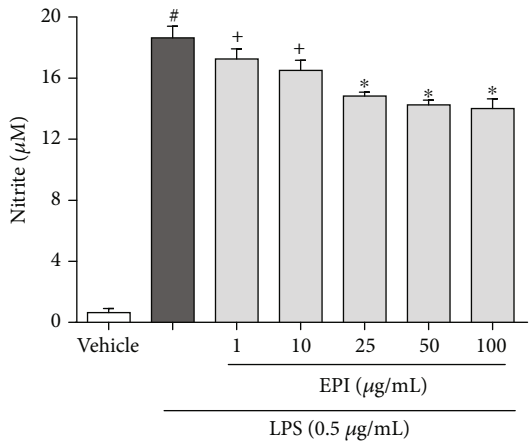

Figure 3: Effect of EPI in LPS-induced NO production. Results are expressed as mean ± S.E.M of nitrite production (μM). # vs. vehicle/RPMI; * vs. LPS group. + vs. EPI 25 μg/mL+LPS ($p < 0.05$ —one-way ANOVA and Bonferroni test), n = 4/group.

2.3. Cell Culture Conditions. Cells were plated on poly-L-lysine-coated 96- or 24-well plates, at a density of 1×10^5 cells/mL or 1×10^6 cells/mL in RPMI-1640 culture medium, supplemented with 10% FBS at 37°C under an atmosphere of 5% CO_2.

2.4. MTT Assay. BV-2 cells (1×10^5 cells/mL) were incubated with different concentrations of EPI (1, 10, 25, 50, and 100 μg/mL), vehicle/control group (DMSO 0.1% in water), or Triton x-100 (0.01%—cytotoxic standard). After 24 hours, the MTT bromide salt (3[4,5-dimethylthiazol-2-yl]-2,5-diphenyltetrazolium bromide) was added to cell suspension at a concentration of 0.5 mg/mL. After 90 minutes of incubation, the plate was centrifuged at 800 g and the supernatant was discarded. Finally, 150 μL of DMSO was added for solubilization of the metabolized formazan salt. The plate was stirred constantly for 15 minutes using a shaker, and the absorbance was measured in a microplate reader at 560 nm [25].

2.5. Lactate Dehydrogenase Activity. The assay was performed using the LDH Kit (Liquiform, Minas Gerais, Brazil) according to the manufacturer's instructions. The assay is based on the measurement of the decrease in absorbance of the sample due to oxidation of nicotinamide adenine dinucleotide (NADH), which is proportional to the LDH activity. Microglial cells BV-2 (1×10^5 cells/mL) were plated in 96-well plate and after 1 hour were incubated with EPI diluted in DMSO 0.1% (1, 10, 25, 50, and 100 μg/mL), vehicle/control group (DMSO 0.1%), or Triton x-100 group (0.01%—cytotoxic standard). After 24 hours, the substrate of the LDH enzyme was added to cell supernatants. Absorbance (340 nm) was measured at 37°C.

2.6. NO Measurement. Nitric oxide (NO) production was assessed by nitrite concentration using the Griess reaction. Microglial BV-2 cells (1×10^6 cells/mL) were incubated with EPI (1, 10, 25, 50, and 100 μg/mL) or vehicle/control group (DMSO 0.1%) for one hour, followed by LPS stimulation (0.5 μg/mL). Next, 100 μL of Griess reagent (1% sulfanilamide in 1% H_3PO_4/0.1% N-(1-naphthyl)-ethylenediamine dihydrochloride/1% H_3PO_4/distilled water, 1 : 1 : 1 : 1) was added to 100 μL of cell culture supernatant. Absorbance was measured at 560 nm using a plate reader. Nitrite concentration was obtained from the absorbance values using sodium nitrite (1 μM - 100 μM) as the standard curve [26].

2.7. Measurement of IL-1β, IL-6, TNF-α, and IL-10 Levels. Cytokine production was assessed by enzyme-linked immunosorbent assay (ELISA). BV-2 cells (1×10^6 cells/mL) were pretreated with EPI, 25 μg/mL, or vehicle/control group (DMSO 0.1%) for one hour at 37°C, followed by LPS stimulation (0.5 μg/mL). After 24 hours, IL-1β, IL-6, IL-10, and TNF-α were measured in the cell supernatant according to the manufacturer's instructions (BD Biosciences—San Diego, CA, USA, and R&D Systems—Minnesota, MN,

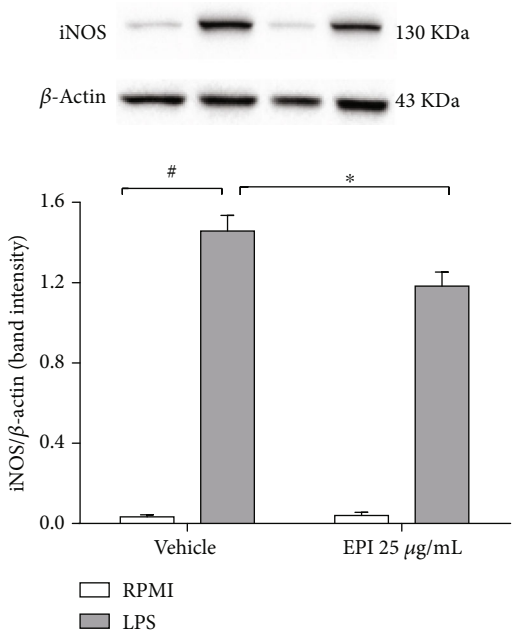

Figure 4: Effect of EPI in LPS-induced iNOS expression in microglia. BV-2 cells were pretreated with EPI (25 μg/mL) for 1 h before the addition of LPS (0.5 μg/mL). Results are expressed as mean ± S.E.M of iNOS/β-actin band intensity. # vs. vehicle/RPMI; * vs. LPS group ($p < 0.05$—two-way ANOVA and Bonferroni test), $n = 4$/group.

USA). Optical density was measured at an absorbance of 450 nm using a microplate reader.

2.8. Western Blot Analysis. Microglial cells (1×10^6 cells/mL) were incubated with EPI 25 μg/mL or vehicle/control group (DMSO 0.1%) for one hour at 37°C, followed by LPS stimulation (0.5 μg/mL) for 1 h or 24 h. After the incubation period, the cells were harvested with ice-cold buffered saline (PBS) and centrifuged at 4°C, 130 g for 5 minutes. The total cell lysate was obtained using radioimmunoprecipitation assay buffer (RIPA buffer) supplemented with protease inhibitors (P2714, Sigma-Aldrich, New York, USA) and phosphatase inhibitors (ab201112, Abcam®, Cambridge, UK). The total lysate was cleared by centrifugation at 12000 g for 10 minutes at 4°C, and the pellet was discarded. Protein concentration was determined using the BCA kit (Bio-Rad Laboratories, CA, USA). Total protein (30 μg) was separated on 10% SDS-polyacrylamide (SDS-PAGE) gel electrophoresis and transferred onto a polyvinylidene fluoride (PVDF) membrane (Bio-Rad Laboratories, CA, USA). Nonspecific binding sites were blocked with 5% non-fatty dry milk solubilized in Tris-buffered saline solution with Tween 0.01% for 1 h at room temperature. Membranes were incubated overnight at 4°C with the following primary specific antibodies: anti-iNOS 1 : 3000 (ab178945), anti-β-actin 1 : 100 (ab8226), and anti-total-ERK1/2 total 1 : 1000 (ab36991) from Abcam; anti-TLR4 1 : 500 (482300) and anti-TREM2 1 : 500 (PA587933) from Thermo Scientific; anti-phospho-NF-κB P65 1 : 1000 (Ser536, #3033S), anti-total-NF-κB P65 1 : 1000 (#6956S), anti-phospho-JNK 1 : 1000 (Thr183/Tyr185, #9255S), anti-total-JNK 1 : 2000 (#9252S), and anti-phospho-ERK1/2 1 : 1000 (Thr202/Tyr204, #9101S) all from Cell Signaling. Next, membranes were washed with TBS-tween and incubated with secondary antibodies anti-mouse (#170-6516, Bio-Rad) or anti-rabbit (SAB3700956, Sigma-Aldrich) (HRP 1 : 3000) for 2 hours. Protein expression was visualized using Western Blot Clarity™ ECL (Bio-Rad Laboratories, Hercules, CA, USA). Immunoreactive signals were detected by chemiluminescence in a photo documenter ChemiDocTM MP Imaging System (Bio-Rad Laboratories, Hercules, CA, USA). Optical densities were measured by Image Lab™ 5.1 Software (Bio-Rad Laboratories, Hercules, CA, USA).

2.9. Statistical Analyses. For statistical analysis, the GraphPad Prism version 6.0 program (GraphPad Software, San Diego, USA) was used. Data were represented as mean ± standard error of the mean (S.E.M). Data normality analysis was performed using the Shapiro-Wilk test. Data that showed normal distribution were analyzed by analysis of variance (one-way or two-way ANOVA) followed by the Bonferroni posttest. Differences were considered significant when $p < 0.05$.

3. Results

3.1. Cell Viability Is Not Affected by EPI. The addition of increasing concentrations of EPI (1, 10, 25, 50, and 100 μg/mL) to BV-2 cells did not affect cell viability assessed LDH enzyme activity (8.8 ± 0.5; 9.1 0.8; 8.8 ± 0.6; 8.9 ± 0.6, and 9.8 ± 0.6 U/L, respectively) compared to vehicle group (DMSO 0.1%: 9.1 ± 0.7 U/L) (Figure 2(a)). In the evaluation of cell viability by MTT, the addition of increasing concentrations of EPI (1, 10, 25, 50, and 100 μg/mL) to the BV-2 cell suspension did not significantly reduce cell viability (Abs 560 nm: 1.3 ± 0.04; 1.3 ± 0.05; 1.2 ± 0.05; 1.2 ± 0.06; 1.2 ± 0.06, respectively) when compared to the vehicle group (Abs 560 nm: 1.3 ± 0.08) (Figure 2(b)). These results demonstrated that EPI does not affect the viability of microglial cells and guided the continuation of studies to investigate the anti-inflammatory/immunomodulatory effect of this alkaloid in BV-2 cells.

3.2. EPI Reduces Nitric Oxide/Nitrite Production in LPS-Stimulated BV-2 Cells. Microglial cells treated with LPS (0.5 μg/mL) exhibited higher concentrations of nitrite in the supernatant (18.6 ± 0.7 μM) compared to the vehicle control group (DMSO 0.1%: 0.6 ± 0.2 μM) (Figure 3). With LPS treatment, the addition of EPI (25, 50, and 100 μg/mL) significantly reduced nitrite levels (14.8 ± 0.2; 14.2 ± 0.3; 14.0 ± 0.6 μM, respectively) when compared to only LPS-treated group (18.6 ± 0.7 μM). Lower concentrations of EPI (1 and 10 μg/mL) were not able to reduce nitrite levels (17.9 ± 0.2; 16.5 ± 0.6 μM, respectively) induced by LPS stimulation. This finding shows a potential anti-inflammatory effect of EPI, which may be related to the inhibition of intracellular pathways such as iNOS, NF-κB, and MAPKs.

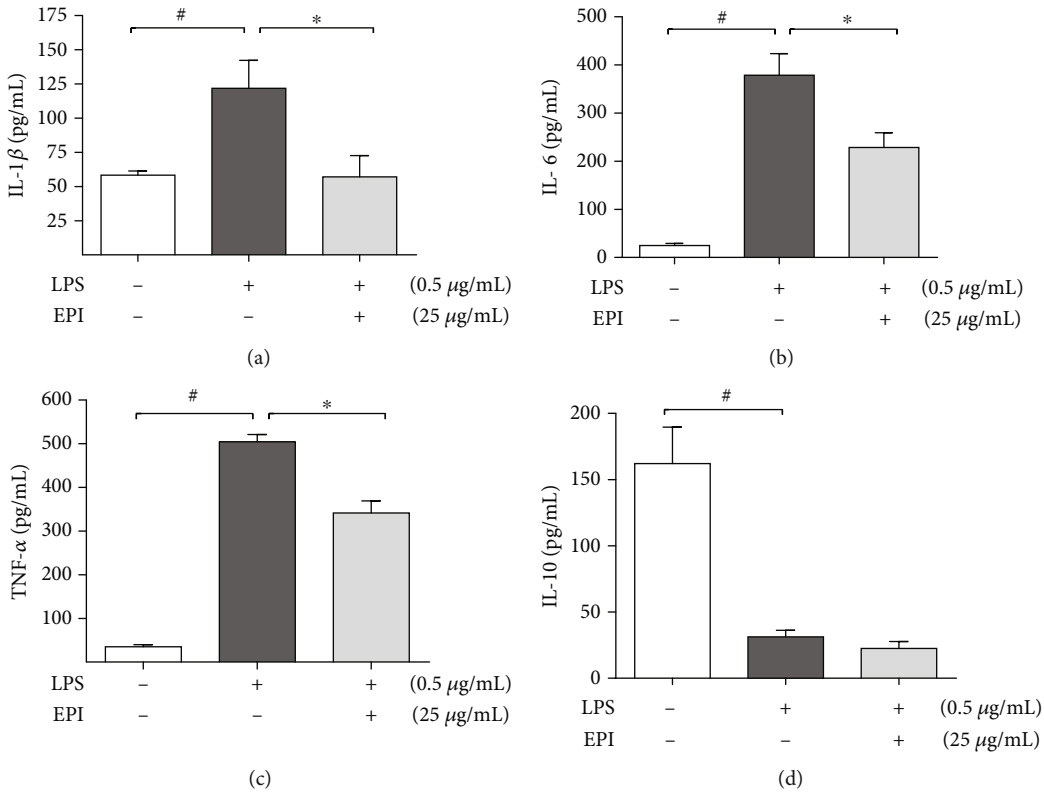

Figure 5: Effects of EPI on inflammatory cytokine release in LPS-stimulated microglia. BV-2 cells were pretreated with EPI (25 μg/mL) for 1 h and incubated with LPS (0.5 μg/mL) for 24 hours. Results are expressed as mean ± S.E.M of IL-1β (a), IL-6 (b), TNF-α (c), and IL-10 (d) production (pg/mL). # vs. vehicle/RPMI; * vs. LPS group ($p < 0.05$—one-way ANOVA and Bonferroni test), $n = 4$/group.

3.3. EPI Reduces the Expression of Inducible Nitric Oxide Synthase (iNOS) and the Production of IL-1 β, IL-6, and TNF-α in Microglial Cell Stimulated with LPS. Microglial cells treated with LPS (0.5 μg/mL) exhibited increased expression of nitric oxide synthase. However, the pretreatment of cells with EPI (25 μg/mL) (iNOS/β-actin band intensity: 1.1 ± 0.06) significantly reduced when compared to the LPS group (iNOS/β-actin band intensity: 1.4 ± 0.07) (Figure 4).

Based on the results obtained so far, the concentration of EPI selected for further studies was 25 μg/mL. Cells exposed to LPS showed an increase about two times in IL-1β concentration (121.0 ± 20.8 pg/mL). Pretreatment with EPI significantly reduced IL-1β production (64.7 ± 17.7 pg/mL) when related to the LPS group, with final values similar to those unstimulated BV-2 cells (58.3 ± 3.0 pg/mL) (Figure 5(a)). The addition of EPI (25 μg/mL) to the cell culture before LPS also significantly reduced IL-6 production (228.4 ± 30.6 pg/mL) showing an average inhibition of 40% when compared to the LPS group (378.7 ± 44.9 pg/mL). Similarly, the increase of TNF-α production observed after exposure of the cells to LPS (504.2 ± 16.9 pg/mL) was partially reversed by EPI (341.5 ± 27.7 pg/mL) corresponding to a reduction of about 34% (see Figures 5(a) and 5(c)). It was also evaluated the effect of EPI on the production of IL-10, an anti-inflammatory cytokine. The cells exposed to LPS reduced in about five times the IL-10 production (31.2 ± 5.0 pg/mL) when related to unstimulated BV-2 cells (162.0 ± 27.6 pg/mL), and EPI (22.5 ± 5.2 pg/mL) did not interfere in the reduction of this cytokine level after exposure to LPS (Figure 5(d)). Taken together, these data show that EPI acts decreasing NO production through direct action on the biosynthesis of this mediator. In addition, the anti-inflammatory effect of this alkaloid seems to be associated to the reduction in the production of proinflammatory cytokines without affecting IL-10 level, an anti-inflammatory cytokine.

3.4. EPI Interferes with TLR4/NF-κB-MAPK Signaling Pathway. Stimulation of microglial cells with LPS (0.5 μg/mL) for 1 hour increased about two times the TLR4 protein expression (2.2 ± 0.3) when compared to the vehicle group (1.26 ± 0.09). However, pretreatment with EPI (25 μg/mL), significantly reduced the protein expression of TLR-4 (1.3 ± 0.1) when related to the LPS group (Figure 6(a)). The addition of EPI (25 μg/mL) to the cells inhibited in about 40% the phosphorylation of the p65 subunit of NF-κB (0.47 ± 0.04) when compared to the LPS group (0.79 ± 0.06). Similar results were observed in the activation of the MAPK signaling pathway. EPI pretreatment reduced phosphorylation of JNK (0.63 ± 0.01) and ERK1/2 (1.74 ± 0.03) compared to the LPS-treated group (1.0 ± 0.01 and 1.74 ± 0.03 for JNK and ERK1/2, respectively) (Figures 6(c) and 6(d)). These data demonstrate that the anti-

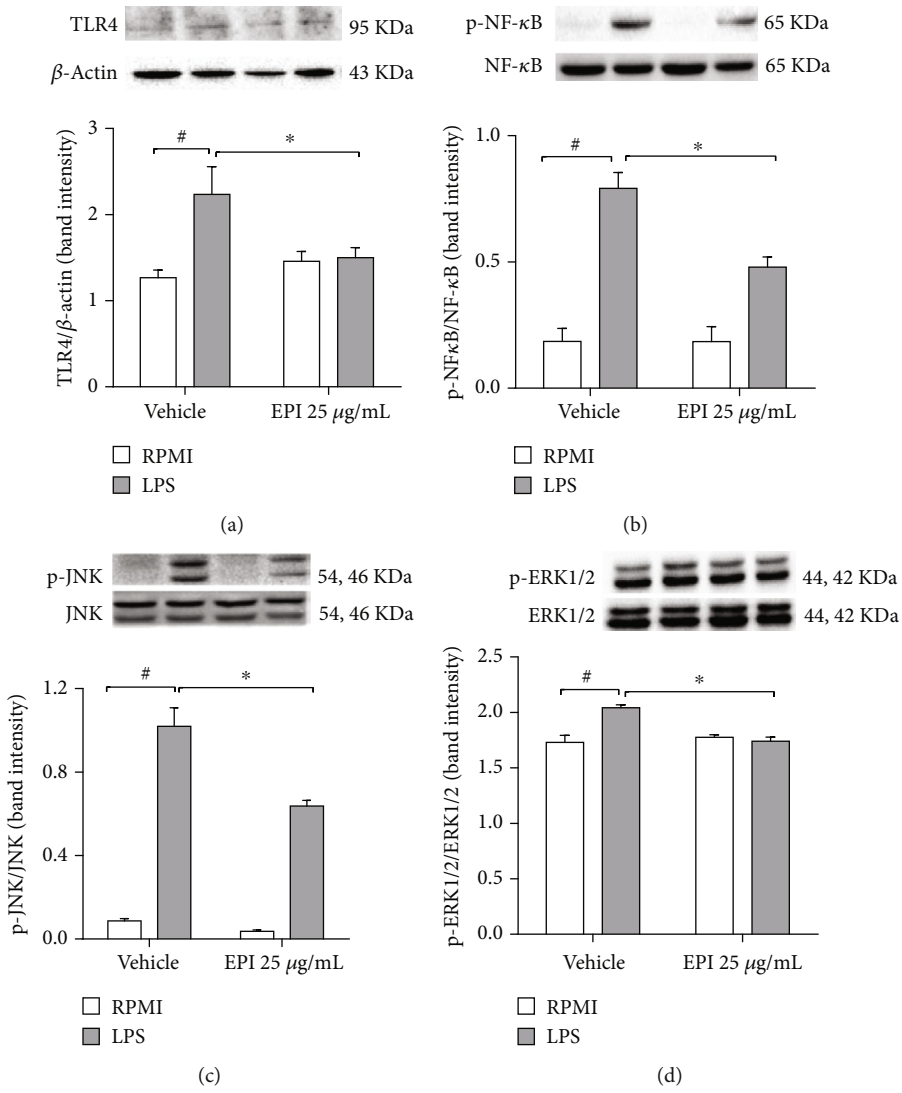

Figure 6: Effect of EPI on TLR4 (a), NF-κB (b), JNK (c), and ERK1/2 (d). BV-2 cells were pretreated with EPI (25 μg/mL) for 1 h, followed by LPS (0.5 μg/mL) for 1 hour. Results are expressed as mean ± S.E.M. # vs. vehicle/RPMI; * vs. vehicle group stimulated with LPS ($p < 0.05$ —two-way ANOVA and Bonferroni test), $n = 4$/group.

inflammatory effect of EPI occurs via the inhibition of TLR4/NF-κB-MAPK (ERK and JNK) signaling pathway in BV-2 microglial cells, which affect the production of inflammatory mediators.

3.5. EPI Does Not Affect the Expression of Triggered Receptor Expressed on Myeloid Cells 2 (TREM2). The addition of LPS (0.5 μg/mL) to BV-2 microglial cell suspension significantly reduced the protein expression of the anti-inflammatory marker TREM2 (0.35 ± 0.1) when compared to the vehicle group (1.3 ± 0.2). However, the cell treatment with EPI 25 μg/mL (0.4 ± 0.2) was not able to significantly interfere with the receptor expression after LPS stimulation (0.3 ± 0.1) (see Figure 7). This data suggests, therefore, that the anti-inflammatory effect of EPI is not related to a modulatory effect in the anti-inflammatory mechanism mediated by the TREM2 receptor.

4. Discussion

This study investigates the anti-inflammatory effects of epiisopiloturine (EPI), an imidazole alkaloid isolated from *P. microphyllus* in LPS-stimulated microglia. Aberrant activation of microglia plays a crucial role in the development and progression of neuroinflammation responsible for progressive neuronal death in neurodegenerative diseases. The alkaloid EPI showed potent anti-inflammatory activity by reducing LPS-induced proinflammatory cytokines (M1 phenotype) through mechanisms associated with MAPK and NF-κB signaling pathways.

A neuroinflammation is a form of inflammatory process restricted to the central nervous system (CNS) and peripheral nervous system (PNS), highly involved with several CNS diseases, including Parkinson's disease, multiple sclerosis, Alzheimer's disease (AD), and more recently neuropathic pain, due to the production of proinflammatory mediators (cytokines

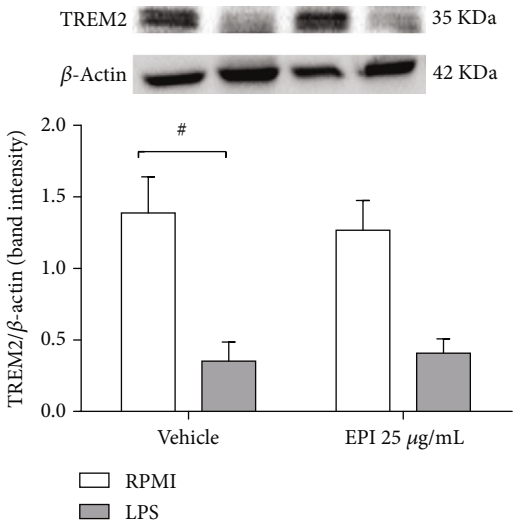

Figure 7: Expression of TREM in BV-2 cells treated with EPI. BV-2 cells were pretreated with EPI 25 μg/mL for 1 h, followed by stimulation with LPS for 1 h. Results are expressed as mean ± of TREM2/β – actin band intensity. # vs. vehicle/RPMI; ($p < 0.05$ —two-way ANOVA and Bonferroni test), $n = 4$/group.

and chemokines) by glial cells [27–29]. Products of oxidative stress are among inflammatory mediators which contribute to the development and progression of these disorders, such as nitric oxide (NO).

Nitric oxide (NO) is a versatile mediator with several homeostatic roles, mainly in the cardiovascular and nervous systems; however, it is also produced in inflammatory processes by innate immune cells [30, 31]. In the central nervous system, NO production is associated with the activation of neuronal NO synthase (nNOS) and endothelial (eNOS), which are constitutively expressed in neurons of the spinal cord/vessels of the brain and vascular systems surrounding motor neurons, respectively. In contrast, the inducible isoform (iNOS) present in astrocytes and microglia is upregulated during inflammatory response [32]. Thus, during the inflammatory process in CNS, studies indicate that NO produced by iNOS contributes to neuronal death by mechanisms dependent on mitochondrial dysfunction, DNA damage, and release of glutamate with consequent excitotoxic cell death [33–37]. Here, we show that treatment of microglial cells with EPI reduced nitric oxide production and iNOS expression induced by LPS. In addition, these effects were not associated with cytotoxic effects of EPI as no changes were observed in the mitochondrial activity or cell membrane permeability assessed by the MTT test and LDH enzyme activity, respectively. These data suggest that EPI reduces NO production acting directly in its biosynthesis and might have consequences on the formation of other reactive species of nitrogen (RNS), such as peroxynitrite (ONOO-). At high concentrations, ONOO- in CNS induces lipid peroxidation, which affects the neuronal Ca^{2+} homeostasis, a molecular marker of AD. These data corroborate a previous study [38] showing that EPI reduced NO production and iNOS expression in intestinal tracts from rats affected by experimental Crohn's disease induced by trinitrobenzene sulfonic acid (TNBS).

The production of proinflammatory mediators (NO, IL-1β, TNF-α, and IL-6) by classically activated microglial cells (M1 profile) is a common process in neuroinflammation [39]. The chronic phenotype of this inflammatory profile (M1) downregulates the neurorepairing microglial profile (M2) responsible for restoring homeostasis in the brain parenchyma through the production of anti-inflammatory mediators such as IL-10, IL-4, TGF-β, and arginase-1 [40]. EPI reduced the increase in LPS-induced inflammatory cytokines in microglial cells. The higher IL-1β levels observed after exposure of the cells to LPS were reversed by EPI, which also prevented the TNF-α and IL-6 overproduction. Such data corroborate previous investigations where EPI was able to decrease the production of proinflammatory cytokines in human neutrophils [20], peritoneal cavity from mice submitted to carrageenan-induced peritonitis model [22], and intestinal inflammation in experimental TNBS-induced Crohn's disease [38].

Considering the promising results, the effectiveness of EPI in interfering with the TLR4 receptor expression induced by LPS in microglial cells was investigated. Toll-like receptors play important role in innate immune activation [16, 17]. They interact with pathogen-associated molecular patterns (PAMPs) including LPS and endogenous molecules (damage-associated molecular patterns (DAMPS)) leading to the expression of proinflammatory mediators [41]. LPS is a potent activation of TLR4, which is expressed in several cells from the immune, vascular, and central nervous system. TLR4 stimulation induces activation of a proinflammatory cascade involving adaptor molecules, activation of NF-κB and MAPK pathways, and consequent cytokine production, including IL-1β, TNF-α, and IL-6. In CNS, TLR4 activation is associated with microglia-mediated neurotoxicity and it is considered therapeutic for ND treatment [42–47]. The EPI induced a significant reduction of the TLR4 expression, which explains the anti-inflammatory effect of this alkaloid. So, for further description of the mechanism of action of EPI, it was evaluated its effect on MAPK and NF-κB pathways in BV-2 microglial cells.

NF-κB and MAPKs are important intracellular activation pathways in the inflammatory response [48–55], and both pathways are potently activated by TLR4. EPI treatment inhibited the expression of the p65 NF-κB subunit in microglial cells stimulated with LPS. The p50 and p65 dimer is the most frequent in the formation of NF-κB and is found in an inactive form in the cytoplasm cells. The LPS-induced NF-κB activation through TLR4 and adaptor molecules (MyD88 and TRIF) results in the phosphorylation of IκB through the IKK complex. In the cell nucleus, the NF-κB dimer initiates transcription of a number of different genes including chemokines, adhesion molecules, TNF-α, and IL-6 [56]. Thus, the result demonstrates that EPI reduced the production of inflammatory mediators by regulating the transcription of coding proinflammatory genes, such as IL-1β, TNF-α, and IL-6. Our results were corroborated by a previous study [20] where we demonstrated that this alkaloid also inhibits the migration of the p65 subunit to the

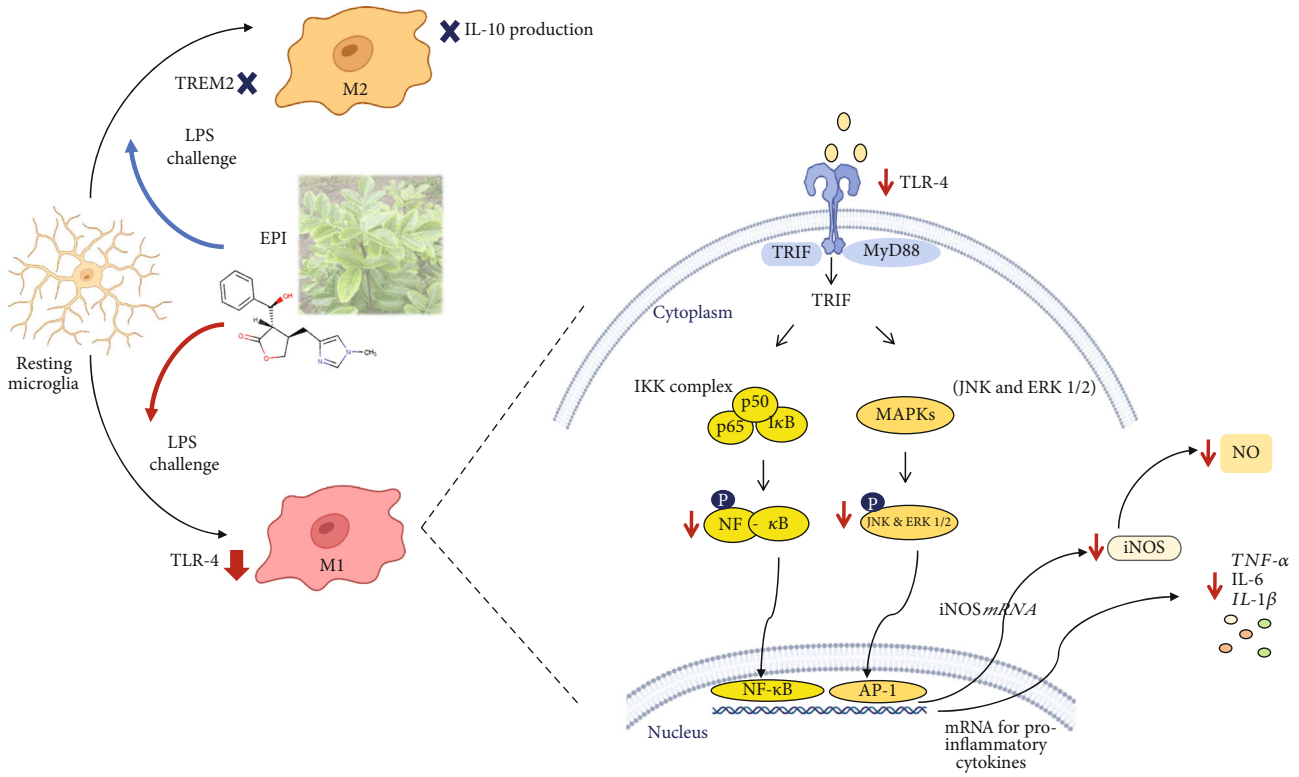

FIGURE 8: Anti-inflammatory effects mediated by the alkaloid epiisopiloturine (EPI) in microglia. EPI inhibits TLR4 expression and phosphorylation of NF-κB p65 and MAPKs (JNK and ERK1/2) induced by LPS.

nucleus in human neutrophils stimulated by fMLP. In addition, we show for the first time that the anti-inflammatory action of EPI is also dependent on its inhibitory effects on MAPK activation, particularly ERK 1/2 and JNK. The ERK and JNK signaling pathways control several cell functions, and JNK also acts in activating transcription factors, including AP-1, and activating transcription factor 2 (ATF-2) [57]. Studies have shown a key role of ERK 1/2 and JNK in a variety of physiological and pathological processes in CNS. Inhibitors of ERK and JNK have been studied as a pharmacological tool for the treatment of AD [58]. Thus, the regulation of these kinases by EPI makes it a promising drug for the treatment of AD.

Taken together, our results indicate that EPI reduces neuroinflammatory response in two different manners: (1) reducing TLR4 expression and (2) interfering with downstream kinases (ERK 1/2 and JNK) and NF-κB pathways (see Figure 8).

No other previous study had proposed this molecular mechanism of action for this alkaloid. Although several studies in the literature already highlight the ability of other alkaloids to inhibit similar intracellular signaling pathways in BV-2 cells, such as protopine obtained from *Corydalis yanhusuo* [59] and isotalatizidine from the species *Aconitum carmichaelii* Debx [60], both present in Chinese medicine.

TREM2 is a microglia-specific receptor for the M2-activation phenotype. The downregulation of this receptor contributes to the TLR4-mediated MAPK signaling pathway and increases Aβ protein accumulation and neuroinflammation in rodents [61–66]. Interestingly, EPI was not able to reverse the inhibition of TREM2 expression induced by LPS activation in BV-2 cells. These data suggest that EPI regulates the inflammatory response in microglial cells acting on TLR4, not affecting the expression of TREM2 (see Figure 8).

Under inflammatory conditions, activated microglia secrete various chemokines, resulting in leukocyte migration, e.g., neutrophils, which migrate from postcapillary venules to the brain, by crossing the blood-brain barrier. Activated neutrophils release various chemical mediators including cytokines, proteases, ROS, and RNS [67, 68]. Thus, the ability of EPI to regulate the proinflammatory mechanisms in microglial and human neutrophils as determined previously by our laboratory [20] makes EPI a potential therapeutic tool for the treatment of neuroinflammatory diseases by regulating central and peripheral innate immunity.

5. Conclusion

The present study demonstrates for the first time the anti-inflammatory activity of imidazole alkaloid epiisopiloturine (EPI) from *P. mycrophyllus* by inhibiting the LPS-induced inflammatory response in microglial cells. Mechanisms underlying these effects are associated with inhibition of TLR4 expression and signal transduction, interfering with downstream kinases (ERK1/2 and JNK), as well as NF-κB pathway with consequent reduction of inflammatory mediators production (NO, IL-1 β, IL-6, TNF-α). Moreover, no effects were observed on TREM2 expression and IL-10 production.

Abbreviations

AD: Alzheimer's disease
AP-1: Activator protein-1
BSA: Bovine serum albumin
CNS: Central nervous system
DMSO: Dimethyl sulfoxide
DNA: Deoxyribonucleic acid
ERK: Extracellular signal-regulated kinase
eNOS: Endothelial nitric oxide synthase
EPI: Epiisopiloturine
FBS: Fetal bovine serum
FMLP: N-formyl-methionyl-leucyl-phenylalanine
IFN-γ: Interferon-gamma
IKK: IkB kinase complex
IL: Interleukin
iNOS: Inducible nitric oxide synthase
JNK: c-Jun N-terminal kinase
LDH: Lactate dehydrogenase
LPS: Lipopolysaccharide
MAPKs: Mitogen-activated protein kinases
MTT: 3-(4,5-Dimethylthiazol-2-yl)-2,5-diphenyltetrazolium bromide
NADH: Nicotinamide adenine dinucleotide
NEED: N-(1-Naphthyl)ethylenediamine dihydrochloride
NF-κB: Nuclear factor-kappa B
NO: Nitric oxide
ND: Neurodegenerative diseases
nNOS: Neuronal nitric oxide synthase
PAMPs: Pathogen-associated molecular patterns
PBS: Phosphate-buffered saline
PRRs: Pattern recognition receptors
RIPA: Radioimmunoprecipitation assay buffer
PMA: Phorbol 12-myristate-13-acetate
PNS: Peripheral nervous system
RNS: Reactive nitrogen species
ROS: Reactive oxygen species
SDS: Sodium dodecyl sulfate
TLR4: Toll-like receptor 4
TNF-α: Tumor necrosis factor-alpha
TGF-β: Transformative growth factor β
TNBS: Trinitrobenzene sulfonic acid
TREM2: Receptor expressed on myeloid cells 2.

Data Availability

The experimental data used to support the findings of this study are included within the article.

Conflicts of Interest

The authors declare that they have no conflict of interest.

Acknowledgments

This work was supported by the Brazilian National Research Council (CNPq) for research fellowships (316948/2021-7) and by the Coordination for the Improvement of Higher Education Personnel (CAPES), the Research Foundation of the State of Ceara (FUNCAP). The authors are grateful to Anidro do Brasil Extraçoes SA and Phytobios Research Development Innovation LTDA for the harvest of *Pilocarpus microphyllus* and for the support in the extraction, purification, and isolation of epiisopiloturine.

References

[1] H. S. Kwon and S. H. Kon, "Neuroinflammation in neurodegenerative disorders: the roles of microglia and astrocytes," *Translational Neurodegeneration*, vol. 9, no. 42, 2020.

[2] F. A. Scorza, A. C. do Carmo, A. C. Fiorini et al., "Sudden unexpected death in Parkinson's disease (SUDPAR): a review of publications since the decade of the brain," *Clinics*, vol. 72, no. 11, pp. 649–651, 2017.

[3] B. Pinter, A. Diem-Zangerl, G. K. Wenning et al., "Mortality in Parkinson's disease: a 38-year follow-up study," *Movement Disorders*, vol. 30, no. 2, pp. 266–269, 2015.

[4] N. H. Ibrahim, M. F. Yahaya, W. Mohamed, S. L. Teoh, C. K. Hui, and J. Kumar, "Pharmacotherapy of Alzheimer's disease: seeking clarity in a time of uncertainty," *Frontiers in Pharmacology*, vol. 24, no. 11, p. 261, 2020.

[5] Q. Li and B. Barres, "Microglia and macrophages in brain homeostasis and disease," *Nature Reviews Immunology*, vol. 18, no. 4, pp. 225–242, 2018.

[6] S. Bachiller, I. Jiménez-Ferrer, A. Paulus et al., "Microglia in neurological diseases: a road map to brain-disease dependent-inflammatory response," *Frontiers in Cellular Neuroscience*, vol. 12, pp. 1–17, 2018.

[7] T. Zhou, Z. Huang, X. Sun et al., "Microglia polarization with M1/M2 phenotype changes in rd1 mouse model of retinal degeneration," *Frontiers in Neuroanatomy*, vol. 11, pp. 1–11, 2017.

[8] K. Takahashi, C. D. P. Rochford, and H. Neumann, "Clearance of apoptotic neurons without inflammation by microglial triggering receptor expressed on myeloid cells-2," *Journal of Experimental Medicine*, vol. 201, no. 4, pp. 647–657, 2005.

[9] R. H. Shin, C. Y. Wang, and C. M. Yang, "NF-kappaB signaling pathways in neurological inflammation: a mini review," *Frontiers in Molecular Neuroscience*, vol. 8, pp. 1–8, 2015.

[10] Y. C. Lu, W. C. Yeh, and P. S. Ohashi, "LPS/TLR4 signal transduction pathway," *Cytokine*, vol. 42, no. 2, pp. 145–151, 2008.

[11] O. Takeuchi and S. Akira, "Pattern recognition receptors and inflammation," *Cell*, vol. 140, no. 6, pp. 805–820, 2010.

[12] M. L. Block, L. Zecca, and J. S. Hong, "Microglia-mediated neurotoxicity: uncovering the molecular mechanisms," *Nature Reviews Neuroscience*, vol. 8, no. 1, pp. 57–69, 2007.

[13] T. Kawai and S. Akira, "Toll-like receptors and their crosstalk with other innate receptors in infection and immunity," *Immunity*, vol. 34, no. 5, pp. 637–650, 2011.

[14] X. Feng, C. Y. Wu, F. H. Burton, H. H. Loh, and L. N. Wei, "β -arrestin protects neurons by mediating endogenous opioid arrest of inflammatory microglia," *Cell Death and Differentiation*, vol. 21, no. 3, pp. 397–406, 2014.

[15] T. Goldmann, P. Wieghofer, P. F. Müller et al., "A new type of microglia gene targeting shows TAK1 to be pivotal in CNS autoimmune inflammation," *Nature Neuroscience*, vol. 16, no. 11, pp. 1618–1626, 2013.

[16] J. Zhang, Y. Zheng, Y. Luo, Y. Du, X. Zhang, and J. Fu, "Curcumin inhibits LPS-induced neuroinflammation by promoting microglial M2 polarization via TREM2/ TLR4/ NF-κB

pathways in BV2 cells," *Immunology*, vol. 116, no. 116, pp. 29–37, 2019.

[17] G. R. Leitner, T. J. Wenzel, N. Marshall, E. J. Gates, and A. Klegeris, "Targeting Toll-like receptor 4 to modulate neuroinflammation in central nervous system disorders," *Expert Opinion on Therapeutic Targets*, vol. 23, no. 10, pp. 865–882, 2019.

[18] Y. J. Feng and Y. Y. Li, "The role of p38 mitogen-activated protein kinase in the pathogenesis of inflammatory bowel disease," *Journal of Digestive Diseases*, vol. 12, no. 5, pp. 327–332, 2011.

[19] S. Li, X. Liu, X. Chen, and L. Bi, "Research progress on anti-inflammatory effects and mechanisms of alkaloids from Chinese medical herbs," *Evid Based Complement Alternat Medicine*, vol. 2020, article 1303524, pp. 1–10, 2020.

[20] T. M. Rocha, N. J. Machado, J. A. C. de Sousa et al., "Imidazole alkaloids inhibit the pro-inflammatory mechanisms of human neutrophil and exhibit anti-inflammatory properties in vivo," *Journal of Pharmacy and Pharmacology*, vol. 71, no. 5, pp. 849–859, 2019.

[21] T. M. Rocha, *Formulação farmacêutica à base de epiisopiloturina, alcaloide de Pilocarpus microphyllus, reduz a hipernocicepção inflamatória: papel da via NO/GMPc/PKG/K+ATP e modulação da resposta 26mmune*, 2021. 19 f. Tese (Doutorado em Farmacologia) – Faculdade de Medicina, Universidade Federal do Ceará, Fortaleza, 2021.

[22] G. Silva, R. O. Silva, S. R. B. Damasceno et al., "Anti-inflammatory and antinociceptive activity of epiisopiloturine, an imidazole alkaloid isolated from Pilocarpus microphyllus," *Journal of Natural Products*, vol. 76, no. 6, pp. 1071–1077, 2013.

[23] L. A. D. Nicolau, N. S. Carvalho, D. M. Pacífico et al., "Epiisopiloturine hydrochloride, an imidazole alkaloid isolated from *Pilocarpus microphyllus* leaves, protects against naproxen-induced gastrointestinal damage in rats," *Biomedicine and Pharmacotherapy*, vol. 87, pp. 188–195, 2017.

[24] L. M. Veras, M. A. Guimaraes, Y. D. Campelo et al., "Activity of epiisopiloturine against Schistosoma mansoni," *Medicinal Chemistry*, vol. 19, no. 13, pp. 2051–2058, 2012.

[25] T. Mosmann, "Rapid colorimetric assay for cellular growth and survival: application to proliferation and cytotoxicity assays," *Journal of Immunological Methods*, vol. 65, no. 1-2, pp. 55–63, 1983.

[26] L. C. Green, D. A. Wagner, J. Glogowski, P. L. Skipper, J. S. Wishnok, and S. R. Tannenbaum, "Analysis of nitrate, nitrite, and [^{15}N]nitrate in biological fluids," *Analytical Biochemistry*, vol. 126, no. 1, pp. 131–138, 1982.

[27] M. Matsuda, Y. Huh, and R. R. Ji, "Roles of inflammation, neurogenic inflammation, and neuroinflammation in pain," *Journal of Anesthesia*, vol. 33, no. 1, pp. 131–139, 2019.

[28] R. R. Ji, T. Berta, and M. Nedergaard, "Glia and pain: is chronic pain a gliopathy?," *Pain*, vol. 154, Supplement 1, pp. S10–S28, 2013.

[29] O. Fatoba, T. Itokazu, and T. Yamashita, "Microglia as therapeutic target in central nervous system disorders," *Journal of Pharmacological Sciences*, vol. 144, no. 3, pp. 102–118, 2020.

[30] P. M. Liy, N. N. A. Puzi, S. Jose, and S. Vidyadaran, "Nitric oxide modulation in neuroinflammation and the role of mesenchymal stem cells," *Experimental Biology and Medicine*, vol. 246, no. 22, pp. 2399–2406, 2021.

[31] J. E. Yuste, E. Tarragon, C. M. Campuzano, and F. Ros-Bernal, "Implications of glial nitric oxide in neurodegenerative diseases," *Frontiers in Cellular Neuroscience*, vol. 9, pp. 1–13, 2015.

[32] W. K. Alderton, C. E. Cooper, and R. G. Knowles, "Nitric oxide synthases: structure, function and inhibition," *Biochemical Journal*, vol. 357, no. 3, pp. 593–615, 2001.

[33] A. Bal-Prince and G. C. Brown, "Inflammatory neurodegeneration mediated by nitric oxide from activated glia-inhibiting neuronal respiration, causing glutamate release and excitotoxicity," *Journal of Neuroscience*, vol. 21, no. 17, pp. 6480–6491, 2001.

[34] V. Calabrese, C. Mancuso, M. Calvani, E. Rizzarelli, D. A. Butterfield, and A. M. Giuffrida Stella, "Nitric oxide in the central nervous system: neuroprotection versus neurotoxicity," *Nature Reviews Neuroscience*, vol. 8, no. 10, pp. 766–775, 2007.

[35] P. E. Chabrier, C. Demerlé-Pallardy, and M. Auguet, "Nitric oxide synthases: targets for therapeutic strategies in neurological diseases," *Cellular and Molecular Life Sciences*, vol. 55, no. 9, pp. 1029–1035, 1999.

[36] S. Lipton, "Pathologically-activated therapeutics for neuroprotection: mechanism of NMDA receptor block by memantine and S-nitrosylation," *Current Drug Targets*, vol. 8, no. 5, pp. 621–632, 2007.

[37] J. S. Pacher, L. Beckman, and L. Liaudet, "Nitric oxide and peroxynitrite in health and disease," *Physiological Reviews*, vol. 87, no. 1, pp. 315–424, 2007.

[38] L. R. de Carvalho, T. V. de Brito, J. S. D. C. Júnior et al., "Epiisopiloturine, an imidazole alkaloid, reverses inflammation and lipid peroxidation parameters in the Crohn disease model induced by trinitrobenzenosulfonic acid in Wistar rats," *Biomedicine and Pharmacotherapy*, vol. 102, pp. 278–285, 2018.

[39] L. Muzio, A. Viotti, and G. Martino, "Microglia in neuroinflammation and neurodegeneration: from understanding to therapy," *Frontiers in Neuroscience*, vol. 15, 2021.

[40] R. Franco and D. Fernández-Suarez, "Alternatively activated microglia and macrophages in the central nervous system," *Progress in Neurobiology*, vol. 131, pp. 65–86, 2015.

[41] H. K. Lee and A. Iwasaki, "Innate control of adaptive immunity: dendritic cells and beyond," *Seminars in Immunology*, vol. 19, no. 1, pp. 48–55, 2007.

[42] Y. Zhou, Y. Chen, C. Xu, H. Zhang, and C. Lin, "TLR4 targeting as a promising therapeutic strategy for Alzheimer disease treatment," *Frontiers in Neuroscience*, vol. 14, article 602508, 2020.

[43] S. Azam, M. Jakaria, I. S. Kim, J. Kim, M. E. Haque, and D. K. Choi, "Regulation of Toll-like receptor (TLR) signaling pathway by polyphenols in the treatment of age-linked neurodegenerative diseases: focus on TLR4 signaling," *Frontiers in Immunology*, vol. 10, no. 5, 2019.

[44] M. M. Buchanan, M. Hutchinson, L. R. Watkins, and H. Yin, "Toll-like receptor 4 in CNS pathologies," *Journal of Neurochemistry*, vol. 114, no. 1, pp. 13–27, 2010.

[45] Y. Li, Y. Xia, S. Yin et al., "Targeting microglial α-synuclein/TLRs/NF-kappaB/NLRP3 inflammasome axis in Parkinson's disease," *Frontiers in Immunology*, vol. 12, pp. 1–16, 2021.

[46] W. Teng, L. Wang, W. Xue, and C. Guan, "Activation of TLR4-mediated NF ? B signaling in hemorrhagic brain in rats," *Mediators of Inflammation*, vol. 2009, Article ID 473276, 6 pages, 2009.

[47] M. L. Zhou, W. Wu, Y. S. Ding et al., "Expression of Toll-like receptor 4 in the basilar artery after experimental subarachnoid hemorrhage in rabbits: a preliminary study," *Brain Research*, vol. 1173, no. 1, pp. 110–116, 2007.

[48] T. Liu, L. Zhang, D. Joo, and S. C. Sun, "NF-κB signaling in inflammation," *Signal Transduction and Targeted Therapy*, vol. 2, no. 1, 2017.

[49] B. C. Albensi, "What is nuclear factor kappa B (NF-κB) doing in and to the mitochondrion?," *Frontiers in Cell and Developmental Biology*, vol. 7, no. 6, pp. 1–7, 2019.

[50] M. G. Dorrington and I. D. C. Fraser, "NF-κB signaling in macrophages: dynamics, crosstalk, and signal integration," *Frontiers in Immunology*, vol. 10, no. 4, 2019.

[51] U. Moens, S. Kostenko, and B. Sveinbjørnsson, "The role of mitogen-activated protein kinase-activated protein kinases (MAPKAPKs) in inflammation," *Genes*, vol. 4, no. 2, pp. 101–133, 2013.

[52] T. Jayakumar, K. C. Lin, C. C. Chang et al., "Targeting MAP2rc/FAK-mediated macrophage migration," *International Journal of Molecular Sciences*, vol. 23, no. 1, p. 92, 2021.

[53] J. Cui, M. Zhang, Y. Q. Zhang, and Z. H. Xu, "JNK pathway: diseases and therapeutic potential," *Acta Pharmacologica Sinica*, vol. 28, no. 5, pp. 601–608, 2007.

[54] J. Sun J and G. Nan, "The extracellular signal-regulated kinase ½ pathway in neurological diseases: a potential therapeutic target (review)," *International Journal Of Molecular Medicine*, vol. 39, no. 6, pp. 1338–1346, 2017.

[55] E. K. Kim and E. J. Choi, "Pathological roles of MAPK signaling pathways in human diseases," *Biochimica et Biophysica Acta–Molecular Basis of Disease*, vol. 1802, no. 4, pp. 396–405, 2010.

[56] S. C. Sun and L. S. C. Ley, "New insights into NF-kappaB regulation and function," *Trends in Immunology*, vol. 29, no. 10, pp. 469–478, 2008.

[57] R. J. Davis, "Signal transduction by the JNK group of MAP kinases," *Cell*, vol. 103, no. 2, pp. 239–252, 2000.

[58] M. A. Bogoyevitch, I. Boehm, A. Oakley, A. J. Ketterman, and R. K. Barr, "Targeting the JNK MAPK cascade for inhibition: basic science and therapeutic potential," *Biochimica et Biophysica Acta*, vol. 1697, no. 1-2, pp. 89–101, 2004.

[59] M. B. Alam, M. K. Ju, Y. G. Kwon, and S. H. Lee, "Protopine attenuates inflammation stimulated by carrageenan and LPS via the MAPK/NF-κB pathway," *Food and Chemical Toxicology*, vol. 131, article 110583, 2019.

[60] S. Shao, H. Xia, M. Hu et al., "Isotalatizidine, a C19-diterpenoid alkaloid, attenuates chronic neuropathic pain through stimulating ERK/CREB signaling pathway-mediated microglial dynorphin a expression," *Journal of Neuroinflammation*, vol. 17, no. 1, pp. 1–11, 2020.

[61] J. B. Ruganzu, X. Peng, Y. He et al., "Downregulation of TREM2 expression exacerbates neuroinflammatory responses through TLR4-mediated MAPK signaling pathway in a transgenic mouse model of Alzheimer's disease," *Molecular Immunology*, vol. 142, pp. 22–36, 2021.

[62] W. Liu, O. Taso, R. Wang et al., "Trem2 promotes anti-inflammatory responses in microglia and is suppressed under pro-inflammatory conditions," *Human Molecular Genetics*, vol. 29, no. 19, pp. 3224–3248, 2020.

[63] R. Owens, K. Grabert, C. L. Davies et al., "Divergent neuroinflammatory regulation of microglial TREM expression and involvement of NF-κB," *Frontiers in Cellular Neuroscience*, vol. 11, pp. 1–14, 2017.

[64] C. D. Schmid, L. N. Sautkulis, P. E. Danielson et al., "Heterogeneous expression of the triggering receptor expressed on myeloid cells-2 on adult murine microglia," *Journal of Neurochemistry*, vol. 83, no. 6, pp. 1309–1320, 2002.

[65] I. R. Turnbull, S. Gilfillan, M. Cella et al., "Cutting edge: TREM-2 attenuates macrophage activation," *The Journal of Immunology*, vol. 177, no. 6, pp. 3520–3524, 2006.

[66] J. Zhou, W. Yu, M. Zhang, X. Tian, Y. Li, and Y. Lü, "Imbalance of microglial TLR4/TREM2 in LPS-treated APP/PS1 transgenic mice: a potential link between Alzheimer's disease and systemic inflammation," *Neurochemical Research*, vol. 44, no. 5, pp. 1138–1151, 2019.

[67] M. Kovács, T. Németh, Z. Jakus et al., "The Src family kinases Hck, Fgr, and Lyn are critical for the generation of the in vivo inflammatory environment without a direct role in leukocyte recruitment," *Journal of Experimental Medicine*, vol. 211, no. 10, pp. 1993–2011, 2014.

[68] C. Tecchio and M. A. Cassatella, "Neutrophil-derived chemokines on the road to immunity," *Seminars in Immunology*, vol. 28, no. 2, pp. 119–128, 2016.

Hindawi
Oxidative Medicine and Cellular Longevity
Volume 2022, Article ID 7836828, 13 pages
https://doi.org/10.1155/2022/7836828

Review Article

Role of Oxidative Stress in Retinal Disease and the Early Intervention Strategies: A Review

Jun Wang[1,2] **Mengling Li**[3] **Ziyue Geng**[4] **Saadullah Khattak**[2] **Xinying Ji**[2] **Dongdong Wu**[2] **and Yalong Dang**[2,5]

[1]*School of Basic Medical Sciences, Henan University, Kaifeng, China*
[2]*Henan International Joint Laboratory for Nuclear Protein Regulation, Henan University, Kaifeng, China*
[3]*College of Acu-Moxibustion and Massage, Shaanxi University of Chinese Medicine, Xianyang, China*
[4]*School of Clinical Medicine, Henan University, Kaifeng, Henan, China*
[5]*Sanmenxia Central Hospital, Sanmenxia, Henan, China*

Correspondence should be addressed to Jun Wang; whb21c@vip.henu.edu.cn, Dongdong Wu; ddwubiomed2010@163.com, and Yalong Dang; dangyalong@haust.edu.cn

Received 11 January 2022; Revised 5 August 2022; Accepted 11 August 2022; Published 14 October 2022

Academic Editor: Francisco Rios

The retina, owing to its cellular anatomy and physical location, is susceptible to generating reactive oxygen species (ROS), which are associated with several major retinal diseases. When ROS exceeds the body's natural antioxidants, the retina is in a state of oxidative stress, which is recognized as the pathogenesis of retinal diseases. The early stage of the pathogenic process is an adaptive change in which oxidative stress and endogenous defense mechanisms occur. If no treatment is applied, the retinal diseases will progress to the pathological stage with neuronal and vascular dysfunction or damage and even blindness. This review summarizes the role of oxidative stress in several common retinal diseases, including retinitis pigmentosa, age-related macular degeneration, diabetic retinopathy, glaucoma, and retinopathy of prematurity. In addition, we discuss the early intervention strategies for these diseases. An outline is provided to identify potential intervention targets for further research. Early intervention for retinal diseases is necessary and urgent and may offer hope to improve patients' quality of life through functional vision.

1. Introduction

The retina is an extension of the brain and is a highly oxygen-consuming organ in the body, relying more on aerobic glycolysis than the brain; it is also highly sensitive to various stimuli [1]. Furthermore, the retina is extremely metabolically active and rich in polyunsaturated fatty acids, which are vulnerable to lipid peroxidation [2]. Under normal conditions, reactive oxygen species (ROS) in the retina are related to physiological signaling and protective mechanisms via the prosurvival extracellular signal-related kinase 1/2 pathway and endoplasmic reticulum stress signaling. ROS production-induced oxidative stress may contribute to the pathogenesis of several retinal degenerative diseases, including diabetic retinopathy (DR), retinal vascular occlusion, retinitis pigmentosa (RP), age-related macular degeneration (AMD), glaucoma, and retinopathy of prematurity (ROP).

The number of people with retinal diseases, including AMD, DR, and glaucoma, is expected to more than double by 2050 [3]. This prediction indicates that there will be a healthcare crisis that not only affects patients with visual disturbance but also the caregivers and entire healthcare system. Thus, there is an urgent need to focus on the prevention of and protection against retinal diseases. This review includes the necessary recommendations and neuroprotective strategies for preventing the progression of vision loss and blindness in individuals with retinal diseases.

In living cells, oxidation-reduction reactions may generate metabolic byproducts—free radicals, which are ROS and

reactive nitrogen species (RNS) [4]. Free radicals are a class of molecules containing one or more unpaired electrons. ROS can be generated via multiple pathways, including endogenous and exogenous substances [4]. ROS are highly active and may react with biomolecules, e.g., proteins, lipid membranes, and DNA, leading to cell damage or functional impairment. Oxidative stress is a condition of oxidation-reduction imbalance characterized by elevated levels of ROS and free radicals or a reduction of antioxidants [5, 6]. Under physiological conditions, the generation of ROS and the scavenging of free radicals may reach a dynamic redox balance. When various excess stimuli (endogenous and/or exogenous) occur, ROS accumulate massively. This may lead to oxidative stress in the corresponding cells and organs [7]. Continuous oxidative stress may ultimately damage cells in target organs. Therefore, the inhibition of ROS generation and scavenging of excessive ROS by various pathways have been used as therapeutic strategies for the treatment of eye diseases. In this review, we will introduce the mechanisms of ROS generation in several retinal diseases, summarize the pathogenetic roles of oxidative stress in their development, and discuss the early intervention pathway of antioxidative stress.

2. Physiological Role of Free Radicals and ROS in Organisms

The free radicals in the human body can be divided into oxygen and nonoxygen radicals. Free oxygen radicals are the predominant category derived from molecular oxygen, and their proportion of oxygen radicals is approximately 95% of the total radicals. Oxygen radicals include hydrogen peroxide (H_2O_2), hydroxyl radicals, superoxide anions ($O2^{-}\cdot$), nitroxides, and peroxynitrite, which are defined as ROS and RNS. ROS/RNS can be produced by the metabolism of normal cells and exogenous stimuli, e.g., chemical drugs, high-pressure oxygen, radiation, mental stress, insomnia, smoking, and pollution [8] Free radicals are highly reactive and short-lived intermediates that have one or more unpaired electrons and exist independently on their own [9, 10]. Under normal conditions, free radicals are important for maintaining homeostasis and defending the body against hazardous invasion [11] by (1) enhancing phagocytosis of leukocytes, (2) promoting synthesis of prostaglandin and lipoxygenases, and (3) relaxing vascular smooth muscle and modulating blood pressure. Endogenous ROS are derived from the mitochondria by escaping electrons to molecular oxygen [12]. The generation sources include NADPH oxidases (Nox), xanthine oxidase, and lipoxygenase on the membranes of endothelial cells and phagocytes [2]. In most cases, the terms "free radicals" and "ROS" are regarded as interchangeable [12]. Healthy organisms always generate low levels of free radicals, and antioxidant defense systems may scavenge them rapidly before they cause oxidative damage to the cell. If the dynamic redox balance is imperfect, ROS/RNS-mediated damage may occur continuously. In other words, oxidative stress injury is generated when the speed of free radical production exceeds the capacity of the cellular defense system, for example, exposure to high oxygen pressure or ionizing radiation [8]. Oxidative stress damages biological macromolecules, e.g., nucleic acids, proteins, and lipids by peroxidation, degeneration, crosslinking, and breakage. Finally, oxidative stress can cause injuries to cell structures and functions, as well as to the tissues and organs in the body [11]. Thus far, increasingly more diseases/disorders are recognized gradually by linking them directly or indirectly with oxidative stress [8]. Some of these disorders are due to free radicals, whereas others may be only secondarily involved. Tissue injured by various processes, such as trauma, toxic substances, and infections, may undergo free radical damage more rapidly than healthy tissues. Tissue destruction and degeneration may increase oxidative damage through processes including metal ion release, phagocyte activation, and disruption of mitochondrial electron transport chains. Iron chelation, superoxide dismutase, catalase, vitamins (C and E), and antioxidants (flavonoids) could have protective effects under various experimental conditions, which further indicate the key role of free radicals in many disorders [13–16]. Additionally, an increasing number of small-molecule drugs have been developed and implemented to target ROS [17].

3. Oxidative Stress and Retinal Pathology

Oxidative stress plays a prominent role in the pathogenesis of many degenerative retinal diseases, such as AMD, DR, and RP. Normal, healthy retinal cells are susceptible to significant light exposure, which may lead to the generation of abundant ROS [18]. However, under pathological conditions, the normal homeostatic mechanisms are destroyed. When the relationship of prooxidative stress and antioxidative stress signaling is unbalanced, it may lead to excessive oxidative stress, inflammatory responses, blood-retinal barrier injury, and retinal tissue damage [18, 19]. Retinal diseases, including photoreceptor degeneration, diabetic retinopathy, and retinal ganglion cell injury, always involve the same process of oxidative stress and apoptosis in the final pathological stages. This review will provide a summary of the effects of oxidative stress in several congenital retinal diseases and possible early intervention strategies.

3.1. Oxidative Stress in RP. RP is an inherited retinal disease caused by different genetic mutations. The pathological process leads to photoreceptor cell degeneration (successive rod and cone cell loss) and eventually results in retinal pigmented epithelium (RPE) dysfunction [2]. The prevalence rate is 1 in 4000 persons worldwide, and there are >1.5 million patients with RP worldwide [20]. The early phenotype of RP is difficult to observe at night, and loss of peripheral vision is caused by apoptosis of rod photoreceptors. Then, vision loss becomes more restricted to the central visual field and is eventually lost [20]. Studies have demonstrated that progressive visual loss in RP is associated with the loss of photoreceptor cells and oxidative stress (Figure 1) [21, 22]. Clinical evidence also showed that 8-oxo-7,8-dyhydro-2′-deoxyguanosine (8-oxo-dG) and protein carbonyl contents were increased in the vitreous and aqueous humor of patients with RP [23, 24]. This finding indicates that

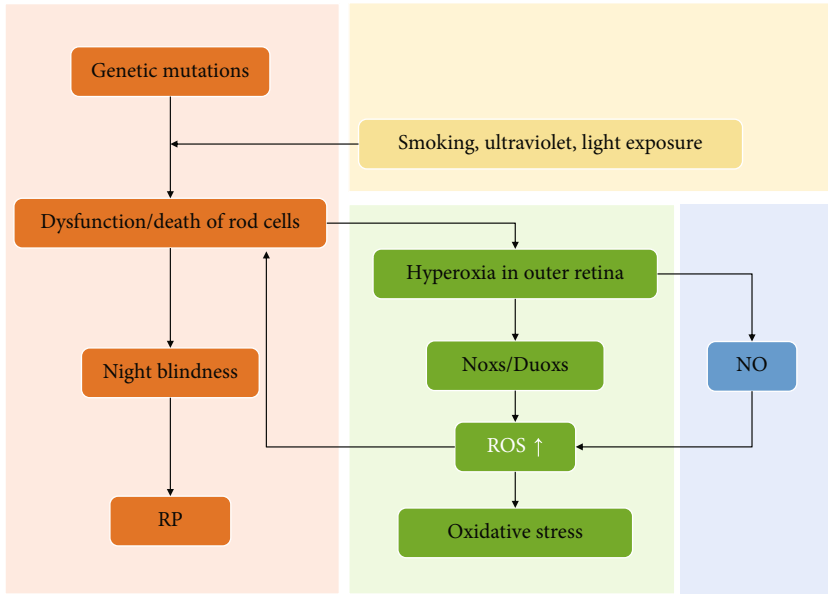

Figure 1: Oxidative stress is involved in the rod cell death-induced clinical feature of RP. ROS: reactive oxygen species; RP: retinitis pigmentosa.

oxidative stress exists in the ocular tissues of patients with RP. In the outer nuclear layer, rods account for 95% of the cells and are more metabolically active than cones. These cells gradually decrease in number as RP progressed [24]. Subsequently, retinal oxygen demand and usage also decrease. Retinal circulation is not regulated; therefore, the oxygen supply to the outer retina increases spontaneously [24]. Hyperoxia in the outer retina can induce Nox and dual oxidase, but not xanthine oxidase, to produce excessive amounts of ROS and contribute to tissue damage [25]. Hyperoxia in the outer retina induced by rod degeneration may activate Nox enzymes and may also activate the high levels of Nox2 in microglia, which have been demonstrated to migrate into the outer retina in RP. This leads to an increase of superoxide radicals and oxidative damage [25, 26]. High levels of nitric oxide in the outer retina are another indirect oxidative stress factor that may react with superoxide radicals to form highly reactive and damaging peroxynitrite radicals. Hence, inhibition of Nox and nitric oxide synthase (NOS) together with antioxidative stress by scavenging ROS directly should be regarded as a strategy to help maintain photoreceptor function in patients with RP.

3.1.1. RP: Intervention Strategy at an Early Stage. RP is a family of inherited diseases. Over 250 gene mutations are associated with the cause of rod death, and it is likely the major pathogenesis of RP [27, 28]. Therefore, RP is difficult to cure at the genetic level despite the development of genotype-phenotype technology that may already characterize each causal gene in RP [29]. Currently, there is no specific pharmacological or genetic treatment for RP [27]. Antioxidants have shown promise as an intervention to delay the reduction of cone cell loss and retard the progress of RP [30]. However, the clinical evidence has not been clarified. The application of antioxidant supplements, such as vitamins A and E, beta-carotene, omega-3, docosahexaenoic acid (DHA), zinc, and docosahexaenoic acid, might be able to slow the decline in peripheral field function [20, 30]. The oral antioxidant N-acetyl cysteine (NAC) for RP was studied in a phase 1 clinical trial [31]. However, its efficacy should be addressed in future studies. In addition, a study showed that smoking is detrimental to patients with RP, as it worsens macular function and structural integrity [32]. Hence, smoking may not benefit patients with RP. Furthermore, ultraviolet and blue light exposure may accelerate vision loss in RP [33, 34]. Wearing protective goggles is a simple and effective method to prevent light damage. Regular to moderate physical activity, not endurance exercise without adaptable physical training, may protect against ROS/RNS damage in eye diseases, including RP [35]. Intraocular pressure may affect the circulation of the outer retinal layer. It is possible that an obvious reduction in choroidal blood flow through the elevation of intraocular pressure may prevent sufficient oxygen supply from the choroid [36]. Therefore, it is reasonable to assume that appropriate eyeball massage may be a preconditioning intervention to the retinal outer layer to improve endogenous antioxidative stress during the early stage of RP. Finally, prevention of consanguinity and reinforcement of genetic counseling before birth is very important in reducing the risk of RP. Antioxidant gene modification may be a potential treatment for late stages of RP in the future; although, transgenic overexpression is not applicable to humans.

3.2. Oxidative Stress in AMD. AMD is a chronic, irreversible disease that primarily affects central vision and is an important cause of blindness worldwide. Accumulations of lipid and protein between the RPE and Bruch's membrane (BrM); loss of photoreceptors, RPE, and retinal neurons; and neovascularization are the main pathological processes.

Multiple risk factors have been reported for AMD including age, light exposure, smoking, obesity, hypertension, poor antioxidant intake, and a hereditary component [37, 38]. Many studies have demonstrated that oxidative stress is involved in the pathogenesis of AMD [39–42]. The levels of oxidative stress markers, including malondialdehyde, protein carbonyls, and 8-hydroxy-2-deoxyg, are increased significantly in the blood serum of patients with AMD [37, 43]. This finding indicates that systemic oxidative stress is associated with AMD. Additionally, a higher level of carboxyethylpyrrole (CEP) and damaged proteins was detected in the BrM of donor eyes with AMD [44]. CEP is formed from DHA during oxidative stress. The outer segments of photoreceptors are abundantly composed of DHA, which increases their vulnerability to oxidative damage. Under stress conditions, photoreceptors must metabolize continuously to regenerate outer segments, producing a unique source of ROS in RPE cells [45]. RPE cells are responsible for phagocytosis of photoreceptor outer segments. ROS overaccumulation may cause disorders in cell structure and function, which in turn increases ROS generation. Taken together, high oxygen metabolism, continuous light exposure, and high concentrations of polyunsaturated fatty acids make the retina prone to retinal damage. Thus, oxidative stress plays important roles in the pathophysiology of AMD (Figure 2).

3.2.1. AMD: Intervention Strategy at an Early Stage. (1) Cigarette smoking has been shown experimentally to be directly linked to the development of AMD and is a major risk factor in epidemiological studies [46, 47]. Therefore, quitting smoking as early as possible is a good strategy to prevent AMD. (2) One of the mechanisms of retinal injury in AMD is the interaction between light exposure and photosensitive molecules (rhodopsin and lipofuscin) [48, 49]. Excessive activation of rhodopsin and light conduction can cause the formation of ROS from the DHA content of the outer segment membranes of the rod and induce photoreceptor cell degeneration [49]. It has been suggested that shorter wavelengths have a higher risk of retinal injury than longer wavelengths [50]. Avoiding exposure to blue light may prevent the increased formation of ROS by photosensitive molecules [51]. (3) Experimental studies have shown that an antioxidation-deficient diet is associated with lipofuscin accumulation and photoreceptor degeneration in the RPE [52]. Increased antioxidants in the diet (vitamins A, C, and E and carotenoids) or serum could protect against AMD progression [49]. A longitudinal clinical study also indicated that the consumption of antioxidants/zinc could decrease the risk of early AMD in a highly susceptible group [53]. Moreover, the topical antioxidant OT-551 (0.45%), investigated in a single-center phase II trial, may improve best-corrected visual acuity [54]. Age-related eye disease studies, antivascular endothelial growth factor (VEGF) injections, and laser therapy are also useful for controlling the progression of wet AMD [55, 56]

3.3. Oxidative Stress in DR. DR, a progressive microvasculature complication of diabetes, is one of the most common causes of blindness in adults of working ages [57, 58]. Approximately 90% of diabetic patients develop DR complications within 25 years of diagnosis [59]. Oxidative stress and inflammation are considered to play key roles in the pathogenesis of DR because the retina has high vascularization and long-term light exposure [60]. Chronic hyperglycemia exposure, resulting in increased ROS production, makes microvessels more vulnerable to oxidative stress. The disturbance of redox homeostasis contributes to the death of neurons in the retina, followed by the rupture of the blood-retinal barrier and increased vascular permeability, leading to advanced DR. In retinal cells under oxidative stress conditions, excessive ROS directly acts on protein and DNA or indirectly acts as a second messenger to affect the pathogenesis of DR (Figure 3) [58, 61, 62]. As the main source of intracellular ROS, mitochondria are abundant in photoreceptors, which are the major O2- contributor in DR [63]. Studies have shown that mitochondrial dysfunction in turn affects the production of ROS in retinal cells, activity of optic nerve cells, and function of photoreceptors. ROS accumulation causes further deterioration [64]. Besides, mitochondrial dysfunction may reduce mitochondrial energy production, leading to optic nerve degeneration [65, 66]. Additionally, the accumulation of byproducts caused by metabolic abnormalities induced by hyperglycemia, e.g., the activation of protein kinase C, hexosamine, polyol flux, and advanced glycation end-products (AGEs), induces oxidative stress through ROS/RNS formation, leading to the death of retinal neurons [58, 67]. Oxygen-derived free radicals, such as hydroperoxyl species, have been shown to cause lipid peroxidation, contributing to the production of ROS to facilitate the senescence of RPE cells, leading to the progression of DR [68–70]. Therefore, oxidative stress plays an important role in DR progression.

3.3.1. DR: Intervention Strategy at an Early Stage. Current therapies for DR, such as anti-VEGF treatment, laser therapy, vitrectomy, and glucocorticoids, focus on the late stage, which may reduce visual loss by temporarily protecting retinal vessels [71, 72]. However, it is still difficult for patients with severe vision loss to reestablish normal vision. As a major factor in the progression of DR, oxidative stress is a hot target at an early stage. Nox, the main enzymatic source of ROS, has been demonstrated to be a direct risk factor for DR, and inhibitors of the Nox family have been studied to prevent the development of DR. For example, diphenyleneiodonium (a Nox inhibitor) can suppress ROS generation, alleviate blood-retinal barrier breakdown, and recover the death of retinal capillary endothelial cells [73, 74]. Nox 1/4 specific inhibitors, GKT136901 and GKT137831, have shown potent effects in DR treatment [75]. Polyphenols are antioxidants that are abundant in vegetables, fruits, beverages, whole grains, etc. Studies have demonstrated the protective effects of DR against various polyphenols, including green tea polyphenols, chlorogenic acid, curcumin, beta-glucogallin, and cocoa polyphenols [76–78]. Resveratrol, the most studied polyphenol, has been shown to activate antioxidant enzymes and inactivate NOS activity with a decrease in ROS/RNS in the blood and retina in various experimental

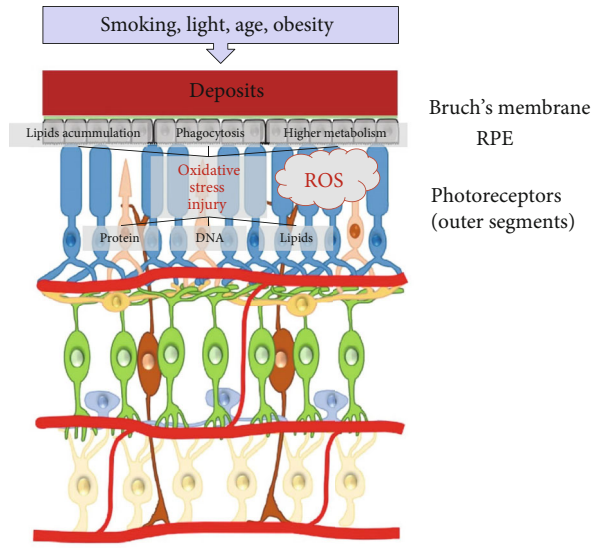

Figure 2: Oxidative stress in AMD. ROS are increased in RPE and photoreceptors since the exposure of environmental risk factors in the early stage of AMD. ROS lead to the deposits of lipid substances, phagocytosis disability, and cell injury in protein, lipids, and DNA, until cell death. AMD: age-related macular degeneration; ROS: reactive oxygen species; RPE: retinal pigmented epithelium.

models [79–81]. The ROS scavengers NAC and duloxetine are effective in the early stages of DR [82]. Nuclear factor erythroid 2-related factor 2 (NRF2) binds to antioxidant response elements to regulate antioxidant protein levels and fight against oxidative stress. Recent studies have shown that activation of the NRF2 pathway provides new insights for DR treatment. The novel NRF2 activator dh404 provides potential protection to the retina in diabetes, including vision-threatening breakdown of the blood–retinal barrier [83, 84]. Herein, the inhibition or clearance of ROS generation provides an early candidate strategy for blindness caused by DR.

3.4. Oxidative Stress in Glaucoma. Glaucoma is a progressive optic neuropathic disease characterized by retinal ganglion cell (RGCs) degeneration and synaptic loss of dendrites and axon terminals and is the most common cause of irreversible blindness worldwide [85]. It was estimated that the number of people with glaucoma will reach 111.8 million by 2040 globally because of the increase in the number of people of advanced age [86, 87]. Although intraocular pressure is the only known risk factor for glaucoma, increasing studies have shown that oxidative stress plays an important role in the pathogenesis of glaucoma [88, 89]. Increased intraocular pressure and advancing age are closely implicated in the pathogenesis of glaucoma. Oxidative stress occurs in the eyes and may explain the potential mechanism underlying the development of glaucoma [90–92]. Moreover, mitochondrial dysfunction is largely related to oxidative stress in the pathogenesis of glaucoma [93, 94]. Especially in the aging retina, oxidative stress and lipid peroxidation are the major risks to activate the inflammatory response, leading to RGC death and apoptosis, aggravating glaucoma (Figure 4) [95]. Exposure to sunlight and a high-oxygen environment causes higher oxidative stress in the eyes than in other tissues, which can further damage the eye tissue [96, 97]. The trabecular meshwork (TM) is the most sensitive tissue in the eye and is vulnerable to oxidative stress [98]. Studies have shown that increased 8-OH-dG levels are found in the TM of patients with glaucoma, indicating the occurrence of DNA oxidative stress damage [99, 100]. In addition, the accumulation of ROS, particularly H_2O_2, was also detected in TM cells, which reduced antioxidant activity and inhibited the secretion of adhesion molecules to TM cells, contributing to cytoskeleton reorganization and eventually resulting in cell loss [91, 101, 102].

3.4.1. Glaucoma: Intervention Strategy at an Early Stage. Early diagnosis and intervention are important to prevent visual loss in patients with glaucoma due to irreversible blindness [103]. Based on the increasing evidence of oxidative stress in glaucomatous tissues, the levels of biomarker candidates related to oxidative stress, e.g., protein carbonyls and AGEs, have been shown to increase significantly in the blood and aqueous humor samples of patients with glaucoma [104]. Oxidative stress is an important risk factor for ocular hypertension, which is a target of glaucoma treatment [105, 106]. Drugs with antioxidant properties, such as valproic acid and spermidine, have been reported to prevent glaucomatous retinal degeneration in glaucoma mouse models [107, 108]. The grafting of antioxidant molecules to drug carriers can also effectively reduce the intraocular pressure in glaucoma [109]. The activation and recruitment of microglia and astrocytes to the edge of the optic nerve are early characteristics of glaucoma [110–112]. Inhibition of ROS can inhibit the byproducts of electron leakage along the electron transport chain during cell respiration and improve mitochondrial dysfunction, contributing to the delay in glaucoma progression [95, 113, 114]. Additionally, data based on a large population have shown that quitting smoking and moderate-intensity aerobic exercise may reduce the risk of glaucoma [115–117]. A balanced diet,

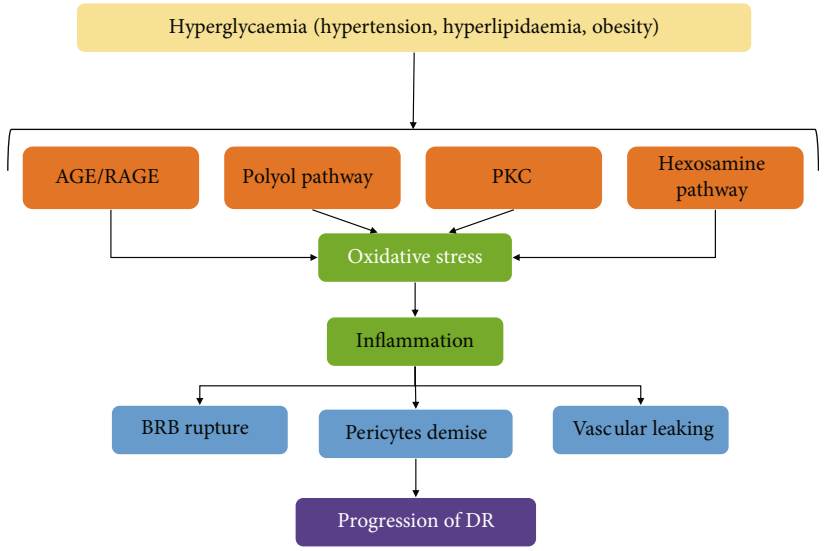

Figure 3: The driving mechanism of oxidative stress in the progression of DR. PKC: protein kinase C; AGEs: advanced glycation end-products; BRB: blood-retinal barrier; DR: diabetic retinopathy.

including vegetables, omega fatty acids, and coffee, may help prevent the occurrence or progression of glaucoma [118]. Studies showed that oxidative stress might be a potential target for the prevention and treatment of glaucoma in the early stages; although, there is no direct clinical evidence.

3.5. Oxidative Stress in ROP. ROP is a complex eye disease characterized by retinal neovascularization in low-birth-weight preterm infants (LBWs), and it is the most common cause of blindness in children [119, 120]. Oxidative stress is a physiological redox imbalance caused by excessive ROS/RNS. It plays a key role in the pathogenesis of ROP and significantly increases the mortality and morbidity of ROP in very LBWs (Figure 5) [119, 121, 122]. There are two phases of ROP: (1) abnormal retinal neovascularization motivated by hypoxia and (2) delayed growth of retinal vascularization induced by supplemental oxygen [123–125]. Clinical data showed a connection between the incidence of ROP in LBWs and unrestricted oxygen exposure, and the corresponding findings have shown that reduced oxygen saturation can decrease the incidence of ROP [126]. For newborns, oxidative stress is a challenge during the process of birth itself. The sharp postnatal transition from a lower oxygen content with an intrauterine environment into a higher oxygen content environment causes oxidative stress in infants, and most preterm infants lack antioxidant enzymes and chemical antioxidants because the increase in key antioxidant enzymes such as superoxide dismutase only occurs in late pregnancy, showing a lower antioxidant ability in premature infants [127, 128]. Retinal hyperoxia in LBWs due to the lack of autoregulation of the blood network in the retina causes an imbalance of prooxidants and antioxidants, contributing to the inflammation of retinal tissue, eventually resulting in the development of ROP [129–131]. Moreover, in ROP, damage of the outer retina occurs along with the increased ROS levels in the inner retina [131, 132].

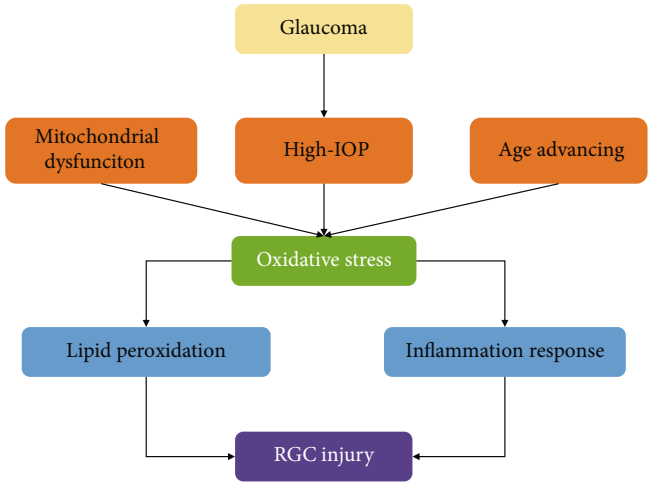

Figure 4: The role of oxidative stress in glaucoma RCG injury. IOP: intraocular pressure; RGC: retinal ganglion cell.

3.5.1. ROP: Intervention Strategy at an Early Stage. Early intervention is an efficient strategy to control the incidence of ROP, a preventable ocular disease [133]. According to the early treatment of ROP, cryotherapy and laser therapy are now effective methods to prevent ROP in preterm infants [134–136]. Strict oxygen limitation effectively reduces the incidence of ROP in LBWs. Flavonoids are a group of antioxidants present in the diet [137, 138]. For example, green tee has been demonstrated to prevent ROP through the inhibition of corneal neovascularization in animal models [139, 140]. Bilberries, a natural source of anthocyanins with high antioxidative properties, can significantly render lipid peroxidation and neovascular proliferation and protect the retinal vasculature after high oxygen therapy, contributing to the suppression of ROP progression [140, 141]. Other flavonoids, e.g., baicalin and luteolin, have also

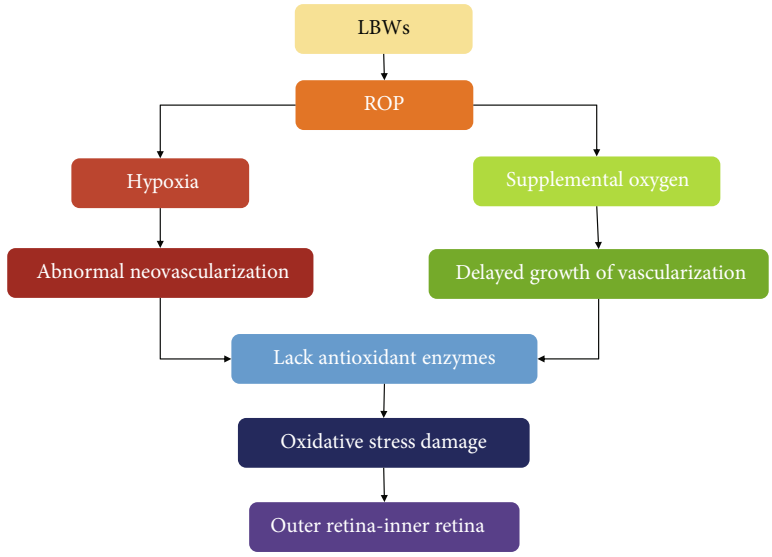

Figure 5: The increased ROS level plays a key role in the pathogenesis of ROP. LBWs: low-birth-weight infants; ROP: retinopathy of prematurity.

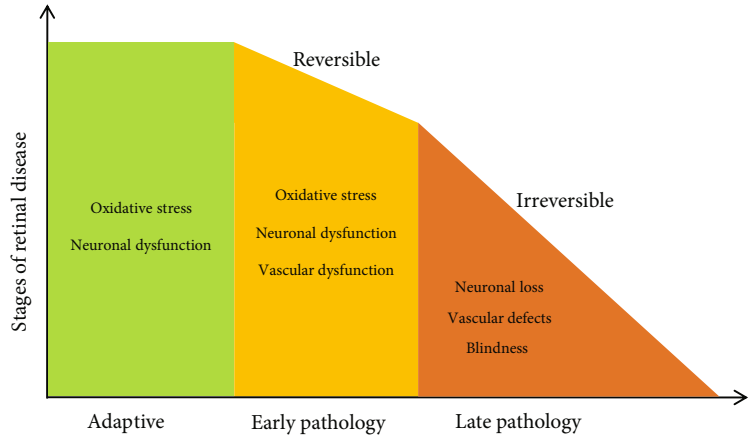

Figure 6: The progression of retinal disease in the hypothetical stages. Effective intervention during the early stage of retinal disease would be most beneficial in protection against vision loss (revised from Machelle T. Pardue, 2018, Prog Retin Eye Res).

been shown to protect against ROP because of their ability to scavenge ROS [142, 143]. Additionally, prenatal supplementation with antioxidants, such as carotenoids and vitamins (A and E), helps to promote normal fetal growth, resulting in a reduction in the birth rate of preterm infants; although, there is no clinical evidence that it can prevent ROP in LBWs [144–147]. Moreover, supplementation with essential fatty acids, e.g., ω-fatty acids, leads to a decrease in ROP development, which can be explained by the antioxidant effect of unsaturated fatty acids that reduces lipid peroxidation [148, 149]. Therefore, it would be a key early intervention strategy to reasonably expect a status with strong antioxidants at birth or provide antioxidant supplementation to reduce the risk of ROP in preterm infants.

4. Summary

An increasing number of people will be diagnosed with retinal diseases in the future. The number of people with vision loss will be 61 million, and that of those with vision impairment will be 470 million by 2050 [3]. The healthcare system will face challenges from millions of people with vision loss and their caregivers. Poor effective treatments currently exist during the advanced disease stage in the clinical setting. Hence, it is important to find ways to detect retinal diseases early and monitor disease progression and treatment efficacy because the adaptive phase and early pathology phase are reversible and are also the most effective phases in retinal diseases (Figure 6) [20].

Oxidative stress plays a critical role in the pathological processes of many types of retinal dysfunctions [150]. Anatomical features of the eye make the retina more susceptible to ROS production, especially with increasing age [151–153]. The retina, especially the photoreceptors and retinal pigment epithelium, is rich in polyunsaturated fatty acids, which are susceptible to lipid peroxidation [50, 154]. Persistent prooxidant factors and decreased antioxidant capacity with age may accelerate oxidative stress. Thus, the increase

in ROS and intracellular Ca^{2+} concentrations are common pathological changes in the retina [50]. Many studies have indicated that oxidant stress injury is the first step to induce the cell death of retinal neurons [24, 50, 155–157]. Ocular diseases share the same cellular mechanisms. In the final stages of retinal disease, there are limited effective treatments that may rescue lost vision.

Therefore, early intervention for retinal diseases is necessary and urgent, and may offer hope to improve patients' quality of life through functional vision. First, management of the source of ROS generation is a key factor in preventing the progression of retinal disease. Various factors that lead to ROS generation should be suppressed, including hyperglycemia, intraocular hypertension, hyperlipidemia, ultraviolet light exposure, ischemia, and obesity. Early reduction of these stressors may ameliorate ROS-induced retinal damage. Second, the application of dietary antioxidants, antioxidant supplementation, or pharmacological inhibitors could be an effective intervention strategy in the early stages of retinal diseases. This approach may scavenge excess free radicals and reduce oxidative stress injury. Third, physical exercise as a rehabilitation treatment has shown pluripotent benefits in multiple systems of the body, including retinal diseases [158, 159]. Recently, exercise has been demonstrated to have protective effects in animal models of retinal diseases via multiple mechanisms, including the BDNF/TrkB signaling pathway, increased blood flow, and modulation of VEGF and its receptors [160, 161]. Retrospective studies in humans have also indicated that exercise treatment for visual disorders can improve visual function and quality of life. Therefore, exercise interventions may be implemented in the early stage of retinal disease. The retina is a metabolically active tissue that is susceptible to oxidative injury. Therefore, hepatic injury or hyperlipidemia may induce metabolic turbulence and negatively affect retinal health. Maintaining blood and liver health is beneficial to the retina.

4.1. Future Directions

(1) Methods for the early detection of retinal dysfunction must be developed to identify the key treatment window and monitor disease progression

(2) Simple, accessible self-screening is needed to address the problem of visual function and obtain a clinical examination

(3) To explore the differences in the therapeutic effects of nonselective antioxidants, general ROS scavengers, specific inhibitors of Nox isoforms, and molecular/genomic target drugs are necessary to curb the progression of retinal diseases

Conflicts of Interest

The authors report no conflicts of interest.

Acknowledgments

The authors thank Editage Editing Service for editing the English text of a draft of this manuscript. This study was supported by the Key R&D and Promotion Projects of Henan Province No. 182102410099 and No. 182102310452.

References

[1] J. B. Hurley, K. J. Lindsay, and J. Du, "Glucose, lactate, and shuttling of metabolites in vertebrate retinas," *Journal of Neuroscience Research*, vol. 93, no. 7, pp. 1079–1092, 2015.

[2] Z. Sahnoun, K. Jamoussi, and K. M. Zeghal, "Free radicals and antioxidants: physiology, human pathology and therapeutic aspects (part II)," *Thérapie*, vol. 53, no. 4, pp. 315–339, 1998.

[3] T. C. Chan, B. J. Wilkinson, D. Deliyanti et al., "The role of reactive oxygen species in the pathogenesis and treatment of retinal diseases," *Experimental Eye Research*, vol. 201, p. 108255, 2020.

[4] "Trends in prevalence of blindness and distance and near vision impairment over 30 years: an analysis for the Global Burden of Disease Study," *The Lancet Global Health*, vol. 9, no. 2, pp. e130–e143, 2021.

[5] M. Valko, C. J. Rhodes, J. Moncol, M. Izakovic, and M. Mazur, "Free radicals, metals and antioxidants in oxidative stress-induced cancer," *Chemico-Biological Interactions*, vol. 160, no. 1, pp. 1–40, 2006.

[6] V. I. Lushchak, "Free radicals, reactive oxygen species, oxidative stress and its classification," *Chemico-Biological Interactions*, vol. 224, pp. 164–175, 2014.

[7] A. Singh, R. Kukreti, L. Saso, and S. Kukreti, "Oxidative stress: a key modulator in neurodegenerative diseases," *Molecules*, vol. 24, no. 8, p. 1583, 2019.

[8] H. Sies and D. P. Jones, "Reactive oxygen species (ROS) as pleiotropic physiological signalling agents," *Nature Reviews. Molecular Cell Biology*, vol. 21, no. 7, pp. 363–383, 2020.

[9] B. Halliwell, "Antioxidants in human health and disease," *Annual Review of Nutrition*, vol. 16, no. 1, pp. 33–50, 1996.

[10] S. Di Meo and P. Venditti, "Evolution of the knowledge of free radicals and other oxidants," *Oxidative Medicine and Cellular Longevity*, vol. 2020, Article ID 9829176, 32 pages, 2020.

[11] B. Halliwell, "Biochemistry of oxidative stress," *Biochemical Society Transactions*, vol. 35, no. 5, pp. 1147–1150, 2007.

[12] B. Halliwell, "Reactive species and antioxidants. Redox biology is a fundamental theme of aerobic life," *Plant Physiology*, vol. 141, no. 2, pp. 312–322, 2006.

[13] B. Halliwell and J. M. Gutteridge, "The importance of free radicals and catalytic metal ions in human diseases," *Molecular Aspects of Medicine*, vol. 8, no. 2, pp. 89–193, 1985.

[14] R. Amarowicz and R. B. Pegg, "Protection of natural antioxidants against low-density lipoprotein oxidation," *Advances in Food and Nutrition Research*, vol. 93, pp. 251–291, 2020.

[15] Q. J. Zhang, T. Li, H. Zhan, and Y. M. Xin, "Inhibitory effects of tea polyphenols and vitamin C on lipid peroxidation induced by FeSO4- cysteine in isolated human plasma and carbon tetrachloride-induced liver free radical injury in mice," *Space Medicine & Medical Engineering*, vol. 14, no. 1, pp. 50–53, 2001.

[16] B. Frei, "Ascorbic acid protects lipids in human plasma and low-density lipoprotein against oxidative damage," *The American Journal of Clinical Nutrition*, vol. 54, no. 6, pp. 1113S–1118S, 1991.

[17] L. J. Rohowetz, J. G. Kraus, and P. Koulen, "Reactive oxygen species-mediated damage of retinal neurons: drug development targets for therapies of chronic neurodegeneration of the retina," *International Journal of Molecular Sciences*, vol. 19, no. 11, p. 3362, 2018.

[18] M. Nita and A. Grzybowski, "The role of the reactive oxygen species and oxidative stress in the pathomechanism of the age-related ocular diseases and other pathologies of the anterior and posterior eye segments in adults," *Oxidative Medicine and Cellular Longevity*, vol. 2016, Article ID 3164734, 23 pages, 2016.

[19] E. B. Domènech and G. Marfany, "The relevance of oxidative stress in the pathogenesis and therapy of retinal dystrophies," *Antioxidants*, vol. 9, no. 4, p. 347, 2020.

[20] M. T. Pardue and R. S. Allen, "Neuroprotective strategies for retinal disease," *Progress in Retinal and Eye Research*, vol. 65, pp. 50–76, 2018.

[21] P. A. Campochiaro and T. A. Mir, "The mechanism of cone cell death in retinitis pigmentosa," *Progress in Retinal and Eye Research*, vol. 62, pp. 24–37, 2018.

[22] S. Usui, B. C. Oveson, S. Y. Lee et al., "NADPH oxidase plays a central role in cone cell death in retinitis pigmentosa," *Journal of Neurochemistry*, vol. 110, no. 3, pp. 1028–1037, 2009.

[23] Y. Murakami, Y. Ikeda, N. Yoshida et al., "MutT homolog-1 attenuates oxidative DNA damage and delays photoreceptor cell death in inherited retinal degeneration," *The American Journal of Pathology*, vol. 181, no. 4, pp. 1378–1386, 2012.

[24] P. A. Campochiaro, R. W. Strauss, L. Lu et al., "Is there excess oxidative stress and damage in eyes of patients with retinitis pigmentosa?," *Antioxidants & Redox Signaling*, vol. 23, no. 7, pp. 643–648, 2015.

[25] S. Usui, K. Komeima, S. Y. Lee et al., "Increased expression of catalase and superoxide dismutase 2 reduces cone cell death in retinitis pigmentosa," *Molecular Therapy*, vol. 17, no. 5, pp. 778–786, 2009.

[26] K. Komeima, B. S. Rogers, and P. A. Campochiaro, "Antioxidants slow photoreceptor cell death in mouse models of retinitis pigmentosa," *Journal of Cellular Physiology*, vol. 213, no. 3, pp. 809–815, 2007.

[27] Y. Morizane, N. Morimoto, A. Fujiwara et al., "Incidence and causes of visual impairment in Japan: the first nation-wide complete enumeration survey of newly certified visually impaired individuals," *Japanese Journal of Ophthalmology*, vol. 63, no. 1, pp. 26–33, 2019.

[28] S. P. Daiger, L. S. Sullivan, and S. J. Bowne, "Genes and mutations causing retinitis pigmentosa," *Clinical Genetics*, vol. 84, no. 2, pp. 132–141, 2013.

[29] S. K. Verbakel, R. van Huet, C. Boon et al., "Non-syndromic retinitis pigmentosa," *Progress in Retinal and Eye Research*, vol. 66, pp. 157–186, 2018.

[30] Y. Murakami, Y. Nakabeppu, and K. H. Sonoda, "Oxidative stress and microglial response in retinitis pigmentosa," *International Journal of Molecular Sciences*, vol. 21, no. 19, p. 7170, 2020.

[31] P. A. Campochiaro, M. Iftikhar, G. Hafiz et al., "Oral N-acetylcysteine improves cone function in retinitis pigmentosa patients in phase I trial," *The Journal of Clinical Investigation*, vol. 130, no. 3, pp. 1527–1541, 2020.

[32] A. Oishi, K. Noda, J. Birtel et al., "Effect of smoking on macular function and retinal structure in retinitis pigmentosa," *Brain Communications*, vol. 2, no. 2, article a117, 2020.

[33] A. V. Meer, T. Berger, F. Muller, A. C. Foldenauer, S. Johnen, and P. Walter, "Establishment and characterization of a unilateral UV-induced photoreceptor degeneration model in the C57Bl/6J mouse," *Translational Vision Science & Technology*, vol. 9, no. 9, p. 21, 2020.

[34] L. Schwartz, P. Y. Boelle, F. D'Hermies, G. Ledanois, and J. Virmont, "Blue light dose distribution and retinitis pigmentosa visual field defects: an hypothesis," *Medical Hypotheses*, vol. 60, no. 5, pp. 644–649, 2003.

[35] J. Kruk, K. Kubasik-Kladna, and H. Y. Aboul-Enein, "The role oxidative stress in the pathogenesis of eye diseases: current status and a dual role of physical activity," *Mini Reviews in Medicinal Chemistry*, vol. 16, no. 3, pp. 241–257, 2015.

[36] M. R. Landers, "Retinal oxygenation via the choroidal circulation," *Transactions of the American Ophthalmological Society*, vol. 76, pp. 528–556, 1978.

[37] Q. Wei, W. Hu, Q. Lou, and J. Yu, "NAD+ inhibits the metabolic reprogramming of RPE cells in early AMD by upregulating mitophagy," *Discovery Medicine*, vol. 27, no. 149, pp. 189–196, 2019.

[38] L. F. Hernandez-Zimbron, R. Zamora-Alvarado, L. P. L. Ochoa-De et al., "Age-related macular degeneration: new paradigms for treatment and management of AMD," *Oxidative Medicine and Cellular Longevity*, vol. 2018, Article ID 8374647, 14 pages, 2018.

[39] S. Abokyi, C. H. To, T. T. Lam, and D. Y. Tse, "Central role of oxidative stress in age-related macular degeneration: evidence from a review of the molecular mechanisms and animal models," *Oxidative Medicine and Cellular Longevity*, vol. 2020, Article ID 7901270, 19 pages, 2020.

[40] Y. Nishimura, H. Hara, M. Kondo, S. Hong, and T. Matsugi, "Oxidative stress in retinal diseases," *Oxidative Medicine and Cellular Longevity*, vol. 2017, Article ID 4076518, 2 pages, 2017.

[41] W. Smith, J. Assink, R. Klein et al., "Risk factors for age-related macular degeneration: pooled findings from three continents," *Ophthalmology*, vol. 108, no. 4, pp. 697–704, 2001.

[42] A. J. Payne, S. Kaja, N. R. Sabates, and P. Koulen, "A case for neuroprotection in ophthalmology: developments in translational research," *Missouri Medicine*, vol. 110, no. 5, pp. 429–436, 2013.

[43] A. J. Payne, S. Kaja, Y. Naumchuk, N. Kunjukunju, and P. Koulen, "Antioxidant drug therapy approaches for neuroprotection in chronic diseases of the retina," *International Journal of Molecular Sciences*, vol. 15, no. 2, pp. 1865–1886, 2014.

[44] C. S. Alge, S. G. Priglinger, A. S. Neubauer et al., "Retinal pigment epithelium is protected against apoptosis by alphaB-crystallin," *Investigative Ophthalmology & Visual Science*, vol. 43, no. 11, pp. 3575–3582, 2002.

[45] L. Ye, T. Yu, Y. Li et al., "Sulforaphane enhances the ability of human retinal pigment epithelial cell against oxidative stress, and its effect on gene expression profile evaluated by microarray analysis," *Oxidative Medicine and Cellular Longevity*, vol. 2013, Article ID 413024, 13 pages, 2013.

[46] T. Matsuura, K. Takayama, H. Kaneko et al., "Nutritional supplementation inhibits the increase in serum malondialdehyde in patients with wet age-related macular degeneration," *Oxidative Medicine and Cellular Longevity*, vol. 2017, Article ID 9548767, 9 pages, 2017.

[47] J. W. Crabb, M. Miyagi, X. Gu et al., "Drusen proteome analysis: an approach to the etiology of age-related macular degeneration," *Proceedings of the National Academy of Sciences of the United States of America*, vol. 99, no. 23, pp. 14682–14687, 2002.

[48] J. G. Meyer, T. Y. Garcia, B. Schilling, B. W. Gibson, and D. A. Lamba, "Proteome and secretome dynamics of human retinal pigment epithelium in response to reactive oxygen species," *Scientific Reports*, vol. 9, no. 1, p. 15440, 2019.

[49] S. Velilla, J. J. Garcia-Medina, A. Garcia-Layana et al., "Smoking and age-related macular degeneration: review and update," *Journal of Ophthalmology*, vol. 2013, Article ID 895147, 11 pages, 2013.

[50] A. L. Wang, T. J. Lukas, M. Yuan, N. Du, J. T. Handa, and A. H. Neufeld, "Changes in retinal pigment epithelium related to cigarette smoke: possible relevance to smoking as a risk factor for age-related macular degeneration," *PLoS One*, vol. 4, no. 4, article e5304, 2009.

[51] S. Jabbehdari and J. T. Handa, "Oxidative stress as a therapeutic target for the prevention and treatment of early age-related macular degeneration," *Survey of Ophthalmology*, vol. 66, no. 3, pp. 423–440, 2021.

[52] J. Wu, S. Seregard, and P. V. Algvere, "Photochemical damage of the retina," *Survey of Ophthalmology*, vol. 51, no. 5, pp. 461–481, 2006.

[53] G. C. Demontis, B. Longoni, and P. L. Marchiafava, "Molecular steps involved in light-induced oxidative damage to retinal rods," *Investigative Ophthalmology & Visual Science*, vol. 43, no. 7, pp. 2421–2427, 2002.

[54] J. J. Wang, G. H. Buitendijk, E. Rochtchina et al., "Genetic Susceptibility, Dietary Antioxidants, and Long-Term Incidence of Age- Related Macular Degeneration in Two Populations," *Ophthalmology*, vol. 121, no. 3, pp. 667–675, 2014.

[55] L. Ho, R. van Leeuwen, J. C. Witteman et al., "Reducing the genetic risk of age-related macular degeneration with dietary antioxidants, zinc, and ω-3 fatty Acids," *Archives of Ophthalmology*, vol. 129, no. 6, pp. 758–766, 2011.

[56] W. T. Wong, W. Kam, D. Cunningham et al., "Treatment of geographic atrophy by the topical administration of OT-551: results of a phase II clinical trial," *Investigative Ophthalmology & Visual Science*, vol. 51, no. 12, pp. 6131–6139, 2010.

[57] E. Y. Chew, T. E. Clemons, E. Agron et al., "Long-Term Effects of Vitamins C and E, β-Carotene, and Zinc on Age-related Macular Degeneration: AREDS Report No. 35," *Ophthalmology*, vol. 120, no. 8, pp. 1604–1611.e4, 2013.

[58] W. M. Amoaku, U. Chakravarthy, R. Gale et al., "Defining response to anti-VEGF therapies in neovascular AMD," *Eye (London, England)*, vol. 29, no. 6, pp. 721–731, 2015.

[59] N. M. Holekamp, "Review of neovascular age-related macular degeneration treatment options," *The American Journal of Managed Care*, vol. 25, 10 Suppl, pp. S172–S181, 2019.

[60] A. L. Ortega, "Oxidative Stress in Diabetic Retinopathy," *Antioxidants*, vol. 10, no. 1, p. 50, 2021.

[61] Q. Kang and C. Yang, "Oxidative stress and diabetic retinopathy: molecular mechanisms, pathogenetic role and therapeutic implications," *Redox Biology*, vol. 37, p. 101799, 2020.

[62] G. D. Calderon, O. H. Juarez, G. E. Hernandez, S. M. Punzo, and Z. D. De la Cruz, "Oxidative stress and diabetic retinopathy: development and treatment," *Eye (London, England)*, vol. 31, no. 8, pp. 1122–1130, 2017.

[63] M. H. Wang, G. Hsiao, and M. Al-Shabrawey, "Eicosanoids and oxidative stress in diabetic retinopathy," *Antioxidants*, vol. 9, no. 6, p. 520, 2020.

[64] H. Ahsan, "Diabetic retinopathy - Biomolecules and multiple pathophysiology," *Diabetes and Metabolic Syndrome: Clinical Research and Reviews*, vol. 9, no. 1, pp. 51–54, 2015.

[65] M. L. Rodriguez, S. Perez, S. Mena-Molla, M. C. Desco, and A. L. Ortega, "Oxidative stress and microvascular alterations in diabetic retinopathy: future therapies," *Oxidative Medicine and Cellular Longevity*, vol. 2019, Article ID 4940825, 18 pages, 2019.

[66] Y. Du, A. Veenstra, K. Palczewski, and T. S. Kern, "Photoreceptor cells are major contributors to diabetes-induced oxidative stress and local inflammation in the retina," *Proceedings of the National Academy of Sciences of the United States of America*, vol. 110, no. 41, pp. 16586–16591, 2013.

[67] T. Bek, "Mitochondrial dysfunction and diabetic retinopathy," *Mitochondrion*, vol. 36, pp. 4–6, 2017.

[68] R. A. Kowluru, "Diabetic retinopathy: mitochondrial dysfunction and retinal capillary cell death," *Antioxidants & Redox Signaling*, vol. 7, no. 11-12, pp. 1581–1587, 2005.

[69] M. Barot, M. R. Gokulgandhi, and A. K. Mitra, "Mitochondrial dysfunction in retinal diseases," *Current Eye Research*, vol. 36, no. 12, pp. 1069–1077, 2011.

[70] M. Nebbioso, A. Lambiase, M. Armentano et al., "Diabetic retinopathy, oxidative stress, and sirtuins: an in depth look in enzymatic patterns and new therapeutic horizons," *Survey of Ophthalmology*, vol. 67, no. 1, pp. 168–183, 2022.

[71] R. R. Robles-Rivera, J. A. Castellanos-Gonzalez, C. Olvera-Montano et al., "Adjuvant therapies in diabetic retinopathy as an early approach to delay its progression: the importance of oxidative stress and inflammation," *Oxidative Medicine and Cellular Longevity*, vol. 2020, Article ID 3096470, 23 pages, 2020.

[72] Q. Chen, L. Tang, G. Xin et al., "Oxidative stress mediated by lipid metabolism contributes to high glucose- induced senescence in retinal pigment epithelium," *Free Radical Biology & Medicine*, vol. 130, pp. 48–58, 2019.

[73] M. M. Gupta and S. Chari, "Lipid peroxidation and antioxidant status in patients with diabetic retinopathy," *Indian Journal of Physiology and Pharmacology*, vol. 49, no. 2, pp. 187–192, 2005.

[74] W. Wang and A. Lo, "Diabetic retinopathy: pathophysiology and treatments," *International Journal of Molecular Sciences*, vol. 19, no. 6, p. 1816, 2018.

[75] D. Zhang, F. L. Lv, and G. H. Wang, "Effects of HIF-1α on diabetic retinopathy angiogenesis and VEGF expression," *European Review for Medical and Pharmacological Sciences*, vol. 22, no. 16, pp. 5071–5076, 2018.

[76] W. Jiao, J. Ji, F. Li et al., "Activation of the Notch-Nox4-reactive oxygen species signaling pathway induces cell death in high glucose-treated human retinal endothelial cells," *Molecular Medicine Reports*, vol. 19, no. 1, pp. 667–677, 2019.

[77] J. Li, J. J. Wang, Q. Yu, K. Chen, K. Mahadev, and S. X. Zhang, "Inhibition of reactive oxygen species by lovastatin downregulates vascular endothelial growth factor expression and ameliorates blood-retinal barrier breakdown in db/db mice:

role of NADPH oxidase 4," *Diabetes*, vol. 59, no. 6, pp. 1528–1538, 2010.

[78] B. Appukuttan, Y. Ma, A. Stempel et al., "Effect of NADPH oxidase 1 and 4 blockade in activated human retinal endothelial cells," *Clinical & Experimental Ophthalmology*, vol. 46, no. 6, pp. 652–660, 2018.

[79] A. P. Laddha and Y. A. Kulkarni, "Tannins and vascular complications of diabetes: an update," *Phytomedicine*, vol. 56, pp. 229–245, 2019.

[80] A. M. Mahmoud, E. S. Abd, and E. S. Abdel-Reheim, "Consumption of polyphenol-rich Morus alba leaves extract attenuates early diabetic retinopathy: the underlying mechanism," *European Journal of Nutrition*, vol. 56, no. 4, pp. 1671–1684, 2017.

[81] D. Kalita, D. G. Holm, D. V. LaBarbera, J. M. Petrash, and S. S. Jayanty, "Inhibition of α-glucosidase, α-amylase, and aldose reductase by potato polyphenolic compounds," *PLoS One*, vol. 13, no. 1, article e191025, 2018.

[82] P. Palsamy and S. Subramanian, "Resveratrol protects diabetic kidney by attenuating hyperglycemia-mediated oxidative stress and renal inflammatory cytokines via Nrf2-Keap1 signaling," *Biochimica et Biophysica Acta*, vol. 1812, no. 7, pp. 719–731, 2011.

[83] S. Bungau, M. M. Abdel-Daim, D. M. Tit et al., "Health benefits of polyphenols and carotenoids in age-related eye diseases," *Oxidative Medicine and Cellular Longevity*, vol. 2019, Article ID 9783429, 22 pages, 2019.

[84] N. Xia, A. Daiber, A. Habermeier et al., "Resveratrol reverses endothelial nitric-oxide synthase uncoupling in apolipoprotein E knockout mice," *The Journal of Pharmacology and Experimental Therapeutics*, vol. 335, no. 1, pp. 149–154, 2010.

[85] S. D. Chalke and P. P. Kale, "Combinational approaches targeting neurodegeneration, oxidative stress, and inflammation in the treatment of diabetic retinopathy," *Current Drug Targets*, vol. 22, no. 16, pp. 1810–1824, 2021.

[86] D. Deliyanti, S. F. Alrashdi, S. M. Tan et al., "Nrf2 activation is a potential therapeutic approach to attenuate diabetic retinopathy," *Investigative Ophthalmology & Visual Science*, vol. 59, no. 2, pp. 815–825, 2018.

[87] Q. Liu, F. Zhang, X. Zhang et al., "Fenofibrate ameliorates diabetic retinopathy by modulating Nrf2 signaling and NLRP3 inflammasome activation," *Molecular and Cellular Biochemistry*, vol. 445, no. 1-2, pp. 105–115, 2018.

[88] S. Alqawlaq, J. T. Huzil, M. V. Ivanova, and M. Foldvari, "Challenges in neuroprotective nanomedicine development: progress towards noninvasive gene therapy of glaucoma," *Nanomedicine (London, England)*, vol. 7, no. 7, pp. 1067–1083, 2012.

[89] Y. C. Tham, X. Li, T. Y. Wong, H. A. Quigley, T. Aung, and C. Y. Cheng, "Global prevalence of glaucoma and projections of glaucoma burden through 2040: a systematic review and meta-analysis," *Ophthalmology*, vol. 121, no. 11, pp. 2081–2090, 2014.

[90] M. Kolko, A. Horwitz, J. Thygesen, J. Jeppesen, and C. Torp-Pedersen, "The prevalence and incidence of glaucoma in Denmark in a fifteen year period: a nationwide study," *PLoS One*, vol. 10, no. 7, article e132048, 2015.

[91] H. Jayaram, "Intraocular pressure reduction in glaucoma: does every mmHg count?," *Taiwan Journal of Ophthalmology*, vol. 10, no. 4, pp. 255–258, 2020.

[92] G. J. Fan, M. H. Shah, and E. C. Chan, "Oxidative stress and the role of NADPH oxidase in glaucoma," *Antioxidants*, vol. 10, no. 2, p. 238, 2021.

[93] K. Kikuchi, Z. Dong, Y. Shinmei et al., "Cytoprotective effect of astaxanthin in a model of normal intraocular pressure glaucoma," *Journal of Ophthalmology*, vol. 2020, Article ID 9539681, 6 pages, 2020.

[94] A. Izzotti, A. Bagnis, and S. C. Sacca, "The role of oxidative stress in glaucoma," *Mutation Research*, vol. 612, no. 2, pp. 105–114, 2006.

[95] S. Seen and L. Tong, "Dry eye disease and oxidative stress," *Acta Ophthalmologica*, vol. 96, no. 4, pp. e412–e420, 2018.

[96] P. G. Sreekumar, D. R. Hinton, and R. Kannan, "The emerging role of senescence in ocular disease," *Oxidative Medicine and Cellular Longevity*, vol. 2020, Article ID 2583601, 19 pages, 2020.

[97] J. T. Eells, "Mitochondrial dysfunction in the aging retina," *Biology*, vol. 8, no. 2, p. 31, 2019.

[98] C. Baudouin, M. Kolko, S. Melik-Parsadaniantz, and E. M. Messmer, "Inflammation in glaucoma: from the back to the front of the eye, and beyond," *Progress in Retinal and Eye Research*, vol. 83, p. 100916, 2021.

[99] P. X. Shaw, T. Stiles, C. Douglas et al., "Oxidative stress, innate immunity, and age-related macular degeneration," *AIMS Molecular Science*, vol. 3, no. 2, pp. 196–221, 2016.

[100] N. Golestaneh, Y. Chu, S. K. Cheng, H. Cao, E. Poliakov, and D. M. Berinstein, "Repressed SIRT1/PGC-1α pathway and mitochondrial disintegration in iPSC-derived RPE disease model of age-related macular degeneration," *Journal of Translational Medicine*, vol. 14, no. 1, p. 344, 2016.

[101] J. Zhao, S. Wang, W. Zhong, B. Yang, L. Sun, and Y. Zheng, "Oxidative stress in the trabecular meshwork (review)," *International Journal of Molecular Medicine*, vol. 38, no. 4, pp. 995–1002, 2016.

[102] S. C. Sacca, A. Pascotto, P. Camicione, P. Capris, and A. Izzotti, "Oxidative DNA damage in the human trabecular Meshwork," *Archives of Ophthalmology*, vol. 123, no. 4, pp. 458–463, 2005.

[103] A. Izzotti, S. C. Sacca, C. Cartiglia, and S. De Flora, "Oxidative deoxyribonucleic acid damage in the eyes of glaucoma patients," *The American Journal of Medicine*, vol. 114, no. 8, pp. 638–646, 2003.

[104] L. Zhou, Y. Li, and B. Y. Yue, "Oxidative stress affects cytoskeletal structure and cell-matrix interactions in cells from an ocular tissue: the trabecular meshwork," *Journal of Cellular Physiology*, vol. 180, no. 2, pp. 182–189, 1999.

[105] O. Masihzadeh, D. A. Ammar, T. C. Lei, E. A. Gibson, and M. Y. Kahook, "Real-time measurements of nicotinamide adenine dinucleotide in live human trabecular meshwork cells: effects of acute oxidative stress," *Experimental Eye Research*, vol. 93, no. 3, pp. 316–320, 2011.

[106] R. Cook, V. Thomas, and R. Martin, "Laser eye procedure is safe and effective as an early treatment for glaucoma," *BMJ*, vol. 366, p. l4235, 2019.

[107] G. Hondur, E. Göktas, X. Yang et al., "Oxidative stress-related molecular biomarker candidates for glaucoma," *Investigative Ophthalmology & Visual Science*, vol. 58, no. 10, pp. 4078–4088, 2017.

[108] C. Lanzi, L. Lucarini, M. Durante et al., "Role of histamine H3 receptor antagonists on intraocular pressure reduction in rabbit models of transient ocular hypertension and

glaucoma," *International Journal of Molecular Sciences*, vol. 20, no. 4, p. 981, 2019.

[109] Q. Liu, W. K. Ju, J. G. Crowston et al., "Oxidative stress is an early event in hydrostatic pressure induced retinal ganglion cell damage," *Investigative Ophthalmology & Visual Science*, vol. 48, no. 10, pp. 4580–4589, 2007.

[110] K. Mahalingam, A. K. Chaurasia, L. Gowtham et al., "Therapeutic potential of valproic acid in advanced glaucoma: a pilot study," *Indian Journal of Ophthalmology*, vol. 66, no. 8, pp. 1104–1108, 2018.

[111] T. Noro, K. Namekata, Y. Azuchi et al., "Spermidine ameliorates neurodegeneration in a mouse model of normal tension glaucoma," *Investigative Ophthalmology & Visual Science*, vol. 56, no. 8, pp. 5012–5019, 2015.

[112] S. F. Chou, L. J. Luo, and J. Y. Lai, "In vivo Pharmacological Evaluations of Pilocarpine-Loaded Antioxidant- Functionalized Biodegradable Thermogels in Glaucomatous Rabbits," *Scientific Reports*, vol. 7, no. 1, p. 42344, 2017.

[113] K. Oikawa, H. J. Ver, L. Teixeira et al., "Sub-region-specific optic nerve head glial activation in glaucoma," *Molecular Neurobiology*, vol. 57, no. 6, pp. 2620–2638, 2020.

[114] A. Sapienza, A. L. Raveu, E. Reboussin et al., "Bilateral neuroinflammatory processes in visual pathways induced by unilateral ocular hypertension in the rat," *Journal of Neuroinflammation*, vol. 13, no. 1, p. 44, 2016.

[115] M. L. Cooper, S. D. Crish, D. M. Inman, P. J. Horner, and D. J. Calkins, "Early astrocyte redistribution in the optic nerve precedes axonopathy in the DBA/2J mouse model of glaucoma," *Experimental Eye Research*, vol. 150, pp. 22–33, 2016.

[116] M. P. Murphy, "How mitochondria produce reactive oxygen species," *The Biochemical Journal*, vol. 417, no. 1, pp. 1–13, 2009.

[117] P. A. Williams, J. M. Harder, N. E. Foxworth et al., "Vitamin B3modulates mitochondrial vulnerability and prevents glaucoma in aged mice," *Science*, vol. 355, no. 6326, pp. 756–760, 2017.

[118] S. M. Law, X. Lu, F. Yu, V. Tseng, S. K. Law, and A. L. Coleman, "Cigarette smoking and glaucoma in the United States population," *Eye (London, England)*, vol. 32, no. 4, pp. 716–725, 2018.

[119] F. Fahmideh, N. Marchesi, A. Barbieri, S. Govoni, and A. Pascale, "Non-drug interventions in glaucoma: putative roles for lifestyle, diet and nutritional supplements," *Survey of Ophthalmology*, vol. 67, no. 3, pp. 675–696, 2022.

[120] C. I. Perez, K. Singh, and S. Lin, "Relationship of lifestyle, exercise, and nutrition with glaucoma," *Current Opinion in Ophthalmology*, vol. 30, no. 2, pp. 82–88, 2019.

[121] J. Kim, H. Aschard, J. H. Kang et al., "Intraocular pressure, glaucoma, and dietary caffeine consumption: a gene-diet interaction study from the UK biobank," *Ophthalmology*, vol. 128, no. 6, pp. 866–876, 2021.

[122] J. H. Park, J. H. Hwang, Y. S. Chang, M. H. Lee, and W. S. Park, "Survival rate dependent variations in retinopathy of prematurity treatment rates in very low birth weight infants," *Scientific Reports*, vol. 10, no. 1, p. 19401, 2020.

[123] Q. P. Li, Z. H. Wang, Y. Y. Li et al., "Retinopathy of prematurity screening in 2185 premature infants," *Zhonghua Yan Ke Za Zhi*, vol. 48, no. 10, pp. 903–907, 2012.

[124] W. L. Stone, D. Shah, and S. M. Hollinger, "Retinopathy of prematurity: an oxidative stress neonatal disease," *Frontiers in Bioscience*, vol. 21, no. 1, pp. 165–177, 2016.

[125] T. Froysaker, "The influence of constrictive pericarditis on the superior vena caval flow pattern," *Scandinavian Journal of Thoracic and Cardiovascular Surgery*, vol. 6, no. 3, pp. 227–233, 1972.

[126] L. E. Smith, A. L. Hard, and A. Hellstrom, "The biology of retinopathy of prematurity: how knowledge of pathogenesis guides treatment," *Clinics in Perinatology*, vol. 40, no. 2, pp. 201–214, 2013.

[127] O. D. Saugstad, "Oxygen and retinopathy of prematurity," *Journal of Perinatology*, vol. 26, Suppl 1, pp. S46–S50, 2006.

[128] W. V. Good, R. J. Hardy, V. Dobson et al., "The incidence and course of retinopathy of prematurity: findings from the early treatment for retinopathy of prematurity study," *Pediatrics*, vol. 116, no. 1, pp. 15–23, 2005.

[129] B. W. Fleck and B. J. Stenson, "Retinopathy of prematurity and the oxygen conundrum: lessons learned from recent randomized trials," *Clinics in Perinatology*, vol. 40, no. 2, pp. 229–240, 2013.

[130] G. Buonocore, S. Perrone, M. Longini et al., "Oxidative stress in preterm neonates at birth and on the seventh day of life," *Pediatric Research*, vol. 52, no. 1, pp. 46–49, 2002.

[131] J. M. Davis and R. L. Auten, "Maturation of the antioxidant system and the effects on preterm birth," *Seminars in Fetal & Neonatal Medicine*, vol. 15, no. 4, pp. 191–195, 2010.

[132] J. E. Lee, "Low IGF-1 suppresses VEGF-survival signaling in retinal endothelial cells: direct correlation with clinical retinopathy of prematurity, by A. Hellström, C. Perruzzi, M. Ju, E. Engström, A Hård, J. Liu, K. Albertson-Wikland, B. Carlsson, A. Niklasson, L. Sjödell, D. LeRoith, D. Senger, and L. Smith. PNAS 98:5804-8, 2001," *Survey of Ophthalmology*, vol. 48, no. 2, pp. 234-235, 2003.

[133] U. Garg, A. Jain, P. Singla, S. Beri, R. Garg, and A. Saili, "Free radical status in retinopathy of prematurity," *Indian Journal of Clinical Biochemistry*, vol. 27, no. 2, pp. 196–199, 2012.

[134] L. Banjac, G. Banjac, J. Kotur-Stevuljevic et al., "Pro-oxidants and antioxidants in retinopathy of prematurity," *Acta Clinica Croatica*, vol. 57, no. 3, pp. 458–463, 2018.

[135] T. E. Zhou, J. C. Rivera, V. K. Bhosle et al., "Choroidal involution is associated with a progressive degeneration of the outer retinal function in a model of retinopathy of prematurity: early role for IL-1β," *The American Journal of Pathology*, vol. 186, no. 12, pp. 3100–3116, 2016.

[136] J. F. Vander, J. A. McNamara, W. Tasman, and G. C. Brown, "Revised indications for early treatment of retinopathy of prematurity," *Archives of Ophthalmology*, vol. 123, no. 3, p. 406, 2005.

[137] J. K. Singh, E. M. Wymore, B. D. Wagner et al., "Relationship between severe bronchopulmonary dysplasia and severe retinopathy of prematurity in premature newborns," *Journal of AAPOS*, vol. 23, no. 4, pp. 209.e1–209.e4, 2019.

[138] S. H. Rodriguez, S. A. Schechet, M. J. Shapiro, and M. P. Blair, "Late visual outcomes in infants treated with primary bevacizumab for type 1 retinopathy of prematurity," *Journal of AAPOS*, vol. 24, no. 3, pp. 149.e1–149.e5, 2020.

[139] M. E. Hartnett, "Advances in understanding and management of retinopathy of prematurity," *Survey of Ophthalmology*, vol. 62, no. 3, pp. 257–276, 2017.

[140] A. Kozlowska and D. Szostak-Wegierek, "Flavonoids–food sources and health benefits," *Roczniki Państwowego Zakładu Higieny*, vol. 65, no. 2, pp. 79–85, 2014.

[141] J. A. Ross and C. M. Kasum, "DIETARYFLAVONOIDS: bioavailability, metabolic effects, and safety," *Annual Review of Nutrition*, vol. 22, no. 1, pp. 19–34, 2002.

[142] Y. Saito, Y. Hasebe-Takenaka, T. Ueda et al., "Effects of green tea fractions on oxygen-induced retinal neovascularization in the neonatal rat," *Journal of Clinical Biochemistry and Nutrition*, vol. 41, no. 1, pp. 43–49, 2007.

[143] Y. Wang, L. Zhao, F. Lu et al., "Retinoprotective effects of bilberry anthocyanins via antioxidant, anti-inflammatory, and anti-apoptotic mechanisms in a visible light-induced retinal degeneration model in pigmented rabbits," *Molecules*, vol. 20, no. 12, pp. 22395–22410, 2015.

[144] J. Tsang, S. A. Wolf, I. M. Pompoes et al., "Potential Effects of Nutraceuticals in Retinopathy of Prematurity," *Lifestyles*, vol. 11, no. 2, p. 79, 2021.

[145] H. Jo, S. H. Jung, H. B. Yim, S. J. Lee, and K. D. Kang, "The effect of baicalin in a mouse model of retinopathy of prematurity," *BMB Reports*, vol. 48, no. 5, pp. 271–276, 2015.

[146] S. W. Park, C. S. Cho, H. O. Jun et al., "Anti-angiogenic effect of luteolin on retinal neovascularization via blockade of reactive oxygen species production," *Investigative Ophthalmology & Visual Science*, vol. 53, no. 12, pp. 7718–7726, 2012.

[147] C. Dani, I. Lori, F. Favelli et al., "Lutein and zeaxanthin supplementation in preterm infants to prevent retinopathy of prematurity: a randomized controlled study," *The Journal of Maternal-Fetal & Neonatal Medicine*, vol. 25, no. 5, pp. 523–527, 2012.

[148] C. Hanson, E. Lyden, J. Furtado et al., "Vitamin E status and associations in maternal-infant dyads in the Midwestern United States," *Clinical Nutrition*, vol. 38, no. 2, pp. 934–939, 2019.

[149] M. S. Bastos, S. A. Rolland, C. M. Costa et al., "Vitamin A and Pregnancy: A Narrative Review," *Nutrients*, vol. 11, no. 3, 2019.

[150] M. L. de Souza, L. V. Mennitti, V. V. de Rosso, and L. P. Pisani, "The role of vitamin a and its pro-vitamin carotenoids in fetal and neonatal programming: gaps in knowledge and metabolic pathways," *Nutrition Reviews*, vol. 79, no. 1, pp. 76–87, 2021.

[151] A. Hellstrom, L. E. Smith, and O. Dammann, "Retinopathy of prematurity," *Lancet*, vol. 382, no. 9902, pp. 1445–1457, 2013.

[152] R. Cayabyab and R. Ramanathan, "Retinopathy of prematurity: therapeutic strategies based on pathophysiology," *Neonatology*, vol. 109, no. 4, pp. 369–376, 2016.

[153] E. Di Marco, J. C. Jha, A. Sharma, J. L. Wilkinson-Berka, K. A. Jandeleit-Dahm, and J. B. de Haan, "Are reactive oxygen species still the basis for diabetic complications?," *Clinical Science (London, England)*, vol. 129, no. 2, pp. 199–216, 2015.

[154] S. C. Sacca, A. M. Roszkowska, and A. Izzotti, "Environmental light and endogenous antioxidants as the main determinants of non-cancer ocular diseases," *Mutation Research*, vol. 752, no. 2, pp. 153–171, 2013.

[155] T. Finkel and N. J. Holbrook, "Oxidants, oxidative stress and the biology of ageing," *Nature*, vol. 408, no. 6809, pp. 239–247, 2000.

[156] S. C. Sacca, S. Gandolfi, A. Bagnis et al., "From DNA damage to functional changes of the trabecular meshwork in aging and glaucoma," *Ageing Research Reviews*, vol. 29, pp. 26–41, 2016.

[157] J. J. Hunter, J. I. Morgan, W. H. Merigan, D. H. Sliney, J. R. Sparrow, and D. R. Williams, "The susceptibility of the retina to photochemical damage from visible light," *Progress in Retinal and Eye Research*, vol. 31, no. 1, pp. 28–42, 2012.

[158] M. B. McGuinness, A. Karahalios, J. A. Simpson et al., "Past physical activity and age-related macular degeneration: the Melbourne collaborative cohort study," *The British Journal of Ophthalmology*, vol. 100, no. 10, pp. 1353–1358, 2016.

[159] P. D. Loprinzi, "Association of accelerometer-assessed sedentary behavior with diabetic retinopathy in the United States," *JAMA Ophthalmology*, vol. 134, no. 10, pp. 1197-1198, 2016.

[160] V. Chrysostomou, S. Galic, P. van Wijngaarden, I. A. Trounce, G. R. Steinberg, and J. G. Crowston, "Exercise reverses age-related vulnerability of the retina to injury by preventing complement-mediated synapse elimination via a BDNF-dependent pathway," *Aging Cell*, vol. 15, no. 6, pp. 1082–1091, 2016.

[161] A. M. Hanif, E. C. Lawson, M. Prunty et al., "Neuroprotective effects of voluntary exercise in an inherited retinal degeneration mouse model," *Investigative Ophthalmology & Visual Science*, vol. 56, no. 11, pp. 6839–6846, 2015.

Hindawi
Oxidative Medicine and Cellular Longevity
Volume 2022, Article ID 3652402, 15 pages
https://doi.org/10.1155/2022/3652402

Research Article

Isorhamnetin Attenuated the Release of Interleukin-6 from β-Amyloid-Activated Microglia and Mitigated Interleukin-6-Mediated Neurotoxicity

Pei-Cih Wei,[1] **Guey-Jen Lee-Chen**,[2] **Chiung-Mei Chen**,[1] **Ying Chen**,[1] **Yen-Shi Lo**,[1] **and Kuo-Hsuan Chang**[1]

[1]*Department of Neurology, Chang Gung Memorial Hospital-Linkou Medical Center, Chang Gung University School of Medicine, Taoyuan, Taiwan*
[2]*Department of Life Science, National Taiwan Normal University, Taipei, Taiwan*

Correspondence should be addressed to Kuo-Hsuan Chang; gophy5128@cgmh.org.tw

Received 16 February 2022; Revised 14 July 2022; Accepted 12 August 2022; Published 15 September 2022

Academic Editor: Francisco Rios

Alzheimer's disease (AD), characterized by the abnormal accumulation of β-amyloid (Aβ), is the most prevalent type of dementia, and it is associated with progressive cognitive decline and memory loss. Aβ accumulation activates microglia, which secrete proinflammatory factors associated with Aβ clearance impairment and cause neurotoxicity, generating a vicious cycle among Aβ accumulation, activated microglia, and proinflammatory factors. Blocking this cycle can be a therapeutic strategy for AD. Using Aβ-activated HMC3 microglial cells, we observed that isorhamnetin, a main constituent of *Oenanthe javanica*, reduced the Aβ-triggered secretion of interleukin- (IL-) 6 and downregulated the expression levels of the microglial activation markers ionized calcium binding adaptor molecule 1 (IBA1) and CD11b and the inflammatory marker nuclear factor-κB (NF-κB). Treatment of the SH-SY5Y-derived neuronal cells with the Aβ-activated HMC3-conditioned medium (HMC3-conditioned medium) or IL-6 increased reactive oxygen species production, upregulated cleaved caspase 3 expression, and reduced neurite outgrowth, whereas treatment with isorhamnetin counteracted these neurodegenerative presentations. In the SH-SY5Y-derived neuronal cells, IL-6 upregulated the phosphorylation of tyrosine kinase 2 (TYK2) and signal transducer and activator of transcription 1 (STAT1), whereas isorhamnetin normalized this abnormal phosphorylation. Overexpression of TYK2 attenuated the neuroprotective effect of isorhamnetin on IL-6-induced neurotoxicity. Our findings demonstrate that isorhamnetin exerts its neuroprotective effect by mediating the neuroinflammatory IL-6/TYK2 signaling pathway, suggesting its potential for treating AD.

1. Introduction

Alzheimer's disease (AD), the most common cause of dementia in older people, is an irreversible and a progressive neurodegenerative disease that slowly impairs cognitive function, memory and thinking, and eventually the ability to perform the simplest daily tasks [1]. With the rapid increase in the aging population in developing and developed countries, AD is becoming a major health problem globally [2]. However, the lack of effective treatment for preventing disease progression necessitates the development of new agents that can halt the pathogenesis of AD. Pathologically, AD is characterized by the presence of senile plaques in the brain [1]. Senile plaques are composed of the β-amyloid (Aβ) peptide, a fragment of the amyloid peptide precursor protein (APP) [3]. Aβ peptides aggregate to form oligomers and other high-order polymerized structures that cause neuronal death through various mechanisms including neuroinflammation, oxidative stress, excitotoxicity, energy depletion, and apoptosis [4].

Neuroinflammation is a prominent feature in AD pathology and a potential target for the treatment and prevention of AD [5]. Neuroinflammation links Aβ peptide deposition to neuronal death by activating microglia through Toll-like receptor 2 [6]. Activated microglia secrete proinflammatory

factors including interleukin- (IL-) 1β [7], IL-6 [8], and tumor necrosis factor- (TNF-) α [7]. The expression levels of IL-1β, IL-6, and TNF-α have been reported to be upregulated in the brains of AD animal models [7, 9] and patients with AD [1]. In addition, an increased risk of AD is associated with the genetic variants of IL-1β [10], IL-6 [11], and TNF-α [12]. Abnormal production of proinflammatory factors causes neurotoxicity and impairs Aβ peptide clearance, forming a vicious cycle among Aβ peptide accumulation, activated microglia, and proinflammatory factors. Blocking this cycle can be a vital strategy for halting neurodegeneration in AD.

Isorhamnetin, a small-molecular compound with an aromatic heterocyclic structure, is the main constituent of the *Oenanthe javanica* extract. Isorhamnetin exerts an anti-inflammatory effect by modulating IκB kinase (IKK)α, IKKβ, and nuclear factor- (NF-) κB [13]. In a rat model, isorhamnetin demonstrated neuroprotection against Aβ peptides [14]. This study investigated the effects of isorhamnetin on microglial activation and neuroinflammation in the cell models of AD. Isorhamnetin inhibited Aβ peptide-mediated microglial activation and exerted a neuroprotective effect on IL-6-mediated neurotoxicity. These findings support the potential of isorhamnetin for use in AD treatment.

2. Materials and Methods

2.1. Maintenance and Neural Induction of SH-SY5Y Cells. SH-SY5Y cells (American Type Culture Collection (ATCC) CRL-2266) were maintained in Dulbecco's modified Eagle medium/nutrient mixture F-12 (DMEM/F12) containing 10% fetal bovine serum (FBS) at 37°C under 5% CO_2. Subsequently, for neuronal differentiation, 20 μM retinoic acid (RA) was added to the culture medium and the cells were incubated for 5 days. The differentiated cells were treated with isorhamnetin (10 μM, Merck), TYK2 inhibitor (1 μM, BMS-986165, AdooQ), or IL-6-neutralized antibody (IL-6 IgG, 5 ng/mL, InvivoGen) for 2 days, respectively.

2.2. HMC3 Cell Culture and Drug Treatment. HMC3 cells (human microglial cells; ATCC CRL-3304) were routinely cultured in DMEM/F12 containing 10% FBS at 37°C under 5% CO2 and 95% relative humidity. The HMC3 cells were activated by the addition of Aβ oligomers (200 nM) for 24 or 48 hours and then treated with isorhamnetin (10 μM) or NF-κB inhibitor EVP4593 (1 μM, Merck) for 48 hours.

2.3. Cell Viability Assessment Using Lactate Dehydrogenase and 2,5-Diphenyl-2H-Tetrazolium Bromide Assays. According to the manufacturer's instructions (Roche), the cells were incubated with 100 μL of lactate dehydrogenase (LDH) reagent at room temperature for 20 min. The absorbance of the samples was measured at 490 nm by using a spectrophotometer. For the 2,5-diphenyl-2H-tetrazolium bromide (MTT) assay, the cells were cultivated with 20 μL of MTT (5 mg/mL in phosphate-buffered saline (PBS)) and incubated at 37°C for 2 hours. Subsequently, the formation of purple formazan crystals was determined by measuring absorbance at 570 nm by using a microplate spectrophotometer.

2.4. Preparation of Aβ Oligomers [15]. Aβ42 peptides were dissolved in hexafluoro-2-propanol (HFIP) and incubated at room temperature for at least 1 hour. To obtain the peptide film, HFIP was removed through evaporation and the resulting peptides were stored at −20°C or −80°C. The resulting film was adjusted to a concentration of 5 mM by using dimethyl sulfoxide and then diluted to achieve appropriate concentrations for experiments.

2.5. Western Blotting. Total proteins were lysed using RIPA buffer containing a protease inhibitor cocktail (Sigma) and a phosphatase inhibitor (Sigma). Thereafter, 60 μg of proteins was separated through 12% sodium dodecyl sulfate-polyacrylamide gel electrophoresis and transferred onto polyvinylidene fluoride membranes. The blocked membrane was hybridized using the following antibodies: glyceraldehyde 3-phosphate dehydrogenase (GAPDH) (1 : 10,000 dilution, Proteintech), NF-κB (1 : 1000 dilution, Cell Signaling), p-NF-κB/p65 (1 : 1000 dilution, Cell Signaling), ionized calcium-binding adaptor molecule 1 (IBA1) (1 : 1000 dilution, WAKO), cleaved caspase 3 (dilution 1 : 1000, Cell Signaling), CD11b (1 : 1000 dilution, WAKO), CD68 (1 : 1000 dilution, Boster), p-IKKα/p-IKK-□ (1 : 1000 dilution, Cell Signaling), IKKα (1 : 1000 dilution, Cell Signaling), IKK□ (1 : 1000 dilution, Cell Signaling), Janus kinase 2 (JAK2) (1 : 1000 dilution, Cell Signaling), p-JAK2 (1 : 1000 dilution, Cell Signaling), tyrosine kinase 2 (TYK2) (1 : 1000 dilution, Cell Signaling), p-TYK2 (1 : 1000 dilution, Cell Signaling), signal transducer and activator of transcription 3 (STAT3) (1 : 1000 dilution, Santa Cruz), p-STAT3 (1 : 1000 dilution, Santa Cruz), signal transducer and activator of transcription 1 (STAT1) (1 : 1000 dilution, Cell Signaling), and p-STAT1 (1 : 1000 dilution, Cell Signaling). The protein expression was detected using horseradish peroxidase-labeled goat anti-mouse or goat anti-rabbit IgG antibody and a chemiluminescent substrate.

2.6. Transfection with Plasmid DNA. The SH-SY5Y cells were transfected with the TYK2 expression vector (Sino Biological) by using the X-treme transfection reagent (Roche) according to the manufacturer's instructions. Subsequently, the expression of TYK2 was confirmed through Western blotting after 48 hours of transfection.

2.7. Reactive Oxidative Species Analysis. The cells were seeded in six-well plates (10^5 cells/well) and differentiated into neuronal cells through treatment with retinoic acid (RA) (20 μM) for 5 days. Subsequently, the neuronal cells were treated with isorhamnetin or IL-6 for 48 hours. For reactive oxygen species (ROS) analysis, the fluorogenic CellROX deep red reagent (Molecular Probes) was added to the live cells, followed by incubation at 37°C for 6 hours. Thereafter, the cells were washed with PBS and red fluorescence (indicating the presence of ROS) was examined using a Leica TCS confocal microscope at the excitation and emission wavelengths of 644 and 665 nm, respectively.

2.8. Neurite Outgrowth Evaluation Using Immunofluorescence Staining. Neurons were cultured on a coverslip and washed with PBS. Subsequently, they were fixed with 4% paraformaldehyde for 20 min at room temperature. After the residual fixation buffer was removed using PBS, the cells were blocked in PBS containing 5% BSA for 20 min at room temperature and then hybridized with the primary antibody tubulin class III (TUBB3) (1 : 5000 dilution, BioLegend) overnight at 4°C. After being washed with PBS, the cells were incubated with an Alexa 488-conjugated secondary antibody in the dark for 1 hour. For cell counting, the cells were stained with 4′,6-diamidino-2-phenylindole (1 : 1000 dilution). Subsequently, the mounted coverslips were examined using a Leica TCS confocal microscope. Neurite outgrowth on the SH-SY5Y-derived neurons (>200 cells) was analyzed using MetaMorph software (Molecular Devices).

2.9. Preparation of HMC3-Conditional Medium. The HMC3 cells were treated by A oligomers (200 nM) for 48 hours, and the medium was replaced with fresh culture medium for 24 hours. The supernatant free from A oligomers was collected for further experiments.

2.10. ELISA. The conditional medium (2 mL) was collected from a 3.5 cm dish seeded with 10^5 HMC3 cells/well after treatment with A oligomers (200 nM) for 24 or 48 hours, followed by isorhamnetin (10 μM) for 48 hours. The collected medium was centrifuged at 1500 rpm for 5 min at room temperature. We used 100 μL of the supernatant for the assessment. The concentrations of the proinflammatory cytokines/factors TNF-α, IL-1β, and IL-6 were analyzed using commercially available ELISA kits according to the manufacturer's protocol (IL-1β: Thermo Fisher; IL-6: R&D; TNF-α: R&D).

2.11. Statistical Analyses. All statistical analyses were performed using Student's t-test or one-way analysis of variance (ANOVA) with Bonferroni's post hoc test by using SPSS 18.0 (SPSS Inc., Chicago, IL, USA).

3. Results

3.1. Activation of Human Microglia by the Synthetic Aβ Oligomer. Studies have revealed that Aβ oligomers activate microglia to secrete proinflammatory factors [7, 8]. Therefore, we treated the human microglial HMC3 cells with Aβ oligomers [15, 16] (Figure 1(a)). Aβ oligomers demonstrated higher fluorescent signals in the thioflavin T assay than did monomeric Aβ (fold change: 2.13, $P < 0.001$, Figure 1(b)). Treatment of the HMC3 cells with Aβ oligomers for 48 hours increased the expression levels of the microglial activation markers CD11b [17] (fold change: 1.40, $P < 0.05$, Figures 1(c) and 1(d)), CD68 [17] (fold change: 1.41, $P < 0.01$, Figures 1(c) and 1(e)), and IBA1 [17] (fold change: 1.21, $P < 0.05$, Figures 1(c) and 1(f)) and the secretion of IL-6 (treatment vs no treatment: 399.60 vs 129.85 pg/mL, $P < 0.01$, Figure 1(g)). By contrast, the secretions of IL-1β (treatment vs no treatment: 0.42 pg/mL vs 0.34 pg/mL, Supplementary Figure 1A) and TNF-α (treatment vs no treatment: 6.73 pg/mL vs 11.21 pg/mL, Supplementary Figure 1A) were not altered by treatment with Aβ oligomers. Twenty-four-hour treatment with Aβ oligomers to HMC3 cells demonstrated consistent results of cytokine releases (Supplementary Figure 1A). These results demonstrated that Aβ oligomers can activate microglia and increase IL-6 secretion from microglia. Given 48 hours treatment with Aβ oligomers to HMC3 cells, it generated relatively pronounced IL-6 secretion compared with 24 hours treatment. Therefore, we chose this condition for further experiments.

3.2. Isorhamnetin Reduced Aβ-Mediated Microglial Activation. Evidence suggests that isorhamnetin has anti-inflammatory properties [18]. We examined whether isorhamnetin exerts an anti-inflammatory effect on microglia (Figure 2(a)). In the time-response experiments, treatment with isorhamnetin for 2 days demonstrated protective effects on Aβ toxicity in HMC3 cells (Supplementary Figure 1B, C). Treatment with Aβ oligomers increased the secretion of IL-6 (366.08 vs 86.92 pg/mL, $P < 0.001$ compared with no treatment, Figure 2(b)), whereas isorhamnetin significantly attenuated the increase in the IL-6 concentration (213.88 pg/mL, $P < 0.01$ compared with Aβ treatment only, Figure 2(b)) in activated HMC3. Meanwhile, Aβ oligomers also upregulated the microglial activation markers CD11b (fold change: 1.75, $P < 0.001$ compared with no treatment, Figures 2(c) and 2(d)), CD68 (fold change: 1.51, $P < 0.001$ compared with no treatment, Figures 2(c) and 2(e)), and IBA1 (fold change: 1.79, $P < 0.001$ compared with no treatment, Figures 2(c) and 2(f)) and impaired HMC3 viability, as observed in MTT (71.71%, $P < 0.01$ compared with no treatment, Figure 2(j)) and LDH assays (76.68%, $P < 0.01$ compared with no treatment, Figure 2(k)). Furthermore, isorhamnetin rescued the impairment of cell viability by Aβ oligomers (MTT: 83.28%, $P < 0.05$ compared with Aβ oligomers; LDH: 87.98%, $P < 0.05$ compared with Aβ oligomers, Figures 2(j) and 2(k)) and normalized the expression levels of CD11b (fold change: 1.37, $P < 0.05$ compared with Aβ treatment only, Figures 2(c) and 2(d)), CD68 (fold change: 1.25, $P < 0.05$ compared with Aβ treatment only, Figures 2(c) and 2(e)), and IBA1 (fold change: 1.46, $P < 0.05$ compared with Aβ treatment only, Figures 2(c) and 2(f)). In addition, treatment with Aβ oligomers increased the phosphorylation of IKKα (fold change: 1.61, $P < 0.01$, Figures 2(c) and 2(g)), IKKβ (fold change: 1.70, $P < 0.001$, Figures 2(c) and 2(h)), and NF-κB (fold change: 2.22, $P < 0.001$, Figures 2(c) and 2(i)), whereas isorhamnetin normalized this abnormal phosphorylation (p-IKKα: fold change: 0.66, $P < 0.001$ compared with Aβ treatment only, Figures 2(c) and 2(g); p-IKKβ: fold change: 0.73, $P < 0.001$ compared with Aβ treatment only, Figures 2(c) and 2(h); and p-NF-κB: fold change: 1.51, $P < 0.01$ compared with Aβ treatment only, Figures 2(c) and 2(i)). Treatment with the NF-κB inhibitor (EVP4593) to Aβ-activated HMC3 cells reduced the expression of CD11b (Aβ vs Aβ/EVP4593: fold change: 1.98 vs 1.29, $P < 0.05$, Supplementary Figure 2A, C), CD68 (Aβ vs Aβ/EVP4593:

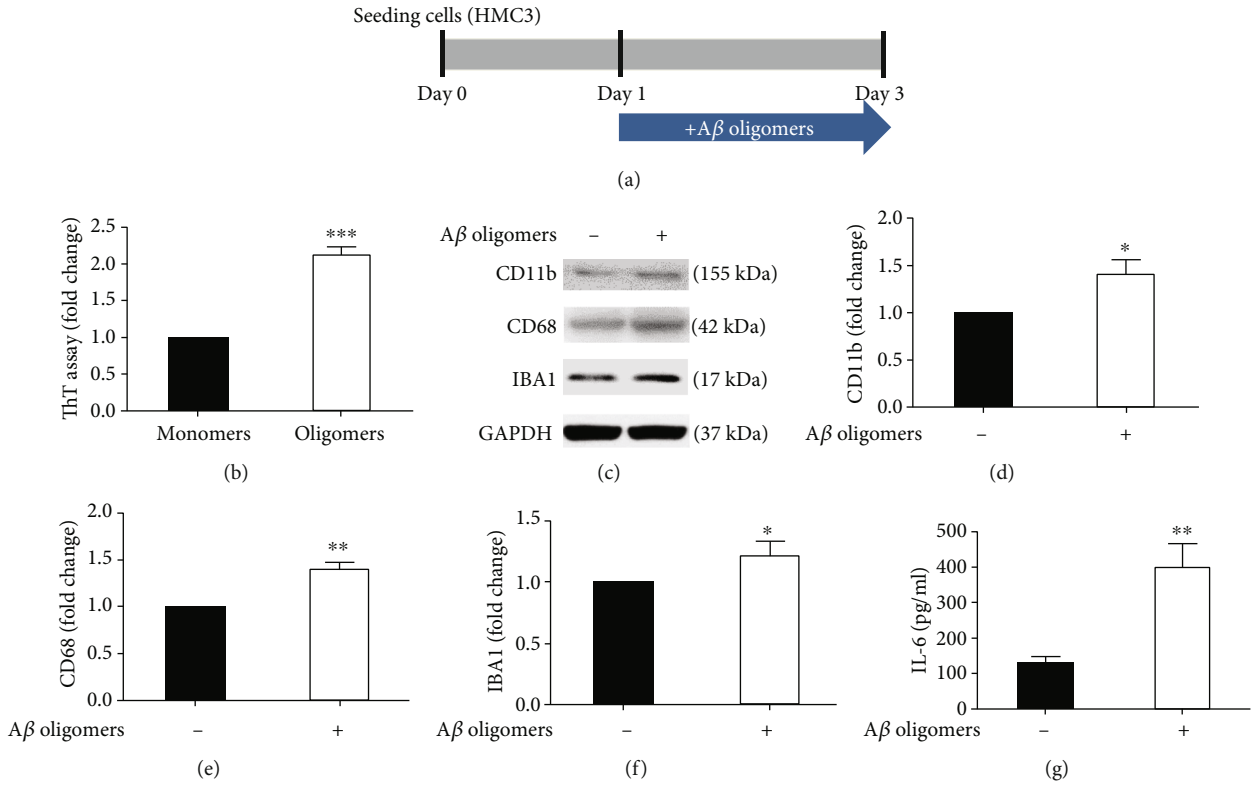

Figure 1: Activation of HMC3 microglia by Aβ oligomers. (a) Experimental flowchart. HMC3 cells were treated with Aβ oligomers (200 nM) for 48 hours. (b) The thioflavin T (ThT) assay demonstrated the misfolding of Aβ by oligomerization. (c–f) Treatment with Aβ oligomers upregulated the expression of the microglia activation markers CD11b, CD68, and IBA1. (g) Treatment with Aβ oligomers increased the IL-6 concentration in the culture medium. Data were analyzed using Student's t-test ($n = 3$, independent assays; $^{*}P < 0.05$, $^{**}P < 0.01$, $^{***}P < 0.001$, means ± SEM).

fold change: 1.71 vs 1.22, $P < 0.01$, Supplementary Figure 2A, D), and IBA1 (Aβ vs Aβ/EVP4593: fold change: 2.16 vs 1.42, $P < 0.05$, Supplementary Figure 2A, E), as well as increased the secretion of IL-6 (Aβ vs Aβ/EVP4593: 389.67 pg/mL vs 256.54 pg/mL, $P < 0.05$, Supplementary Figure 2F). Taken together, these results indicated that isorhamnetin reduced Aβ-mediated activation and IL-6 secretion in microglia.

3.3. Isorhamnetin Had a Neuroprotective Effect on Neurons Exposed to HMC3-Activated Conditional Medium. The SH-SY5Y cells were differentiated into neuronal cells through the addition of retinoic acid (RA) [19] (Figure 3(a)). The findings of MTT and LDH assays indicated the low cytotoxicity of isorhamnetin in the SH-SY5Y cells (LC_{90}: MTT: 10.56 μM, Figure 3(b); LDH: 12.40 μM, Figure 3(c)). Compared with no treatment, treatment with isorhamnetin resulted in a comparable number of $TUBB3^{+}$ neurons ($TUBB3^{+}$ neurons: isorhamnetin vs no treatment: 51.22% vs 50.38%, Figures 3(d) and 3(e)) and well-developed neurite outgrowth (neurite outgrowth, fold change: 1.02, Figures 3(d) and 3(f)). These results demonstrated that isorhamnetin resulted in low neurotoxicity and did not affect neuronal differentiation.

To investigate the anti-neuroinflammatory and neuroprotective effects of isorhamnetin, we exposed the SH-SY5Y-derived neuronal cells to the HMC3-conditioned medium and then treated them with isorhamnetin (Figure 4(a)). Given that treatment with Aβ oligomers significantly increased the secretion of IL-6 from the HMC3 cells, we treated the SH-SY5Y-derived neuronal cells with IL-6 at a concentration equal to that present in the HMC3-conditioned medium (350 pg/mL; Figure 2(b)). The results of MTT and LDH assays revealed that treatment with the HMC3-conditioned medium and IL-6 reduced cell viability (conditioned medium, MTT: 65.82%, $P < 0.01$, Figure 4(b); LDH: 62.17%, $P < 0.01$, Figure 4(c)), whereas isorhamnetin attenuated the impairment of cell viability (MTT: 81.39%, $P < 0.05$ compared with the HMC3-conditioned medium only, Figure 4(b); LDH: 79.53%, $P < 0.05$ compared with the HMC3-conditioned medium only, Figure 4(c)). Similarly, treatment with IL-6 impaired cell viability (MTT: 62.91%, $P < 0.01$, Figure 4(b); LDH: 60.34%, $P < 0.01$, Figure 4(c)), which was rescued by isorhamnetin treatment (MTT: 82.20%, $P < 0.05$ compared with IL-6 only, Figure 4(b); LDH: 76.31%, $P < 0.05$ compared with IL-6 only, Figure 4(c)).

Evidence suggests that neuroinflammation contributes to oxidative damage to neurons in AD [20]. Therefore, we assessed the production of ROS and neurite outgrowth. Treatment with the HMC3-conditioned medium increased ROS production (fold change: 1.87, $P < 0.01$ compared with control, Figures 4(d) and 4(e)) and reduced neurite outgrowth (fold change:0.43, $P < 0.01$ compared with control, Figures 4(d) and 4(f)). Isorhamnetin attenuated the

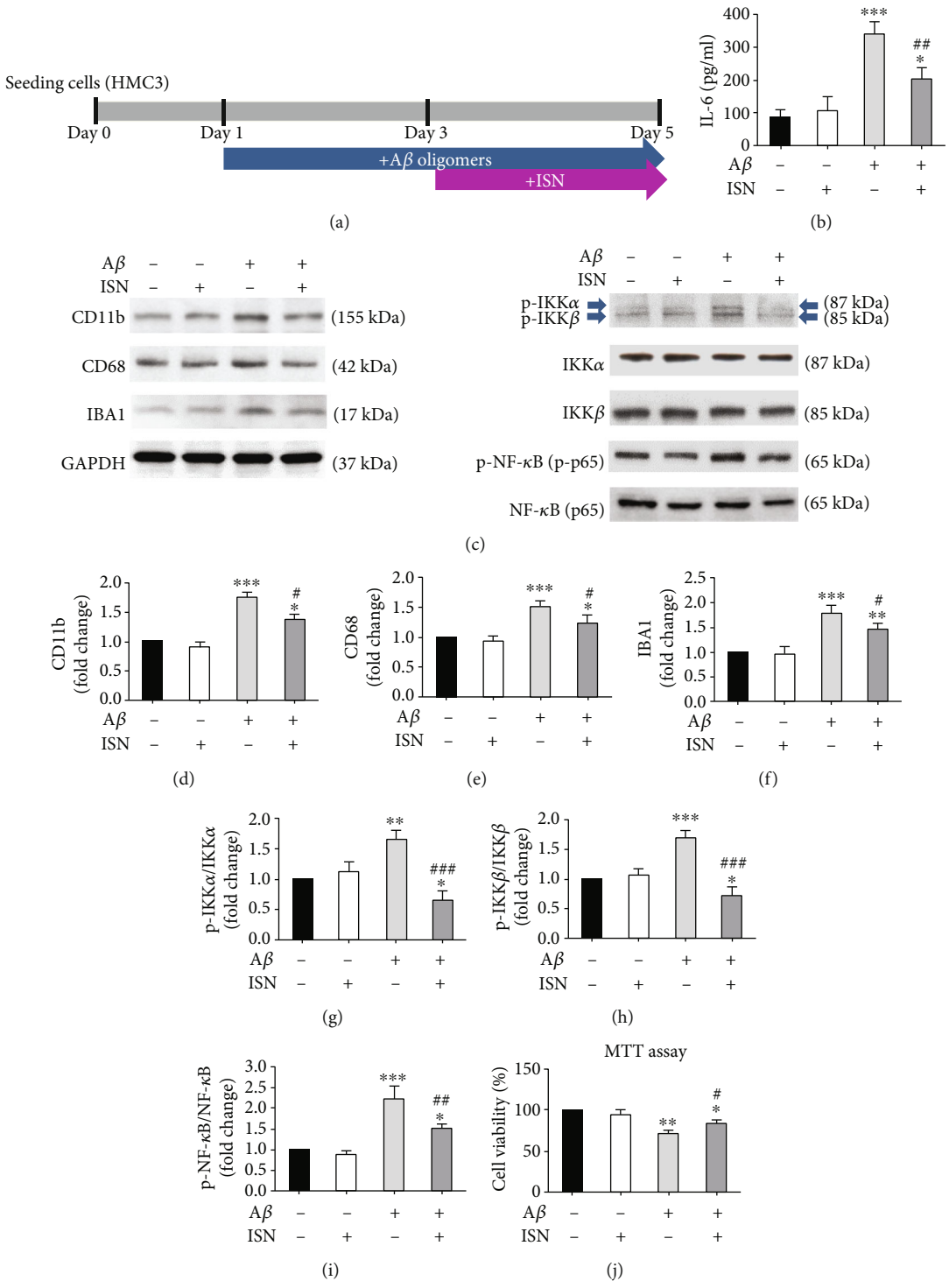

Figure 2: Continued.

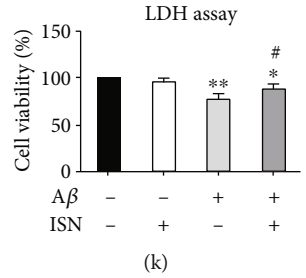

Figure 2: Isorhamnetin reduced the IL-6 concentration and NF-κB/p65 phosphorylation in Aβ-activated microglial cells. (a) Experimental flowchart. (b) Aβ (200 nM) increased the secretion of IL-6 on HMC cells, whereas cotreatment with isorhamnetin (10 μM) reduced the secretion of IL-6. (c–i) HMC3 cells with the upregulated expression of the microglial activation markers CD11b, CD68, and IBA1 increased the phosphorylation of IKKα, IKKβ, and NF-κB. Isorhamnetin cotreatment reduced the expression of CD11b, CD68, and IBA1 and normalized the phosphorylation of IKKα, IKKβ, and NF-κB. (j, k) Aβ reduced cell viability, as observed in MTT and LDH assays, whereas isorhamnetin improved cell viability. Data were analyzed using one-way ANOVA with Bonferroni's post hoc test ($^{*}P < 0.05$, $^{**}P < 0.01$, and $^{***}P < 0.001$ (control vs Aβ); $^{\#}P < 0.05$, $^{\#\#}P < 0.01$, and $^{\#\#\#}P < 0.001$ (Aβ vs Aβ/ISN), $n = 3$; means ± SEM). Aβ: Aβ oligomers; ISN: isorhamnetin.

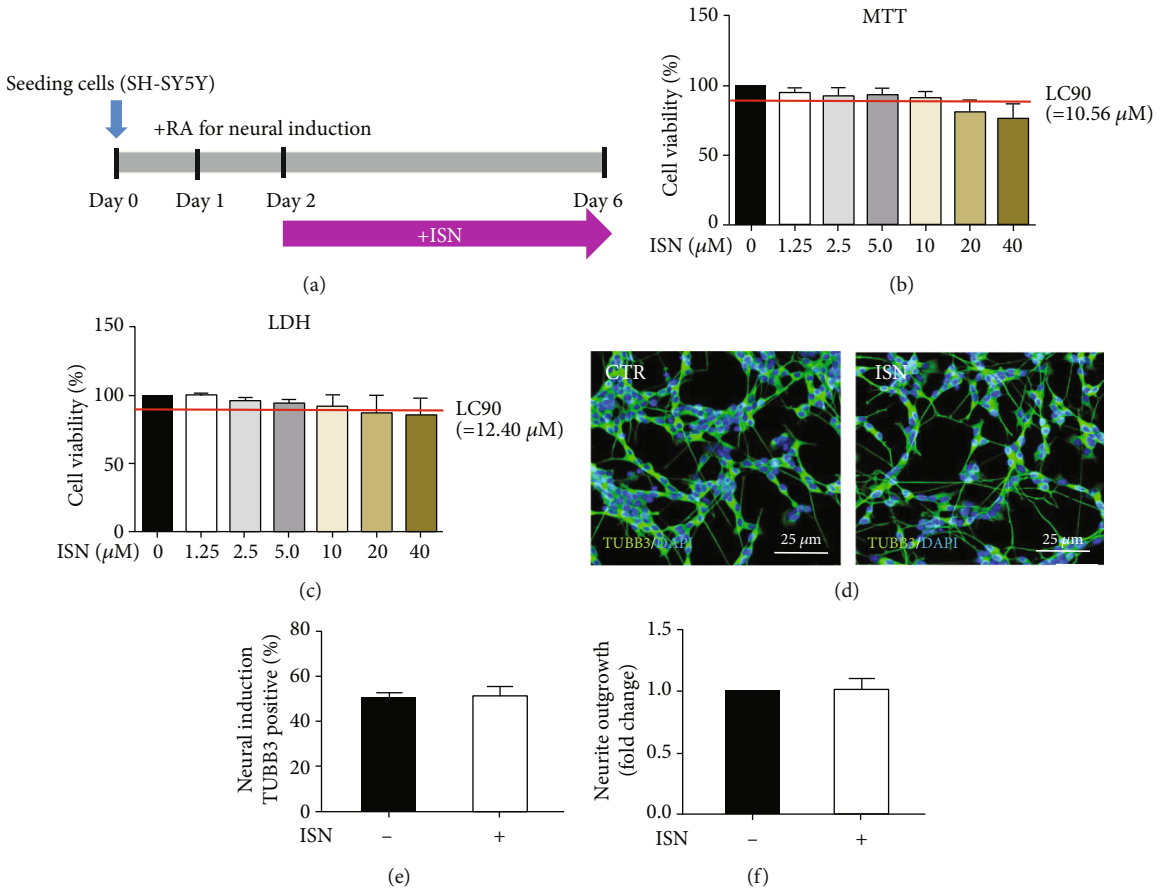

Figure 3: Neurotoxicity of isorhamnetin. (a) Experimental flowchart. SH-SY5Y cells were treated with isorhamnetin for 4 days. (b, c) LC_{90} determined by performing MTT and LDH assays. (d–f) Comparison of neurite outgrowth and the neuronal marker (TUBB3) between neurons treated without and with isorhamnetin (10 μM). Quantification of TUBB3-positive cells and neurite outgrowth through MetaMorph software. Data were analyzed using Student's t-test (independent assays, $n = 3$; means ± SEM). Scale bar, 25 μm. ISN: isorhamnetin.

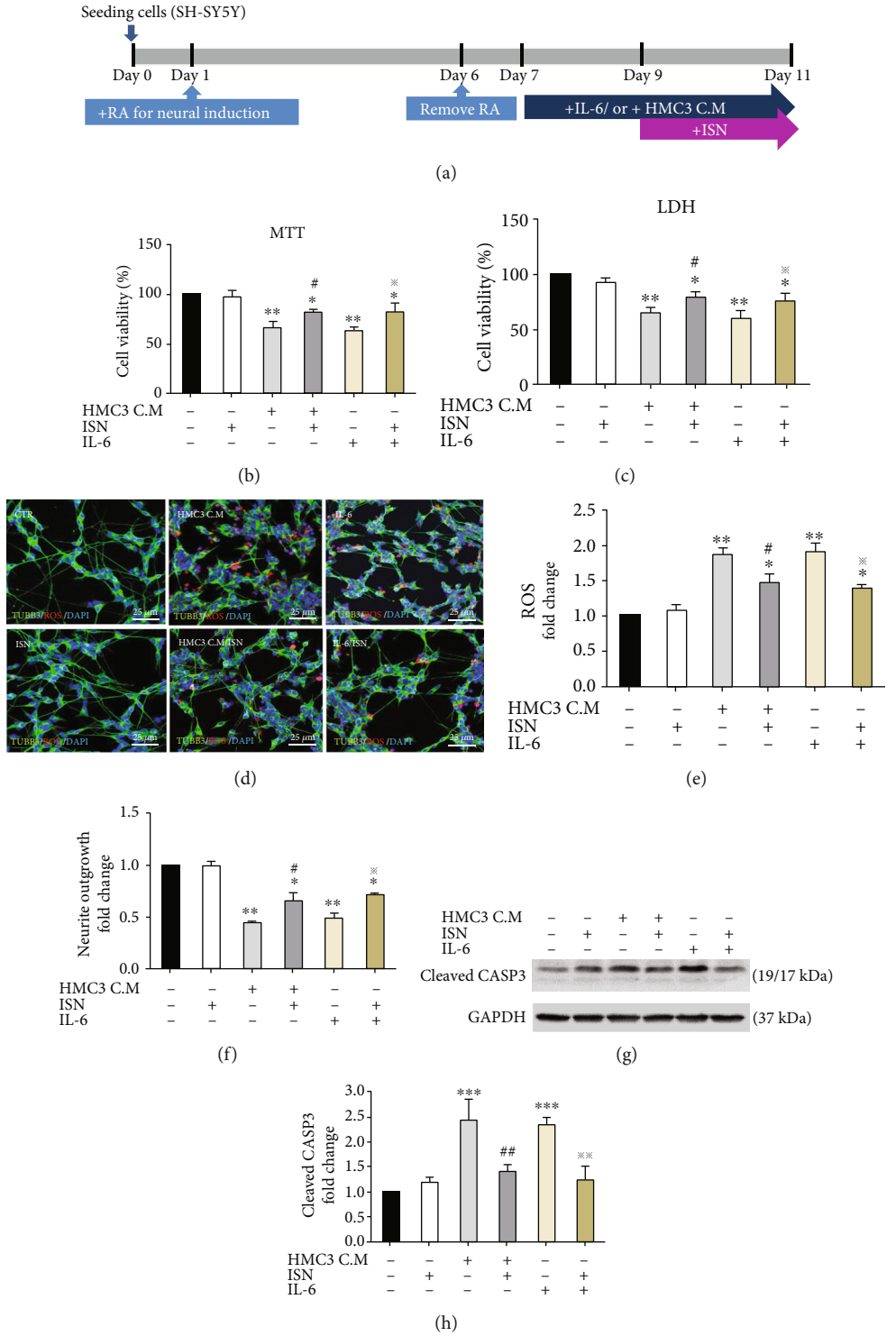

Figure 4: Isorhamnetin reduced ROS production, improved neurite outgrowth, and reduced apoptosis in the neurons treated with the HMC3-conditioned medium or IL-6. (a) Experimental design of neuroinflammation induced by treatment with the conditioned medium from Aβ-treated HMC3 cells or IL-6 (350 pg/mL). (b, c) Isorhamnetin (10 μM) maintained the viability of SH-SY5Y cells treated with the HMC3-conditioned medium or IL-6. (d–f) Isorhamnetin reduced the ROS level and attenuated neurite outgrowth impaired by treatment with the HMC3-conditioned medium or IL-6. Images were examined using MetaMorph software. Scale bar, 25 μm. (g, h) Western blotting indicated that neurons treated with the HMC3-conditioned medium or IL-6 increased the expression of cleaved caspase 3, whereas cotreatment with isorhamnetin reduced the expression of cleaved caspase 3. Data were analyzed using one-way ANOVA with Bonferroni's post hoc test ($^{*}P < 0.05$, $^{**}P < 0.01$, and $^{***}P < 0.001$ (control vs HMC3 C.M; control vs IL-6); $^{\#}P < 0.05$, $^{\#\#}P < 0.01$ (HMC3 C.M vs HMC3 C.M/ISN); $^{※}P < 0.05$, $^{※※}P < 0.01$ (IL-6 vs IL-6/ISN), $n = 3$; means ± SEM). HMC3 C.M: HMC3-conditional medium; ISN: isorhamnetin.

increased ROS production (fold change: 1.48, $P < 0.05$ compared with the HMC3-conditional medium only, Figures 4(d) and 4(e)) and impaired neurite outgrowth (fold change: 0.58, $P < 0.05$ compared with the HMC3-conditional medium only, Figures 4(d) and 4(f)). Furthermore, ROS production (fold change: 1.91, $P < 0.01$ compared with control, Figures 4(d) and 4(e)) and neurite outgrowth impairment (fold change: 0.52, $P < 0.01$ compared with control, Figures 4(d) and 4(f)) were enhanced by IL-6 treatment, whereas isorhamnetin attenuated the increased ROS production (fold change: 1.39, $P < 0.05$ compared with IL-6 only, Figures 4(d) and 4(e)) and impaired neurite growth (fold change: 0.66, $P < 0.05$ compared with IL-6 only, Figures 4(e) and 4(f)). The expression level of cleaved caspase 3 was increased following treatment with the HMC3-conditioned medium (fold change: 2.43, $P < 0.001$ compared with control, Figures 4(g) and 4(h)) or IL-6 (fold change: 2.30, $P < 0.001$ compared with control, Figures 4(g) and 4(h)). Isorhamnetin attenuated the increase in the expression level of cleaved caspase 3 caused by treatment with the HMC3-conditioned medium (fold change: 1.40, $P < 0.01$ compared with the conditioned medium only, Figures 4(g) and 4(h)) or IL-6 (fold change:1.24, $P < 0.01$ compared with IL-6 only, Figures 4(g) and 4(h)).

To further confirm the role of IL-6 as the main toxic cytokine to neurons, we treated SH-SY5Y-derived neuronal cells with IL-6 IgG and HMC3-conditioned medium concomitantly. IL-6 IgG reduced the levels of cleaved-caspase 3 (HMC3-conditioned medium vs HMC3-conditioned medium/IL-6 IgG: fold change: 2.91 vs 1.88, $P < 0.05$, Supplementary Figure 3A-B) and ROS (HMC3-conditioned medium vs HMC3-conditioned medium/IL-6 IgG: fold change: 4.24 vs 2.55, $P < 0.05$, Supplementary Figure 3C-D) compared with those exposed to HMC3-conditioned medium only. Moreover, treatment with IL-6 IgG improve the neurite outgrowth (HMC3-conditioned medium vs HMC3-conditioned medium/IL-6 IgG: fold change: 0.50 vs 0.71, $P < 0.05$, Supplementary Figure 3C, E). Taken together, these results indicated that IL-6 is the main neurotoxic constituent in HMC3-conditioned medium. Isorhamnetin demonstrated a neuroprotective effect against this neuroinflammation-mediated neurotoxicity.

3.4. Isorhamnetin Exerted a Neuroprotective Effect by Modulating the TYK2/STAT1 Pathway. It has shown that IL-6 activates canonical JAK2/STAT3 and noncanonical TYK2/STAT1 pathways to upregulate neuronal apoptosis [21, 22]. Therefore, we explored the potential of isorhamnetin to demonstrate neuroprotection by modulating these pathways (Figure 5(a)). Treatment with IL-6 or HMC3-conditional medium enhanced the phosphorylation of TYK2 (IL-6 treatment, fold change: 2.03, $P < 0.05$; HMC3-conditioned medium treatment, fold change: 1.97, $P < 0.01$, compared with no treatment, Figures 5(b) and 5(c)) and STAT1 (IL-6 treatment, fold change: 3.05, $P < 0.05$; HMC3-conditioned medium treatment, fold change: 1.95, $P < 0.01$, compared with no treatment, Figures 5(b) and 5(d)), as well as increased the expression level of cleaved caspase 3 (IL-6 treatment, fold change: 1.81, $P < 0.01$; HMC3-conditioned medium treatment, fold change: 2.39, $P < 0.001$, compared with no treatment, Figures 5(b) and 5(e)). Isorhamnetin normalized the phosphorylation of TYK2 (fold change: 1.05, $P < 0.05$ compared with IL-6 only; fold change: 1.28, $P < 0.05$ compared with HMC3-conditioned medium only, Figures 5(b) and 5(c)), STAT1 (fold change: 0.93, $P < 0.05$ compared with IL-6 only; fold change: 1.37, $P < 0.05$ compared with HMC3-conditioned medium only, Figures 5(b) and 5(d)), and cleaved caspase 3 (fold change: 1.03, $P < 0.05$ compared with IL-6 only; fold change: 1.70, $P < 0.05$ compared with HMC3-conditioned medium only, Figures 5(b) and 5(e)). Furthermore, treatment with the TYK2 inhibitor consistently normalized the expression level of cleaved caspase 3 (HMC3-conditioned medium vs HMC3-conditioned medium/inhibitor: fold change: 1.81 vs 1.02, $P < 0.001$; IL-6 vs IL-6/inhibitor, fold change: 1.58 vs 1.17, $P < 0.05$, Supplementary Figure 4A-B). On the other hand, the phosphorylation of JAK2 and STAT3 was not affected by treatment with HMC3-conditioned medium, IL-6, or isorhamnetin (Figures 5(b), 5(f), and 5(g)). These results indicated that isorhamnetin provided neuroprotection against IL-6-mediated neurotoxicity by modulating the TYK2/STAT1 pathway.

3.5. Isorhamnetin Counteracted Apoptotic Activation and Preserved Neuronal Viability Even under TYK2 Overexpression. To confirm the role of TYK2 in the neuroprotective effect of isorhamnetin, we overexpressed TYK2 in the SH-ST5Y-derived neuronal cells under treatment with the HMC3-conditional medium, IL-6, and isorhamnetin (Figure 6(a)). Under treatment with either the HMC3-conditional medium or IL-6, TYK2 overexpression significantly increased the phosphorylation of STAT1 (HMC3-conditioned medium treatment, fold change: 2.13, $P < 0.001$; IL-6 treatment, fold change: 1.65, $P < 0.01$, Figures 6(b) and 6(d)), the expression level of cleaved caspase 3 (HMC3-conditional medium treatment, fold change: 1.83, $P < 0.001$; IL-6 treatment, fold change: 1.96, $P < 0.001$, Figures 6(b) and 6(e)), and the levels of ROS (HMC3-conditional medium treatment, fold change: 1.58, $P < 0.01$; IL-6 treatment, fold change: 1.45, $P < 0.01$, Figures 7(a) and 7(b)) as well as impaired neurite outgrowth (HMC3-conditional medium treatment, fold change: 0.74, $P < 0.05$; IL-6 treatment, fold change: 0.71, $P < 0.05$, Figures 7(a) and 7(c)). In addition, TYK2 overexpression counteracted the effects of isorhamnetin on the reduction of the phosphorylation of TYK2 (HMC3-conditioned medium/isorhamnetin vs overexpressed TYK2/HMC3-conditioned medium/isorhamnetin, fold change: 0.60 vs 1.57, $P < 0.01$; IL-6/isorhamnetin vs overexpressed TYK2/IL-6/isorhamnetin, fold change: 0.56 vs 1.38, $P < 0.01$, Figures 6(b) and 6(c)) and STAT1 (HMC3-conditioned medium/isorhamnetin vs overexpressed TYK2/HMC3-conditioned medium/isorhamnetin, fold change: 0.69 vs 1.49, $P < 0.01$; IL-6/isorhamnetin vs overexpressed TYK2/IL-6/isorhamnetin, fold change: 0.71 vs 1.23, $P < 0.01$, Figures 6(b) and 6(d)), the expression level of cleaved caspase 3 (HMC3-conditioned medium/isorhamnetin vs overexpressed TYK2/HMC3-conditioned medium/isorhamnetin, fold change: 0.52 vs 1.27, $P < 0.01$; IL-6/

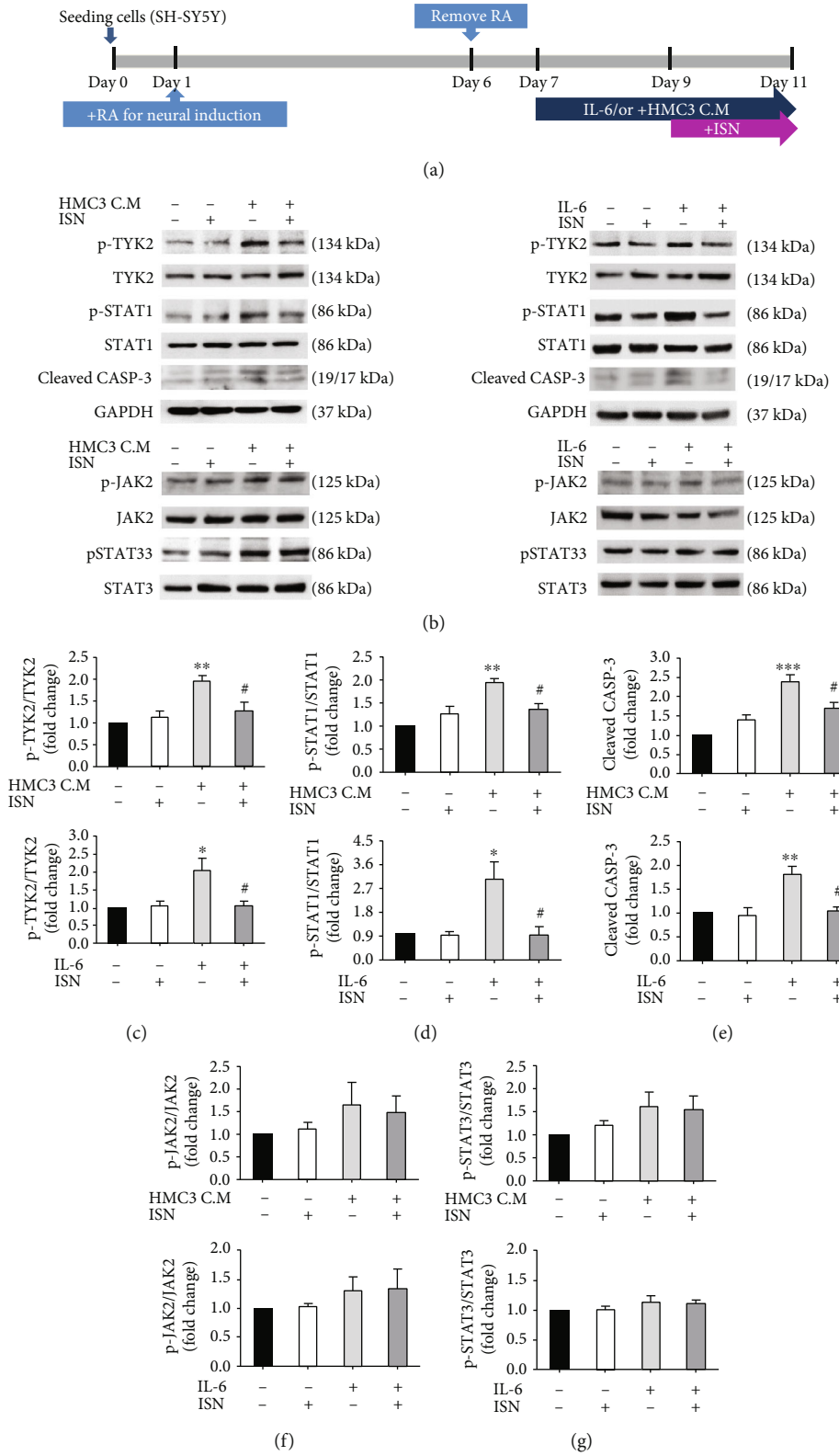

Figure 5: Isorhamnetin exerted neuroprotective effects by modulating the TYK2/STAT1 pathway. (a) Experimental design scheme. (b–g) Western blotting revealed the modulation of TYK2/STAT1 signaling and cleaved caspase 3 in the neurons treated with IL-6 (350 pg/mL) and/or isorhamnetin (10 μM) or HMC3-conditioned medium and/or isorhamnetin. Isorhamnetin impeded the activities of the apoptotic and TYK2/STAT1 pathway. Data were analyzed using one-way ANOVA with Bonferroni's post hoc test ($^{*}P < 0.05$, $^{**}P < 0.01$, and $^{***}P < 0.001$ (control vs IL-6; control vs IL-6/ISN and control vs HMC3 C.M; control vs HMC3 C.M/ISN); $^{\#}P < 0.05$ (IL-6 vs IL-6/ISN and HMC3 C.M vs HMC3 C.M/ISN), $n = 3$; means ± SEM). HMC3 C.M: HMC3-conditional medium; ISN: isorhamnetin.

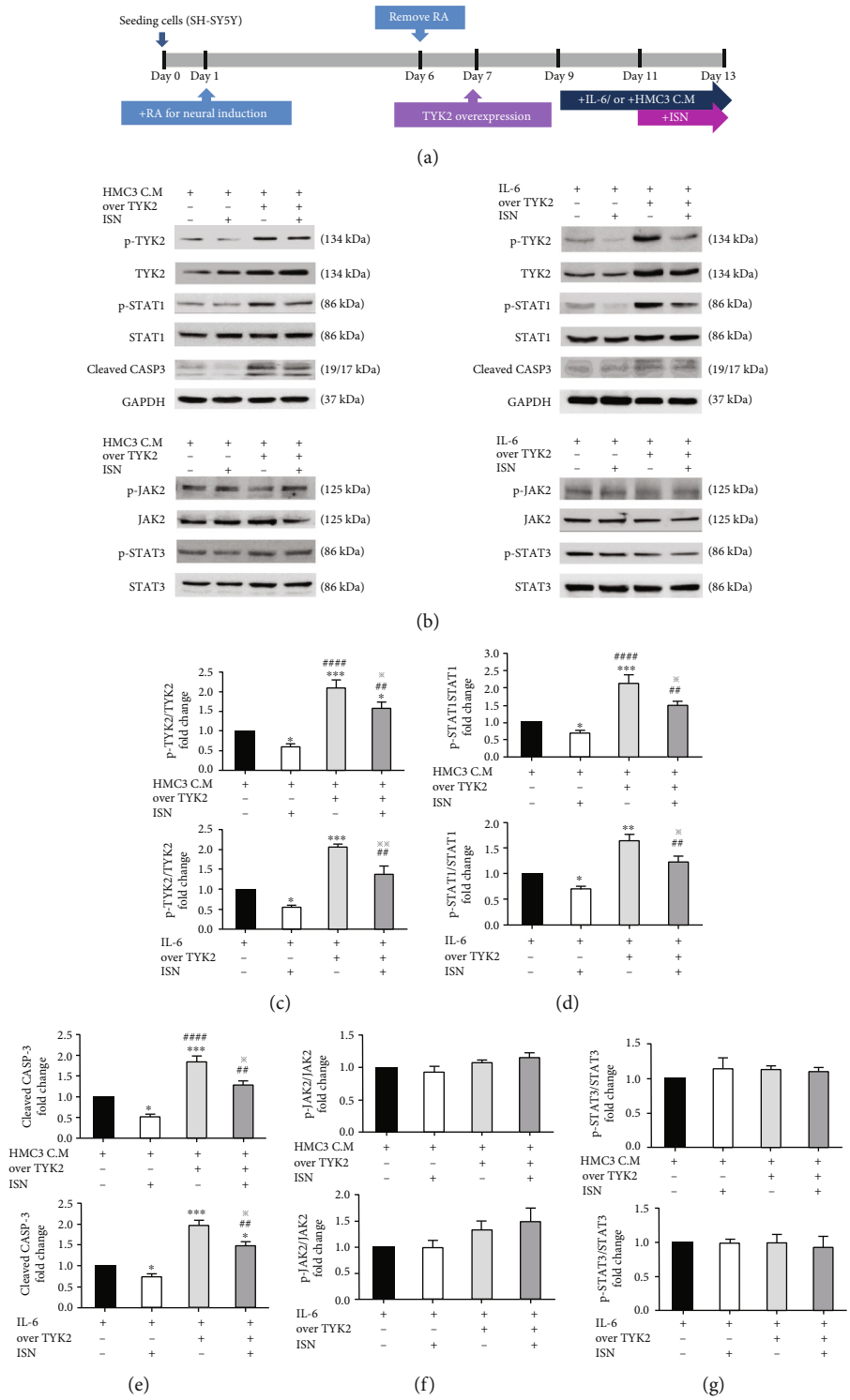

Figure 6: Isorhamnetin-induced neuroprotection attenuated the effect of TYK2 overexpression. (a) Experimental design scheme. (b–g) Immunoblots revealed TYK2/STAT1, JAK2/STAT3 signaling, and cleaved caspase 3 in HMC3-conditioned medium- or IL-6- (350 pg/mL) stimulated neurons treated with TYK2 overexpression and 10 μM isorhamnetin. Isorhamnetin abrogated the activities of apoptosis and the TYK2/STAT1 pathway. Data were analyzed using one-way ANOVA with Bonferroni's post hoc test ($^{*}P < 0.05$, $^{**}P < 0.01$, $^{***}P < 0.001$ (HMC3 C.M vs HMC3 C.M/ISN; HMC3 C.M vs overTYK2/HMC3 C.M; HMC3 C.M vs overTYK2/HMC3 C.M/ISN and IL-6 vs IL-6/ISN; IL-6 vs overTYK2/IL-6; IL-6 vs overTYK2/IL-6/ISN); $^{\#\#}P < 0.01$, $^{\#\#\#\#}P < 0.0001$ (HMC3 C.M/ISN vs overTYK2/HMC3 C.M; HMC3 C.M/ISN vs overTYK2/HMC3 C.M/ISN and IL-6/ISN vs overTYK2/IL-6; IL-6/ISN vs overTYK2/IL-6/ISN); $^{※}P < 0.05$, $^{※※}P < 0.01$ (overTYK2/HMC3 C.M vs overTYK2/HMC3 C.M/ISN and overTYK2/IL-6 vs overTYK2/IL-6/ISN), $n = 3$; means ± SEM). HMC3 C.M: HMC3-conditioned medium; ISN: isorhamnetin; overTYK2: overexpressed TYK2.

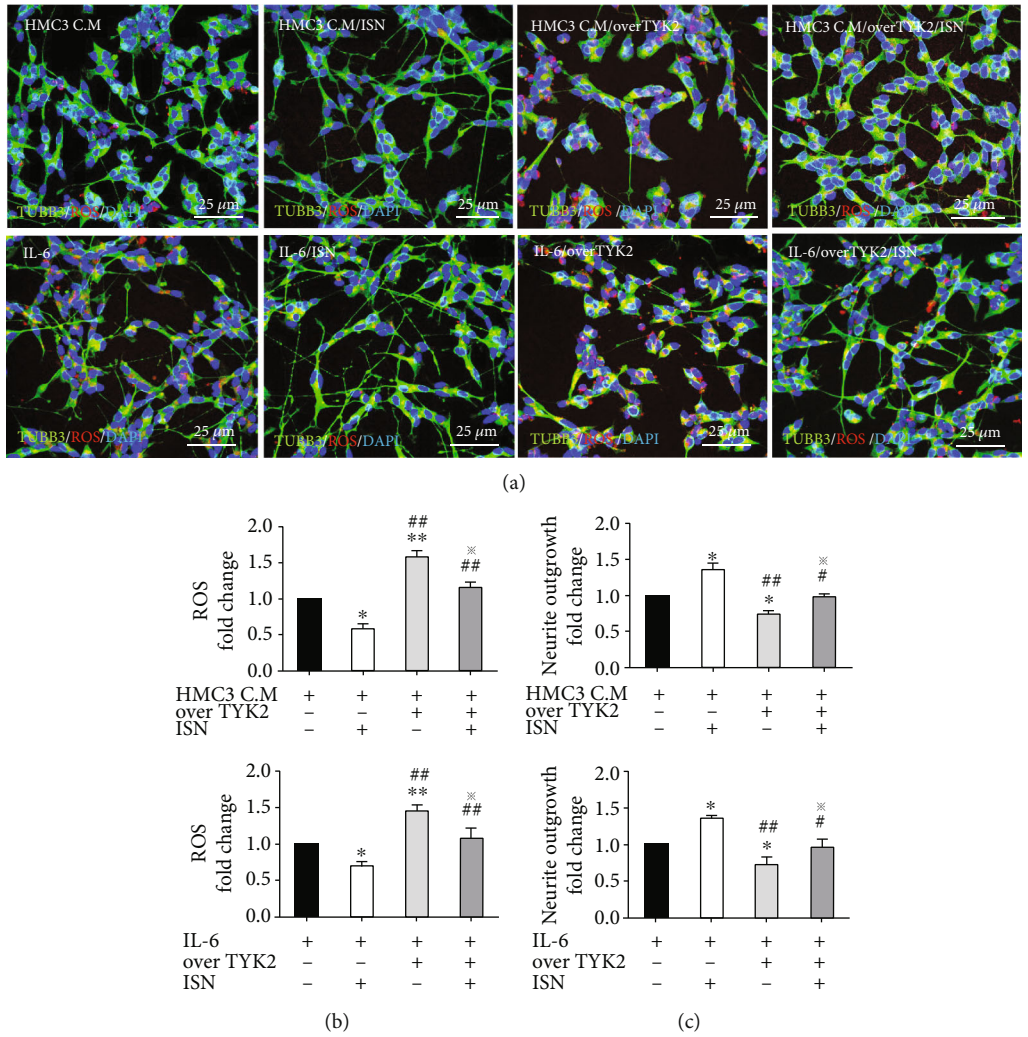

Figure 7: Isorhamnetin alleviated the impaired neurite growth and ROS overproduction induced by TYK2 overexpression. (a–c) Compared with TYK2 overexpression only, SH-SY5Y-derived neuronal cells cotreated with TYK2 overexpression and isorhamnetin (10 μM) exhibited lower ROS intensity, as measured through fluorescent staining. Measurement of neurite outgrowth differed between cotreatment with TYK2 overexpression and isorhamnetin and TYK2 overexpression only, as examined using MetaMorph software. Scale bar, 25 μm. Data were analyzed using one-way ANOVA with Bonferroni's post hoc test ($^{*}P < 0.05$, $^{**}P < 0.01$ (HMC3 C.M vs HMC3 C.M/ISN; HMC3 C.M vs overTYK2/HMC3 C.M; HMC3 C.M vs overTYK2/HMC3 C.M/ISN and IL-6 vs IL-6/ISN; IL-6 vs overTYK2/IL-6; IL-6 vs overTYK2/IL-6/ISN); $^{\#}P < 0.05$, $^{\#\#}P < 0.01$ (HMC3 C.M/ISN vs overTYK2/HMC3 C.M; HMC3 C.M/ISN vs overTYK2/HMC3 C.M/ISN and IL-6/ISN vs overTYK2/IL-6; IL-6/ISN vs overTYK2/IL-6/ISN); $^{※}P < 0.05$ (overTYK2/HMC3 C.M vs overTYK2/HMC3 C.M/ISN and overTYK2/IL-6 vs overTYK2/IL-6/ISN), $n = 3$; means ± SEM). HMC3 C.M: HMC3-conditioned medium; ISN: isorhamnetin; overTYK2: overexpressed TYK2.

isorhamnetin vs overexpressed TYK2/IL-6/isorhamnetin, fold change: 0.74 vs 1.48, $P < 0.01$, Figures 6(b) and 6(e)), the level of ROS (HMC3-conditioned medium/isorhamnetin vs overexpressed TYK2/HMC3-conditioned medium/isorhamnetin, fold change: 0.59 vs 1.16, $P < 0.01$; IL-6/isorhamnetin vs overexpressed TYK2/IL-6/isorhamnetin, fold change: 0.71 vs 1.08, $P < 0.01$, Figures 7(a) and 7(b)), and the impairment of neurite outgrowth (HMC3-conditioned medium/isorhamnetin vs overexpressed TYK2/HMC3-conditioned medium/isorhamnetin, fold change: 1.40 vs 0.98, $P < 0.05$; IL-6/isorhamnetin vs overexpressed TYK2/IL-6/isorhamnetin, fold change: 1.36 vs 0.97, $P < 0.05$, Figures 7(a) and 7(c)). The phosphorylation of JAK2 and STAT3 was not affected by either TYK2 overexpression or isorhamnetin treatment (Figures 6(b), 6(f), and 6(g)). These results indicated that isorhamnetin exerted its neuroprotective effect by mediating TYK2 expression or phosphorylation.

4. Discussion

Elucidating interactions between neuroinflammation and neurodegeneration can facilitate the development of new treatment strategies for AD. In this study, we established cell models to mimic neurodegenerative interactions among Aβ-activated microglia, inflammatory factors, and neurons. The results reveal that the Aβ-activated NF-κB inflammatory signaling pathway upregulated the expression of the microglial

activation markers CD11b, CD68, and IBA1 and increased the secretion of IL-6 from the HMC3 microglial cells. Both the HMC3-conditioned medium and IL-6 reduced cell viability, impaired neurite outgrowth, and increased ROS production and cleaved caspase 3 expression in the SH-SY5Y-derived neuronal cells. We observed that isorhamnetin attenuated the neuroinflammation and neurodegeneration induced by the HMC3-conditioned medium and IL-6. Furthermore, the results indicate that isorhamnetin suppressed neuroinflammation by deactivating the TYK2/STAT1 signaling pathway. These findings indicate the role of IL-6 in the nonautonomous interaction between microglia and neurons in AD. Furthermore, the findings demonstrate that the neuroprotective effect of isorhamnetin involves mediation of the noncanonical IL-6 signaling pathway, thus indicating the potential of isorhamnetin for use in AD treatment (Figure 8).

Our study demonstrates that IL-6 was the main constituent in the HMC3 conditional medium that regulated the neuroinflammatory interaction between microglia and neurons for neurodegeneration (Figures 2 and 4). Isorhamnetin suppressed the activation of the NF-κB pathway, downregulated the expression of the microglial activation markers, and reduced the secretion of IL-6 from the Aβ-activated microglia (Figure 2). In lipopolysaccharide-induced BV2 mouse microglial cells, isorhamnetin reduced oxidative stress by reactivating TLR4 and the NF-κB pathway [23]. Moreover, isorhamnetin was reported to attenuate oxidative stress and neurotoxicity by upregulating NRF2/HO-1 [24]. Similar to isorhamnetin, Gx-50, a natural compound derived from *Zanthoxylum bungeanum*, suppressed the activation of TLR4 and its downstream MyD88 and TRAF6 and reduced the expression levels of TNF-α, IL-1β, nitric oxide (NO), prostaglandin E2, inducible NO synthase, and cyclooxygenase-2 in Aβ-activated primary rat microglia and APP$^+$ transgenic mice [7]. In addition, KHG26792, a novel azetidine derivative, attenuated the activation of the NF-κB signaling pathway and reduced the expression levels of IL-6, IL-1β, TNF-α, NO, ROS, and NADHP oxidase in Aβ-treated rat primary microglia [25]. These compounds exert neuroprotective effects possibly by mediating neuroinflammation, and the neuroprotective potential of these compounds should be further explored in neuronal and animal models for AD.

The canonical downstream pathway of IL-6 in inflammatory cells and microglia involves the activation of JAK2 and STAT3. IL-6 upregulated the expression of STAT3 in rodent neurons [26, 27]. However, the downstream signaling of IL-6 in human neurons remains contentious. The phosphorylation of STAT3 was upregulated on SH-SY5Y cells exposed to a high IL-6 concentration (10 ng/mL) [27]. In this study, we observed that HMC3-conditioned medium and a low IL-6 concentration (350 pg/mL; this concentration was equal to that in the HMC3-conditioned medium) caused neurotoxicity without upregulating the JAK2/STAT3 signaling pathway in the SH-SY5Y-derived neuronal cells (Figure 5). However, the noncanonical TYK2/STAT1 phosphorylation was upregulated following treatment with a low IL-6 concentration. TYK2, a member of the JAK family,

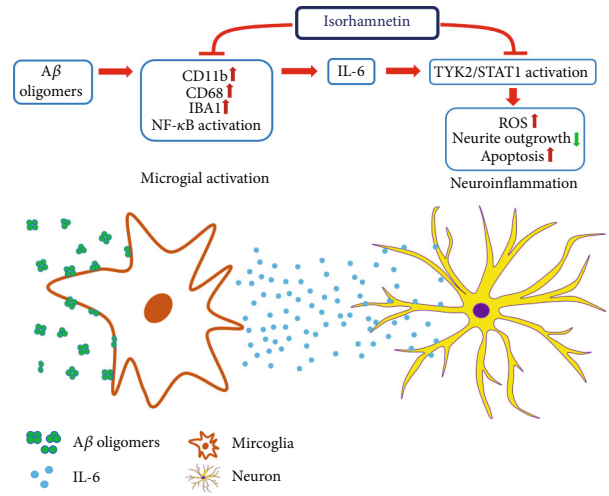

Figure 8: The anti-inflammatory and neuroprotective effects of isorhamnetin on Alzheimer's disease. Aβ oligomers activate microglia to secrete IL-6, which further upregulates the TYK2/STAT1 pathway to increase production of reactive oxygen species (ROS), impair neurite outgrowth, and upregulate apoptosis on neurons (neuroinflammation). Isorhamnetin attenuates microglial activation and IL-6 secretion and downregulates the TYK2/STAT1 pathway to reduce IL-6-mediated neuroinflammation.

is associated with the intracellular domain of various cytokines that affect inflammatory responses [28]. In addition, the activation of the TYK2/STAT signaling pathway is associated with inflammatory responses, apoptosis, and ROS production [21, 22, 29]. Knockout of TYK2 mitigated neuronal death in APP/PS1 transgenic mice [23]. Our results indicate that isorhamnetin downregulated TYK2/STAT1 phosphorylation to attenuate the neurotoxic effects of IL-6, whereas TYK2 overexpression attenuated the neuroprotective effect of isorhamnetin (Figures 6 and 7). These results highlight the role of TYK2/STAT1 signaling in AD pathogenesis and isorhamnetin in protection against neuroinflammation.

Isorhamnetin, the main constituent of flavonoids, possesses antioxidative properties [30, 31]. In addition to protection against neuroinflammation, isorhamnetin exerts antioxidative and neurotropic effects. Isorhamnetin potentiated the effect of the nerve growth factor on the neurite outgrowth of PC12 cells [32]. In mice treated with scopolamine, isorhamnetin reduced oxidative stress and suppressed cholinergic signaling pathways, reduced cholinesterase activity [33], and improved impairment in spatial and nonspatial learning and memory [34]. Furthermore, treatment with isorhamnetin in stroke mice improved the integrity of the blood-brain barrier and reduced the levels of IL-1β, IL-6, and TNF-α in the ischemic cortex [35]. Together with our findings, these results suggest the pleiotropic effects of isorhamnetin for neuroprotection. Isorhamnetin can effectively penetrate the blood-brain barrier [36] and thus can be used for treating neurological diseases. Furthermore, our results reveal that isorhamnetin exhibite neuroprotection in the SH-SY5Y-derived neuronal cells following IL-6 treatment, suggesting that isorhamnetin can reduce neuroinflammation-mediated neurodegeneration.

In conclusion, our study indicates the pivotal role of IL-6 in mediating nonautonomous interactions between microglia and neurons in AD and that the TYK2/STAT1 signaling pathway can be a target for treating neuroinflammation in AD. In addition, our results demonstrate that isorhamnetin alleviates neuroinflammation by deactivating the TYK2/STAT1 signaling pathway. These findings provide new insights into neuroinflammatory pathogenesis as well as a novel therapeutic target for AD. Additional animal studies should be conducted to validate our findings.

Data Availability

The datasets generated during the current study are available from the corresponding author upon reasonable request.

Conflicts of Interest

The authors declare no competing interests.

Authors' Contributions

P.-C.W. did the execution of experiments, data analysis and interpretation, and paper drafting; C.-M.C. and G.-J.L.-C. did the conceptual design and data interpretation; Y.C. and Y.-S.L. did the execution of experiments; K.-H.C. did the conceptual design, data analysis and interpretation, funding acquisition, and drafting and finalizing of the paper.

Acknowledgments

This study was supported by grants from the Chang Gung Memorial Hospital, Taipei, Taiwan (CMRPG3L0042) and Ministry of Science and Technology, Taiwan (MOST106-2314-B-182-037-MY2, MOST108-2811-B-182-531, MOST109-2811-B-182-526, and MOST110-2811-B-182-534).

Supplementary Materials

Supplementary Figure 1: time-response experiments of Aβ oligomers and isorhamnetin in HMC3 cells. (A) Treatment with Aβ oligomers (200 nM) for 24 or 48 hours increased IL-6 release, whereas the secretions of IL-1β and TNF-α were not affected by Aβ oligomers. (B) Experimental flowchart. HMC3 cells activated by Aβ were treated with isorhamnetin (10 μM) for 24 or 48 hours. (C) In Aβ-activated HMC3 cells, treatment with isorhamnetin for 24 hours did not reduce the secretion of IL-6, while 48-hour treatment reduced the IL-6 secretion to baseline. Data were analyzed using one-way ANOVA with Bonferroni's post hoc test ($^{*}P < 0.05$, $^{**}P < 0.01$ (control vs Aβ); $^{\#\#}P < 0.05$ (Aβ vs Aβ/ISN), $n = 3$; means ± SEM). Aβ: Aβ oligomers; ISN: isorhamnetin. Supplementary Figure 2: NF-κB inhibitor suppressed the Aβ-induced activation of HMC3 cells. (A) Western blot in HMC3 cells treated with Aβ oligomers (200 nM) or EVP4593 (NF-κB inhibitor, 1 μM). Treatment with EVP4593 for 48 hours reduced phosphorylation of NF-κB (B), the expression of CD11b (C), CD68 (D), IBA1(E), and IL-6 secretion (F). Data were analyzed using one-way ANOVA with Bonferroni's post hoc test or Student's t-test ($^{*}P < 0.05$, $^{**}P < 0.01$, and $^{***}P < 0.001$ (control vs Aβ); $^{\#}P < 0.05$, $^{\#\#}P < 0.01$, and $^{\#\#\#}P < 0.001$ (Aβ vs Aβ/EVP4593), $n = 3$; means ± SEM). Aβ: Aβ oligomers; EVP4593: NF-κB inhibitor. Supplementary Figure 3: IL-6 IgG neutralized the effect of HMC3 activated-conditional medium on SH-SY5Y-derived neurons. (A-B) IL-6 IgG (5 ng/mL for 48 hours) reduced the expression cleaved caspase 3 in SH-SY5Y-derived neurons treated with HMC3-conditioned medium. (C-D) IL-6 IgG reduced ROS production in SH-SY5Y-derived neurons treated with HMC3-conditioned medium. (E) The impaired neurite outgrowth by HMC3-conditioned medium was rescued by IL-6-neutralizing antibody. Images were measured using MetaMorph software. Scale bar, 25 μm. Data were analyzed using one-way ANOVA with Bonferroni's post hoc test ($^{*}P < 0.05$, $^{***}P < 0.001$ (control vs HMC3 C.M; control vs HMC3 C.M/IL-6 IgG); $^{\#}P < 0.05$ (HMC3 C.M vs HMC3 C.M/IL-6 IgG), $n = 3$; means ± SEM). HMC3 C.M: HMC3-conditioned medium; IL-6 IgG: IL-6 neutralized antibody. Supplementary Figure 4: TYK2 inhibitor suppressed IL-6 or HMC3-conditioned medium induced apoptosis in SH-SY5Y-derived neurons. (A-B) In SH-SY5Y-derived neurons, the upregulation of cleaved caspase 3 by IL-6 (350 pg/mL) or HMC3-conditioned medium was counteracted by treatment with the TYK2 inhibitor (1 μM) for 48 hours. Data were analyzed using one-way ANOVA with Bonferroni's post hoc test ($^{**}P < 0.01$, $^{***}P < 0.001$ (control vs IL-6; control vs HMC3 C.M); $^{\#}P < 0.05$ (IL-6 vs IL-6/TYK2 inhibitor); $^{\times\times\times}P < 0.001$ (HMC3 C.M vs HMC3 C.M/TYK2 inhibitor), $n = 3$; means ± SEM). HMC3 C.M: HMC3 activated-conditioned medium. *(Supplementary Materials)*

References

[1] H. W. Querfurth and F. M. LaFerla, "Alzheimer's Disease," *New England Journal of Medicine*, vol. 362, no. 4, pp. 329–344, 2010.

[2] R. J. Caselli, T. G. Beach, R. Yaari, and E. M. Reiman, "Alzheimer's disease a century later," *The Journal of Clinical Psychiatry*, vol. 67, no. 11, pp. 1784–1800, 2006.

[3] C. L. Masters, G. Simms, N. A. Weinman, G. Multhaup, B. L. McDonald, and K. Beyreuther, "Amyloid plaque core protein in Alzheimer disease and down syndrome," *Proceedings of the National Academy of Sciences of the United States of America*, vol. 82, no. 12, pp. 4245–4249, 1985.

[4] M. S. Parihar and T. Hemnani, "Alzheimer's disease pathogenesis and therapeutic interventions," *Journal of Clinical Neuroscience*, vol. 11, no. 5, pp. 456–467, 2004.

[5] Z. Cai, M. D. Hussain, and L. J. Yan, "Microglia, neuroinflammation, and beta-amyloid protein in Alzheimer's disease," *The International Journal of Neuroscience*, vol. 124, no. 5, pp. 307–321, 2014.

[6] S. Liu, Y. Liu, W. Hao et al., "TLR2 is a primary receptor for Alzheimer's amyloid β peptide to trigger neuroinflammatory activation," *Journal of Immunology*, vol. 188, no. 3, pp. 1098–1107, 2012.

[7] S. Shi, D. Liang, Y. Chen et al., "Gx-50 reduces β-amyloid-induced TNF-α, IL-1β, NO, and PGE2 expression and inhibits NF-κB signaling in a mouse model of Alzheimer's disease,"

European Journal of Immunology, vol. 46, no. 3, pp. 665–676, 2016.

[8] B. Li, K. Bedard, S. Sorce, B. Hinz, M. Dubois-Dauphin, and K. H. Krause, "NOX4 expression in human microglia leads to constitutive generation of reactive oxygen species and to constitutive IL-6 expression," *Journal of Innate Immunity*, vol. 1, no. 6, pp. 570–581, 2009.

[9] A. Escrig, C. Canal, P. Sanchis et al., "IL-6 trans-signaling in the brain influences the behavioral and physio- pathological phenotype of the Tg2576 and 3xTgAD mouse models of Alzheimer's disease," *Brain, Behavior, and Immunity*, vol. 82, pp. 145–159, 2019.

[10] J. A. Nicoll, R. E. Mrak, D. I. Graham et al., "Association of interleukin-1 gene polymorphisms with Alzheimer's disease," *Annals of Neurology*, vol. 47, no. 3, pp. 365–368, 2000.

[11] C. Capurso, V. Solfrizzi, A. D'Introno et al., "Interleukin 6-174 G/C promoter gene polymorphism and sporadic Alzheimer's disease: geographic allele and genotype variations in Europe," *Experimental Gerontology*, vol. 39, no. 10, pp. 1567–1573, 2004.

[12] S. M. McCusker, M. D. Curran, K. B. Dynan et al., "Association between polymorphism in regulatory region of gene encoding tumour necrosis factor α and risk of Alzheimer's disease and vascular dementia: a case-control study," *Lancet*, vol. 357, no. 9254, pp. 436–439, 2001.

[13] J. H. Yang, S. C. Kim, B. Y. Shin et al., "*O* -methylated flavonol isorhamnetin prevents acute inflammation through blocking of NF-κB activation," *Food and Chemical Toxicology*, vol. 59, pp. 362–372, 2013.

[14] A. Iida, T. Usui, F. Zar Kalai, J. Han, H. Isoda, and Y. Nagumo, "Protective effects of Nitraria retusa extract and its constituent isorhamnetin against amyloid β-induced cytotoxicity and amyloid β aggregation," *Bioscience, Biotechnology, and Biochemistry*, vol. 79, no. 9, pp. 1548–1551, 2015.

[15] B. A. Chromy, R. J. Nowak, M. P. Lambert et al., "Self-assembly of Aβ1-42 into globular neurotoxins," *Biochemistry*, vol. 42, no. 44, pp. 12749–12760, 2003.

[16] N. Janabi, S. Peudenier, B. Héron, K. H. Ng, and M. Tardieu, "Establishment of human microglial cell lines after transfection of primary cultures of embryonic microglial cells with the SV40 large T antigen," *Neuroscience Letters*, vol. 195, no. 2, pp. 105–108, 1995.

[17] C. Dello Russo, N. Cappoli, I. Coletta et al., "The human microglial HMC3 cell line: where do we stand? A systematic literature review," *Journal of Neuroinflammation*, vol. 15, no. 1, p. 259, 2018.

[18] S. Chirumbolo, "Anti-inflammatory action of isorhamnetin," *Inflammation*, vol. 37, no. 4, pp. 1200-1201, 2014.

[19] Y. C. Chen, Y. J. Chiu, C. H. Lin et al., "Indole compound NC009-1 augments APOE and TRKA in Alzheimer's disease cell and mouse models for neuroprotection and cognitive improvement," *Journal of Alzheimer's Disease*, vol. 67, no. 2, pp. 737–756, 2019.

[20] U. Ganguly, U. Kaur, S. S. Chakrabarti et al., "Oxidative stress, neuroinflammation, and NADPH oxidase: implications in the pathogenesis and treatment of Alzheimer's disease," *Oxidative Medicine and Cellular Longevity*, vol. 2021, Article ID 7086512, 19 pages, 2021.

[21] J. Wan, A. K. Fu, F. C. Ip et al., "Tyk2/STAT3 signaling mediates beta-amyloid-induced neuronal cell death: implications in Alzheimer's disease," *The Journal of Neuroscience*, vol. 30, no. 20, pp. 6873–6881, 2010.

[22] S. Dedoni, M. C. Olianas, and P. Onali, "Interferon-β induces apoptosis in human SH-SY5Y neuroblastoma cells through activation of JAK–STAT signaling and down-regulation of PI3K/Akt pathway," *Journal of Neurochemistry*, vol. 115, no. 6, pp. 1421–1433, 2010.

[23] S. Y. Kim, C. Y. Jin, C. H. Kim et al., "Isorhamnetin alleviates lipopolysaccharide-induced inflammatory responses in BV2 microglia by inactivating NF-κB, blocking the TLR4 pathway and reducing ROS generation," *International Journal of Molecular Medicine*, vol. 43, no. 2, pp. 682–692, 2019.

[24] Y. Wu, L. Fan, Y. Wang, J. Ding, and R. Wang, "Isorhamnetin alleviates high glucose- aggravated inflammatory response and apoptosis in oxygen-glucose deprivation and reoxygenation-induced HT22 hippocampal neurons through Akt/SIRT1/Nrf2/HO-1 signaling pathway," *Inflammation*, vol. 44, no. 5, pp. 1993–2005, 2021.

[25] S. J. Yang, J. Kim, S. E. Lee, J. Y. Ahn, S. Y. Choi, and S. W. Cho, "Anti-inflammatory and anti-oxidative effects of 3-(naphthalen-2-yl(propoxy)methyl)azetidine hydrochloride on β-amyloid-induced microglial activation," *BMB Reports*, vol. 50, no. 12, pp. 634–639, 2017.

[26] R. A. Quintanilla, D. I. Orellana, C. Gonzalez-Billault, and R. B. Maccioni, "Interleukin-6 induces Alzheimer-type phosphorylation of tau protein by deregulating the cdk5/p35 pathway," *Experimental Cell Research*, vol. 295, no. 1, pp. 245–257, 2004.

[27] K. W. Park, S. E. Nozell, and E. N. Benveniste, "Protective role of STAT3 in NMDA and glutamate-induced neuronal death: negative regulatory effect of SOCS3," *PLoS One*, vol. 7, no. 11, article e50874, 2012.

[28] K. Ghoreschi, A. Laurence, and J. J. O'Shea, "Janus kinases in immune cell signaling," *Immunological Reviews*, vol. 228, no. 1, pp. 273–287, 2009.

[29] J. J. O'Shea and R. Plenge, "JAK and STAT signaling molecules in immunoregulation and immune-mediated disease," *Immunity*, vol. 36, no. 4, pp. 542–550, 2012.

[30] G. Gong, Y. Y. Guan, Z. L. Zhang et al., "Isorhamnetin: a review of pharmacological effects," *Biomedicine & Pharmacotherapy*, vol. 128, article 110301, 2020.

[31] J. H. Yang, B. Y. Shin, J. Y. Han et al., "Isorhamnetin protects against oxidative stress by activating Nrf2 and inducing the expression of its target genes," *Toxicology and Applied Pharmacology*, vol. 274, no. 2, pp. 293–301, 2014.

[32] S. L. Xu, R. C. Choi, K. Y. Zhu et al., "Isorhamnetin, a flavonol aglycone from Ginkgo biloba L., induces neuronal differentiation of cultured PC12 cells: potentiating the effect of nerve growth factor," *Evidence-based Complementary and Alternative Medicine*, vol. 2012, Article ID 278273, 11 pages, 2012.

[33] D. N. Olennikov, N. I. Kashchenko, N. K. Chirikova, A. Akobirshoeva, I. N. Zilfikarov, and C. Vennos, "Isorhamnetin and quercetin derivatives as anti-acetylcholinesterase principles of marigold (calendula officinalis) flowers and preparations," *International Journal of Molecular Sciences*, vol. 18, no. 8, p. 1685, 2017.

[34] I. O. Ishola, M. O. Osele, M. C. Chijioke, and O. O. Adeyemi, "Isorhamnetin enhanced cortico-hippocampal learning and memory capability in mice with scopolamine-induced amnesia: role of antioxidant defense, cholinergic and BDNF signaling," *Brain Research*, vol. 1712, pp. 188–196, 2019.

[35] J. J. Zhao, J. Q. Song, S. Y. Pan, and K. Wang, "Treatment with Isorhamnetin protects the brain against ischemic injury in mice," *Neurochemical Research*, vol. 41, no. 8, pp. 1939–1948, 2016.

[36] L. Rangel-Ordóñez, M. Nöldner, M. Schubert-Zsilavecz, and M. Wurglics, "Plasma levels and distribution of flavonoids in rat brain after single and repeated doses of standardized Ginkgo biloba extract EGb 761®," *Planta Medica*, vol. 76, no. 15, pp. 1683–1690, 2010.

Hindawi
Oxidative Medicine and Cellular Longevity
Volume 2022, Article ID 6906722, 14 pages
https://doi.org/10.1155/2022/6906722

Research Article

Anxiolytic Effect of Carvedilol in Chronic Unpredictable Stress Model

Caren Nádia Soares de Sousa,[1] **Ingridy da Silva Medeiros**,[1] **Germana Silva Vasconcelos**,[1] **Gabriel Ângelo de Aquino**,[1] **Francisco Maurício Sales Cysne Filho**,[1] **Jamily Cunha de Almeida**,[1] **Ana Paula Negreiros Nunes Alves**,[2] **Danielle S. Macêdo**,[1] **Luzia Kalyne Almeida Moreira Leal**,[3] **and Silvânia Maria Mendes Vasconcelos**[1]

[1]*Neuropsychopharmacology Laboratory, Drug Research and Development Center, Department of Physiology and Pharmacology, Faculty of Medicine, Federal University of Ceará, Fortaleza, Ceará, Brazil*
[2]*Histopathology Laboratory, Drug Research and Development Center, Department of Physiology and Pharmacology, Faculty of Medicine, Federal University of Ceará, Fortaleza, Ceará, Brazil*
[3]*Center for Pharmaceutical and Cosmetic Studies, Faculty of Pharmacy, Dentistry and Nursing, Department of Pharmacy, Federal University of Ceará, Fortaleza, Ceará, Brazil*

Correspondence should be addressed to Luzia Kalyne Almeida Moreira Leal; kalyne@ufc.br
and Silvânia Maria Mendes Vasconcelos; silvania_vasconcelos@yahoo.com.br

Received 26 October 2021; Revised 13 July 2022; Accepted 25 July 2022; Published 19 August 2022

Academic Editor: Alin Ciobica

Anxiety disorders are the most prevalent psychiatric disorders being also a comorbid state of other diseases. We aimed to evaluate the anxiolytic-like effects of carvedilol (CVD), a drug used to treat high blood pressure and heart failure with potent antioxidant effects, in animals exposed to chronic unpredictable stress (CUS). To do this, female Swiss mice were exposed to different stressors for 21 days. Between days 15 and 21, the animals received oral CVD (5 or 10 mg/kg) or the antidepressant desvenlafaxine (DVS 10 mg/kg). On the 22nd day, behavioral tests were conducted to evaluate locomotor activity (open field) and anxiety-like alterations (elevated plus-maze—EPM and hole board—HB tests). After behavioral determinations, the animals were euthanized, and the adrenal gland, blood and brain areas, prefrontal cortex (PFC), and hippocampus were removed for biochemical analysis. CUS reduced the crossings while increased rearing and grooming, an effect reversed by both doses of CVD and DVS. CUS decreased the number of entries and permanence time in the open arms of the EPM, while all treatments reversed this effect. CUS reduced the number of head dips in the HB, an effect reversed by CVD. The CUS reduced weight gain, while only CVD5 reversed this effect. A reduction in the cortical layer size of the adrenal gland was observed in stressed animals, which CVD reversed. Increased myeloperoxidase activity (MPO) and interferon-γ (IFN-γ), as well as reduction of interleukin-4 (IL-4) induced by CUS, were reversed by CVD. DVS and CVD increased IL-6 in both brain areas. In the hippocampus, DVS caused an increase in IFN-γ. Our data show that CVD presents an anxiolytic effect partially associated with immune-inflammatory mechanism regulation.

1. Introduction

Affective disorders, including anxiety, are associated with several comorbidities and impact the quality of life and social relationships [1–4]. In addition, these disorders are one of the leading causes of disease-related disability, especially among women.

Although anxiety etiology is not entirely understood, many theories have been proposed to explain its pathogenesis, including an interaction between biological, social, and psychological factors [5–8]. Among the risk factors for anxiety, environmental stressors are the most relevant. Indeed, environmental stressors may disrupt the hypothalamic-pituitary-adrenal axis (HPA) and contribute to the degree and duration of neuroinflammatory-driven diseases [9–12]. The chronic unpredictable stress model simulates the chronic exposure to stress factors leading to the development of major chronic mood disorders like anxiety and depression [13]. This animal model induces higher levels of cytokines in the hippocampus, like interleukin- (IL-) 1β, IL-6, and IL-2, and decreases motivated behavior [14]. Additionally, evidence points to the induction of peripheral oxidative and inflammatory (increase in TNF-α, IL-1β, and IL-6 inflammatory markers and a decrease in IL-10) alterations by CUS [15].

Regarding inflammatory mechanisms in anxiety, recent studies have pointed to myeloperoxidase (MPO), an enzyme mainly produced by neutrophils, as an important marker for anxiety since this enzyme is one of the links between oxidative stress and inflammation [16]. In addition, deregulation between proinflammatory and anti-inflammatory cytokines has also been found in patients with anxiety and reported as one of the mechanisms associated with the pathophysiology of anxiety [17].

Anxiety disorders are a cluster of mental disorders that include, for example, generalized anxiety disorder, social anxiety disorder (social phobia), panic, and phobias. Due to the heterogeneity of this mental disorder, the first-line interventions vary between serotonin reuptake inhibitors, cognitive behavioral therapy, and benzodiazepines. Unfortunately, less than 60% of patients respond to these treatments. Moreover, many still have residual symptoms or remain refractory to treatment; therefore, the search for new therapeutic strategies is urgent [18]. Stress-induced neuroinflammation may be involved in treatment resistance [19, 20].

Carvedilol (CVD) is a noncardioselective β-blocker with no negative hemodynamic and metabolic effects associated with typical blockers [21, 22]. In addition, CVD has significant antioxidant, anti-inflammatory, and cardioprotective properties in various neuropsychiatric disorders [23–28].

Despite the evidence on CVD's anxiolytic, antioxidant, and anti-inflammatory properties, no previous studies have addressed immune-inflammatory alterations as underlying mechanisms of this drug against stress-related disorders. Therefore, in this study, desvenlafaxine (DVS) was included as an antianxiety drug since it treats anxiety disorders like generalized anxiety disorder and anxiety symptoms of depression [29].

Therefore, considering CVD's antioxidant and anti-inflammatory properties [30–32], the present study is aimed at evaluating the potential anxiolytic-like effects of CVD against the CUS model, providing a rationale for the repurposing of this antihypertensive drug for the treatment of anxiety.

2. Material and Methods

2.1. Animals. Female Swiss mice (30-32g) were provided by the Drug Research and Development Center (NPDM) animal facility from the Universidade Federal do Ceará. Female mice were used due to women's higher prevalence of anxiety in relation to men [33]. Mice were kept in a controlled temperature environment ($22 \pm 1°C$), with a standard 12-hour light/dark cycle, and received water and food ad libitum, except in periods of stress, following the experimental protocol. The study followed the ethical principles of the Brazilian College of Animal Experimentation (COBEA) and the National Council to Control Animal Experimentation (CONCEA), which comply with the international rules of scientific research involving animals [34]. The Local Ethics Committee approved the project (protocol number 26/2017).

2.2. Drugs

2.2.1. Carvedilol. Carvedilol (CVD, Lab. Biosintética, Aché, Brazil) was diluted in distilled water and administered orally (by gavage) for seven consecutive days at a dose of 5 (CVD5) or 10 (CVD10) mg/kg in a volume of 10 ml/kg. According to the body surface area calculation [35], the doses of 5 and 10 mg/kg in mice are equivalent to the CVD's human antihypertensive doses of 12.5 and 25 mg/day, respectively.

2.2.2. Desvenlafaxine. Desvenlafaxine monohydrate succinate (DVS-Lab. Wyeth, Brazil) was macerated and dissolved in distilled water and administered orally (by gavage) for seven consecutive days at 10 mg/kg in a volume of 10 ml/kg. DVS dose was determined based on previous studies from our laboratory [36, 37].

2.3. Experimental Protocol. Mice were subjected to varying stressors for 21 days [38], as represented in Table 1. In addition, the CUS model was used to study anxiety-like changes induced by exposure to stress [39].

On the twenty-second day of the protocol, the animals received the last dose of water, CVD, or DVS. After 1 hour, open field, elevated plus maze, and hole board tests were conducted. In addition, an observer blinded to the experimental groups recorded the mice's behavior. Immediately after the behavioral tests, the animals were euthanized by rapid decapitation, and their adrenals, blood, and brains were removed for further neurochemical and histological analysis. Figure 1 depicts the experimental design of the study.

To minimize the stress caused by behavioral tests and the number of animals used, the 160 animals used here were randomly distributed into two cohorts: (I) 80 animals were used to assess weight gain, open field and histological analysis of the adrenal gland, and measurement of MPO activity in the prefrontal cortex (PFC) and hippocampus; and (II) 80 animals were used to assess elevated plus maze and hole

Table 1: Daily stressors used in chronic unpredictable stress induction. Adapted from Kumar, Kuhad, and Chopra [38].

Day	Time/period	Stressors
1st	5 min/morning	Swimming in cold water (12°C)
2nd	30s/afternoon	Tail pinch
3rd	24 h/night	Water and food deprivation
4th	12h/night	Night lighting
5th	—	No stress
6th	15 min/morning	Swimming in water at room temperature (23 ± 2°C)
7th	60s/afternoon	Tail pinch
8th	5 min/morning	Swimming in cold water (12°C)
9th	12h/night	Night lighting
10th	—	No stress
11th	10 min/morning	Swimming in water at room temperature (23 ± 2°C)
12th	90s/afternoon	Tail pinch
13th	5 min/morning	Swimming in cold water (12°C)
14th	24 h/afternoon	Water and food deprivation
15th	12h/night	Night lighting
16th	—	No stress
17th	24 h/morning	Water and food deprivation
18th	60s/afternoon	Tail pinch
19th	15 min/morning	Swimming in water at room temperature (23 ± 2°C)
20th	12 h/night	Night lighting
21st	5 min/morning	Swimming in cold water (12 °C)

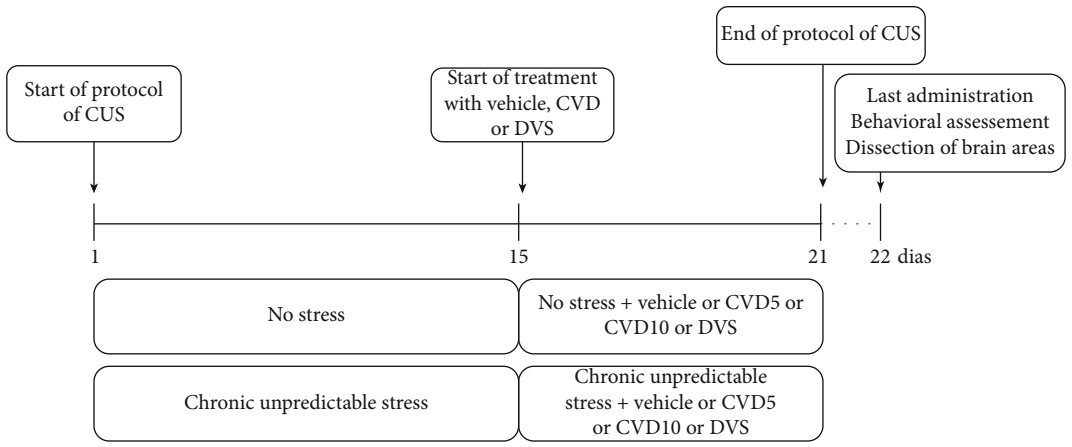

Figure 1: Schematic overview of the experimental design. CUS: chronic unpredictable stress; CVD: carvedilol; DVS: desvenlafaxine.

board performance, as well as corticosterone and cytokine concentrations.

Considering that the animals were randomly divided into two experimental blocks, the number of animals used between the tests varied due to the expected exclusions caused by animals that presented discrepant or stereotyped behavior throughout the experimental protocol. In addition, biochemical and histological tests also require a smaller number of animals for an accurate analysis of the data given the methodology used.

The number of animals was calculated using the "resource equation" method. This method is used when it is not possible to assume effect sizes. According to this method, the value "E" is measured based on the degree of freedom of ANOVA [40]. Based on this calculation, it was decided to use a minimum of 6 animals/group.

2.4. Behavioral Assessment

2.4.1. Open Field Test. The open field area was made of transparent acrylic walls and a black floor (30 cm × 30 cm × 15 cm) divided into nine equal-area squares. Rearing and grooming behaviors were evaluated for five minutes [41].

2.4.2. Elevated Plus-Maze Test. The elevated plus-maze test for mice consisted of two perpendicular open arms

(30 × 5 cm) and two perpendicular closed arms (30 × 5 × 25 cm). The open and closed arms were connected by a central platform (5 × 5 cm). The maze was 45 cm above the floor. Each animal was placed at the center of the apparatus and was observed for 5 min to evaluate the following parameters: the number of entries in the open arm (NEOA), number of entries in the closed arms (NECA), the permanence time in open arms (PTOA), and permanence time in closed arms (PTCA) [42].

2.4.3. Hole Board Test. This test was conducted in an apparatus with 16 evenly spaced holes with built-in infrared sensors (Ugo Basile, Brazil). In brief, the number of head dips into the holes was counted for 5 min for each animal [43].

2.5. Weight Measurement. Each animal's weight (g) was recorded throughout the experimental protocol every two days. Weight measurement was performed between 9 and 10 a.m. At the end of the protocol (21st day), the animals' weight gain (g) was verified in relation to the first day of the experimental protocol.

2.6. Adrenal Gland Area and Corticosterone Evaluation. The adrenals were removed and fixed in 10% buffered formaldehyde until paraffinization. Then, the adrenals were cut and stained with hematoxylin-eosin to measure the cortical zone area of the adrenal gland. The analysis was performed using the ImageJ2 version (Wayne Rasband, National Institutes of Health, USA, disponível no endereço eletrônico http://rsbweb.nih.gov/ij/index.html.) and expressed in mm^2.

Serum corticosterone levels were measured using a corticosterone ELISA kit (Thermo Fisher Scientific, Waltham, MA, USA). The range of the detectable level was 78,125-10,000 pg/mL, determined by absorbance of 450 nm.

2.7. Neurochemical Assessment. The neurochemical determinations were conducted in the prefrontal cortex and hippocampus. For the MPO assay, brain regions were immediately homogenized and tested. Then, the brain areas were stored at -80°C until assayed to measure interleukin concentrations.

2.7.1. Myeloperoxidase Activity (MPO). In a 0.5% hexadecyltrimethylammonium bromide solution, the brain areas were homogenized in 50 mM phosphate buffer (HTAB, pH 6). They were then centrifuged (40,000 g for 15 minutes at 4°C), and the MPO activity in the supernatant (0.1 mL) was measured using a spectrophotometer at 0 and 3 minutes (460 nm) [44]. For MPO units (U) calculation, we subtracted the values of the absorbances at baseline and after 3 min and calculated using a standard MPO curve. Thus, the results were expressed as U of MPO/mg of tissue.

2.7.2. Interleukin- (IL-) 4, IL-6, and Interferon- (IFN-) γ Concentrations. The PFC and HC were homogenized in 8 volumes of PBS buffer with protease inhibitors (EMD Biosciences) and phosphatase (Sigma-Aldrich) to be later centrifuged (10,000 rpm, 5 min). The supernatant was used without dilution. According to the manufacturer's protocol, the concentration of cytokines in 50 μL of samples was determined by ELISA (R&D Systems, Minneapolis, MN, USA) and expressed in pg/g of tissue.

2.8. Statistical Analysis. The statistical analysis was performed with GraphPad Prism 8.0 for Windows, GraphPad Software (San Diego, CA, USA). Two-way ANOVA considering the factors "treatment" (vehicle, CVD5, CVD10, and DVS) and "CUS model" (control and CUS) was used to evaluate behavioral data, MPO activity, body weight, and area of cortical and medullary adrenal zones. One-way ANOVA was used to evaluate data on cytokines and corticosterone. In both conditions, a Turkey post hoc test was performed.

Considering that no significant changes in the behavioral evaluations were observed between nonstressed mice treated with the drugs and the control group, we decided to perform the other assessments, i.e., weight changes, MPO activity, serum corticosterone, and cytokines only in the groups exposed to CUS and control, to reduce the number of animals used in the experiments.

All results are expressed as means ± S.E.M (standard error of the mean). Before ANOVA, Kolmogorov-Smirnov (distance) test was conducted to verify the normal distribution of the data. For all analyses, was considered the significance level at $\alpha = 0.05$.

3. Results

3.1. CVD and DVS Revert Locomotor Alterations Induced by the CUS-Model. In the analysis of locomotor activity (Figure 2(a)), CUS caused a significant reduction in the number of crossings when compared with the control group ($P < 0.001$), while CVD ($P < 0.001$), in both doses, and DVS ($P < 0.0001$) reversed this effect (two-way ANOVA results: interaction ($F(3, 40) = 5.802$, $P = 0.0022$); main effect of "treatment" ($F(3, 40) = 9.800$, $P < 0.0001$); and "CUS" ($F(1, 40) = 8.408$, $P = 0.0060$)).

Besides that, rearing behavior (Figure 2(b)) increased in animals exposed to CUS in relation to control ($P < 0.01$), while all treatments reversed this alteration ($P < 0.01$) (two-way ANOVA results: interaction ($F(3, 40) = 7.428$, $P = 0.0005$); main effect of "treatment" ($F(3, 40) = 3.158$, $P = 0.0350$)).

In the evaluation of grooming behavior (Figure 2(c)), there was an increase by CUS in relation to control mice ($P < 0.0001$), while CVD at both doses and DVS significantly reversed this alteration ($P < 0.0001$) (two-way ANOVA results: interaction ($F(3, 42) = 51.49$, $P < 0.0001$); main effect of "treatment" ($F(3, 42) = 50.58$, $P < 0.0001$); and "CUS" ($F(1, 42) = 85.28$, $P < 0.0001$)).

3.2. CVD and DVS Reverse Anxiety-Like Behavior Induced by the CUS-Model. CUS caused a decrease in the number of entries (Figure 3(a); $P < 0.001$) and permanence time (Figure 3(c); $P < 0.0001$) in the open arms and an increase in the number of entries (Figure 3(b); $P < 0.0001$) and permanence time (Figure 3(d); $P < 0.0001$) in the closed arms when compared with the control group. Treatment with CVD5 (NEOA: $P < 0.0001$; NECA: $P < 0.001$; PTOA: $P < 0.0001$; PTCA: $P < 0.0001$), CVD10 (NEOA: $P < 0.0001$;

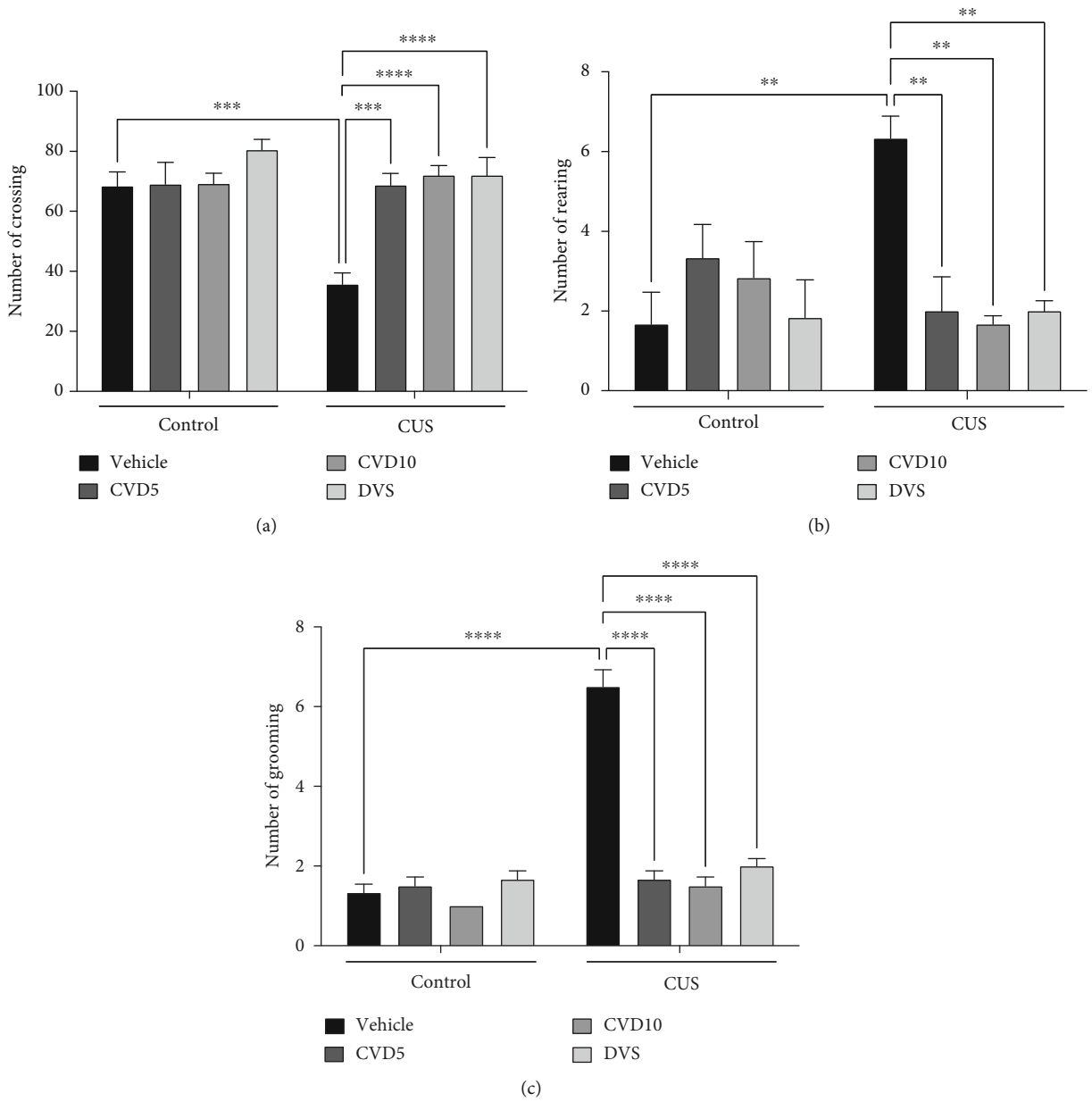

Figure 2: Effects of CVD and DVS treatment in the open field parameters, crossings (a), rearing (b), and grooming (c) in mice subjected to the CUS model. The animals were subjected to different stressors for 21 days. Between the 15th and 21st days of the stress protocol, mice received CVD (5 or 10 mg/kg, p.o.) or DVS (10 mg/kg, p.o.). On the 22nd day, the animals were submitted to the open field test, 1 h after administering drugs, without applying stressors. Each column represents the mean ± SEM ($n = 6 - 9$ animals/group). $^{**}P < 0.01$, $^{***}P < 0.001$, and $^{****}P < 0.0001$ according to Tukey's multiple comparison test. Abbreviations: CUS: chronic unpredictable stress; CVD: carvedilol; DVS: desvenlafaxine.

NECA: $P < 0.0001$; PTOA: $P < 0.0001$; PTCA: $P < 0.0001$), or DVS (NEOA: $P < 0.0001$; NECA: $P < 0.01$; PTOA: $P < 0.0001$; PTCA: $P < 0.0001$) reversed all alterations caused by CUS in this test. Interestingly, treatment with DVS in the absence of CUS increased the permanence time in the closed arms compared with control ($P < 0.01$) (two-way ANOVA results: NEOA interaction ($F(3, 63) = 15.99$, $P < 0.0001$); NECA interaction ($F(3, 63) = 7.895$, $P = 0.0001$); PTOA interaction ($F(3, 63) = 14.44$, $P < 0.0001$); and PTCA interaction ($F(3, 63) = 15.63$, $P < 0.0001$)).

In the analysis of the number of head dips (Figure 4), CUS exposure decreased the number of head dips in relation to the control group ($P < 0.05$). Only CVD, in both doses, reversed the alterations caused by CUS ($P < 0.05$) (two-way ANOVA results: interaction ($F(3, 43) = 8.712$, $P = 0.0001$)).

3.3. Effects of CUS and Anxiolytic Strategies on Body Weight. The CUS model reduced the mice's weight (Figure 5) gain when compared with the control ($P < 0.001$), while only the treatment with CVD5 ($P < 0.001$) reversed this effect

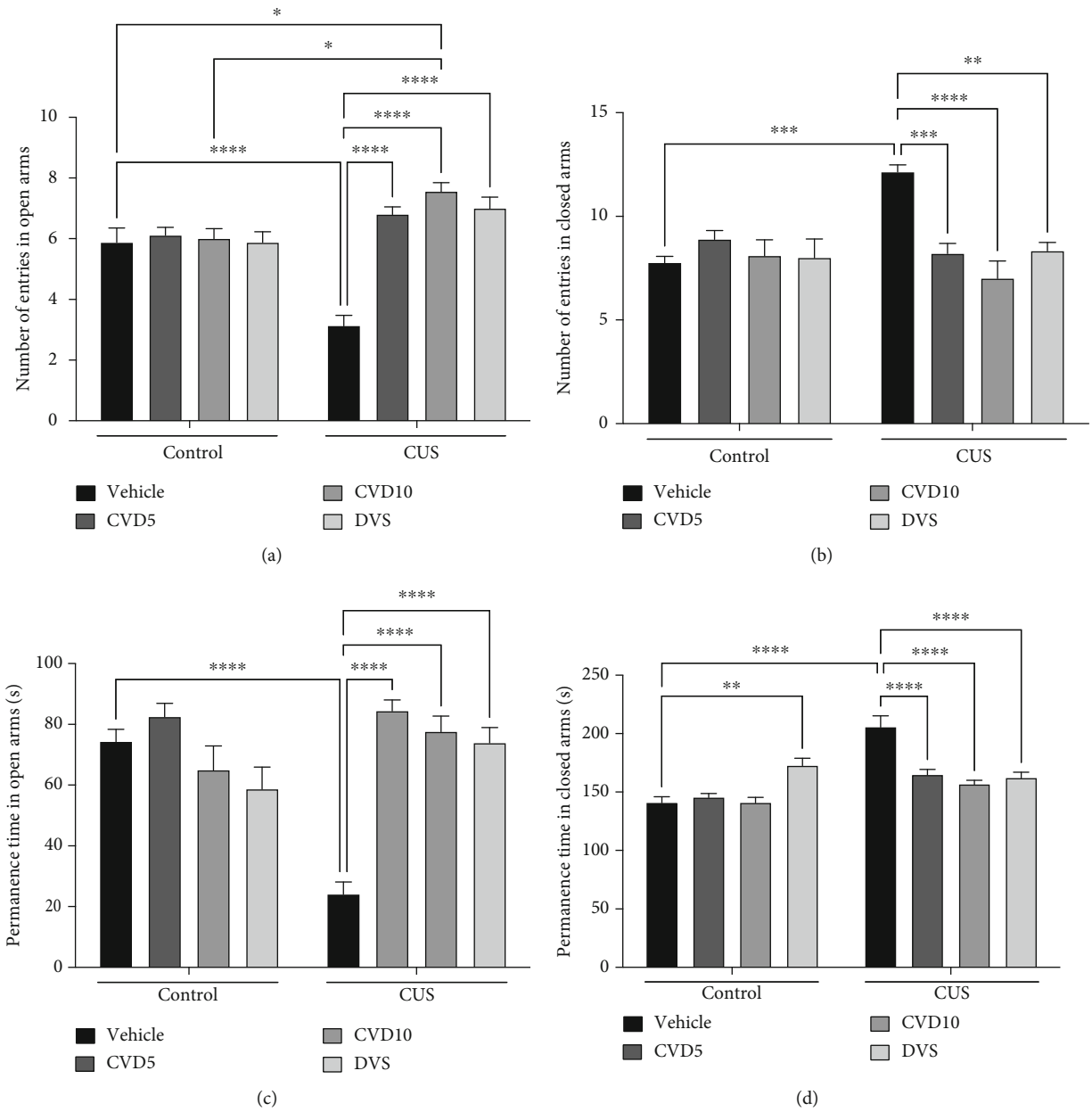

Figure 3: Effects of CVD and DVS treatment on plus-maze test parameters, number of entries in open arms-NEOA (a) and closed arms-NECA (b), and permanence time in open arms-PTOA (c) and closed arms-PTCA (d), in the CUS model. The animals were subjected to different stressors for 21 days. Between the 15th and 21st days of the stress protocol, the mice received CVD (5 or 10 mg/kg, p.o.) or DVS (10 mg/kg, p.o.). On the 22nd day, the animals were submitted to the elevated plus-maze test, 1 h after administering drugs, without the application of stressors. Each column represents the mean ± SEM ($n = 8 - 10$ animals/group). $^{*}P < 0.05$, $^{**}P < 0.01$, $^{***}P < 0.001$, and $^{****}P < 0.0001$ according to Tukey's multiple comparison test. Abbreviations: CUS: chronic unpredictable stress; CVD: carvedilol; DVS: desvenlafaxine; NEOA: number of entries in open arms; NECA: number of entries in closed arms; PTOA: permanence time in open arms; PTCA: permanence time in closed arms.

(two-way ANOVA results: interaction ($F(3, 56) = 5.615$, $P = 0.0019$)).

3.4. Effects of CUS and Anxiolytic Strategies on Cortical Adrenal Zone Area and Corticosterone Levels. The assessment of the cortical adrenal zone area (Figure 6(a)) showed that CUS caused an increase in the cortical adrenal zone area when compared with the control group ($P < 0.01$), while CVD5 ($P < 0.001$), CVD10 ($P < 0.01$), and DVS ($P < 0.001$) reversed this effect. On the other hand, no statistically significant effect was observed in the measurement of serum corticosterone (Figure 6(b)).

3.5. Effects of CVD and DVS Treatment on MPO Activity. In the evaluation of MPO activity in the PFC (Figure 7(a)), CUS increased MPO activity in this brain area when

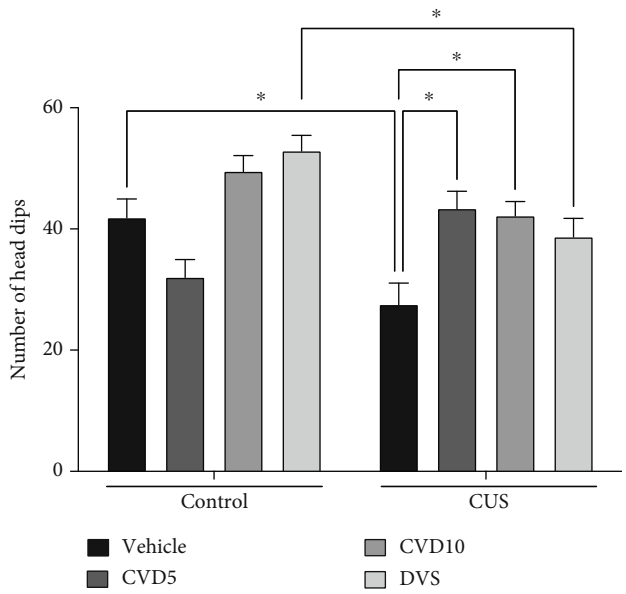

Figure 4: Effects of CVD and DVS treatment on hole board test in a CUS model. The animals were subjected to different stressors for 21 days. Between the 15th and 21st days of the stress protocol, the mice received CVD (5 or 10 mg/kg, p.o.) or DVS (10 mg/kg, p.o.). On the 22nd day, the animals were submitted to the hole board test, 1 h after administering drugs, without the application of stressors. Each column represents the mean ± SEM ($n = 6 - 8$ animals/group). $^{*}P < 0.05$ according to Tukey's multiple comparison test. Abbreviations: CUS: chronic unpredictable stress; CVD: carvedilol; DVS: desvenlafaxine.

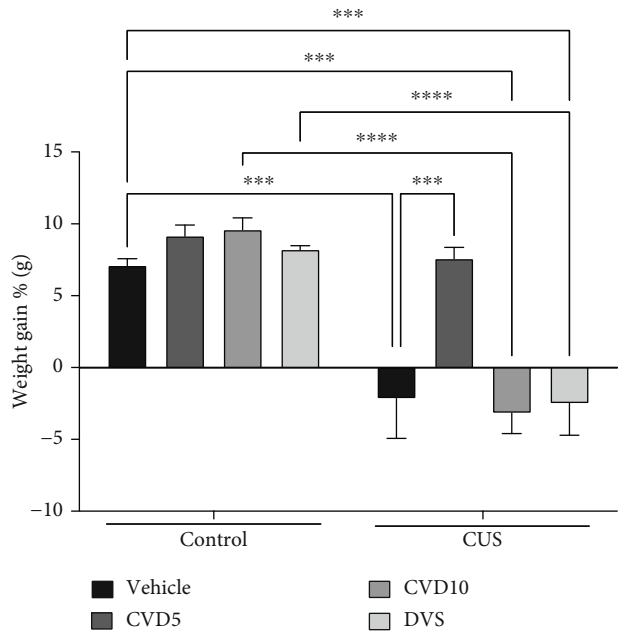

Figure 5: Effects of CVD and DVS treatment on weight gain in the CUS model. The animals were subjected to different stressors for 21 days. Between the 15th and 21st days of the stress protocol, the mice received CVD (5 or 10 mg/kg, p.o.) or DVS (10 mg/kg, p.o.). The animals' weight was recorded in grams every 2 days throughout the experimental protocol. The weight gain was calculated based on changes in body weight from day 21 relative to the bodyweight on day 1. Each column represents the weight gain ± SEM ($n = 8$ animals/group). $^{***}P < 0.001$, and $^{****}P < 0.0001$ according to Tukey's multiple comparison test. Abbreviations: CUS: chronic unpredictable stress; CVD: carvedilol; DVS: desvenlafaxine.

compared with the control ($P < 0.001$), while only CVD treatment, in both doses, reversed the CUS effect ($P < 0.01$) (two-way ANOVA results: main effect of "treatment" ($F(3, 45) = 7.357$; $P = 0.0004$) and "CUS" ($F(1, 45) = 21.03$; $P < 0.0001$)).

In the analysis of MPO activity in the hippocampus (Figure 7(b)), CUS increased MPO activity in this brain area when compared with the control ($P < 0.01$), while treatment with CVD5 ($P < 0.0001$), CVD10 ($P < 0.001$), and DVS ($P < 0.05$) reversed CUS effect (two-way ANOVA results: interaction ($F(3, 43) = 6.457$; $P = 0.0010$)).

3.6. Effects of CVD and DVS Treatment on Brain Cytokine Concentrations. In the PFC (Figure 8(a)), CUS caused a significant decrease in IL-4 concentrations when compared with the control group ($P < 0.01$). In this area, none of the treatments reversed the effect caused by CUS.

On the other hand, no changes were observed in the hippocampus (Figure 8(b)).

CUS did not alter IL-6 levels in the PFC (Figure 8(c)) in relation to the control group. However, treatment with DVS ($P < 0.0001$), CVD5 ($P < 0.05$), or CVD10 ($P < 0.05$) significantly increased IL-6 concentrations when compared to control group.

Like the effects in the PFC, CUS did not cause any change in IL-6 concentrations in the hippocampus (Figure 8(d)) compared with the control group. However, all treatments significantly increased the concentrations of this cytokine when compared with the control and CUS groups ($P < 0.001$).

In the PFC (Figure 8(e)), CUS caused a significant increase in IFN-γ concentrations when compared with the control group ($P < 0.01$). Only the CVD10 treatment reversed the effect caused by CUS ($P < 0.05$). CUS did not cause changes in the concentrations of IFN-γ in the hippocampus (Figure 8(f)) when compared with the control group ($F(4, 25) = 3.699$; $P = 0.0169$). On the other hand, treatment with DVS induced higher concentrations of this cytokine compared with the control group ($P < 0.05$).

4. Discussion

In the present study, CUS induced behavioral alterations that mimic anxiety in apparatus that are well-validated for this end, namely, plus-maze and role board tests [36, 45–48]. In this regard, we observed decreased number of entries and time spent in the open arms, increased entries and permanence time in the closed arms of the plus-maze, and decreased head dips in the role board test. Additionally, we observed reduced weight gain, increased adrenal area, and proinflammatory alterations in brain areas related to mood regulation, namely, PFC and hippocampus. The administration of CVD reversed all behavioral and some neuroinflammatory alterations induced by CUS and weight

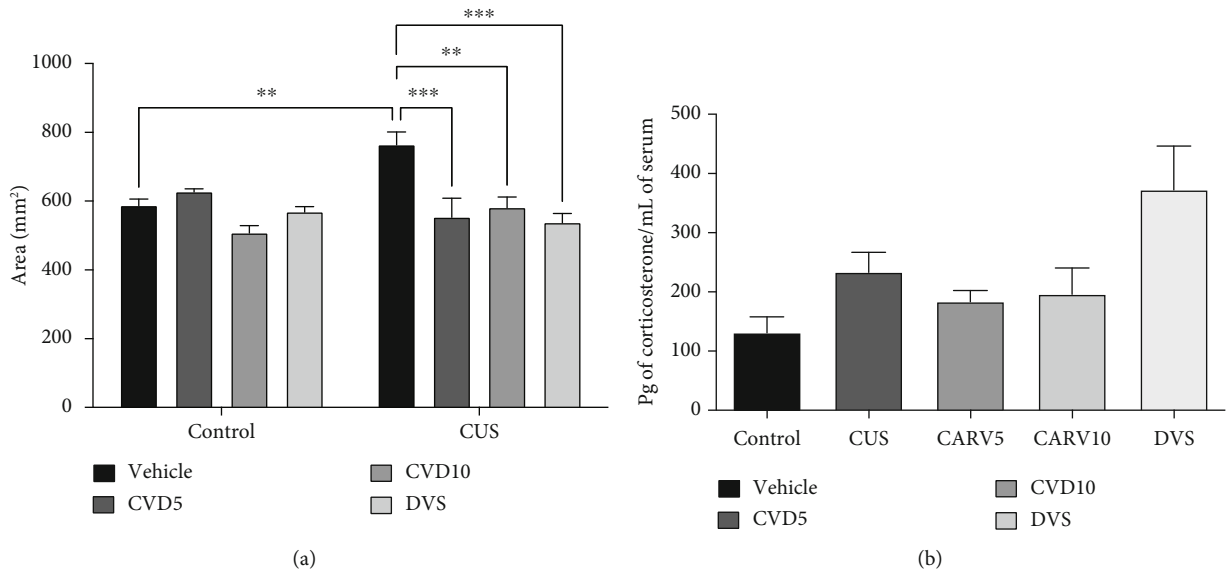

Figure 6: Effects of CVD and DVS treatment on adrenal cortex area (a) and corticosterone serum concentrations (b) in a CUS model. The animals were subjected to different stressors for 21 days. Between the 15th and 21st days of the stress protocol, the mice received CVD (5 or 10 mg/kg, p.o.) or DVS (10 mg/kg, p.o.). On the 22nd day, the animals were euthanized, and their blood and adrenals were collected. Each column represents the mean ± SEM ($n = 4 - 5$ animals/group). $^{**}P < 0.01$, $^{***}P < 0.001$ according to Tukey's multiple comparison test. Abbreviations: CUS: chronic unpredictable stress; CVD: carvedilol; DVS: desvenlafaxine.

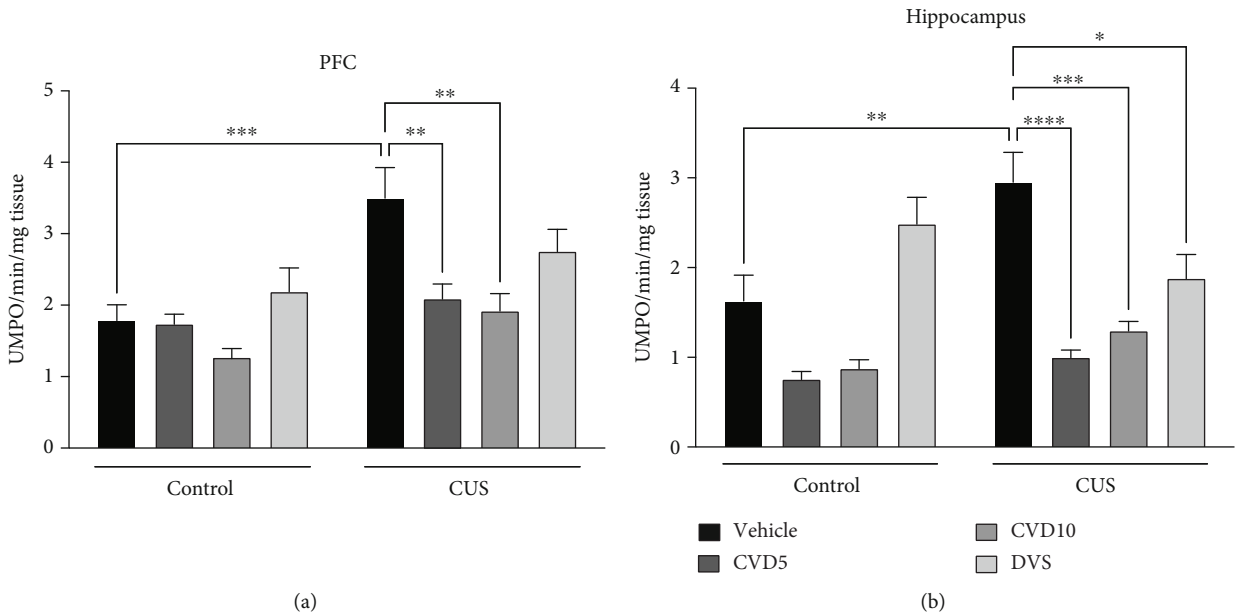

Figure 7: Effects of CVD and DVS treatment on myeloperoxidase (MPO) activity in the prefrontal cortex (a) and hippocampus (b). The animals were subjected to different stressors for 21 days. Between the 15th and 21st days of the stress protocol, the mice received CVD (5 or 10 mg/kg, p.o.) or DVS (10 mg/kg, p.o.). On the 22nd day, the animals were euthanized. Each column represents the mean ± SEM ($n = 6 - 8$ animals/group). $^{*}P < 0.05$, $^{**}P < 0.01$, $^{***}P < 0.001$, and $^{****}P < 0.0001$ according to Tukey's multiple comparison test. Abbreviations: CUS: chronic unpredictable stress; CVD: carvedilol; DVS: desvenlafaxine; MPO: myeloperoxidase; PFC: prefrontal cortex; HC: hippocampus.

gain changes. On the other hand, DVS, used here as an antidepressant drug to treat anxiety disorders, could not reverse weight gain and some proinflammatory alterations induced by CUS. Our results revealed that CVD might be an important strategy for treating anxiety disorders.

Repeated exposure to stress induces adaptive changes in the brain involving the cumulative action of glucocorticoids that facilitate the development of stress-related psychiatric disorders, including anxiety [49]. For example, anxiety disorders are marked by excessive fear and autonomic nervous

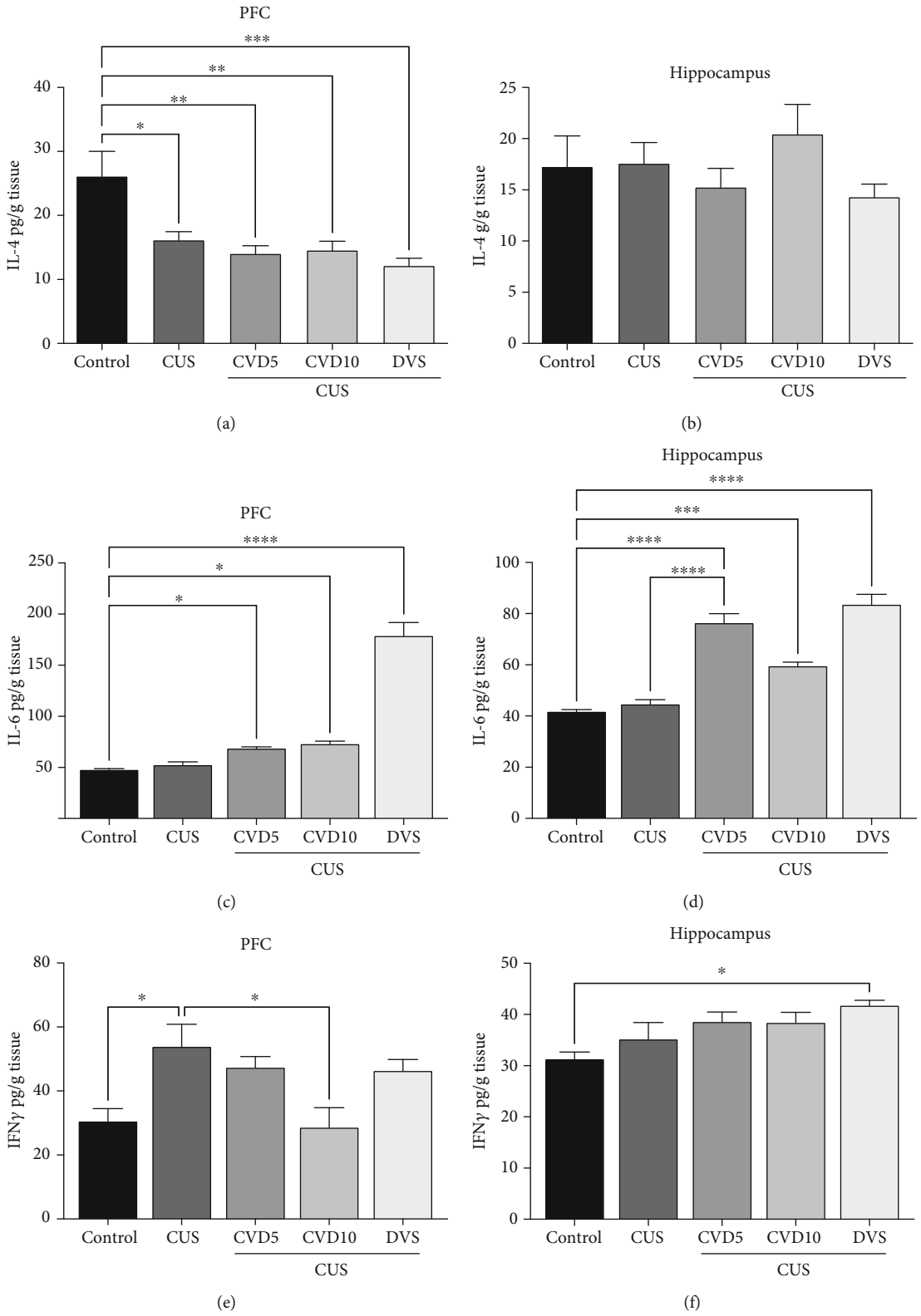

Figure 8: Effects of CVD and DVS treatment on IL-4 ((a) prefrontal cortex; (b) hippocampus), IL-6 ((c) prefrontal cortex; (d) hippocampus), and IFN-γ ((e) prefrontal cortex; (f) hippocampus) concentrations. The animals were subjected to different stressors for 21 days. Between the 15th and 21st days of the stress protocol, the mice received CVD (5 or 10 mg/kg, p.o.) or DVS (10 mg/kg, p.o.). On the 22nd day, the animals were euthanized and had the prefrontal cortex and hippocampus dissected. Each column represents the significance ± SEM ($n = 6 - 8$ animals/group). $^{*}P < 0.05$, $^{**}P < 0.01$, $^{***}P < 0.001$, and $^{****}P < 0.0001$ according to Tukey's multiple comparison test. Abbreviations: CUS: chronic unpredictable stress; CVD: carvedilol; DVS: desvenlafaxine; IL-4: interleukin-4; IL-6: interleukin-6; IFN-γ: interferon-γ; PFC: prefrontal cortex; HC: hippocampus.

system activity changes, like increased heart rate and blood pressure [50]. To date, antidepressant drug treatment is the clinical standard for all anxiety disorders [51].

In the present study, we performed the open field test besides performing validated tests to evaluate anxiety-like behaviors in rodents, namely, plus-maze and role board tests, to expand the behavioral assessment. We observed that CUS caused a reduction in locomotor activity (evaluated by the number of crossings), a behavioral alteration already reported in different animal models of anxiety [36, 52, 53]. Psychomotor retardation is an important symptom of generalized anxiety disorder [54–56]. Other important parameters measured in the open field test and relevant for anxiety were rearing and grooming behaviors. Indeed, previous findings have shown a relationship between altered rearing and anxiety in animal models [57, 58]. Regarding grooming, we observed higher levels in CUS-exposed animals. This parameter is extensively investigated in animal models of anxiety [29, 59, 60]. Our results, therefore, reinforce the idea that CUS causes anxiety-like behavior.

We observed that both CVD and DVS improved psychomotor performance and anxiety-related parameters evaluated in the open field test [56, 61]. It deserves to be mentioned that the anxiolytic effect of DVS is already well established in the literature [29, 36, 62], which is not true for CVD.

Accumulated evidence reveals that stress is associated with the activation of neuroendocrine pathways culminating in the development of anxiety disorders. One of the mechanisms related to this dysregulation is the activation of beta-adrenergic receptors in glial cells and some brain regions. Thus, the blockade of these receptors seems to be an important anxiolytic strategy already observed in animal models and human studies [63–67]. Indeed, we observed that CVD was superior to DVS in regulating anxiety-like alterations induced by CUS, probably due to its nonselective blockade of adrenergic receptors.

Weight changes are often observed in patients with depression and anxiety, and this symptom is considered for the diagnostic classification [54]. In this regard, the literature has already documented that stress promotes the mobilization of the body's energy reserves as an adaptation mechanism to respond to threatening situations. Furthermore, stress-induced hyperactivation of the HPA axis and the sympathetic nervous system causes a positive and dialectical regulatory mechanism between these two systems associated with anorexia hypophagia and weight loss [68, 69].

Our findings showed that CVD5 reversed the weight changes caused by CUS. This effect is probably associated with the adrenergic blocking action of CVD, considering that the stimulation of lipolysis and the release of fatty acids from adipose tissue and glycogenolysis and gluconeogenesis in the liver are activities regulated by alpha- and beta-adrenergic receptors [70, 71]. However, this appears to be a dose-dependent effect, as only the lowest dose reversed the weight loss caused by CUS.

In line with stress deregulation of the HPA axis [72, 73], CUS increased the adrenal cortical layer area. However, this alteration was reversed by both CVD and DVS. This effect is probably related to a regulation of stress-induced adrenocorticotropic hormone (ACTH) stimulation on cells in this region, especially the glomerulus layer [72, 74].

Given the importance of proinflammatory alterations as underlying mechanisms of anxiety, we decided to investigate the activity of MPO and the levels of pro- and anti-inflammatory cytokines in the PFC and hippocampus. We observed that CUS induced increased activity of MPO in the PFC and hippocampus, which was reversed in both brain areas by the two doses of CVD and only in the hippocampus by DVS. MPO is produced by leukocytes [75–77], representing an important link between these oxidative mechanisms and inflammation [78]. Furthermore, this enzyme is an important biomarker for mental disorders [76].

Previous studies indicate that the microglial reactivity observed in stressful situations is associated with noradrenaline's direct activation of beta-adrenergic receptors. This beta-adrenergic activation of microglia cells contributes to synthesizing and releasing inflammatory mediators and oxidative stress [75, 79, 80]. Since CVD is a nonselective beta-blocker with alpha-blocker properties, this drug seems to present advantages for treating neuropsychiatric disorders associated with a dysregulation in adrenergic and inflammatory mechanisms.

Among the cytokines involved in the pathophysiology of anxiety, IL-4 stands out for its anti-inflammatory activity. Here, we observed that CUS caused a reduction in IL-4 concentrations in the PFC. This result is in line with studies indicating that low concentrations of IL-4 are associated with anxiety symptoms [81]. However, in our experimental conditions, the drugs could not reverse CUS-induced alterations in IL-4. Therefore, the observed absence of effects may probably be related to the short administration time of these drugs (only 7 days).

Besides being related to the neurobiology of anxiety [49, 82, 83], in our results, we did not observe CUS-induced alterations in IL-6 levels in the PFC, nor in the hippocampus. Furthermore, several studies indicate that the chronic stress protocol of 28 days or more can be more robust when mimicking a greater variety of neurochemical and behavioral changes, including changes in brain cytokines. Finally, it is worth noting that the stressors used in the protocol and the sex of the animals can influence the observed findings [84–86] since females are less prone to developing brain inflammatory alterations compared with males [87].

On the other hand, treatments with CVD or DVS increased IL-6 concentrations in relation to control animals. This is an intriguing result that must be further explored. Indeed, the cellular expression of the membrane-bound and soluble forms of IL-6R (Interleukin-6 receptor) and its receptor, gp130 (Glycoprotein 130) is modulated by many factors, including proteases, cytokines, chemical drugs, and intracellular signaling pathways, contributing to IL-6 pro- and anti-inflammatory effects [88]. In addition, IL-6 regulates the HPA axis, and possibly the alteration observed here is related to this effect [49].

Several studies have reported high circulating levels of IFN-γ in anxiety patients [89, 90]. In addition, some anxiolytics can antagonize IFN-γ signaling [91–93].

Here, CVD10 reversed the increase in IFN-γ caused by CUS in the PFC. Corroborating this idea, previous findings indicate that treatment with selective serotonin reuptake inhibitors decreases the expression of IFN-γ mRNA in patients with anxiety [94]. Despite this, in our results, DVS did not reverse the CUS-induced increase in PFC IFN-γ levels but instead increased the levels of this cytokine in the hippocampus. This result is divergent from the literature and requires further investigation.

Clinical and preclinical studies have already reported the anxiolytic effect of CVD, strengthening the data presented here [63, 64, 66, 67]. However, studies addressing neuroinflammatory mechanisms underlying the action of this drug are still scarce, mainly using stress models of anxiety.

5. Conclusion

The present study is the first to demonstrate that anti-inflammatory mechanisms underlie CVD anxiolytic action in an animal model of anxiety/depression induced by CUS. We also showed here that the effect of CVD was superior to DVS in some parameters, revealing that the nonselective blockade of adrenergic receptors combined with antioxidant and possibly immunoregulatory effects of this drug is relevant for the reversal of behavioral and neurobiological alterations induced by repeated stress exposure. Besides that, cardiovascular changes like hypertension or heart failure are commonly observed in anxiety patients emphasizing the repurposing of CVD as a therapeutic alternative for patients with depression and anxiety, therefore reducing the need for polypharmacy and the side effects observed in the current pharmacotherapy.

Data Availability

The behavioral and neurochemical data used to support the findings of this study are included within the article.

Conflicts of Interest

The authors declare no conflicts of interest.

Acknowledgments

This study was supported by grants from the Brazilian government Institutions CNPq, CAPES, and FUNCAP.

References

[1] A. Canuto, K. Weber, M. Baertschi et al., "Anxiety disorders in old age: psychiatric comorbidities, quality of life, and prevalence according to age, gender, and country," *American Journal of Geriatric Psychiatry*, vol. 26, no. 2, pp. 174–185, 2018.

[2] S. Giovanoli, H. Engler, A. Engler, J. Richetto, M. Voget, R. Willi, and C. Winter, Eds.M. A. Riva, P. B. Mortensen, J. Feldon, and M. Schedlowski, "Stress in Puberty Unmasks Latent Neuropathological Consequences of Prenatal Immune Activation in Mice," *Science*, S. Giovanoli, H. Engler, A. Engler, J. Richetto, M. Voget, R. Willi, and C. Winter, Eds., vol. 339, no. 6123, pp. 1095–1099, 2013.

[3] S. Korkmaz, A. Kazgan, S. Çekiç, A. S. Tartar, H. N. Balcı, and M. Atmaca, "The anxiety levels, quality of sleep and life and problem-solving skills in healthcare workers employed in COVID-19 services," *Journal of Clinical Neuroscience*, vol. 80, pp. 131–136, 2020.

[4] A. Koyuncu, E. İnce, E. Ertekin, and R. Tükel, "Comorbidity in social anxiety disorder: diagnostic and therapeutic challenges," *Drugs in Context*, vol. 8, pp. 1–13, 2019.

[5] E. Assary, J. P. Vincent, R. Keers, and M. Pluess, "Gene-environment interaction and psychiatric disorders: review and future directions," *Seminars in Cell and Developmental Biology*, vol. 77, pp. 133–143, 2018.

[6] A. A. Bartlett, R. Singh, and R. G. Hunter, "Anxiety and epigenetics," *In Advances in Experimental Medicine and Biology*, vol. 978, pp. 145–166, 2017.

[7] M. A. Schiele and K. Domschke, "Epigenetics at the crossroads between genes, environment and resilience in anxiety disorders," *Genes, Brain and Behavior*, vol. 17, no. 3, 2018.

[8] C. Ziegler, M. A. Schiele, and K. Domschke, "Patho- and therapyepigenetics of mental disorders," *Der Nervenarzt*, vol. 89, no. 11, pp. 1303–1314, 2018.

[9] J. C. Felger, "Imaging the role of inflammation in mood and anxiety-related disorders," *Current Neuropharmacology*, vol. 16, no. 5, pp. 533–558, 2018.

[10] V. Michopoulos, A. Powers, C. F. Gillespie, K. J. Ressler, and T. Jovanovic, "Inflammation in fear- and anxiety-based disorders: PTSD, GAD, and beyond," *Neuropsychopharmacology*, vol. 42, no. 1, pp. 254–270, 2017.

[11] L. S. Novaes, N. Barreto, R. F. P. dos Santos et al., "Environmental enrichment protects against stress-induced anxiety: role of glucocorticoid receptor, ERK, and CREB signaling in the basolateral amygdala," *Neuropharmacology*, vol. 113, pp. 457–466, 2017.

[12] J. M. Peirce and K. Alviña, "The role of inflammation and the gut microbiome in depression and anxiety," *Journal of Neuroscience Research*, vol. 97, no. 10, pp. 1223–1241, 2019.

[13] S. Monteiro, S. Roque, D. de Sá-Calçada, N. Sousa, M. Correia-Neves, and J. J. Cerqueira, "An efficient chronic unpredictable stress protocol to induce stress-related responses in C57BL/6 mice," *Frontiers in Psychiatry*, vol. 6, 2015.

[14] K. D. Mograbi, D. Suchecki, S. G. da Silva, L. Covolan, and C. Hamani, "Chronic unpredictable restraint stress increases hippocampal pro-inflammatory cytokines and decreases motivated behavior in rats," *Stress*, vol. 23, no. 4, pp. 427–436, 2020.

[15] A. L. López-López, H. J. Bonilla, M. del Carmen et al., "Chronic unpredictable mild stress generates oxidative stress and systemic inflammation in rats," *Physiology & Behavior*, vol. 161, pp. 15–23, 2016.

[16] M. Maes, K. L. Bonifacio, N. R. Morelli et al., "Generalized anxiety disorder (GAD) and comorbid major depression with GAD are characterized by enhanced nitro-oxidative stress, increased lipid peroxidation, and lowered lipid-associated antioxidant defenses," *Neurotoxicity Research*, vol. 34, no. 3, pp. 489–510, 2018.

[17] B. Li, T. Gao, and D. Jing, "Neuroimmune imbalance: the key for the treatment of anxiety?," *Journal of Immunological Sciences*, vol. 3, no. 3, pp. 14–16, 2019.

[18] A. Bystritsky, "Treatment-resistant anxiety disorders," *Molecular Psychiatry*, vol. 11, no. 9, pp. 805–814, 2006.

[19] V. Michopoulos, A. Powers, C. F. Gillespie, K. J. Ressler, and T. Jovanovic, "Inflammation in fear-and anxiety-based

disorders: PTSD, GAD, and beyond," *Neuropsychopharmacology*, vol. 42, no. 1, pp. 254–270, 2017.

[20] S. Rooney, A. Sah, M. S. Unger et al., "Neuroinflammatory alterations in trait anxiety: modulatory effects of minocycline," *Translational Psychiatry*, vol. 10, no. 1, p. 256, 2020.

[21] G. Leonetti and C. G. Egan, "Use of carvedilol in hypertension: an update," *Vascular Health and Risk Management*, vol. 8, pp. 307–322, 2012.

[22] E. V. Veiga, M. S. Nogueira, E. C. Cárnio et al., "7ª Diretriz Brasileira de Hipertensão Arterial," *Revista Da Sociedade Brasileira De Cardiologia*, vol. 107, no. 3, pp. 83–89, 2013.

[23] R. F. Araújo Júnior, TO Souza, C. A. Medeiros et al., "Carvedilol decrease IL-1β and TNF-α, inhibits MMP-2, MMP-9, COX-2, and RANKL expression, and up-regulates OPG in a rat model of periodontitis," *PLoS One*, vol. 8, no. 7, 2013.

[24] A. J. Fatani, K. A. Al-Hosaini, M. M. Ahmed, H. M. Abuohashish, M. Y. Parmar, and S. S. Al-Rejaie, "Carvedilol attenuates inflammatory biomarkers and oxidative stress in a rat model of ulcerative colitis," *Drug Development Research*, vol. 76, no. 4, pp. 204–214, 2015.

[25] Y. Karatas, S. L. Cengiz, H. Esen, A. Toker, and C. Savas, "Effect of carvedilol on secondary damage in experimental spinal cord injury in rats," *Turkish Neurosurgery*, vol. 25, no. 6, pp. 930–935, 2014.

[26] A. Kumar, S. Dogra, and A. Prakash, "Effect of carvedilol on behavioral, mitochondrial dysfunction, and oxidative damage against d-galactose induced senescence in mice," *Naunyn-Schmiedeberg's Archives of Pharmacology*, vol. 380, no. 5, pp. 431–441, 2009.

[27] S. Olapour, A. R. Assareh, M. T. Jalali, H. Yaghooti, and S. Ayashi, "Role of antioxidant property of carvedilol in mild to moderate hypertensive patients: a prospective open-label study," *Indian Journal of Pharmacology*, vol. 48, no. 4, pp. 372–376, 2016.

[28] G. C. de Souza, J. A. Gomes, A. I. de Góis Queiroz et al., "Preclinical evidences for an antimanic effect of carvedilol," *Neural Plasticity*, vol. 2015, Article ID 692541, 10 pages, 2015.

[29] K. A. Tourian, Q. Jiang, and P. T. Ninan, "Analysis of the effect of desvenlafaxine on anxiety symptoms associated with major depressive disorder: pooled data from 9 short-term, double-blind, placebo-controlled trials," *CNS Spectrums*, vol. 15, no. 3, pp. 187–193, 2010.

[30] S. J. C. Davies and C. Allgulander, "Anxiety and cardiovascular disease," *Modern Trends in Pharmacopsychiatry*, vol. 29, pp. 85–97, 2013.

[31] C. A. Emdin, A. Odutayo, C. X. Wong, J. Tran, A. J. Hsiao, and B. H. M. Hunn, "Meta-analysis of anxiety as a risk factor for cardiovascular disease," *American Journal of Cardiology*, vol. 118, no. 4, pp. 511–519, 2016.

[32] P. J. Tully, N. J. Harrison, P. Cheung, and S. Cosh, "Anxiety and cardiovascular disease risk: a review," *Current Cardiology Reports*, vol. 18, no. 12, 2016.

[33] C. Kuehner, "Why is depression more common among women than among men?," *The Lancet Psychiatry*, vol. 4, no. 2, pp. 146–158, 2017.

[34] National Institutes of Health, *Guide for the Care and Use of Laboratory Animals-Institute of Laboratory Animal Research-National Research Council*, National Academies Press, 1996.

[35] S. Reagan-Shaw, M. Nihal, and N. Ahmad, "Dose translation from animal to human studies revisited," *FASEB Journal: Official Publication of the Federation of American Societies for Experimental Biology*, vol. 22, no. 3, pp. 659–661, 2008.

[36] M. C. Silva, C. N. Chaves, S. de Sousa et al., "Augmentation therapy with alpha-lipoic acid and desvenlafaxine: a future target for treatment of depression?," *Naunyn-Schmiedeberg's Archives of Pharmacology*, vol. 386, no. 8, pp. 685–695, 2013.

[37] C. N. Sousa, G. S. Vasconcelos, I. da Silva Medeiros et al., "Neuroprotective evidence of alpha-lipoic acid and desvenlafaxine on memory deficit in a neuroendocrine model of depression," *Naunyn-Schmiedeberg's Archives of Pharmacology*, vol. 391, no. 8, pp. 803–817, 2018.

[38] B. Kumar, A. Kuhad, and K. Chopra, "Neuropsychopharmacological effect of sesamol in unpredictable chronic mild stress model of depression: behavioral and biochemical evidences," *Psychopharmacology*, vol. 214, no. 4, pp. 819–828, 2011.

[39] A. C. Campos, M. V. Fogaça, D. C. Aguiar, and F. S. Guimarães, "Animal models of anxiety disorders and stress," *Revista Brasileira de Psiquiatria*, vol. 35, Supplement 2, pp. S101–S111, 2013.

[40] J. Charan and N. Kantharia, "How to calculate sample size in animal studies?," *Journal of Pharmacology and Pharmacotherapeutics*, vol. 4, no. 4, pp. 303–306, 2013.

[41] J. Archer, "Tests for emotionality in rats and mice: a review," *Animal Behaviour*, vol. 21, no. 2, pp. 205–235, 1973.

[42] R. G. Lister, "The use of a plus-maze to measure anxiety in the mouse," *Psychopharmacology*, vol. 92, no. 2, pp. 180–185, 1987.

[43] G. Clark, A. G. Koester, and D. W. Pearson, "Exploratory behavior in chronic disulfoton poisoning in mice," *Psychopharmacologia*, vol. 20, no. 2, pp. 169–171, 1971.

[44] P. P. Bradley, D. A. Priebat, R. D. Christensen, and G. Rothstein, "Measurement of cutaneous inflammation: estimation of neutrophil content with an enzyme marker," *Journal of Investigative Dermatology*, vol. 78, no. 3, pp. 206–209, 1982.

[45] A. Bali and A. S. Jaggi, "Preclinical experimental stress studies: protocols, assessment and comparison," *European Journal of Pharmacology*, vol. 746, pp. 282–292, 2015.

[46] R. D. C. Chaves, A. S. V. Mallmann, N. F. Oliveira et al., "Reversal effect of riparin IV in depression and anxiety caused by corticosterone chronic administration in mice," *Pharmacology Biochemistry and Behavior*, vol. 180, pp. 44–51, 2019.

[47] D. Garabadu and V. Kumar, "Celecoxib potentiates the antianxiety and anticompulsive-like activity of fluoxetine against chronic unpredictable mild stress in experimental animals," *Behavioural Pharmacology*, vol. 30, no. 2, pp. 251–259, 2019.

[48] V. Mehta, A. Parashar, and M. Udayabanu, "Quercetin prevents chronic unpredictable stress induced behavioral dysfunction in mice by alleviating hippocampal oxidative and inflammatory stress," *Physiology and Behavior*, vol. 171, pp. 69–78, 2017.

[49] M. Girotti, J. J. Donegan, and D. A. Morilak, "Influence of hypothalamic IL-6/Gp130 receptor signaling on the HPA axis response to chronic stress," *Psychoneuroendocrinology*, vol. 38, no. 7, pp. 1158–1169, 2013.

[50] J. M. Martinez, A. Garakani, H. Kaufmann, C. J. Aaronson, and J. M. Gorman, "Heart rate and blood pressure changes during autonomic nervous system challenge in panic disorder patients," *Psychosomatic Medicine*, vol. 72, no. 5, pp. 442–449, 2010.

[51] A. Y. Bespalov, M. M. van Gaalen, and G. Gross, "Antidepressant treatment in anxiety disorders," *Current Topics in Behavioral Neurosciences*, vol. 2, pp. 361–390, 2010.

[52] N. B. Gawali, V. D. Bulani, M. S. Gursahani, P. S. Deshpande, P. S. Kothavade, and A. R. Juvekar, "Agmatine attenuates chronic unpredictable mild stress-induced anxiety, depression-like behaviours and cognitive impairment by modulating nitrergic signalling pathway," *Brain Research*, vol. 1663, pp. 66–77, 2017.

[53] X. Sun, M. Wang, Y. Wang et al., "Melatonin produces a rapid onset and prolonged efficacy in reducing depression-like behaviors in adult rats exposed to chronic unpredictable mild stress," *Neuroscience Letters*, vol. 642, pp. 129–135, 2017.

[54] American Psychiatric Association, "*Cautionary statement for forensic use of DSM-5*," *American Journal of Psychiatry*, vol. 5, 2013.

[55] P. C. Koo, C. Berger, G. Kronenberg et al., "Combined cognitive, psychomotor and electrophysiological biomarkers in major depressive disorder," *European Archives of Psychiatry and Clinical Neuroscience*, vol. 269, no. 7, pp. 823–832, 2019.

[56] V. Thomas-Ollivier, E. Foyer, S. Bulteau et al., "Cognitive component of psychomotor retardation in unipolar and bipolar depression: is verbal fluency a relevant marker? Impact of repetitive transcranial stimulation," *Psychiatry and Clinical Neurosciences*, vol. 71, no. 9, pp. 612–623, 2017.

[57] M. L. Seibenhener and M. C. Wooten, "Use of the open field maze to measure locomotor and anxiety-like behavior in mice," *Journal of Visualized Experiments*, vol. 96, no. 96, article e52434, 2015.

[58] O. Sturman, P.-L. Germain, and J. Bohacek, "Exploratory rearing: a context- and stress-sensitive behavior recorded in the open-field test," *Stress*, vol. 21, no. 5, pp. 443–452, 2018.

[59] M. A. Katzman, X. Wang, D. B. Wajsbrot, and M. Boucher, "Effects of desvenlafaxine versus placebo on MDD symptom clusters: a pooled analysis," *Journal of Psychopharmacology*, vol. 34, no. 3, pp. 280–292, 2020.

[60] S. G. Kornstein, C. J. Guico-Pabia, and R. S. Fayyad, "The effect of desvenlafaxine 50 mg/day on a subpopulation of anxious/depressed patients: a pooled analysis of seven randomized, placebo-controlled studies," *Human Psychopharmacology*, vol. 29, no. 5, pp. 492–501, 2014.

[61] L. L. Beheydt, D. Schrijvers, L. Docx, F. Bouckaert, W. Hulstijn, and B. Sabbe, "Psychomotor retardation in elderly untreated depressed patients," *Frontiers in Psychiatry*, vol. 5, 2015.

[62] B. M. Gupta, S. H. Zargar, M. Arora, and V. R. Tandon, "Efficacy and safety of escitalopram versus desvenlafaxine in the treatment of major depression: a preliminary 1-year prospective randomized open label comparative trial," *Perspectives in Clinical Research*, vol. 7, no. 1, pp. 45–50, 2016.

[63] Ż. Brudkowska, M. Tomczyk, K. Jusiak, H. Karakuła-Juchnowicz, and E. Rudnicka-Drożak, "The role of beta-adrenolytic drugs in treating anxiety disorders," *Current Problems of Psychiatry*, vol. 19, no. 3, pp. 209–224, 2018.

[64] R. O. Margatho, E. K. Hamasato, D. G. Cruz et al., "Beta-adrenergic antagonist prevents anxiety like behavior and natural killer cells migration to the spleen in a model of cohabitation with sick partners," *Brain, Behavior, and Immunity.*, vol. 49, pp. e45–e46, 2015.

[65] C. Song, K. C. Berridge, and A. V. Kalueff, "'Stressing' rodent self-grooming for neuroscience research," *Nature Reviews Neuroscience*, vol. 17, no. 9, p. 591, 2016.

[66] A. V. Srinivasan, "Propranolol: a 50-year historical perspective," *Annals of Indian Academy of Neurology*, vol. 22, no. 1, pp. 21–26, 2019.

[67] H. Zhu, Z. Liu, Y. Zhou et al., "Lack of *B*2-AR increases anxiety-like behaviors and rewarding properties of cocaine," *Frontiers in Behavioral Neuroscience*, vol. 11, 2017.

[68] J. N. Flak, B. Myers, M. B. Solomon, J. M. Mcklveen, E. G. Krause, and J. P. Herman, "Role of paraventricular nucleus-projecting norepinephrine/epinephrine neurons in acute and chronic stress," *The European Journal of Neuroscience*, vol. 39, no. 11, pp. 1903–1911, 2014.

[69] C. Rabasa and S. L. Dickson, "Impact of stress on metabolism and energy balance," *Current Opinion in Behavioral Sciences*, vol. 9, pp. 71–77, 2016.

[70] T. J. Bartness, Y. Liu, Y. B. Shrestha, and V. Ryu, "Neural innervation of white adipose tissue and the control of lipolysis," *Frontiers in Neuroendocrinology*, vol. 35, no. 4, pp. 473–493, 2014.

[71] R. S. Sherwin and L. Saccà, "Effect of epinephrine on glucose metabolism in humans: contribution of the liver," *The American Journal of Physiology*, vol. 247, no. 2, pp. E157–E165, 1984.

[72] I. Berger, M. Werdermann, S. R. Bornstein, and C. Steenblock, "The adrenal gland in stress–adaptation on a cellular level," *The Journal of Steroid Biochemistry and Molecular Biology*, vol. 190, pp. 198–206, 2019.

[73] L. Cai, R. Li, W. J. Tang, G. Meng, H. Xiang Yang, and W. Ting Ni, "Antidepressant-like effect of geniposide on chronic unpredictable mild stress- induced depressive rats by regulating the hypothalamus-pituitary-adrenal axis," *European Neuropsychopharmacology*, vol. 25, no. 8, pp. 1332–1341, 2015.

[74] Y. M. Ulrich-Lai, H. F. Figueiredo, M. M. Ostrander, D. C. Choi, W. C. Engeland, and J. P. Herman, "Chronic stress induces adrenal hyperplasia and hypertrophy in a subregion-specific manner," *American Journal of Physiology-Endocrinology and Metabolism*, vol. 291, no. 5, pp. E965–E973, 2006.

[75] M. A. Calcia, D. R. Bonsall, P. S. Bloomfield, S. Selvaraj, T. Barichello, and O. D. Howes, "Stress and neuroinflammation: a systematic review of the effects of stress on microglia and the implications for mental illness," *Psychopharmacology*, vol. 233, no. 9, pp. 1637–1650, 2016.

[76] K. Pravalika, D. Sarmah, H. Kaur et al., "Myeloperoxidase and neurological disorder: a crosstalk," *ACS Chemical Neuroscience*, vol. 9, no. 3, pp. 421–430, 2018.

[77] G. Singhal and B. T. Baune, "Microglia: an interface between the loss of neuroplasticity and depression," *Frontiers in Cellular Neuroscience*, vol. 11, 2017.

[78] G. Ndrepepa, "Myeloperoxidase - a bridge linking inflammation and oxidative stress with cardiovascular disease," *Clinica Chimica Acta*, vol. 493, pp. 36–51, 2019.

[79] L. Hertz, D. Lovatt, S. A. Goldman, and M. Nedergaard, "Adrenoceptors in brain: cellular gene expression and effects on astrocytic metabolism and $[Ca^{2+}]_i$," *Neurochemistry International*, vol. 57, no. 4, pp. 411–420, 2010.

[80] K. F. Tanaka, H. Kashima, H. Suzuki, K. Ono, and M. Sawada, "Existence of functional *B*1- and *B*2-adrenergic receptors on microglia," *Journal of Neuroscience Research*, vol. 70, no. 2, pp. 232–237, 2002.

[81] D. R. Goldsmith, M. H. Rapaport, and B. J. Miller, "A meta-analysis of blood cytokine network alterations in psychiatric patients: comparisons between schizophrenia, bipolar disorder

and depression," *In Molecular Psychiatry*, vol. 21, no. 12, pp. 1696–1709, 2016.

[82] G. E. Hodes, C. Ménard, and S. J. Russo, "Integrating interleukin-6 into depression diagnosis and treatment," *Neurobiology of Stress*, vol. 4, pp. 15–22, 2016.

[83] J. C. Zhang, W. Yao, C. Dong et al., "Blockade of interleukin-6 receptor in the periphery promotes rapid and sustained antidepressant actions: a possible role of gut-microbiota-brain axis," *Translational Psychiatry*, vol. 7, no. 5, p. e1138, 2017.

[84] I. M. Balmus, A. Ciobica, I. Antioch, R. Dobrin, and D. Timofte, "Oxidative stress implications in the affective disorders: main biomarkers, animal models relevance, genetic perspectives, and antioxidant approaches," *Oxidative Medicine and Cellular Longevity*, vol. 2016, Article ID 3975101, 25 pages, 2016.

[85] R. O. Cojocariu, I. M. Balmus, R. Lefter et al., "Camelina sativa methanolic and ethanolic extract potential in alleviating oxidative stress, memory deficits, and affective impairments in stress exposure-based irritable bowel syndrome mouse models," *Oxidative Medicine and Cellular Longevity*, vol. 2020, Article ID 9510305, 20 pages, 2020.

[86] R. O. Cojocariu, I. M. Balmus, R. Lefter et al., "Behavioral and oxidative stress changes in mice subjected to combinations of multiple stressors relevant to irritable bowel syndrome," *Brain Sciences*, vol. 10, no. 11, pp. 1–19, 2020.

[87] B. S. Mello, A. J. Ferreira, M. C. Filho et al., "Sex influences in behavior and brain inflammatory and oxidative alterations in mice submitted to lipopolysaccharide-induced inflammatory model of depression," *Journal of Neuroimmunology*, vol. 320, pp. 133–142, 2018.

[88] J. Wolf, S. Rose-John, and C. Garbers, "Interleukin-6 and its receptors: a highly regulated and dynamic system," *Cytokine*, vol. 70, no. 1, pp. 11–20, 2014.

[89] J. Dahl, H. Ormstad, C. D. Hans et al., "The plasma levels of various cytokines are increased during ongoing depression and are reduced to normal levels after recovery," *Psychoneuroendocrinology*, vol. 45, pp. 77–86, 2014.

[90] F. M. Schmidt, N. Lichtblau, J. Minkwitz et al., "Cytokine levels in depressed and non-depressed subjects, and masking effects of obesity," *Journal of Psychiatric Research*, vol. 55, pp. 29–34, 2014.

[91] D. Brustolim, R. Ribeiro-dos-Santos, R. E. Kast, E. L. Altschuler, and M. B. P. Soares, "A new chapter opens in anti-inflammatory treatments: the antidepressant bupropion lowers production of tumor necrosis factor-alpha and interferon- gamma in mice," *International Immunopharmacology*, vol. 6, no. 6, pp. 903–907, 2006.

[92] M. Kubera, A. H. Lin, G. Kenis, E. Bosmans, D. Van Bockstaele, and M. Maes, "Anti-inflammatory effects of antidepressants through suppression of the interferon-γ/interleukin-10 production ratio," *Journal of Clinical Psychopharmacology*, vol. 21, no. 2, pp. 199–206, 2001.

[93] M. Maes, C. Song, A. H. Lin et al., "Negative immunoregulatory effects of antidepressants: inhibition of interferon-γ and stimulation of interleukin-10 secretion," *Neuropsychopharmacology*, vol. 20, no. 4, pp. 370–379, 1999.

[94] C. W. Tsao, Y. S. Lin, J. T. Cheng et al., "Serotonin transporter MRNA expression is decreased by lamivudine and ribavirin and increased by interferon in immune cells," *Scandinavian Journal of Immunology.*, vol. 63, no. 2, pp. 106–115, 2006.

Hindawi
Oxidative Medicine and Cellular Longevity
Volume 2022, Article ID 8729398, 23 pages
https://doi.org/10.1155/2022/8729398

Research Article

Activation of LRP1 Ameliorates Cerebral Ischemia/Reperfusion Injury and Cognitive Decline by Suppressing Neuroinflammation and Oxidative Stress through TXNIP/NLRP3 Signaling Pathway in Mice

Cheng-Jie Yang,[1,2] **Xin Li**,[1,2] **Xiao-Qing Feng**,[1,2] **Ye Chen**,[2,3] **Jian-Guo Feng**,[1,2] **Jing Jia**,[1,2] **Ji-Cheng Wei**,[1] **and Jun Zhou**[1,2]

[1]*Department of Anesthesiology, The Affiliated Hospital of Southwest Medical University, Luzhou, China*
[2]*Laboratory of Anesthesiology, Southwest Medical University, Luzhou, China*
[3]*Department of Traditional Chinese Medicine, The Affiliated Hospital of Southwest Medical University, Luzhou, China*

Correspondence should be addressed to Jun Zhou; scjunzhou@gmail.com

Received 24 May 2022; Accepted 3 August 2022; Published 18 August 2022

Academic Editor: Francisco Rios

Cerebral ischemia/reperfusion (I/R) injury is a clinical event associated with high morbidity and mortality. Neuroinflammation plays a crucial role in the pathogenesis of I/R-induced brain injury and cognitive decline. Low-density lipoprotein receptor-related protein-1 (LRP1) can exert strong neuroprotection in experimental intracerebral hemorrhage. However, whether LRP1 can confer neuroprotective effects after cerebral I/R is yet to be elucidated. The present study is aimed at investigating the effects of LRP1 activation on cerebral I/R injury and deducing the underlying mechanism involving TXNIP/NLRP3 signaling pathway. Cerebral I/R injury was induced in mice by bilateral common carotid artery occlusion. LPR1 ligand, apoE-mimic peptide COG1410, was administered intraperitoneally. To elucidate the underlying mechanism, overexpression of TXNIP was achieved via the hippocampal injection of AAV-TXNIP before COG1410 treatment. Neurobehavioral tests, brain water content, immunofluorescence, Western blot, enzyme-linked immunosorbent assay, HE, and terminal deoxynucleotidyl transferase dUTP nick end labeling staining were performed. Our results showed that the expressions of endogenous LRP1, TXNIP, NLRP3, procaspase-1, and cleaved caspase-1 were increased after cerebral I/R. COG1410 significantly ameliorated cerebral I/R-induced neurobehavioral deficits, brain edema, histopathological damage, and poor survival rate. Interestingly, COG1410 inhibited microglia proinflammatory polarization and promoted anti-inflammatory polarization, decreased oxidative stress, attenuated apoptosis, and inhibited the expression of the TXNIP/NLRP3 signaling pathway. However, the benefits of COG1410 were abolished by TXNIP overexpression. Thus, our study suggested that LRP1 activation with COG1410 attenuated cerebral I/R injury at least partially related to modulating microglial polarization through TXNIP/NLRP3 signaling pathway in mice. Thus, COG1410 treatment might serve as a promising therapeutic approach in the management of cerebral I/R patients.

1. Introduction

Cerebral ischemia/reperfusion (I/R) injury is a potentially life-threatening disorder with high morbidity and mortality [1, 2]. Primary ischemic insult is initiated due to insufficient oxygen and glucose delivery that supports cellular homeostasis [3]. On the other hand, restoring blood flow to the brain may cause a series of secondary pathological cascades, including excitotoxicity, neuroinflammation, oxidative stress, apoptosis, and death, or developing severe neurological deficits within the first several weeks due to delayed neuronal cell death [4, 5]. This phenomenon suggested that preventing and treating delayed neuronal necrosis are essential in addition to restoring cerebral blood flow in

the treatment of cerebral I/R injury. However, a lack of specific neuroprotective agents for cerebral I/R injury necessitates the investigation of the underlying mechanism and finding effective therapeutic strategies.

Microglia are innate immune cells in the brain and homologous to macrophages in the peripheral system. Microglia play a vital role in the neuroinflammation of brain injury. Depending on the type of stimulus, activated microglia have distinct functions related to the M1/M2 microglial polarization [6]. The M1 phenotypes of microglia are proinflammatory, releasing tumor necrosis factor-a (TNF-α), interleukin-6 (IL-6), and inducible nitric oxide synthase (iNOS). Conversely, the M2 phenotypes of microglia are anti-inflammatory and conducive to the production of IL-10, transforming growth factor-β (TGF-β), and arginase-1 (Arg-1) [7]. Thus, microglial polarization modulation towards the anti-inflammatory M2 phenotype might be a promising therapeutic target, which ameliorates cerebral I/R injury.

Low-density lipoprotein receptor-related protein-1 (LRP1) is a multifunctional receptor with two main biological functions in endocytosis and in the regulation of cell signaling pathways, which is widely expressed in neurons and glial cells in the central nervous system (CNS) [8–10]. Apolipoprotein E (*APOE* = gene, apoE = protein), one of the ligands of LRP1, is synthesized by astrocytes and oligodendrocytes in the brain [11]. Human APOE consists of three different isoforms: APOEε2, APOEε3, and APOEε4. Previous studies demonstrated that both human apoE3 and murine apoE exert neuroprotection by interacting with its receptor LRP1, while the APOEε4 isoform exhibits a poor prognosis in acute and chronic neurological diseases [12–14]. ApoE protein is 34 kilodaltons (kDa) and cannot permeate through the blood-brain barrier, making it difficult to use clinically. COG1410, a small molecule ApoE-mimetic peptide, is derived from the apoE receptor binding region [15]. Some studies showed that COG1410 has multiple neuroprotective properties, including anti-inflammation, antioxidation, and antiapoptosis, by activating its receptor LRP1 [16–18]. However, whether LRP1 activation with COG1410 can relieve I/R-induced cerebral damage and its underlying mechanism is yet unknown.

Nucleotide-binding oligomerization domain-like receptor protein 3 (NLRP3) inflammasome is composed of oligomerized NLRP3, apoptosis-associated speck-like protein (ASC), and procaspase-1 and is widely distributed in the microglia [19]. Previous studies found that NLRP3 inflammasomes promote inflammation and apoptosis by activating microglia in the cerebral I/R injury [20]. Moreover, oxidative stress is one of the crucial factors in cerebral I/R injury. Thioredoxin-interacting protein (TXNIP), an endogenous inhibitor of thioredoxin (TRX), plays a vital role in maintaining cellular redox balance [21, 22]. Previous studies demonstrated that TXNIP aggravates oxidative stress and promotes inflammatory response by activating the NLRP3 inflammasome. Therefore, TXNIP is also considered a potential target for the treatment of some I/R injuries [23, 24]. Nevertheless, the role of LRP1 and the TXNIP/NLRP3 signaling pathway in the microglial polarization modulation after cerebral I/R injury is yet to be elucidated.

In the present study, we hypothesized that activation of LRP1 with an apoE mimic, COG1410, alleviates cerebral I/R injury by regulating the polarization of microglia via inhibition of the TXNIP/NLRP3 signaling pathway.

2. Materials and Methods

2.1. Animals. The current study was approved by the Animal Care Committee of Southwest Medical University (China). Adult male *C57BL/6* mice, weighing 18–22 g, were purchased from Chengdu Dossy Experimental Animals Co., Ltd. (China). The animals were housed in cages in a temperature-controlled room ($22 \pm 2^{\circ}$C) with an alternating 12-h light/dark cycle and acclimatized for one week. Before the study, the mice were fasted for 8 h but were allowed water ad libitum. All procedures were performed according to the National Institutes of Health guidelines for the use of experimental animals.

2.2. Experimental Design. The experimental flow diagram is illustrated in Figure 1.

2.2.1. Experiment 1. To evaluate the time course of endogenous LRP1, TXNIP, NLRP3, procaspase-1, and cleaved caspase-1 expression and histopathological changes in the hippocampal tissues of mice after cerebral I/R, the mice were randomized into five groups: sham, 6, 12, 24, and 72 h after I/R ($n = 14$/group). Western blot analysis was performed to assess the protein level of LRP1, TXNIP, NLRP3, procaspase-1, and cleaved caspase-1. Then, hematoxylin and eosin (HE) staining was used for histopathological examination of the hippocampal tissues. Additionally, the cellular localization of LRP1 with neurons (neuronal nuclei, NeuN), astrocytes (glial fibrillary acidic protein, GFAP), or microglia (calcium-binding adaptor molecule 1, Iba-1) was evaluated by double immunofluorescence staining in the sham and I/R-72 h group ($n = 3$/group).

2.2.2. Experiment 2. To determine the beneficial effects of LRP1 activation on neurobehavioral functions, brain water content (BWC), and histopathological changes at 72 h after cerebral I/R, the mice were randomized into five groups: sham, I/R + Vehicle, I/R + COG1410 (0.5 mg/kg), I/R + COG1410 (1.0 mg/kg), and I/R + COG1410 (2.0 mg/kg) ($n = 24$/group). The BWC and histopathological changes were tested at 72 h after reperfusion, while Morris water maze (MWM) was performed for neurobehavior tests on days 3–8 after cerebral I/R.

2.2.3. Experiment 3. To assess the roles of LRP1 activation on microglia, neuroinflammation, and apoptosis at 72 h after cerebral I/R, the mice were randomly divided into three groups for Western blot, enzyme-linked immunosorbent assay (ELISA), immunofluorescence, and terminal deoxynucleotidyl transferase dUTP nick end labeling (TUNEL) staining: sham, I/R + Vehicle, and I/R + COG1410 ($n = 14$/group).

2.2.4. Experiment 4. In order to investigate the underlying mechanism of TXNIP/NLRP3 pathway in LRP1 mediated

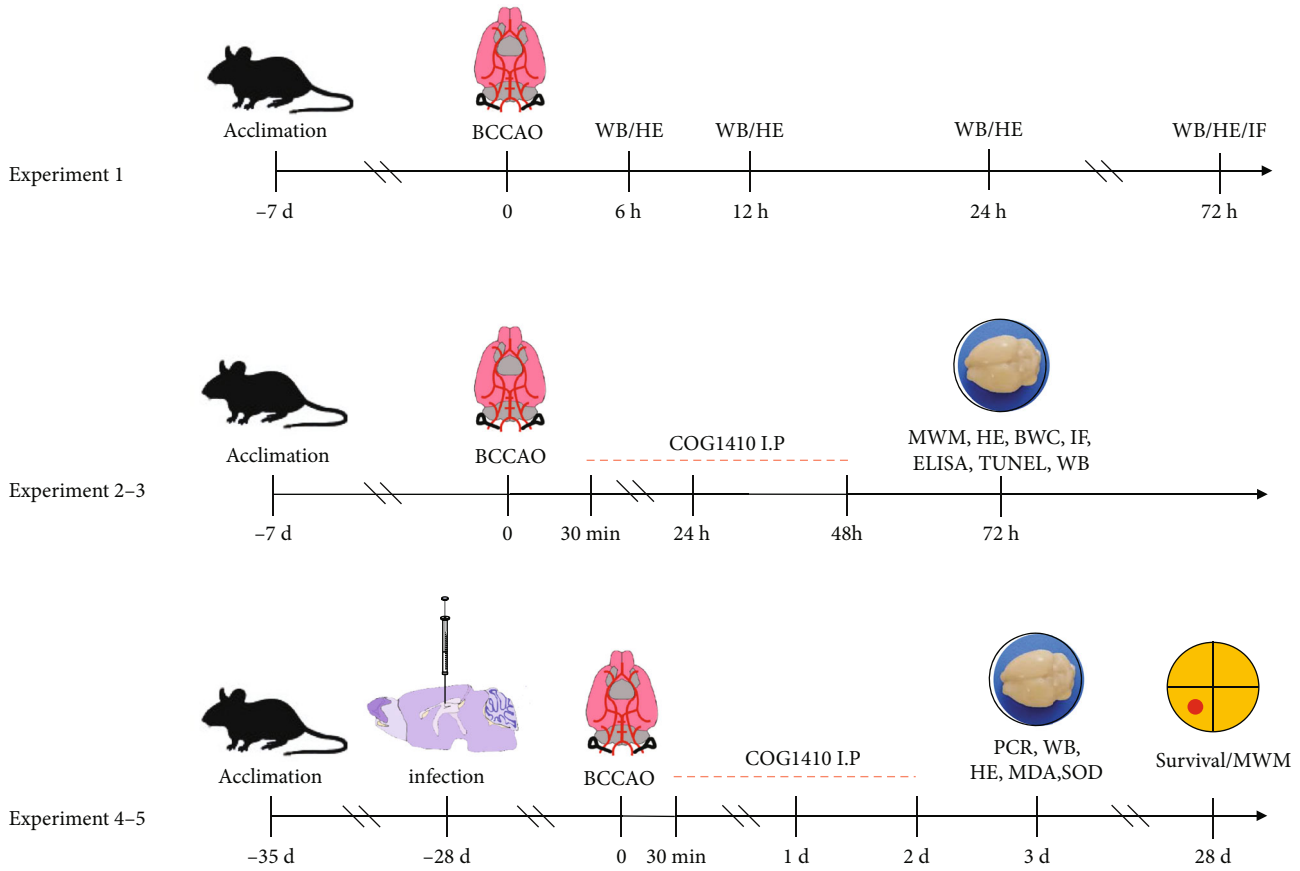

Figure 1: Experimental design and animal groups. BCCAO: bilateral common carotid artery occlusion; WB: Western blot; HE: hematoxylin and eosin; IF: immunofluorescence; BWC: brain water content; MWM: Morris water maze; ELISA: enzyme-linked immunosorbent assay; TUNEL: terminal deoxynucleotidyl transferase dUTP nick end labeling; h: hour; d: day.

microglia polarization-modulating, the mice were randomized into five groups: sham, I/R + Vehicle, I/R + COG1410, I/R + COG1410 + AAV-NC, and I/R + COG1410 + AAV-TXNIP ($n = 14$/group). Histopathological changes, the level of oxidative stress, the release of inflammatory factors, and Western blot analysis were performed at 72 h after cerebral I/R. Moreover, the mice were randomly divided into three groups, naïve, naïve + AAV-NC, and naïve + AAV-TXNIP ($n = 6$/group), to verify the efficacy of AAV-TXNIP on TXNIP overexpression via qRT-PCR and Western blot.

2.2.5. Experiment 5. To explore the underlying mechanism of TXNIP/NLRP3 pathway in LRP1-mediated long-term neuroprotective effect, the mice were randomly divided into five groups: sham, I/R + Vehicle, I/R + COG1410, I/R + COG1410 + AAV-NC, and I/R + COG1410 + AAV-TXNIP ($n = 15$/group). The survival rates of different groups were monitored at 28 days after cerebral I/R, and WMW was conducted on days 28–33 after cerebral I/R.

2.3. Cerebral I/R Model. The model of cerebral I/R was established using bilateral common carotid artery occlusion (BCCAO) as described previously [25]. Briefly, mice were anesthetized with pentobarbital sodium (45 mg/kg, intraperitoneally). Then, the trachea was exposed by a 0.5 cm midline neck incision, and the bilateral common carotid arteries (CCAs) were separated from the vagus nerve. Subsequently, the bilateral CCAs were occluded with the microvascular clamp, with the right CCA clamped first. After 30 min of ischemia, both CCAs were reperfused. In the sham operation group mice, the same procedures were performed without CCA occlusion. After infiltration with 0.25% bupivacaine, the wound was closed by sterile sutures. During the surgery, the body temperature of mice was maintained with a heating pad.

2.4. Intraperitoneal Administration. COG1410 (acetyl-AS-Aib-LRKL-Aib-KRLL-amide synthesized by GL Biochem, Shanghai, China) was diluted with saline to different concentrations (0.5 mg/kg, 1.0 mg/kg, and 2.0 mg/kg), as described previously (Laskowitz et al., 2007). A volume of 100 μL COG1410 was administered intraperitoneally at 30 min, 24 h, and 48 h after reperfusion. The mice in the sham and I/R + Vehicle groups received equal volumes of saline at the same time point.

2.5. AAV Injection. The TXNIP overexpression mouse model was established on day 28 before BCCAO, as described previously [26]. Briefly, the adeno-associated virus vectors (AAV-TXNIP and AAV-NC) were constructed by

Syngentech Co., Ltd. (Beijing, China). Before exposing the skull, the mice were anesthetized with pentobarbital sodium in a stereotaxic apparatus (RWD, Shenzhen, China). A volume of 1.5 μL of the AAV vectors was injected stereotaxically into the bilateral hippocampal CA1 area (AP-2.0 mm; ML±1.0 mm; DV 2.0 mm) at a rate of 0.5 μL/min, following which the needle was kept in place for 5 min and screwed out slowly. The skin incision was sutured, and the mice were housed in a single cage after they awoke from anesthesia.

2.6. Specimen Collection. The mice were sacrificed at 6, 12, 24, or 72 h after reperfusion under deep anesthesia. Some animals were perfused transcardially with ice-cold saline, and then, the hippocampal tissues were separated on ice, frozen in liquid nitrogen, and stored at -80°C for Western blot, ELISA, detection of oxidative stress, and RT-PCR. The other mice were perfused transcardially with 4% paraformaldehyde for HE, TUNEL, and immunofluorescence staining.

2.7. Morris Water Maze Test. The function of spatial learning and memory for mice was assessed using the Morris water maze (MWM) test [27]. The maze (Xinruan, Shanghai, China) consisted of a round tank (height 50 cm, diameter 120 cm), a platform (diameter 10 cm), and a camera analysis system. The tank was divided into four quadrants, and filled up to a depth of 30 cm with mixed milk water (22 ± 1°C). The mice were trained for four trials per day for five consecutive days during the place navigation test. In every trial, mice were placed in a different start quadrant and allowed to find the platform submerged below 1 cm of the water surface within a maximum duration of 60 s; the escape latency was recorded. On day 6, in the probe trial, the platform was withdrawn, and the mice were allowed to navigate freely in water for 60 s. The number of times crosses over the removed platform, duration in the target quarter (%), and swimming speed was recorded during the trial.

2.8. Histopathological Examination. Whole-brain tissues were fixed in 4% paraformaldehyde, embedded in paraffin, and sliced into 3 μm-thick coronal sections. The sections were stained with HE and observed under a light microscope (Olympus, Tokyo, Japan) by two experienced pathologists blinded to the study. The number of normal neurons per square millimeter (cells/mm^2) was calculated according to the size of the CA1 subregion in four high-magnification fields of each section, and the average was considered.

2.9. Brain Water Content. The brain water content (BWC) was estimated by the wet-to-dry brain weight ratio as described previously [28]. Briefly, the whole brains were harvested under deep anesthesia and immediately weighed to obtain the wet weight. Then, the brain tissues were baked at 65°C for 48 h to obtain the dry weight. BWC = (wet weight − dry weight)/wet weight × 100%.

2.10. Assessment of Apoptosis. The brains were dehydrated with 30% sucrose and sliced into 8 μm-thick coronal frozen sections using a cryostat (Leica, Germany). The apoptosis of cells in the hippocampus was detected using the TUNEL staining, according to the manufacturer's protocol (#12156792910, Roche, Basel, Switzerland) [29]. The numbers of TUNEL-positive cells were counted in the CA1 subregion of the hippocampus. Four random high-magnification fields per section over a microscopic field of 400x magnification were averaged. Data were presented as the ratio of TUNEL-positive cells (%).

2.11. Immunofluorescence Staining. Immunofluorescence staining was performed as described previously [30]. Briefly, the frozen sections were incubated with primary antibody at 4°C overnight: mouse anti-Iba1 (1 : 200, #GT10312, Invitrogen, USA), mouse anti-GFAP (1 : 200, #3670S, Cell Signaling Technology (CST), USA), mouse anti-NeuN (1 : 200, #ab104224, Abcam, USA), rabbit anti-LRP1 (1 : 200, #64099S, CST, USA), rabbit anti-TXNIP (1 : 200, #14715S, CST, USA), and rabbit anti-NLRP3 (1 : 200, #15101S, CST, USA). After washing with phosphate-buffered saline (PBS), the sections were incubated with the corresponding secondary antibody (Cy3-labeled goat anti-rabbit IgG, FITC-labeled goat anti-mouse IgG) (1 : 200, #S0011, #0007, Affinity, USA) at room temperature for 1 h, followed by DAPI (#C0060, Solarbio, China) staining. Finally, the sections were visualized, and images were captured using a fluorescence microscope.

2.12. Detection of Inflammatory Factors. Hippocampal tissue homogenates were prepared and clarified by centrifugation at 12000 rpm at 4°C for 15 min. TNF-α, IL-6, IL-1β, and IL-18 levels were measured in the supernatants of hippocampal tissues using the ELISA kits (#MM-0132M1, #MM-0163M1, #MM-0040M1, #MM-0169M1, Meimian Jiangsu, China) by the manufacturer's instruction as described previously [31].

2.13. Detection of Oxidative Stress. Hippocampal tissue homogenates were prepared, and lysates were collected by centrifugation at 3000 rpm at 4°C for 10 min. The ROS and MDA content and SOD and GSH-Px activity in the supernatant of hippocampal tissues were detected by commercial biochemical kits (#E004-1-1, #A003-1-2, #A001-3-2, #A005-1-2, Nanjing Jiancheng, China) as described previously [32, 33].

2.14. qRT-PCR. Total RNA was extracted from the hippocampal tissues using an RNA simple total RNA kit (#DP419, Tiangen, Beijing, China) following the standard protocol. This isolated RNA was reverse-transcribed into cDNA using the ReverTra Ace qPCR RT Master Mix (#FSQ-201, Toyobo, Japan) according to the manufacturer's protocol. Then, the cDNA was amplified using SuperReal PreMix Plus (SYBR Green) (#FP205-02, Tiangen, Beijing, China) on a real-time PCR system (Roche). The amplification parameters were as follows: 95°C for 15 min, followed by five cycles of 95°C for 10 s and 60°C for 32 s. β-Actin was used as an internal reference for the quantification of the *TXNIP* gene expression level. The relative mRNA expression level in the naive group (target mRNA/β-*actin* value) was set as the normalization to calculate the fold-changes of the mRNA level in other groups. The primer sequences are listed in Table 1.

Table 1: The PCR primers sequences.

Genes	Primer sequences
TXNIP	Forward: 5′-ATACTCCTTGCTGATCTACG-3′
	Reverse: 5′-TGGGGTATCTGGGATGTTTA-3′
β-Actin	Forward: 5′-TTTGCAGCTCCTTCGTTGC-3′
	Reverse: 5′-TCGTCATCCATGGCGAACT-3′

Abbreviation: TXNIP: thioredoxin-interacting protein.

2.15. Western Blot Analysis. The protein in the hippocampal tissue sample was estimated using an enhanced BCA protein assay kit (#P0012, Beyotime, Shanghai, China). An equivalent of 30 μg protein was separated on the sodium dodecyl sulfate-polyacrylamide gel electrophoresis (SDS-PAGE) and transferred to a polyvinylidene fluoride membrane (PVDF; Amersham Biosciences, NJ, USA) or a nitrocellulose membrane (Beyotime). Then, the membrane was blocked with 5% nonfat milk at room temperature for 1 h and probed with the primary antibodies at 4°C overnight: anti-LRP1 (1 : 1000, #64099S, CST), anti-TXNIP (1 : 1000, #14715S, CST), anti-NLRP3 (1 : 1000, #15101S, CST), anti-caspase-1 (1 : 200, #SC-56036, Santa Cruz, USA), anti-Iba-1 (1 : 1000, #17198S, CST), anti-iNOS (1 : 1000, #AF0199, Affinity, USA), anti-Arg-1 (1 : 1000, #DF6657, Affinity), anti-Bcl-2 (1 : 1000, #ab59348, Abcam, USA), anti-Bax (1 : 1000, #50599-2-Ig, Proteintech, China), anti-cleaved caspase-3 (1 : 1000, #19677-1-AP, Proteintech), and anti-β-actin (1 : 5000, #6609-1-Ig, Proteintech), followed by incubation with the appropriate horseradish peroxidase- (HRP-) labeled secondary antibody (1 : 5000, #SE131, #SE134, Solarbio, China) at room temperature for 1 h. Then, the membranes were developed using enhanced chemiluminescence (ECL; Amersham, Buckinghamshire, UK). Finally, the immunoreactive bands were analyzed using Image J software (version 1.31; National Institutes of Health (NIH), Bethesda, MD, USA).

2.16. Statistical Analysis. The GraphPad Prism 8.3 statistical software (GraphPad Software, San Diego, CA, USA) was used for statistical analysis. All data were expressed as the mean and standard error of the mean (mean ± SEM). One-way analysis of variance (ANOVA) and Tukey's post hoc test were used for comparisons. For the training phase of the WMW test, the escape latency over time was analyzed by two-way repeated-measures ANOVA. Kaplan-Meier survival curves were analyzed using the log-rank test. $P < 0.05$ was considered statistically significant.

3. Results

3.1. Time Course of Histopathological Changes and the Endogenous Protein Levels of LRP1, TXNIP, and NLRP3 Inflammasome in the Hippocampus after Cerebral I/R. HE staining was performed to determine the histopathological changes in the hippocampal tissues on the animal models. The results showed that the total normal cells of the CA1 region started decreasing at 6 h and were the lowest at 72 h after cerebral I/R injury (Figures 2(a) and 2(b)). Furthermore, Western blot analysis showed that the protein level of LRP1 was significantly increased in the I/R group compared to the sham group at 12-72 h after surgery. The protein level of TXNIP was significantly increased in the I/R group compared to the sham group at 6 h and 72 h postsurgery. The protein level of NLRP3 was significantly increased in the I/R group compared to the sham group at 72 h after surgery. The protein level of procaspase-1 and cleaved caspase-1 was significantly increased in the I/R group compared to the sham group at 24-72 h after surgery (Figures 2(d)–2(i)).

Double immunofluorescence staining of LRP1 with microglia (Iba-1), neurons (NeuN), and astrocytes (GFAP) was performed in the sham group and I/R-72 h group. The cellular colocalization of LRP1 with Iba-1, NeuN, and GFAP was detected in the CA1 subregion of the hippocampus, and the number of LRP1-positive microglia, neurons, and astrocytes was increased at 72 h after cerebral I/R (Figure 2(c)).

3.2. COG1410 Ameliorated Short-Term Neurological Deficits, Brain Edema, and Histopathological Damage at 72 H after Cerebral I/R. In the place navigation test, the escape latency for the mice to find the platform was significantly prolonged in the I/R + Vehicle group compared to the sham group. However, a significantly shorter escape latency was observed on training days 4-5 in the I/R + COG1410 (1.0 mg/kg and 2.0 mg/kg) groups (Figure 3(a)). In the probe trial, the mice in the I/R + Vehicle group required fewer platform crossings and less time percentage in the target quarter compared to the sham group, while the reference memory deficits were improved by COG1410 treatment (1.0 mg/kg and 2.0 mg/kg). Also, no significant differences were observed in the swimming speed among each group (Figures 3(b)–3(e)).

The results of HE staining showed that the structure of the hippocampal CA1 region was regular morphology in the sham group. However, many injured neurons, characterized by shrunken and stained dark, were observed in the hippocampal CA1 region of the mice after cerebral I/R. Moreover, fewer normal neurons of the hippocampal CA1 area and higher BWC of the whole brain tissues were observed in the I/R + Vehicle group compared to the sham group mice at 72 h after cerebral I/R. Compared to the animals treated with vehicles, administration of 1.0 mg/kg and 2.0 mg/kg COG1410 significantly attenuated the histopathological damage and brain edema (Figures 4(a)–4(c)). Based on the MWM test, histopathological results, and BWC, the dose of 1.0 mg/kg was selected for subsequent experiments.

3.3. COG1410 Reduced Apoptosis of Hippocampal Cells at 72 H after Cerebral I/R. The cell apoptosis of the hippocampal CA1 region in mice was evaluated by the TUNEL method. Apoptotic cells were not detected in the sham group. The number of apoptotic cells was significantly increased in the hippocampal CA1 region after 72 h of reperfusion. These changes were alleviated by COG1410

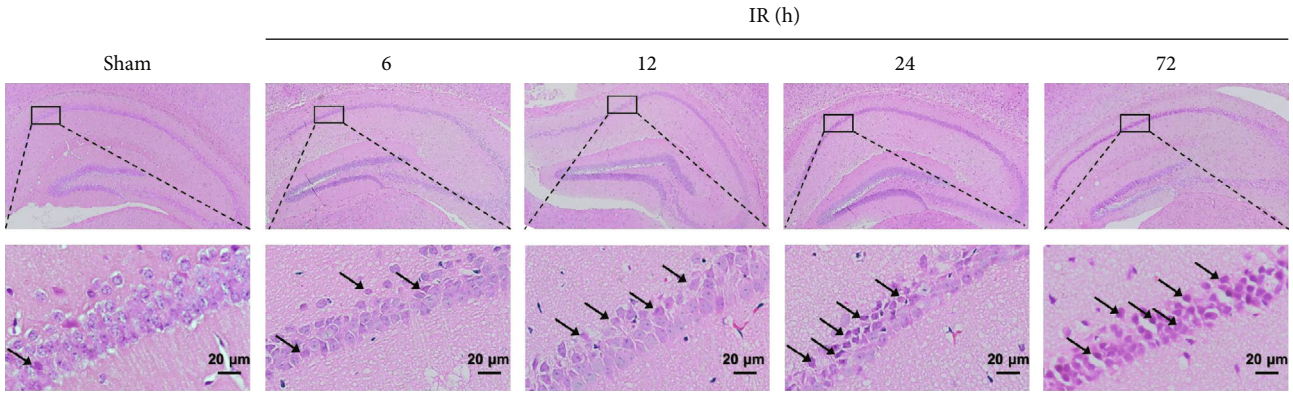

(a)

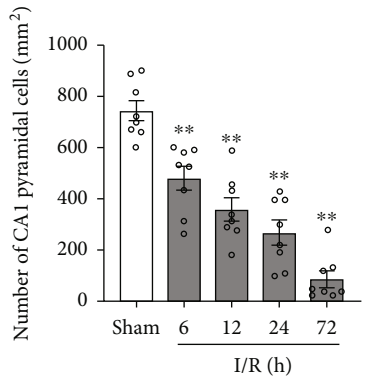

(b)

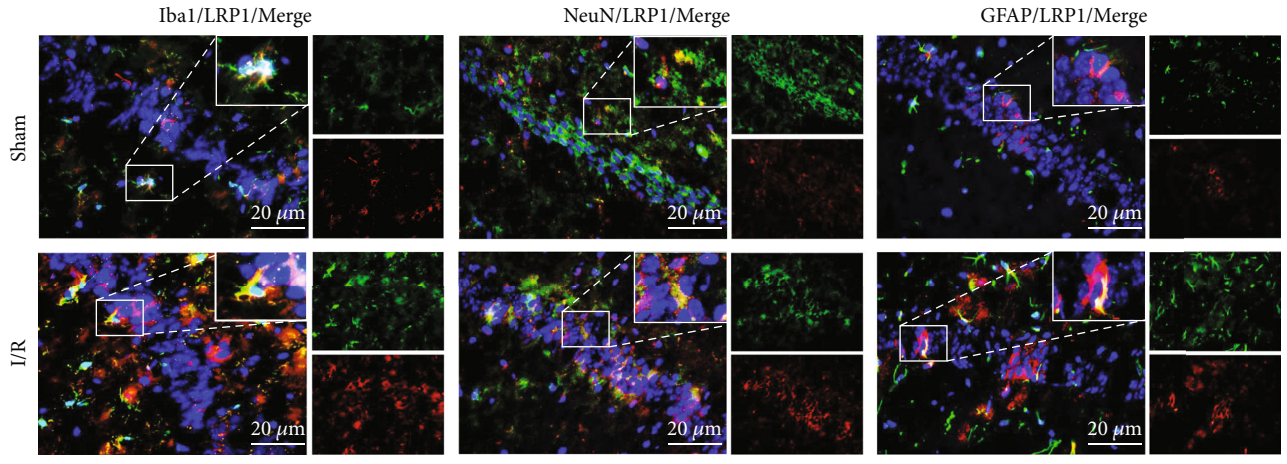

(c)

Figure 2: Continued.

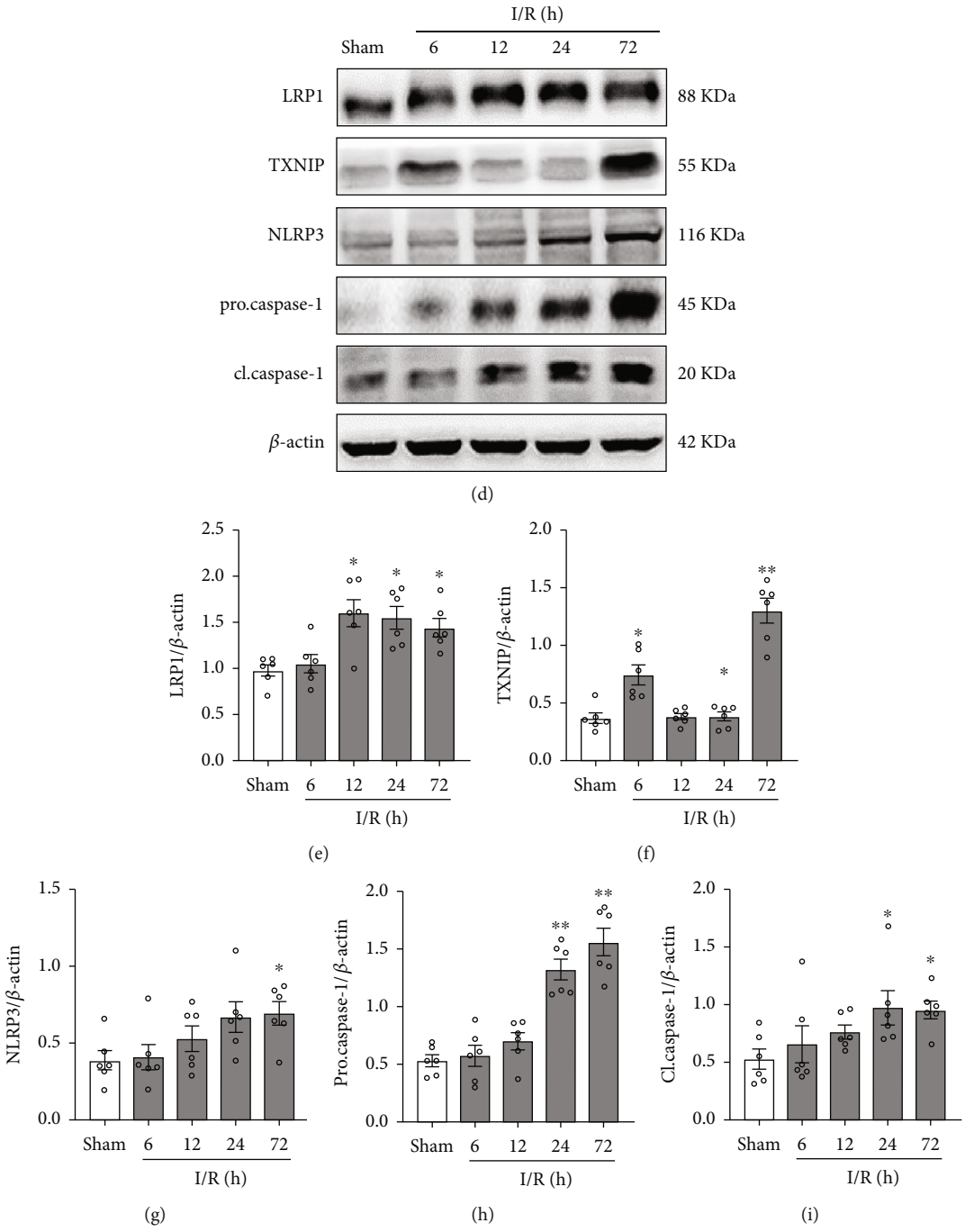

Figure 2: Effects of cerebral I/R on histopathological changes, and the expressions of LRP1, TXNIP, and NLRP3 inflammasome. (a) HE staining of hippocampal CA1 area (×400), scale bar = 20 μm; the arrows indicate injured neurons. (b) Quantitative analysis of normal neurons in the hippocampal CA1 area. (c) Double immunofluorescence staining (IF) of LRP1 (red) with microglia (Iba-1, green), neurons (NeuN, green), and astrocytes (GFAP, green) in the hippocampal CA1 region at 72 h after cerebral I/R. Nuclei were stained with DAPI (blue), scale bar = 20 μm. (d) Representative bands of Western blot data. (e–i) Quantitative analysis of the Western blot bands. Data were represented as mean ± SEM. Western blot, $n = 6$ per group; HE staining, $n = 8$ per group; double immunofluorescence staining, $n = 3$ per group. $^{*}P < 0.05$, $^{**}P < 0.01$ vs. sham group.

treatment, manifested as a decreased number of TUNEL-positive cells (Figures 5(a) and 5(c)).

Furthermore, the Western blot data indicated that the protein levels of cleaved caspase-3 and Bax increased in the I/R + Vehicle group compared to the sham group, while that decreased significantly in the I/R + COG group compared to the I/R + Vehicle group (Figures 5(b), 5(d), and 5(e)). In addition, the protein levels of Bcl-2 were significantly lower

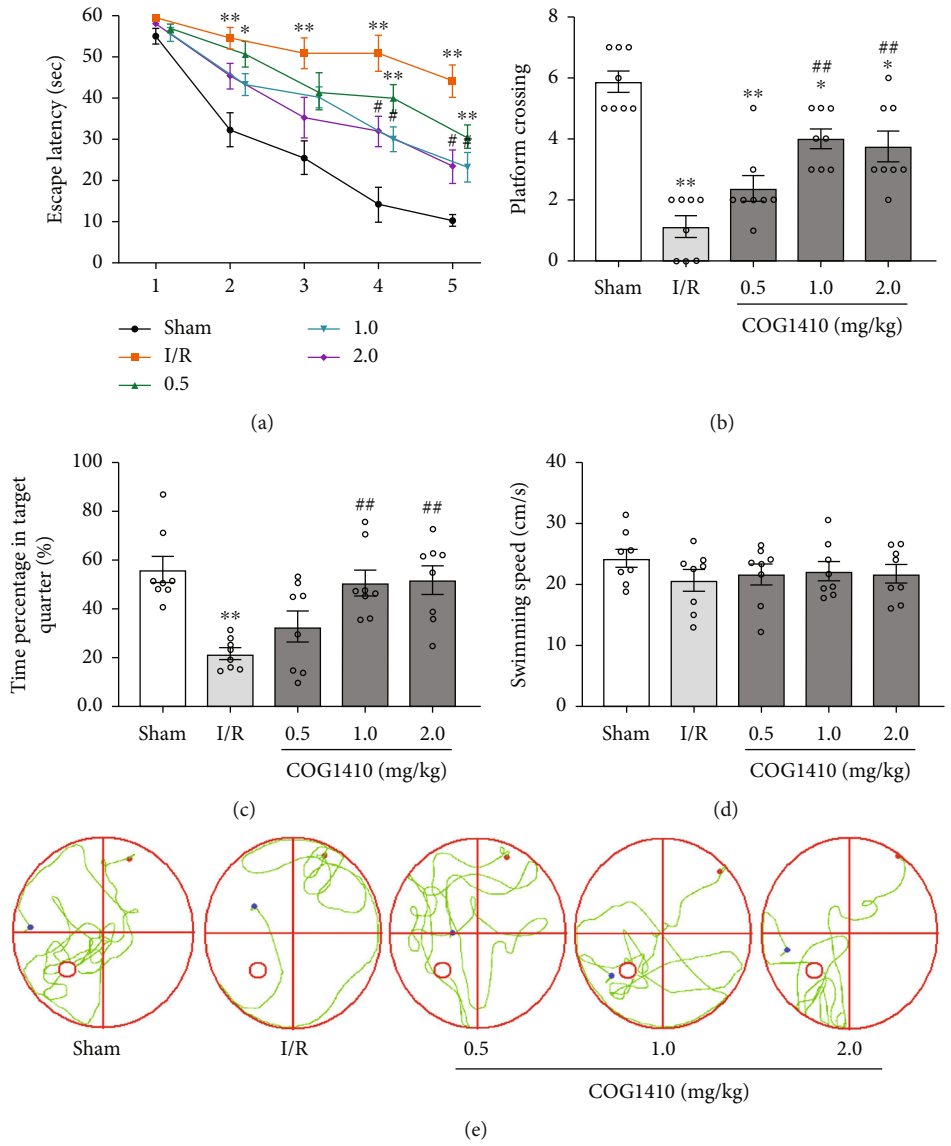

Figure 3: Effects of COG1410 on the neurological functions at 72 h after cerebral I/R. (a) Escape latency of mice in the training trials. (b) Frequency of platform crossing in the probe trial. (c) Percentage of time spent in the target quadrant in the probe trial. (d) Swimming speed in the probe trial. (e) Swimming trajectory of mice of each group in the probe trial. Data were represented as mean ± SEM ($n = 8$). $^{*}P < 0.05$, $^{**}P < 0.01$ vs. sham group; $^{\#}P < 0.05$, $^{\#\#}P < 0.01$ vs. I/R + Vehicle group.

in the I/R + Vehicle group compared to the sham group but were increased in the I/R + COG group compared to the I/R + Vehicle group (Figures 5(b) and 5(f)).

3.4. COG1410 Promoted M1-to-M2 Phenotypic Polarization of Microglia and Alleviated Inflammatory Response. Immunofluorescence staining with Iba-1 antibody was performed at 72 h after cerebral I/R. The sham group showed fewer Iba-1-positive cells with ramified thin processes. However, compared to the sham group, the number of Iba-1-positive cells was significantly increased, and the microglial cells showed considerable branch retraction, thickening, and amoeba-like morphology in the I/R + Vehicle group, while the I/R + COG group showed less microglial activation than the I/R + Vehicle group (Figure 6(a)).

Upon activation, microglial polarized to M1 or M2 phenotypes with distinct proinflammatory and immunosuppressive functions, among which iNOS was an M1 phenotype marker and Arg-1 was an M2 phenotype marker. The Western blot data indicated that the protein levels of Iba-1 and iNOS were upregulated in the I/R + Vehicle group compared to the sham group but were significantly lower in the I/R + COG group compared to the I/R + Vehicle group (Figures 6(b)–6(d)). Moreover, the protein level of Arg-1 was increased in the I/R + Vehicle group compared to the sham group and was significantly higher in the I/R + COG group compared to the I/R + Vehicle group (Figures 6(b) and 6(e)).

Next, we detected the expression of inflammatory factors, including IL-1β, IL-18, TNF-α, and IL-6 in each group

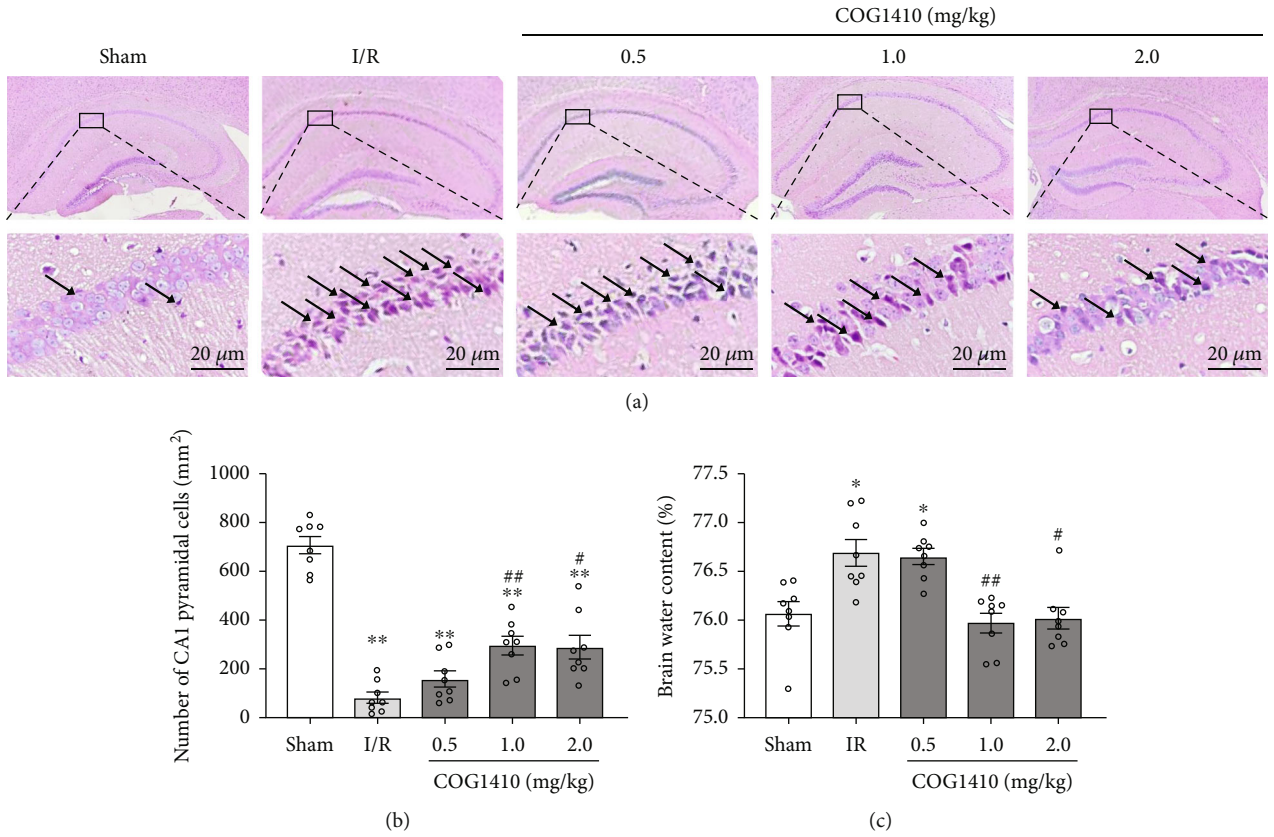

Figure 4: Effects of COG1410 on the histopathological damage and BWC at 72 h after cerebral I/R. (a) HE staining of hippocampal CA1 area (×400), scale bar = 20 μm; the arrows indicate injured neurons. (b) Quantitative analysis of normal neurons in the hippocampal CA1 area. (c) BWC. Data were represented as mean ± SEM ($n = 8$). $^{*}P < 0.05$, $^{**}P < 0.01$ vs. sham group; $^{\#}P < 0.05$, $^{\#\#}P < 0.01$ vs. I/R + Vehicle group.

by ELISA. As shown in Figures 6(f)–6(i), the levels of inflammatory factors were significantly increased in the I/R + Vehicle group compared to the sham group, while a significantly decreased expression of the inflammatory factors was observed in the I/R + COG group compared to the I/R + Vehicle group.

3.5. COG1410 Inhibited TXNIP/NLRP3 Signaling Pathway in the Hippocampus after Cerebral I/R. Western blot was used to detect the levels of LRP1, TXNIP, NLRP3, procaspase-1, and cleaved caspase-1 in the hippocampus of mice at 72 h after cerebral I/R. The results showed that the levels of these proteins increased in the I/R + Vehicle group compared to the sham group. Interestingly, the expression levels of TXNIP, NLRP3, procaspase-1, and cleaved caspase-1 decreased significantly in the I/R + COG group compared to the I/R + Vehicle group. However, no statistically significant difference was observed between the I/R + Vehicle group and the I/R + COG group concerning the LRP1 level (Figures 7(b) and 7(e)–7(i)).

Double immunofluorescence staining was performed to verify the cellular localization of the TXNIP/NLRP3 signaling pathway after cerebral I/R. The results showed that TXNIP/NLRP3 signaling pathway was colocalized with microglia in the hippocampus of mice at 72 h after cerebral I/R. Moreover, quantitative analysis showed that the number of TXNIP-positive and NLRP3-positive microglia increased significantly in the I/R + Vehicle group compared to the sham group, while the number of the TXNIP-positive and NLRP3-positive microglia was significantly decreased in the I/R + COG group compared to the I/R + Vehicle group (Figures 7(a), 7(c), and 7(d)).

3.6. Overexpression of TXNIP Reversed the Effects of COG1410 on M2 Microglial Polarization, Apoptosis, Oxidative Stress, and Inflammation. AAV vectors with green fluorescence were injected into the hippocampus 28 days before BCCAO. The overexpression efficacy of AAV-TXNIP was verified by Western blot and qRT-PCR. The results showed that both the mRNA and protein levels of TXNIP were significantly increased in the AAV-TXNIP group compared to the AAV-NC group (Figures 8(a)–8(c)).

Strikingly, compared to vehicle treatment after cerebral I/R, COG1410 treatment had no effect on the protein level of LRP1, but it significantly decreased the protein levels of TXNIP, NLRP3, procaspase-1, cleaved caspase-1, M1 microglial phenotype marker Iba-1 and iNOS, and proapoptotic proteins cleaved caspase-3 and Bax and increased the levels of M2 microglial phenotype marker Arg-1 and antiapoptotic protein Bcl-2. When the TXNIP protein was overexpressed in the I/R + COG + AAV-TXNIP group, the effects of COG1410 on the TXNIP/NLRP3

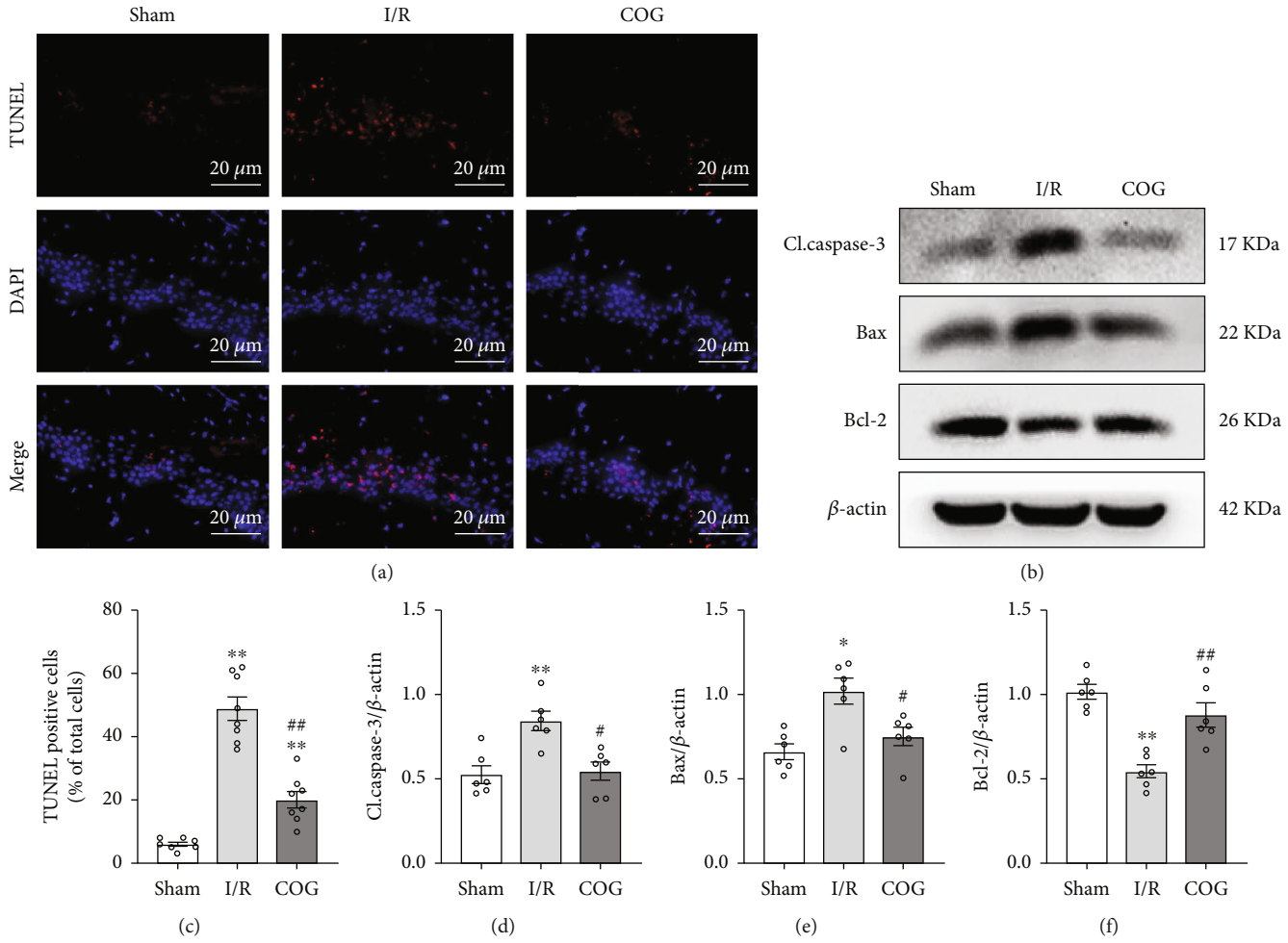

Figure 5: Effects of COG1410 on hippocampal apoptosis at 72 h after cerebral I/R. (a) Representative images of TUNEL staining in the hippocampal CA1 area (×400); nuclei were labeled with blue fluorescence (DAPI), and TUNEL-positive cells were labeled with red fluorescence, scale bars = 20 μm. (b) Representative bands of Western blot data. (c) Quantitative analyses of TUNEL-positive cells in the hippocampal area. (d–f) Quantitative analysis of the Western blot bands. Data were represented as mean ± SEM. Western blot, $n = 6$ per group; TUNEL staining, $n = 8$ per group. $^{*}P < 0.05$, $^{**}P < 0.01$ vs. sham group; $^{\#}P < 0.05$, $^{\#\#}P < 0.01$ vs. I/R + Vehicle group.

signaling pathway inhibition, M2 microglial polarization, and antiapoptosis were reversed compared to the I/R + COG + AAV-NC group (Figures 8(d)–8(o)).

The results of HE staining showed that the normal neuronal cells in the hippocampus were significantly increased in the I/R + COG group compared to the I/R + Vehicle group and that in the I/R + COG + AAV-TXNIP group was also decreased compared to the I/R + COG + AAV-NC group (Figures 9(a) and 9(b)). Since TXNIP plays a vital role in maintaining the balance of cellular redox, we assessed the degree of oxidative stress via ROS and MDA content and GSH-Px and SOD activity and found that the degree of oxidative stress was significantly reduced with COG1410 treatment after cerebral I/R. Nevertheless, the antioxidative effect of COG1410 was abolished when the TXNIP protein was overexpressed (Figures 9(c)–9(f)). Meanwhile, we found that the levels of inflammatory factors, including IL-1β, IL-18, TNF-α, and IL-6, were significantly reduced with COG1410 treatment after cerebral I/R. However, the anti-inflammatory effect of COG1410 was abolished when the TXNIP protein was overexpressed (Figures 9(g)–9(j)).

3.7. COG1410 Improved Survival Rate and Long-Term Neurological Functions through the TXNIP/NLRP3 Signaling Pathway after Cerebral I/R. To evaluate the long-term effects of COG1410 on cerebral I/R mice, a 28-day survival rate for different groups was observed. Interestingly, the survival rate was significantly decreased in the I/R + Vehicle group compared to the sham group, while that of the cerebral I/R mice was improved by COG1410 treatment. However, the effect of COG1410 on improving the survival rate of cerebral I/R mice was abolished after overexpression of TXNIP (Figure 10(a)). The results of the MWM test showed that compared to the sham group, the learning and memory function were impaired in the mice 28 days after cerebral I/R. The neurological deficits of cerebral I/R mice were alleviated with COG1410 treatment, while the neuroprotective function of COG1410 was reversed by TXNIP overexpression (Figures 10(b)–10(f)).

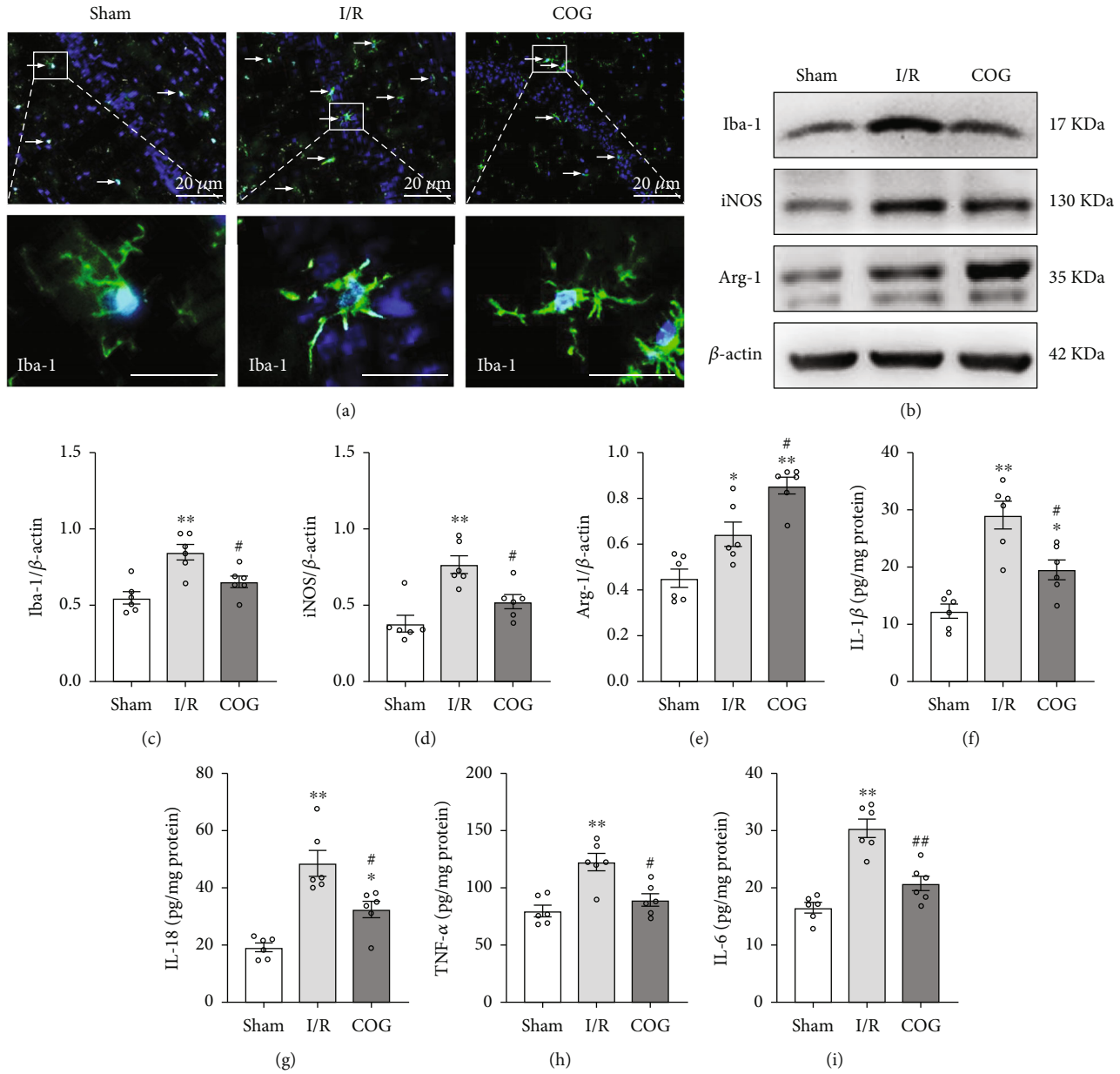

Figure 6: Effects of COG1410 on microglial polarization and proinflammatory factors at 72 h after cerebral I/R. (A) Representative images of Iba-1 immunofluorescence staining in hippocampal CA1 area (×200); nuclei were labeled with blue fluorescence (DAPI), and Iba-1 was labeled with green fluorescence, scale bars = 20 μm. (b) Representative bands of Western blot data. (c–e) Quantitative analysis of the Western blot bands. (f–i) Quantitative analysis of the inflammatory factors including IL-1β, IL-18, TNF-α, and IL-6. Data were represented as mean ± SEM. Western blot and ELISA, $n = 6$ per group; immunofluorescence staining, $n = 3$ per group. $^{*}P < 0.05$, $^{**}P < 0.01$ vs. sham group; $^{\#}P < 0.05$, $^{\#\#}P < 0.01$ vs. I/R + Vehicle group.

4. Discussion

In the current study, we first investigated the beneficial effects of LRP1 activation and explored its underlying mechanism in the cerebral I/R mouse model. Next, we demonstrated that LRP1 activation with COG1410 regulated microglia polarization, decreased brain edema, reduced oxidative stress, suppressed apoptosis in the hippocampus, and improved both short- and long-term neurological functions after cerebral I/R. In addition, LRP1 activation was associated with the downregulation of TXNIP, NLRP3, procaspase-1, cleaved caspase-1, Iba-1, iNOS, IL-1β, IL-18, IL-6, TNF-α, cleaved caspase-3, Bax, ROS, and MDA and the upregulation of Arg-1, Bcl-2, GSH-Px, and SOD after cerebral I/R. However, overexpression of TXNIP reversed the beneficial effects of LRP1 activation on microglial polarization, inflammation, oxidative stress, apoptosis, and neurological functions. These results suggested that LRP1 activation attenuates neuroinflammation, apoptosis, and oxidative stress after cerebral I/R, which was, at least partially, related to microglial polarization mediated by the inhibition of the TXNIP/NLRP3 signaling pathway.

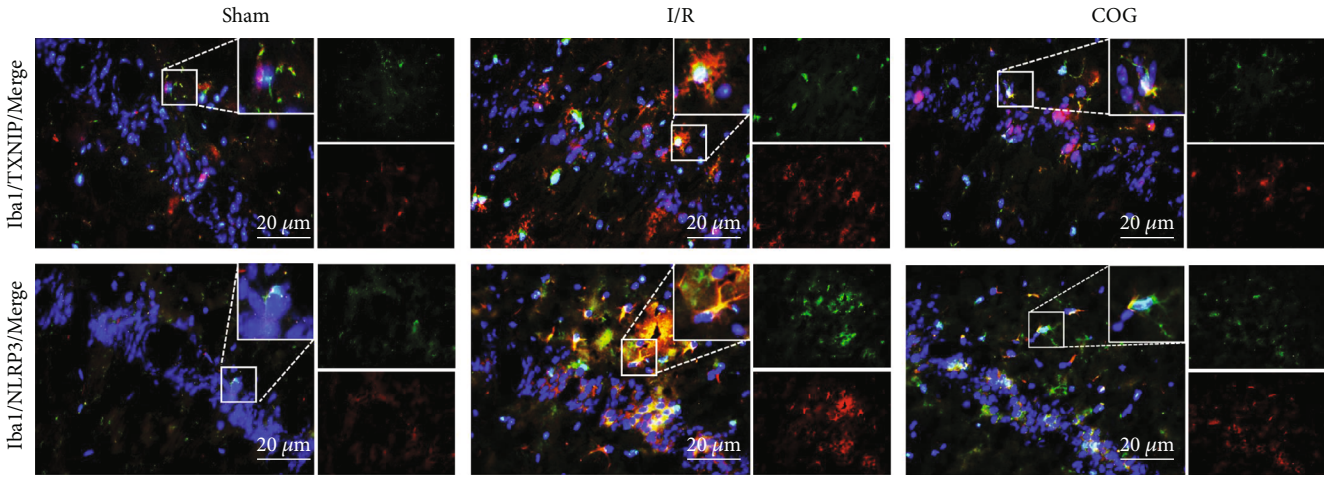

(a)

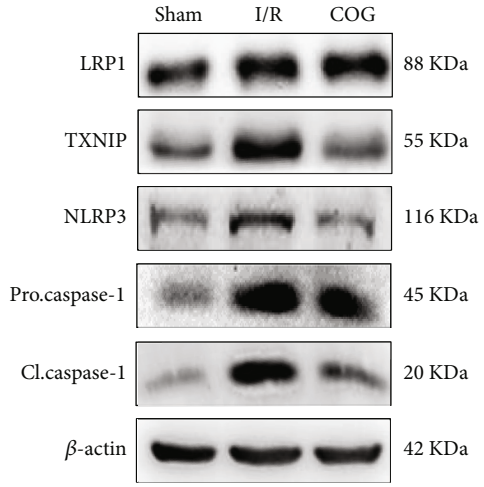

(b)

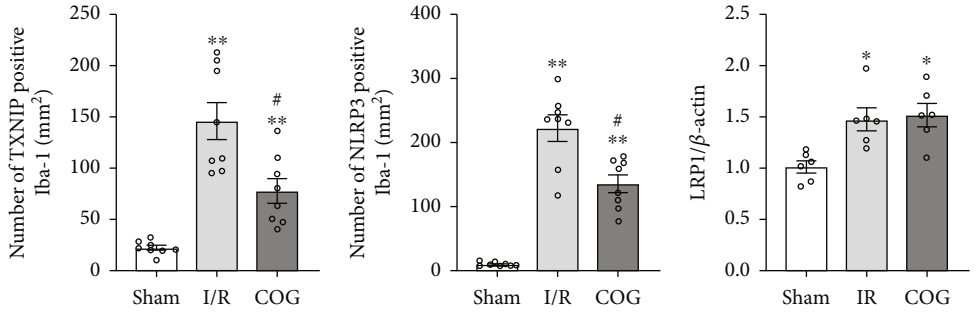

(c) (d) (e)

Figure 7: Continued.

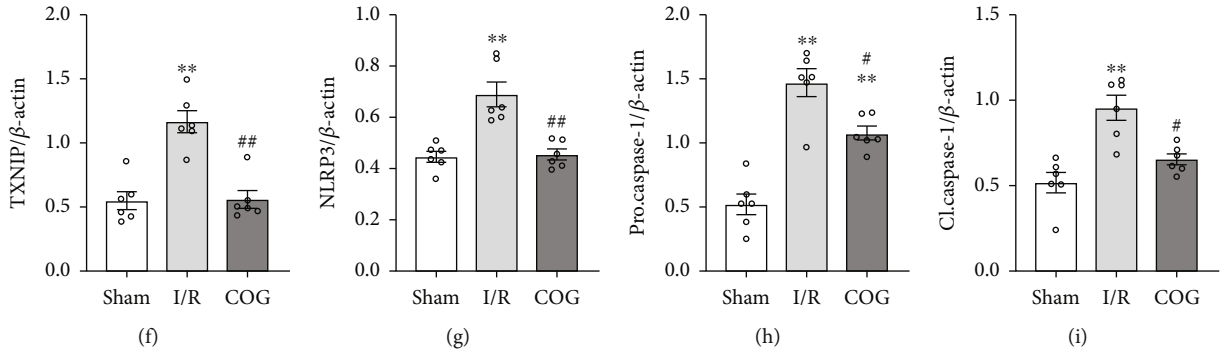

Figure 7: Effects of COG1410 on the TXNIP/NLRP3 signaling pathway at 72 h after cerebral I/R. (a) Representative images of the colocalization of TXNIP and NLRP3 (red) with microglia (Iba-1, green) in the hippocampal area. (b) Representative bands of Western blot data. (c, d) Quantitative analysis of TXNIP-positive and NLRP3-positive microglia. (e–i) Quantitative analysis of the Western blot bands. Data were represented as mean ± SEM. Western blot, $n = 6$ per group; double immunofluorescence staining, $n = 8$ per group. $^{*}P < 0.05$, $^{**}P < 0.01$ vs. sham group; $^{\#}P < 0.05$, $^{\#\#}P < 0.01$ vs. I/R + Vehicle group.

In the present study, a BCCAO-induced cerebral I/R mice model was used. The hippocampal neurons are related to the functions of spatial learning and memory, of which the CA1 neurons are most vulnerable to ischemic damage. Transient BCCAO delays hippocampal neuron death and is often used to study the mechanism of cerebral I/R injury [34]. However, the BCCAO model shows great variability due to the presence of posterior communicating arteries (PcomA). Previous studies have confirmed that C57BL/6 mice have less PcomA patency, which is ideal for establishing a BCCAO animal model [35–37]. In this study, HE staining was used to determine the success of the mice model. The results of the histopathological analysis showed that the number of normal hippocampal pyramid cells significantly decreased 72 h after BCCAO, which was consistent with previous studies [38, 39].

The Morris water maze experiment, as a classic experiment for mouse behavioral evaluation, is divided into two parts: the positioning navigation experiment and the space exploration experiment [28, 29]. In this study, the Morris water maze experiment was performed on days 3-8 after cerebral I/R. The positioning navigation experiment was carried out on days 3-7 after cerebral I/R (training days 1-5), and the space exploration experiment was carried out on days 8 after cerebral I/R. The positioning navigation experiment evaluates the learning ability, and the space exploration experiment evaluates the memory ability. Considering that learning is a process, when all mice are in the initial learning phase, they cannot show differences in neurobehavioral deficits. Therefore, it is speculated that there are two possible reasons for the difference between the Morris water maze experiment and the activation of LRP1/TXNIP/NLRP3. Firstly, the neurobehavioral deficits might have appeared on day 3 after cerebral I/R (training day 1), while the mice among different groups were undergoing training in the positioning navigation experiment at this time, so there were no differences in escape latency. Secondly, the expressions of the LRP1/TXNIP/NLRP3 pathway in this experiment were markedly increased at 3 days after cerebral I/R injury; however, they might be further upregulated on days 4-5 after cerebral I/R (training days 2-3). This might be consistent with the changing trend in the results of neurobehavioral deficits.

Microglia, a hallmark of neuroinflammation, plays a critical role in the delayed neuronal death caused by cerebral I/R. Activated microglia causes endocytosis of cell debris and participates in tissue repair in the early stage of cerebral I/R. However, overactivated brain microglia release inflammatory factors, such as TNF-α and IL-6, and participate in chronic inflammation, causing delayed neuronal death, brain edema, and neurological deficits [40, 41]. In this study, the results of double immunofluorescence staining showed that the LRP1 was colocalized with microglia, neurons, and astrocytes in the CA1 subregion of the hippocampus at 72 h after cerebral I/R. Previous study indicated that direct protein-protein binding effects of apoE with its signal receptor LRP1 enable microglia to exert immunosuppressive and neuroprotective effects in neuroinflammation caused by hemorrhagic stroke, traumatic brain injury, and multiple sclerosis [42]. Another study has shown that activation of LRP1 with COG1410 promotes microglial M1 to M2 phenotypic shift, and LRP1 was expressed in M2 phenotypes but not in M1 phenotypes of activated microglia in subarachnoid hemorrhage (SAH) mice [43]. In the present study, we found that the activation of LRP1 by COG1410 significantly decreased the iNOS-positive M1 phenotypes but increased the Arg-1 positive M2 phenotypes of activated microglia. Moreover, apoE-mimic peptide COG1410 treatment significantly inhibited neuroinflammation, reduced apoptosis in the hippocampal CA1 area, decreased brain edema, and improved short- and long-term neurological function after cerebral I/R in mice.

Furthermore, how LRP1 regulates microglial M1 to M2 phenotypic shift after cerebral I/R is yet to be elucidated. The potential mechanism involves the cleavage of the intracellular domain of the LRP1 after interacting with its ligand. The cytoplasmic fragment of LRP1 may have functions in the cytoplasm or the nucleus via protein cascades or transcriptional regulation [44]. A previous study showed that the C-terminal fragment of LRP1 regulates microglial activation via inhibited JNK phosphorylation after the binding between apoE-mimic peptide COG1410 and LRP1 [45].

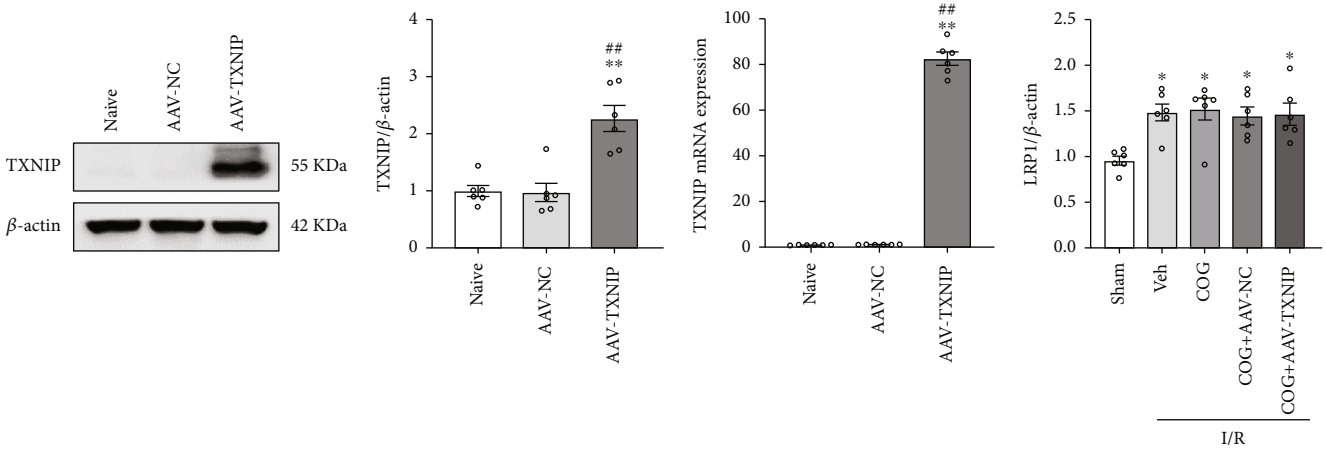

(a) (b) (c) (d)

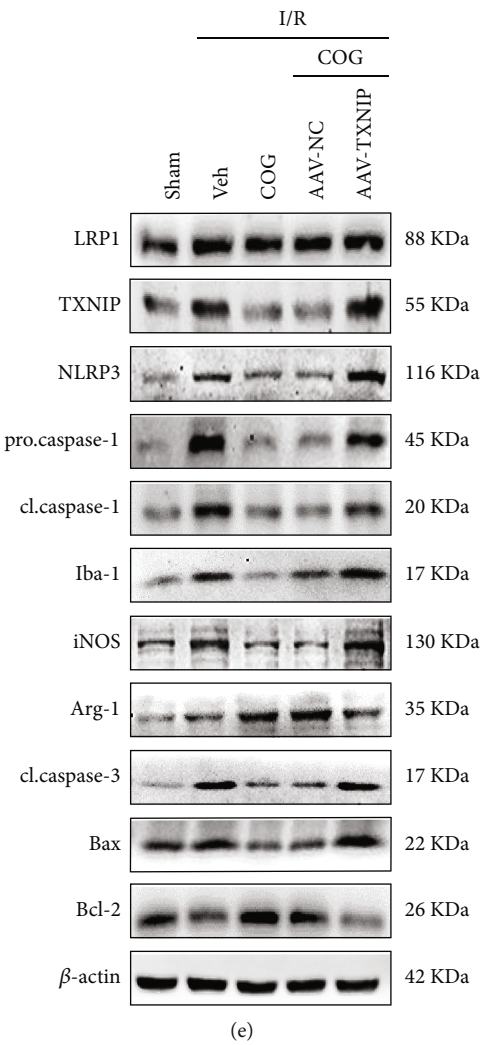

(e)

Figure 8: Continued.

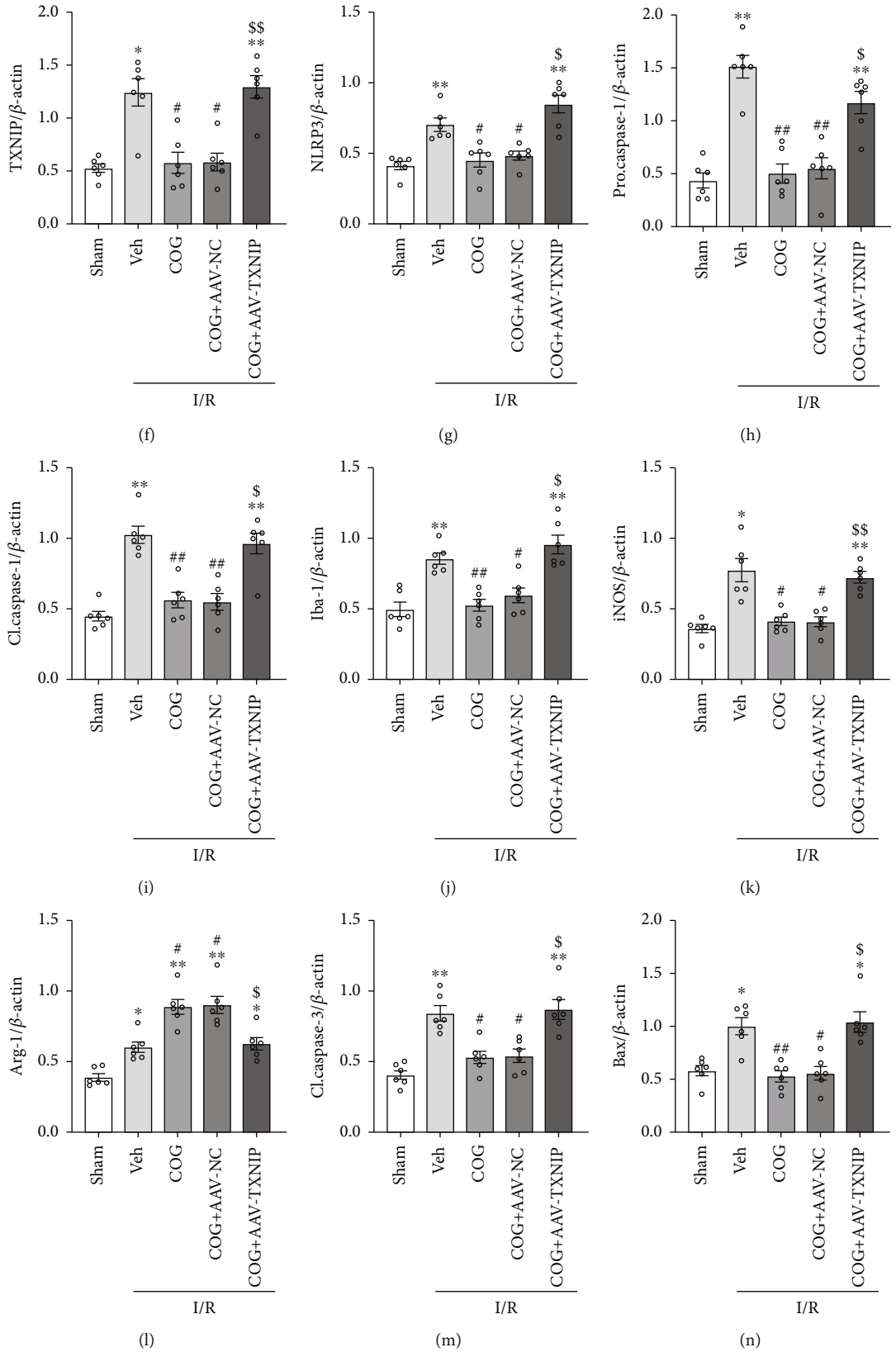

Figure 8: Continued.

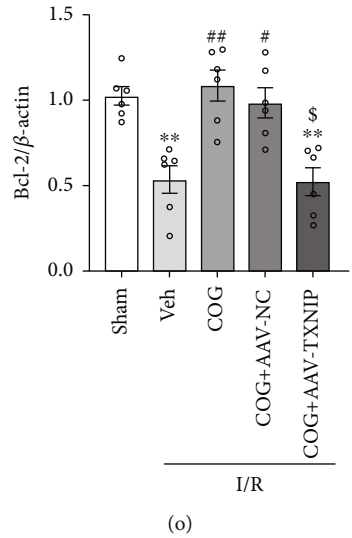

Figure 8: Overexpression of TXNIP reversed the beneficial effects of COG1410 on M2 microglial polarization and apoptosis at 72 h after cerebral I/R. (a–c) TXNIP-overexpression efficacy evaluation. Data were represented as mean ± SEM ($n = 6$). $^{*}P < 0.05$, $^{**}P < 0.01$ vs. naive group; $^{\#}P < 0.05$, $^{\#\#}P < 0.01$ vs. AAV-NC group. (e) Representative bands of Western blot data. (d, f–o) Quantitative analysis of the Western blot bands. Data were represented as the mean ± SEM ($n = 6$). $^{*}P < 0.05$, $^{**}P < 0.01$ vs. sham group; $^{\#}P < 0.05$, $^{\#\#}P < 0.01$ vs. I/R + Vehicle group; $^{\$}P < 0.05$, $^{\$\$}P < 0.01$ vs. I/R + COG1410 + AAV-NC group.

Another study found that stimulation of LRP1 by apoE-mimic peptide COG1410 modulated microglial polarization through Shc1/PI3K/Akt signaling pathway [43]. Nonetheless, the mechanisms of LRP1 underlying microglial phenotypic shift in cerebral I/R are yet to be elucidated. TRX is a vital intracellular antioxidant substance that exists as TRX/TXNIP under physiological conditions. The generation of a large number of reactive oxygen species (ROS) increases the expression of TXNIP and activates the NLRP3 inflammasome during the postischemic reperfusion phase [46].

LRP1 is a transmembrane receptor composed of a transmembrane β chain of 85 kDa noncovalently to an extracellular α chain of 515 kDa. It mainly exerts its biological functions in two ways of endocytosis and signal transduction. At present, the specific mechanism of LRP1 signal transduction remains to be elucidated. Previous studies have demonstrated that different motifs in the intracellular domain of the LRP1 β chain (LRP1-ICD) have different functions: YXXL motifs are related to endocytosis, while NPXY motifs can bind to various proteins in the cytoplasm (such as DAB1, FE65, JIP1, PSD-95, ShcA, and CED-6/GULP). When LRP1 binds to its ligand, LRP1-ICD of the LRP1 β chain can be cleaved through regulated intramembranous proteolysis (RIP), and the released fragments can play a protein cascade role in the cytoplasm or translocate to the nucleus to regulate transcription [4–7]. In this experiment, we found that the expression of TXNIP decreased after the cerebral I/R mice were treated with the LRP1 agonist COG1410. Interestingly, the expression of LRP1 did not change significantly for the cerebral I/R mice that TXNIP was overexpressed. It is speculated that LRP1 acts as an upstream signal of TXNIP and regulates the expression of TXNIP through the protein cascade or transcriptional regulation of LRP1-ICD.

As an important antioxidant in cells, TRX has two types: TRX1 and TRX2. TRX1 is distributed in the cytoplasm, nucleus, and plasma membrane, while TRX2 is distributed in the mitochondria. TXNIP is an endogenous inhibitor of TRX and exists as the composition TRX/TXNIP complex under physiological conditions. During oxidative stress, an increase in ROS leads to a decrease in TRX in the nucleus, accompanied by free TXNIP increases and translocates to the cytoplasm and mitochondria, where it binds TRX1 and TRX2, respectively, resulting in an increase in apoptosis signal-regulating kinase 1 (ASK-1) and causing apoptosis and aggravate oxidative stress. At the same time, TXNIP can directly bind to NLRP3 and activate the NLRP3 inflammasome, further aggravating oxidative stress [22]. Previous studies have also demonstrated that the regulation of NLRP3 by TXNIP is dependent on ROS [47, 48]. In this study, it was found that the decrease and increase of TXNIP correspond to the decrease and increase of oxidative stress, respectively. It is speculated that the increased ROS during oxidative stress activates TXNIP/NLRP3 pathway and activated NLRP3 inflammasome will further aggravate oxidative stress and form a vicious cycle.

Activation of the NLRP3 inflammasome appears to occur in two steps. The first step involves priming or initiating a signal in which many PAMPs or DAMPs are recognized by TLRs, leading to activation of nuclear factor kappa B- (NF-κB-) mediated signaling, which in turn upregulates transcription of inflammasome-related components, including inactive NLRP3, proIL-1β, and proIL-18. The second step of inflammasome activation is the oligomerization of NLRP3 and subsequent assembly of NLRP3, ASC, and procaspase-1 into a complex. This triggers the transformation of procaspase-1 to caspase-1, as well as the production and secretion of mature IL-1β and IL-18. To date, several

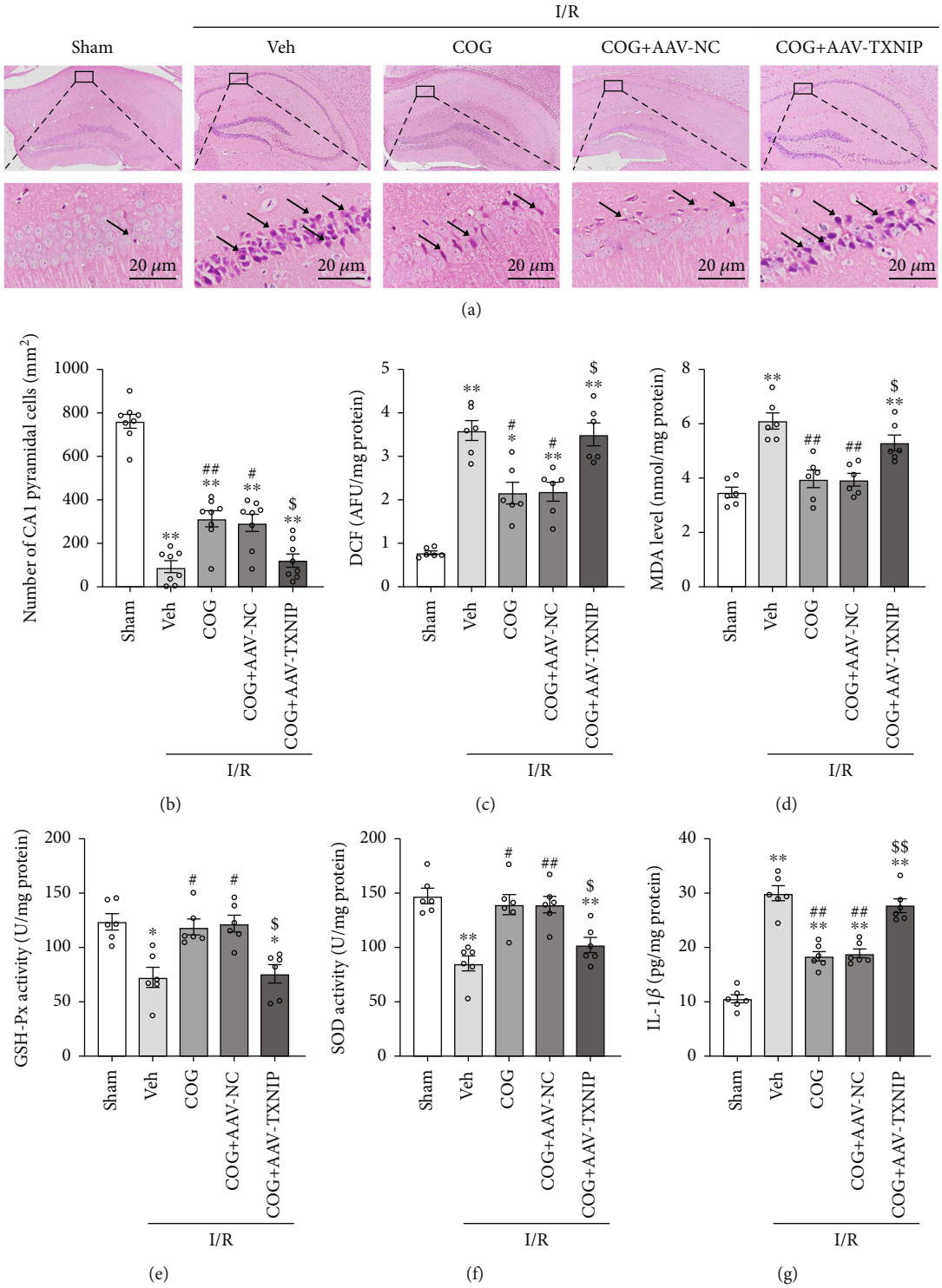

Figure 9: Continued.

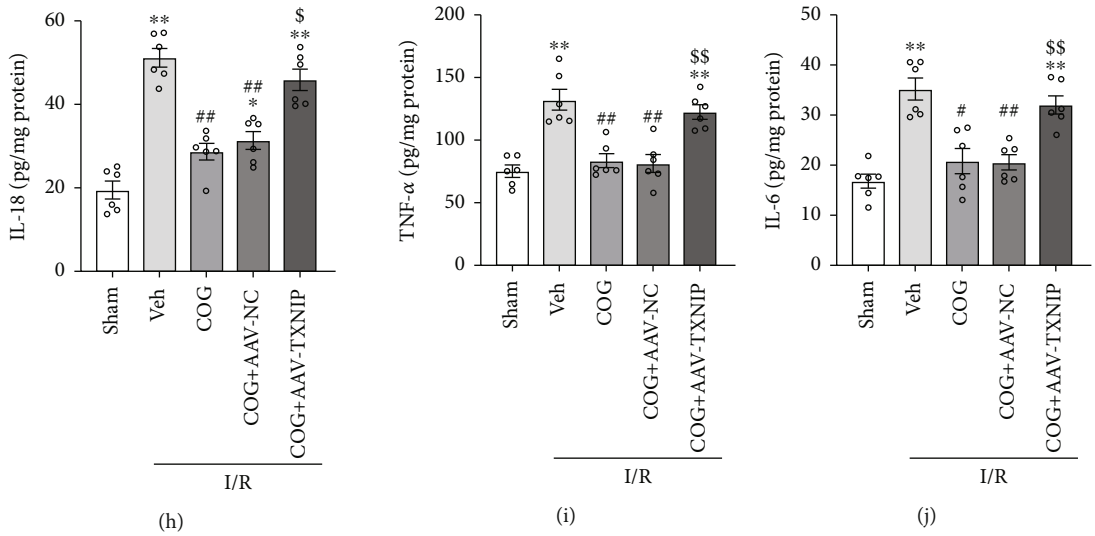

Figure 9: Overexpression of TXNIP reversed the beneficial effects of COG1410 on histopathological damage, oxidative stress, and inflammation at 72 h after cerebral I/R. (a) HE staining of hippocampal CA1 area (×400), scale bar = 20 μm; the arrows indicate injured neurons. (b) Quantitative analysis of normal neurons in the hippocampal CA1 area. (c–f) Quantitative analysis of the oxidative stress markers (ROS, MDA, GSH-Px, and SOD). (g–j) Quantitative analysis of the inflammatory factors including IL-1β, IL-18, TNF-α, and IL-6. Data were represented as mean ± SEM. HE staining, $n = 8$ per group; oxidative stress markers and inflammatory factors, $n = 6$ per group. $^{*}P < 0.05$, $^{**}P < 0.01$ vs. sham group; $^{\#}P < 0.05$, $^{\#\#}P < 0.01$ vs. I/R + Vehicle group; $^{\$}P < 0.05$, $^{\$\$}P < 0.01$ vs. I/R + COG1410 + AAV-NC group.

stimuli (such as ATP, ROS, cell debris, silica, asbestos, amyloid-β, and alum) have been found as the activator of the second step of inflammasome activation. Meanwhile, a variety of NLRP3-inflammasome activators including ATP, ROS, and silica were shown to result in TXNIP dissociation from TRX and binding to the NLRP3 inflammasome. TXNIP binding is an essential step for NLRP3 inflammasome activation. On the other hand, some studies demonstrated that the NLRP3 inflammasome and its downstream IL-1β activate the microglial M1 phenotypes [49, 50]. The activated M1 microglia, in turn, promote inflammation and oxidative stress, thus forming a vicious circle [51, 52]. Therefore, the TXNIP/NLRP3 signaling pathway is speculated to play a major role in regulating the polarization of microglia. The current study found that microglial M1 phenotypes are elevated, accompanied by TXNIP, NLRP3, procaspase-1, and cleaved caspase-1 upregulation after cerebral I/R, while increased microglial M2 phenotypes are accompanied by TXNIP, NLRP3, procaspase-1, and cleaved caspase-1 downregulation after COG1410 treatment. In addition, the results of double immunofluorescence staining showed that the number of TXNIP-positive and NLRP3-positive microglia were increased in the hippocampus of mice after cerebral I/R, while these types of cells were decreased after COG1410 treatment. Also, hippocampal apoptosis induced by cerebral I/R was observed, as indicated by increased positive cells in TUNEL staining, upregulated proapoptotic proteins cleaved caspase-3 and Bax, and downregulated anti-apoptotic protein Bcl-2. Previous studies have shown that cleaved caspase-1 catalyzed by activated NLRP3 inflammasomes promotes the mature release of IL-1β and IL-18 to regulate inflammation and apoptosis [53]. Some studies also found that TXNIP promotes apoptosis by activating proapoptotic protein signal-regulating kinase (ASK-1) and inducing the release of cytochrome-C from mitochondria [54]. Therefore, it could be deduced that apoptosis is also significantly reduced following the inhibition of the TXNIP/NLRP3 signaling pathway by activating LRP1 in this study.

To further verify the correlation between LRP1 and the TXNIP/NLRP3 signaling pathway, the TXNIP protein was overexpressed through the hippocampal injection of AAV vectors in this study. TXNIP overexpression with AAV-TXNIP significantly reversed the effects of LRP1 activation on TXNIP/NLRP3 pathway inhibition, M2 microglial polarization, antiapoptosis, anti-inflammatory, and antioxidant, while the LRP1 levels remained unchanged. These data suggested that LRP1 activation promotes M2 microglial polarization by inhibiting the TXNIP/NLRP3 pathway after cerebral I/R in mice.

Nevertheless, the present study had some limitations. Firstly, we only found that the activation of LRP1 affects the TXNIP/NLRP3 signaling pathway; however, the specific mechanism needs further study. Secondly, apoE is bound and internalized via receptor-mediated endocytosis by some receptors, such as the low-density lipoprotein receptor (LDLR), apoE receptor 2 (apoEr2), and triggering the receptor expressed on myeloid cells 2 (TREM2) in the CNS. How the apoE-mimic peptide COG1410 affects these receptors and the related pathways need to be investigated further. Thirdly, we did not fully explore the mechanism by which NLRP3 modulates microglia/macrophage polarization. A previous study has demonstrated that curcumin protected against ischemic stroke by modulating microglia/macrophage polarization toward an anti-inflammatory phenotype through NF-κB suppression and NLRP3 inflammasome inhibition. Meanwhile, NLRP3 knockdown in vivo

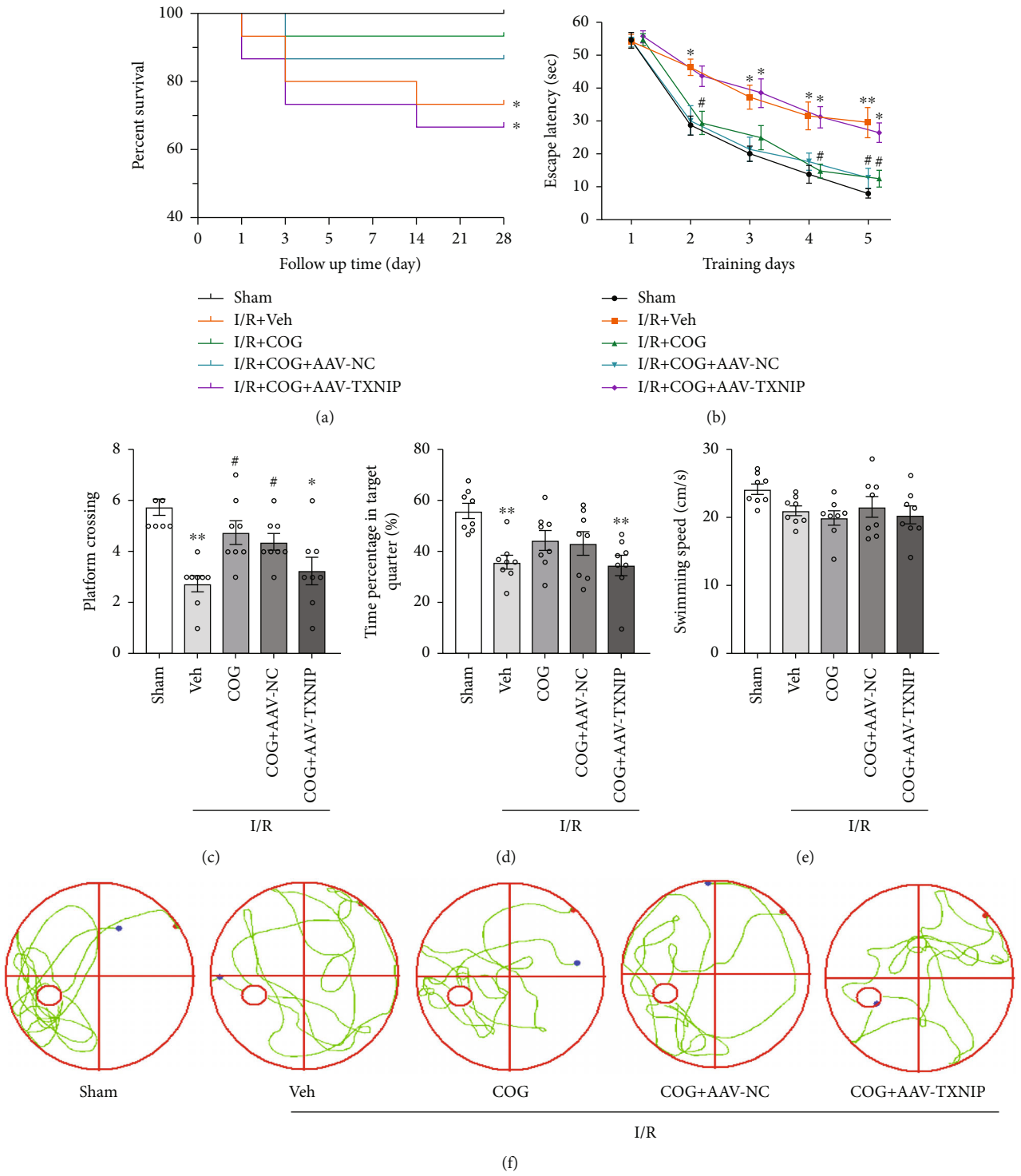

Figure 10: COG1410 improved the survival rate and long-term neurological function 28 days after cerebral I/R. (a) The survival rate in different groups. (b) Escape latency of mice in the training trials. (c) Frequency of platform crossing in the probe trial. (d) Percentage of time spent in the target quadrant in the probe trial. (e) Swimming speed in the probe trial. (f) Swimming trajectory of mice of each group in the probe trial. Data were represented as mean ± SEM. Survival rate, $n = 15$ per group; MWM, $n = 8$ per group. $^{*}P < 0.05$, $^{**}P < 0.01$ vs. sham group; $^{\#}P < 0.05$, $^{\#\#}P < 0.01$ vs. I/R + Vehicle group.

significantly inhibited microglia/macrophage pyroptosis and ameliorated cerebral ischemia injury [55]. Further research has shown that MiR-423-5p could decrease the polarization of microglia/macrophage cells of the M1 phenotype by inhibiting the mRNA expression of NLRP3 in a spinal cord injury animal model [56]. Another study also found that Tranilast, an NLRP3 inflammasome inhibitor, could promote the polarization of microglia/macrophage from M1

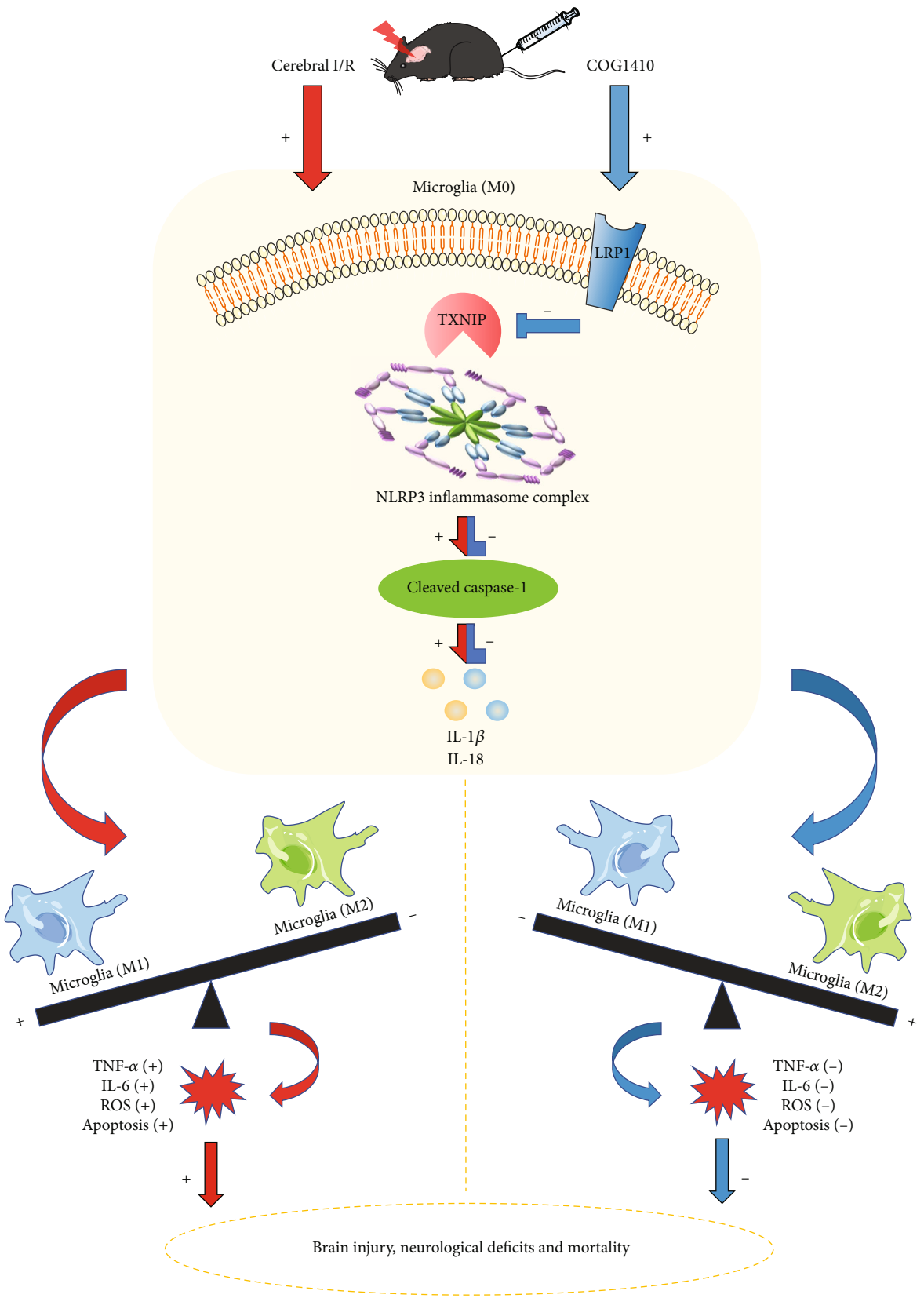

Figure 11: The mechanism map of the protective properties of COG1410 against cerebral I/R injury. Inflammation, oxidative stress, and apoptosis were triggered by cerebral I/R, which resulted in brain injury, neurological deficits, and even mortality. COG1410 treatment could improve the changes mentioned above. Mechanistically, COG1410 of LRP1 agonist shifted microglia towards the M2 phenotype by inhibiting the TXNIP/NLRP3 signaling pathway. The activation was labeled with "+," and the inhibition was labeled with "-."

type to M2 type and ameliorate ischemic stroke by inhibiting the NLRP3/caspase-1 pathway in a murine model of distal middle cerebral artery occlusion [57]. The activation of the NLRP3 inflammasome triggers the transformation of procaspase-1 to caspase-1, as well as the production and secretion of mature IL-1β and IL-18. Interestingly, some research supported a potential role for IL-1β as one of the potential supporting factors of M1 over M2 microglia/macrophage polarization. Administration of an IL-1β neutralizing antibody led to upregulation of the M2 marker, Ym1, and corresponding downregulation of the proinflammatory cytokine, cleaved IL-1β in LPS-activated BV2 microglia cell [58]. Likewise, our study found that inhibition of NLRP3 inflammasome promotes the polarization of microglia from M1 type to M2 type. The current study found that administration of COG1410 led to downregulation of the expressions of TXNIP, NLRP3, caspase-1, IL-1β, the M1 markers iNOS, and TNF-α, while the M2 marker Arg-1 was upregulated in cerebral I/R injury mice. It is speculated that COG1410 could regulate microglia phenotype polarization through TXNIP/NLRP3/caspase-1/IL-1β pathway. At the same time, inflammation is a multimolecular cascade, and hence, the possibility of involvement of multiple pathway regulation is likely and requires further study. Finally, the clinical translation of this study needs to be further elucidated.

5. Conclusions

This study demonstrated that LRP1 activation by apoE-mimic peptide COG1410 attenuated neuroinflammation, apoptosis, and oxidative stress and could improve short- and long-term neurological deficits and mortality after cerebral I/R, which was, at least in part, related to microglial polarization mediated by the inhibition of TXNIP/NLRP3 signaling pathway (Figure 11). Therefore, apoE-mimic peptide COG1410 may be a promising treatment agent in patients after cerebral I/R injury.

Data Availability

The data used to support the findings of this study are included within the article and are available from the corresponding author upon request.

Disclosure

This study has been stored on a preprint server Research Square [59].

Conflicts of Interest

The authors declare that they have no conflicts of interest.

Authors' Contributions

Cheng-Jie Yang, Xin Li, and Xiao-Qing Feng contributed equally to this work. Jun Zhou and Ji-Cheng Wei conceived and designed the experiments. Cheng-Jie Yang, Xin Li, and Xiao-Qing Feng performed the experiments. Ye Chen and Cheng-Jie Yang analyzed the data. Jian-Guo Feng and Jing Jia contributed the reagents/materials/analysis tools. Jun Zhou wrote the paper. All authors read and approved the manuscript.

Acknowledgments

This study was supported by grants from the National Natural Science Foundation of China (no. 81873930), partly by grants from the Department of Science and Technology of Sichuan Province (no. 2020YJ0189), the Talent Development Project of The Affiliated Hospital of Southwest Medical University (no. 20063), and the Youth Program of Southwest Medical University (no. 2021ZKQN057). We are grateful to Dr. Dan-Li Zhu for her excellent technical assistance.

References

[1] S. Virani, A. Alonso, H. Aparicio et al., "Heart disease and stroke statistics-2021 update: a report from the American heart association," *Circulation*, vol. 143, no. 8, pp. e254–e743, 2021.

[2] R. Madathil, R. Hira, M. Stoeckl, F. Sterz, J. Elrod, and G. Nichol, "Ischemia reperfusion injury as a modifiable therapeutic target for cardioprotection or neuroprotection in patients undergoing cardiopulmonary resuscitation," *Resuscitation*, vol. 105, pp. 85–91, 2016.

[3] S. E. Khoshnam, A. Sarkaki, L. Khorsandi et al., "Vanillic acid attenuates effects of transient bilateral common carotid occlusion and reperfusion in rats," *Biomedicine & Pharmacotherapy*, vol. 96, pp. 667–674, 2017.

[4] V. Gupta, D. K. Dhull, J. Joshi, S. Kaur, and A. Kumar, "Neuroprotective potential of azilsartan against cerebral ischemic injury: possible involvement of mitochondrial mechanisms," *Neurochemistry International*, vol. 132, article 104604, 2020.

[5] S. Spray and L. Edvinsson, "Improved assessment of outcomes following transient global cerebral ischemia in mice," *Experimental Brain Research*, vol. 234, no. 7, pp. 1925–1934, 2016.

[6] Y. Lu, M. Zhou, Y. Li, Y. Li, Y. Hua, and Y. Fan, "Minocycline promotes functional recovery in ischemic stroke by modulating microglia polarization through STAT1/STAT6 pathways," *Biochemical Pharmacology*, vol. 186, article 114464, 2021.

[7] X. Xiong, L. Liu, and Q. Yang, "Functions and mechanisms of microglia/macrophages in neuroinflammation and neurogenesis after stroke," *Progress in Neurobiology*, vol. 142, pp. 23–44, 2016.

[8] C. Brifault, A. Gilder, E. Laudati, M. Banki, and S. Gonias, "Shedding of membrane-associated LDL receptor-related protein-1 from microglia amplifies and sustains neuroinflammation," *The Journal of Biological Chemistry*, vol. 292, no. 45, pp. 18699–18712, 2017.

[9] G. Wang, A. Manaenko, A. Shao et al., "Low-density lipoprotein receptor-related protein-1 facilitates heme scavenging after intracerebral hemorrhage in mice," *Journal of Cerebral Blood Flow and Metabolism*, vol. 37, no. 4, pp. 1299–1310, 2017.

[10] R. Sun, M. Peng, P. Xu et al., "Low-density lipoprotein receptor (LDLR) regulates NLRP3-mediated neuronal pyroptosis following cerebral ischemia/reperfusion injury," *Journal of Neuroinflammation*, vol. 17, no. 1, p. 330, 2020.

[11] X. Qin, H. You, F. Cao et al., "Apolipoprotein E mimetic peptide increases cerebral glucose uptake by reducing blood-brain barrier disruption after controlled cortical impact in mice: an F-fluorodeoxyglucose PET/CT study," *Journal of Neurotrauma*, vol. 34, no. 4, pp. 943–951, 2017.

[12] J. Peng, X. Qin, J. Pang et al., "Apolipoprotein E ε4: a possible risk factor of intracranial pressure and white matter perfusion in good-grade aneurysmal subarachnoid hemorrhage patients at early stage," *Frontiers in Neurology*, vol. 8, p. 150, 2017.

[13] H. Wu, J. Ruan, X. Zhang, H. Xia, Y. Jiang, and X. Sun, "Association of promoter polymorphism of apolipoprotein E gene with cerebral vasospasm after spontaneous SAH," *Brain Research*, vol. 1362, pp. 112–116, 2010.

[14] H. Wilkins, S. Koppel, R. Bothwell, J. Mahnken, J. Burns, and R. Swerdlow, "Platelet cytochrome oxidase and citrate synthase activities in APOE ε4 carrier and non-carrier Alzheimer's disease patients," *Redox Biology*, vol. 12, pp. 828–832, 2017.

[15] S. Chen, J. Peng, P. Sherchan et al., "TREM2 activation attenuates neuroinflammation and neuronal apoptosis via PI3K/Akt pathway after intracerebral hemorrhage in mice," *Journal of Neuroinflammation*, vol. 17, no. 1, p. 168, 2020.

[16] D. T. Laskowitz, S. E. McKenna, P. Song et al., "COG1410, a novel apolipoprotein E-based peptide, improves functional recovery in a murine model of traumatic brain injury," *Journal of Neurotrauma*, vol. 24, no. 7, pp. 1093–1107, 2007.

[17] D. T. Laskowitz, B. Lei, H. N. Dawson et al., "The apoE-mimetic peptide, COG1410, improves functional recovery in a murine model of intracerebral hemorrhage," *Neurocritical Care*, vol. 16, no. 2, pp. 316–326, 2012.

[18] Y. Wu, J. Pang, J. Peng et al., "An apoE-derived mimic peptide, COG1410, alleviates early brain injury via reducing apoptosis and neuroinflammation in a mouse model of subarachnoid hemorrhage," *Neuroscience Letters*, vol. 627, pp. 92–99, 2016.

[19] J. Slusarczyk, E. Trojan, K. Wydra et al., "Beneficial impact of intracerebroventricular fractalkine administration on behavioral and biochemical changes induced by prenatal stress in adult rats: possible role of NLRP3 inflammasome pathway," *Biochemical Pharmacology*, vol. 113, pp. 45–56, 2016.

[20] M. Heneka, R. McManus, and E. Latz, "Inflammasome signalling in brain function and neurodegenerative disease," *Nature Reviews. Neuroscience*, vol. 19, no. 10, pp. 610–621, 2018.

[21] J. B. Nyandwi, Y. S. Ko, H. Jin, S. P. Yun, S. W. Park, and H. J. Kim, "Rosmarinic acid inhibits oxLDL-induced inflammasome activation under high- glucose conditions through downregulating the p38-FOXO1-TXNIP pathway," *Biochemical Pharmacology*, vol. 182, article 114246, 2020.

[22] M. Pan, F. Zhang, K. Qu, C. Liu, and J. Zhang, "TXNIP: a double-edged sword in disease and therapeutic outlook," *Oxidative Medicine and Cellular Longevity*, vol. 2022, Article ID 7805115, 14 pages, 2022.

[23] Y. R. Yan, L. Zhang, Y. N. Lin et al., "Chronic intermittent hypoxia-induced mitochondrial dysfunction mediates endothelial injury via the TXNIP/NLRP3/IL-1β signaling pathway," *Free Radical Biology & Medicine*, vol. 165, pp. 401–410, 2021.

[24] Y. Jia, R. Cui, C. Wang et al., "Metformin protects against intestinal ischemia-reperfusion injury and cell pyroptosis via TXNIP-NLRP3-GSDMD pathway," *Redox Biology*, vol. 32, article 101534, 2020.

[25] L. Li, B. Deng, S. Wang et al., "Asynchronous therapy targeting Nogo-a enhances neurobehavioral recovery by reducing neuronal loss and promoting neurite outgrowth after cerebral ischemia in mice," *Journal of Drug Targeting*, vol. 24, no. 1, pp. 13–23, 2016.

[26] B. Liu, Y. Cao, F. Shi et al., "The overexpression of RBM3 alleviates TBI-induced behaviour impairment and AD- like tauopathy in mice," *Journal of Cellular and Molecular Medicine*, vol. 24, no. 16, pp. 9176–9188, 2020.

[27] D. Song, Y. Chen, C. Chen, L. Chen, and O. Cheng, "GABAB receptor antagonist promotes hippocampal neurogenesis and facilitates cognitive function recovery following acute cerebral ischemia in mice," *Stem Cell Research & Therapy*, vol. 12, no. 1, p. 22, 2021.

[28] B. Yang, L. Y. Zhang, Y. Chen et al., "Melatonin alleviates intestinal injury, neuroinflammation and cognitive dysfunction caused by intestinal ischemia/reperfusion," *International Immunopharmacology*, vol. 85, article 106596, 2020.

[29] Y. Chen, Y. Lei, L. Mo et al., "Electroacupuncture pretreatment with different waveforms prevents brain injury in rats subjected to cecal ligation and puncture via inhibiting microglial activation, and attenuating inflammation, oxidative stress and apoptosis," *Brain Research Bulletin*, vol. 127, pp. 248–259, 2016.

[30] Y. Zhang, S. L. Tan, J. Du et al., "Dexmedetomidine alleviates neuroinflammation, restores sleep disorders and neurobehavioral abnormalities in rats with minimal hepatic encephalopathy," *International Immunopharmacology*, vol. 96, article 107795, 2021.

[31] L. Yang, Y. Guo, X. Fan et al., "Amelioration of coagulation disorders and inflammation by hydrogen-rich solution reduces intestinal ischemia/reperfusion injury in rats through NF-κB/NLRP3 pathway," *Mediators of Inflammation*, vol. 2020, Article ID 4359305, 12 pages, 2020.

[32] Y. Jia, Z. Li, Y. Feng et al., "Methane-rich saline ameliorates sepsis-induced acute kidney injury through anti-inflammation, antioxidative, and antiapoptosis effects by regulating endoplasmic reticulum stress," *Oxidative Medicine and Cellular Longevity*, vol. 2018, Article ID 4756846, 10 pages, 2018.

[33] X. Fan, J. Du, M. H. Wang et al., "Irisin contributes to the hepatoprotection of dexmedetomidine during intestinal ischemia/reperfusion," *Oxidative Medicine and Cellular Longevity*, vol. 2019, Article ID 7857082, 15 pages, 2019.

[34] M. Cai, P. Phan, J. Hong et al., "The neuroprotective effect of eupatilin against ischemia/reperfusion-induced delayed neuronal damage in mice," *European Journal of Pharmacology*, vol. 689, no. 1-3, pp. 104–110, 2012.

[35] F. Barone, D. Knudsen, A. Nelson, G. Feuerstein, and R. Willette, "Mouse strain differences in susceptibility to cerebral ischemia are related to cerebral vascular anatomy," *Journal of Cerebral Blood Flow and Metabolism*, vol. 13, no. 4, pp. 683–692, 1993.

[36] K. Kitagawa, M. Matsumoto, G. Yang et al., "Cerebral ischemia after bilateral carotid artery occlusion and intraluminal suture occlusion in mice: evaluation of the patency of the posterior communicating artery," *Journal of Cerebral Blood Flow and Metabolism*, vol. 18, no. 5, pp. 570–579, 1998.

[37] G. Zhen and S. Dore, "Optimized protocol to reduce variable outcomes for the bilateral common carotid artery occlusion model in mice," *Journal of Neuroscience Methods*, vol. 166, no. 1, pp. 73–80, 2007.

[38] S. Tajiri, S. Oyadomari, S. Yano et al., "Ischemia-induced neuronal cell death is mediated by the endoplasmic reticulum stress pathway involving CHOP," *Cell Death and Differentiation*, vol. 11, no. 4, pp. 403–415, 2004.

[39] X. Lei, L. Lei, Z. Zhang, and Y. Cheng, "Neuroprotective effects of lycopene pretreatment on transient global cerebral ischemia-reperfusion in rats: the role of the Nrf2/HO1 signaling pathway," *Molecular Medicine Reports*, vol. 13, no. 1, pp. 412–418, 2016.

[40] J. Park, J. Park, J. Ahn et al., "Transient cerebral ischemia induces albumin expression in microglia only in the CA1 region of the gerbil hippocampus," *Molecular Medicine Reports*, vol. 16, no. 1, pp. 661–665, 2017.

[41] B. He, X. Wang, Y. He et al., "Gamma ray-induced glial activation and neuronal loss occur before the delayed onset of brain necrosis," *The FASEB Journal*, vol. 34, no. 10, pp. 13361–13375, 2020.

[42] T. Chuang, Y. Guo, S. Seki et al., "LRP1 expression in microglia is protective during CNS autoimmunity," *Acta Neuropathologica Communications*, vol. 4, no. 1, p. 68, 2016.

[43] J. Peng, J. Pang, L. Huang et al., "LRP1 activation attenuates white matter injury by modulating microglial polarization through Shc1/PI3K/Akt pathway after subarachnoid hemorrhage in rats," *Redox Biology*, vol. 21, article 101121, 2019.

[44] P. Boucher and J. Herz, "Signaling through LRP1: protection from atherosclerosis and beyond," *Biochemical Pharmacology*, vol. 81, no. 1, pp. 1–5, 2011.

[45] L. Yang, C. Liu, H. Zheng et al., "LRP1 modulates the microglial immune response via regulation of JNK and NF-κB signaling pathways," *Journal of Neuroinflammation*, vol. 13, no. 1, p. 304, 2016.

[46] S. Nasoohi, S. Ismael, and T. Ishrat, "Thioredoxin-interacting protein (TXNIP) in cerebrovascular and neurodegenerative diseases: regulation and implication," *Molecular Neurobiology*, vol. 55, no. 10, pp. 7900–7920, 2018.

[47] Z. Li, T. Liu, Y. Feng et al., "PPARγ Alleviates Sepsis-Induced Liver Injury by Inhibiting Hepatocyte Pyroptosis via Inhibition of the ROS/TXNIP/NLRP3 Signaling Pathway," *Oxidative Medicine and Cellular Longevity*, vol. 2022, Article ID 1269747, 15 pages, 2022.

[48] L. Minutoli, D. Puzzolo, M. Rinaldi et al., "ROS-mediated NLRP3 inflammasome activation in brain, heart, kidney, and testis ischemia/reperfusion injury," *Oxidative Medicine and Cellular Longevity*, vol. 2016, Article ID 2183026, 10 pages, 2016.

[49] X. Cao, Y. Wang, and L. Gao, "CHRFAM7A overexpression attenuates cerebral ischemia-reperfusion injury via inhibiting microglia pyroptosis mediated by the NLRP3/Caspase-1 pathway," *Inflammation*, vol. 44, no. 3, pp. 1023–1034, 2021.

[50] K. Campagno and C. Mitchell, "The P2X7 receptor in microglial cells modulates the endolysosomal axis, autophagy, and phagocytosis," *Frontiers in Cellular Neuroscience*, vol. 15, article 645244, 2021.

[51] M. Catani, V. Gasperi, T. Bisogno, and M. Maccarrone, "Essential dietary bioactive lipids in neuroinflammatory diseases," *Antioxidants & Redox Signaling*, vol. 29, no. 1, pp. 37–60, 2018.

[52] S. Q. Du, X. R. Wang, W. Zhu et al., "Acupuncture inhibits TXNIP-associated oxidative stress and inflammation to attenuate cognitive impairment in vascular dementia rats," *CNS Neuroscience & Therapeutics*, vol. 24, no. 1, pp. 39–46, 2018.

[53] K. Wang, Q. Lv, Y. M. Miao, S. M. Qiao, Y. Dai, and Z. F. Wei, "Cardamonin, a natural flavone, alleviates inflammatory bowel disease by the inhibition of NLRP3 inflammasome activation _via_ an AhR/Nrf2/NQO1 pathway," *Biochemical Pharmacology*, vol. 155, pp. 494–509, 2018.

[54] J. Lu and A. Holmgren, "Thioredoxin system in cell death progression," *Antioxidants & Redox Signaling*, vol. 17, no. 12, pp. 1738–1747, 2012.

[55] Y. Ran, W. Su, F. Gao et al., "Curcumin ameliorates white matter injury after ischemic stroke by inhibiting microglia/macrophage pyroptosis through NF-κB suppression and NLRP3 inflammasome inhibition," *Oxidative Medicine and Cellular Longevity*, vol. 2021, Article ID 1552127, 25 pages, 2021.

[56] J. Cheng, J. Hao, X. Jiang et al., "Ameliorative effects of miR-423-5p against polarization of microglial cells of the M1 phenotype by targeting a NLRP3 inflammasome signaling pathway," *International Immunopharmacology*, vol. 99, article 108006, 2021.

[57] H. Jia, X. Qi, L. Fu et al., "NLRP3 inflammasome inhibitor ameliorates ischemic stroke by reprogramming the phenotype of microglia/macrophage in a murine model of distal middle cerebral artery occlusion," *Neuropathology*, vol. 42, no. 3, pp. 181–189, 2022.

[58] R. Thakkar, R. Wang, J. Wang, R. K. Vadlamudi, and D. W. Brann, "17β-estradiol regulates microglia activation and polarization in the hippocampus following global cerebral ischemia," *Oxidative Medicine and Cellular Longevity*, vol. 2018, Article ID 4248526, 2018.

[59] https://www.researchsquare.com/article/rs-1657100/v1.

Hindawi
Oxidative Medicine and Cellular Longevity
Volume 2022, Article ID 6125711, 13 pages
https://doi.org/10.1155/2022/6125711

Research Article

Preventing Axonal Sodium Overload or Mitochondrial Calcium Uptake Protects Axonal Mitochondria from Oxidative Stress-Induced Alterations

Rebecca Ulshöfer,[1,2,3] Helena Bros,[4] Anja Erika Hauser,[5,6] Raluca Aura Niesner,[6,7] Friedemann Paul,[1,2,3,8] Bimala Malla,[2] and Carmen Infante-Duarte[1,2,3]

[1]*Experimental and Clinical Research Center (ECRC), A Cooperation between Charité-Universitätsmedizin Berlin and Max-Delbrück-Center for Molecular Medicine, 13125 Berlin, Germany*
[2]*Charité-Universitätsmedizin Berlin, Corporate Member of Freie Universität Berlin, Humboldt Universität zu Berlin and Berlin Institute of Health, 10117 Berlin, Germany*
[3]*Max-Delbrück-Center for Molecular Medicine (MDC) in the Helmholtz Association, 13125 Berlin, Germany*
[4]*Charité-Universitätsmedizin Berlin, Institute for Medical Immunology, Augustenburger Platz 1, 13353 Berlin, Germany*
[5]*Charité-Universitätsmedizin Berlin, Medizinische Klinik mit Schwerpunkt Rheumatologie und Klinische Immunologie, Charité Platz 1, 10117 Berlin, Germany*
[6]*Deutsches Rheuma-Forschungszentrum, a Leibniz Institute, Charité Platz 1, 10117 Berlin, Germany*
[7]*Dynamic and Functional In Vivo Imaging, Veterinary Medicine, Freie Universität Berlin, Germany*
[8]*Charité-Universitätsmedizin Berlin, NeuroCure Clinical Research Center, Charité Platz 1, 10117 Berlin, Germany*

Correspondence should be addressed to Carmen Infante-Duarte; carmen.infante@charite.de

Bimala Malla and Carmen Infante-Duarte contributed equally to this work.

Received 23 June 2021; Revised 2 May 2022; Accepted 5 May 2022; Published 24 May 2022

Academic Editor: Luzia Kalyne Almeida Moreira Leal

In neuroinflammatory and neurodegenerative disorders such as multiple sclerosis, mitochondrial damage caused by oxidative stress is believed to contribute to neuroaxonal damage. Previously, we demonstrated that exposure to hydrogen peroxide (H_2O_2) alters mitochondrial morphology and motility in myelinated axons and that these changes initiate at the nodes of Ranvier, where numerous sodium channels are located. Therefore, we suggested that mitochondrial damage may lead to ATP deficit, thereby affecting the efficiency of the sodium-potassium ATPase and eventually leading to sodium overload in axons. The increased intra-axonal sodium may revert the axonal sodium-calcium exchangers and thus may lead to a pathological calcium overload in the axoplasm and mitochondria. Here, we used the explanted murine ventral spinal roots to investigate whether modulation of sodium or calcium influx may prevent mitochondrial alterations in myelinated axons during exogenous application of H_2O_2 inducing oxidative stress. For that, tetrodotoxin, an inhibitor of voltage-gated sodium ion channels, and ruthenium 360, an inhibitor of the mitochondrial calcium uniporter, were applied simultaneously with hydrogen peroxide to axons. Mitochondrial shape and motility were analyzed. We showed that inhibition of axonal sodium influx prevented oxidative stress-induced morphological changes (i.e., increase in circularity and area and decrease in length) and preserved mitochondrial membrane potential, which is crucial for ATP production. Blocking mitochondrial calcium uptake prevented decrease in mitochondrial motility and also preserved membrane potential. Our findings indicate that alterations of both mitochondrial morphology and motility in the contexts of oxidative stress can be counterbalanced by modulating intramitochondrial ion concentrations pharmacologically. Moreover, motile mitochondria show preserved membrane potentials, pointing to a close association between mitochondrial motility and functionality.

1. Introduction

Multiple sclerosis (MS) is a chronic inflammatory disease of the central nervous system (CNS) that affects approximately 2.5 million people worldwide [1]. The pathological hallmarks of MS include inflammation, demyelination, and neurodegeneration; however, its pathogenesis and the relationship between those three aspects are not completely understood [1].

In this context, mitochondria have emerged as one of the key players that are affected by inflammation and contribute to neuroaxonal loss [2–4]. During neuroinflammatory events in MS, activated CNS-invading leukocytes, as well as microglia, are potential sources of reactive oxygen species (ROS), mainly via increased activation of nicotinamide adenine dinucleotide phosphate (NADPH) oxidases [5–8]. It is assumed that excessive ROS production may lead to oxidative stress and consequently to the inhibition of adenosine triphosphate (ATP) production. Activation of oxidative phosphorylation under pathological stress conditions may also lead to increased chances of electron slippage to oxygen and the formation of additional detrimental ROS [9–11]. In a physiological state, cells have mechanisms to cope with increased ROS production [12, 13]. However, sustained inflammation and oxidative stress may lead to irreversible damage in mitochondria and affect the survivability of the cells [14].

To investigate the impact of oxidative stress on neuroaxonal mitochondria, we have developed an ex vivo model to monitor mitochondrial alterations in murine spinal roots [15, 16]. We focused on ventral spinal roots because they consist predominantly of efferent motor axons and are thicker than dorsal roots making them easier to handle. Using this model, we previously showed that oxidative stress alters both mitochondrial morphology (increases mitochondrial circularity and decreases mitochondrial area and length) and mitochondrial motility (reduces the percentage of moving mitochondria, length of their trajectories and their velocity) [17]. We also observed that, following an oxidative insult, all these alterations consistently initiate at the nodes of Ranvier [17].

In axons, voltage-gated sodium channels (NaV) are mainly located near the nodes of Ranvier [18]. In the presence of oxidative stress, mitochondrial damage may lead to reduced ATP generation [19] and the consequent failure of the sodium-potassium-ATPase (Na^+/K^+-ATPase), leading to sodium (Na^+) accumulation inside the axons [20]. Moreover, in a degeneration paradigm using dorsal root ganglion cells, it has been demonstrated that influx of Na^+ via NaV contributes to intraneuronal Na^+ accumulation [13]. To compensate for the excess of intracellular Na^+ in the presence of a dysfunctional Na^+/K^+-ATPase, the axonal sodium-calcium exchanger (NCX) may start acting in a reverse mode, causing axonal calcium (Ca^{2+}) overload [5, 13, 20].

High cytosolic Ca^{2+} concentration directly impacts mitochondria, which in turn are part of the Ca^{2+} buffering system of cells [13, 21, 22]. Tightly regulated intracellular Ca^{2+} homeostasis is crucial because an excessive mitochondrial Ca^{2+} uptake may lead to the opening of the permeability transition pore (PTP), resulting in apoptosis [9, 14]. A mitochondrial Ca^{2+} uniporter (MCU) transports Ca^{2+} into the mitochondrial matrix [19]. It has been shown that overexpression of MCU and subsequent mitochondrial Ca^{2+} overload results in neuronal death, both *in vitro* and *in vivo* [23]. Moreover, mitochondria are linked to motor proteins via Miro-1/2, which have Ca^{2+}-sensing structures, suggesting that mitochondrial motility is also Ca^{2+}-sensitive [18]. Although during physiological state, a slight increase in mitochondrial Ca^{2+} appears to directly stimulate mitochondrial ATP production by activating Ca^{2+}-sensitive enzymes of Krebs' Cycle [21], high levels of Ca^{2+} may lead to the suppression of mitochondrial movement [20].

In neuroinflammation, the assumption that alteration of ion concentrations and neuronal damage are connected is supported by the beneficial effects of ion channel blockers reported in experimental autoimmune encephalitis (EAE), where blocking NaV or voltage-gated Ca^{2+} channels attenuates the disease course [13, 24]. Hence, we hypothesized that the abnormal activity of ion channels at the nodes of Ranvier following oxidative stress may cause the observed mitochondrial alterations [5, 13, 24].

Thus, we investigated here if preventing Na^+ overload within axons and Ca^{2+} overload within mitochondria using the NaV blocker tetrodotoxin (TTX) and the MCU inhibitor ruthenium 360 (Ru360), respectively, would protect both mitochondria and axons from oxidative-stress mediated damage.

2. Material and Methods

2.1. Ethics Statement. All experimental procedures were approved by the regional animal study committee of Berlin (Landesamt für Gesundheit und Soziales Berlin). Animal experiments were conducted in strict accordance with Directive 2010/63/EU of the European Parliament and of the European Council of 22 September 2010. Female and male mice (8-10 weeks old) were used for the experiments. The mice were housed and maintained in a temperature-controlled environment on a 12 h light-dark cycle.

2.2. Preparation and Maintenance of Ventral Spinal Roots. Ventral spinal roots were prepared as described previously [15]. Briefly, C57BL/6 mice were deeply anesthetized with isoflurane before cervical dislocation. After separating the connective tissue, the dorsal side of the spinal cord was exposed, and the vertebrae were cut laterally from rostral to caudal. The spinal cord was sectioned at the thoracic level and the ventral spinal roots were cut distal to the spinal cord. Together with the attached spinal roots, the explanted spinal cord was then placed into artificial cerebrospinal fluid (aCSF), saturated with carbogen (95% O_2 and 5% CO_2), and adjusted to a pH of 7.3-7.4. Under a dissecting microscope, the lumbar ventral roots were finally selected and separated from the spinal cord. Explanted ventral roots were maintained in aCSF, containing the following solutions: Solution I – 124 mM NaCl, 1.25 mM NaH_2PO_4, 10.0 mM Glucose, 1.8 mM $MgSO_4$, 1.6 mM $CaCl_2$, 3.00 mM KCl;

Solution II – 26.0 mM $NaHCO_3$. Both solutions were mixed immediately before use.

2.3. Induction of Oxidative Stress and Treatment Groups. All experiments were conducted in a submerged incubation chamber (Brain Slice Keeper-BSK 6 Scientific Systems Design Inc., Ontario, Canada), allowing up to five different treatment conditions and continuous carbogen perfusion of each submersion well throughout the entire process. Although the BSK 6 has 6 individual tubes to supply gas to each of the six wells, one tube had to be used to carbogenate the aCSF stock and therefore only 5 wells were available for the experiments.

To assess the effect of TTX and Ru360 on mitochondrial alterations induced by oxidative stress, we assigned spinal roots randomly to the following experimental groups: a) Negative controls of TTX experiments consisted of axons incubated with aCSF for 30 min at room temperature (RT). Negative controls of Ru360 experiments consisted of axons incubated with the corresponding solvent dimethyl sulfoxide (DMSO) at 1 μl/ml (0,001%) for 30 min at RT. This concentration corresponded to the one used to solve Ru360. DMSO does not exert an effect on investigated mitochondrial parameters (data not shown). We also refer to the negative groups as "untreated groups". b) In the oxidatively-stressed control group, ventral spinal roots were incubated with 100 μM H_2O_2 for 30 min at RT along with the corresponding vehicle (aCSF for TTX experiments, DMSO for Ru360 experiments). We also refer to this group as "positive control". c) Effects of blocking NaV channels on spinal roots were investigated by incubating the spinal roots with 100 nM or 1 μM TTX along with 100 μM H_2O_2. d) Effects of blocking mitochondrial Ca^{2+} influx were determined by incubation with 5, 10, or 20 μM Ru360 along with 100 μM H_2O_2.

2.4. Labeling of Mitochondria, Microscopy, and Analysis of Mitochondrial Dynamics (Morphology and Motility). After incubation with the treatments, transected ventral spinal roots were washed and transferred into aCSF containing 100 nM MitoTracker® Orange CMTMRos (Life Technologies, Darmstadt, Germany) dissolved in DMSO for 30 min at RT and then washed again with fresh aCSF.

Microscopy and imaging analysis of the ventral spinal roots were performed as previously described [15]. For microscopy, spinal roots were placed on a glass coverslip and transferred to an imaging chamber containing carbogenated aCSF. A custom-built nylon net was placed on top of the spinal roots to prevent them from moving during image acquisition. For all experiments, an inverted laser-scanning confocal microscope adapted for live-cell imaging was used. Experiments with Na^+ channel blockade were imaged with an LSM 710 (Carl Zeiss, Jena, Germany). Experiments with Ca^{2+} channel blockade were conducted using a Nikon Scanning Confocal A1Rsi+. MitoTracker® Orange was excited at 561 nm with a diode-pumped solid-state (DPSS) laser. Visualization of mitochondria was performed through a 100x (LSM 710, Carl Zeiss) or 60x (Nikon Scanning Confocal A1Rsi+) oil immersion objective. Regions of interest (ROI) were chosen based on the following criteria: 1) clearly visible node of Ranvier 2) well-labeled mitochondria 3) axon with intact myelin sheath and no signs of membrane disruption in regions adjacent to the selected ROI 4) areas at least 2 mm away from the end of the roots. Scrutinizing the spinal roots from the proximal to the distal end, three separate ROI were chosen. For each ROI, a time-lapse (60-second duration, 2 s/frame) with a resolution of 512x512 pixels was recorded. Exposure time and laser power were reduced to minimize photobleaching and phototoxicity.

The first frame of every time-lapse video was used to assess mitochondrial morphology with an automated analysis tool of the Volocity®6.3 software (Perkin Elmer, Rodgau, Germany). To determine the changes in mitochondrial morphology, the following parameters were analyzed: shape factor (4πX [Area/Perimeter^2]), a measure of circularity ranging from 0 to 1, in which "1" indicates a perfect circle, length (μm) and area (μm^2) of an individual mitochondrion. To assess motility, mitochondria were tracked manually using Volocity®6.3 software (Perkin Elmer, Rodgau, Germany). Any mitochondrion with a displacement of $\geq 1\,\mu$m was considered "mobile". For experiments with Ru360, mobile mitochondria were further analyzed for track length (μm), the measure of the real distance traveled by a mitochondrion, and velocity (μm/s).

Under physiological and pathological conditions, mitochondrial populations display high heterogeneity within one cell due to their adaption to different energetic states. Thus, to minimize selection bias, large amounts of mitochondria in different axons of several experiments were analyzed and matched.

2.5. Assessment of Mitochondrial Membrane Potential. To determine mitochondrial membrane potential, spinal roots were stained with 20 μg/ml 5,5′,6,6′-tetrachloro-1,1′,3,3′-tetraethylbenzimidazolylcarbocyanine iodide (JC-1; Life Technologies, Darmstadt, Germany) in aCSF at RT for 1 h. JC-1 accumulates in mitochondria with intact membrane potential and negative charge. Sufficient accumulation due to unaltered mitochondrial membrane potential leads to the formation of J aggregates and a shift in emitted fluorescence from green (529 nm) to red (590 nm) [25]. To minimize background noise, roots were washed with fresh aCSF before imaging. JC-1 was excited with dual illumination with argon (514 nm) and DPSS (561 nm) lasers.

Red/green fluorescence ratio of JC-1 stained mitochondria determined at a Nikon Scanning Confocal A1Rsi+microscope was used for the analysis of mitochondrial membrane potential. Results of the red/green fluorescence ratio of individual mitochondrion were normalized to the average red/green fluorescence ratio of the untreated group as established by others [26].

2.6. Statistical Analysis. Acquired data were analyzed with Prism 8 Software (GraphPad, CA, USA). All datasets were first subjected to D'Agostino and Pearson omnibus K2 normality test and Shapiro-Wilk normality test for Gaussian distribution. Data fitting the criteria for normal distribution were subsequently analyzed using a one-way ANOVA with

Bonferroni's post hoc test. Data following a non-parametric distribution were analyzed using a Kruskal-Wallis test followed by a Dunn's post hoc multiple comparisons test. p values ≤ 0.05 were considered significant. The significance of the data was further depicted as $*$ implying $p \leq 0.05$, $**$ implying $p \leq 0.01$, $***$ implying $p \leq 0.001$, and $****$ implying $p \leq 0.0001$. All data are shown in mean ± SEM.

3. Results

3.1. Blocking Axonal Na^+ Influx Prevents Oxidative Stress-Induced Morphological Changes in Mitochondria. To investigate the effect of Na^+ channel blockade on mitochondrial morphology, the explanted ventral spinal roots were treated with 100 μM H_2O_2 alone, or 100 μM H_2O_2 along with different concentrations of TTX (100 nM or 1 μM). Explants were then imaged using a confocal microscope (Figure 1(a)). Shape factor (Figure 1(b)), mitochondrial length (Figure 1(c)), and mitochondrial area (Figure 1(d)) were analyzed.

During oxidative stress, mitochondrial shape factor (untreated: 0.4148 ± 0.0060; H_2O_2: 0.4854 ± 0.0074) and area (untreated: $0.4043 \pm 0.0124\,\mu m^2$; H_2O_2: $0.7557 \pm 0.0335\,\mu m^2$) increased while mitochondrial length decreased (untreated: $1.684 \pm 0.0375\,\mu m$; H_2O_2: $1.5800 \pm 0.0431\,\mu m$; Figures 1(b) and 1(c)). All observed morphological changes induced by oxidative stress were prevented with 100 nM of TTX (shape factor = 0.4202 ± 0.0079; length = $1.8990 \pm 0.0702\,\mu m$; area = $0.5247 \pm 0.0268\,\mu m^2$; Figures 1(b)–1(d)). In contrast, 1 μM of TTX did not affect the H_2O_2-induced increase in shape factor (0.5030 ± 0.0072; Figure 1(b)), but significantly reduced length ($1.4400 \pm 0.0362\,\mu m$, Figure 1(c)) and increased mitochondrial area in comparison to oxidative stress conditions ($1.0150 \pm 0.0377\,\mu m^2$; Figure 1(d)).

3.2. Blocking Axonal Na^+ Influx Prevents Oxidative Stress-Induced Changes of Mitochondria Motility. Next, we performed time-lapse imaging and analyzed mitochondrial motility parameters under the above-mentioned experimental conditions (Figure 2(a)). We analyzed the percentage of manually tracked motile mitochondria (Figure 2(b)). The untreated group with aCSF alone showed an average percentage of motile mitochondria of about 16% ($15.890 \pm 1.395\%$), while in the presence of 100 μM H_2O_2 only around 5% ($5.044 \pm 1.228\%$) of mitochondria were motile (Figure 2(b)). Blocking Na^+ influx with 1 μM TTX prevented the oxidative stress-induced reduction of motile mitochondria ($11.460 \pm 1.826\%$; Figure 2(b)). The effect of 100 nM TTX was not significant compared to the H_2O_2-treated group (Figure 2(b)).

3.3. Blocking Mitochondrial Ca^{2+} Uptake Prevents Oxidative Stress-Induced Alterations of Mitochondrial Length. Then, we examined the influence of mitochondrial Ca^{2+} on mitochondrial morphology. Oxidative stress was induced again with 100 μM H_2O_2. Blocking mitochondrial Ca^{2+} influx via mitochondrial Ca^{2+} uniporter channels was performed by simultaneous incubation of mitochondria with H_2O_2 and 5, 10, or 20 μM Ru360. We observed that H_2O_2 led to a decrease in mitochondrial length (untreated: $1.9260 \pm 0.0343\,\mu m$; H_2O_2: $1.6920 \pm 0.0302\,\mu m$) and area (untreated: $1.0890 \pm 0.0292\,\mu m^2$; H_2O_2: $0.9756 \pm 0.0268\,\mu m^2$) compared to the untreated group (Figures 3(c) and 3(d)). However, shape factor did not increase under H_2O_2-treatment (untreated: 0.4703 ± 0.0072; H_2O_2: 0.4841 ± 0.0071) when compared to the untreated group (Figure 3(b)). Blocking mitochondrial Ca^{2+} influx with 5 μM Ru360 prevented changes in shape factor (0.4474 ± 0.0090, Figure 3(b)). A similar trend was observed in roots treated with 10 μM Ru360 (0.4741 ± 0.0083; Figure 3(b)). However, at 20 μM, Ru360 induced an even more pronounced increase in shape factor values (0.5214 ± 0.0095) when compared to the H_2O_2-treated group (Figure 3(b)). Incubation with 5 μM Ru360 did not increase mitochondrial length compared to the H_2O_2-treated group ($1.881 \pm 0.0426\,\mu m$, Figure 3(c)). In the presence of 10 μM Ru360, mitochondrial length increased ($1.7780 \pm 0.0390\,\mu m$; Figure 3(c)), while at 20 μM Ru360 promoted decrease in mitochondrial length compared to treatment with oxidative stress alone (Figure 3(c)). Regarding area, we did not observe significant alterations in either of the treatment groups (Figure 3(d)).

3.4. Blocking Mitochondrial Ca^{2+} Uptake Prevents Reduction of Mitochondrial Motility in Stressed Axons. To investigate the effect of blocking MCU on oxidative stress-induced alterations in mitochondrial motility, we incubated explanted ventral spinal roots with DMSO alone, DMSO plus 100 μM H_2O_2, or with 100 μM H_2O_2 along with three different concentrations (5, 10 or 20 μM) of Ru360 (Figure 4(a)).

In the untreated group, we observed an average of 7% ($7.103\% \pm 0.997$) of moving mitochondria (Figure 4(b)). H_2O_2 at 100 μM caused a significant reduction in motile mitochondria ($1.447\% \pm 0.507$) as well as a decrease in track length (untreated: $8.2722 \pm 0.8433\,\mu m$; H_2O_2-treated: $2.8750 \pm 0.6442\,\mu m$) and track velocity (untreated: $0.2094 \pm 0.0210\,\mu m/s$; H_2O_2-treated: $0.1265 \pm 0.0320\,\mu m/s$) (Figures 4(a)–4(c)). H_2O_2-induced decrease in percentage of motile mitochondria, mitochondrial track length, and track velocity was prevented with 10 μM Ru360 (% of moving mitochondria: $7.393 \pm 1.861\%$; track length: $8.9410 \pm 0.7597\,\mu m$; track velocity: $0.2293 \pm 0.0243\,\mu m/s$; Figures 4(a)–4(c)) and 20 μM Ru360 (% of moving mitochondria: $3.549 \pm 1.124\%$; track length: $4.989 \pm 0.6025\,\mu m$; track velocity: $0.1384 \pm 0.0280\,\mu m/s$; Figures 4(a)–4(c)). However, in spinal roots treated with 5 μM Ru360, only H_2O_2-induced changes for track length (μm, Figure 4(c)) were prevented. No effects were observed on percentage of moving mitochondria or track velocity ((% of moving mitochondria: $5.205 \pm 1.325\%$; track velocity: $0.1331 \pm 0.0235\,\mu$ m/s, Figures 4(a) and 4(d)).

3.5. Blocking Axonal Na^+ Influx Prevents Oxidative Stress-Induced Reduction of Mitochondrial Membrane Potential. Next, we investigated whether inhibition of axonal Na^+ influx may preserve mitochondrial functionality altered by H_2O_2. Four groups of spinal roots were treated for 30 min

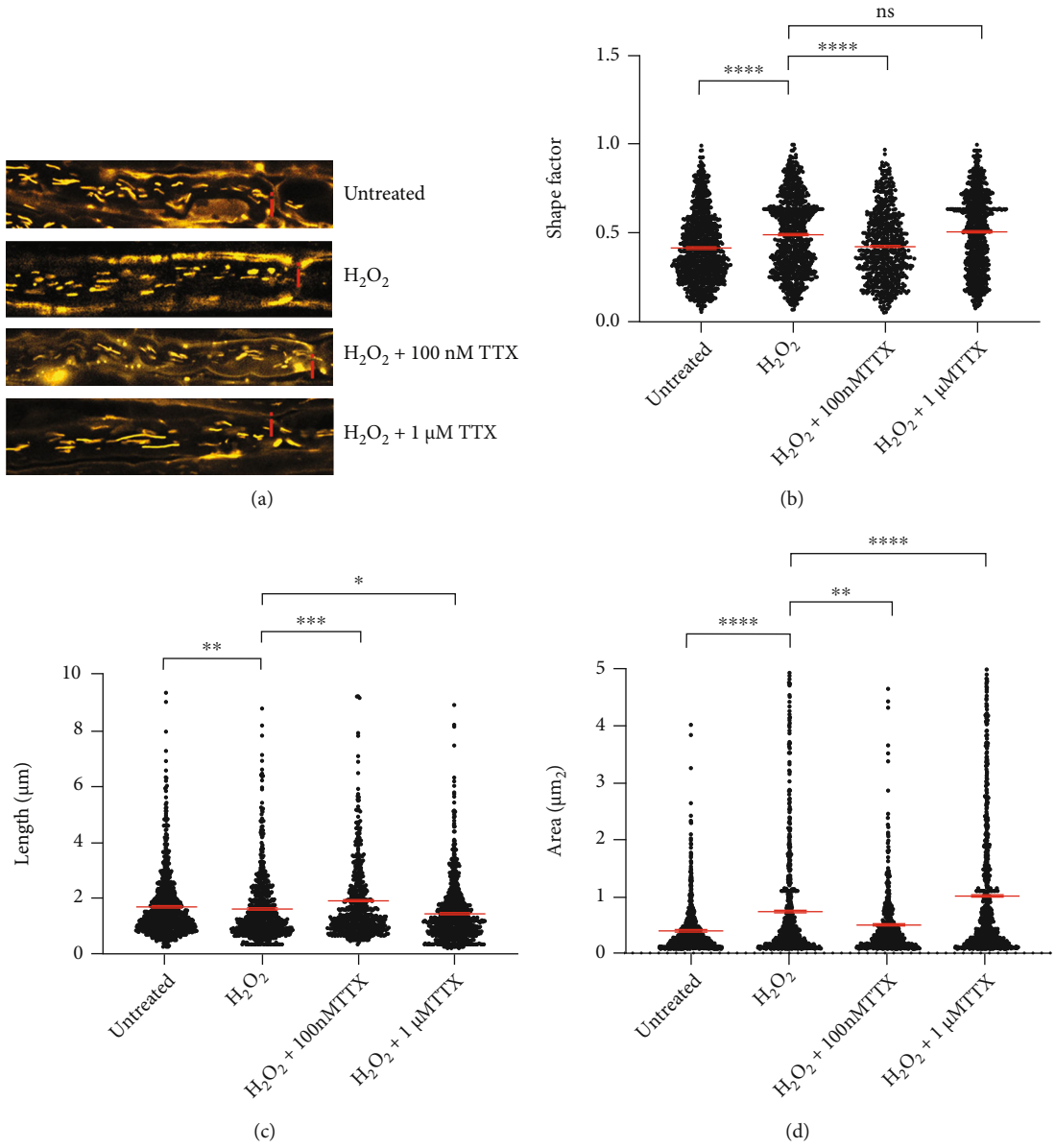

Figure 1: Blocking axonal Na^+ influx with tetrodotoxin (TTX) prevents oxidative stress-induced mitochondrial morphology alterations. (a) Representative original images of all different experimental conditions; axons incubated with aCSF alone contained elongated mitochondria; incubation with 100 μM H_2O_2 led to the generation of smaller and rounder mitochondria, and some diffuse MitoTracker® distribution; axon simultaneously incubated with 100 μM H_2O_2 and 100 nM TTX contained elongated mitochondria; axon simultaneously incubated with 100 μM H_2O_2 and 1 μM TTX contained short mitochondria but with increased area. (b–d) Shape factor (b), length (c), and area (d) of mitochondria located near the nodes of Ranvier in axons incubated with the above-mentioned treatments. Nodes of Ranvier are marked with a red "i". $^*p \leq 0.05$, $^{**}p \leq 0.01$, $^{***}p \leq 0.001$, and $^{****}p \leq 0.0001$. The error bars represent the standard error of mean; $n = 6$ animals and 22 roots; untreated 7 roots, H_2O_2 6 roots, H_2O_2+100 nM TTX 4 roots, and H_2O_2+1 μM TTX 5 roots.

with either aCSF alone (vehicle control group), 100 μM H_2O_2, 100 μM H_2O_2+1 μM TTX or 1 μM TTX alone, respectively. Since the incubation chamber permitted the simultaneous assessment of maximally 5 conditions, only the 1 μM TTX concentration, which showed best protecting effects in Figure 2(a), was tested in these experiments. Treated spinal roots were then incubated for 30 min with the ratiometric indicator JC-1. The red/green fluorescence ratio is an indication of the mitochondrial membrane potential and thereby mitochondrial ability to produce ATP (Figure 5(a)).

The application of 100 μM H_2O_2 resulted in a shift to green fluorescence (0.6374 ± 0.0291; Figures 5(a) and 5(b)), as a sign of a loss of mitochondrial membrane potential. 1 μM TTX applied simultaneously with 100 μM H_2O_2 prevented the loss of mitochondrial membrane potential (untreated: 1.0000 ± 0.0297; 1 μM TTX: 1.2410 ± 0.0432; Figures 5(a) and 5(b)). TTX alone led to higher

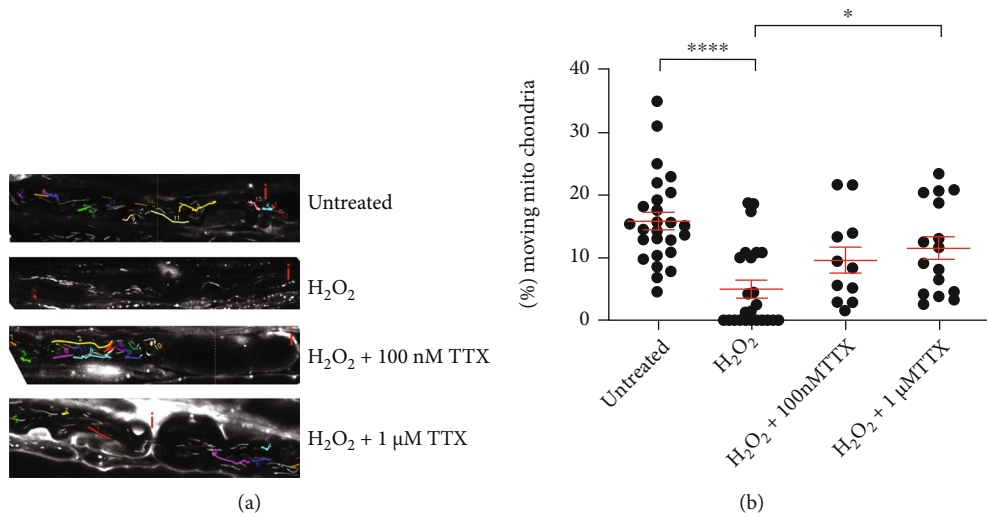

Figure 2: Blocking axonal Na^+ influx with TTX barely affects mitochondrial motility parameters altered due to oxidative stress. (a) Representative original images of all different experimental conditions: axon incubated with aCSF alone contained multiple moving mitochondria that c5over larger distances in the axon; 100 μM H_2O_2 induced a strong reduction of motile mitochondria; axons simultaneously incubated with 100 μM H_2O_2 and 100 nM TTX or 1 μM TTX contained more motile mitochondria, covering longer distances. (b) Percentage of moving mitochondria per axon. Nodes of Ranvier are marked with a red "i". $^*p \leq 0.05$, $^{****}p \leq 0.0001$. The error bars represent the standard error of mean; $n = 6$ animals and 22 roots; untreated 7 roots, H_2O_2 6 roots, H_2O_2+100 nM TTX 4 roots, and H_2O_2+1 μM TTX 5 roots.

mitochondrial membrane potential than in the untreated group (TTX: 1.1270 ± 0.0309; Figures 5(a) and 5(b)).

3.6. Blocking Mitochondrial Ca^{2+} Uptake Prevents Oxidative Stress-Induced Reduction of Mitochondrial Membrane Potential. To assess effects of Ca^{2+} uptake on mitochondrial functionality, four groups of spinal roots were treated for 30 min with either DMSO (vehicle control group), DMSO +100 μM H_2O_2, 100 μM H_2O_2+10 μM Ru360 or 10 μM Ru360 alone, respectively. We selected 10 μM Ru360 for these experiments because it was the concentration that showed the best protection against oxidative stress-induced loss of motility (Figure 4(a)). Treated spinal roots were then incubated for 30 min with the ratiometric indicator JC-1. The red/green fluorescence ratio is an indication of the mitochondrial membrane potential and thereby mitochondrial ability to produce ATP (Figure 6(a)).

The application of 100 μM H_2O_2 resulted in a shift to green fluorescence (0.5638 ± 0.0250; Figures 6(a) and 6(b)), as a sign of a severe loss of mitochondrial membrane potential. 10 μM Ru360 applied simultaneously with 100 μM H_2O_2 prevented the loss of mitochondrial membrane potential and restored it to values close to the untreated group (untreated: 1.0000 ± 0.0383; 10 μM Ru360: 0.8507 ± 0.0395; Figures 6(a) and 6(b)). With Ru360 alone, we did not observe any effects on mitochondrial membrane potential in comparison to DMSO treated condition (Figures 6(a) and 6(b)).

4. Discussion

Mitochondrial alterations linked to oxidative stress [9] are reported to occur in the early stages of MS [4, 12] and are believed to contribute to neurodegenerative processes observed in MS patients [2, 27–29]. Therefore, mitochondria have emerged as potential therapeutic targets to limit disease progression [30, 31]. In this study, we investigated using an ex vivo model of peripheral axons [17] whether the effects of oxidative stress on mitochondria can be prevented by targeting pathological ion alterations affecting, in particular, the levels of axonal Na^+ and mitochondrial Ca^{2+}.

In this model, oxidative stress was induced by a 30-minute incubation with 100 μM H_2O_2, a concentration that led to reversible structural and functional alterations in mitochondria [32]. We observed oxidative stress-induced decrease in mitochondrial length (Figures 1(c) and 3(c)) as well as a decrease in the number of motile mitochondria (Figures 2(b) and 4(b)). Additionally, consistent with our previous reports [16, 33] and those of others describing inhibition of axonal transport by oxidative stress [34–36], we observed a decrease in both track length and track velocity of mitochondria exposed to 100 μM H_2O_2 (Figures 4(c) and 4(d)). The observed reduction in mitochondrial length supports previous findings of our group [17] and may be the consequence of an increase in the fission process, which is induced in stressed and damaged mitochondria to get rid of the damaged portion [37].

We also expected that oxidative stress would damage mitochondria and reduce their functionality in our model causing ATP depletion as it has been reported for highly energy-dependent neuronal cells [9, 38]. We showed a decrease in mitochondrial membrane potential under oxidative stress conditions (Figures 5(a), 5(b), 6(a), and 6(b)). As an intact mitochondrial membrane potential is an important determinant for mitochondrial ATP production via oxidative phosphorylation [39], we assumed ATP depletion in oxidatively injured mitochondria. In a novel CNS model established in our lab, we were indeed able to show decreased ATP levels upon oxidative stress induced by

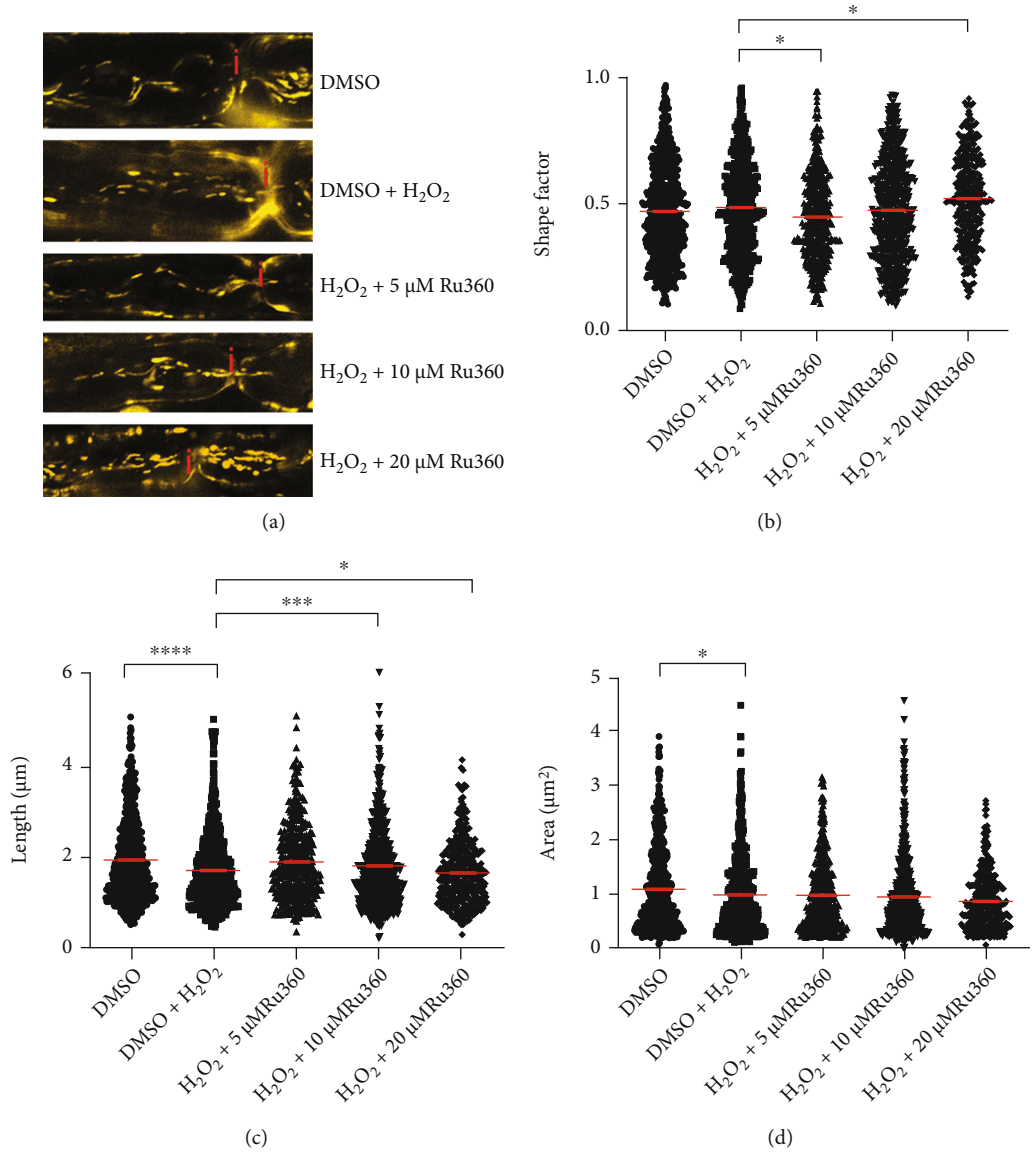

Figure 3: Blocking mitochondrial Ca^{2+} influx with Ru360 alters mitochondrial morphology. (a) Representative original images of all different experimental conditions; axon incubated with DMSO alone showed elongated mitochondria; 100 μM H_2O_2 induced shorter and smaller mitochondria; axonal mitochondria exposed to 100 μM H_2O_2 and 5 μM Ru360 showed slightly longer and less round morphology than mitochondria exposed to H_2O_2 alone; incubation with 100 μM H_2O_2 and 10 μM Ru360 led to the formation of longer mitochondria compared with H_2O2 control; axon incubated with 100 μM H_2O_2 and 20 μM Ru360 showed shorter mitochondria than oxidative stress control. (b–d) Mitochondrial shape factor (b), length (c), and area (d) of single mitochondria. Nodes of Ranvier are marked with a red "i". $^{*}p \leq 0.05$, $^{***}p \leq 0.001$, and $^{****}p \leq 0.0001$. The error bars represent the standard error of mean; $n = 7$ animals and 29 roots; DMSO 7 roots, H_2O_2 7 roots, H_2O_2+5 μM Rui360 4 roots, H_2O_2+10 μM Ru360 7 roots, and H_2O_2+20 μM Ru360 4 roots.

100 μM H_2O_2 [33]. Thus, our paradigm of stressed mitochondria in explanted roots may serve in the future to examine effects of antioxidative interventions on ATP levels.

We previously reported that alterations of mitochondria during oxidative stress initiate at the nodes of Ranvier [17]. NaVs are abundantly present at the nodes of Ranvier and are important for saltatory conduction [40, 41]. In MS lesions, the expression of these channels is reported to be altered [42–44]. In this line, during exposure to H_2O_2, blocking NaV with 100 nM TTX prevented the decrease in length and increase in shape factor and area (Figures 1(a)–1(c)). In contrast, 1 μM TTX along with H_2O_2 led to the generation of short mitochondria that display however large areas (Figures 1(b) and 1(c)). A large mitochondrial area could reflect either detrimental swelling [45, 46] or fusion [1, 35]. We speculate that in the group treated with H_2O_2 and 1 μM TTX, transient mitochondrial fusion followed by fission as reported by Liu et al. [45] may occur. Transient fusion seems to be central for maintaining metabolism and motility [45]. In this line, we observed that 1 μM TTX could

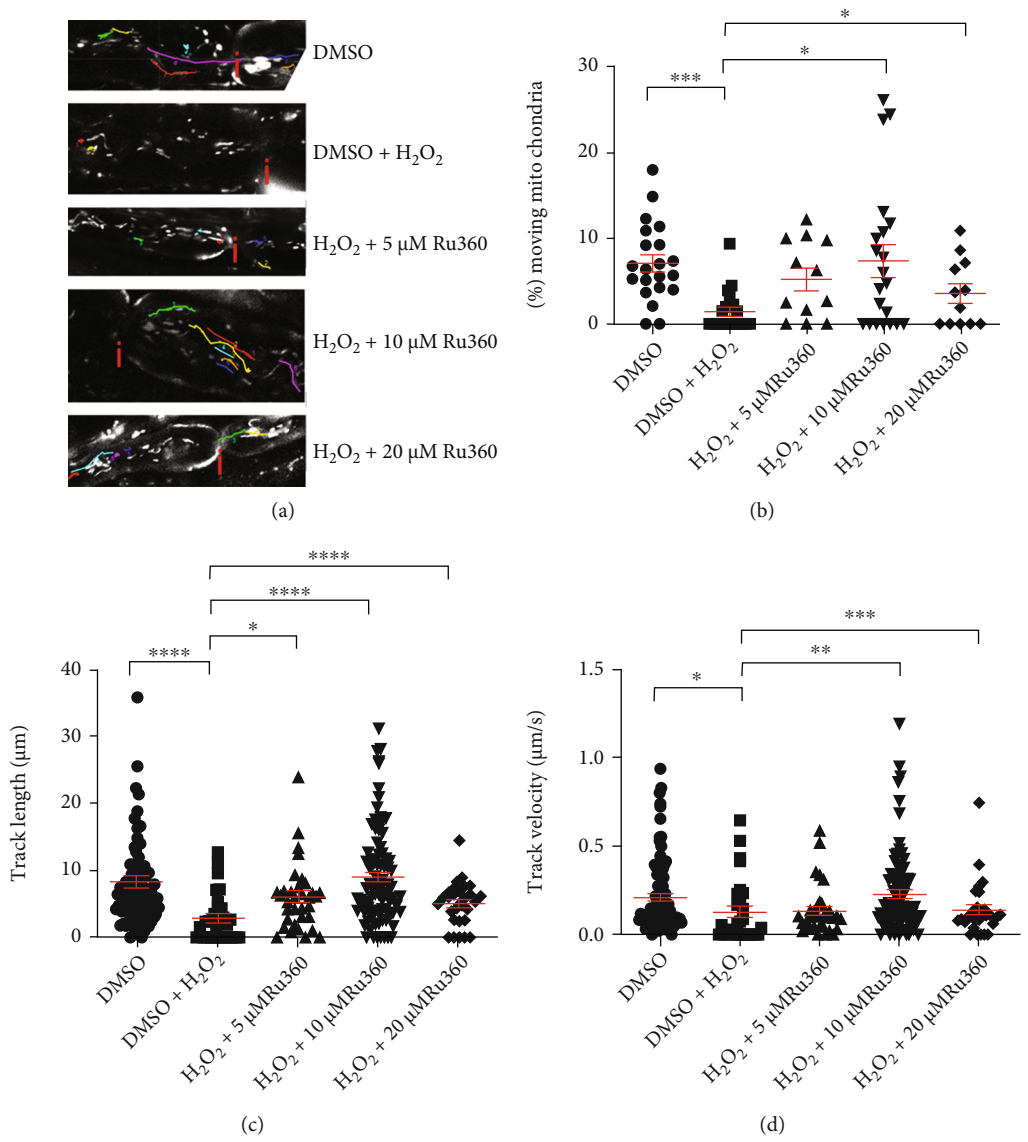

Figure 4: Blocking mitochondrial Ca^{2+} uptake with Ru360 prevents oxidative stress-induced loss of mitochondrial motility. (a) Representative original images of all different experimental conditions: axon incubated with DMSO alone contained multiple moving mitochondria that cover larger distances in the axon.; axon incubated with 100 μM H_2O_2, showed few motile mitochondria with short track length; simultaneous incubation with 100 μM H_2O_2 and 5 or 20 μM Ru360 led to more motile mitochondria that move longer distances; axon simultaneously incubated with 100 μM H_2O_2 and 10 μM Ru360 showed nearly normal mitochondrial motility. (b–d) Quantification of the percentage of motile mitochondria (a), track length (b), and track velocity (c). Nodes of Ranvier are marked with a red "i". $^*p \leq 0.05$, $^{**}p \leq 0.01$, $^{***}p \leq 0.001$, and $^{****}p \leq 0.0001$. The error bars represent the standard error of mean; $n = 7$ animals and 29 roots; DMSO 7 roots, H_2O_2 7 roots, H_2O_2+5 μM Rui360 4 roots, H_2O_2+10 μM Ru360 7 roots, and H_2O_2+20 μM Ru360 4 roots.

prevent the motility decrease and the loss of membrane potential observed in mitochondria exposed to H_2O_2 (Figures 2(a), 5(a), and 5(b)).

Interestingly, 1 μM TTX alone induced an elevation of the mitochondrial membrane potential when compared to the untreated group. This may reflect a state defined as mitochondrial hyperpolarization [46, 47]. We hypothesize that the presence of TTX and the consequent reduce Na^+ influx may lead to a diminished activity of the ATP-dependent Na^+/K^+-ATPase and induce an increase of ATP. Thus, in our setup, hyperpolarization may be generated by the ATP-consuming reverse action mode of complex V [46]. The exact mechanism underlying the elevation of the mitochondrial membrane potential with TTX alone will be part of future investigations.

Subsequently to Na^+ overload, intra-axonal Ca^{2+} accumulation occurs via reverse action mode of NCX, as described in other studies [13, 48]. During axonal Ca^{2+} overload, mitochondria may uptake Ca^{2+} and function as an intracellular Ca^{2+} buffering system [49]. However, excessive intramitochondrial Ca^{2+} may affect mitochondrial function and motility. It has been shown that dynamin-related protein 1 (Drp1), responsible for mitochondrial fission, as well as Miro, connecting mitochondria via other proteins to

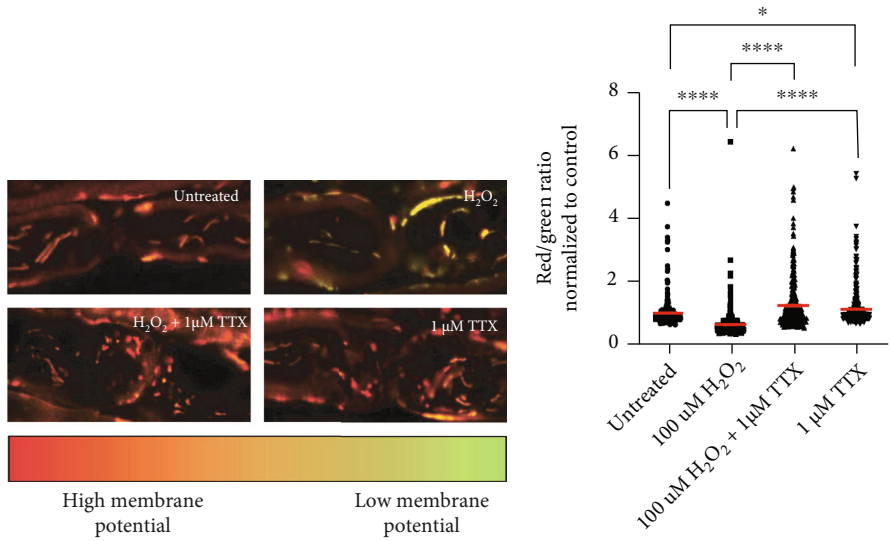

Figure 5: Blocking axonal Na^+ influx with TTX prevents loss of mitochondrial membrane potential. (a) Representative images of axons in the different treatment groups. The upper left image shows mitochondrial membrane potential in untreated condition. Oxidative stress led to loss of mitochondrial membrane potential (upper right image) and a shift to green fluorescence. TTX prevented the H_2O_2 effects (lower left image). The lower right image shows that the application of TTX alone led to preserved mitochondrial membrane potential. (b) Data represent normalized values of individual mitochondria to the mean of the control group (red/green ratio = 1 ± 0.0383). $^{****}p \leq 0.0001$. The error bars represent the standard error of mean; $n = 3$ animals and 12 roots; untreated 3 roots, H_2O_2 3 roots, H_2O_2+1 μM TTX 3 roots, and 1 μM TTX 3 roots.

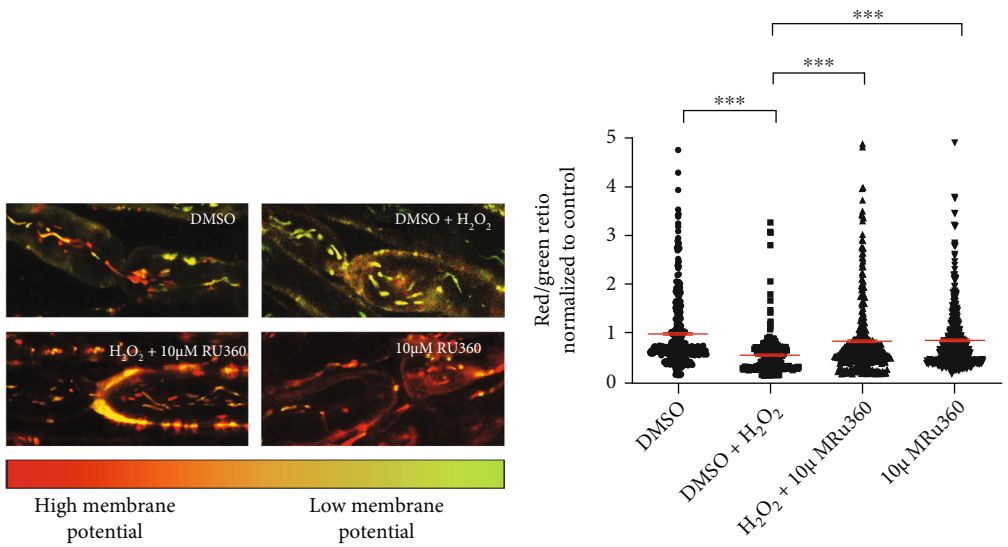

Figure 6: Blocking mitochondrial Ca^{2+} uptake with Ru360 prevents loss of mitochondrial membrane potential. (a) Representative images of axons in the different treatment groups. The upper left image shows mitochondrial membrane potential under negative control conditions containing mitochondria with high (red) and low (green) mitochondrial membrane potential. Oxidative stress led to loss of mitochondrial membrane potential (upper right image) and a shift to green fluorescence. Ru360 prevented the H_2O_2 effects (lower left image). The lower right image shows that the application of the Ru360 alone had no effects on mitochondrial functionality compared to control group. (b) Data represent normalized values of individual mitochondria to the mean of the control group (red/green ratio = 1 ± 0.0383). $^{***}p \leq 0.001$. The error bars represent the standard error of mean; $n = 5$ animals and 20 roots; DMSO 5 roots, H_2O_2 5 roots, H_2O_2+10 μM Ru360 5 roots, and 10 μM Ru360 5 roots.

motor proteins, are directly or indirectly controlled by Ca^{2+} [29, 50–52]. Moreover, mitochondrial swelling seems to be Ca^{2+}-related, too [53]. In this case, we demonstrated that inhibition of Ca^{2+} influx into mitochondria with 10 μM Ru360 completely prevents oxidative stress-induced reduction of mitochondrial length and all motility parameters (Figures 3(b) and 4(a)–4(c)). Further, with 10 μM Ru360, we observed preserved mitochondrial membrane potential (Figures 5(a) and 5(b)). Thus, a rise in intramitochondrial Ca^{2+} concentration appears to contribute to mitochondrial alterations during oxidative stress in our model. In the motility experiments, we observed a biphasic effect of Ru360 with similar absolute values for 5 and 20 μM and a clearly different response for 10 μM Ru360. This biphasic effect was observed in all investigated mitochondrial motility parameters, i.e., percentage of motile mitochondria, mitochondrial track length, and track velocity (Figures 3(a)–3(c)).

Our data confirm previous studies that indicated that ion concentrations show no linear correlation with mitochondrial morphology, motility, or membrane potential [54, 55]. While a slight increase in mitochondrial Ca^{2+} concentration may increase mitochondrial ATP production and be beneficial [55], elevated levels of mitochondrial Ca^{2+} may lead to the opening of the PTP with possible detrimental effects [56]. In addition, PTP opening does not only depend on ion concentrations but also on ATP/ADP levels, mitochondrial ROS, fatty acids, and magnesium levels [57–59]. ROS function as signaling molecules, reversibly oxidizing defined structures and thereby regulating transcription or enzyme activity [6, 31, 60–62]. ROS regulates among others the activity of MCU [63], as well as of voltage-gated sodium channels, including NaV1.7 [64]. These potential cellular mechanisms to cope with increased ROS should be kept in mind when dealing with oxidative stress and ion alterations.

Ru360 is a specific inhibitor of the MCU [65, 66]. However, blocking MCU may not result in a complete inhibition of mitochondrial Ca^{2+} influx. As described in metabolically inhibited cells [47], a reverse action mode of mitochondrial Na^+/Ca^{2+}-exchanger may enhance intramitochondrial Ca^{2+} in stressed axons. Additionally, mitochondria closely interact with the endoplasmic reticulum (ER), forming mitochondria-associated membranes (MAMs) [67]. MAMs play a role in the exchange of Ca^{2+} or metabolites [68, 69], mitochondrial fusion and fission processes, and induction of apoptosis [70].

Mitochondria possess different mechanisms of Ca^{2+} influx [71], but also of Ca^{2+} efflux. The two most important mechanisms are via mitochondrial Na^+/Ca^{2+}-exchanger and via $2H^+/Ca^{2+}$-exchanger [71, 72]. Mitochondrial Ca^{2+} uptake is therefore most likely directly influenced by intraaxonal Na^+ concentration because this affects mitochondrial Ca^{2+} efflux mechanisms via mitochondrial Na^+/Ca^{2+}-exchanger. Interestingly, a reverse action mode is also described for mitochondrial Na^+/Ca^{2+}-exchanger in metabolically inhibited cells [48]. Thus, blocking either axonal Na^+ influx or mitochondrial Ca^{2+} uptake may likely indirectly interfere with other pathways, for example via mitochondria-associated membranes (MAMs) or mitochondrial Na^+/Ca^{2+}-exchanger of a tightly regulated and interconnected Na^+- Ca^{2+}-homeostasis.

5. Limitations of the Study

One technical limitation of our setup was the restricted number of experimental conditions that could be conducted simultaneously within one experiment. The size of the incubation chamber and the narrow time-window, in which transplants could be imaged ex vivo, permitted only the comparison of maximally five different culture conditions. Therefore, using this setup, we were unable to compare effects on mitochondria of different concentrations of inhibitors both in the absence and the presence of the oxidative insult.

Therefore, using this setup, we were able to show only effects on mitochondria of different concentrations of inhibitors in the oxidative stress paradigm and not in the absence of H_2O_2.

Moreover, although our data indicate that modulation of Ca^{2+} influx with Ru360 protects mitochondria from oxidative stress-induced damage, we could not define which Ca^{2+} concentrations are protective and which concentrations are detrimental for mitochondria. Basically, we attested that the explanted root model was not suitable for intraaxonal Ca^{2+}quantification using, for instance, Ca^{2+}-sensitive dyes or roots from Ca^{2+} reporter mice.

6. Conclusion

In conclusion, explanted murine spinal roots appear to be a suitable model to investigate oxidative stress-induced ion alterations affecting axonal mitochondria, in particular, Na^+ and Ca^{2+} overload. Using the model, we demonstrated that inhibition of axonal Na^+ influx prevented oxidative stress-induced alterations of mitochondrial morphology. On the other hand, blocking mitochondrial Ca^{2+} uptake prevented the oxidative stress-induced reduction of both mitochondrial motility and mitochondrial membrane potential, which is crucial for ATP production.

The fact that H_2O_2-induced alterations in mitochondria morphology and motility were prevented by pharmacologic inhibitors of NaV and MCU indicates a direct participation of Na^+ and Ca^{2+} on oxidative stress-mediated mitochondrial changes. Further investigations in this direction are needed to explore the therapeutic potential of the modulation of Na^+ and Ca^{2+} ion channel for mitochondrial protection during oxidative stress.

Data Availability

The main data supporting the findings of this study are listed in Tables 1–6 of the Supplementary Materials.

Conflicts of Interest

The authors declare that there is no conflict of interest regarding the publication of this paper.

Authors' Contributions

Bimala Malla and Carmen Infante-Duarte contributed equally to this work.

Acknowledgments

We thank the Core Facility Advanced Medical Bioimaging (AMBIO) at Charité Universitätsmedizin Berlin for imaging infrastructure and technical support. The study was supported by the Charité Universitätsmedizin and by a fellowship from Berlin Institute of Health (BIH) to R. Ulshöfer. The work of C. Infante-Duarte was supported by the DFG (SFB1340-1, Project B05), and the work of R. Niesner and A. E. Hauser was supported by the DFG (SFB1444, Project 14).

Supplementary Materials

Supplementary 1. Table 1: summary of morphology parameters of untreated mitochondria, mitochondria under H_2O_2 treatment alone, and mitochondria treated with H_2O_2 in the presence of 100 nM and 1 μM TTX.

Supplementary 2. Table 2: summary of motility parameters of untreated mitochondria, mitochondria under H_2O_2 treatment alone, and mitochondria treated with H_2O_2 in the presence of 100 nM and 1 μM TTX.

Supplementary 3. Table 3: summary of morphology parameters of untreated mitochondria, mitochondria under H_2O_2 treatment alone, and mitochondria treated with H_2O_2 in the presence of 5 μM, 10 μM, and 20 μM Ru360.

Supplementary 4. Table 4: summary of motility parameters of untreated mitochondria, mitochondria under H_2O_2 treatment alone, and mitochondria treated with H_2O_2 in the presence of 5 μM, 10 μM, and 20 μM Ru360.

Supplementary 5. Table 5: summary of the red-green ratio normalized to untreated mitochondria, mitochondria treated with 100 μM H_2O_2 alone or in the presence of 1 μM TTX, and mitochondria treated with 1 μM TTX alone.

Supplementary 6. Table 6: summary of the red-green ratio normalized to untreated mitochondria, mitochondria treated with 100 μM H_2O_2 alone or in the presence of 10 μM Ru360, and mitochondria treated with 10 μM Ru360 alone.

References

[1] A. J. Thompson, S. E. Baranzini, J. Geurts, B. Hemmer, and O. Ciccarelli, "Multiple sclerosis," *The Lancet*, vol. 391, no. 10130, pp. 1622–1636, 2018.

[2] K. G. Su, G. Banker, D. Bourdette, and M. Forte, "Axonal degeneration in multiple sclerosis: the mitochondrial hypothesis," *Current Neurology and Neuroscience Reports*, vol. 9, no. 5, pp. 411–417, 2009.

[3] L. Haider, "Inflammation, iron, energy failure, and oxidative stress in the pathogenesis of multiple sclerosis," *Oxidative Medicine and Cellular Longevity*, vol. 2015, Article ID 725370, 10 pages, 2015.

[4] S. Patergnani, V. Fossati, M. Bonora et al., "Mitochondria in multiple sclerosis: molecular mechanisms of pathogenesis," *International Review of Cell and Molecular Biology*, vol. 328, pp. 49–103, 2017.

[5] S. G. Waxman, "Axonal conduction and injury in multiple sclerosis: the role of sodium channels," *Nature Reviews Neuroscience*, vol. 7, no. 12, pp. 932–941, 2006.

[6] K. Ohl, K. Tenbrock, and M. Kipp, "Oxidative stress in multiple sclerosis: central and peripheral mode of action," *Experimental Neurology*, vol. 277, pp. 58–67, 2016.

[7] A. A. Mossakowski, J. Pohlan, D. Bremer et al., "Tracking CNS and systemic sources of oxidative stress during the course of chronic neuroinflammation," *Acta Neuropathologica*, vol. 130, no. 6, pp. 799–814, 2015.

[8] H. Radbruch, D. Bremer, R. Guenther et al., "Ongoing oxidative stress causes subclinical neuronal dysfunction in the recovery phase of EAE," *Frontiers in Immunology*, vol. 7, no. 92, 2016.

[9] A. Federico, E. Cardaioli, P. Da Pozzo, P. Formichi, G. N. Gallus, and E. Radi, "Mitochondria, oxidative stress and neurodegeneration," *Journal of the Neurological Sciences*, vol. 322, no. 1-2, pp. 254–262, 2012.

[10] B. Kadenbach, "Introduction to mitochondrial oxidative phosphorylation," *Advances in Experimental Medicine and Biology*, vol. 748, pp. 1–11, 2012.

[11] D. F. Wilson, "Oxidative phosphorylation: regulation and role in cellular and tissue metabolism," *The Journal of Physiology*, vol. 595, no. 23, pp. 7023–7038, 2017.

[12] I. Nikić, D. Merkler, C. Sorbara et al., "A reversible form of axon damage in experimental autoimmune encephalomyelitis and multiple sclerosis," *Nature Medicine*, vol. 17, no. 4, pp. 495–499, 2011.

[13] A. K. Persson, I. Kim, P. Zhao, M. Estacion, J. A. Black, and S. G. Waxman, "Sodium channels contribute to degeneration of dorsal root ganglion neurites induced by mitochondrial dysfunction in an in vitro model of axonal injury," *The Journal of Neuroscience*, vol. 33, no. 49, pp. 19250–19261, 2013.

[14] V. Pegoretti, K. A. Swanson, J. R. Bethea, L. Probert, U. L. M. Eisel, and R. Fischer, "Inflammation and oxidative stress in multiple sclerosis: consequences for therapy development," *Oxidative Medicine and Cellular Longevity*, vol. 2020, Article ID 7191080, 19 pages, 2020.

[15] H. Bros, R. Niesner, and C. Infante-Duarte, "An ex vivo model for studying mitochondrial trafficking in neurons," *Methods in Molecular Biology*, vol. 1264, pp. 465–472, 2015.

[16] B. Malla, S. Cotten, R. Ulshoefer et al., "Teriflunomide preserves peripheral nerve mitochondria from oxidative stress-mediated alterations," *Therapeutic Advances in Chronic Disease*, vol. 11, 2020.

[17] H. Bros, J. M. Millward, F. Paul, R. Niesner, and C. Infante-Duarte, "Oxidative damage to mitochondria at the nodes of Ranvier precedes axon degeneration in ex vivo transected axons," *Experimental Neurology*, vol. 261, pp. 127–135, 2014.

[18] J. Wang, S.-W. Ou, and Y.-J. Wang, "Distribution and function of voltage-gated sodium channels in the nervous system," *Channels*, vol. 11, no. 6, pp. 534–554, 2017.

[19] X. Wang, W. Wang, L. Li, G. Perry, H.-g. Lee, and X. Zhu, "Oxidative stress and mitochondrial dysfunction in Alzheimer's disease," *Biochimica et Biophysica Acta (BBA) - Molecular Basis of Disease*, vol. 1842, no. 8, pp. 1240–1247, 2014.

[20] G. Criste, B. Trapp, and R. Dutta, "Axonal loss in multiple sclerosis: causes and mechanisms," *Handbook of Clinical Neurology*, vol. 122, pp. 101–113, 2014.

[21] Y. Lin, L.-L. Li, W. Nie et al., "Brain activity regulates loose coupling between mitochondrial and cytosolic Ca^{2+} transients," *Nature Communications*, vol. 10, no. 1, p. 5277, 2019.

[22] G. Csordás, P. Várnai, T. Golenár et al., "Imaging interorganelle contacts and local calcium dynamics at the ER-mitochondrial interface," *Molecular Cell*, vol. 39, no. 1, pp. 121–132, 2010.

[23] V. Granatiero, M. Pacifici, A. Raffaello, D. De Stefani, and R. Rizzuto, "Overexpression of mitochondrial calcium uniporter causes neuronal death," *Oxidative Medicine and Cellular Longevity*, vol. 2019, Article ID 1681254, 15 pages, 2019.

[24] B. Schattling, B. Eggert, and M. A. Friese, "Acquired channelopathies as contributors to development and progression of multiple sclerosis," *Experimental Neurology*, vol. 262, pp. 28–36, 2014.

[25] F. Sivandzade, A. Bhalerao, and L. Cucullo, "Analysis of the mitochondrial membrane potential using the cationic JC-1 dye as a sensitive fluorescent probe," *Bio-Protocol*, vol. 9, no. 1, article e3128, 2019.

[26] S. M. Kilbride, J. E. Telford, and G. P. Davey, "Complex I controls mitochondrial and plasma membrane potentials in nerve terminals," *Neurochemical Research*, vol. 46, no. 1, pp. 100–107, 2021.

[27] M. E. Witte, D. J. Mahad, H. Lassmann, and J. van Horssen, "Mitochondrial dysfunction contributes to neurodegeneration in multiple sclerosis," *Trends in Molecular Medicine*, vol. 20, no. 3, pp. 179–187, 2014.

[28] D. Mahad, H. Lassmann, and D. Turnbull, "Review: mitochondria and disease progression in multiple sclerosis," *Neuropathology and Applied Neurobiology*, vol. 34, no. 6, pp. 577–589, 2008.

[29] C. S. Palmer, L. D. Osellame, D. Stojanovski, and M. T. Ryan, "The regulation of mitochondrial morphology: intricate mechanisms and dynamic machinery," *Cellular Signalling*, vol. 23, no. 10, pp. 1534–1545, 2011.

[30] P. H. Reddy and T. P. Reddy, "Mitochondria as a therapeutic target for aging and neurodegenerative diseases," *Current Alzheimer Research*, vol. 8, no. 4, pp. 393–409, 2011.

[31] A. K. Camara, E. J. Lesnefsky, and D. F. Stowe, "Potential therapeutic benefits of strategies directed to mitochondria," *Antioxidants & Redox Signaling*, vol. 13, no. 3, pp. 279–347, 2010.

[32] M. Gülden, A. Jess, J. Kammann, E. Maser, and H. Seibert, "Cytotoxic potency of H2O2 in cell cultures: impact of cell concentration and exposure time," *Free Radical Biology and Medicine*, vol. 49, no. 8, pp. 1298–1305, 2010.

[33] B. Malla, A. Liotta, H. Bros et al., "Teriflunomide preserves neuronal activity and protects mitochondria in brain slices exposed to oxidative stress," *International Journal of Molecular Sciences*, vol. 23, no. 3, p. 1538, 2022.

[34] C. Fang, D. Bourdette, and G. Banker, "Oxidative stress inhibits axonal transport: implications for neurodegenerative diseases," *Molecular Neurodegeneration*, vol. 7, no. 1, p. 29, 2012.

[35] O. Errea, B. Moreno, A. Gonzalez-Franquesa, P. M. Garcia-Roves, and P. Villoslada, "The disruption of mitochondrial axonal transport is an early event in neuroinflammation," *Journal of Neuroinflammation*, vol. 12, no. 1, p. 152, 2015.

[36] R. Isonaka, H. Hiruma, and T. Kawakami, "Inhibition of axonal transport caused by tert-butyl hydroperoxide in cultured mouse dorsal root ganglion neurons," *Journal of Molecular Neuroscience*, vol. 45, no. 2, pp. 194–201, 2011.

[37] M. Carinci, B. Vezzani, S. Patergnani et al., "Different roles of mitochondria in cell death and inflammation: focusing on mitochondrial quality control in ischemic stroke and reperfusion," *Biomedicine*, vol. 9, no. 2, p. 169, 2021.

[38] M. T. Islam, "Oxidative stress and mitochondrial dysfunction-linked neurodegenerative disorders," *Neurological Research*, vol. 39, no. 1, pp. 73–82, 2017.

[39] M. D. Brand, "The efficiency and plasticity of mitochondrial energy transduction," *Biochemical Society Transactions*, vol. 33, no. 5, pp. 897–904, 2005.

[40] S. A. Freeman, A. Desmazières, D. Fricker, C. Lubetzki, and N. Sol-Foulon, "Mechanisms of sodium channel clustering and its influence on axonal impulse conduction," *Cellular and Molecular Life Sciences*, vol. 73, no. 4, pp. 723–735, 2016.

[41] A. H. Seidl, "Regulation of conduction time along axons," *Neuroscience*, vol. 276, pp. 126–134, 2014.

[42] J. A. Black, J. Newcombe, B. D. Trapp, and S. G. Waxman, "Sodium channel expression within chronic multiple sclerosis plaques," *Journal of Neuropathology and Experimental Neurology*, vol. 66, no. 9, pp. 828–837, 2007.

[43] M. J. Craner, J. Newcombe, J. A. Black, C. Hartle, M. L. Cuzner, and S. G. Waxman, "Molecular changes in neurons in multiple sclerosis: altered axonal expression of Nav1.2 and Nav1.6 sodium channels and Na^+/Ca^{2+} exchanger," *Proceedings of the National Academy of Sciences of the United States of America*, vol. 101, no. 21, pp. 8168–8173, 2004.

[44] A. Bouafia, J. L. Golmard, V. Thuries et al., "Axonal expression of sodium channels and neuropathology of the plaques in multiple sclerosis," *Neuropathology and Applied Neurobiology*, vol. 40, no. 5, pp. 579–590, 2014.

[45] X. Liu, D. Weaver, O. Shirihai, and G. Hajnóczky, "Mitochondrial 'kiss-and-run': interplay between mitochondrial motility and fusion-fission dynamics," *The EMBO Journal*, vol. 28, no. 20, pp. 3074–3089, 2009.

[46] M. Forkink, G. R. Manjeri, D. C. Liemburg-Apers et al., "Mitochondrial hyperpolarization during chronic complex I inhibition is sustained by low activity of complex II, III, IV and V," *Bioenergetics*, vol. 1837, no. 8, pp. 1247–1256, 2014.

[47] A. Y. Abramov, T. K. Smulders-Srinivasan, D. M. Kirby et al., "Mechanism of neurodegeneration of neurons with mitochondrial DNA mutations," *Brain: a Journal of Neurology*, vol. 133, no. 3, pp. 797–807, 2010.

[48] I. Smets, A. Caplanusi, S. Despa et al., "Ca^{2+} uptake in mitochondria occurs via the reverse action of the Na^+/Ca^{2+} exchanger in metabolically inhibited MDCK cells," *American Journal of Physiology Renal Physiology*, vol. 286, no. 4, pp. F784–F794, 2004.

[49] D. G. Nicholls, "Mitochondrial calcium function and dysfunction in the central nervous system," *Biochimica et Biophysica Acta (BBA)-Bioenergetics*, vol. 1787, no. 11, pp. 1416–1424, 2009.

[50] P. Mishra and D. C. Chan, "Metabolic regulation of mitochondrial dynamics," *The Journal of Cell Biology*, vol. 212, no. 4, pp. 379–387, 2016.

[51] G. M. Cereghetti, A. Stangherlin, O. M. de Brito et al., "Dephosphorylation by calcineurin regulates translocation of Drp1 to mitochondria," *Proceedings of the National Academy*

of Sciences of the United States of America, vol. 105, no. 41, pp. 15803–15808, 2008.

[52] Y. Chen and Z. H. Sheng, "Kinesin-1-syntaphilin coupling mediates activity-dependent regulation of axonal mitochondrial transport," *The Journal of Cell Biology*, vol. 202, no. 2, pp. 351–364, 2013.

[53] A. A. Courtes, N. R. de Carvalho, D. F. Gonçalves et al., "Guanosine protects against Ca^{2+}-induced mitochondrial dysfunction in rats," *Biomedicine & Pharmacotherapy*, vol. 111, pp. 1438–1446, 2019.

[54] R. Bagur and G. Hajnóczky, "Intracellular Ca^{2+} sensing: its role in calcium homeostasis and signaling," *Molecular Cell*, vol. 66, no. 6, pp. 780–788, 2017.

[55] E. J. Griffiths and G. A. Rutter, "Mitochondrial calcium as a key regulator of mitochondrial ATP production in mammalian cells," *Biochimica et Biophysica Acta (BBA)-Bioenergetics*, vol. 1787, no. 11, pp. 1324–1333, 2009.

[56] T. I. Peng and M. J. Jou, "Oxidative stress caused by mitochondrial calcium overload," *Annals of the New York Academy of Sciences*, vol. 1201, no. 1, pp. 183–188, 2010.

[57] N. Naumova and R. Šachl, "Regulation of cell death by mitochondrial transport systems of calcium and Bcl-2 proteins," *Membranes*, vol. 10, no. 10, p. 299, 2020.

[58] K. N. Belosludtsev, M. V. Dubinin, N. V. Belosludtseva, and G. D. Mironova, "Mitochondrial Ca^{2+} transport: mechanisms, molecular structures, and role in cells," *Biochemistry Biokhimiia*, vol. 84, no. 6, pp. 593–607, 2019.

[59] S. Golshani-Hebroni, "Mg^{++} requirement for MtHK binding, and Mg^{++} stabilization of mitochondrial membranes via activation of MtHK & MtCK and promotion of mitochondrial permeability transition pore closure: a hypothesis on mechanisms underlying Mg^{++}'s antioxidant and cytoprotective effects," *Gene*, vol. 581, no. 1, pp. 1–13, 2016.

[60] A. Kumar and R. R. Ratan, "Oxidative stress and Huntington's disease: the good, the bad, and the ugly," *Journal of Huntington's Disease*, vol. 5, no. 3, pp. 217–237, 2016.

[61] J. R. Stone and S. Yang, "Hydrogen peroxide: a signaling messenger," *Antioxidants & Redox Signaling*, vol. 8, no. 3-4, pp. 243–270, 2006.

[62] D. F. Stowe and A. K. Camara, "Mitochondrial reactive oxygen species production in excitable cells: modulators of mitochondrial and cell function," *Antioxidants & Redox Signaling*, vol. 11, no. 6, pp. 1373–1414, 2009.

[63] N. Nemani, S. Shanmughapriya, and M. Madesh, "Molecular regulation of MCU: implications in physiology and disease," *Cell Calcium*, vol. 74, pp. 86–93, 2018.

[64] R. Patel and F. Sesti, "Oxidation of ion channels in the aging nervous system," *Brain Research*, vol. 1639, pp. 174–185, 2016.

[65] K. C. Reed and F. L. Bygrave, "A low molecular weight ruthenium complex inhibitory to mitochondrial Ca^{2+} transport," *FEBS Letters*, vol. 46, no. 1-2, pp. 109–114, 1974.

[66] C. L. Moore, "Specific inhibition of mitochondrial Ca^{++} transport by ruthenium red," *Biochemical and Biophysical Research Communications*, vol. 42, no. 2, pp. 298–305, 1971.

[67] N. Bernard-Marissal, R. Chrast, and B. L. Schneider, "Endoplasmic reticulum and mitochondria in diseases of motor and sensory neurons: a broken relationship?," *Cell Death & Disease*, vol. 9, no. 3, p. 333, 2018.

[68] C. Giorgi, S. Missiroli, S. Patergnani, J. Duszynski, M. R. Wieckowski, and P. Pinton, "Mitochondria-associated membranes: composition, molecular mechanisms, and physiopathological implications," *Antioxidants & Redox Signaling*, vol. 22, no. 12, pp. 995–1019, 2015.

[69] R. Rizzuto, S. Marchi, M. Bonora et al., "Ca^{2+} transfer from the ER to mitochondria: when, how and why," *Biochimica et Biophysica Acta (BBA) - Bioenergetics*, vol. 1787, no. 11, pp. 1342–1351, 2009.

[70] M. Krols, G. van Isterdael, B. Asselbergh et al., "Mitochondria-associated membranes as hubs for neurodegeneration," *Acta Neuropathologica*, vol. 131, no. 4, pp. 505–523, 2016.

[71] R. F. Feissner, J. Skalska, W. E. Gaum, and S.-S. Sheu, "Crosstalk signaling between mitochondrial Ca^{2+} and ROS," *Frontiers in Bioscience*, vol. 14, no. 4, pp. 1197–1218, 2009.

[72] P. Pizzo, I. Drago, R. Filadi, and T. Pozzan, "Mitochondrial Ca^{2+} homeostasis: mechanism, role, and tissue specificities," *Pflügers Archiv - European Journal of Physiology*, vol. 464, no. 1, pp. 3–17, 2012.

Hindawi
Oxidative Medicine and Cellular Longevity
Volume 2022, Article ID 7157444, 26 pages
https://doi.org/10.1155/2022/7157444

Research Article

Effect of Ethyl Acetate Fraction from *Eucommia ulmoides* Leaves on $PM_{2.5}$-Induced Inflammation and Cognitive Dysfunction

Min Ji Kim,[1] Jin Yong Kang,[1,2] Jong Min Kim,[1] Jong Hyun Moon,[1] Hyo Lim Lee,[1] Hye Rin Jeong,[1] Min Ji Go,[1] Uk Lee,[3] and Ho Jin Heo[1]

[1]*Division of Applied Life Science (BK21), Institute of Agriculture and Life Science, Gyeongsang National University, Jinju 52828, Republic of Korea*
[2]*World Institute of Kimchi an Annex of Korea Food Research Institute, Gwangju, Republic of Korea*
[3]*Division of Special Forest Products, National Institute of Forest Science, Suwon 16631, Republic of Korea*

Correspondence should be addressed to Ho Jin Heo; hjher@gnu.ac.kr

Received 15 February 2022; Revised 31 March 2022; Accepted 19 April 2022; Published 14 May 2022

Academic Editor: Silvânia Maria Mendes Vasconcelos

This study aimed to evaluate the protective effect of the ethyl acetate from *Eucommia ulmoides* leaves (EFEL) on $PM_{2.5}$-induced cognitive impairment in BALB/c mice. EFEL improved $PM_{2.5}$-induced cognitive decline by improving spontaneous alternative behavioral and long-term memory ability. EFEL increased ferric reducing activity power (FRAP) in serum. In addition, EFEL increased superoxide dismutase (SOD) and reduced glutathione (GSH) contents and inhibited the production of malondialdehyde (MDA) in lung and brain tissues. EFEL also restored the mitochondrial function by regulating reactive oxygen species (ROS) production, mitochondrial membrane potential (MMP) level, and ATP level in lung and brain tissues. EFEL ameliorated the cholinergic system by regulating the acetylcholine (ACh) content and acetylcholinesterase (AChE) activity in the brain tissue and the expression of AChE and choline acetyltransferase (ChAT) in the whole brain and hippocampal tissues. EFEL reduced $PM_{2.5}$-induced excessive expression of inflammatory protein related to the lung, whole brain, olfactory bulb, and hippocampus. Physiological compounds of EFEL were identified as 5-O-caffeolyquinic acid, rutin, quercetin, and quercetin glycosides. As a result, EFEL has anti-inflammation and anti-amnesic effect on $PM_{2.5}$-induced cognitive impairment by regulating the inflammation and inhibiting the lung and brain tissue dysfunction, and its effect is considered to be due to the physiological compounds of EFEL.

1. Introduction

Air pollution is an environmental issue that is becoming a global problem, and its harmful effect on the human body is gradually increasing [1]. According to the World Health Organization (WHO), air pollution causes stroke, heart disease, lung cancer, and respiratory diseases, resulting in approximately 3.0 million deaths annually [2]. Particulate matter (PM), one of the causes of air pollution, is generated from construction sites, factories, and automobile exhaust gas and is composed of organic ions such as sulfate, nitrate, and ammonium ion, carbon, and mineral components [3]. PM is classified as PM_{10}, which is smaller than 10 μm in diameter, and $PM_{2.5}$, which is smaller than 2.5 μm in diameter [4]. $PM_{2.5}$ can easily reach the bronchi and lungs because it cannot be filtered by the cilia. The $PM_{2.5}$ deposited in the respiratory system causes reactive oxygen species (ROS), oxidative stress, inflammation, and apoptosis, inducing respiratory diseases such as asthma, pneumonia, chronic cough, disruption of calcium homeostasis, and mediating of inflammatory responses [5]. $PM_{2.5}$ exposure increases the ROS and inflammation factors by oxidative stress and inflammatory response in lung tissue [6]. Also, $PM_{2.5}$ that has penetrated into the alveoli can pass through the air-blood barrier and circulate throughout the body, where it can be deposited in the brain tissue [7]. Also, inflammatory cytokines produced by the inflammation of lung tissue circulate whole body

through blood and affect the central neuronal system [8]. As a result, inflammation induced by nanoparticles exposure leads to neuronal dysfunction such as loss of neurons and disruption of synapses, resulting in learning and memory impairment [9]. In addition, $PM_{2.5}$ directly reaches the olfactory bulb, passing through the blood-brain barrier (BBB), which induces nervous system dysfunction and causes neuroinflammation and neurodegenerative diseases [10]. The $PM_{2.5}$ absorbed induces an excessive inflammatory response, which leads to cell apoptosis in the brain by producing ROS and inflammatory cytokines [11].

Eucommia ulmoides is a plant in the family *Eucommiaceae* and is widely cultivated in China, Japan, and Korea [12]. *Eucommia ulmoides* has various compounds such as flavonoids, lignans, iridoids, and phenols, and its barks and leaves are used as herbal medicines for the prevention of hypertension, diabetes, and hepotoxicity [13–15]. According to previous studies, *Eucommia ulmoides* leaves extract decreased the levels of total cholesterol, LDH cholesterol, and free fatty acids in serum and decreased the activity of hepatic fatty acid synthase and HMG-CoA enzyme in a high-fat diet-induced hamster model [16]. The water extract of *Eucommia ulmoides* leaves showed antioxidant activity in the liver of a CCl_4-induced hepatotoxicity model and decreased GOT, GPT, LDH, and ALP levels in serum [15]. *Eucommia ulmoides* extract improved motor dysfunction in 1-methyl-4-phenyl-1,2,3,6-tetrahydropyridine (MPTP-)-induced Parkinson's model mice through pole and rotarod tests and increased the levels of dopamine and its metabolites such as 3,4-dihydroxyphenylacetic acid and homovanillic acid in striatum. Also, *Eucommia ulmoides* extract showed a protective effect on neuroinflammation by reducing the levels of TNF-α, IL-1β, and IL-6 in the blood [17]. In addition, it was confirmed that *Eucommia ulmoides* improved the neurotoxicity of amyloid beta-induced-PC12 cells [18]. However, the studies on the physiological activities of the *Eucommia ulmoides* leaves are mainly focused on the improvement effect of hepatoxicity and lipid metabolism, especially there are few studies on *Eucommia ulmoides* leaves related to the effect on $PM_{2.5}$-induced inflammation and cognitive dysfunction. Therefore, in this study, anti-inflammatory and amnesic effects were confirmed using the ethyl acetate fraction from *Eucommia ulmoides* leaves in $PM_{2.5}$-induced BALB/c mice, and the potential availability as a functional food material for the prevention of $PM_{2.5}$-induced cognitive impairment was evaluated.

2. Materials and Methods

2.1. Sample Preparation. Eucommia ulmoides leaves were purchased from Yeongcheon, Gyeongsangbuk-do, Korea, in April 2019 and verified by the National Institute of Forest Science (Suwon, Korea). The sample was extracted in 40% ethanol for 2 h at 40°C and evaporated using a vacuum rotary evaporator (N-N series, Eyela Co., Tokyo, Japan). After that, the extract was sequentially fractionated using *n*-hexane, chloroform, and ethyl acetate and lyophilized. According to previous study, ethyl acetate fraction from *Eucommia ulmoides* leaves (EFEL) was presented as the significant total phenolic and flavonoid contents and antioxidant activities, and it was used for this study (Supplementary Figures 1 and 2) [19].

2.2. Animal Experiment Design. The experimental animals (BALB/c, 6-week, male) were bred in certain temperature (22 ± 2°C) and humidity (50 ± 5%) conditions. All experiments were performed according to the guidelines of Animal Care and Use Committee of the Gyeongsang National University (approval number: GNU-200302-M0007; approval day: 03/02/2020). Mice were randomly divided to 4 groups: control (clean air exposure), $PM_{2.5}$ ($PM_{2.5}$ exposure), EFEL 20 ($PM_{2.5}$ exposure + EFEL 20 mg/kg of body weight), and EFEL 40 ($PM_{2.5}$ exposure + EFEL 40 mg/kg of body weight) ($n = 20$ per group; 7 for *in vivo* tests; 5 for *ex vivo* tests; 5 for mitochondrial activity tests; and 3 for western blot analysis). $PM_{2.5}$, EFEL 20, and EFEL 40 groups were exposed to $PM_{2.5}$ at a constant concentration ($500\,\mu g/m^3$) in whole body exposure chamber, and the control group was exposed to filtered air the same time. Clean air and $PM_{2.5}$ were exposed 5 hours per day for 12 weeks. EFEL was dissolved in clean drinking water according to the dose and ingested in mice by oral administration once a day for 12 weeks.

2.3. In Vivo Behavioral Tests

2.3.1. Y-Maze Test. The Y-maze consists of the length (33 cm), height (15 cm), and width (10 cm), respectively. Mice were placed at the end of one arm, and the movement of each mouse was recorded by a smart video tracking system (Smart 3.0, Panlab, Barcelona, Spain) for 8 min [20, 21]. In Y-maze test, evaluated behavioral parameters were total distance and triplet (%) of spontaneous alternative behavior. Total distance was similar in all groups, indicating that all mice were behaviorally normal. Triplet measures the sequential entry into the three arms of the maze.

2.3.2. Morris Water Maze Test. Morris water maze consists of stainless circular pool (90 cm in diameter and 30 cm deep) and divided into quadrants (N, S, E, and W zones) with visual clues, and a platform was placed in the center of the W zone. In Morris water maze test, evaluated behavioral parameters were escape times for platform in W zone of pool through hidden tests and retention time in W zone through probe test. In the hidden test, the escape time to the platform was measured for 4 days (maximum time: 60 sec). In the probe test, the platform was removed retention time in the W zone, and movements of mice were recorded using a smart video tracking system (Smart 3.0, Panlab) [21, 22]. After all in vivo tests were completed, mice were sacrificed using CO_2 inhalation.

2.4. Serum FRAP Analysis. After the behavioral test, the serum obtained by centrifugation at 10,000×*g* for 10 min at 4°C was used to measure ferric reducing/antioxidant power (FRAP). Serum was reacted with FRAP reagent consisting of 10 mM 2-4-5-tripyridyl-S-triazine (TPTZ): 20 mM $FeCl_3$: 0.3 M sodium acetate buffer (pH 3.6) (1 : 1 : 10), and then, the reaction was measured by a microplate reader at 593 nm.

2.5. Sample Preparation. The lung and brain homogenates using 10 volumes phosphate buffer saline (PBS, pH 7.4) were used for evaluation of antioxidant system such as superoxide dismutase (SOD) and malondialdehyde (MDA) contents, and cholinergic system, such as acetylcholine (ACh) and acetylcholinesterase (AChE), and homogenate using 10 mM phosphate buffer with 1 mM EDTA (pH 6.0) were used for evaluation of reduced glutathione (GSH) content.

2.6. Antioxidant System Analysis

2.6.1. SOD Contents. The supernatant obtained by centrifuging the lung and brain homogenates at 400×*g* for 10 min at 4°C was extracted using 10 volumes of cell extraction buffer. The extracted samples were centrifuged at 14,000×*g* for 5 min at 4°C, and the supernatants were used for the experiment according to manufacturer's protocol (Dojindo Molecular Technologies, Rockville, MD, USA). The absorbance was measured at 450 nm (Epoch2, BioTek, Winooski, VT, USA) [21, 23].

2.6.2. Reduced GSH Contents. The supernatants obtained by centrifuging at 10,000×*g* for 15 min at 4°C of lung and brain homogenate were mixed with 5% metaphosphoric acid (1 : 1), and the mixtures were centrifuged at 2,000×*g* for 2 min at 4°C. The supernatants were mixed with 0.26 M tris-HCl, 0.65 N NaOH, and 1 M o-phthaldialdehyde and reacted for 15 min. Fluorescence was measured by a fluorescence microplate reader (Infinite 200, Tecan Co., San Jose, CA, USA) at emission (420 nm) and excitation (320 nm) wave [21, 24].

2.6.3. MDA Production. The supernatants obtained by centrifuging at 5,000 rpm for 10 min at 4°C of lung and brain homogenate were reacted with 1% phosphoric acid and 0.67% TBA in water bath for 95°C for 1 h. The mixtures were spun down, and the absorbance of supernatant was measured at 532 nm (Epoch2, BioTek) [21, 25].

2.7. Cholinergic System. The supernatant obtained by centrifuging the brain tissue homogenate at 14,000×*g* for 30 min at 4°C was used for ACh levels and AChE activity [21, 26]. For ACh levels, 2 M hydroxylamine: 3.5 N NaOH (1 : 1) mixture was reacted with the obtained supernatant at room temperature, and then, 0.5 N HCl and 0.37 M $FeCl_3$ were added, and the absorbance was measured at 540 nm using microplate reader (Epoch2, BioTek).

To evaluate the AChE activity, 50 mM sodium phosphate buffer was reacted with the obtained supernatant at 37°C for 15 min. After that, AChE solution composed to acetyl thiocholine and 5,5'dithio-bis (2-nitroenzoic acid) (DTNB) was added, and absorbance was measured at 405 nm using microplate reader (Epoch, BioTek).

2.8. Mitochondrial Extraction. Lung and brain tissues were homogenized into a mitochondrial isolation (MI) buffer including 215 mM mannitol, 75 mM sucrose, 0.1% bovine serum albumin (BSA), 20 mM HEPES (Na^+), and 20 mM EDTA using a bullet blender (BBY24M, Next Advance Inc., Averill Park, NY, USA). The pellet obtained by centrifuge (13,000×*g*, 10 min at 4°C) was mixed with MI buffer containing 0.1% digitonin. The mitochondrial sample and MI buffer without 20 mM EDTA were mixed and centrifuged at 13,000×*g* for 15 min at 4°C. The pellet obtained was mixed with the EDTA-free MI buffer and centrifuged at 10,000×*g* for 10 min at 4°C [21, 27]. The obtained pellet mixed with EDTA-free MI buffer was used to measure ROS content and mitochondrial membrane potential (MMP).

2.8.1. Mitochondrial ROS Production. ROS content and MMP activity used quantified protein by Bradford assay [28]. The mitochondrial extract (0.80 mg/mL) was used to measure ROS contents, and the mitochondrial extract and 25 μM dichlorofluorescin diacetate (DCF-DA) reagent were mixed and reacted in the dark for 20 min. Fluorescence of mixture was measured by a fluorescence microplate reader (Infinite 200, Tecan Co.) at emission (485 nm) and excitation (535 nm) wave.

2.8.2. Mitochondrial Membrane Potential. The mitochondrial extract (1.20 mg/mL) was used to measure MMP activity, and the mitochondrial extract was reacted with EDTA-free MI buffer containing 5 mM pyruvate and malate and 1 μM tetraethylbenzimidazolyl-carbocyanine iodide (JC-1) in the dark for 20 min. Fluorescence of mixture was measured by a fluorescence microplate reader (Infinite 200, Tecan Co.) at emission (535 nm) and excitation (590 nm) wave.

2.8.3. Mitochondrial ATP Content. The mitochondrial extract was quantified at the same concentration by Bradford assay. The pellet obtained by centrifugation (10,000×*g* for 10 min at 4°C) was reacted with 1% trichloroacetic acid (TCA), and it was mixed with 25 mM Tris-acetate buffer (pH 7.7) and centrifuged at 10,000×*g* for 15 min at 4°C. The obtained supernatants were measured for ATP level using ATP assay kit (Promega, Corp., Madison, WI, USA).

2.9. Western Blot Assay for Protein Expression. After mice brain tissue removal, olfactory bulb and hippocampal tissue were isolated. Lung, whole brain, olfactory bulb, and hippocampus tissues were homogenized with ProtinExTM animal cell/tissue (Gene All Biotechnology, Seoul, Korea) containing 1% protease inhibitor cocktails (Thermo Fisher Scientific, Rockford, IL, USA). And homogenates were immediately centrifuged at 13,000×*g* for 10 min at 4°C. The obtained supernatants were quantified with the same concentration protein using a Bradford reagent (Bio-rad, Hercules, CA, USA) according to Bradford assay. After that, supernatants were mixed with 1× loading dye and boiled at 95°C for 5 min in water bath. The proteins were separated on sodium dodecyl sulfate polyacrylamide gel (SDS-PAGE) and transferred to a polyvinylidene difluoride (PVDF) membrane (Millipore, Billerica, MA, USA). The membranes were blocked with 5% skim milk solution and incubated with primary antibody (1 : 1000) for overnight at 4°C. After incubation, the membranes were incubated with secondary antibody (1 : 2000) for 1 h at room temperature [21]. Finally, protein expression was detected with ProNA™ ECL Ottimo (TransLab, Daejeon, Korea) using an iBright CL 1000Imaging System (Thermo Fischer Scientific, Rockford, IL, USA).

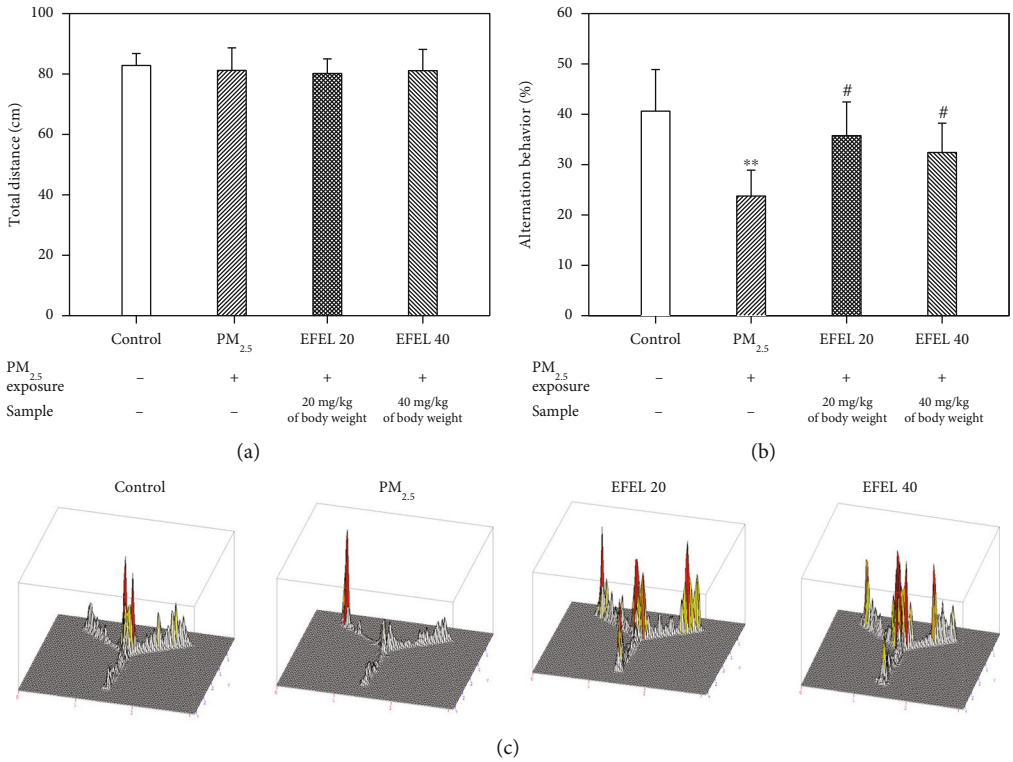

Figure 1: Protective effect of ethyl acetate fraction from *Eucommia ulmoides* leaves (EFEL) in $PM_{2.5}$-induced mice. (a) Number of arm entries; (b) spontaneous alternation behavior; and (c) 3D moving path in Y-maze test. Results shown are mean ± SD ($n = 7$). Data were statistically represented at ∗ which is significantly different from the control group and # which is significantly different from $PM_{2.5}$ group; ∗ and $\#p < 0.05$; and ∗∗and $\#\#p < 0.01$.

The density of the expressed protein was quantified using the iBright Analysis System (Thermo Fischer Scientific).

2.10. Identification of Physiologically Compounds Using UPLC Q-TOF/MS². To identify the physiologically compounds of EFEL, ultraperformance liquid chromatography-ion mobility separation-quadrupole time of flight/tandem mass spectrometry (UPLC-Q-TOF/MS^2, Vion, Waters Corp., Milford, MA, USA) was performed. EFEL was dissolved in 100% methanol and filtered using 0.2 μm membrane filters. UPLC separation was performed using an ACQUITY UPLC BEH C_{18} column (2.1 × 100 mm and 1.7 μm particle size, Waters Corp.). The flow rate was 0.60 mL/min. The mobile phases were composed as solvent A (0.1% formic acid in distilled water) and solvent B (0.1% formic acid in acetonitrile), and the analysis conditions were conducted as follows: a gradient elution of 40% A and 60% B at 0–1 min, 40% A and 60% B at 1–8 min, 100% B at 8–9 min, 100% B at 9-9.50 min, and 40% A and 60% B at 9.50–12 min. The conditions of negative electrospray ionization (ESI) were conducted as follows: ramp collision energy, 10–30 V; capillary voltage, 2.5 kV; source temperature, 100°C; desolvation temperature, 250°C; and mass range, 50–1000 m/z.

2.11. Statistical Analysis. All experiment results were expressed as mean ± standard deviation (SD). The mean value was verified for significance differences by Duncan's multiple range test ($p < 0.05$) using SAS software (Version 9.4, SAS institute, Cary, NC, USA).

3. Results

3.1. In Vivo Behavior Tests

3.1.1. Y-Maze Test. In the Y-maze test, the total distance of each mice showed no significant difference in all groups (Figure 1(a)) (control: 85.25 ± 3.28; $PM_{2.5}$ group: 79.88 ± 7.87; EFEL 20 group: 79.14 ± 6.45; and EFEL 40 group: 80.66 ± 4.83). These results indicated that all mice had the same motor performance. In the results of spontaneous alternation behavior, the $PM_{2.5}$ group (23.71% ± 5.13 (p value 0.00)) showed reduced spontaneous alternation behavior compared to the control group (40.54% ± 8.25). However, the EFEL groups showed increased spontaneous alternation behavior compared to the $PM_{2.5}$ group (EFEL 20 group: 33.56% ± 6.67 (p value 0.02); EFEL 40 group: 32.33% ± 5.82 (p value 0.06)) (Figure 1(b)).

3.1.2. Morris Water Maze Test. The results of the Morris water maze test are shown in Figure 2. It was confirmed that the escape time of the $PM_{2.5}$ group (51.70 sec ± 10.31 (p value 0.04)) was longer than the control group (28.75 sec ± 15.87). The escape times of the EFEL groups (EFEL 20 group, 23.94 sec ± 7.91 (p value 0.01); EFEL 40 group, 33.78 sec ± 11.31 (p value 0.01)) were shorter compared to the $PM_{2.5}$ group. In

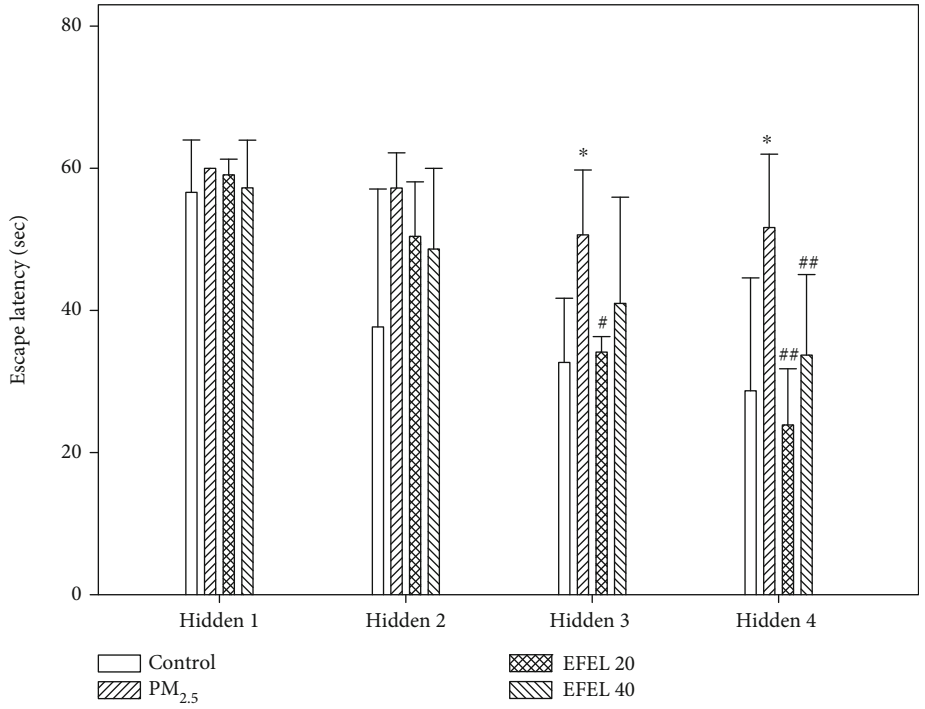

(a)

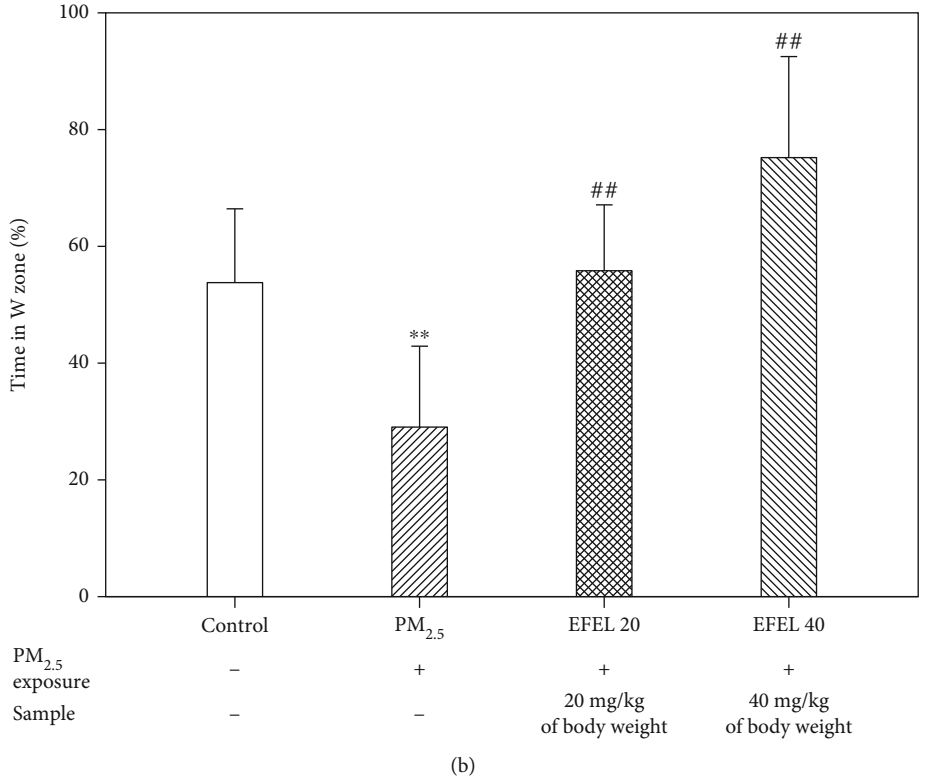

(b)

Figure 2: Continued.

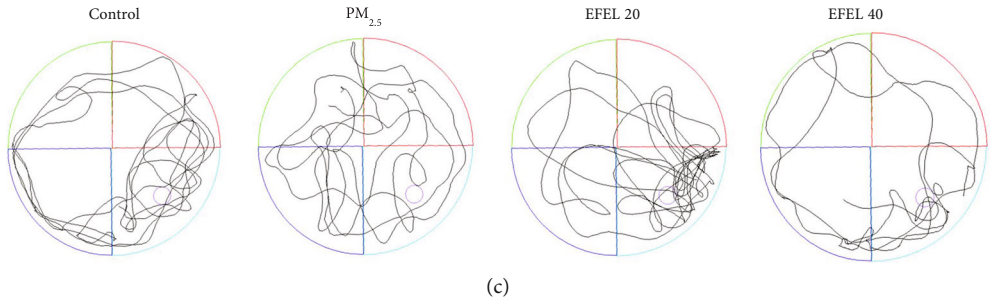

Figure 2: Protective effect of ethyl acetate fraction from *Eucommia ulmoides* leaves (EFEL) in $PM_{2.5}$-induced mice. (a) Escape latency; (b) time in W zone; and (c) 2D moving path in Morris water maze test. Results shown are mean ± SD ($n = 7$). Data were statistically represented at ∗ which is significantly different from the control group and #which is significantly different from $PM_{2.5}$ group; ∗ and #$p < 0.05$; and ∗∗ and ##$p < 0.01$.

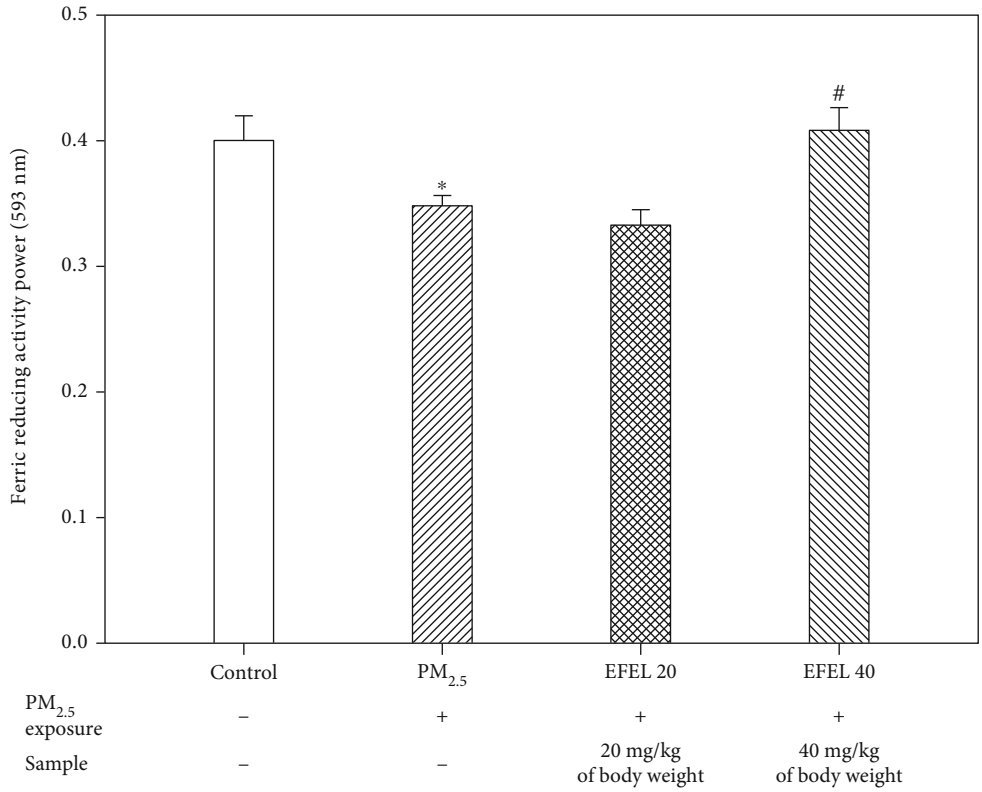

Figure 3: Ferric reducing/antioxidant power of ethyl acetate fraction from *Eucommia ulmoides* leaves (EFEL) on $PM_{2.5}$-induced mice in serum. Results shown are mean ± SD ($n = 3$). Data were statistically represented at ∗which is significantly different from the control group and #which is significantly different from $PM_{2.5}$ group; ∗ and #$p < 0.05$; and ∗∗and ##$p < 0.01$.

the probe test, the retention time in the W zone of the $PM_{2.5}$ group (29.11% ± 13.85 (p value 0.00)) was decreased compared to the control group (53.80% ± 12.64). However, the EFEL groups (EFEL 20 group, 55.85% ± 11.26 (p value 0.01); EFEL 40 group, 75.16% ± 17.28 (p value 0.00)) increased the retention time in the W zone compared to the $PM_{2.5}$ group (Figure 2(b)).

3.2. Serum FRAP Analysis. Serum FRAP activity is shown in Figure 3. Serum FRAP activity was lowered in the $PM_{2.5}$ group (0.35 ± 0.008 (p value 0.02)) and improved in the EFEL groups (EFEL 20, 0.33 ± 0.01 (p value 0.12); and EFEL 40, 0.41 ± 0.02 (p value 0.02)) similarly to the control group (0.40 ± 0.02).

3.3. Antioxidant System. The results of SOD, reduced GSH, and MDA content in the lung and brain tissues are presented in Figure 4. The SOD content in the lung tissue of the $PM_{2.5}$ group (3.90 ± 0.56 unit/mg of protein (p value 0.21)) decreased compared to the control group (4.45 ± 0.30 unit/mg of protein). However, SOD contents of the EFEL groups (EFEL 20, 4.58 ± 0.20 unit/mg of protein (p value 0.03); EFEL 40, 5.76 ± 0.49 unit/mg of protein (p value 0.00)) were increased compared to the $PM_{2.5}$ group

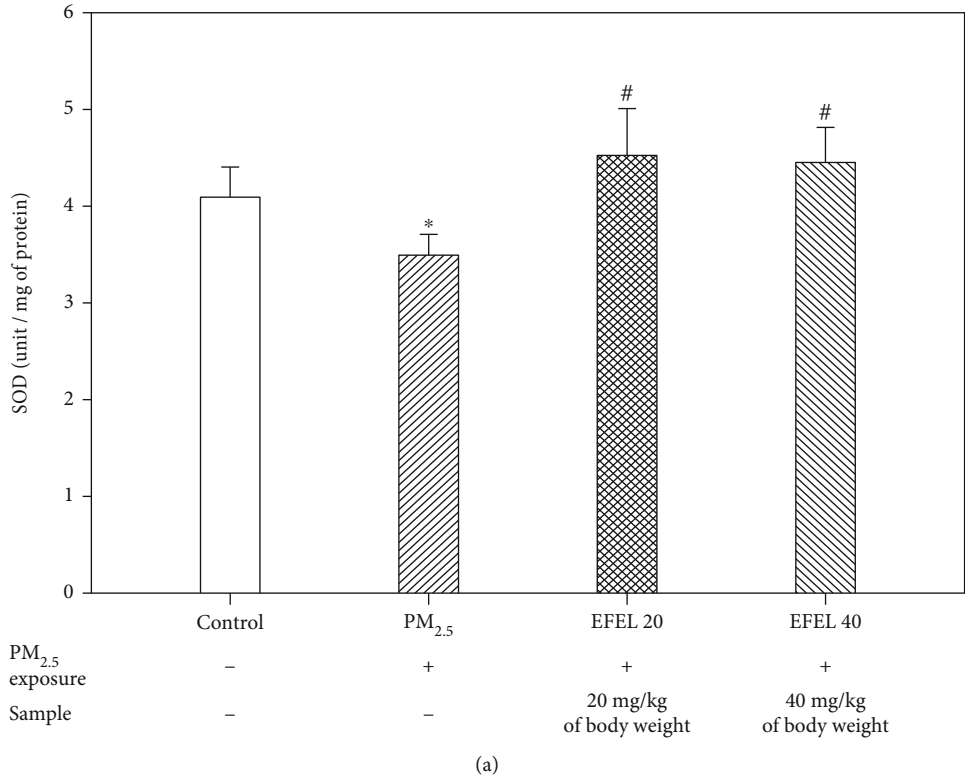

(a)

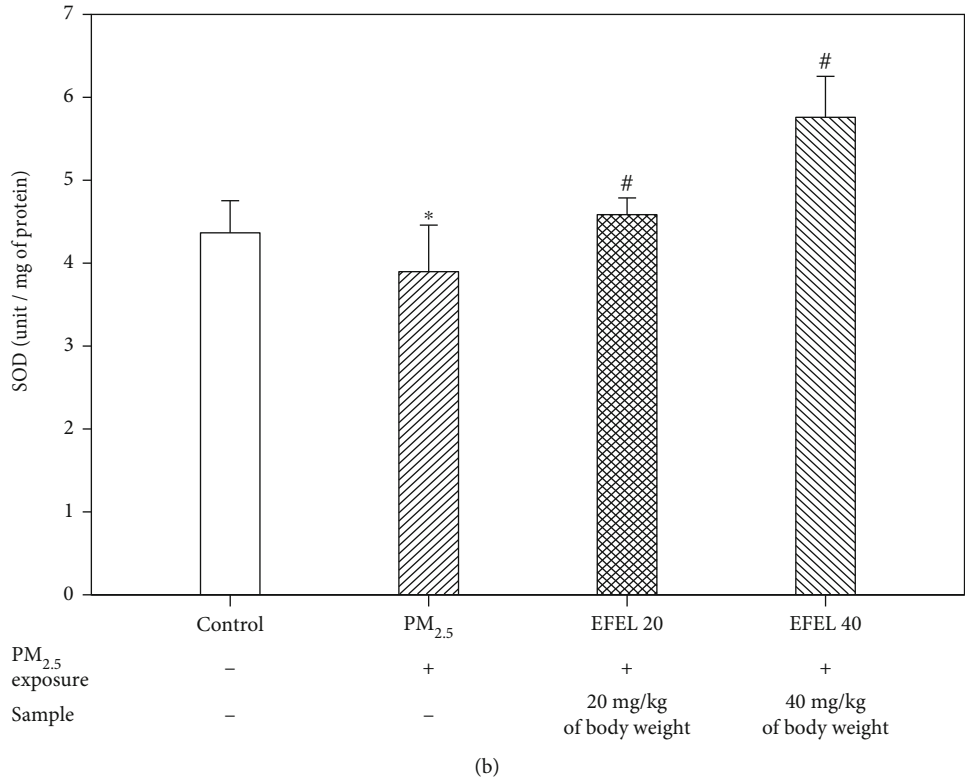

(b)

Figure 4: Continued.

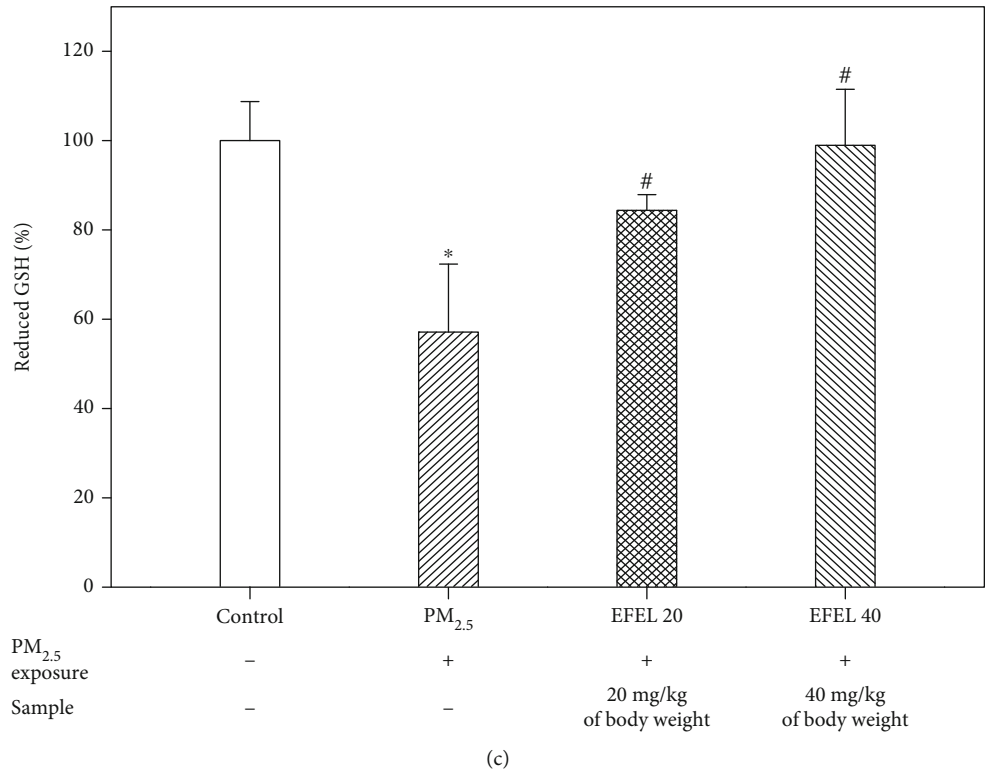

(c)

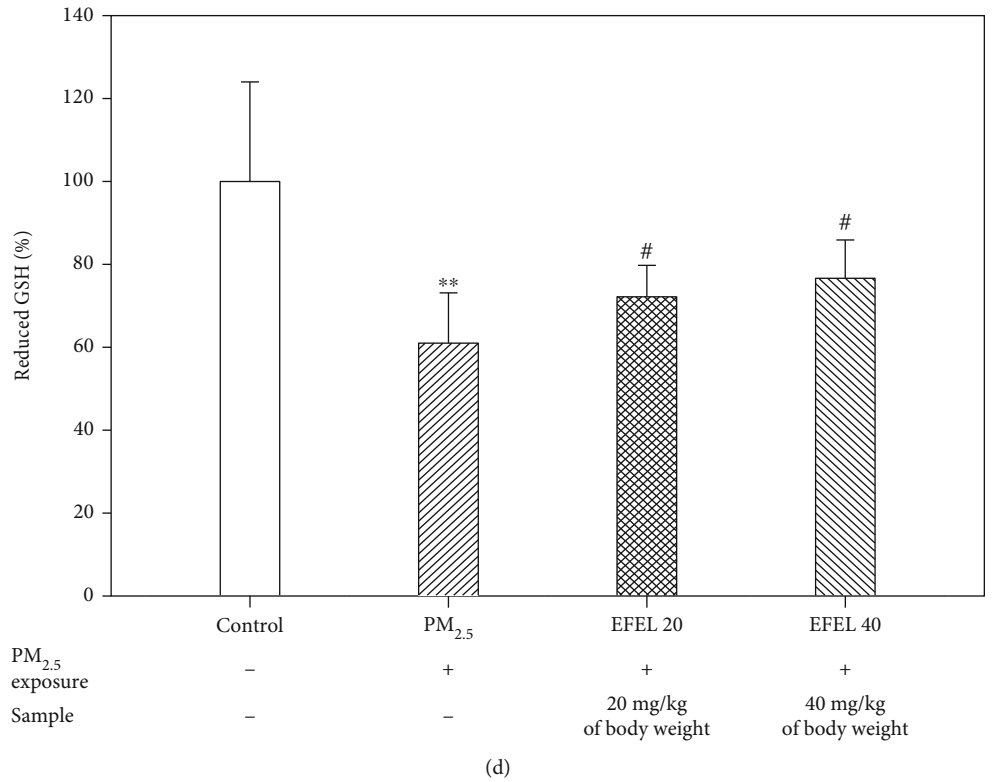

(d)

Figure 4: Continued.

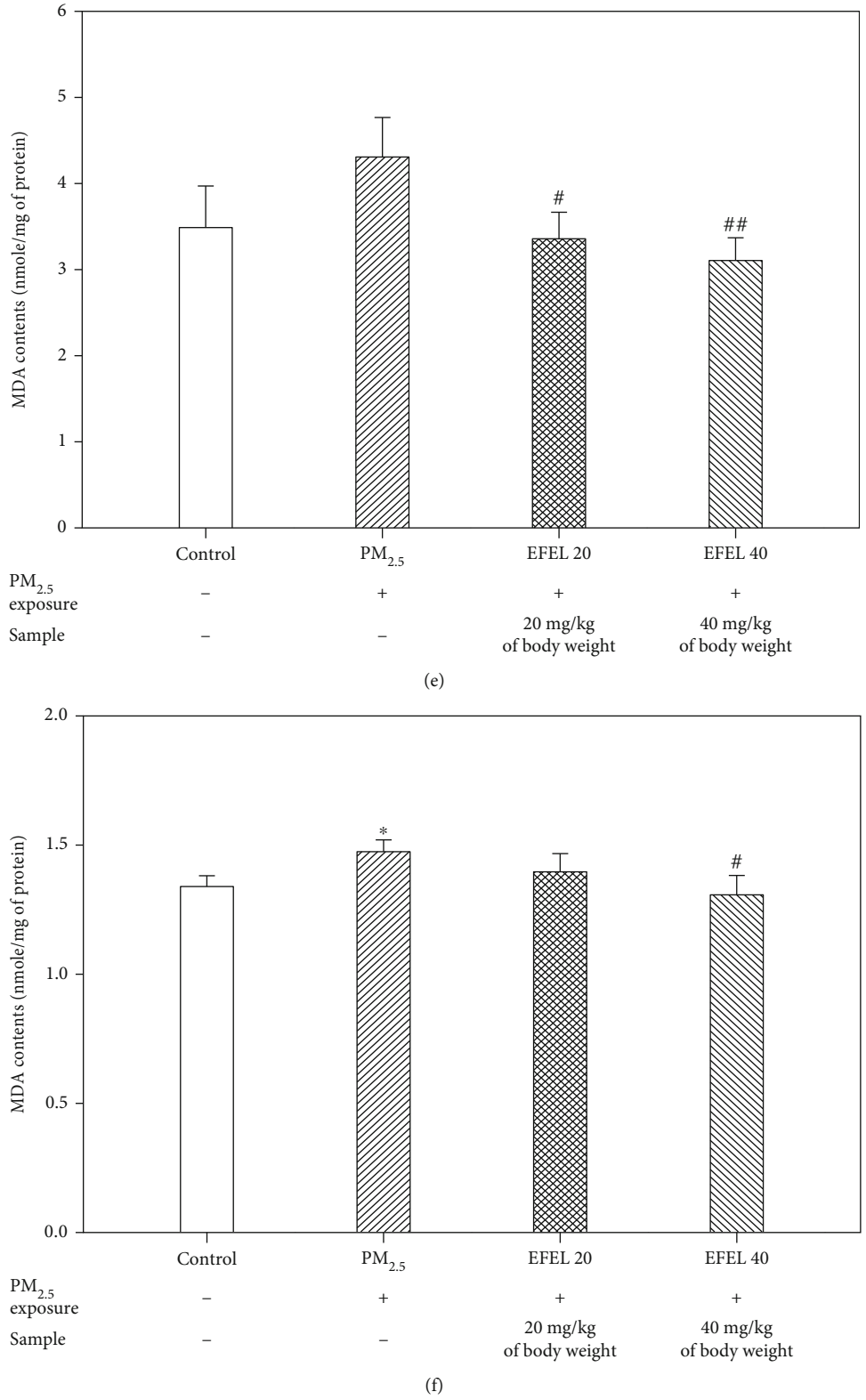

Figure 4: Protective effect of ethyl acetate fraction from *Eucommia ulmoides* leaves (EFEL) on antioxidant system in $PM_{2.5}$-induced mice. Superoxide dismutase (SOD) content in the brain (a) and lung (b). Reduced GSH content in the brain (c) and lung (d). Malondialdehyde (MDA) content in the brain (e) and lung (f). Results shown are mean ± SD ($n = 5$). Data were statistically represented at ∗which is significantly different from the control group and # which is significantly different from $PM_{2.5}$ group; ∗ and #$p < 0.05$; and ∗∗ and ##$p < 0.01$.

(Figure 4(a)). The reduced GSH content (61.00 ± 12.12% of control (p value 0.01)) in lung tissues of the $PM_{2.5}$ group decreased compared with the control group (100 ± 24.01 %). However, the EFEL groups increased the reduced GSH content (EFEL 20, 72.19 ± 7.56% of control (p value 0.03); EFEL 40, 76.62 ± 9.28% of control (p value 0.03)) compared to the $PM_{2.5}$ group (Figure 4(c)). MDA content in lung tissues of the $PM_{2.5}$ group (1.47 ± 0.05 nmole/mg of protein (p value 0.02)) increased compared with the control group (1.34 ± 0.04 nmole/mg of protein). However, the EFEL groups had decreased MDA production (EFEL 20, 1.39 ± 0.07 nmole/mg of protein (p value 0.25); EFEL 40, 1.31 ± 0.08 nmole/mg of protein (p value 0.04)) compared to the $PM_{2.5}$ group (Figure 4(e)).

The SOD content in the brain tissue of the $PM_{2.5}$ group (3.50 ± 0.22 unit/mg of protein (p value 0.02)) decreased compared to the control group (4.10 ± 0.31 unit/mg of protein). It also decreased in the EFEL groups (EFEL 20, 4.53 ± 0.48 unit/mg of protein (p value 0.04); EFEL 40, 4.46 ± 0.36 unit/mg of protein (p value 0.04)) compared to the $PM_{2.5}$ groups (Figure 4(b)). The reduced GSH content in the brain tissue of the $PM_{2.5}$ group (57.11 ± 15.22% of control (p value 0.02)) decreased compared to the control group (100 ± 14.25%). However, the EFEL groups increased the reduced GSH content (EFEL 20, 84.38 ± 3.51% of control (p value 0.03); EFEL 40, 98.93 ± 12.55% of control (p value 0.02)) compared to $PM_{2.5}$ (Figure 4(d)). MDA content in the brain tissue of the $PM_{2.5}$ group (4.32 ± 0.46 nmole/mg of protein (p value 0.13)) increased compared with the control group (3.50 ± 0.47 nmole/mg of protein). The EFEL groups saw decreased MDA production (EFEL 20, 3.37 ± 0.30 nmole/mg of protein (p value 0.04); EFEL 40, 3.11 ± 0.26 nmole/mg of protein (p value 0.00)) compared to the $PM_{2.5}$ group (Figure 4(f)).

3.4. Cholinergic System. The cholinergic system with acetylcholinesterase (AChE) and choline acetyltransferase (ChAT) is shown in Figure 5. $PM_{2.5}$ significantly increased the activity of AChE (108.52 ± 4.07% of control (p value 0.14)), and the EFEL groups (EFEL 20, 91.37 ± 3.79% of control (p value 0.01); EFEL 40, 83.35 ± 1.47% of control (p value 0.00)) decreased the activity of AChE. In addition, $PM_{2.5}$ decreased ACh content (1.68 ± 0.08 mM/mg of protein (p value 0.00)) compared with the control group (2.18 ± 0.17 mM/mg of protein). And the EFEL groups (EFEL 20, 1.71 ± 0.06 mM/mg of protein (p value 0.53); EFEL 40, 1.95 ± 0.07 mM/mg of protein (p value 0.02)) increased ACh content compared with the $PM_{2.5}$ group (Figures 5(a) and 5(b)). In addition, Figures 5(c) and 5(d) show band images of the whole brain and hippocampal expression levels of AChE and ChAT acting on the degradation and synthesis of ACh, respectively. $PM_{2.5}$ showed an increased AChE expression level (whole brain, 1.28 ± 0.14 (p value 0.08); hippocampus, 1.42 ± 0.01 (p value 0.00)) compared with the control group (whole brain, 1.00 ± 0.11; hippocampus, 1.00 ± 0.04). However, EFEL 40 decreased the AChE expression level (whole brain, 0.81 ± 0.07 (p value 0.01); hippocampus, 0.83 ± 0.20 (p value 0.04)). Also, $PM_{2.5}$ showed a reduced ChAT expression level (whole brain, 0.33 ± 0.14 (p value 0.05); hippocampus, 0.58 ± 0.21 (p value 0.10)) compared with the control group (whole brain, 1.00 ± 0.27; hippocampus, 1.00 ± 0.39). However, EFEL 40 increased the ChAT expression level (whole brain, 1.01 ± 0.24 (p value 0.02); hippocampus, 0.77 ± 0.17 (p value 0.08)) (Figures 5(e) and 5(f)).

3.5. Mitochondrial Activity. The ROS content, MMP and ATP level measured from the mitochondrial extract of mice lung and brain tissue are shown in Figure 6. The lungs of the $PM_{2.5}$ group showed excessive ROS content (136.41 ± 25.46 % of control (p value 0.04)), while EFEL 20 and 40 had decreased the ROS content (76.13 ± 15.57% of control (p value 0.05) and 61.11 ± 25.64% of control (p value 0.05)) (Figure 6(a)). MMP was decreased in the lungs of the $PM_{2.5}$ group (74.13 ± 26.41% of control (p value 0.06)), and EFEL 20 and 40 had an increased MMP level (132.74 ± 11.03% of control (p value 0.04) and 160.73 ± 3.49% of control (p value 0.01)) (Figure 6(c)). The ATP level was decreased in the lungs of the $PM_{2.5}$ group (0.17 ± 0.05 nmole/mg of protein (p value 0.04)) compared with the control group (0.31 ± 0.02 nmole/mg of protein), while the EFEL 20 and 40 groups showed 0.20 ± 0.05 nmole/mg of protein (p value 0.59) and 0.25 ± 0.03 nmole/mg of protein (p value 0.09), respectively (Figure 6(e)).

The brain of the $PM_{2.5}$ group showed excessive ROS content (133.68 ± 16.92% of control (p value 0.05)), while EFEL 20 and 40 had decreased ROS content (80.62 ± 10.60 % of control (p value 0.01) and 73.12 ± 11.64% of control (p value 0.02), respectively) (Figure 6(b)). MMP was decreased in the brain of the $PM_{2.5}$ group (73.59 ± 12.21% of control (p value 0.05)) and EFEL 20 and 40 have an increased MMP level (111.11 ± 19.68% of control (p value 0.01) and 152.17 ± 22.89% of control (p value 0.01), respectively) (Figure 6(d)). The ATP level decreased in the brain of the $PM_{2.5}$ group (0.09 ± 0.02 nmole/mg of protein (p value 0.04)) compared with the control group (0.32 ± 0.07 nmole/mg of protein), and the EFEL 20 and 40 groups showed 0.08 ± 0.01 nmole/mg of protein (p value 0.41) and 0.10 ± 0.05 nmole/mg of protein (p value 0.73), respectively (Figure 6(f)).

3.6. Western Blot Analysis

3.6.1. Inflammatory Cytokine Expression Level in the Lung. Figure 7 shows the expression of protein mediating inflammatory responses in $PM_{2.5}$-exposed mice lung tissue. The expression levels of TLR4, p-JNK, p-IκBα, caspase-1, TNF-α, and IL-1β (63.64 ± 0.54% (p value 0.14), 58.75 ± 0.29% (p value 0.01), 42.84 ± 0.29% (p value 0.04), 336.12 ± 0.78 % (p value 0.01), 61.37 ± 0.51% (p value 0.10), and 93.42 ± 0.57% (p value 0.09), respectively) in the $PM_{2.5}$ group were up-regulated compared to the control group. However, the expression levels of the EFEL 40 group (59.65 ± 0.16% (p value 0.11), 45.81 ± 0.20% (p value 0.10), 53.04 ± 0.13% (p value 0.06), 178.49 ± 0.93% (p value 0.03), 55.78 ± 0.19% (p value 0.13), and 80.04 ± 0.23% (p value 0.12), respectively) were down-regulated compared to the $PM_{2.5}$ group (Figures 7(b)–7(g)).

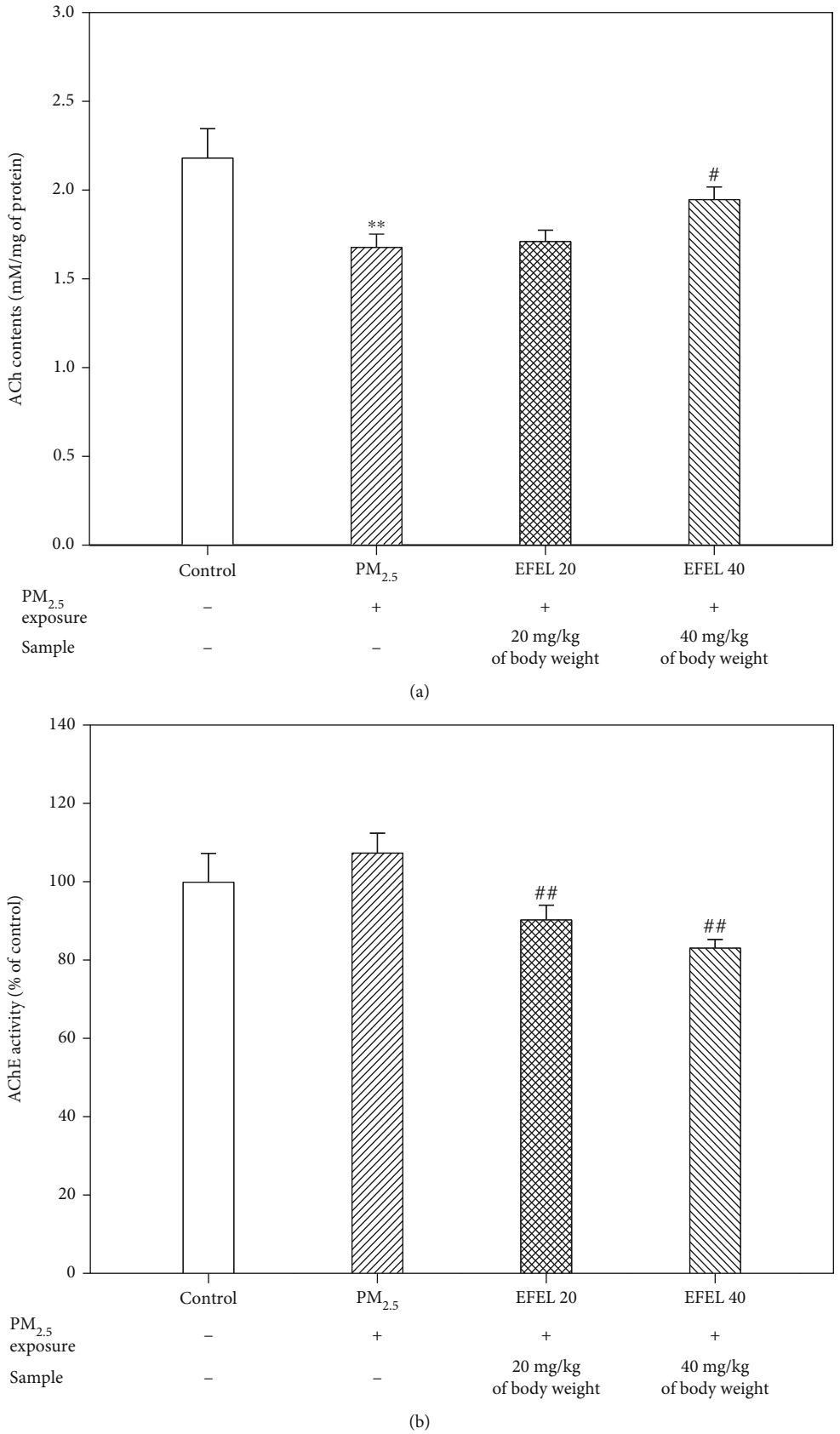

Figure 5: Continued.

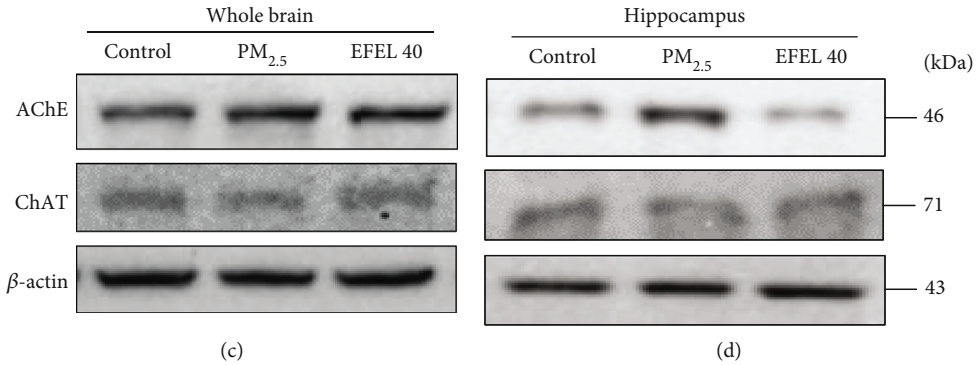

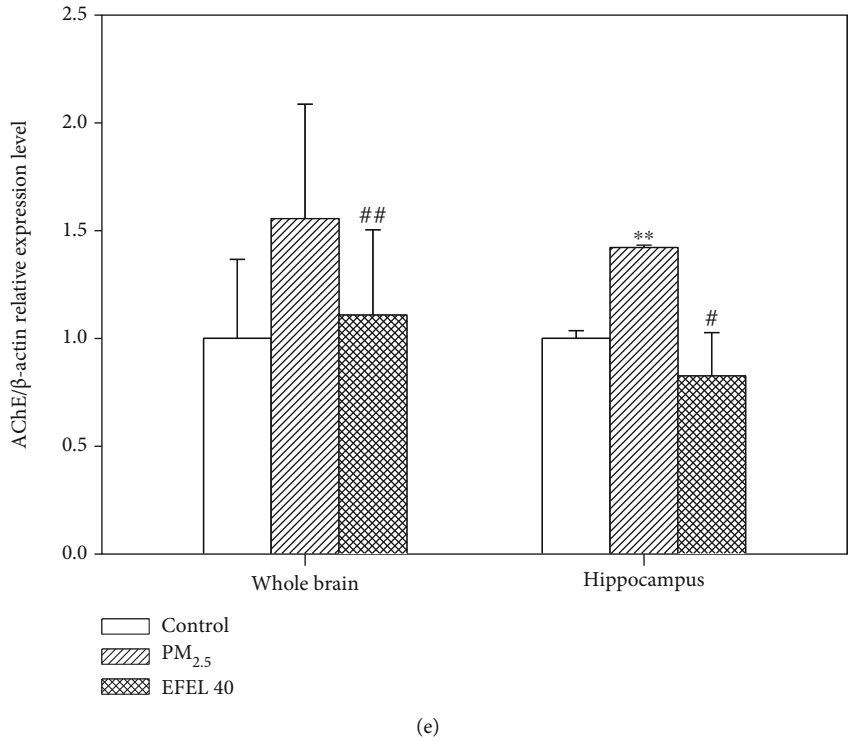

Figure 5: Continued.

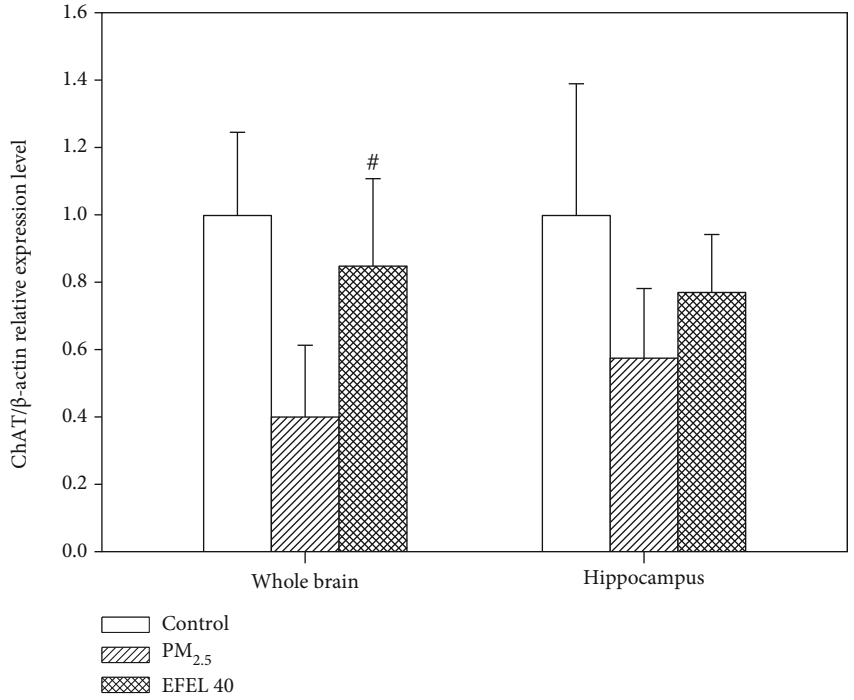

(f)

Figure 5: Protective effect of ethyl acetate fraction from *Eucommia ulmoides* leaves (EFEL) on cholinergic dysfunction in $PM_{2.5}$-induced mice. (a) Acetylcholine (ACh) contents. (b) Acetylcholinesterase (AChE) activity in the whole brain. Acetylcholinesterase and choline acetyltransferase (ChAT) band image in the whole brain (c) and hippocampus (d). AChE and ChAT expression level in the whole brain (e and f) and hippocampal (g and h). Results shown are mean ± SD ($n = 5$). Data were statistically represented at $*$ which is significantly different from the control group and # which is significantly different from $PM_{2.5}$ group; $*$ and $\#p < 0.05$; and $**$ and $\#\#p < 0.01$.

3.6.2. Inflammation Protein Expression Level in the Whole Brain, Olfactory Bulb, and Hippocampus. Figure 8 shows the expression of protein-mediating inflammatory responses in $PM_{2.5}$-exposed mice brain tissue. The expression levels of *p*-JNK (whole brain, 72.92 ± 0.47% (*p* value 0.02); olfactory bulb, 101.53 ± 0.76% (*p* value 0.10); and hippocampus, 177.29 ± 0.46% (*p* value 0.01)), *p*-IκBα (whole brain, 42.36 ± 0.34% (*p* value 0.15); olfactory bulb, 16.16 ± 0.20% (*p* value 0.19); and hippocampus, 84.52 ± 0.28% (*p* value 0.07)), caspase-1 (whole brain, 55.55 ± 0.53% (*p* value 0.07); olfactory bulb, 114.27 ± 0.85% (*p* value 0.10); and hippocampus, 65.08 ± 0.22% (*p* value 0.15)), IL-1β (whole brain, 17.90 ± 0.09% (*p* value 0.15); olfactory bulb, 81.84 ± 0.12% (*p* value 0.04); and hippocampus, 49.81 ± 0.23% (*p* value 0.06)), and TNF-α (whole brain, 11.44 ± 0.26% (*p* value 0.55); olfactory bulb, 104.60 ± 0.87% (*p* value 0.12); hippocampus, 92.56 ± 0.16% (*p* value 0.04)) in the $PM_{2.5}$ group were up-regulated compared to the control group. However, the expression levels of *p*-JNK (whole brain, 12.54 ± 0.46% (*p* value 0.49); olfactory bulb, 82.63 ± 0.47% (*p* value 0.07); and hippocampus, 129.49 ± 0.32% (*p* value 0.01)), *p*-IκBα (whole brain, 32.28 ± 0.21% (*p* value 0.27); olfactory bulb, 52.20 ± 0.24% (*p* value 0.06); and hippocampus, 63.72 ± 0.31% (*p* value 0.16)), caspase-1 (whole brain, 44.71 ± 0.40% (*p* value 0.16); olfactory bulb, 105.39 ± 0.35 % (*p* value 0.12); and hippocampus, 62.70 ± 0.33% (*p* value 0.18)), IL-1β (whole brain, 6.08 ± 0.19% (*p* value 0.59); olfactory bulb, 86.09 ± 0.38% (*p* value 0.04); and hippocampus, 49.54 ± 0.14% (*p* value 0.14)), and TNF-α (whole brain, 26.24 ± 0.22% (*p* value 0.01); olfactory bulb, 82.42 ± 0.34% (*p* value 0.09); and hippocampus, 75.44 ± 0.47% (*p* value 0.14)) in the EFEL 40 group were down-regulated compared to the $PM_{2.5}$ group (Figures 8(b)–8(f)).

3.6.3. Apoptosis Protein Expression Level in the Brain. Figure 9 shows the expression of amyloid-β and *p*-tau protein in mice whole brain, olfactory bulb, and hippocampus. The amyloid-β expression level increased 62.76 ± 0.33% (*p* value 0.00), 69.75 ± 0.51% (*p* value 0.08), and 56.00 ± 0.40 % (*p* value 0.18) in the whole brain, olfactory bulb, and hippocampus compared to the control group, respectively. And EFEL decreased the expression level (whole brain, 48.89 ± 0.25% (*p* value 0.08); olfactory bulb, 78.83 ± 0.31% (*p* value 0.12); and hippocampus, 65.79 ± 0.24% (*p* value 0.02)) compared to the $PM_{2.5}$ group. The *p*-tau expression level increased 101.62 ± 0.71% (*p* value 0.03), 31.90 ± 0.05% (*p* value 0.20), and 231.82 ± 0.57% (*p* value 0.02) in the whole brain, olfactory bulb, and hippocampus compared to the control group, respectively. And EFEL decreased the expression level (whole brain, 53.38 ± 0.21% (*p* value 0.22); olfactory bulb, 68.36 ± 0.28% (*p* value 0.03); and hippocampus, 214.58 ± 0.34% (*p* value 0.02)) compared to the $PM_{2.5}$ group (Figures 9(b) and 9(c)).

3.7. Identification of Bioactive Compounds Using UPLC Q-TOF/MS². The major physiological compounds of EFEL

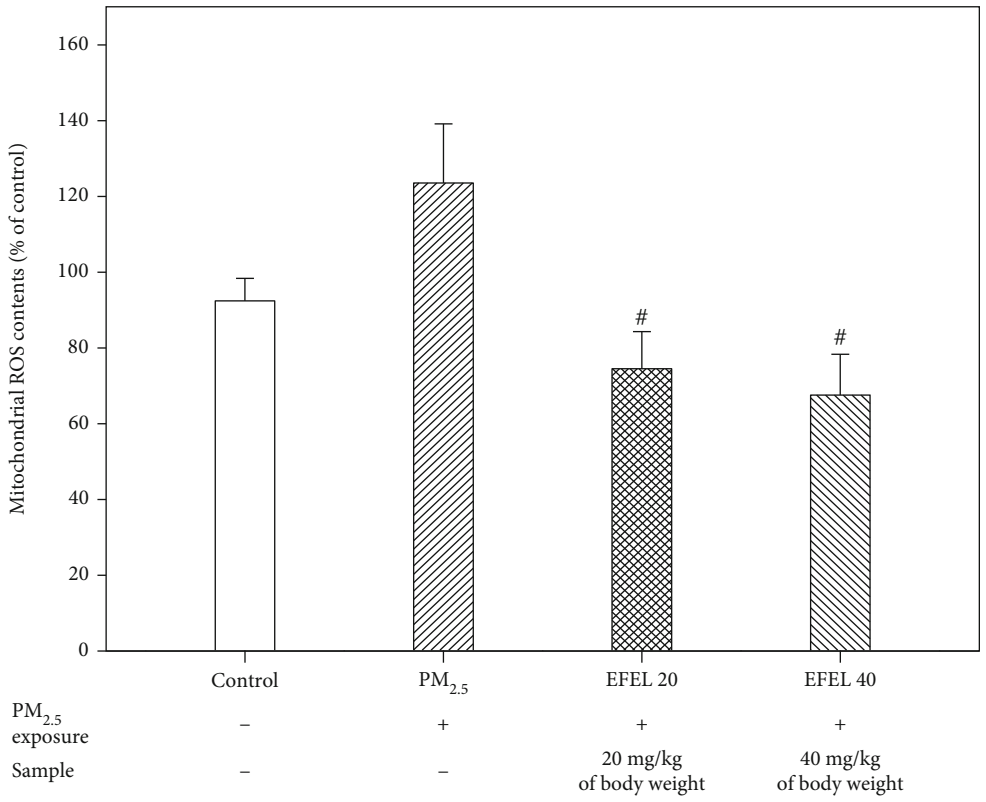

(a)

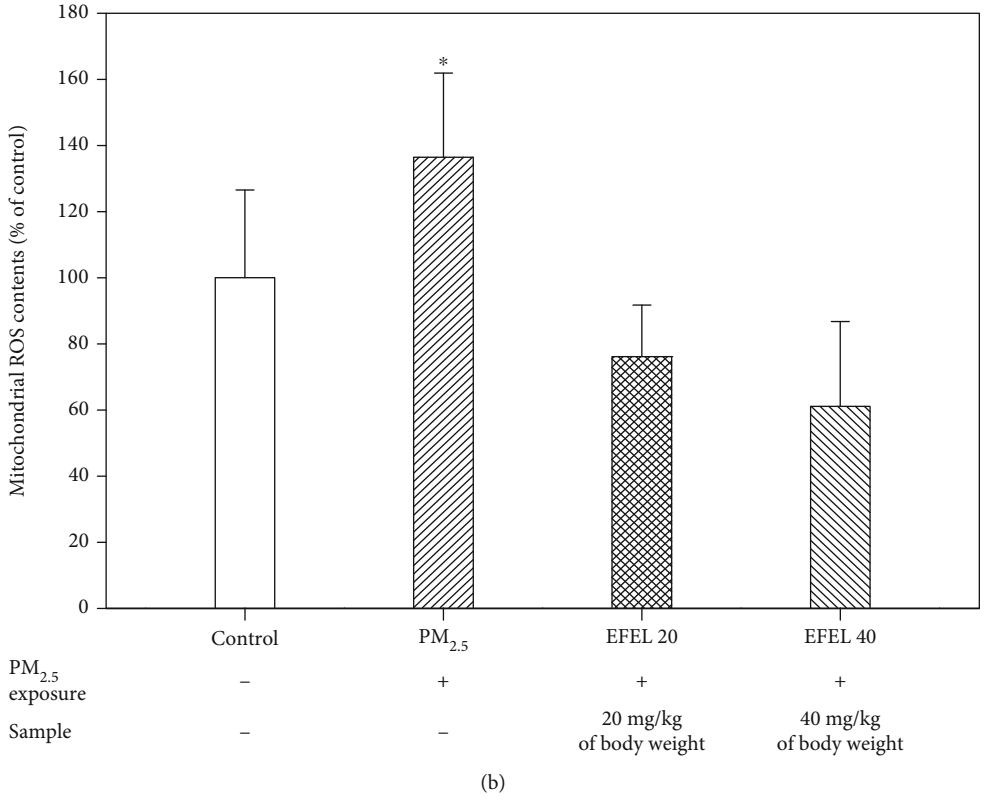

(b)

Figure 6: Continued.

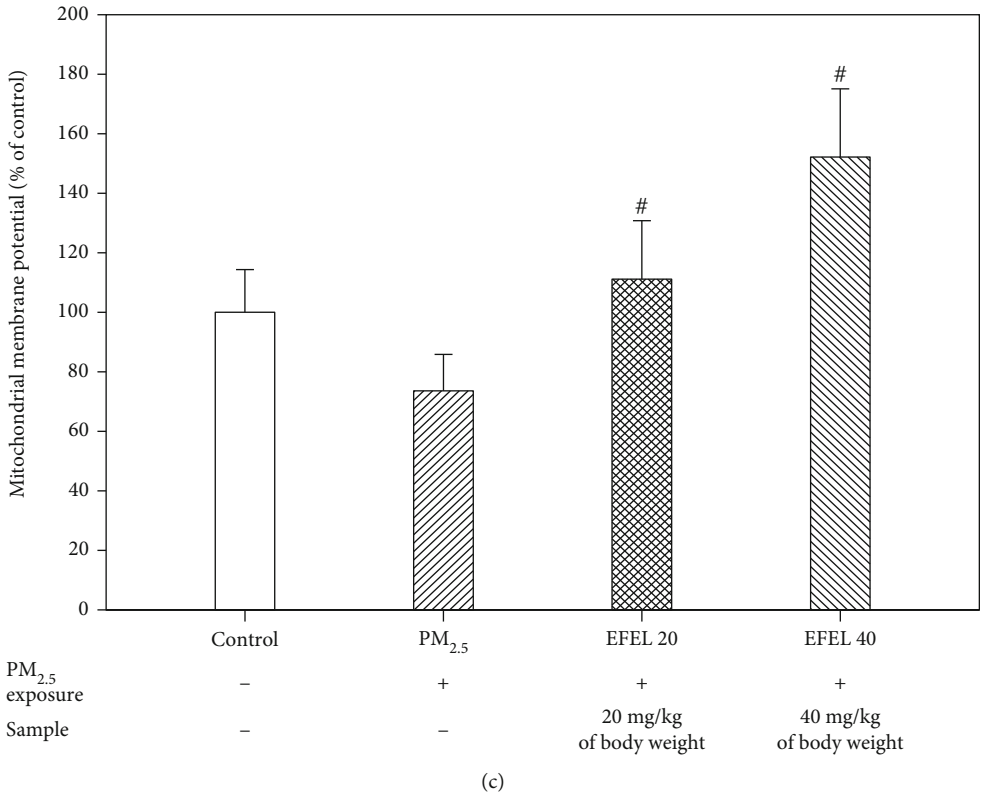

(c)

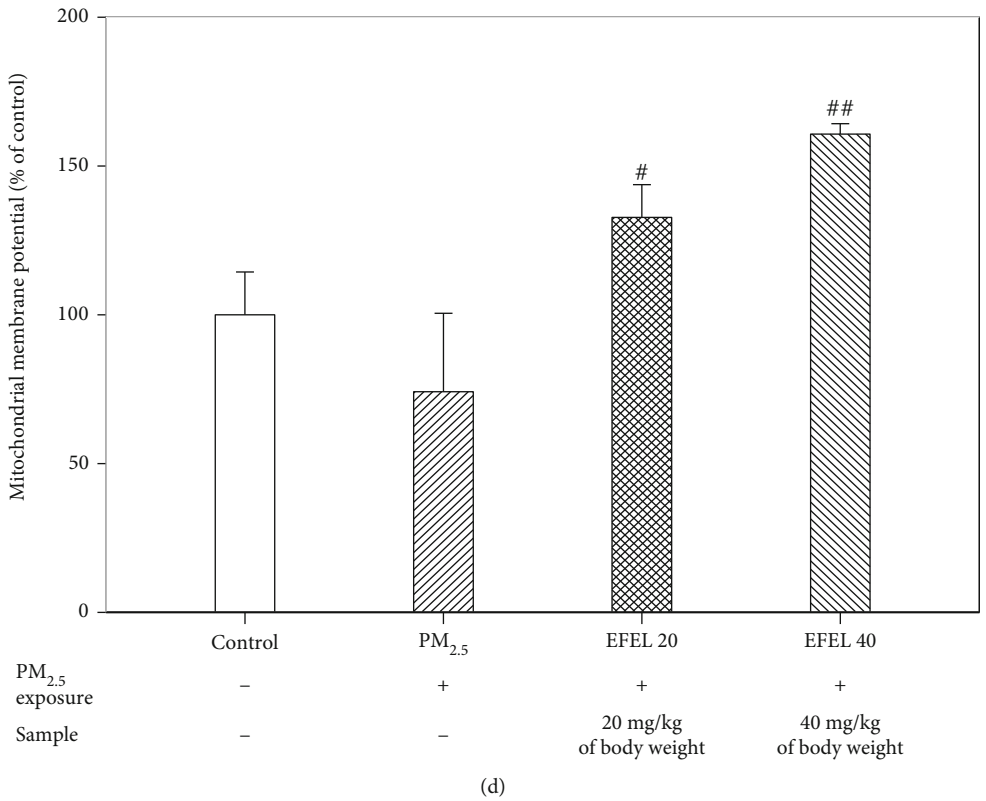

(d)

Figure 6: Continued.

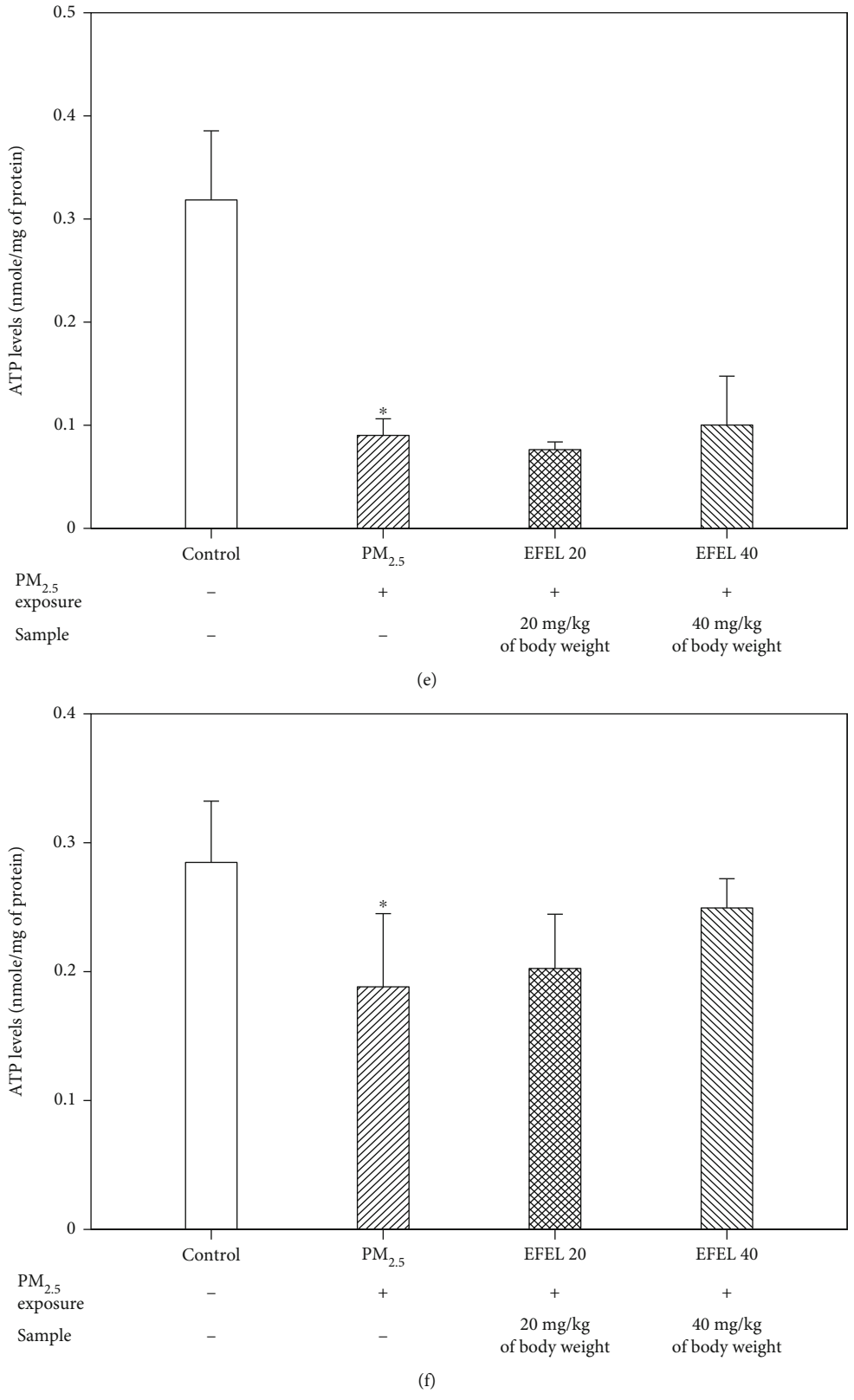

Figure 6: Mitochondrial activity of ethyl acetate fraction from *Eucommia ulmoides* leaves (EFEL) on $PM_{2.5}$-induced mice in brain and lung. Mitochondrial reactive oxygen species (ROS) contents in the brain (a) and lung (b). Mitochondrial membrane potential (MMP) activity in the brain (c) and lung (d). Mitochondrial ATP contents in the brain (e) and lung (f). Results shown are mean ± SD ($n = 5$). Data were statistically represented at $*$ which is significantly different from the control group and # which is significantly different from $PM_{2.5}$ group; $*$ and $\#p < 0.05$; and $**$ and $\#\#p < 0.01$.

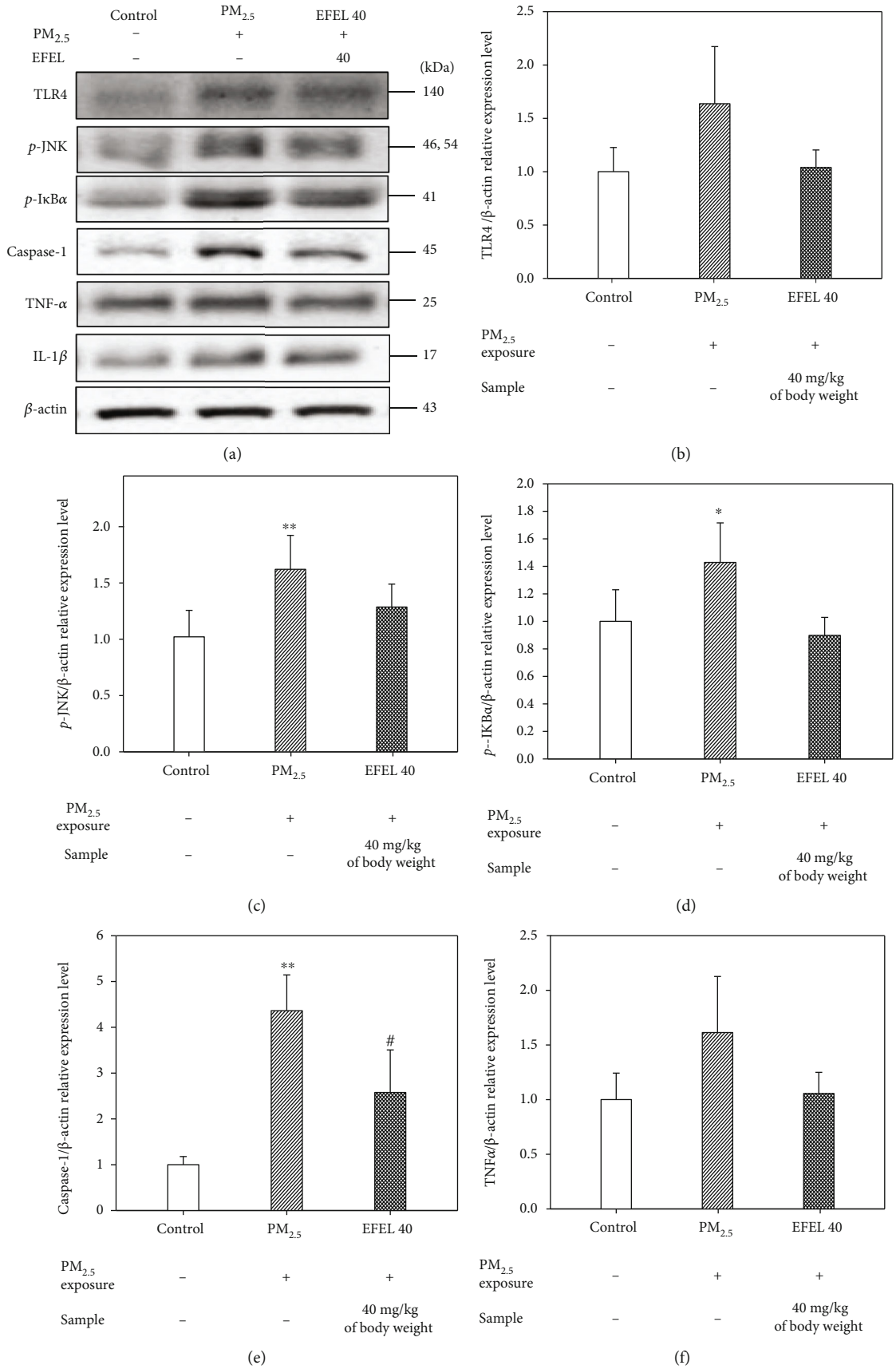

Figure 7: Continued.

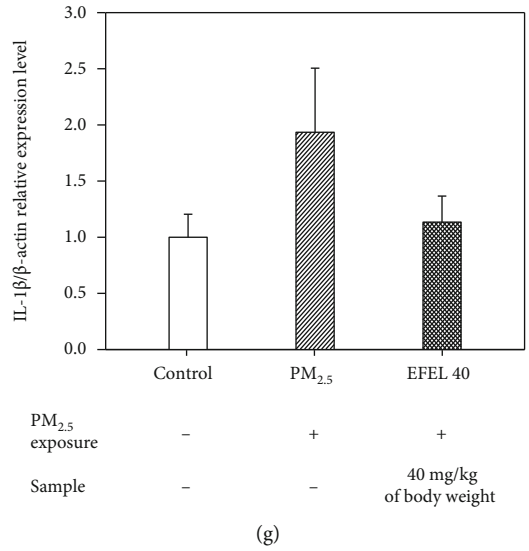

Figure 7: Expression levels of protein related to inflammation pathway in lung tissue. (a) band image; (b) TLR4; (c) *p*-JNK; (d) *p*-Iκb-*α*; (e) caspase-1; (f) TNF-*α*; and (g) IL-1*β*. Results shown are mean ± SD ($n = 3$). Data were statistically represented at ∗ which is significantly different from the control group and # which is significantly different from $PM_{2.5}$ group; ∗ and $\#p < 0.05$; and ∗∗ and $\#\#p < 0.01$.

were identified using UPLC IMS Q-TOF/MS^2 analysis (Figure 10 and Table 1). The MS spectra were obtained in negative ion mode $[M-H]^-$ as compound A, 707 m/z (RT: 2.84 min); compound B, 609 m/z (RT: 3.15 min); compound C, 463 m/z (RT: 3.22 min); compound D, 505 m/z (RT:3.28 min); compound E, 489 m/z (RT: 3.44 min); and compound F, 301 m/z (RT: 3.84 min). When the main fragments were compared with a previous study, these peaks were identified as 5-O-caffeoylquinic acid (compound A) [29], rutin (compound B) [30], quercetin-O-hexoside (compound C) [30], quercetin-O-acetylhexoside (isomer) (compound D) [31], luteolin-O-acetylhexoside (compound E) [29], and quercetin (compound F) [30].

4. Discussion

$PM_{2.5}$ exposure induces oxidative stress and inflammation in respiratory system [32]. Because $PM_{2.5}$ have small diameter, it is not filtered by the nasal mucosa and is deposited in the lungs and alveoli [5]. The release of proinflammatory cytokines (TNF-*α*, IL-6, and IFN-*γ*) produced by inflammation in the respiratory system, which circulate through the blood vessels throughout the body, results in systemic inflammation [32]. Also, $PM_{2.5}$ and inflammatory cytokines that pass through the blood brain barrier (BBB) promote neuroinflammation, which leads to cognitive and learning deficits by neuronal damage, and $PM_{2.5}$ can directly penetrate the olfactory bulb tissue through the olfactory nerve [33]. In this study, $PM_{2.5}$ induced cognitive dysfunction, while EFEL improved the spontaneous alternative behavior and long-term memory ability of $PM_{2.5}$-induced mice by regulating the inflammation and inhibited the tissues dysfunction in lung and brain tissues. *Eucommia ulmoides* bark showed neuroprotective effects by improving spontaneous alternative behavior and long-term memory ability in mice with amyloid-*β*-induced cognitive impairment [34]. Also, rutin as a bioactive substance within EFEL inhibited the long-term memory deficit in cadmium-induced rats, and quercetin improved the levels of spontaneous alternative behavior and short-term memory deficit in a TMT-induced mice model [35, 36]. In this study, EFEL containing quercetin and its derivatives improved spontaneous alternation behavior and long-term memory ability in $PM_{2.5}$-induced cognitive dysfunction. Therefore, EFEL can be used as a material that improves cognitive dysfunction in $PM_{2.5}$-induced mice.

$PM_{2.5}$ can induce oxidative stress, which leads to a breakdown of the body's antioxidant system such as SOD and GSH. According to a study by Liu and Meng [37], the $PM_{2.5}$ exposure decreased SOD and reduced GSH levels in the brain, lung, liver, and kidney of mice. Also, increased ROS due to an imbalance in the antioxidant system by $PM_{2.5}$ exposure can also cause direct damage to cells and tissues [38]. The imbalance of the antioxidant system by ROS and $PM_{2.5}$ can easily induce lipid peroxidation of unsaturated fatty acids in the brain tissue [39]. Similar to this study, $PM_{2.5}$ reduced SOD and GSH levels and increased MDA levels in mice lung and brain tissues. However, EFEL inhibited the reduction of SOD and GSH levels and the production of MDA levels. The extract of *Eucommia ulmoides* bark increased the content of reduced GSH and the activity of catalase in the kidneys of cadmium-induced kidney toxicity mice [40] and increased the SOD and GSH-Px levels in the serum of streptozotocin-induced diabetic rats [41]. The macranthoin extracted from *Eucommia ulmoides* increased the level of SOD level and GSH content in H_2O_2-induced PC12 cells [42]. Also, the extract from *Eucommia ulmoides* leaves inhibited the production of MDA in the serum of streptozotocin-induced diabetic rats. Rutin increased the activities of SOD, GSH, catalase, and GPx on copper sulfate-induced brain damage of rats [43]. In addition, quercetin inhibited the MDA production on D-galactose-induced mice brain [44]. In this study, EFEL might not only

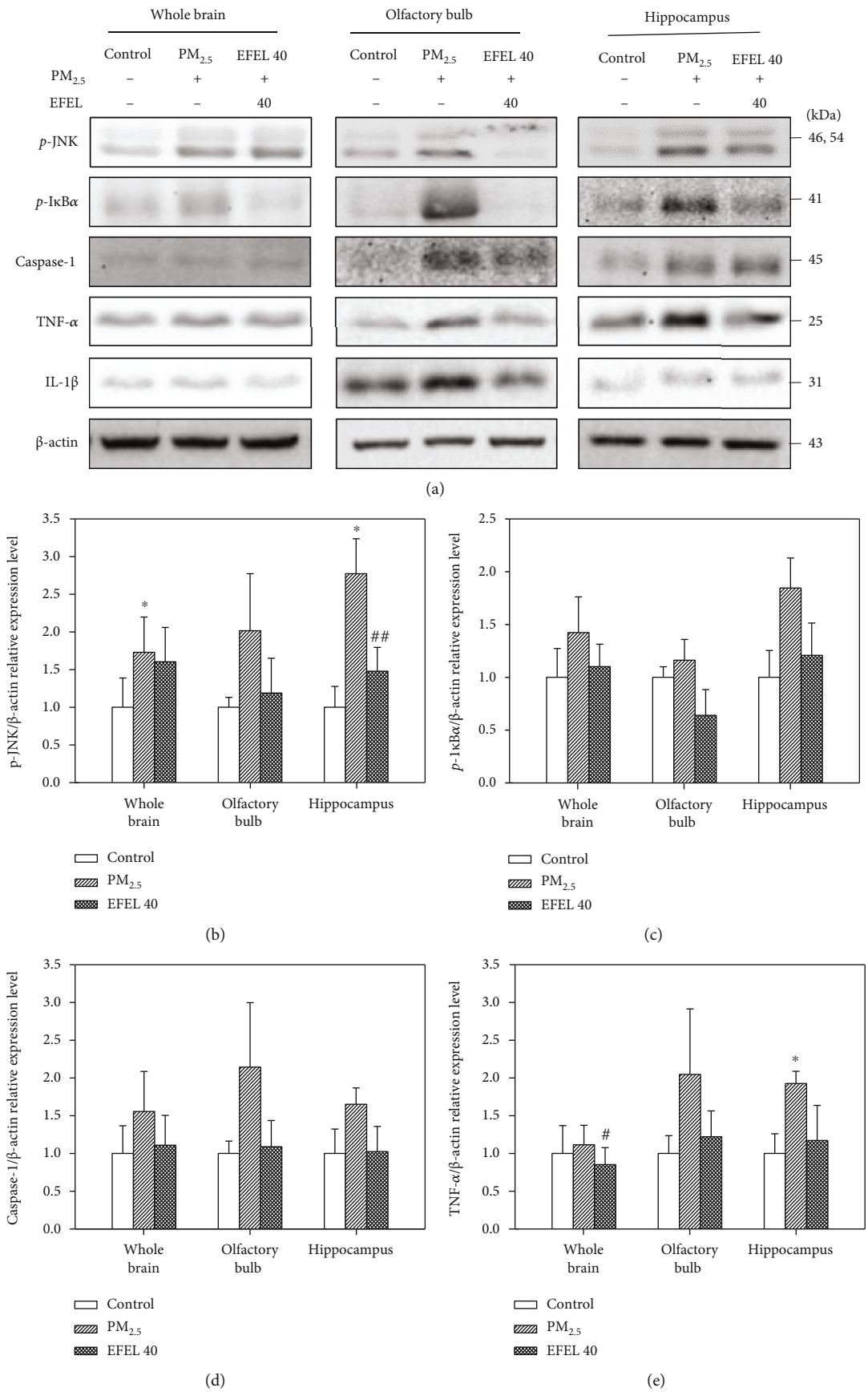

Figure 8: Continued.

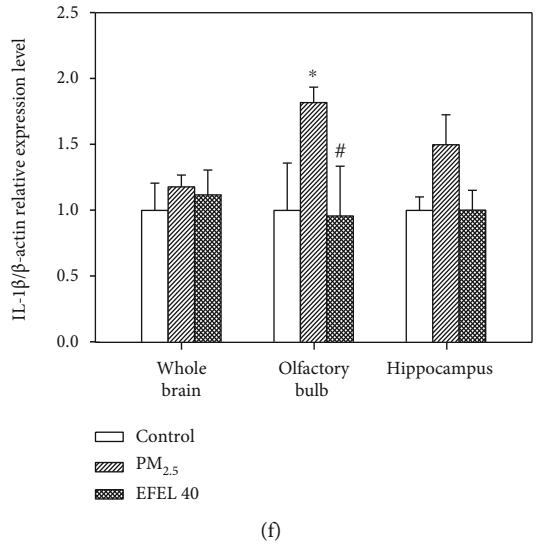

(f)

Figure 8: Expression levels of protein related to inflammation pathway in the whole brain, olfactory bulb and hippocampus tissues. (a) Band images; (b) *p*-JNK; (c) *p*-IκBα; (d) caspase-1; (e) TNF-α; and (f) IL-1β relative expression level in olfactory bulb, whole brain, and hippocampus. Results shown are mean ± SD ($n = 3$). Data were statistically represented at $*$ which is significantly different from the control group and # which is significantly different from $PM_{2.5}$ group; $*$ and $\#p < 0.05$; and $**$ and $\#\#p < 0.01$.

regulate the reduction of SOD and GSH contents, but also inhibit the production of MDA. It was suggested that the intake of EFEL improved the $PM_{2.5}$-induced damaged antioxidant system in lung and brain tissues.

The cholinergic system, which plays role the of neurotransmission in learning and memory ability, is highly correlated with oxidative stress and inflammation. Disruption of the cholinergic system due to increased inflammatory response leads to an abnormal neurotransmission system through the activation of the microglia and apoptosis pathway, and it is directly related to cognitive impairment [45]. $PM_{2.5}$-induced oxidative stress and neuroinflammation induce disruption of the cholinergic system, which is a characteristic of neurodegenerative diseases such as Alzheimer's and Parkinson's diseases [46]. In this study, $PM_{2.5}$-induced cholinergic system dysfunction and EFEL decreased the activity of AChE and increased the content of ACh and regulated the expression of AChE and ChAT in the whole brain and hippocampus tissues. The hippocampus functions related to learning and memory ability are easily affected by cholinergic dysfunction [47]. In the hippocampus tissues of cognitive impairment patients, acetylcholine (ACh) content was showed decreasing [48]. Therefore, the expression level of ChAT and AChE, which synthesize and degrade of ACh, were measured in the whole brain and hippocampus tissues. The bark of *Eucommia ulmoides* decreased AChE activity in the hippocampal and cortex of scopolamine-induced learning and cognitive impairment mice [49]. In addition, rutin as a physiological compound of *Eucommia ulmoides* leaves decreased AChE activity in the hippocampus and cortex of cadmium-induced rat [35]. Quercetin reduced the activity of AChE in the synaptosome, cerebral cortex, hippocampus, and striatum of the brain tissue on streptozotocin-induced diabetes rat model [50]. Also, quercetin regulated the mRNA expression levels of AChE and ChAT in the frontal cortex and hippocampus tissues on cadmium-induced mice [51]. In this study, EFEL decreased the activity of AChE and increased the content of ACh in $PM_{2.5}$-induced cholinergic dysfunction. In addition, EFEL regulated the expression level of AChE and ChAT in the whole brain and hippocampus tissues. Therefore, it was confirmed that EFEL improves cognitive impairment by regulating the cholinergic system in $PM_{2.5}$-induced neurotoxicity.

$PM_{2.5}$ can damage the mitochondrial structure and ATP synthesis metabolite [52]. In a previous study, exposure to $PM_{2.5}$ increased the expression of genes that induce mitochondrial fission in the nasal mucosa of rat [53]. In this study, the intake of EFEL ameliorated excessive ROS production and loss of MMP and ATP in the lung and brain mitochondria of $PM_{2.5}$-induced mice. Exposure to $PM_{2.5}$ decreased membrane potential and increased intracellular ROS levels in human bronchial epithelial cells (BEAS-2B) [54]. In addition, the bark extract of *Eucommia ulmoides* reduced the ROS level and improved the loss of MMP in H_2O_2-induced human neuroblastoma cells (SH-SY5Y) [55]. The rutin contained in *Eucommia ulmoides* improved the sodium nitroprusside-induced reduction of MMP in PC12 cells [56]. In addition, the quercetin contained in *Eucommia ulmoides* increased the SOD and ATP contents and improved the loss of MMP in the mitochondria of chloral hydrate-induced traumatic brain injury mice [57]. As a result, $PM_{2.5}$ exposure induced mitochondrial dysfunction of lung and brain tissue, and EFEL reduced ROS production and inhibited the loss of MMP and ATP levels in mitochondria.

$PM_{2.5}$ entering through the respiratory tract induces oxidative stress and inflammatory responses, which can secrete various inflammatory cytokines such as interleukin (IL)-1, IL-16, MCP-1, TNF-α, and C(cysteine)-X(noncysteine)-C (cysteine) motif (CXC) chemokines such as CXC chemokine ligand 1(CXCL1) and CXC chemokine ligand 8 (CXCL8) in lung tissue [58, 59]. $PM_{2.5}$ and inflammatory cytokines circulating in the whole body pass the BBB and attack brain

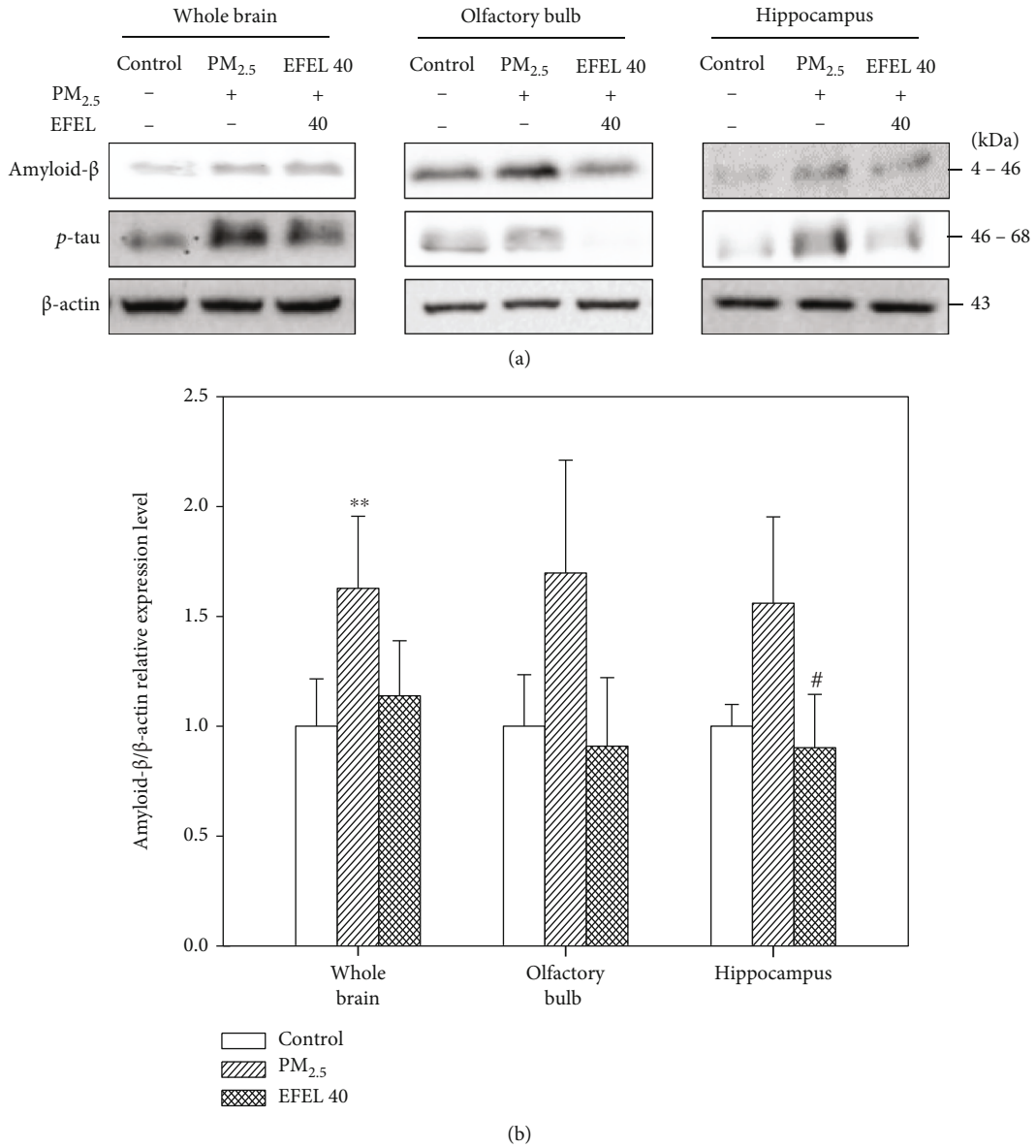

Figure 9: Continued.

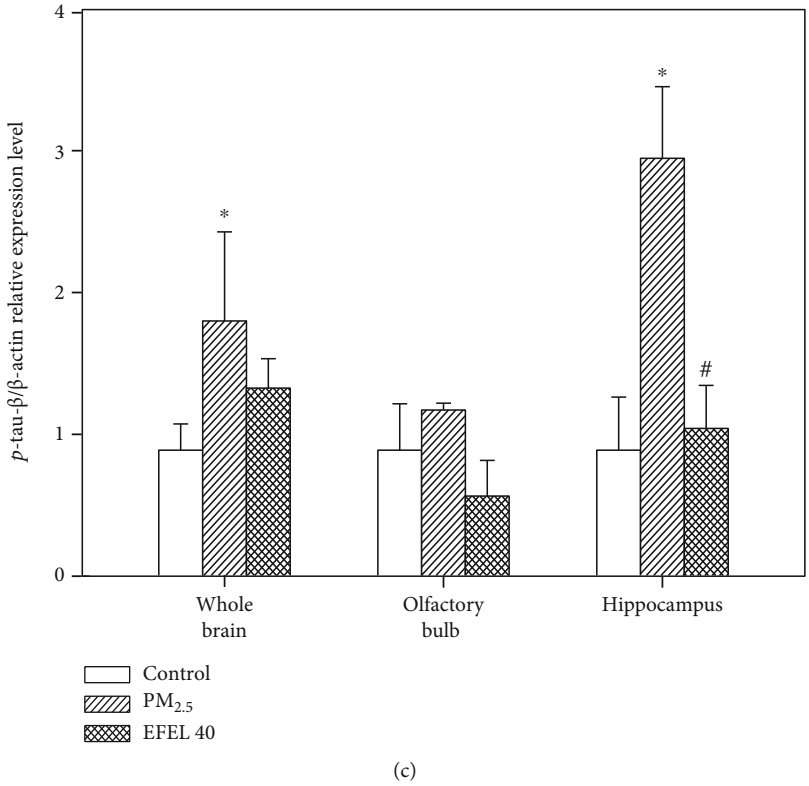

Figure 9: Expression levels of protein related to apoptosis in the whole brain, olfactory bulb, and hippocampus tissues. (a) Band images; (b) amyloid-β; and (c) p-tau relative expression in the whole brain, olfactory bulb, and hippocampus. Results shown are mean ± SD ($n = 3$). Data were statistically represented at $*$ which is significantly different from the control group and # which is significantly different from $PM_{2.5}$ group; $*$ and $\#p < 0.05$; and $**$ and $\#\#p < 0.01$.

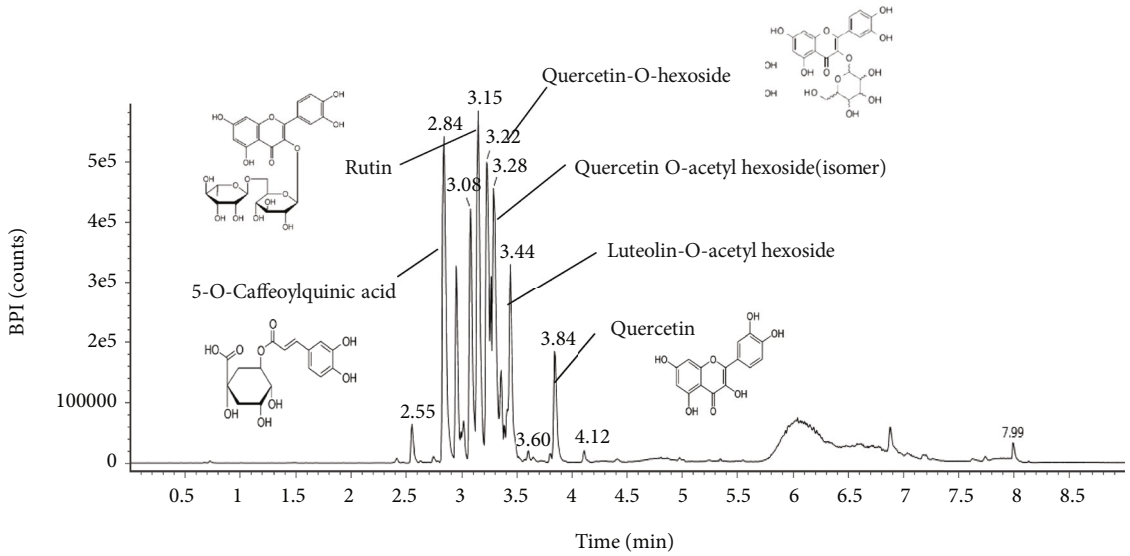

Figure 10: Ultraperformance liquid chromatography-ion mobility separation-quadrupole time of flight/tandem mass spectrometry (UPLC Q-TOF/MS^2) chromatographic profile of ethyl acetate fraction from *Eucommia ulmoides* leaves (EFEL).

tissue, and $PM_{2.5}$ deposited in the olfactory bulb promotes neuroinflammation [60, 61]. The excessive inflammatory response in the brain disrupts the neurotransmitter system, which leads to hippocampus damage to learning and memory [62]. The stimulation of TLR4 as a membrane receptor increases the expression level of phosphorylation extracellular signal-related kinase (ERK), c-Jun N-terminal kinase (JNK), and p-NFκB and p-IκBα, stimulating the secretion of inflammatory cytokines such as IL-1β and TNF-α [63]. Also, $PM_{2.5}$ exposure increases the activity of poly (ADP-

Table 1: Bioactive compounds identified from ethyl acetate fraction of *Eucommia ulmoides* leaves (EFEL).

No.	RT (min)	Parent Ion (m/z)	MS^2 fragment (m/z)	Compound
1	2.84	707	354, 353	5-O-Caffeoylquinic acid
2	3.15	609	301	Rutin
3	3.22	463	301	Quercetin-O-hexoside
4	3.28	505	301, 300	Quercetin-O-acetyl hexoside (isomer)
5	3.44	489	285	Luteolin-O-acetyl hexoside
6	3.84	301	179, 151	Quercetin

ribose) polymerase (PARP)-1, which promotes the formation of amyloid-β, and shows excessive activity of glial cells as evidence of neuroinflammation [64]. Exposure to $PM_{2.5}$ increased the levels of soluble and insoluble amyloid-β and phosphorylated tau protein in mouse brain tissue [65, 66]. In this study, EFEL reduced the expression levels of protein related to inflammatory responses in the lung and brain tissues of mice and decreased the expression levels of amyloid-β and *p*-tau in the brain tissue. Polysaccharides extracted from *Eucommia ulmoides* leaves regulated the TLR4-NFκB pathway in hepatic ischemia-reperfusion injury mice [67]. *Eucommia ulmoides* bark reduced the expression level of *p*-JNK, *p*-ERK, TNF-α, and IL-1β in LPS-induced microglial BV-2 cells [68]. Also, rutin as a physiological compound of EFEL decreased the expression of TNF-α, IL-1β, IL-6, *p*-ERK, and *p*-JNK and decreased the expression level of IκB in LPS-induced lung injury mice [69]. Quercetin contained in *Eucommia ulmoides* decreased the expression levels of *p*-ERK, *p*-JNK, and *p*-p65 in okadaic acid-induced hippocampal neurons and reduced the expression levels of amyloid-$\beta_{1\text{-}42}$ and phosphorylation tau protein in aged triple transgenic Alzheimer's disease model mice [70, 71]. In this study, EFEL down-regulated the expression levels of *p*-JNK, *p*-IκBα, caspase-1, IL-1β, and TNF-α in the lung and the expression levels of *p*-JNK, *p*-IκBα, caspase-1, IL-1β, and TNF-α in olfactory bulb caused by $PM_{2.5}$ toxicity. These results suggest that the regulation of pulmonary inflammation decreases the inflammatory factor passing through the blood, thereby reducing the expression of the neuroinflammatory factor in hippocampus tissues. In addition, EFEL reduced the expression levels of amyloid-β and *p*-tau in the brain tissue. Therefore, EFEL can be used as a functional food material to improve $PM_{2.5}$-induced inflammatory response and cognitive impairment by regulating inflammation.

5. Conclusions

In this study, the protective effect of the ethyl acetate fraction of *Eucommia ulmoides* leaves (EFEL) against $PM_{2.5}$-induced excessive inflammation and cognitive impairment in BALB/c mice was confirmed. EFEL increased the level of spontaneous alternation behavior and protected the long-term memory ability of $PM_{2.5}$-induced mice. EFEL inhibited the antioxidant deficit and mitochondrial damage in $PM_{2.5}$-induced lung and brain tissues and attenuated cerebral cholinergic dysfunction. EFEL regulated the protein expression level related to inflammation in the lung and brain tissues. Inhibition of inflammation in lung tissue by EFEL indicates reduced neuroinflammation in the whole brain, olfactory bulb, and hippocampus, which improved the learning and memory decline in mice. EFEL inhibited damage to mitochondria and antioxidant systems in lung and brain tissues, and consequently protected against the cognitive impairment induced by $PM_{2.5}$. In conclusion, it is suggested that *Eucommia ulmoides* leaves could be used as a material for functional food to improve $PM_{2.5}$-induced cognitive impairment by regulating the inflammatory response.

Data Availability

The research data used to support the findings of this study are included within the article.

Conflicts of Interest

The authors declare that there is no conflict of interest regarding the publication of this paper.

Acknowledgments

This study was supported by the National Research Foundation of Korea (2018R1D1A3B0 704339814).

Supplementary Materials

Figure 1: EFEL increased the cell viability on $PM_{2.5}$-induced cytotoxicity of RPMI 2650 (nasal cell), A549 (lung cell), HT22 (hippocampus cell), MC-IXC (human neuronal cells), and BV-2 (microglia cell) cells. Figure 2 EFEL inhibited the ROS formation on $PM_{2.5}$-induced cytotoxicity of RPMI 2650 (nasal cell), A549 (lung cell), HT22 (hippocampus cell), MC-IXC (human neuronal cells), and BV-2 (microglia cell) cells. *(Supplementary Materials)*

References

[1] M. Kampa and E. Castanas, "Human health effects of air pollution," *Environmental Pollution*, vol. 151, no. 2, pp. 362–367, 2008.

[2] World Health Organization, "Ambient air pollution: A global assessment of exposure and burden of disease," *Clean Air Journal*, vol. 26, no. 2, p. 6, 2016.

[3] E. Stone, J. Schauer, T. A. Quraishi, and A. Mahmood, "Chemical characterization and source apportionment of fine and

coarse particulate matter in Lahore, Pakistan," *Atmospheric Environment*, vol. 44, no. 8, pp. 1062–1070, 2010.

[4] G. Polichetti, S. Cocco, A. Spinali, V. Trimarco, and A. Nunziata, "Effects of particulate matter (PM_{10}, $PM_{2.5}$ and PM_1) on the cardiovascular system," *Toxicology*, vol. 261, no. 1-2, pp. 1–8, 2009.

[5] Y. F. Xing, Y. H. Xu, M. H. Shi, and Y. X. Lian, "The impact of $PM_{2.5}$ on the human respiratory system," *Journal of Thoracic Disease*, vol. 8, no. 1, p. 69, 2016.

[6] S. Y. Kyung and S. H. Jeong, "Particulate-matter related respiratory diseases," *Tuberculosis Respiratory Disease*, vol. 83, no. 2, pp. 116–121, 2020.

[7] F. Liu, Y. Huang, F. Zhang et al., "Macrophages treated with particulate matter $PM_{2.5}$ induce selective neurotoxicity through glutaminase-mediated glutamate generation," *Journal of Neurochemistry*, vol. 134, no. 2, pp. 315–326, 2015.

[8] Y. Wang, L. Xiong, and M. Tang, "Toxicity of inhaled particulate matter on the central nervous system: neuroinflammation, neuropsychological effects and neurodegenerative disease," *Journal of Applied Toxicology*, vol. 37, no. 6, pp. 644–667, 2017.

[9] T. T. Win-Shwe, S. Yamaoto, Y. Fujitani, S. Hirano, and H. Fujimaki, "Nanoparticle-rich diesel exhaust affects hippocampal-dependent spatial learning and NMDA receptor subunit expression in female mice," *Nanotoxicology*, vol. 6, no. 5, pp. 543–553, 2012.

[10] X. Zhu, X. Ji, Y. Shou et al., "Recent advances in understanding the mechanisms of $PM_{2.5}$-mediated neurodegenerative diseases," *Toxicology Letters*, vol. 329, pp. 31–37, 2020.

[11] S. M. Lucas, N. J. Rothwell, and R. M. Gibson, "The role of inflammation in CNS injury and disease," *British Journal of Pharmacology*, vol. 147, no. S1, pp. S232–S240, 2006.

[12] H. Y. Kim, B. H. Moon, H. J. Lee, and D. H. Choi, "Flavonol glycosides from the leaves of _Eucommia ulmoides_ O. with glycation inhibitory activity," *Journal of Ethnopharmacology*, vol. 93, no. 2-3, pp. 227–230, 2004.

[13] C. Y. Kwan, C. X. Chen, T. Deyama, and S. Nishibe, "Endothelium-dependent vasorelaxant effects of the aqueous extracts of the Eucommia ulmoides Oliv. leaf and bark: implications on their antihypertensive action," *Vascular Pharmacology*, vol. 40, no. 5, pp. 229–235, 2003.

[14] S. A. Park, M. S. Choi, M. J. Kim et al., "Hypoglycemic and hypolipidemic action of Du-zhong (Eucommia ulmoides Oliver) leaves water extract in C57BL/KsJ-db/db mice," *Journal of Ethnopharmacology*, vol. 107, no. 3, pp. 412–417, 2006.

[15] M. Y. Hung, T. Y. C. Fu, P. H. Shih, C. P. Lee, and G. C. Yen, "Du-Zhong (*Eucommia ulmoides* Oliv.) leaves inhibits CCl_4-induced hepatic damage in rats," *Food and Chemical Toxicology*, vol. 44, no. 8, pp. 1424–1431, 2006.

[16] M. S. Choi, U. J. Jung, H. J. Kim et al., "Du-zhong (Eucommia ulmoides Oliver) leaf extract mediates hypolipidemic action in hamsters fed a high-fat diet," *The American Journal of Chinese Medicine*, vol. 36, no. 1, pp. 81–93, 2008.

[17] S. Fan, Q. Yin, D. Li et al., "Anti-neuroinflammatory effects of Eucommia ulmoides Oliv. In a Parkinson's mouse model through the regulation of p38/JNK-Fosl2 gene expression," *Journal of Ethnopharmacology*, vol. 260, article 113016, 2020.

[18] Y. Zhou, M. Liang, W. Li et al., "Protective effects of *Eucommia ulmoides* Oliv. bark and leaf on amyloid β-induced cytotoxicity," *Environmental Toxicology and Pharmacology*, vol. 28, no. 3, pp. 342–349, 2009.

[19] M. J. Kim, J. Y. Kang, S. K. Park et al., "Protective effect of Eucommia ulmoides oliver leaves against $PM_{2.5}$-induced oxidative stress in neuronal cells in vitro," *Korean Journal of Food Science and Technology*, vol. 53, no. 4, pp. 423–433, 2021.

[20] K. Kraeuter, P. C. Guest, and Z. Sarnyai, "The Y-maze for assessment of spatial working and reference memory in mice," *Humana Press*, vol. 1916, pp. 105–111, 2019.

[21] J. M. Kim, S. K. Park, J. Y. Kang et al., "Green tea seed oil suppressed Aβ1–42-induced behavioral and cognitive deficit via the Aβ-related Akt pathway," *International Journal of Molecular Sciences*, vol. 20, no. 8, p. 1865, 2019.

[22] K. Bromley-Brits, Y. Deng, and W. Song, "Morris water maze test for learning and memory deficits in Alzheimer's disease model mice," *Journal of Visualized Experiments*, vol. 53, no. 53, article e2920, 2011.

[23] U. Song, H. Jun, B. Waldman et al., "Functional analyses of nanoparticle toxicity: a comparative study of the effects of TiO2 and Ag on tomatoes (*Lycopersicon esculentum*)," *Ecotoxicology and Environmental Safety*, vol. 93, pp. 60–67, 2013.

[24] P. J. Hissin and R. Hilf, "A fluorometric method for determination of oxidized and reduced glutathione in tissues," *Analytical Biochemistry*, vol. 74, no. 1, pp. 214–226, 1976.

[25] J. Lu, Y. Zheng, D. Wu, L. Luo, D. Sun, and Q. Shan, "Ursolic acid ameliorates cognition deficits and attenuates oxidative damage in the brain of senescent mice induced by D-galactose," *Biochemical Pharmacology*, vol. 74, no. 7, pp. 1078–1090, 2007.

[26] G. L. Ellman, K. D. Courtney, V. Andres, and R. M. Reatherstone, "A new and rapid colorimetric determination of acetylcholinesterase activity," *Biochemical Pharmacology*, vol. 7, no. 2, pp. 88–95, 1961.

[27] D. M. Wang, S. Q. Li, W. L. Wu, X. Y. Zhu, Y. Wang, and H. Y. Yuan, "Effects of long-term treatment with quercetin on cognition and mitochondrial function in a mouse model of Alzheimer's disease," *Neurochemical Research*, vol. 39, no. 8, pp. 1533–1543, 2014.

[28] M. M. Bradford, "A rapid and sensitive method for the quantitation of microgram quantities of protein utilizing the principle of protein-dye binding," *Analytical Biochemistry*, vol. 72, no. 1-2, pp. 248–254, 1976.

[29] S. C. Gouveia and P. C. Castilho, "Phenolic composition and antioxidant capacity of cultivated artichoke, Madeira cardoon and artichoke-based dietary supplements," *Food Research International*, vol. 48, no. 2, pp. 712–724, 2012.

[30] E. J. Llorent-Martínez, G. Zengin, D. Lobine, L. Molina-García, A. Mollica, and M. F. Mahomoodally, "Phytochemical characterization, *In Vitro* and *in silico* approaches for three hypericum species," *New Journal of Chemistry*, vol. 42, no. 7, pp. 5204–5214, 2018.

[31] M. E. Karar and N. Kuhnert, "UPLC-ESI-Q-TOF-MS/MS characterization of phenolics from Crataegus monogyna and Crataegus laevigata (Hawthorn) leaves, fruits and their herbal derived drops (Crataegutt Tropfen)," *Journal of Chemical Biology & Therapeutics*, vol. 1, no. 102, article 2572-0406, 2015.

[32] L. Guan, X. Geng, C. Stone et al., "$PM_{2.5}$ exposure induces systemic inflammation and oxidative stress in an intracranial atherosclerosis rat model," *Environmental Toxicology*, vol. 34, no. 4, pp. 530–538, 2019.

[33] X. Chen, J. Guo, Y. Huang et al., "Urban airborne $PM_{2.5}$-activated microglia mediate neurotoxicity through glutaminase-

containing extracellular vesicles in olfactory bulb," *Environmental Pollution*, vol. 264, article 114716, 2020.

[34] S. H. Kwon, H. K. Lee, J. A. Kim et al., "Neuroprotective effects of *Eucommia ulmoides* Oliv. bark on amyloid beta$_{25-35}$-induced learning and memory impairments in mice," *Neuroscience Letters*, vol. 487, no. 1, pp. 123–127, 2011.

[35] G. Oboh, A. A. Adebayo, A. O. Ademosun, and O. G. Olowokere, "Rutin restores neurobehavioral deficits via alterations in cadmium bioavailability in the brain of rats exposed to cadmium," *Neurotoxicology*, vol. 77, pp. 12–19, 2020.

[36] G. N. Choi, J. H. Kim, J. H. Kwak et al., "Effect of quercetin on learning and memory performance in ICR mice under neurotoxic trimethyltin exposure," *Food Chemistry*, vol. 132, no. 2, pp. 1019–1024, 2012.

[37] X. Liu and Z. Meng, "Effects of airborne fine particulate matter on antioxidant capacity and lipid peroxidation in multiple organs of rats," *Inhalation Toxicology*, vol. 17, no. 9, pp. 467–473, 2005.

[38] X. Jin, B. Xue, Q. Zhou, R. Su, and Z. Li, "Mitochondrial damage mediated by ROS incurs bronchial epithelial cell apoptosis upon ambient $PM_{2.5}$ exposure," *The Journal of Toxicological Sciences*, vol. 43, no. 2, pp. 101–111, 2018.

[39] R. Dua and K. D. Gill, "Aluminium phosphide exposure: implications on rat brain lipid peroxidation and antioxidant defence system," *Pharmacology & Toxicology*, vol. 89, no. 6, pp. 315–319, 2001.

[40] E. Liu, L. Han, J. Wang et al., "Eucommia ulmoides bark protects against renal injury in cadmium-challenged rats," *Journal of Medicinal Food*, vol. 15, no. 3, pp. 307–314, 2012.

[41] H. Fu, X. Bai, L. Le et al., "Eucommia ulmoides Oliv. leaf extract improves erectile dysfunction in streptozotocin-induced diabetic rats by protecting endothelial function and ameliorating hypothalamic-pituitary-gonadal axis function," *Evidence-based Complementary and Alternative Medicine*, vol. 2019, Article ID 1782953, 2019.

[42] W. Hu, G. Wang, P. Li et al., "Neuroprotective effects of macranthoin G from Eucommia ulmoides against hydrogen peroxide-induced apoptosis in PC12 cells via inhibiting NF-κB activation," *Chemico-Biological Interactions*, vol. 224, pp. 108–116, 2014.

[43] J. Arowoogun, O. O. Akanni, A. O. Adefisan, S. E. Owumi, A. S. Tijani, and O. A. Adaramoye, "Rutin ameliorates copper sulfate-induced brain damage via antioxidative and anti-inflammatory activities in rats," *Journal of Biochemical and Molecular Toxicology*, vol. 35, no. 1, article 22623, 2021.

[44] S. W. Sun, H. Q. Yu, H. Zhang, Y. L. Zheng, J. J. Wang, and L. Luo, "Quercetin attenuates spontaneous behavior and spatial memory impairment in d-galactose-treated mice by increasing brain antioxidant capacity," *Nutrition Research*, vol. 27, no. 3, pp. 169–175, 2007.

[45] N. Zaghloul, M. E. Addorisio, H. A. Silverman et al., "Forebrain cholinergic dysfunction and systemic and brain inflammation in murine sepsis survivors," *Frontiers in Immunology*, vol. 8, p. 1673, 2017.

[46] Y. Shou, Y. Huang, X. Zhu, C. Liu, Y. Hu, and H. Wang, "A review of the possible associations between ambient $PM_{2.5}$ exposures and the development of Alzheimer's disease," *Ecotoxicology and Environmental Safety*, vol. 174, pp. 344–352, 2019.

[47] K. Shiozaki, E. Iseki, H. Hino, and K. Kosaka, "Distribution of m1 muscarinic acetylcholine receptors in the hippocampus of patients with Alzheimer's disease and dementia with Lewy bodies–an immunohistochemical study," *Journal of the Neurological Sciences*, vol. 193, no. 1, pp. 23–28, 2001.

[48] M. J. Parent, M. A. Bedard, A. Aliaga et al., "Cholinergic Depletion in Alzheimer's Disease Shown by [18F] FEOBV Autoradiography," *International Journal of Molecular Imaging*, vol. 2013, 6 pages, 2013.

[49] S. H. Kwon, S. X. Ma, H. J. Joo, S. Y. Lee, and C. G. Jang, "Inhibitory effects of Eucommia ulmoides Oliv. bark on scopolamine-induced learning and memory deficits in mice," *Biomolecules & Therapeutics*, vol. 21, no. 6, pp. 462–469, 2013.

[50] R. M. Maciel, F. B. Carvalho, A. A. Olabiyi et al., "Neuroprotective effects of quercetin on memory and anxiogenic-like behavior in diabetic rats: role of ectonucleotidases and acetylcholinesterase activities," *Biomedicine & Pharmacotherapy*, vol. 84, pp. 559–568, 2016.

[51] R. Gupta, R. K. Shukla, L. P. Chandravanshi et al., "Protective role of quercetin in cadmium-induced cholinergic dysfunctions in rat brain by modulating mitochondrial integrity and MAP kinase signalling," *Molecular Neurobiology*, vol. 54, no. 6, pp. 4560–4583, 2017.

[52] X. Miao, W. Li, B. Niu et al., "Mitochondrial dysfunction in endothelial cells induced by airborne fine particulate matter (<2.5 μm)," *Journal of Applied Toxicology*, vol. 39, no. 10, pp. 1424–1432, 2019.

[53] Z. Guo, Z. Hong, W. Dong et al., "$PM_{2.5}$-induced oxidative stress and mitochondrial damage in the nasal mucosa of rats," *International Journal of Environmental Research and Public Health*, vol. 14, no. 2, p. 134, 2017.

[54] L. Yang, Y. Wang, Z. Lin et al., "Mitochondrial OGG1 protects against $PM_{2.5}$-induced oxidative DNA damage in BEAS-2B cells," *Experimental and Molecular Pathology*, vol. 99, no. 2, pp. 365–373, 2015.

[55] S. H. Kwon, M. J. Kim, S. X. Ma et al., "*Eucommia ulmoides* Oliv. Bark. protects against hydrogen peroxide-induced neuronal cell death in SH-SY5Y cells," *Journal of Ethnopharmacology*, vol. 142, no. 2, pp. 337–345, 2012.

[56] R. Wang, Y. Sun, H. Huang, L. Wang, J. Chen, and W. Shen, "Rutin, a natural flavonoid protects PC12 cells against sodium nitroprusside-induced neurotoxicity through activating PI3K/Akt/mTOR and ERK1/2 pathway," *Neurochemical Research*, vol. 40, no. 9, pp. 1945–1953, 2015.

[57] X. Li, H. Wang, Y. Gao et al., "Protective effects of quercetin on mitochondrial biogenesis in experimental traumatic brain injury via the Nrf2 signaling pathway," *PLoS One*, vol. 11, no. 10, article 0164237, 2016.

[58] T. Fujii, S. Hayashi, J. C. Hogg, R. Vincent, and S. F. Van Eeden, "Particulate matter induces cytokine expression in human bronchial epithelial cells," *American Journal of Respiratory Cell and Molecular Biology*, vol. 25, no. 3, pp. 265–271, 2001.

[59] J. S. Kim, H. Choi, J. M. Oh et al., "Effect of fluticasone propionate on human nasal fibroblasts exposed to urban particulate matter," *Auris Nasus Larynx*, vol. 47, no. 3, pp. 415–424, 2020.

[60] S. M. MohanKumar, A. Campbell, M. Block, and B. Veronesi, "Particulate matter, oxidative stress and neurotoxicity," *Neurotoxicology*, vol. 29, no. 3, pp. 479–488, 2008.

[61] S. Christen-Zaech, R. Kraftsik, O. Pillevuit et al., "Early olfactory involvement in Alzheimer's disease," *Canadian Journal of Neurological Sciences*, vol. 30, no. 1, pp. 20–25, 2003.

[62] F. Serrano and E. Klann, "Reactive oxygen species and synaptic plasticity in the aging hippocampus," *Ageing Research Reviews*, vol. 3, no. 4, pp. 431–443, 2004.

[63] L. Chen, H. Deng, H. Cui et al., "Inflammatory responses and inflammation-associated diseases in organs," *Oncotarget*, vol. 9, no. 6, pp. 7204–7218, 2018.

[64] S. Jang, E. W. Kim, Y. Zhang et al., "Particulate matter increases beta-amyloid and activated glial cells in hippocampal tissues of transgenic Alzheimer's mouse: Involvement of PARP-1," *Biochemical and Biophysical Research Communications*, vol. 500, no. 2, pp. 333–338, 2018.

[65] B. Sahu, A. R. Mackos, A. M. Floden, L. E. Wold, and C. K. Combs, "Particulate matter exposure exacerbates amyloid-β plaque deposition and gliosis in APP/PS1 mice," *Journal of Alzheimer's Disease*, vol. 80, pp. 1–14, 2021.

[66] R. Gao, T. Ku, X. Ji, Y. Zhang, G. Li, and N. Sang, "Abnormal energy metabolism and tau phosphorylation in the brains of middle-aged mice in response to atmospheric $PM_{2.5}$ exposure," *Journal of Environmental Sciences*, vol. 62, pp. 145–153, 2017.

[67] W. Gao, Z. Feng, S. Zhang et al., "Anti-inflammatory and antioxidant effect of Eucommia ulmoides polysaccharide in hepatic ischemia-reperfusion injury by regulating ROS and the TLR-4-NF-κB pathway," *BioMed Research International*, vol. 2020, Article ID 1860637, 2020.

[68] S. H. Kwon, S. X. Ma, J. Y. Hwang et al., "The anti-inflammatory activity of Eucommia ulmoides oliv. bark. involves NF-κB suppression and Nrf2-dependent HO-1 induction in BV-2 microglial cells," *Biomolecules & Therapeutics*, vol. 24, no. 3, p. 268, 2016.

[69] C. H. Yeh, J. J. Yang, M. L. Yang, Y. C. Li, and Y. H. Kuan, "Rutin decreases lipopolysaccharide-induced acute lung injury via inhibition of oxidative stress and the MAPK-NF-κB pathway," *Free Radical Biology and Medicine*, vol. 69, pp. 249–257, 2014.

[70] W. Jiang, T. Luo, S. Li et al., "Quercetin protects against okadaic acid-induced injury via MAPK and PI3K/Akt/GSK3β signaling pathways in HT22 hippocampal neurons," *PLoS One*, vol. 11, no. 4, article 0152371, 2016.

[71] M. Sabogal-nGuáqueta, J. I. Munoz-Manco, J. R. Ramírez-Pineda, M. Lamprea-Rodriguez, E. Osorio, and G. P. Cardona-Gómez, "The flavonoid quercetin ameliorates Alzheimer's disease pathology and protects cognitive and emotional function in aged triple transgenic Alzheimer's disease model mice," *Neuropharmacology*, vol. 93, pp. 134–145, 2015.

Hindawi
Oxidative Medicine and Cellular Longevity
Volume 2022, Article ID 8659587, 13 pages
https://doi.org/10.1155/2022/8659587

Research Article

MicroRNA-299a-5p Protects against Spinal Cord Injury through Activating AMPK Pathway

Zong-Ze Zhang, Shu-Yue Xian, Chong Bao, and Feng Chen

Department of Anesthesiology, Zhongnan Hospital of Wuhan University, China

Correspondence should be addressed to Feng Chen; chenfeng@znhospital.cn

Received 12 November 2021; Revised 20 March 2022; Accepted 7 April 2022; Published 13 May 2022

Academic Editor: Silvânia Maria Mendes Vasconcelos

Objective. Inflammation and oxidative stress are implicated in the pathogenesis of spinal cord injury (SCI). The present study is aimed at investigating the function and molecular basis of microRNA-299a-5p (miR-299a-5p) during SCI in mice. *Methods*. Mice were exposed to SCI surgery and then intrathecally injected with the agomir, antagomir, or matched negative controls of miR-299a-5p to overexpress or silence miR-299a-5p. To inhibit AMP-activated protein kinase (AMPK), mice were intraperitoneally injected with compound C (CC). To overexpress pH domain and leucine-rich repeat protein phosphatase 1 (PHLPP1), lentiviral vectors were used. *Results*. The miR-299a-5p expression in the spinal cord was dramatically reduced by SCI stimulation. The miR-299a-5p agomir prevents, while the miR-299a-5p antagomir exacerbates inflammation, oxidative stress, and SCI in mice. Mechanistically, we found that miR-299a-5p directly inhibited PHLPP1 and subsequently activated AMPK pathway. The PHLPP1 overexpression of AMPK inhibition with either genetic or pharmacologic methods dramatically abolished the miR-299a-5p agomir-mediated protective effects against SCI. *Conclusion*. miR-299a-5p protects against spinal cord injury through activating AMPK pathway.

1. Introduction

Spinal cord injury (SCI) is a devastating central nervous system damage that can cause motor, sensory, and autonomic dysfunction, while no effective therapies are currently available. Multiple mechanisms are implicated in the pathogenesis of SCI, including inflammation and oxidative stress. Upon SCI, microglia cells, the resident macrophages in the spinal cord, are activated and then produce massive proinflammatory cytokines, resulting in inflammatory damage and leukocyte infiltration [1, 2]. In addition, the blood-spinal cord barrier (BSCB) is severely disrupted immediately after SCI and lasting for at least 28 days, which also exacerbates tissue edema, leukocyte extravasation, and inflammation [3]. Moreover, the level of reactive oxygen species (ROS) in the spinal cord is elevated by SCI and contributes to the progression of SCI by triggering peroxidation of lipid, protein, and nucleic acid [2, 4]. Based on these contexts, it is desirable to prevent SCI through targeting inflammation and oxidative stress.

AMP-activated protein kinase (AMPK) is a serine/threonine protein kinase and mainly involves in regulating cellular energy homeostasis. In addition, it also participates in some other biological processes, such as inflammation and oxidative stress [5–8]. Emerging studies have demonstrated that AMPK activation effectively inhibits the phosphorylation and activation of nuclear factor-κB (NF-κB), thereby preventing SCI-induced inflammation and motor dysfunction [9]. Besides, AMPK activation could also suppress the activation of nucleotide-binding domain-like receptor protein 3 (NLRP3) inflammasome, an intracellular multiprotein complex to promote the processing, maturation, and secretion of multiple proinflammatory cytokines [10, 11]. Transcriptional factor nuclear factor E2-related factor 2 (NRF2) plays an important role in maintaining cellular redox homeostasis through increasing the expression of antioxidant enzymes, including NAD (P)H: quinone oxidoreductase 1 (NQO1), superoxide dismutase 2 (SOD2), and catalase (CAT) [12, 13]. Hu et al. recently identified that AMPK activation dramatically elevated the NRF2 expression

and eventually reduced SCI-induced oxidative stress and functional impairment [14]. Therefore, finding novel regulators of AMPK, especially endogenous activators, is critical to treat SCI.

MicroRNAs (miRs) are endogenous small noncoding RNAs to regulate gene expressions through binding to the 3′-untranslational region (3′-UTR) of targeted messenger RNAs, and they are shown to be responsible for the progression of SCI [15–17]. Most studies about miR-299a-5p mainly focus on its role in regulating tumor growth and chemotherapy sensitivity; however, its function and molecular basis during SCI remain unclear [18]. Sun et al. previously revealed a correlation between miR-299a-5p and sepsis-related inflammation and acute kidney injury [19]. And the predicted targets of miR-299a-5p are known to affect inflammation and oxidative stress [20]. Based on these results, we hypothesize that miR-299a-5p may be implicated in the pathogenesis of inflammation, oxidative stress, and SCI in mice.

2. Materials and Methods

2.1. Chemicals. Compound C (CC, #S7840) was purchased from Selleck Chemicals (Houston, TX, USA). Evans blue dye (#E2129), 2′,7′-dichlorofluorescin diacetate (DCFH-DA, #D6883), and lucigenin (#M8010) were purchased from Sigma-Aldrich (St. Louis, MO, USA). Amplex™ Red Hydrogen Peroxide/Peroxidase Assay Kit (#A22188) and NE-PER™ Nuclear and Cytoplasmic Extraction Reagents (#78833) were purchased from Thermo Fisher Scientific (Waltham, MA, USA). Commercial kits to detect myeloperoxidase (MPO, #ab155458), malondialdehyde (MDA, #ab118970), 3-nitrotyrosine (3-NT, #ab116691), 8-hydroxy-2-deoxyguanosine (8-OHdG, #ab201734), total SOD (#ab65354) activity, total antioxidant capacity (#ab65329), and capase-1 (casp1, #ab273268) activity were purchased from Abcam (Cambridge, UK). Interleukin-6 (IL-6, #M6000B), tumor necrosis factor-α (TNF-α, #MTA00B), IL-1β (#MLB00C), and IL-18 (#7625) ELISA kits were purchased from R&D Systems (Minneapolis, MN, USA). TransAM® NF-κB p65 assay kit (#40096) and TransAM NRF2 assay kit (#50296) were obtained from Active Motif (Carlsbad, CA, USA). The following primary antibodies were purchased from Cell Signaling Technology (Danvers, MA, USA): anti-phospho-NF-κB p65 (p-p65, #3033), anti-total p65 (t-p65, #8242), anti-p-AMPK (#2535), and anti-t-AMPK (#5831). Anti-NLRP3 (#ab263899), anti-apoptosis-associated speck-like protein (ASC, #ab47092), anti-glyceraldehyde-3-phosphate dehydrogenase (GAPDH, #ab8245), and anti-NRF2 (#ab62352) were purchased from Abcam. Anti-casp1 p10 (#sc-56036) was purchased from Santa Cruz Biotechnology (Dallas, Texas, USA), while anti-pH domain and leucine-rich repeat protein phosphatase 1 (PHLPP1, #67640-1-Ig) were purchased from Proteintech Group, Inc. (Rosemont, IL, USA). The micrON mmu-miR-299a-5p agomir (#miR40000377-4-5), agomir negative control (agomir-NC, #miR4N0000001-4-5), micrOFF mmu-miR-299a-5p antagomir (#miR30000377-4-5), and antagomir-NC (#miR3N0000001-4-5) were purchased from Guangzhou RiboBio Co., Ltd. (Guangzhou, China). Lentivirus carrying the full-length mouse PHLPP1 (NM_133821.3) or the scramble control (Ctrl) was synthetized by Shanghai Genechem Co., Ltd. (Shanghai, China).

2.2. Animals. Twelve-week-old male C57BL/6 mice were group-housed at five per cage with free access to food and water in a 12/12 h light-dark cycle at 22-25°C, and the feeding conditions were kept in a specific pathogen-free barrier system at Wuhan University. Animal experimental procedures were approved by the Ethics Committee of Zhongnan Hospital of Wuhan University (Approval no. ZN2022099). The SCI mouse model was established according to previous studies [2, 21]. Briefly, mice were anesthetized by isoflurane and received a laminectomy with the spinal cord exposed at the T8 vertebral level. Then, the vertebral column was stabilized and subjected to a 60 kdyn contusion using the Infinite Horizons Impactor (Precision Systems and Instrumentation, Fairfax Station, VA, USA). The successful surgery was confirmed by the trembled body, stretched and turned legs, and dropped tail. Penicillin sodium solution was administered once daily for 3 consecutive days postsurgery for disinfection, and 2 mL sterile saline was subcutaneously injected to help rehydration. After SCI, bladders were manually voided twice daily until bladder function was restored. In the sham-operated groups, mice were exposed to a laminectomy at the T8 vertebral level without injury. To overexpress or inhibit miR-299a-5p, mice were intrathecally injected with the agomir, antagomir, or matched NC of miR-299a-5p at a dose of 0.5 nmol per mouse according to previous studies [17, 22]. To inhibit AMPK, 20 mg/kg CC was intraperitoneally injected once two days from 1 week before SCI surgery [10]. To overexpress PHLPP1, SCI mice were injected with 2 μL lentivirus (1×10^8 TU/mL) at rostral and caudal sites 3 mm from the lesion epicenter with approximately 0.5 mm in depth [23]. All mice were sacrificed 7 days after SCI surgery for molecular detection except special annotations.

2.3. Behavioral Analysis and Sensitivity to Mechanical and Thermal Stimulation. Basso Mouse Scale (BMS) score was calculated before or at 1, 3, 7, 14, and 28 days after SCI to evaluate hindlimb function as previously described [3, 21]. In brief, mice were placed in an open field, and the posterior ankle joint mobility, trunk position and stability, coordination of front and rear limbs, paw posture, toe clearance, and tail position were recorded by two observers blind to the experimental condition, from 0 (no ankle movement) to 9 (normal gait) for scoring. Mechanical allodynia and thermal sensitivity were measured according to a previous study at 28 days after SCI [2].

2.4. Evaluation of BSCB Permeability. BSCB permeability was evaluated by measuring the extravasation of Evans blue dye at 28 days after SCI as previously described [3]. Briefly, mice were intravenously injected with 2% Evans blue dye and allowed circulating for 3 h. Next, the spinal cord lesion was collected, homogenized, and incubated in 50%

trichloroacetic acid solution at 60°C for 24 h. After that, the supernatants were collected and detected at 620 nm excitation and 680 emission using a spectrophotometer.

2.5. Quantitative Real-Time PCR. Total RNA was extracted using TRIzol Reagent (Thermo Fisher Scientific), and then 2 μg total RNA was reversely transcribed to cDNA using the first strand cDNA synthesis kit (Roche, Base, Switzerland) according to previous studies [24–26]. Quantitative real-time PCR was then done using the SYBR Green Master mix (Roche) on the LightCycler 480 system (Roche), and GAPDH as well as U6 was selected as the internal controls for mRNA or miRNA, respectively. Relative mRNA levels were calculated using $2^{-\Delta\Delta Ct}$ formula. The thermocycling conditions were provided as below: 95°C for 30 sec, 40 cycles at 95°C for 5 sec, and 60°C for 30 sec. The primer sequences were provided as below: miR-299a-5p, forward, 5′-ACAC TCCAGCTGGGTGGTTTACCGTCCCAC-3′ and reverse, 5′-CTCAACTGGTGTCGTGGAGTCGGCAATTCAGTTG AGATGTATGT-3′; U6, forward, 5′-CTCGCTTCGGCAGC ACA-3′ and reverse, 5′-AACGCTTCACGAATTTGCGT-3′; NQO-1, forward, 5′-AGGATGGGAGGTACTCGAA TC-3′ and reverse, 5′-AGGCGTCCTTCCTTATATGCTA-3′; SOD2, forward, 5′-CAGACCTGCCTTACGACTA TGG-3′ and reverse, 5′-CTCGGTGGCGTTGAGATTG TT-3′; CAT, forward, 5′-AGCGACCAGATGAAGC AGTG-3′ and reverse, 5′-TCCGCTCTCTGTCAAAGTG TG-3′; PHLPP1, forward, 5′-AGGGTCCCGGAGACGA TAAG-3′ and reverse, 5′-AGGGCGGAGATGTCTTTTG C-3′; GAPDH, forward, 5′-AGGTCGGTGTGAACGGATT TG-3′ and reverse, 5′-TGTAGACCATGTAGTTGAGGT CA-3′.

2.6. Western Blot. Total proteins were extracted using RIPA lysis buffer containing protease/phosphatase inhibitor cocktail, and the concentrations were quantified by Pierce™ BCA Protein Assay kit as previously described [27–30]. Then, the proteins were separated by 10% SDS-PAGE, transferred onto PVDF membranes, and incubated with the primary antibodies at 4°C overnight. On the second day, the membranes were incubated with horseradish peroxidase-conjugated secondary antibodies and then visualized using the electrochemiluminescence detection system on a Chemi-Doc XRS+ Image System (Bio-Rad; Hercules, California, USA). Next, the images were analyzed using Image Lab software (Version 6.0) and normalized to match total proteins or GAPDH.

2.7. Analysis of ROS Level. The level of intracellular ROS level was measured using DCFH-DA probe as previously described by us and the others [25, 31, 32]. Briefly, the spinal cord was homogenized and incubated with 50 μmol/L DCFH-DA solution at 37°C for 30 min, and then the fluorescent intensities were determined at 504/524 nm to evaluate intracellular ROS level. To evaluate the level of hydrogen peroxide, the spinal cord was homogenized and reacted with the Amplex™ Red reagent according to the manufacturer's instructions, with the absorbance measured at 560 nm. Superoxide anion was quantified by incubating with 5 mmol/L lucigenin at 37°C for 10 min, and the luminescence intensity was measured at 30 sec intervals for 3-5 min.

2.8. Biochemical Analysis. The activities of MPO, casp1 activity, total SOD, and TAOC were determined by commercial kits according to the manufacturer's instructions. To evaluate NF-κB and NRF2 transcriptional activities, nuclear extracts were prepared using the NE-PER™ Nuclear and Cytoplasmic Extraction Reagents and then incubated with the TransAM® NF-κB p65 Kit or TransAM NRF2 Kit. In separated studies, the fresh spinal cord homogenates were exposed to enzyme-linked immunosorbent assay (ELISA) detection of the IL-6, TNF-α, IL-1β, and IL-18 using commercial ELISA kits. The levels of MDA, 3-NT, and 8-OHdG were determined as previously described by us and the others [25, 31, 33].

2.9. Luciferase Reporter Assay. The wild type and truncated 3′-UTR of PHLPP1 across the seed binding region (NM_133821.3) were obtained from GeneCopoeia (Rockville, MD, USA) and amplified using PCR, which were then cloned into the pGL3-Basic plasmid (Promega, Madison, Wisconsin, USA) downstream of the luciferase reporter gene. Next, these plasmids as well as pRL-TK plasmid were transfected into HEK293T cells with or without the miR-299a-5p agomir using Lipofectamine 3000 for 48 h. The luciferase activity was measured using the Dual-Luciferase Report Assay System (Promega) as we recently described, and changes in the ratio of firefly luciferase and Renilla luciferase were measured to evaluate the interaction between miR-299a-5p and PHLPP1 3′-UTR [25, 34, 35].

2.10. Statistical Analysis. Data are expressed as the mean ± standard deviation and analyzed using SPSS 23.0 software. Two-tailed unpaired Student's t-test was used to compare 2 groups, while one-way analysis of variance (ANOVA) followed by the Tukey posthoc test was conducted to compare the differences among 3 or more groups. Before one-way ANOVA analysis, Gaussian distribution was conducted using D'Agostino and Pearson omnibus normality test. $P < 0.05$ was considered statistically significant.

3. Results

3.1. The miR-299a-5p Agomir Prevents SCI in Mice. We first detect the alteration of miR-299a-5p level during SCI. As shown in Figure 1(a), the miR-299a-5p expression in the spinal cord was dramatically reduced by SCI stimulation but partially restored at 14 or 28 days after SCI. To investigate the function of miR-299a-5p, mice were treated with the miR-299a-5p agomir to overexpression its expression in the spinal cord (Figure 1(b)). BMS scoring data indicated that treatment with the miR-299a-5p agomir significantly prevented SCI-induced motor dysfunction in mice (Figure 1(c)). In addition, the hypersensitivity to mechanical and thermal stimulation in SCI mice was also improved by the miR-299a-5p agomir, as determined by the enhanced

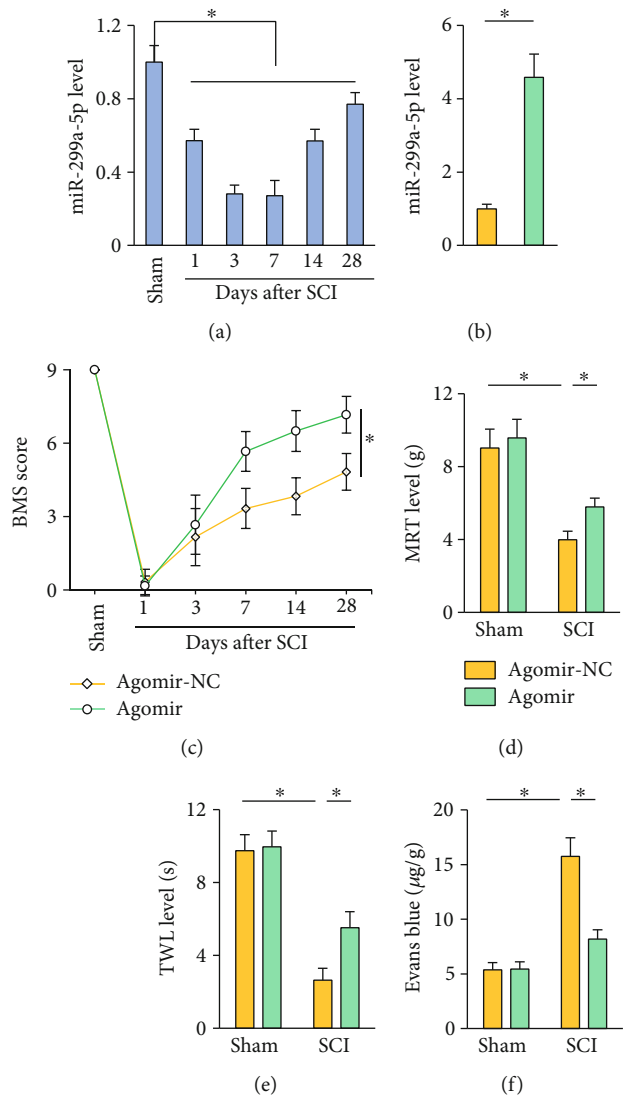

Figure 1: The miR-299a-5p agomir prevents SCI in mice. (a) The expression of miR-299a-5p in the spinal cord after SCI. (b) The expression of miR-299a-5p in mice treated with the miR-299a-5p agomir or agomir-NC. (c) BMS score. (d, e) Sensitivities to mechanical and thermal stimulation. (f) Extravasation of Evans blue dye. $n = 6$ for each groups. Data are expressed as the mean ± standard deviation, and $P < 0.05$ was considered statistically significant.

mechanical response threshold (MRT) and thermal withdrawal latency (TWL) (Figures 1(d) and 1(e)). BSCB disruption contributes to the progression of SCI, and accordingly, we identified a significant leakage of Evans blue dye in SCI mice, which could be alleviated by the miR-299a-5p agomir (Figure 1(f)). Collectively, we demonstrate that the miR-299a-5p agomir prevents SCI in mice.

3.2. The miR-299a-5p Antagomir Exacerbates SCI in Mice. We then investigated whether downregulating the miR-299a-5p expression could further aggravated SCI in mice by treating mice with the miR-299a-5p antagomir (Figure 2(a)). As shown in Figure 2(b), the miR-299a-5p antagomir did not affect motor function under basal conditions but dramatically delayed the recovery of motor function in SCI mice. SCI-induced mechanical allodynia and thermal hypersensitivity were also exacerbated by the miR-299a-5p antagomir (Figure 2(c)). Moreover, treatment with the miR-299a-5p antagomir further disrupted BSCB integrity upon SCI surgery, as evidenced by the increased leakage of Evans blue dye (Figure 2(d)). Collectively, we demonstrate that the miR-299a-5p antagomir exacerbates SCI in mice.

3.3. The miR-299a-5p Agomir Inhibits SCI-Induced Inflammation and NLRP3 Inflammasome. Inflammation contributes to the progression of SCI, and we then evaluated whether it is involved in the protective role against SCI by the miR-299a-5p agomir. MPO activity, an index to determine neutrophils infiltration, was significantly increased in SCI mice but decreased in those treated with the miR-299a-5p agomir (Figure 3(a)). And the miR-299a-5p agomir also reduced IL-6 and TNF-α levels in the spinal cord from SCI mice (Figure 3(b)). NF-κB is a central transcriptional factor to elicit the expression of multiple proinflammatory

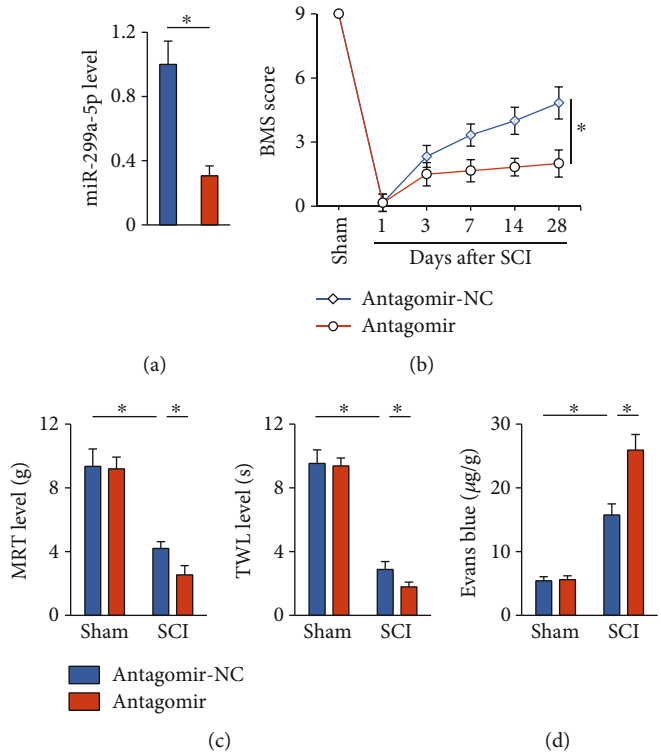

FIGURE 2: The miR-299a-5p antagomir exacerbates SCI in mice. (a) The expression of miR-299a-5p in mice treated with the miR-299a-5p antagomir or antagomir-NC. (b) BMS score. (c) Sensitivities to mechanical and thermal stimulation. (d) Extravasation of Evans blue dye. $n = 6$ for each groups. Data are expressed as the mean ± standard deviation, and $P < 0.05$ was considered statistically significant.

cytokines, and its activation accelerates the development of SCI [3, 36]. And we found that treatment with the miR-299a-5p agomir dramatically suppressed p65 phosphorylation and activation (Figures 3(c) and 3(d)). NLRP3 inflammasome is essential for the processing, maturation, and secretion of intracellular proinflammatory cytokines (e.g., IL-1β and IL-18) and participates SCI-induced inflammation and motor dysfunction [2, 37]. Intriguingly, the expression and activity of NLRP3 inflammasome components were evidently reduced in the miR-299a-5p agomir-treated SCI mice, as determined by the decreased NLRP3, ASC, and casp1 p10 expression and casp1 activity (Figures 3(e) and 3(f)). Accordingly, the levels of IL-1β and IL-18 in SCI mice were also reduced by the miR-299a-5p agomir (Figure 3(g)). Taken together, our findings reveal that the miR-299a-5p agomir inhibits SCI-induced inflammation and NLRP3 inflammasome.

3.4. The miR-299a-5p Agomir Suppresses SCI-Induced Oxidative Stress. Oxidative stress is another feature and pathological factor of SCI. As expected, SCI surgery significantly increased the level of ROS in the spinal cord, as indicated by the elevated ROS, hydrogen peroxide, and superoxide anion levels, which were all reduced in the presence of the miR-299a-5p agomir (Figures 4(a) and 4(b)). Excessive ROS triggers peroxidation of lipid, protein, and nucleic acid, eventually leading neuron loss and motor dysfunction during SCI. As shown in Figure 4(c), treatment with the miR-299a-5p agomir significantly reduced the levels of MDA, 3-NT, and 8-OHdG. NRF2 plays critical roles in orchestrating the transcription of various antioxidant enzymes, and its suppression contributes to the progression of SCI. In line with the decreased oxidative stress, we found that the miR-299a-5p agomir dramatically restored the NRF2 expression in SCI mice (Figures 4(d) and 4(e)). Besides, NRF2 transcriptional activity was enhanced in the miR-299a-5p agomir-treated SCI mice, as further confirmed by the increased mRNA levels of downstream targets, including NQO-1, SOD2, and CAT (Figures 4(f) and 4(g)). Accordingly, SCI-induced suppression on TAOC and total SOD activity was significantly prevented by the miR-299a-5p agomir (Figure 4(h)). These data indicate that the miR-299a-5p agomir suppresses SCI-induced oxidative stress.

3.5. The miR-299a-5p Antagomir Exacerbates SCI-Induced Inflammation and Oxidative Stress. In contrast with the protective phenotypes in the miR-299a-5p agomir-treated SCI mice, we found that treatment with the miR-299a-5p antagomir significantly promoted neutrophil infiltration to the spinal cord upon SCI stimulation (Figure 5(a)). Accordingly, SCI-induced elevations of IL-6, TNF-α, IL-1β, and IL-18 levels were also amplified in the presence of the miR-299a-5p antagomir (Figures 5(b) and 5(c)). In addition, the miR-299a-5p antagomir-treated mice also exhibited increased oxidative stress under SCI stress, as evidenced by the increased ROS, MDA, 3-NT, and 8-OHdG productions and decreased TAOC level (Figures 5(d)–5(f)). Yet, no difference of survival rate was observed between groups (data

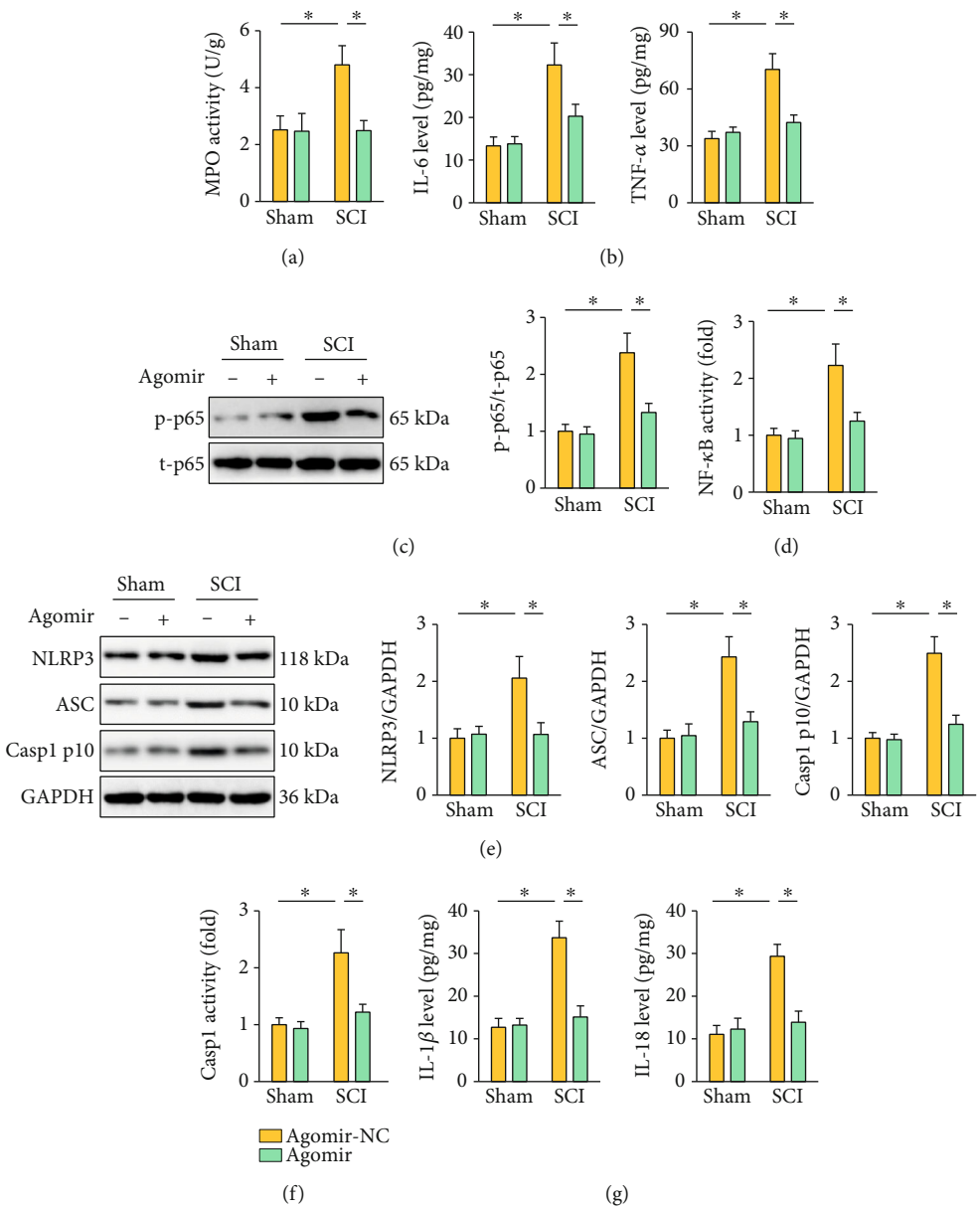

Figure 3: The miR-299a-5p agomir inhibits SCI-induced inflammation and NLRP3 inflammasome. (a) MPO activity in the spinal cord from mice treated with the miR-299a-5p agomir or agomir-NC. (b) IL-6 and TNF-α levels in the spinal cord. (c) Western blot images and quantification of p65 phosphorylation. (d) Relative NF-κB transcriptional activity. (e) Western blot images and quantification of NLRP3, ASC, and casp1 p10. (f) Relative casp1 activity. (g) IL-1β and IL-18 levels in the spinal cord. $n = 6$ for each groups. Data are expressed as the mean ± standard deviation, and $P < 0.05$ was considered statistically significant.

not shown). Taken together, we suppose that the miR-299a-5p antagomir exacerbates SCI-induced inflammation and oxidative stress.

3.6. The miR-299a-5p Agomir Protects against SCI in Mice through Activating AMPK. Given the multifunctional role of AMPK and its involvement in the pathogenesis of SCI, we then tried to investigate whether the miR-299a-5p agomir prevented SCI through activating AMPK. As shown in Figures 6(a) and 6(b), the miR-299a-5p agomir increased, while the miR-299a-5p antagomir decreased AMPK phosphorylation in SCI mice. To further validate the necessity of AMPK, SCI mice were treated with CC to inhibit AMPK. Intriguingly, CC treatment completely blocked the inhibitory role of the miR-299a-5p agomir on SCI-induced inflammation, as evidenced by the increased IL-6, TNF-α, IL-1β, and IL-18 levels (Figures 6(c) and 6(d)). In addition, the miR-299a-5p agomir failed to suppress oxidative stress in SCI mice in the presence with CC (Figures 6(e) and 6(f)). In line with the molecular alterations, CC treatment abrogated the miR-299a-5p agomir-mediated protections against SCI-induced motor dysfunction, mechanical allodynia, and thermal hypersensitivity (Figures 6(g) and 6(h)). And BSCB disruption was further exacerbated in the miR-299a-5p

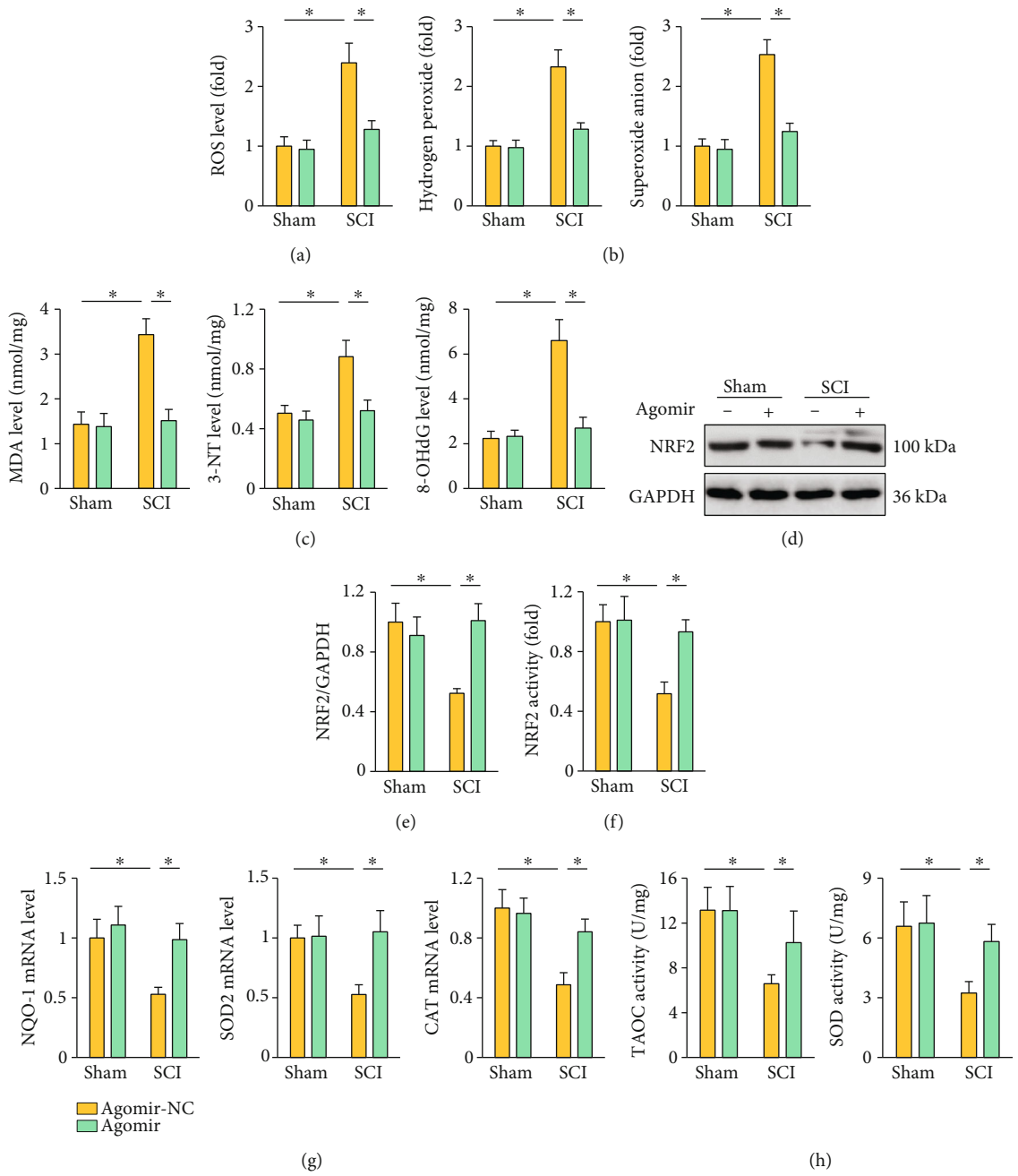

Figure 4: The miR-299a-5p agomir suppresses SCI-induced oxidative stress. (a) ROS level detected by DCFH-DA probe. (b) Quantification of hydrogen peroxide and superoxide anion in the spinal cord. (c) The levels of MDA, 3-NT, and 8-OHdG. (d)–(f) Relative levels of NRF2 protein and transcriptional activity. (g) The mRNA levels of NQO-1, SOD2, and CAT in the spinal cord. (h) Quantification of TAOC and total SOD activities. $n = 6$ for each groups. Data are expressed as the mean ± standard deviation, and $P < 0.05$ was considered statistically significant.

agomir-treated SCI mice by CC, as confirmed by the increased Evans blue leakage to spinal cord (Figure 6(i)). Our findings suggest that the miR-299a-5p agomir protects against SCI in mice through activating AMPK.

3.7. The miR-299a-5p Agomir Activates AMPK through Downregulating PHLPP1. Finally, we explored the possible mechanism through which the miR-299a-5p agomir activated AMPK. Using the online TargetScan software, PHLPP1 was selected for further investigation due to its role in dephosphorylating AMPK and tissue injury [38, 39]. As shown in Figure 7(a), a conserved binding site was found in the PHLPP1 3′-UTR. And results using luciferase reporter assay further validate the directly interaction between miR-299a-5p and PHLPP1 3′-UTR (Figure 7(b)). In addition, the protein and mRNA levels of PHLPP1 in

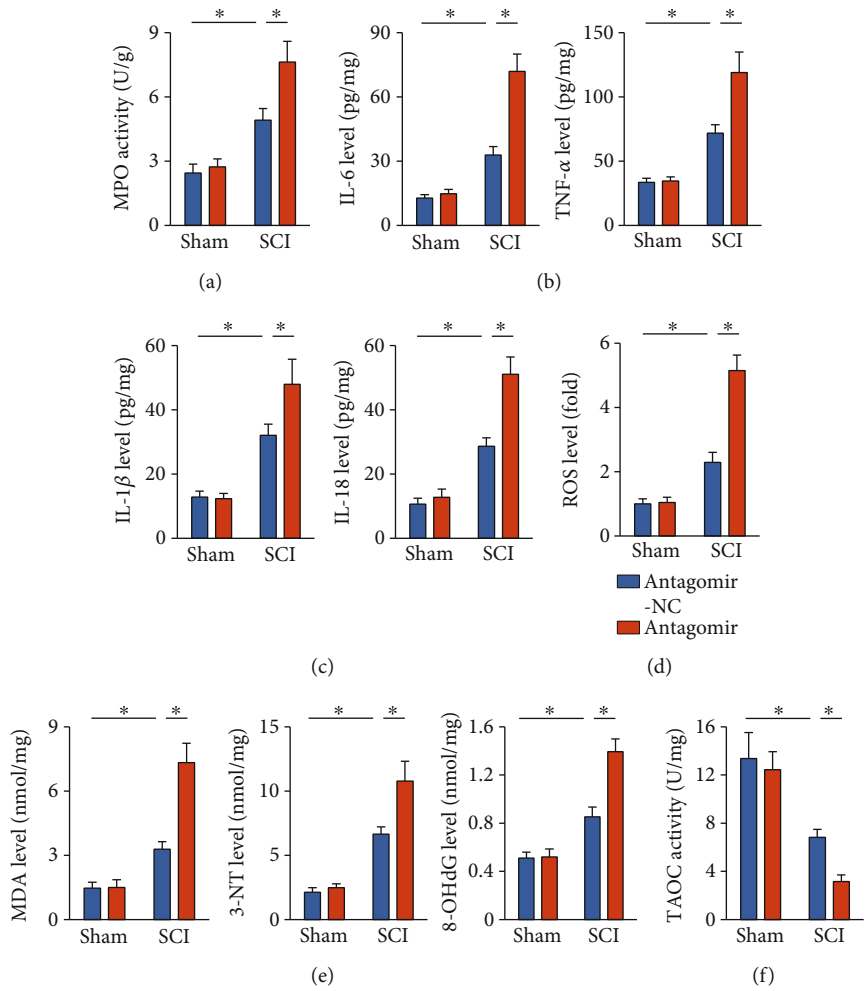

Figure 5: The miR-299a-5p antagomir exacerbates SCI-induced inflammation and oxidative stress. (a) MPO activity in the spinal cord from mice treated with the miR-299a-5p antagomir or antagomir-NC. (b) IL-6 and TNF-α levels in the spinal cord. (c) IL-1β and IL-18 levels in the spinal cord. (d) ROS level detected by DCFH-DA probe. (e) The levels of MDA, 3-NT, and 8-OHdG. (f) Quantification of TAOC activity. $n = 6$ for each groups. Data are expressed as the mean ± standard deviation, and $P < 0.05$ was considered statistically significant.

SCI mice were decreased by the miR-299a-5p agomir, while increased by the miR-299a-5p antagomir (Figures 7(c)–7(e)). To validate the necessity of PHLPP1 in regulating AMPK by miR-299a-5p, mice were injected with lentiviral vectors to overexpress PHLPP1 in vivo, and the efficiency was presented in Figure 7(f). As shown in Figure 7(g), the PHLPP1 overexpression completely abrogated the miR-299a-5p agomir-mediated AMPK activation in SCI mice. And the antiinflammatory and antioxidant capacities of the miR-299a-5p agomir were blocked in PHLPP1-overexpressed SCI mice (Figures 7(h) and 7(i)). Accordingly, the PHLPP1 overexpression abolished the miR-299a-5p agomir-mediated protective effects against SCI-induced motor dysfunction, mechanical allodynia, and thermal hypersensitivity (Figures 7(j)–7(l)). And BSCB disruption was further exacerbated in the miR-299a-5p agomir-treated SCI mice by the PHLPP1 overexpression (Figure 7(m)). In general, we prove that the miR-299a-5p agomir activates AMPK through downregulating PHLPP1.

4. Discussion

SCI is a devastating neurotrauma with severe and insufferable sequelae, such as motor deficits, neuropathic pain, and hypersensitivity. The present study found that the miR-299a-5p expression was downregulated during SCI, and that the miR-299a-5p agomir dramatically prevented SCI-induced inflammation, oxidative stress, and motor and sensory dysfunction. Conversely, treatment with the miR-299a-5p antagomir further exacerbated SCI in mice. Mechanistically, we observed that the miR-299a-5p agomir activated, while the miR-299a-5p antagomir inhibited AMPK pathway in SCI mice, and that AMPK inhibitor completely blocked the beneficial effects of the miR-299a-5p agomir in vivo. Further findings identified a conserved binding site of miR-299a-5p in PHLPP1 3′-UTR, and treatment with the miR-299a-5p agomir significantly decreased the PHLPP1 expression in SCI mice. Yet, the PHLPP1 overexpression blocked AMPK activation by the miR-299a-5p agomir in

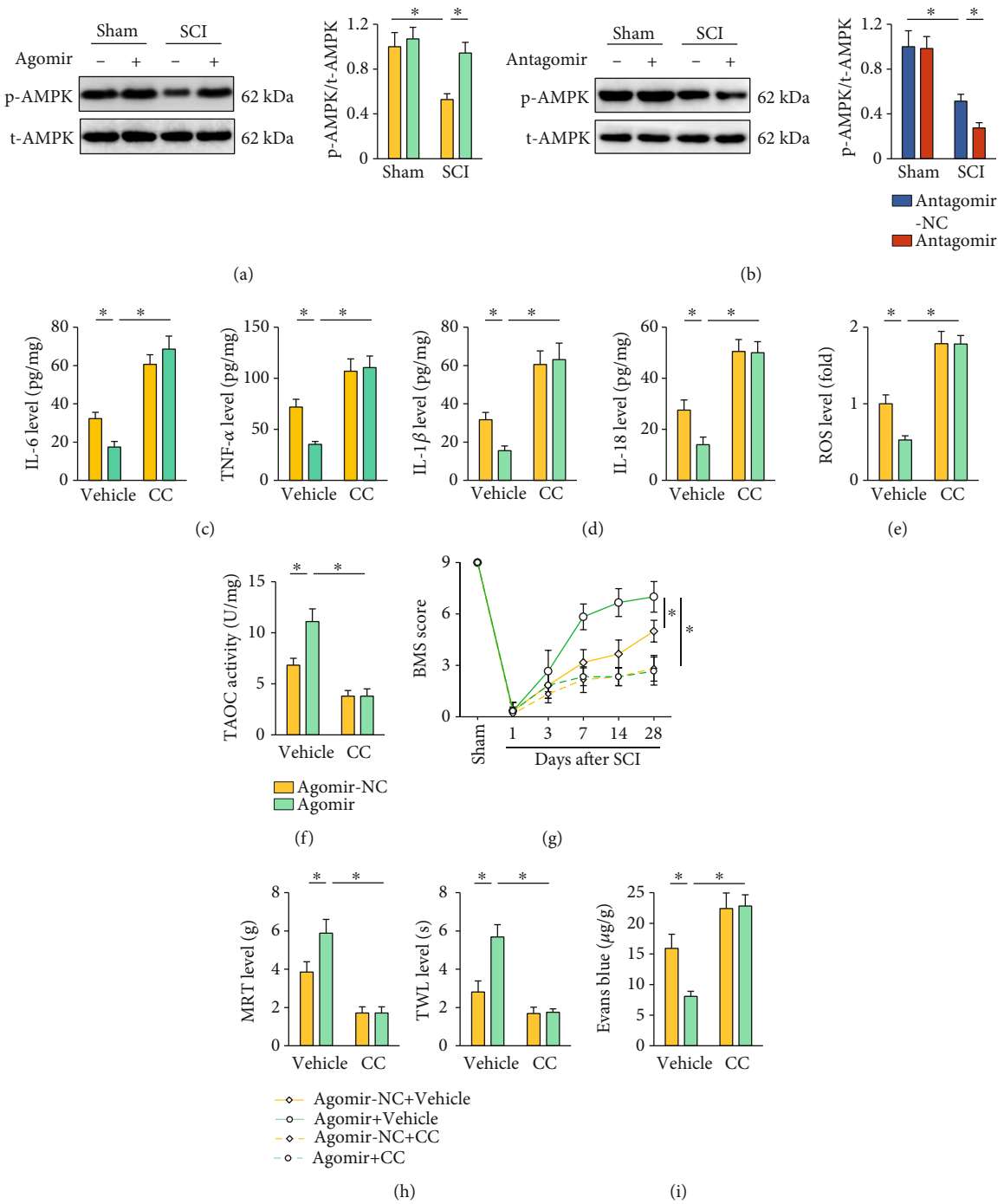

FIGURE 6: The miR-299a-5p agomir protects against SCI in mice through activating AMPK. (a, b) Western blot images and quantification of AMPK phosphorylation in mice treated with the miR-299a-5p agomir or antagomir. (c) IL-6 and TNF-α levels in the spinal cord. (d) IL-1β and IL-18 levels in the spinal cord. (e) ROS level detected by DCFH-DA probe. (f) Quantification of TAOC activity. $n = 6$ for each groups. (g) BMS score. (h) Sensitivities to mechanical and thermal stimulation. (i) Extravasation of Evans blue dye. $n = 6$ for each groups. Data are expressed as the mean ± standard deviation, and $P < 0.05$ was considered statistically significant.

SCI mice, accompanied by an increased inflammation and oxidative stress. To the best of our knowledge, this is the first study about the pathophysiological role and molecular basis of miR-299a-5p during SCI progression.

Inflammation, manifested as extensive microglia cell activation and infiltrations of leukocytes, is a key feature and pathogenic factor of SCI [1]. Upon SCI, microglia cells are activated to synthetize multiple proinflammatory cytokines, which in turn recruit the infiltration of peripheral immune cells to the lesion and further amplify the inflammatory response [40]. The BSCB plays critical roles in controlling the movement of molecules, liquids, or cells between blood vessels and spinal cord, and its structural and functional integrities are required for the

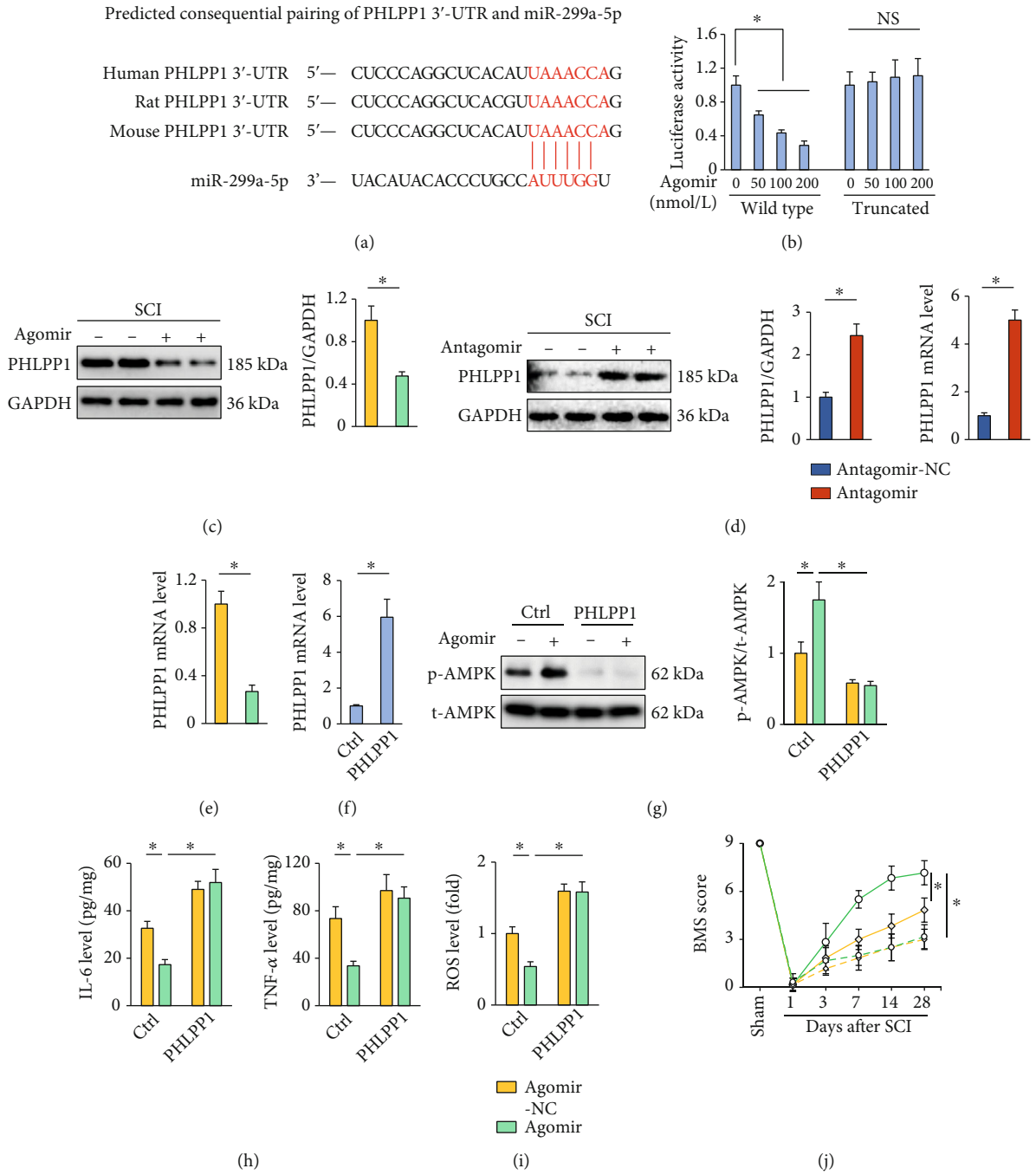

Figure 7: Continued.

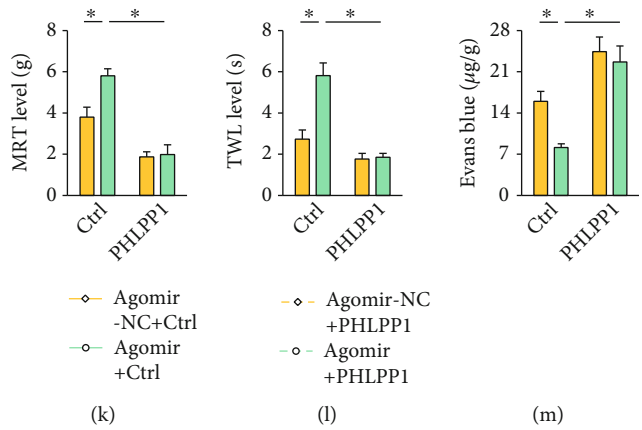

Figure 7: The miR-299a-5p agomir activates AMPK through downregulating PHLPP1. (a) The PHLPP1 3′-UTR contains a conserved binding site for miR-299a-5p. (b) The luciferase assay indicated that miR-299a-5p directly bound to the PHLPP1 3′-UTR. (c)–(e) Quantification of PHLPP1 protein and mRNA levels in SCI mice treated with the agomir, antagomir, or matched NC of miR-299a-5p. (f) The mRNA levels of PHLPP1 in mice with or without PHLPP1 overexpression. (g) Western blot images and quantification of AMPK phosphorylation in the miR-299a-5p agomir-treated mice with or without PHLPP1 overexpression. (h) IL-6 and TNF-α levels in the spinal cord. (i) ROS level detected by DCFH-DA probe. (j) BMS score. (k, l) Sensitivities to mechanical and thermal stimulation. (m) Extravasation of Evans blue dye. $n = 6$ for each groups. Data are expressed as the mean ± standard deviation, and $P < 0.05$ was considered statistically significant.

microenvironment homeostasis of the spinal cord. However, BSCB breakdown occurs as early as 5 min after SCI, accompanied by the infiltration of neutrophils and macrophages to the spinal cord [41]. The present study demonstrated that treatment with the miR-299a-5p agomir could prevent SCI-induced BSCB disruption and tissue inflammation in mice. NLRP3 inflammasome is essential for the processing and maturation of proinflammatory cytokines, and its activation contributes to SCI progression. Previous studies have shown that NLRP3 inactivation dramatically protects against motor dysfunction and sensory hypersensitivity in SCI mice [2, 4]. Consistently, we herein observed that SCI-induced activation of NLRP3 inflammasome was blunted by the miR-299a-5p agomir, accompanied by reduced IL-1β and IL-18 expressions in the spinal cord. Apart from inflammation, excessive ROS functions as another contributor of SCI. Findings from us and other laboratories have shown that the endogenous antioxidant capacities were suppressed by SCI surgery, followed by uncontrolled ROS generation [2, 3]. In addition, neurons in the spinal cord are especially vulnerable to free radicals due to the negligible regenerative capacities. Moreover, ROS overproduction also triggers the dissociation of thioredoxin interacting protein from thioredoxin, which subsequently interacts with and activates NLRP3 inflammasome [42]. Our findings revealed that SCI-induced inflammation and oxidative stress were dramatically reduced by the miR-299a-5p agomir.

miR-299a-5p is identified as a tumor suppressor in various human cancers, including breast cancer, hepatocellular cancer, thyroid cancer, and colorectal cancer [18, 43]. Yet, very few studies have been down in the context of noncancer diseases. Huang et al. previously demonstrated that miR-299a-5p was downregulated in human islets and β-cell under glucolipotoxic conditions, and that miR-299a-5p inhibition promoted β-cell apoptosis and impaired β-cell function in glucolipotoxic settings [44]. Herein, we found that the miR-299a-5p expression was decreased in the spinal cord upon SCI stimulation. The miR-299a-5p agomir alleviated, while the miR-299a-5p antagomir further exacerbated inflammation, oxidative stress, motor dysfunction, and sensory hypersensitivity in SCI mice. Mechanistically, we identified PHLPP1 as a direct target of miR-299a-5p in regulating AMPK and SCI. PHLPP1 is a novel serine/threonine protein phosphatase and directly dephosphorylates many downstream kinases, such as AKT and STAT1 [39, 45]. Behera et al. previously demonstrated that PHLPP1 also interacted with and directly dephosphorylated AMPK Thr172 in myoblasts without influencing its conventional upstream kinase [38]. Consistently, Balamurugan et al. recently also found that the overexpression of PHLPP1 significantly reduced the phosphorylation of AMPK Thr172 [46]. PHLPP1 is traditionally identified to participate in the pathogenesis of various human tumors; however, emerging studies reveal that it also plays critical roles in regulating inflammation, oxidative stress, and tissue injury. Wen et al. previously demonstrated that PHLPP1 deletion protected intestinal epithelial cells against inflammation-induced apoptosis and improved colitis in mice [47]. And PHLPP1 deficiency also reduced inflammation and prevented cardiomyocyte death and cardiac dysfunction [48]. Consistently, we found that PHLPP1 suppression evidently blocked SCI-induced inflammation and NLRP3 inflammasome in mice. Additionally, Mathur et al. found that PHLPP1 silence enhanced NRF2 expression and nuclear localization, thereby alleviating high glucose-induced oxidative stress and apoptosis during diabetic nephropathy [49]. And results from Zhang et al. also indicated that PHLPP1 knockdown promoted the nuclear expression and transcriptional activity of NRF2, preventing oxidative stress and apoptosis in high glucose-treated retinal ganglion cells [50]. In line with these

findings, we also found that PHLPP1 inhibition by the miR-299a-5p agomir significantly elevated the NRF2 expression and transcriptional activity in SCI mice, thereby reducing oxidative damage in SCI mice.

In summary, our study identifies an involvement of miR-299a-5p in SCI progression.

Data Availability

Data supporting the findings of this work are available from the corresponding author upon reasonable request.

Conflicts of Interest

The authors declare that they have no competing interests.

References

[1] N. A. Silva, N. Sousa, R. L. Reis, and A. J. Salgado, "From basics to clinical: a comprehensive review on spinal cord injury," *Progress in Neurobiology*, vol. 114, pp. 25–57, 2014.

[2] J. Qian, W. Zhu, M. Lu, B. Ni, and J. Yang, "D-β-Hydroxybutyrate promotes functional recovery and relieves pain hypersensitivity in mice with spinal cord injury," *British Journal of Pharmacology*, vol. 174, no. 13, pp. 1961–1971, 2017.

[3] X. Ge, P. Tang, Y. Rong et al., "Exosomal miR-155 from M1-polarized macrophages promotes EndoMT and impairs mitochondrial function via activating NF-κB signaling pathway in vascular endothelial cells after traumatic spinal cord injury," *Redox Biology*, vol. 41, article 101932, 2021.

[4] Z. Liu, X. Yao, B. Sun et al., "Pretreatment with kaempferol attenuates microglia-mediate neuroinflammation by inhibiting MAPKs-NF-κB signaling pathway and pyroptosis after secondary spinal cord injury," *Free Radical Biology & Medicine*, vol. 168, pp. 142–154, 2021.

[5] C. Hu, X. Zhang, W. Wei et al., "Matrine attenuates oxidative stress and cardiomyocyte apoptosis in doxorubicin-induced cardiotoxicity _via_ maintaining AMPK _α_ /UCP2 pathway," *Acta Pharmaceutica Sinica B*, vol. 9, no. 4, pp. 690–701, 2019.

[6] L. Yang, X. Li, A. Jiang et al., "Metformin alleviates lead-induced mitochondrial fragmentation via AMPK/Nrf2 activation in SH-SY5Y cells," *Redox Biology*, vol. 36, article 101626, 2020.

[7] T. Zhang, J. Liu, S. Shen, Q. Tong, X. Ma, and L. Lin, "SIRT3 promotes lipophagy and chaperon-mediated autophagy to protect hepatocytes against lipotoxicity," *Cell Death and Differentiation*, vol. 27, no. 1, pp. 329–344, 2020.

[8] X. Zhang, Z. G. Ma, Y. P. Yuan et al., "Rosmarinic acid attenuates cardiac fibrosis following long-term pressure overload via AMPKα/Smad3 signaling," *Cell Death & Disease*, vol. 9, no. 2, pp. 1–14, 2018.

[9] X. Jiang, Z. Shen, J. Chen et al., "Irisin protects against motor dysfunction of rats with spinal cord injury via adenosine 5'-monophosphate (AMP)-activated protein kinase-nuclear factor kappa-B pathway," *Frontiers in Pharmacology*, vol. 11, article 582484, 2020.

[10] W. L. Jiang, K. C. Zhao, W. Yuan et al., "MicroRNA-31-5p exacerbates lipopolysaccharide-induced acute lung injury via inactivating Cab39/AMPKαPathway," *Oxidative Medicine and Cellular Longevity*, vol. 2020, Article ID 8822361, 14 pages, 2020.

[11] P. Wan, W. Su, Y. Zhang et al., "LncRNA H19 initiates microglial pyroptosis and neuronal death in retinal ischemia/reperfusion injury," *Cell Death and Differentiation*, vol. 27, no. 1, pp. 176–191, 2020.

[12] Q. Gao, G. Zhang, Y. Zheng et al., "SLC27A5 deficiency activates NRF2/TXNRD1 pathway by increased lipid peroxidation in HCC," *Cell Death and Differentiation*, vol. 27, no. 3, pp. 1086–1104, 2020.

[13] G. Warpsinski, M. J. Smith, S. Srivastava et al., "Nrf2-regulated redox signaling in brain endothelial cells adapted to physiological oxygen levels: consequences for sulforaphane mediated protection against hypoxia-reoxygenation," *Redox Biology*, vol. 37, article 101708, 2020.

[14] H. Hu, N. Xia, J. Lin et al., "Zinc regulates glucose metabolism of the spinal cord and neurons and promotes functional recovery after spinal cord injury through the AMPK signaling pathway," *Oxidative Medicine and Cellular Longevity*, vol. 2021, Article ID 4331625, 27 pages, 2021.

[15] J. Qiao, J. Zhao, S. Chang et al., "MicroRNA-153 improves the neurogenesis of neural stem cells and enhances the cognitive ability of aged mice through the notch signaling pathway," *Cell Death and Differentiation*, vol. 27, no. 2, pp. 808–825, 2020.

[16] L. L. Lv, Y. Feng, M. Wu et al., "Exosomal miRNA-19b-3p of tubular epithelial cells promotes M1 macrophage activation in kidney injury," *Cell Death and Differentiation*, vol. 27, no. 1, pp. 210–226, 2020.

[17] S. Ni, Z. Luo, L. Jiang et al., "UTX/KDM6A deletion promotes recovery of spinal cord injury by epigenetically regulating vascular regeneration," *Molecular Therapy*, vol. 27, no. 12, pp. 2134–2146, 2019.

[18] Z. Wang, L. He, W. Sun et al., "miRNA-299-5p regulates estrogen receptor alpha and inhibits migration and invasion of papillary thyroid cancer cell," *Cancer Management and Research*, vol. 10, pp. 6181–6193, 2018.

[19] J. Sun, X. Cai, J. Shen, G. Jin, and Q. Xie, "Correlation between single nucleotide polymorphisms at the 3′-UTR of theNFKB1-gene and Acute kidney injury in sepsis," *Genetic Testing and Molecular Biomarkers*, vol. 24, no. 5, pp. 274–284, 2020.

[20] K. A. Padgett, R. Y. Lan, P. C. Leung et al., "Primary biliary cirrhosis is associated with altered hepatic microRNA expression," *Journal of Autoimmunity*, vol. 32, no. 3-4, pp. 246–253, 2009.

[21] H. Liu, J. Zhang, X. Xu et al., "SARM1 promotes neuroinflammation and inhibits neural regeneration after spinal cord injury through NF-κB signaling," *Theranostics*, vol. 11, no. 9, pp. 4187–4206, 2021.

[22] B. Sabirzhanov, J. Matyas, M. Coll-Miro et al., "Inhibition of microRNA-711 limits angiopoietin-1 and Akt changes, tissue damage, and motor dysfunction after contusive spinal cord injury in mice," *Cell Death & Disease*, vol. 10, no. 11, pp. 1–14, 2019.

[23] M. Patel, Y. Li, J. Anderson et al., "Gsx1 promotes locomotor functional recovery after spinal cord injury," *Molecular Therapy*, vol. 29, no. 8, pp. 2469–2482, 2021.

[24] X. Zhang, C. Hu, Y. P. Yuan et al., "Endothelial ERG alleviates cardiac fibrosis via blocking endothelin-1-dependent paracrine mechanism," *Cell Biology and Toxicology*, vol. 37, no. 6, pp. 873–890, 2021.

[25] C. Bao, J. Zhang, S. Y. Xian, and F. Chen, "MicroRNA-670-3p suppresses ferroptosis of human glioblastoma cells through targeting ACSL4," *Free Radical Research*, vol. 55, no. 7, pp. 853–864, 2021.

[26] X. Zhang, C. Hu, N. Zhang et al., "Matrine attenuates pathological cardiac fibrosis via RPS5/p38 in mice," *Acta Pharmacologica Sinica*, vol. 42, no. 4, pp. 573–584, 2021.

[27] C. Hu, X. Zhang, N. Zhang et al., "Osteocrin attenuates inflammation, oxidative stress, apoptosis, and cardiac dysfunction in doxorubicin-induced cardiotoxicity," *Clinical and Translational Medicine*, vol. 10, no. 3, article e124, 2020.

[28] W. Zhan, X. Liao, Z. Chen et al., "LINC00858 promotes colorectal cancer by sponging miR-4766-5p to regulate PAK2," *Cell Biology and Toxicology*, vol. 36, no. 4, pp. 333–347, 2020.

[29] Y. Zhu, L. Yang, J. Xu et al., "Discovery of the anti-angiogenesis effect of eltrombopag in breast cancer through targeting of HuR protein," *Acta Pharmaceutica Sinica B*, vol. 10, no. 8, pp. 1414–1425, 2020.

[30] X. Zhang, C. Hu, X. P. Yuan et al., "Osteocrin, a novel myokine, prevents diabetic cardiomyopathy via restoring proteasomal activity," *Cell Death & Disease*, vol. 12, no. 7, pp. 1–12, 2021.

[31] X. Zhang, C. Hu, C. Y. Kong et al., "FNDC5 alleviates oxidative stress and cardiomyocyte apoptosis in doxorubicin-induced cardiotoxicity via activating AKT," *Cell Death and Differentiation*, vol. 27, no. 2, pp. 540–555, 2020.

[32] C. Hu, X. Zhang, P. Song et al., "Meteorin-like protein attenuates doxorubicin-induced cardiotoxicity via activating cAMP/PKA/SIRT1 pathway," *Redox Biology*, vol. 37, article 101747, 2020.

[33] C. Hu, X. Zhang, M. Hu et al., "Fibronectin type III domain-containing 5 improves aging-related cardiac dysfunction in mice," *Aging Cell*, vol. 21, no. 3, article e13556, 2022.

[34] X. Han, H. Jiang, J. Qi et al., "Novel lncRNA UPLA1 mediates tumorigenesis and prognosis in lung adenocarcinoma," *Cell Death & Disease*, vol. 11, no. 11, pp. 1–12, 2020.

[35] T. Valente, G. Dentesano, M. Ezquerra et al., "CCAAT/enhancer binding protein δ is a transcriptional repressor of α-synuclein," *Cell Death and Differentiation*, vol. 27, no. 2, pp. 509–524, 2020.

[36] E. Sanchez-Lopez, E. M. Ghia, L. Antonucci et al., "NF-κB-p62-NRF2 survival signaling is associated with high ROR1 expression in chronic lymphocytic leukemia," *Cell Death and Differentiation*, vol. 27, no. 7, pp. 2206–2216, 2020.

[37] C. Zeng, F. Duan, J. Hu et al., "NLRP3 inflammasome-mediated pyroptosis contributes to the pathogenesis of non-ischemic dilated cardiomyopathy," *Redox Biology*, vol. 34, article 101523, 2020.

[38] S. Behera, B. Kapadia, V. Kain et al., "ERK1/2 activated PHLPP1 induces skeletal muscle ER stress through the inhibition of a novel substrate AMPK," *Biochimica et Biophysica Acta - Molecular Basis of Disease*, vol. 1864, pp. 1702–1716, 2018.

[39] K. C. Katsenelson, J. D. Stender, A. T. Kawashima et al., "PHLPP1 counter-regulates STAT1-mediated inflammatory signaling," *eLife*, vol. 8, article 48609, 2019.

[40] W. Liu, P. Tang, J. Wang et al., "Extracellular vesicles derived from melatonin-preconditioned mesenchymal stem cells containing USP29 repair traumatic spinal cord injury by stabilizing NRF2," *Journal of Pineal Research*, vol. 71, no. 4, article e12769, 2021.

[41] P. J. Horner, P. G. Popovich, B. B. Mullin, and B. T. Stokes, "A quantitative spatial analysis of the blood-spinal cord barrier: II. Permeability after intraspinal fetal transplantation," *Experimental Neurology*, vol. 142, no. 2, pp. 226–243, 1996.

[42] X. Dai, R. Liao, C. Liu et al., "Epigenetic regulation of TXNIP-mediated oxidative stress and NLRP3 inflammasome activation contributes to SAHH inhibition-aggravated diabetic nephropathy," *Redox Biology*, vol. 45, article 102033, 2021.

[43] L. A. Shevde, B. J. Metge, A. Mitra et al., "Spheroid-forming subpopulation of breast cancer cells demonstrates vasculogenic mimicry via hsa-miR-299-5p regulated de novo expression of osteopontin," *Journal of Cellular and Molecular Medicine*, vol. 14, no. 6B, pp. 1693–1706, 2010.

[44] Q. Huang, W. You, Y. Li et al., "Glucolipotoxicity-inhibited-miR-299-5pregulates pancreatic β-cell function and survival," *Diabetes*, vol. 67, no. 11, pp. 2280–2292, 2018.

[45] B. Lupse, K. Annamalai, H. Ibrahim et al., "Inhibition of PHLPP1/2 phosphatases rescues pancreatic β-cells in diabetes," *Cell Reports*, vol. 36, no. 5, article 109490, 2021.

[46] B. Keerthana, R. Medishetti, J. Kotha et al., "PHLPP1 promotes neutral lipid accumulation through AMPK/ChREBP-dependent lipid uptake and fatty acid synthesis pathways," *iScience*, vol. 25, no. 2, article 103766, 2022.

[47] Y. A. Wen, X. Li, T. Goretsky, H. L. Weiss, T. A. Barrett, and T. Gao, "Loss of PHLPP protects against colitis by inhibiting intestinal epithelial cell apoptosis," *Biochimica et Biophysica Acta*, vol. 1852, no. 10, pp. 2013–2023, 2015.

[48] Y. Tan, T. Li, M. Hu et al., "PHLPP1 deficiency ameliorates cardiomyocyte death and cardiac dysfunction through inhibiting Mcl-1 degradation," *Cellular Signalling*, vol. 92, article 110281, 2022.

[49] A. Mathur, V. K. Pandey, and P. Kakkar, "Activation of GSK3β/β-TrCP axis via PHLPP1 exacerbates Nrf2 degradation leading to impairment in cell survival pathway during diabetic nephropathy," *Free Radical Biology & Medicine*, vol. 120, pp. 414–424, 2018.

[50] X. Zhang, Y. Lu, N. He, and F. Wang, "Downregulation of PHLPP1 ameliorates high glucose-evoked injury in retinal ganglion cells by attenuating apoptosis and oxidative stress through enhancement of Nrf2 activation," *Experimental Cell Research*, vol. 397, no. 2, article 112344, 2020.

Hindawi
Oxidative Medicine and Cellular Longevity
Volume 2022, Article ID 4139330, 23 pages
https://doi.org/10.1155/2022/4139330

Research Article

URB597 and Andrographolide Improve Brain Microvascular Endothelial Cell Permeability and Apoptosis by Reducing Oxidative Stress and Inflammation Associated with Activation of Nrf2 Signaling in Oxygen-Glucose Deprivation

Da-Peng Wang,[1] **Kai Kang**,[2] **Jun Sun**,[1] **Qi Lin**,[3] **Qiao-Li Lv**,[4] **and Jian Hai**[1]

[1]*Department of Neurosurgery, Tong Ji Hospital, School of Medicine, Tong Ji University, Shanghai 200065, China*
[2]*Department of Research and Surveillance Evaluation, Shanghai Center for Health Promotion, Shanghai 200040, China*
[3]*Department of Pharmacy, Institutes of Medical Sciences, Shanghai Jiao Tong University School of Medicine, Shanghai 200025, China*
[4]*Department of Head and Neck Surgery, Jiangxi Key Laboratory of Translational Cancer Research, Jiangxi Cancer Hospital, Nanchang University, Jiangxi 330029, China*

Correspondence should be addressed to Qiao-Li Lv; lvqiaoli2008@126.com and Jian Hai; haijiandoct@zoho.com.cn

Received 7 December 2021; Revised 17 April 2022; Accepted 21 April 2022; Published 12 May 2022

Academic Editor: Francisco Rios

Ischemic stroke, a cerebrovascular disease worldwide, triggers a cascade of pathophysiological events, including blood-brain barrier (BBB) breakdown. Brain microvascular endothelial cells (BMECs) play a vital role in maintaining BBB function. The injury of BMECs may worsen neurovascular dysfunction and patients' prognosis. Therefore, uncover the principal molecular mechanisms involved in BBB disruption in stroke becomes pressing. The endocannabinoid system (ECS) has been implicated in increasingly physiological functions, both in neurometabolism and cerebrovascular regulation. Modulating its activities by the fatty acid amide hydrolase (FAAH) shows anti-inflammatory characteristics. Andrographolide (AG), one Chinese herbal ingredient, has also attracted attention for its role in immunomodulatory and as a therapeutic target in BBB disorders. Recently, the FAAH inhibitor URB597 and AG have important regulatory effects on neuronal and vascular cells in ischemia. However, the effects of URB597 and AG on BMEC permeability and apoptosis in oxygen-glucose deprivation (OGD) and the underlying mechanisms remain unclear. To address these issues, cultured BMECs (bEnd.3 cells) were exposed to OGD. The cell viability, permeability, tube formation, and apoptosis were assessed following treatment with URB597, AG, and cotreatment. Mitochondrial membrane potential (MMP), reactive oxygen species (ROS), superoxide dismutase (SOD), catalase (CAT), malondialdehyde (MDA), proinflammatory factors, tight junction (TJ) proteins, and oxidative stress-mediated Nrf2 signaling were also investigated. Results revealed that OGD broke the endothelial barrier, cell viability, MMP, and tube formation, which was reversed by URB597 and AG. OGD-induced enhancement of ROS, MDA, and apoptosis was reduced after drug interventions. URB597 and AG exhibited antioxidant/anti-inflammatory and mitochondrial protective effects by activating Nrf2 signaling. These findings indicated that URB597 and AG protect BMECs against OGD-induced endothelial permeability impairment and apoptosis by reducing mitochondrial oxidative stress and inflammation associated with activation of Nrf2 signaling. URB597 and AG showing the vascular protection may have therapeutic potential for the BBB damage in ischemic cerebrovascular diseases.

1. Introduction

Ischemic stroke with a high rate of morbidity and mortality is becoming the major cause of adult long-term disability worldwide [1]. In stroke, there is not enough blood supply to provide nutrients and oxygen to ischemic zones, triggering a series of pathophysiological changes, such as inflammatory response, ischemia and hypoxia, and blood-brain barrier (BBB) leakage. BBB dysfunction is a critical neurovascular damage process, which devotes to hemorrhagic transformation and poor prognosis in patients [2]. The BBB is composed of three cellular elements, namely, glial end-feet, pericytes, and brain microvascular endothelial cells (BMECs) [3]. BMECs play a vital part in maintaining the structural and functional integrity of BBB, whereas disruption of microvascular can be found in ischemic cerebrovascular diseases [4]. How do BMECs respond to ischemia and hypoxia in an in vitro model of stroke (oxygen-glucose deprivation, OGD), as well as the underlying mechanisms involved in BBB impairment, remains confusing.

The endocannabinoid system (ECS) comprises endogenous cannabinoid receptors 1 and 2 (CB1 and CB2), the two endocannabinoid ligands N-arachidonoylethanolamine (anandamide, AEA) and 2-arachidonoylglycerol (2AG), and endocannabinoid anabolic and catabolic enzymes, such as monoacylglycerol lipase and fatty acid amide hydrolase (FAAH) [5]. The ECS is involved in modulating neural development, synaptic plasticity, endothelium-dependent vasorelaxation, cerebrovascular regulation, microvascular endothelial barrier, and BBB function [6]. The effects of the ECS on cardiovascular and cerebrovascular cells and circulatory system are not only by CBs but also other atypical cannabinoid receptor-manners. Mestre et al. have found that endocannabinoid (AEA) reduces leukocyte transmigration in a model of BBB by inhibiting vascular cell adhesion molecule-1 in brain endothelial cells associated with CB1 activation [7]. In ischemia-reperfusion injury, pharmacological CB2 offers a new strategy for the protection of blood-spinal cord barrier permeability [8]. The ECS may importantly modulate BBB function under physiological and pathophysiological conditions in a very complex manner. Nevertheless, the underlying pathophysiological characteristics are poorly understood. FAAH inhibitors can also upregulate the level of ECS, which improves ischemic neuronal and vascular injury. FAAH inactivation is emerging as a potential strategy to treat stroke [9]. However, the possible effects of FAAH inhibitors on BMECs as well as BBB permeability during OGD have not yet been systematically investigated.

Andrographolide (AG) is a major active compound of the Asian herb plant *Andrographis paniculate* (green chiretta), which possesses diverse biomedical effects including antineoplastic, antibacterial, anti-inflammatory, and antioxidant properties [10]. Growing evidence indicates that AG with the beneficial neurofunctional regulation exhibits therapeutic effects in Alzheimer's disease (AD) and ischemic brain damage [11]. AG can reduce the total Aβ burden in aged Octodon degus [12]. And we previously reported that AG could suppress cerebral ischemia-induced hippocampal neuronal apoptosis and astroglial activation [13, 14]. Recently, the effects of AG on BBB permeability in ischemic stroke gained attention. Pharmacodynamic studies have revealed that AG can cross the BBB and protect against the MCAO-induced primary cerebral endothelial cells injury [15], but the underlying mechanisms remain unclear.

To clarify these issues, in this study, we explored the potential effects of FAAH inhibitor URB597 and AG on mice BMECs (bEnd.3 cells), as well as the underlying mechanisms associated with its therapeutic potential in modulating BBB permeability in OGD.

2. Materials and Methods

2.1. OGD Treatment. To mimic cerebral ischemia in vitro, bEnd.3 cells (No. CL-0598, Procell Life Science & Technology Co., Ltd, Wuhan, China) were exposed to OGD as reported previously [16]. Briefly, cells were cultured in RPMI 1640 medium (Gibco, Herndon, USA) containing 10% fetal bovine serum (Gibco, Herndon, USA), 100 U/mL penicillin, and 100 U/mL streptomycin (Hyclone Laboratories, Logan, USA) in a humidified incubator at 37°C with 5% CO_2 and 95% air. Then, cells were transferred from the RPMI 1640 medium to DMEM without glucose (Gibco, USA) in 6-well plates, then subsequently cultured in a humidified incubator at 37°C with 5% CO_2 and 95% N_2 for 24 hours.

2.2. Experimental Groups and Drug Treatment. To assess the effects of OGD on bEnd.3 cells and choose the optimum duration of OGD, the cell viability was measured after 4-24 h of OGD in bEnd.3cells. For drug concentration screening, URB597 and AG (No. HY-10864, No. HY-N0191, Med Chem Express Co., Ltd, Shanghai, China) were dissolved in dimethylsulfoxide (DMSO, Med Chem Express, Shanghai, China) and diluted with serum-free RPMI 1640 at different concentrations (0.5 μM, 1 μM, 2 μM, 5 μM, and 10 μM), respectively. Then, cells were added with different concentrations of URB597 and AG before OGD treatment. After 6 h of OGD, cells were incubated in a maintenance medium for 12 h under normal conditions subsequent experiments. Experimental treatment groups were as follows: (1) the control group was cultured without OGD exposure (the Con group), (2) the OGD treatment (the OGD group), (3) the URB597 (2 μM) treatment during OGD (the URB group), (4) the AG (10 μM) treatment during OGD (the AG group), and (4) the URB597 and AG cotreatment during OGD (the URB + AG group).

2.3. Cell Viability Assay. A 3-(4,5-dimethyl-2-thiazolyl)-2,5-diphenyl-2-H-tetrazolium bromide (MTT) method was used to assay cell viability. In brief, the cells in different groups were incubated for another 4 h at 37°C and 5% CO_2 in a sterile incubator, following added 20 μl of MTT. The supernatant was removed, and the cells were lysed in 150 μl of DMSO. A microplate reader (Epoch, BioTek, USA) was used to measure the absorbance (OD) at 490 nm. Cell viability was expressed as a percentage of the control [17].

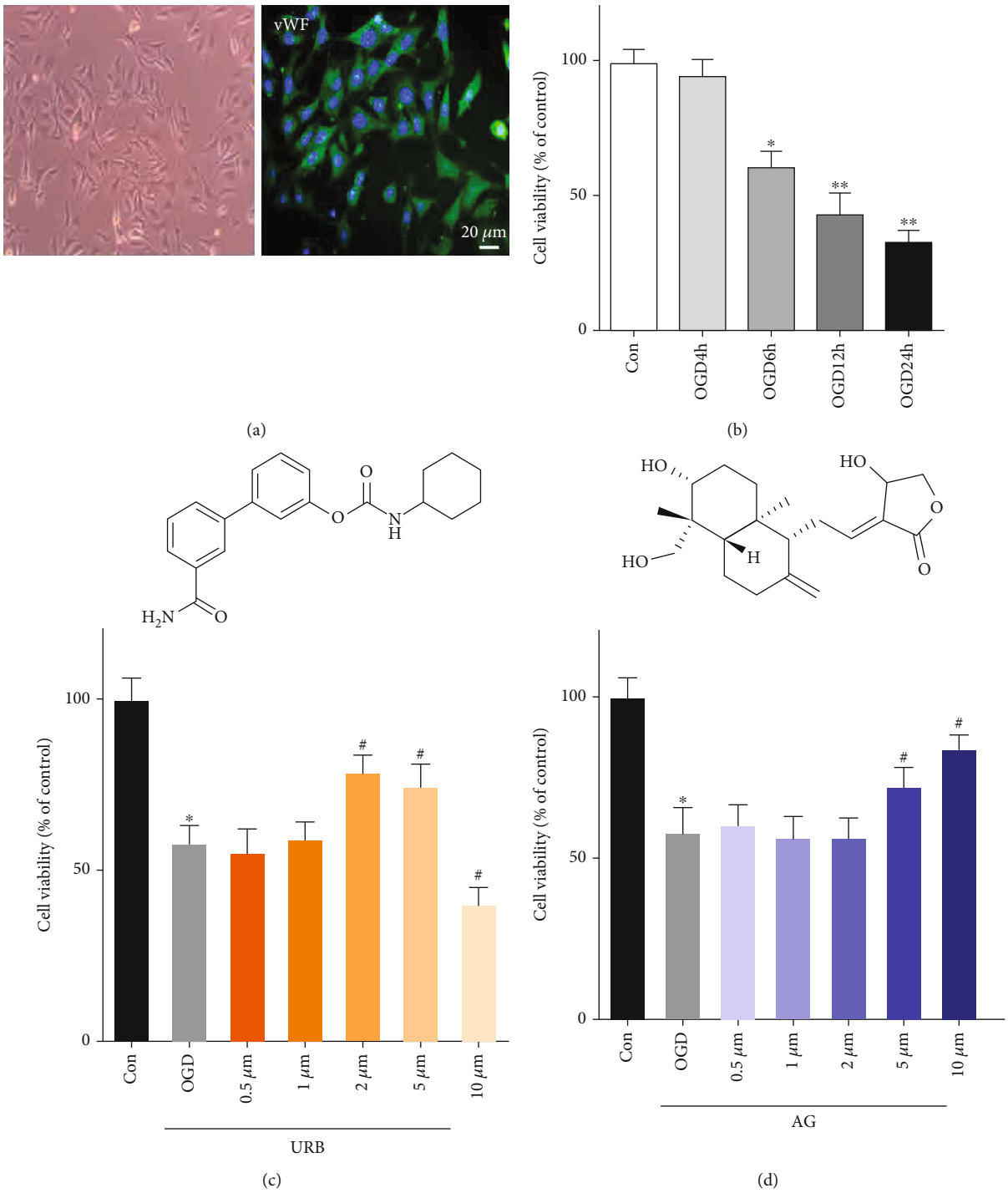

Figure 1: Effects of URB and AG on the cell viability of BMECs subjected to OGD. (a) Morphology and fluorescent staining of BMECs. (b) The cell viability was measured after 4–24 h of OGD by MTT. (c, d) The cell viability was measured after being treated with URB597 and AG (0.5 μM, 1 μM, 2 μM, 5 μM, and 10 μM) subjected subsequently to 6 h of OGD by MTT. $^{*}p < 0.05$, $^{**}p < 0.01$ *vs.* Con, $^{\#}p < 0.05$ *vs.* OGD, ($n = 6$).

2.4. LDH Leakage Assay. LDH release was detected using the LDH activity kit (Beyotime, Shanghai, China) as previously described [18]. Briefly, 50 μl supernatant from each sample was transferred into a new plate, mixed with 50 μl kit's reaction mixture, and incubated for 10 min at room temperature. Stop solution was then added. The OD values at 490 nm and 630 nm were measured using a microplate reader (Epoch, BioTek, USA).

2.5. The Tube Formation Assay. For tube formation analysis, Matrigel basement membrane matrix with growth factor-reduced (BD Biosciences, San Jose, CA, USA) was used as

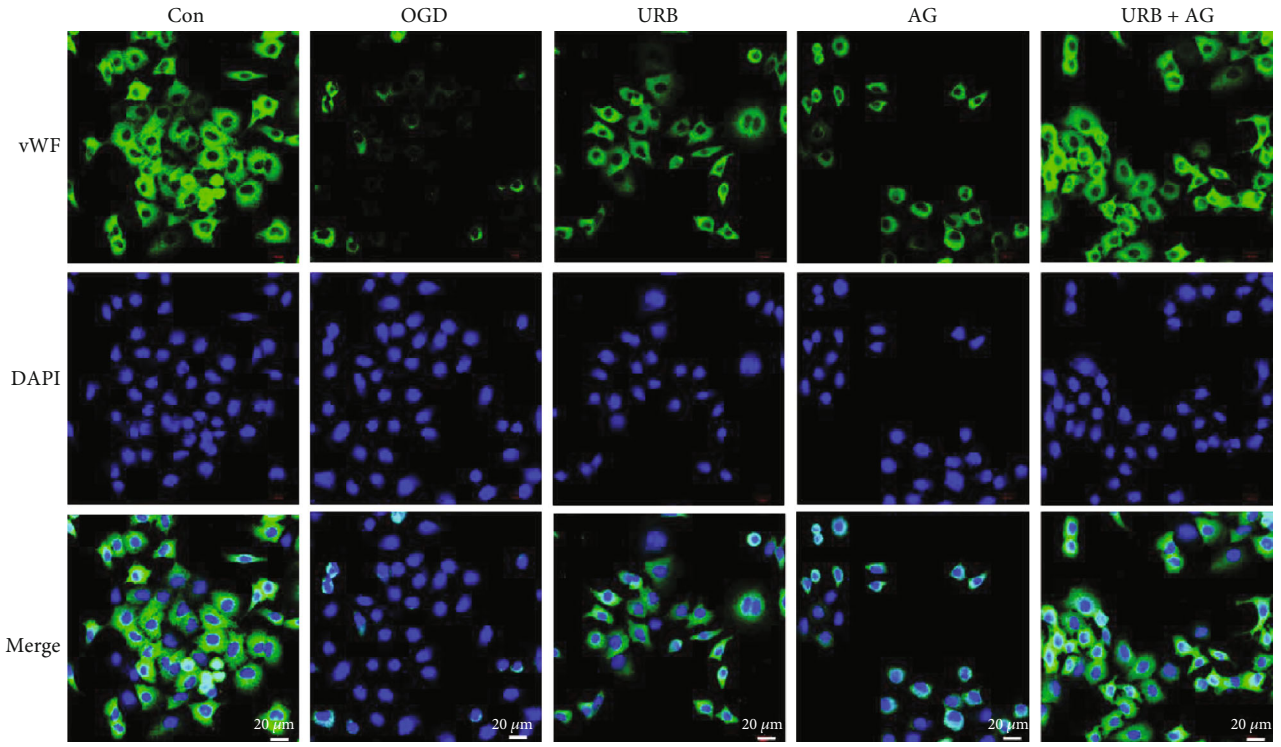

(a)

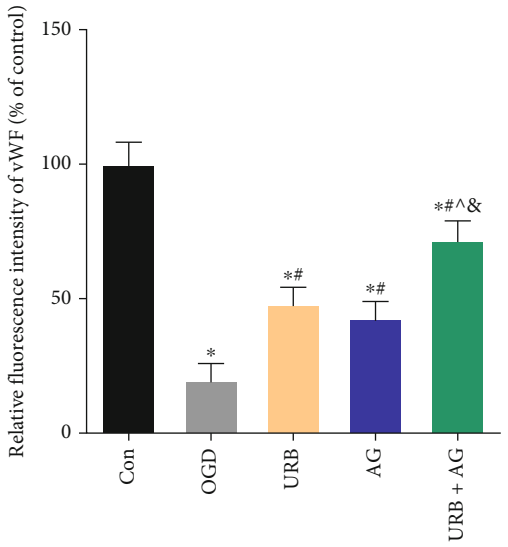

(b)

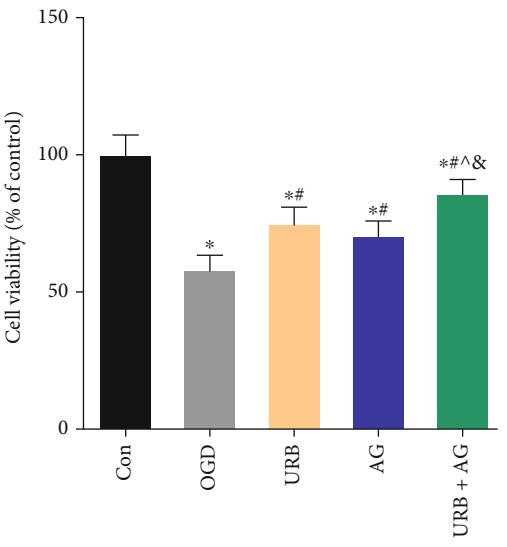

(c)

Figure 2: Continued.

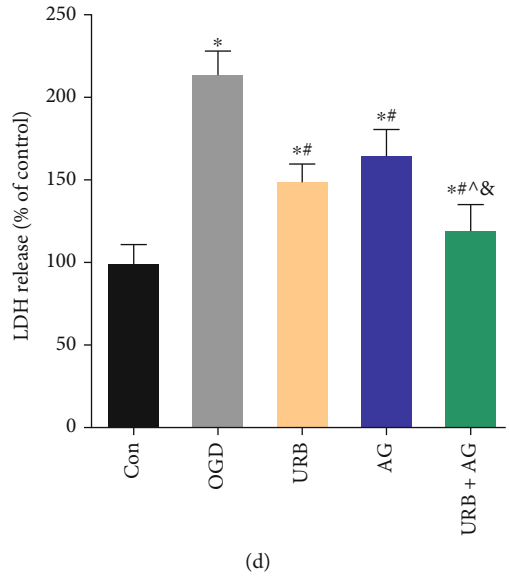

Figure 2: Effects of URB and AG on the cell growth and LDH release of BMECs subjected to OGD. (a, b) Representative vWF (green) immunofluorescence for BMECs. (c, d) Statistical analysis of the cell viability (MTT method) and LDH release. $^{*}p < 0.05$, vs. Con, $^{\#}p < 0.05$ vs. OGD, $^{\wedge}p < 0.05$ vs. URB, $^{\&}p < 0.05$ vs. AG, ($n = 6$). Magnificent: 200×, scale bar 20 μm.

previously described [19]. First, the matrix was thawed at 4°C overnight and incubated at 37°C for 30 mins [20]. After Matrigel polymerization, the pretreated bEnd.3 cells were resuspended and seeded onto the primary Matrigel (60 μl). The plate was transferred to a humidified incubator for 12 h incubation. Images were taken using a microscope (Olympus, Tokyo, Japan) with magnification at ×40 from 3 randomly selected optical fields. The tube formation assay was analyzed and interpreted by an experimenter blinded to the details of the study using the Wim Tube software (Wimasis, Munich, Germany). The number and length of the capillary-like tube were quantified.

2.6. Brain Microvascular Endothelial Barrier Permeability Assay. To estimate the integrity of the cell monolayer, transendothelial electrical resistance (TEER) was first measured using a Millicell-Electrical Resistance System (Millipore, Bedford, MA) with an electrode as described previously [17]. One electrode was put into the upper Transwell insert compartment, and the other electrode was inserted into the lower compartment inside a cell culture hood at room temperature [21]. The resistance was measured daily at regular intervals until cells reached a consistent resistance. Triplicate measurements were recorded for each monolayer with values expressed as Ω cm^2.

Brain microvascular endothelial barrier permeability was also tested using the flux of Evans blue (EB) dye-labeled albumin (Sigma, MU, USA) across the cell monolayer. EB-albumin (50 μl of 2% concentration) was added to the apical surface of bEnd.3 cell monolayers in the culture insert for 1 h before the end of the OGD, whereas bovine serum albumin (150 μl of 4% concentration) was added to the lower chamber. The media in the lower chamber was collected to detect the absorbance of EB at the wavelength of 630 nm using a microplate reader (Epoch, BioTek, USA), after incubation at 37°C for 1 h.

2.7. Oxidative Stress Assay. Intracellular oxidative stress was evaluated by using the determination of superoxide dismutase (SOD), catalase (CAT), malondialdehyde (MDA), and the 2,7-dichlorofluorescein diacetate (DCF-DA) with commercial kits (Beyotime, Shanghai, China) [16]. Experiments were performed in 96-well plates for each condition at least in triplicate. For the ROS assay, cells were incubated with 5 μM DCF-DA solution at 37°C and 5% CO_2 for 30 mins, after being centrifuged at 1000 rpm for 5 min and washed twice with PBS. Then, the mean fluorescence intensity (MFI) was evaluated using a fluorometric microplate reader (FilterMax F5, Molecular Devices, Sunnyvale, USA). The excitation and emission wavelengths were set at 485 and 535 nm, respectively.

2.8. Mitochondrial Membrane Potential (MMP, $\Delta\psi m$) Measurement. According to the instruction of the JC-1 kit (Beyotime, Shanghai, China), cells were plated in 96-well plates at a density of 1×10^4/well after 24 h treatment for measuring $\Delta\psi$m. In brief, the cells were washed twice with PBS and incubated with JC-1 staining medium (2 μM) at 37°C for 20 mins. The cells were observed under a fluorescence microscope (Zeiss, Jena, Thuringia, Germany) after washing with PBS. The level of cellular red and green fluorescence was analyzed by Image J (NIH, Bethesda, MD). Values are expressed as the rate of the red/green fluorescence intensity by an investigator blinded to the grouping information.

2.9. q-Reverse Transcription-Polymerase Chain Reaction (qRT-PCR). The total RNA of BMECs was obtained by using the TRIzol reagent. The RNA concentration and purity were

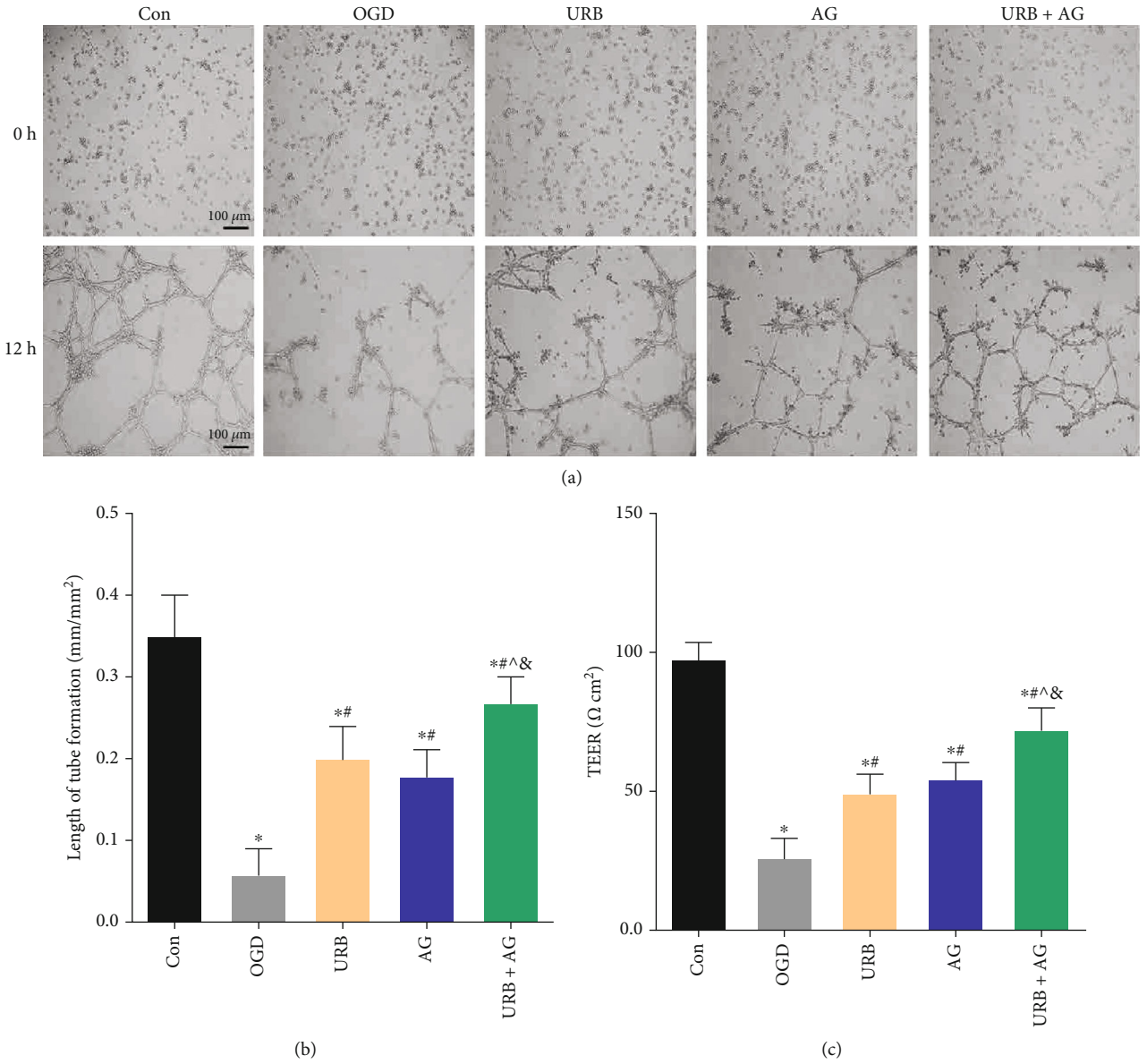

Figure 3: Continued.

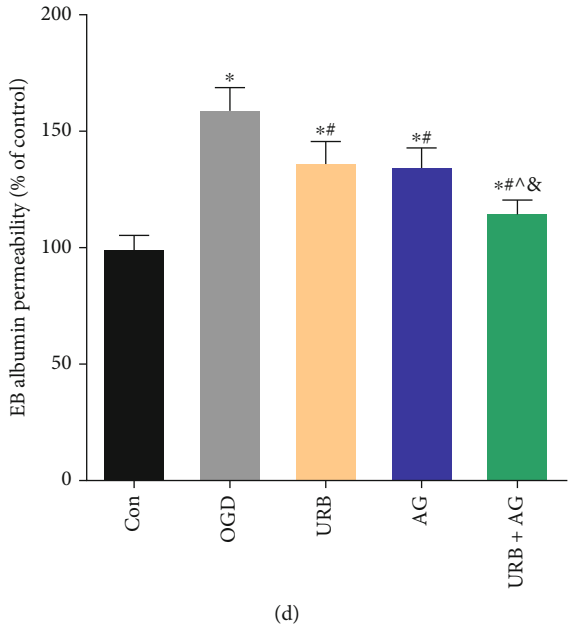

(d)

Figure 3: Effects of URB and AG on the tube formation and barrier function of BMECs subjected to OGD. (a) Representative the tube formation in each group. (b) Statistical analysis of length of tube formation. (c) The barrier property of BMECs monolayer was evaluated by TEER assay. (d) Effect of URB and AG on the barrier was also evaluated using EB albumin assays. $^{*}p < 0.05$, *vs.* Con, $^{\#}p < 0.05$ *vs.* OGD, $^{\wedge}p < 0.05$ *vs.* URB, $^{\&}p < 0.05$ *vs.* AG, ($n = 6$). Magnificent: 100×, scale bar 100 μm.

detected by using a Nanodrop Spectrophotometer (ND-100, Thermo, Waltham, MA) at the 260/280 nm ratio. The total RNA was dissolved in 10 μl DEPC-treated water. The reverse transcription and cDNA production were performed by using a PrimeScript RT reagent kit (RR047A, Takara Holdings Inc., Tokyo, Japan) according to the manufacturer's protocol. The cDNA fragment was amplified by PCR using the following specific primers: TNF-α forward: 5′-CAT CTT CTC AAA ATT CGA GTG ACA A-3′, reverse: 5′-TGG GAG TAG ACA AGG TAC AAC CC-3′; IL-1β forward: 5′-TCA TTG TGG CTG TGG AGA AG-3′, reverse: 5′-AGG CCA CAG GTA TTT TGT CG-3′; iNOS forward: 5′-GAC GAG ACG GAT AGG CAG AG-3′, reverse: 5′-CAC ATG CAA GGA AGG GAA CT-3′; β-actin forward: 5′-TGT GAT GGT GGG AAT GGG TCA G-3′, reverse: 5′-TTT GAT GTC ACG CAC GAT TTC C-3′. The expression of specific mRNAs was validated by performing quantitative real-time PCR with One-Step SYBR PrimeScript RT-PCR Kit (Perfect Real Time, RR066A, Takara Bio Inc., Japan). The relative gene expression level was evaluated by using the 2-$\Delta\Delta$Ct method, which was normalized to endogenous GAPDH expressions.

2.10. Western Blot Analysis. The total protein of BMECs was extracted by using RIPA buffer (Beyotime, Shanghai, China). The protein samples were quantified via a BCA assay kit (Beyotime, Shanghai, China). Subsequently, 30 μg protein in each group was separated by using SDS-PAGE and transferred onto 0.45 μm polyvinylidene fluoride (PVDF) membranes (Millipore, MA, USA). The membranes were blocked in 5% skim milk. Next, the membranes were incubated overnight with primary antibody against ZO-1 (1 : 1000, ab221547, Abcam, Cambridge, MA, USA), Occludin (1 : 1000, ab216327, Abcam), Claudin 5 (1 : 1000, ab131259, Abcam), Nrf2 (1 : 1000, bs-1074R, Bioss, Beijing, China), and HO-1 (1 : 1000, ab52947, Abcam) at 4°C and then interacted with secondary antibody for 2 hours. Protein bands were revealed by the enhanced chemiluminescence (ECL) method. β-Actin (1 : 5000, Abcam, ab227387) was used as a loading reference.

2.11. Flow Cytometry Analysis. To estimate the proportions of apoptosis cells, cellular sedimentation was measured by using flow cytometry. After treatment, the BMECs were detached with 0.25% trypsin containing no EDTA (Thermo Fisher) and then centrifuged at 3000 rpm, after which the supernatant was discarded. The cells were resuspended in PBS, centrifuged, and with the supernatant removed again. The cell apoptosis was quantified by using the Annexin V Apoptosis Detection kit (K201-100; BioVision, Milpitas, CA, USA). The Annexin-V-FITC/PI staining solution was compounded by HEPES buffer (Thermo Fisher), Annexin-VFITC/PI (50 : 1 : 2). The cells were resuspended with the prepared dye at 100 μl per tube. And the tube was protected from light. After incubating for 15 min at ambient temperature, the cells were lysed with 1 mL HEPES buffer. Finally, the cells were collected into flow tubes, and the cell apoptosis was measured on the flow cytometer at 488 nm (Epoch, BioTek, USA).

2.12. Immunofluorescence Staining. Immunofluorescence staining was used to detect the expression of vWF (No. sc-365712, Santa Cruz Biotechnology, Dallas, Texas, USA), ZO-1, Occludin, and Nrf2. First, using 4% paraformaldehyde, fix the cells at room temperature for 10 minutes then

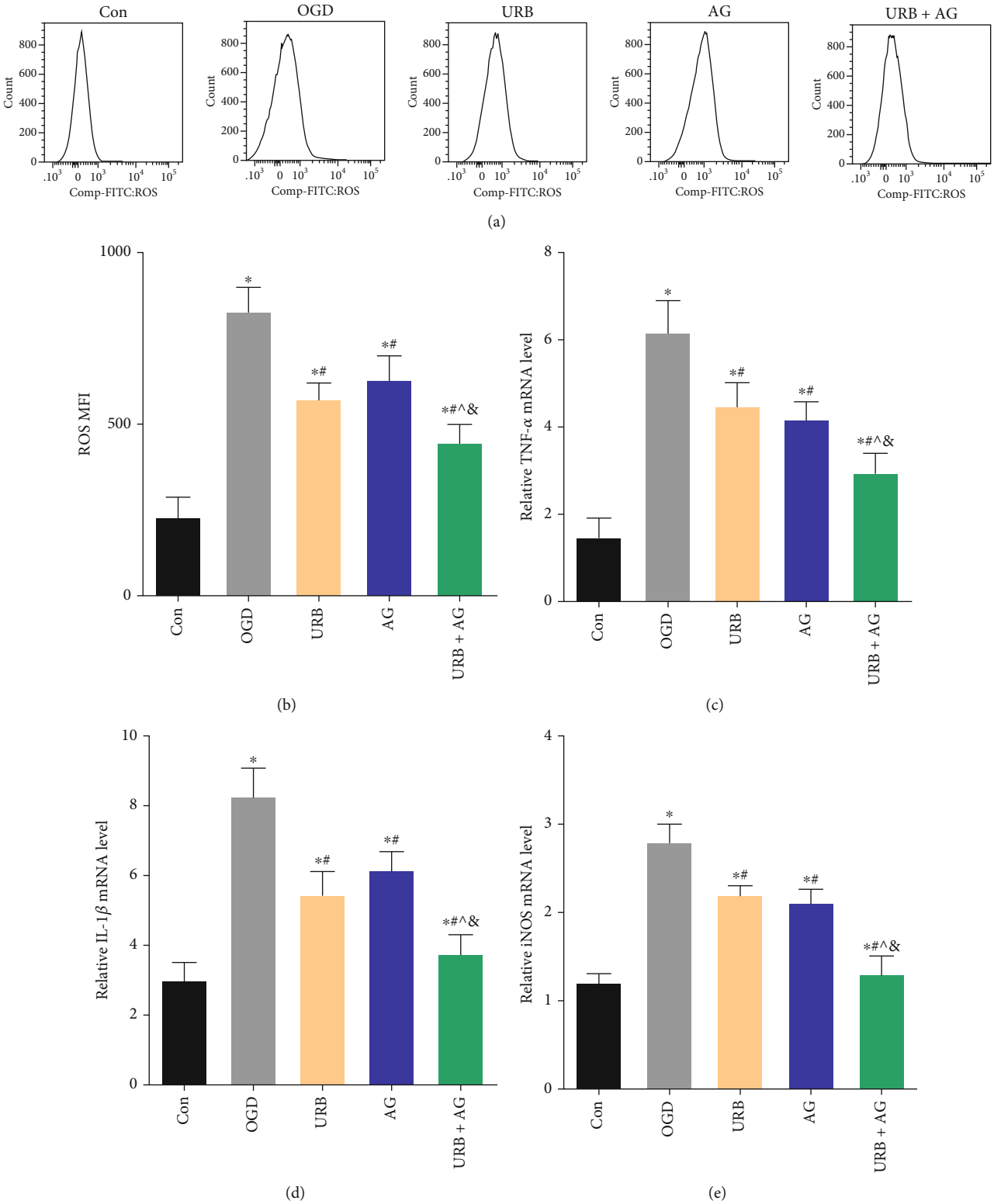

Figure 4: Continued.

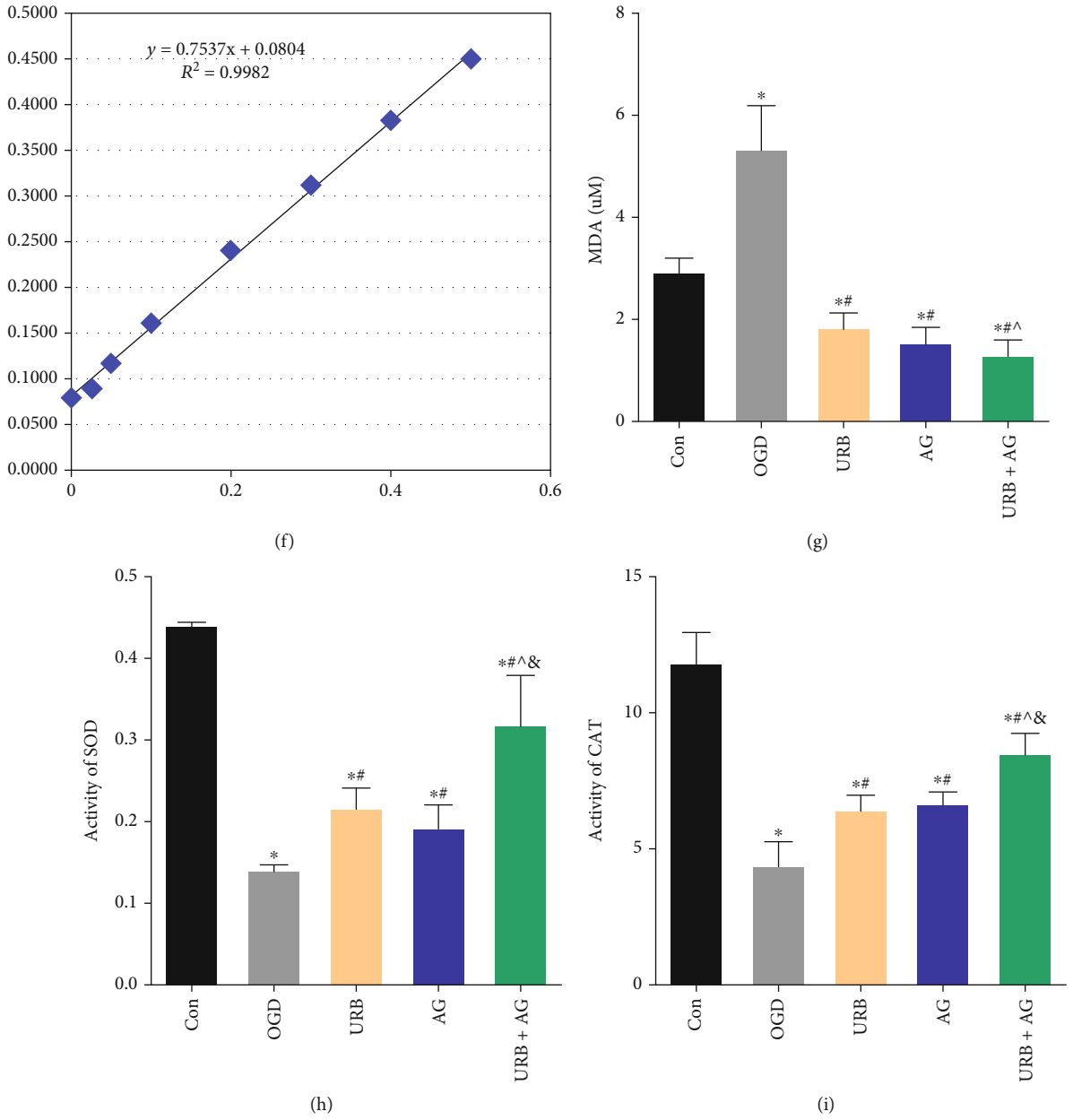

Figure 4: Effects of URB and AG on mitochondria ROS and inflammatory responses of BMECs subjected to OGD. (a) Representative histograms of flow cytometric evaluation of the cell-associated DCF-DA. (b) Quantitative analysis of cellular ROS levels. (c)–(e) Quantitative analysis of relative mRNA levels of TNF-α, IL-1β, and iNOS. (f) Standard protein curve. (g)–(i) Quantification of MDA level and activities of SOD and CAT in BMECs. $^{*}p < 0.05$, vs. Con, $^{\#}p < 0.05$ vs. OGD, $^{\wedge}p < 0.05$ vs. URB, $^{\&}p < 0.05$ vs. AG, ($n = 6$).

washing twice in PBS. Next, the cells were permeabilized in Triton X-100 solution (0.5% TritonX-100 dissolved in PBS) for 30 minutes and treated with 5% bovine serum albumin (BSA) in PBS for 30 minutes. After removal of the blocking solution, cells were incubated with rabbit anti-ZO-1, Occludin, and Nrf2 monoclonal antibody at 1 : 200 dilution in 5% BSA overnight at 4°C. Subsequently, fluorescent dye-conjugated secondary antibody was added and incubated with the cells for 2 hours away from light. Finally, the immunofluorescence images were examined using a fluorescent microscope. The mean fluorescence intensity was estimated from 4 fields of view in each sample by an investigator without knowing the treatment.

2.13. Terminal Deoxynucleotidyl Transferase dUTP Nick End Labeling (TUNEL) Assay. Cells were plated in 24-well flat-bottomed plates at a density of 1×105 cells per well, fixed with 4% paraformaldehyde for 30 minutes, and then permeabilized by 0.2% TritonX-100 for 5 minutes. The apoptosis levels were detected by using Apoptosis Detection Kit (Ribo-Bio, China). Adding 50 μL of TUNEL detection solution to each well and incubating for one hour at room temperature

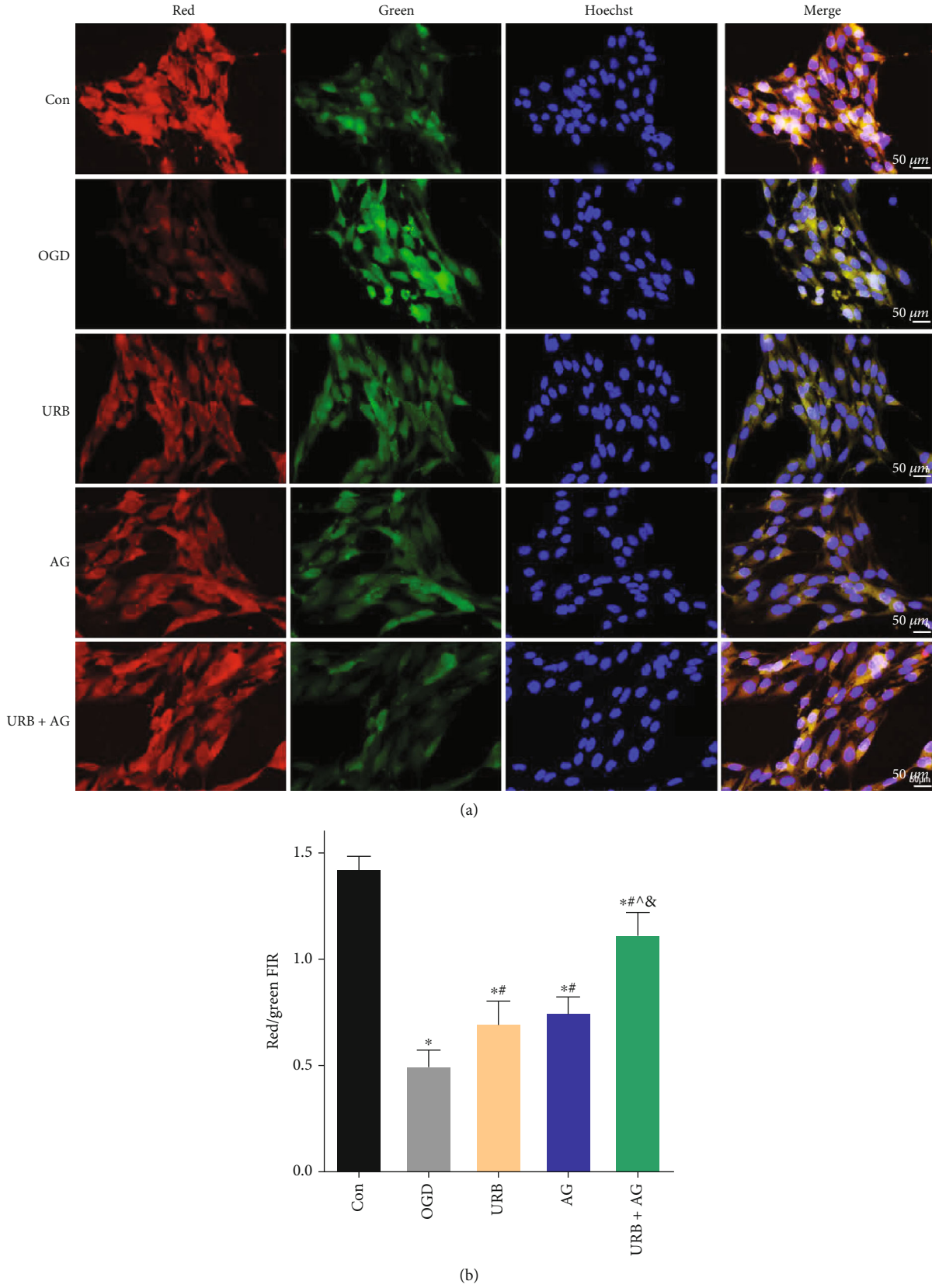

Figure 5: Effects of URB and AG on mitochondrial membrane potential (MMP) of BMECs subjected to OGD. (a) Representative immunofluorescence of mitochondrial JC-1 in BMECs. (b) MMP as estimated by JC-1 red/green fluorescence intensity rate (FIR). $^{*}p < 0.05$, *vs.* Con, $^{\#}p < 0.05$ *vs.* OGD, $^{\wedge}p < 0.05$ *vs.* URB, $^{\&}p < 0.05$ *vs.* AG, ($n = 6$). Magnificent: 400×, scale bar 50 μm.

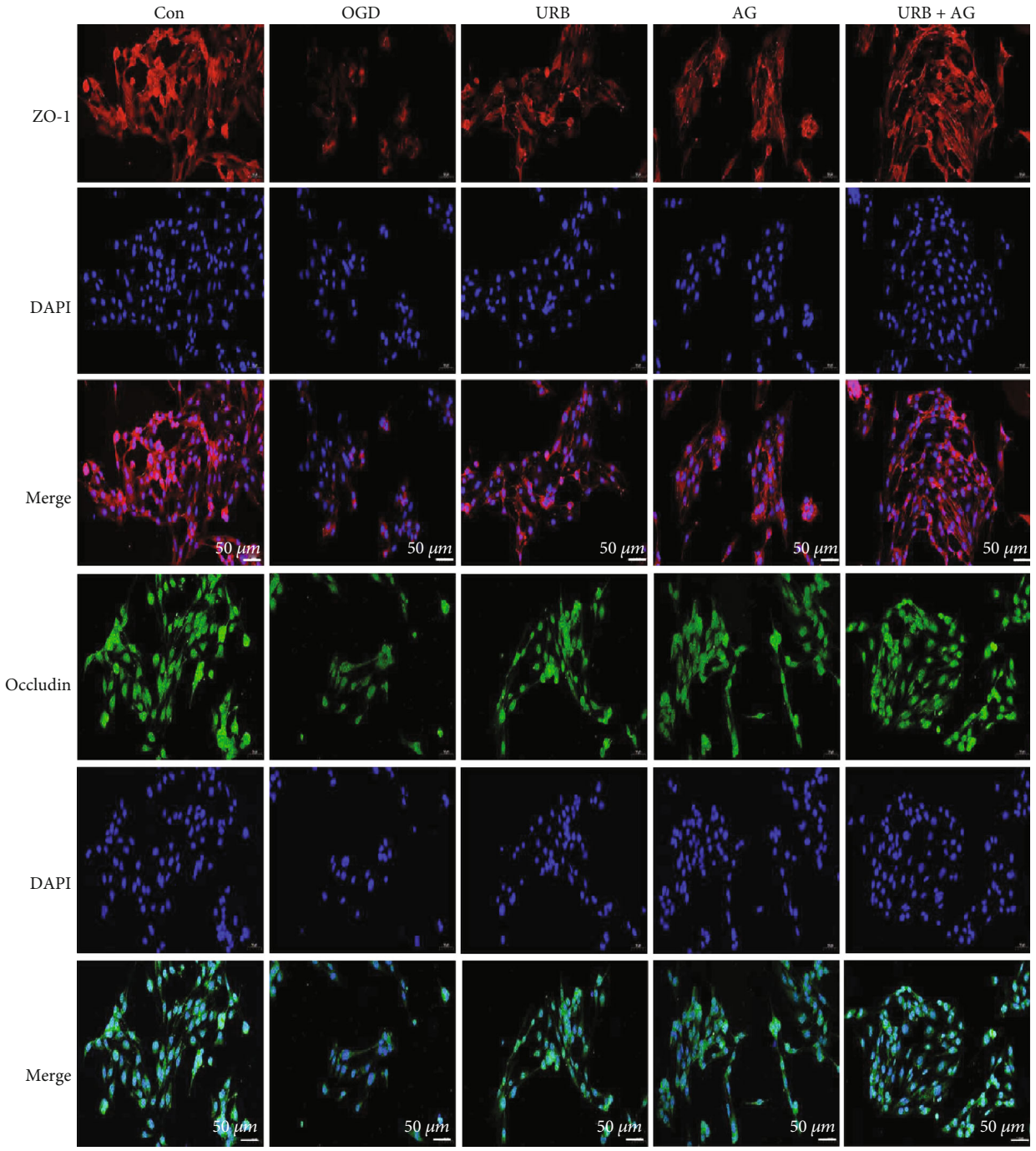

(a)

Figure 6: Continued.

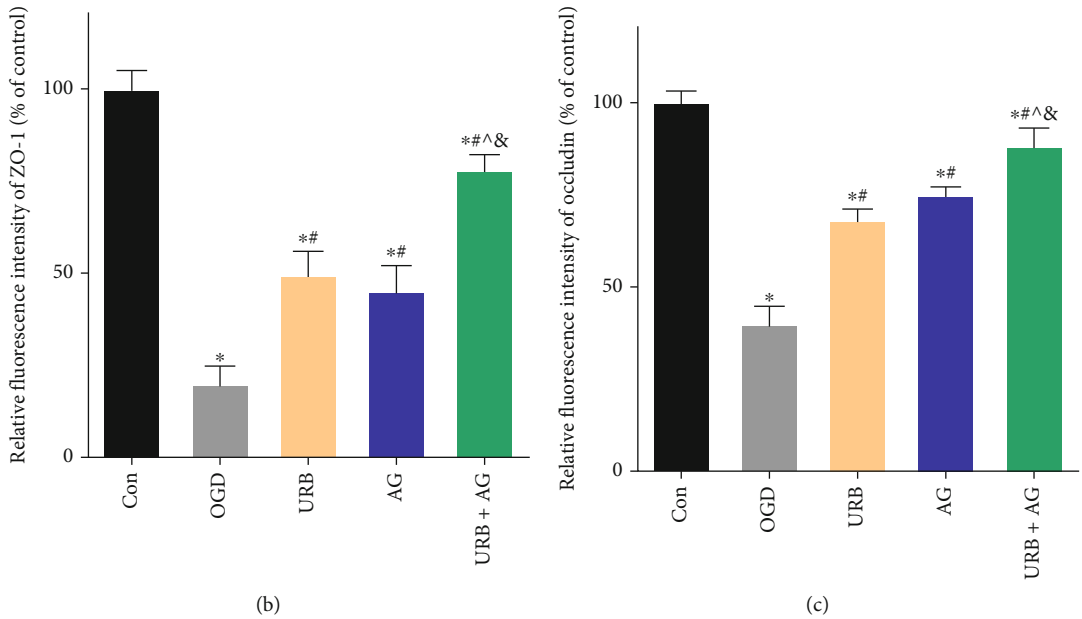

Figure 6: Effects of URB and AG on the distribution and expression of TJ proteins of BMECs subjected to OGD. (a) Representative ZO-1 (red) and Occludin (green) immunofluorescence staining in BMECs. (b, c) Quantitative analysis of relative fluorescence intensity of ZO-1 and Occludin. $^{*}p < 0.05$, *vs.* Con, $^{\#}p < 0.05$ *vs.* OGD, $^{\wedge}p < 0.05$ *vs.* URB, $^{\&}p < 0.05$ *vs.* AG, ($n = 6$). Magnificent: 400×, scale bar 50 μm.

in the dark. The numbers of TUNEL-positive cells were observed under a fluorescence microscope (Olympus).

2.14. Small Interfering RNA (siRNA) Transfection. Nrf2 siRNA was purchased from RiboBio Co., Ltd. (siG2006160258184354, RiboBio, Guangzhou, China). Transfection of negative control (NC) siRNA and Nrf2 into BMECs with Lipofectamine 3000 (Thermo Fisher, UT, USA) is according to the manufacturer's instructions. Cells were then harvested 72 hours later for Western blotting to assess the expression of Nrf2 and HO-1.

2.15. Statistical Analysis. All data, presented as the mean ± standard error of the mean (SEM), were analyzed by two technicians blinded to the details of the group using SPSS 22.0 software (IBM, USA) and GraphPad Prism 6.0 software (San Diego, CA). The student's *t*-test was used for comparison between two groups. One-way analysis of variance (ANOVA) followed by a Bonferroni post hoc test was used for comparison among multiple groups. A p value less than 0.05 was considered statistically significant for all tests.

3. Results

3.1. The Effects of Different Concentrations of URB597 and AG on the Viability of bEnd.3 Cells in OGD. As shown in Figure 1(a), cells were examined for morphology and growth status and identified by immunofluorescence stain of vWF. Then, we investigated the deleterious effects of different durations of OGD on the viability of bEnd.3 cells using MTT assay. As time went on, the viability of cells deteriorated (Figure 1(b)). The viability of cells significantly decreased in the OGD 6 h compared with the control, which is approximately 60.2% of the control. The viability of the cell was reduced more than 50% after 12 h and 24 h of OGD. Then, the bEnd.3 cells were treated with URB597 ($C_{20}H_{22}N_2O_3$) and AG ($C_{20}H_{30}O_5$) at different concentrations (0.5 μM, 1 μM, 2 μM, 5 μM, and 10 μM) subjected subsequently to 6 h of OGD (Figures 1(c) and 1(d)). As shown in Figure 1(c), URB597 (2 μM and 5 μM) treatment increased the viability of cells compared with the OGD. On the contrary, the URB597 treatment with higher concentration led to the viability of cells decreased. 5 μM and 10 μM of AG treatment protected 72.6% and 84.3% of the cells, respectively. The results indicate that URB597 with the concentration of 2 μM and AG with the concentration of 10 μM are propitious to bEnd.3 cells subjects to OGD.

3.2. URB597 and AG Increase the Viability of bEnd.3 Cells in OGD. To further determine whether URB597 treatment, AG treatment, as well as cotreatment promote cell growth and survival under conditions of OGD, we assessed the fluorescence staining of vWF (Figure 2(a)). After 6 h of OGD, vWF fluorescence intensity was significantly reduced ($p < 0.05$ vs. Con). However, URB597 treatment and AG treatment significantly increased the expression of vWF (all $p < 0.05$, vs. OGD group). Compared with the fluorescence intensity of vWF in the URB group and the AG group, vWF expression is higher in the URB + AG group (all $p <$ 0.05) (Figure 2(b)). In the MTT assay, OGD caused a decline in cell survival and growth with OD values decreasing during culture, which was reversed in the drug intervention groups (Figure 2(c)). In addition, LDH leakage as a marker for cell degradation was also monitored. As shown in Figure 2(d), LDH leakage increased in the OGD group compared with the control group ($p < 0.05$). URB597 (2 μM) and AG (10 μM) treatment significantly reduced it (all $p < 0.05$, vs. OGD group). Meanwhile, the inhibition is more obvious

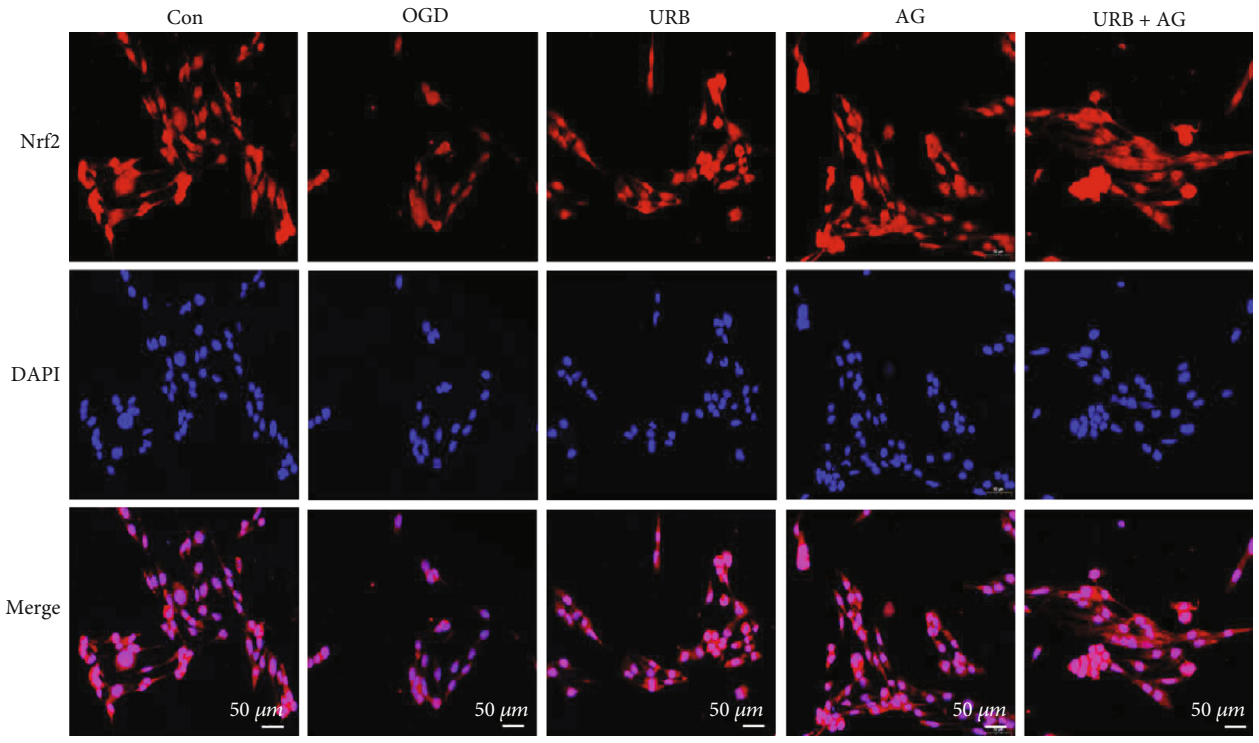

(a)

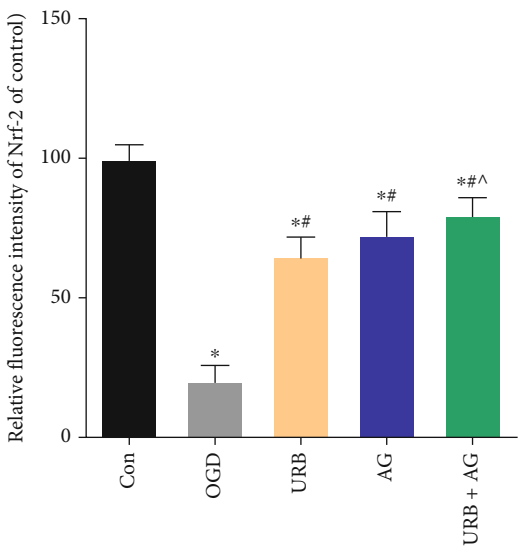

(b)

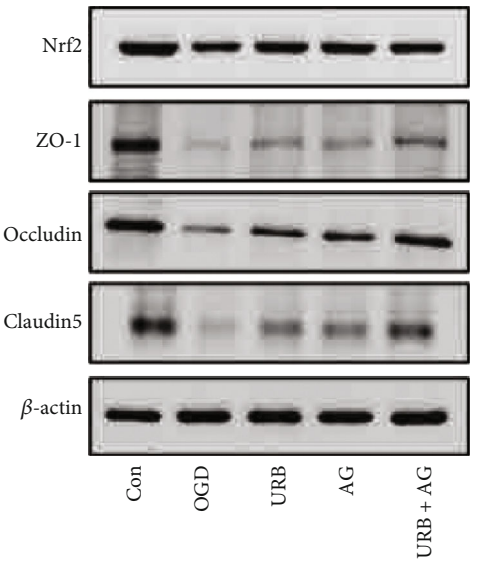

(c)

Figure 7: Continued.

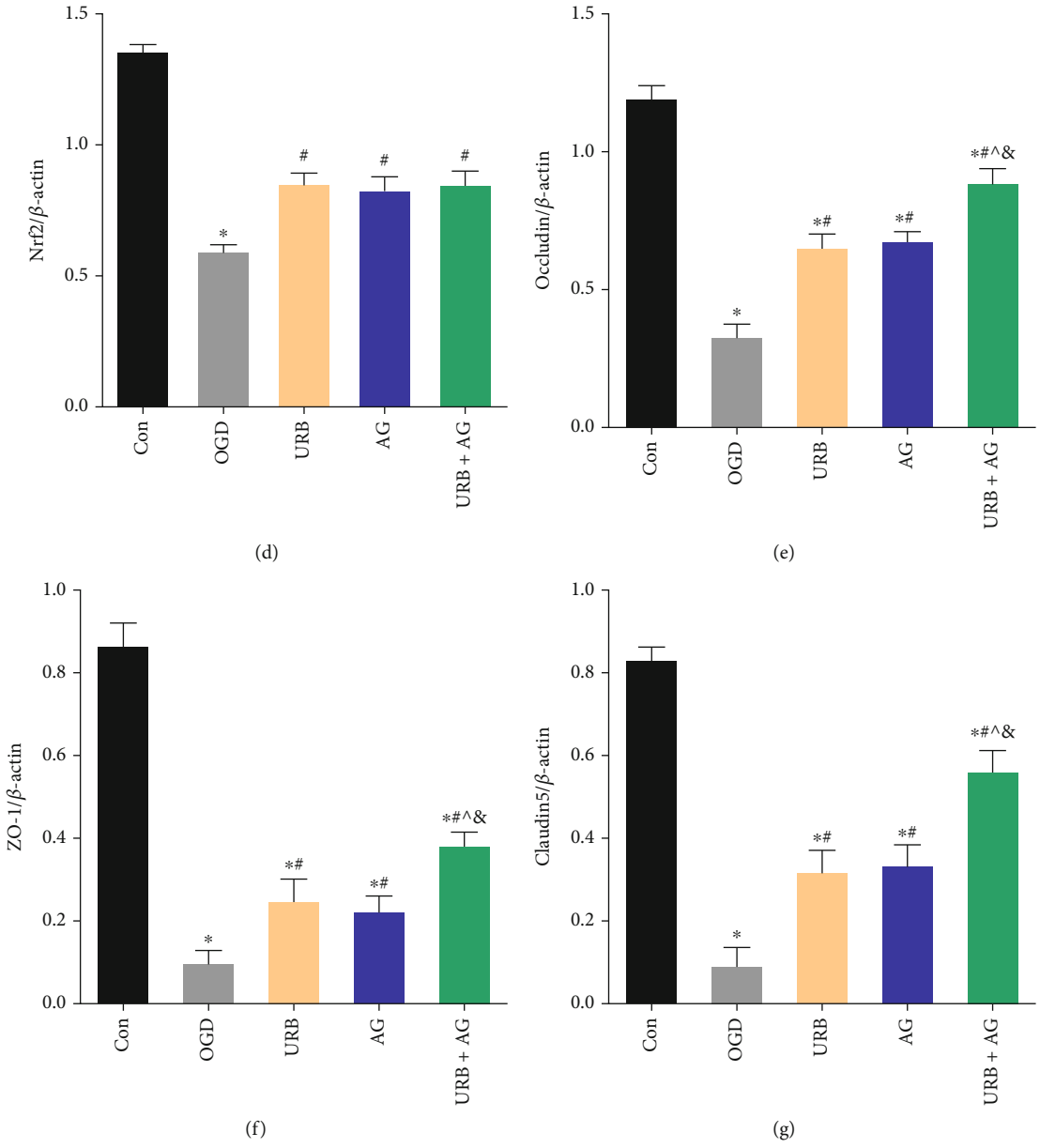

Figure 7: Continued.

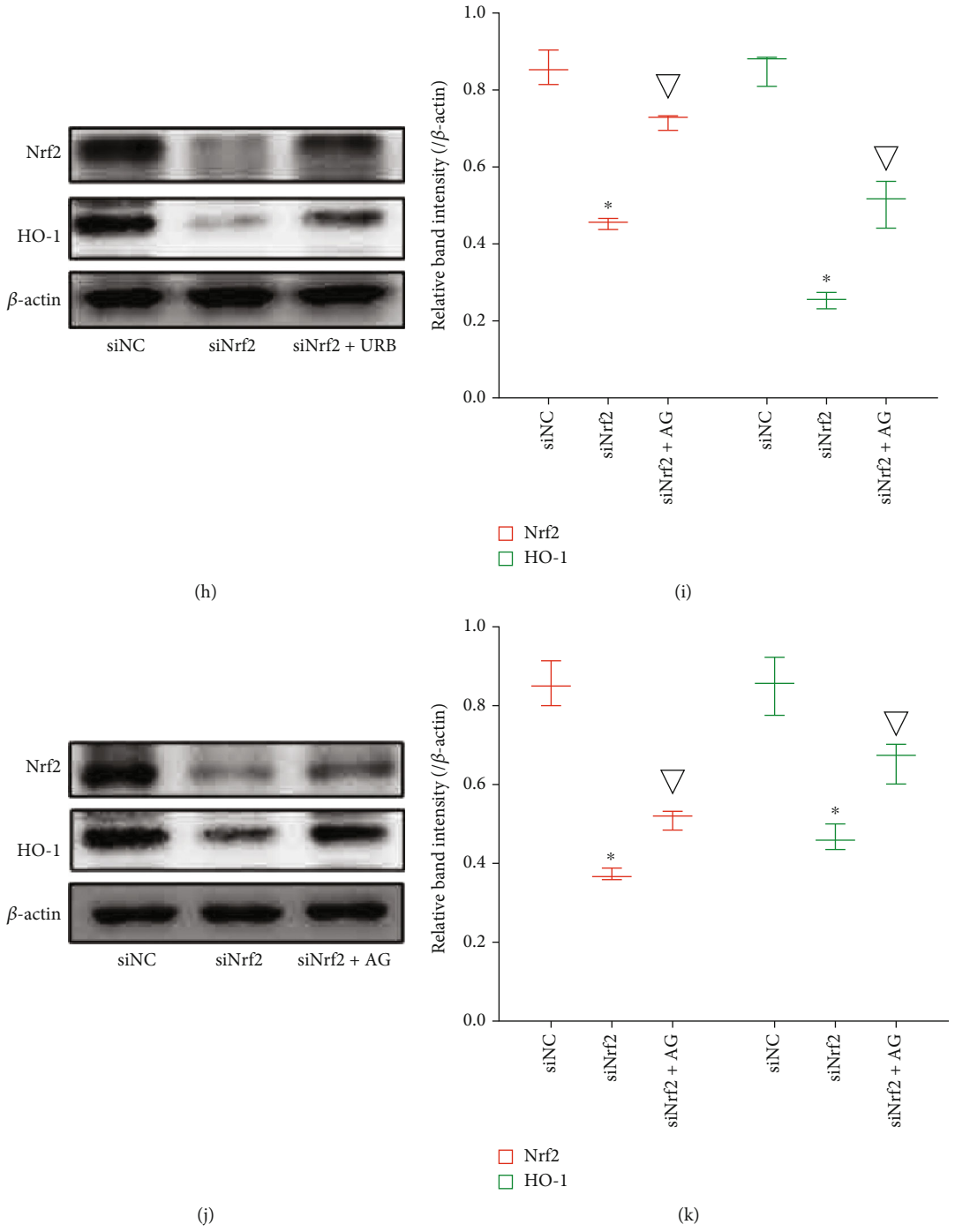

Figure 7: Effects of URB and AG on activation of Nrf2 and TJ proteins of BMECs subjected to OGD. (a) Representative Nrf2 (red) immunofluorescence staining in BMECs. (b) Quantitative analysis of relative fluorescence intensity of Nrf2. (c) Representative Western blot bands of Nrf2, ZO-1, Occludin, and Claudin 5. (d)–(g) Quantitative analysis of the expressions of proteins. (h)–(k) The level of Nrf2, HO-1 after siRNA, URB, and AG treatment. $^{*}p < 0.05$, *vs.* Con/siNC, $^{\#}p < 0.05$ *vs.* OGD, $^{\wedge}p < 0.05$ *vs.* URB, $^{\&}p < 0.05$ *vs.* AG, $^{\triangledown}p < 0.05$ *vs.* siNrf2, ($n = 3$). Magnificent: 400×, scale bar 50 μm.

in cotreatment group ($p < 0.05$, vs. URB group; $p < 0.05$, vs. AG group). Taken together, these results suggested that UBR597 and AG increased the survival and growth of endothelial cells during OGD in vitro.

3.3. URB597 and AG Promote the Tube Formation in bEnd.3 Cells Subjected to OGD. Previous studies suggested that ECS and AG were involved in endothelial cell angiogenesis [22]. To further investigate the effects of URB597 and AG on the tube formation of BMECs, the total pipe length of the tube-like structure in bEnd.3cells that had been treated with URB597, AG, and both, was measured after 12 h of culture under OGD. At the beginning of the OGD (0 h), there are no differences were found among groups; however, the

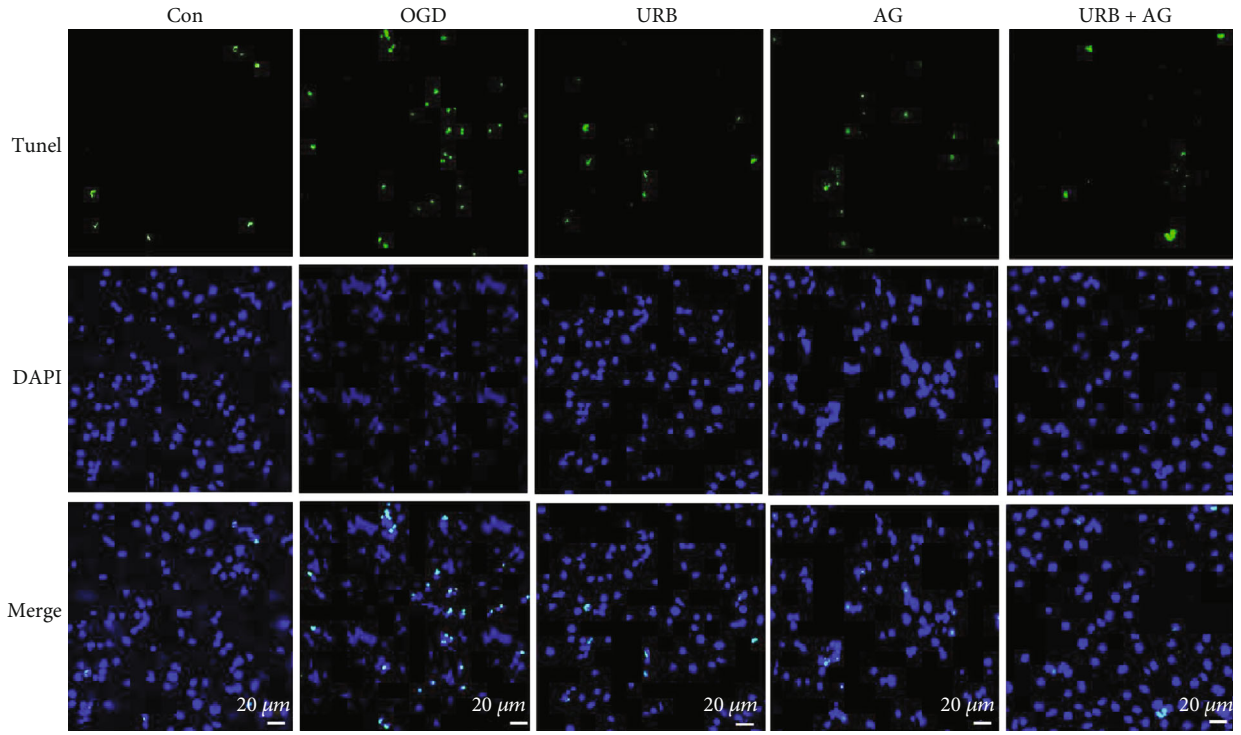

(a)

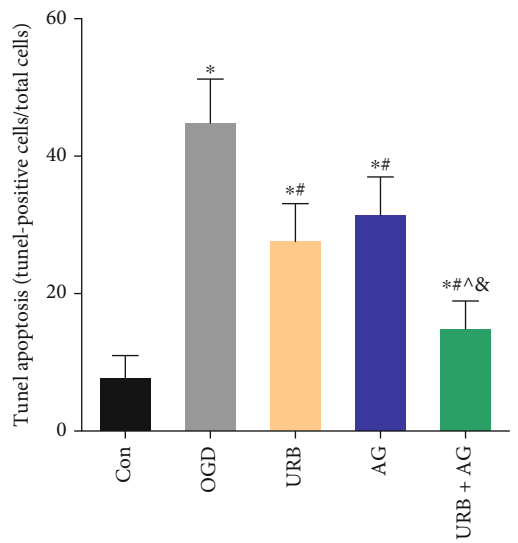

(b)

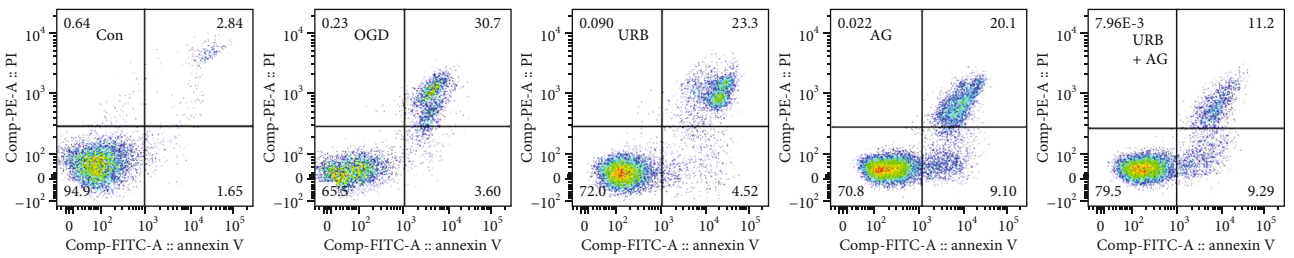

(c)

Figure 8: Continued.

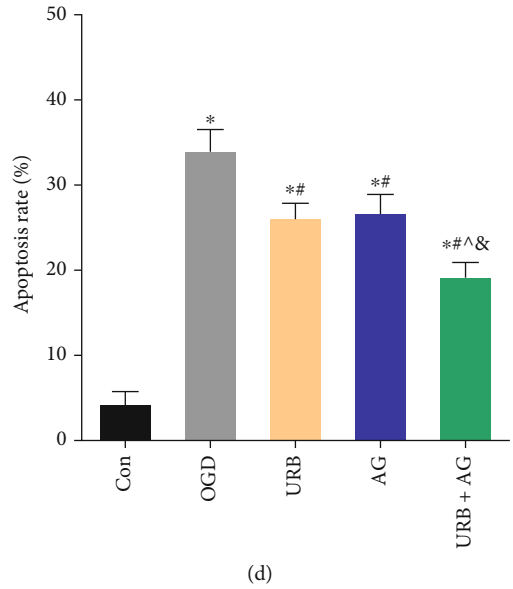

Figure 8: Effects of URB and AG on apoptosis. (a) Representative TUNEL staining in BMECs. (b) Quantitative analysis of the apoptosis rate in TUNEL. (c, d) Cellar apoptosis was detected by Annexin V-FITC/PI flow cytometry analysis. $^{*}p < 0.05$, vs. Con, $^{\#}p < 0.05$ vs. OGD, $^{\wedge}p < 0.05$ vs. URB, $^{\&}p < 0.05$ vs. AG, ($n = 6$). Magnificent: 200×, scale bar 20 μm.

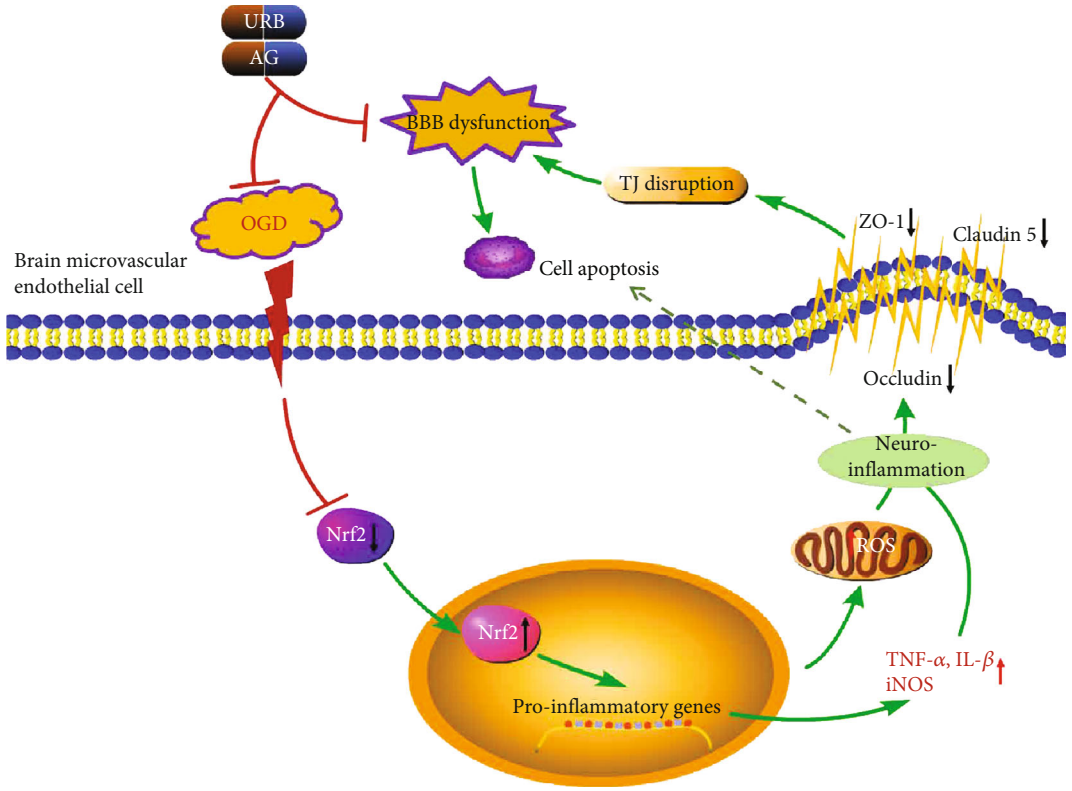

Figure 9: Possible mechanisms of URB and AG against OGD-induced BBB dysfunction and apoptosis. OGD inactivates the Nrf2 signaling, leading to the increase of proinflammatory factors and mitochondrial ROS. These cause a decrease in TJ protein expression and TJ degeneration in BMECs. The FAAH inhibitor URB597 and AG ameliorate BBB permeability and apoptosis by reducing oxidative stress and inflammation and activating Nrf2 signaling in OGD.

tube-like structure was different after 12 h of OGD (Figure 3(a)). Statistical results show that the total pipe length of the tube-like structure in the OGD group was significantly decreased compared to the cells in the Con group ($p < 0.05$). This reduction was reversed by pretreatment with URB597, AG, and combination (all $p < 0.05$, vs. OGD

group) (Figure 3(b)). Thus, this result indicated that URB597 and AG treatments promote the tube formation of BMECs in OGD.

3.4. URB597 and AG Revert OGD-Induced Endothelial Barrier Leakage. The microvascular endothelial barrier is one important basis of the BBB, and its leakage was measured using TEER and EB-albumin assay. TEER, a measure of ion flux, was destroyed by OGD leading to declining over time [17]. The cell permeability was measured at 4 h of OGD, as the cell viability was not affected by OGD at that point (supplementary figure). As shown in Figure 3(c), the reduction of TEER induced by OGD was significantly improved by URB treatment ($p < 0.05$, vs. OGD group). A similar increment was found after treating with AG ($p < 0.05$, vs. OGD group). In the cotreatment group, the TEER was also raised.

Instead, with the opening of ion channels, the EB-albumin permeability significantly raised in OGD ($p < 0.05$, vs. Con group) (Figure 3(d)). URB treatment and AG treatment reduced the EB-albumin leakage. In addition, the EB-albumin level in the combination therapy group was lower levels than those in the URB group and the AG group ($p < 0.05$, respectively) and had the optimal effectiveness in suppressing endothelial barrier leakage (Figure 3(d)). These results above demonstrated that treatment with URB and AG reverted microvascular endothelial barrier leakage induced by OGD, showing the protective effect on endothelial cell permeability.

3.5. URB597 and AG Inhibit OGD-Induced Mitochondrial Oxidative Stress Inflammatory Response. Oxidative stress and inflammatory response are critical pathological processes in cerebral ischemia injury, and their intimate interactions mediate neuronal damage, endothelial cell permeability dysfunction, causing the accumulation of mitochondrial ROS [23]. We found that the level of ROS was upregulated in OGD cells ($p < 0.05$, vs. Con group) (Figures 4(a) and 4(b)). Compared with the control cells, proinflammatory factors' mRNAs, TNF-α, IL-1β, and iNOS, were upregulated in the OGD group (all $p < 0.05$) (Figures 4(c)–4(e)). In addition, cells in the OGD group presented decreased levels of SOD and CAT ($p < 0.05$, respectively, vs. Con group) and increased MDA ($p < 0.05$, vs. Con group) (Figures 4(f)–4(i)). Those elevated ROS, MDA, and inflammatory factors were inhibited by URB597 treatment, AG treatment, and cotreatment (all $p < 0.05$, vs. OGD group). Moreover, the cotreatment had the optimal effectiveness in antioxidation and anti-inflammation (all $p < 0.05$, vs. URB + AG group) (Figures 4(a)–4(i)). Therefore, these data showed that URB597 and GA inhibited OGD-induced mitochondrial oxidative stress and the resultant inflammatory response.

3.6. URB597 and AG Attenuate OGD-Induced MMP Injury. To determine whether ROS permeabilizes the mitochondrial membrane, MMP was measured using the cyanine dye JC-1. The accumulation of JC-1 in these organelles results in the formation of J-aggregates (high MMP, red fluorescence), which is in addition to the typical green fluorescence of J-monomers (low MMP) [24]. The decrease in the ratio between the red and green fluorescence intensity is a marker of mitochondrial damage. As shown in Figure 5, OGD led to a significant decrease in the MMP of BMECs ($p < 0.05$, vs. Con group). However, the decrease in OGD-induced MMP was notably alleviated in the URB group, the AG group, and the URB + AG group (all $p < 0.05$, vs. OGD group) (Figure 5(a)). In addition, URB597 combined with AG treatment was more effective than single treatment ($p < 0.05$, vs. URB + AG group) (Figure 5(b)). These findings confirmed that the URB597 and AG treatments attenuated OGD-induced mitochondrial depolarization, as they have synergistic protective effects on MMP in OGD.

3.7. URB597 and AG Upregulate the Expression of the Tight Junction (TJ) Proteins and Activate Nrf2 Signaling in OGD. The BBB is one of the most robust physical barriers, comprised of TJ proteins in BMECs [25]. We further investigated the effects of URB and AG on TJ membrane proteins, including ZO-1, Occludin, and Claudin 5, against OGD-induced injury. As shown in Figures 6 and 7, OGD led to decreasing expression of ZO-1, Occludin, and Claudin 5. After URB and AG treatment, the relative fluorescence intensity of ZO-1 and Occludin was elevated (all $p < 0.05$, vs. OGD group) (Figures 6(a)–6(c)). Western blot analysis revealed that ZO-1, Occludin, and Claudin 5 expressions were markedly reduced in the OGD group as compared to the Con group (all $p < 0.05$, vs. Con group) (Figures 7(c) and 7(e)–7(g)). These reductions were reversed by URB treatment, AG treatment, and cotreatment. Compared with the URB group or AG group, the upregulation effect of TJ proteins was the most significant in the URB + AG group (all $p < 0.05$) (Figures 6(b) and 6(c), Figures 7(e)–7(g)). These findings suggested that URB and AG could promote the expressions of ZO-1, Occludin, and Claudin 5 of BMECs in the condition of OGD.

To clarify the mechanism underlying the effects of URB and AG, we investigated changes in Nrf2 signaling in each group. The Nrf2 protein with the red fluorescence was mainly expressed in cytoplasm and nucleus (Figure 7(a)). OGD decreased the relative fluorescence intensity of Nrf2 level, which was reversed by URB treatment and AG treatment (all $p < 0.05$, vs. OGD group) (Figure 7(b)). More significant increase was found in the URB + AG group ($p < 0.05$, vs. URB group) (Figure 7(b)). Western blot analysis revealed that Nrf2 expression was downregulated by OGD (Figures 7(c) and 7(d)). However, URB treatment, AG treatment, and cotreatment increased the level of Nrf2 protein. In addition, compared with the siNC group, the levels of Nrf2 and HO-1 were deceased following siRNA silencing. However, the expression of Nrf2 as well as its downstream HO-1 was increased after URB597 and AG treatment, respectively (Figures 7(h)–7(k)) ($p < 0.05$, vs. siNrf2 group). All of these results suggested that URB597 and AG could upregulate the expression of TJ proteins and activate Nrf2 signaling in OGD.

3.8. URB597 and AG Suppress OGD-Induced Apoptosis. MMP and endothelial barrier impairment are hallmark events in triggering the early stage of energy deterioration, pathological changes, and cell apoptosis [26]. First, the cell apoptotic ratio was determined by TUNEL fluorescence staining (Figure 8(a)). The number of TUNEL-positive apoptotic cells with green fluorescence was very obvious in the OGD group ($p < 0.05$, vs. Con group). However, the URB597 treatment and the AG treatment significantly reduced the number of green fluorescent cells (all $p < 0.05$, vs. OGD group). Furthermore, the TUNEL-positive apoptotic cells continued to decrease in the cotreatment group compared with the URB group and the AG group (all $p < 0.05$) (Figure 8(b)).

To further confirm the antiapoptotic effect of URB597 and AG, we detected cell apoptosis by Annexin V-FITC/PI flow cytometry analysis. As shown in Figure 8(c), the apoptotic rate was $34.3 \pm 2.2\%$ in the OGD group, which was greatly increased compared with the control group ($p < 0.05$) (Figure 8(d)). Cells pretreated with AG and URB597 had a reduced apoptotic rate with $26.2 \pm 1.7\%$ and $24.5 \pm 1.5\%$, respectively. The antiapoptotic effect of combined treatment was more effective than single treatment ($p < 0.05$, vs. URB + AG group) (Figure 8(d)). These results were consistent with the staining of TUNEL fluorescence. All of these findings suggested that URB597 combined with AG could mitigate OGD-induced TUNEL-positive cellar apoptosis levels better.

4. Discussion

BMECs form a barrier that is highly restrictive to the passage of solutes between nervous tissue and circulating blood [27]. It is a vital structure for maintaining BBB function and brain homeostasis that is vulnerably disrupted in various neurological diseases. Traumatic brain injury can, directly and indirectly, cause BMECs barrier rupture [28]. In an experimental animal model of stroke, cerebral ischemia destroys the BBB permeability, leading to an increase of brain EB content and brain water content [29]. In the present study, microvascular endothelial barrier function is disrupted in OGD, showing the TEER decline. TEER, a strong indicator of the integrity of the cellular barriers, is inversely related to the fractional area of pathways open to water and small molecules across a cell monolayer [30]. One potential mechanism for this decline is that OGD can open multiple ion channels, such as calcium ion channels [31]. We also found that EB leakage was increased by OGD, which is in line with previous reports [32]. Furthermore, BBB microvascular network is developed via vasculogenesis [33]. In cell viability and tube formation assay, the cellular activity and the length of a tubular structure in the OGD group were significantly decreased. These data demonstrate that OGD destroys the endothelial growth and barrier function, causing increased permeability of BMECs.

Biochemical characteristics of BBB damage include decreased expression and altered organization of TJ constituent proteins [4]. To evaluate the changes of TJ structural and regulatory proteins, we performed the fluorescence staining and western blotting for ZO-1, occludin, and Claudin-5. As shown in Figure 6, the lower immunostaining of ZO-1 and occludin together with the shift of intracellular localization of ZO-1 and occludin from the membrane to the cytoplasm in BMECs in the OGD group is indicating the altered TJ structures induced by OGD. In western blotting, OGD led to a significant reduction in levels of ZO-1, occludin, and Claudin-5 proteins. Since the frayed TJ structure has been shown to result in disruption of BBB integrity compared to intact TJ [34], likely, increased frayed TJ formations, as well as the decreased expression of TJ proteins in BMECs was, at least in part, causally implicated in permeability damage in OGD. In addition, endothelial barrier dysfunction involved in ischemic cerebrovascular pathogenesis may be a trigger, or consequence, of oxidative stress and inflammatory responses [35]. Here, a robust inflammatory response is activated by OGD with proinflammatory cytokine mRNA (TNF-α, IL-1β, and iNOS) upregulation, which is one of the most important mechanisms for cellular metabolism and barrier function disorder. As inflammation after stroke not only lead to the remodeling of TJ but also promote cellular ROS accumulating [36]. ROS were considered as one of the key factors in cellular damage and tissue injury. Mitochondria are the main organelles of cellular ROS production, which are necessary for numerous fundamental functions, including respiration and oxidative energy production, regulation of the intracellular homeostasis [37]. During OGD events, BMEC cannot utilize mitochondrial mechanisms that allow it to maintain normal energy and metabolism, that producing ROS and inflammatory factors in excess and even worse MMP dysfunction. MMP impairment further triggers a series of cascades, including mitochondrial permeability damage and cell apoptosis [38]. In this study, accumulation of ROS levels combined with an imbalance of oxidant and antioxidant enzymes (descended SOD and CAT, elevated MDA) is demonstrated in OGD. When the greater imbalance occurs in favor of the ROS, mitochondrial oxidative stress and BMEC barrier damage ensue.

URB597, a relatively selective inhibitor of FAAH, promotes activities of ECS by enhancing its ligand and receptor levels. ECS is a physiological system with the capacity to mitigate cardiovascular and cerebrovascular disorders through neuronal and endothelial actions [39]. In our previous study, URB597 showed neuroprotective effects on primary cultured hippocampal neurons against OGD-induced neuronal apoptosis by activating CB1-brain-derived neurotrophic factor signaling [16]. Furthermore, we recently found that URB597 could improve neurovascular unit damage via suppressing neuroinflammation and ROS in rats with chronic cerebral ischemia [40]. In this study, we have demonstrated that the novel vascular protective effects of URB597 are involved with anti-inflammation and antioxidation. Levels of ROS and proinflammatory cytokines were significantly decreased in URB597 treatment. OGD-induced mitochondrial MMP disruption was also prevented by URB597. Meanwhile, URB597 improved the BMECs permeability damage compared with that in the OGD group. The clear mitochondrial protective action combined with anti-

inflammation and antioxidation is probably the key underlying mechanism for keeping the BMECs barrier. Indeed, basic research results accumulated since the late 1990s indicate that the moderating effects of ECS on vascular endothelium actualize via attenuating vascular inflammation [41]. ECS can regulate redox function at multiple levels, with a range of downstream effects of cells and tissues. In cardiovascular aging and atherosclerosis, FAAH knockout can decrease age-related cardiac dysfunction, myocardial nitrative stress, and inflammatory gene expression [42]. Another reason for this endothelial protection is that reduction of TJ proteins, ZO-1, Occludin, and Claudin 5, induced by OGD was reserved by URB597 treatment. For morphological evidence, URB597 is proven to reduce ultrastructural deterioration of TJ and improve capillary endothelium breakage and vague basal lamina in cerebral ischemia [40].

AG's ability to prevent or mediate neurodegeneration and oxidative stress in cerebral ischemia in vivo was confirmed [11, 13, 15]. However, the study of modulated effects of AG on BBB function in stroke in vitro or in vivo models has been reported rarely. Yen et al. have reported that AG modulates the oxidative stress-related signaling pathways in primary cerebral endothelial cells to provide positive protection against OGD, maintaining the integrity of the endothelial barrier [43]. In hCMEC/D3, AG-loaded nanoparticles improve the permeation of AG without damaging BBB [44]. In this study, AG ameliorates the permeability of BMECs at various inflammation-mediated mechanisms, including antioxidative stress, inhibition of proinflammatory factors, and protecting mitochondria under the condition of OGD. Like URB597, AG upregulates the expression of ZO-1, Occludin, and Claudin 5 and keeps restoration of BBB integrity. Interestingly, in URB597 and AG cotreatment, we find a novel biological action is that the AG and URB597 display the positive synergistic protective effect on BMEC permeability and survival. However, AG (at 50 and 100 μM concentrations) was reported to induce cerebral endothelial cell apoptosis via arresting cell cycle at the G_0/G_1 phase in cerebral ischemia/reperfusion model in vitro [45]. The discrepancy between this result and ours can be explained by differences in the duration of OGD and the dosage of AG that were used. Both AG and URB597 have a favorable safety profile in a time-dependent and dose-dependent manner [10, 11, 46].

Nrf2, a member of the cap-n-collar family of basic leucine zipper proteins, is basically bound in the cytoplasm to Kelch-like ECH-associated protein 1 (Keap1), directing it to ubiquitination and subsequent degradation by the proteasome [47]. Activating Nrf2 signaling shows neuroprotection against cerebral ischemia by antioxidative stress and antiapoptosis [48]. A deficiency of Nrf2 protein has been observed in neurodegenerative diseases, vascular inflammatory disorders, and stroke [49]. Nrf2 knock-out mice with more serious cerebral infarction, inflammatory damages, and neurological deficits were found compared with wild-type mice [50]. Physiological and pharmacological actions of URB597 and AG in treating many diseases are related to the regulation of the Nrf2. There is a simultaneous increase in Nrf2 expression in the brain of rats with hypertension caused by intraperitoneal injection with URB597 [51]. AG attenuates neurovascular injuries induced by cerebral ischemia via activating Nrf2 signaling, inhibiting inflammatory response [43, 52]. In this OGD model of BMECs, both URB597 and AG enhanced Nrf2 expression and may further cause Nrf2 to translocate into the nucleus. That results in subsequently suppressing the transcription of downstream targets (HO-1), proinflammatory genes, and oxidative metabolism. Excessive ROS is the primary stimulus of vascular dysfunction, which generates large numbers of potentially harmful intermediates that cause imbalances between prooxidants and antioxidants in vascular endothelial cells [53]. Furthermore, the decreasing Nrf-2 and HO-1 following siRNA silencing was reversed by URB treatment and AG treatment, respectively. These findings reveal that the protective effects of URB597 and AG on OGD-induced BMEC barrier damage and apoptosis are associated with activation of the Nrf2 signaling cascade. In addition, the role of URB597 and AG in modulating the Nrf2 pathway may be related to the fact that both can inhibit nuclear factor kappa light chain enhancer of activated B cells (NF-κB) signaling. There is a complex cross-talk between the Nrf2 and NF-κB pathway, and NF-κB can modulate Nrf2 transcription and activity, whereas Nrf2 counteracts NF-κB-driven inflammatory response [54].

There are some limitations to this study. Under stress conditions (excessive accumulation of ROS and inflammatory stress), Nrf2-Keap1 interaction is disrupted, and Nrf2 translocates into the nucleus encoding proteins (i.e., HO-1) that counterbalance impairments in inflammatory and redox control [55]. Therefore, it would be more helpful to confirm Nrf2 is mediating these vascular protective effects if nuclear translocation of Nrf2 was also accessed. Second, mitochondrial oxidative stress is accessed by testing the levels of ROS, SOD, CAT, and MDA, but mitochondrial-specific probes such as MitoSOX are more suitable for measurement of mitochondrial ROS than DCF-DA. In addition, our demonstration of endothelial barrier preservation would benefit from additional experiments, such as check the levels of the inflammatory cytokines by ELISA, Evans blue staining for BBB permeability, and transmission electron microscope for BBB ultrastructure in vivo. The limitations should be further improved in animal experiments.

To our knowledge, the present study demonstrates for the first time that the FAAH inhibitor URB597 and AG protects BMECs against OGD-induced permeability impairment and apoptosis (proposed mechanism of URB and AG shown in Figure 9). This vascular protection is closely associated with activation of the Nrf2 signaling as well as anti-inflammatory and antioxidative effects, providing a new potential strategy for the treatment of endothelial barrier damage in ischemic cerebrovascular diseases.

Data Availability

The data that support the findings of this study are available from the corresponding authors (Qiao-Li Lv, lvqiaoli2008@126.com; Jian Hai, haijiandoct@zoho.com.cn) upon reasonable request.

Conflicts of Interest

The authors declare no conflict of interest.

Authors' Contributions

Conception and design of the study were DP. W, QL. L, and J.H; analysis and interpretation of data were K. K, J. S, Q. L, and DP. W; drafting the manuscript was DP. W and K.K; revision of manuscript for important intellectual content was QL. L and J.H. All authors read and approved the final manuscript. Da-Peng Wang, Kai Kang, and Jun Sun contributed equally to this work and should be identified as the co-first authors.

Acknowledgments

This study was supported by the National Nature Science Foundation of China (82001383 and 81974207), Program of Shanghai Municipal Health Commission (20204Y0074), and The Distinguished Young Scholars Fund of Jiangxi Cancer Hospital (2021DYS01). We thank the editor and reviewers for their valuable comments on this study.

References

[1] W. J. Powers, "Acute ischemic stroke," *The New England Journal of Medicine*, vol. 383, no. 3, pp. 252–260, 2020.

[2] Y. Li, W. Zhong, Z. Jiang, and X. Tang, "New progress in the approaches for blood-brain barrier protection in acute ischemic stroke," *Brain Research Bulletin*, vol. 144, pp. 46–57, 2019.

[3] B. Obermeier, R. Daneman, and R. M. Ransohoff, "Development, maintenance and disruption of the blood-brain barrier," *Nature Medicine*, vol. 19, no. 12, pp. 1584–1596, 2013.

[4] W. Abdullahi, D. Tripathi, and P. T. Ronaldson, "Blood-brain barrier dysfunction in ischemic stroke: targeting tight junctions and transporters for vascular protection," *American Journal of Physiology. Cell Physiology*, vol. 315, no. 3, pp. C343–C356, 2018.

[5] R. Mechoulam and L. A. Parker, "The endocannabinoid system and the brain," *Annual Review of Psychology*, vol. 64, no. 1, pp. 21–47, 2013.

[6] H. Lowe, N. Toyang, B. Steele, J. Bryant, and W. Ngwa, "The endocannabinoid system: a potential target for the treatment of various diseases," *International Journal of Molecular Sciences*, vol. 22, no. 17, p. 9472, 2021.

[7] L. Mestre, P. M. Iñigo, M. Mecha et al., "Anandamide inhibits Theiler's virus induced VCAM-1 in brain endothelial cells and reduces leukocyte transmigration in a model of blood brain barrier by activation of CB (1) receptors," *Journal of Neuroinflammation*, vol. 8, no. 1, p. 102, 2011.

[8] M. C. Yang, H. Z. Zhang, Z. Wang, F. L. You, and Y. F. Wang, "The molecular mechanism and effect of cannabinoid-2 receptor agonist on the blood-spinal cord barrier permeability induced by ischemia-reperfusion injury," *Brain Research*, vol. 1636, pp. 81–92, 2016.

[9] L. Cristino, T. Bisogno, and V. Di Marzo, "Cannabinoids and the expanded endocannabinoid system in neurological disorders," *Nature Reviews. Neurology*, vol. 16, no. 1, pp. 9–29, 2020.

[10] R. A. Burgos, P. Alarcón, J. Quiroga, C. Manosalva, and J. Hancke, "Andrographolide, an anti-inflammatory multitarget drug: all roads lead to cellular metabolism," *Molecules*, vol. 26, no. 1, p. 5, 2021.

[11] J. Lu, Y. Ma, J. Wu et al., "A review for the neuroprotective effects of andrographolide in the central nervous system," *Biomedicine & Pharmacotherapy*, vol. 117, article 109078, 2019.

[12] C. B. Lindsay, J. M. Zolezzi, D. S. Rivera, P. Cisternas, F. Bozinovic, and N. C. Inestrosa, "Andrographolide reduces Neuroinflammation and oxidative stress in aged Octodon degus," *Molecular Neurobiology*, vol. 57, no. 2, pp. 1131–1145, 2020.

[13] D. P. Wang, H. Yin, Q. Lin et al., "Andrographolide enhances hippocampal BDNF signaling and suppresses neuronal apoptosis, astroglial activation, neuroinflammation, and spatial memory deficits in a rat model of chronic cerebral hypoperfusion," *Naunyn-Schmiedeberg's Archives of Pharmacology*, vol. 392, no. 10, pp. 1277–1284, 2019.

[14] D. P. Wang, S. H. Chen, D. Wang et al., "Neuroprotective effects of andrographolide on chronic cerebral hypoperfusion-induced hippocampal neuronal damage in rats possibly via PTEN/AKT signaling pathway," *Acta Histochemica*, vol. 122, no. 3, article 151514, 2020.

[15] G. Graverini, V. Piazzini, E. Landucci et al., "Solid lipid nanoparticles for delivery of andrographolide across the blood-brain barrier: in vitro and in vivo evaluation," *Colloids and Surfaces. B, Biointerfaces*, vol. 161, pp. 302–313, 2018.

[16] D. P. Wang, K. Y. Jin, P. Zhao, Q. Lin, K. Kang, and J. Hai, "Neuroprotective effects of VEGF-A nanofiber membrane and FAAH inhibitor URB597 against oxygen-glucose deprivation-induced ischemic neuronal injury," *International Journal of Nanomedicine*, vol. 16, pp. 3661–3678, 2021.

[17] G. S. Cao, H. L. Chen, Y. Y. Zhang et al., "YiQiFuMai powder injection ameliorates the oxygen-glucose deprivation-induced brain microvascular endothelial barrier dysfunction associated with the NF-κB and ROCK1/MLC signaling pathways," *Journal of Ethnopharmacology*, vol. 183, pp. 18–28, 2016.

[18] Y. Zhang, X. Li, S. Qiao et al., "Occludin degradation makes brain microvascular endothelial cells more vulnerable to reperfusion injury in vitro," *Journal of Neurochemistry*, vol. 156, no. 3, pp. 352–366, 2021.

[19] J. Cheng, H. L. Yang, C. J. Gu et al., "Melatonin restricts the viability and angiogenesis of vascular endothelial cells by suppressing HIF-1α/ROS/VEGF," *International Journal of Molecular Medicine*, vol. 43, no. 2, pp. 945–955, 2019.

[20] O. El Atat, A. Fakih, and M. El-Sibai, "RHOG activates RAC1 through CDC42 leading to tube formation in vascular endothelial cells," *Cells*, vol. 8, no. 2, p. 171, 2019.

[21] A. C. Marcos, M. Siqueira, L. Alvarez-Rosa et al., "Toxoplasma gondii infection impairs radial glia differentiation and its potential to modulate brain microvascular endothelial cell function in the cerebral cortex," *Microvascular Research*, vol. 131, article 104024, 2020.

[22] L. Al-Eitan, A. Alhusban, and S. Alahmad, "Effects of the synthetic cannabinoid XLR-11 on the viability and migration rates of human brain microvascular endothelial cells in a clinically-relevant model," *Pharmacological Reports*, vol. 72, no. 6, pp. 1717–1724, 2020.

[23] H. Chen, Y. He, S. Chen, S. Qi, and J. Shen, "Therapeutic targets of oxidative/nitrosative stress and neuroinflammation in ischemic stroke: applications for natural product efficacy with omics and systemic biology," *Pharmacological Research*, vol. 158, article 104877, 2020.

[24] K. Elefantova, B. Lakatos, J. Kubickova, Z. Sulova, and A. Breier, "Detection of the mitochondrial membrane potential by the

cationic dye JC-1 in L1210 cells with massive overexpression of the plasma membrane ABCB1 drug transporter," *International Journal of Molecular Sciences*, vol. 19, no. 7, p. 1985, 2018.

[25] Y. Hashimoto and M. Campbell, "Tight junction modulation at the blood-brain barrier: current and future perspectives," *Biochimica et Biophysica Acta - Biomembranes*, vol. 1862, no. 9, article 183298, 2020.

[26] D. Song, X. Jiang, Y. Liu, Y. Sun, S. Cao, and Z. Zhang, "Asiaticoside attenuates cell growth inhibition and apoptosis induced by Aβ1-42 via inhibiting the TLR4/NF-κB signaling pathway in human brain microvascular endothelial cells," *Frontiers in Pharmacology*, vol. 9, p. 28, 2018.

[27] M. Segarra, M. R. Aburto, and A. Acker-Palmer, "Blood-brain barrier dynamics to maintain brain homeostasis," *Trends in Neurosciences*, vol. 44, no. 5, pp. 393–405, 2021.

[28] A. Jarrahi, M. Braun, M. Ahluwalia et al., "Revisiting traumatic brain injury: from molecular mechanisms to therapeutic interventions," *Biomedicine*, vol. 8, no. 10, p. 389, 2020.

[29] Z. X. Chen, Q. Q. Xu, C. S. Shan et al., "Borneol for regulating the permeability of the blood-brain barrier in experimental ischemic stroke: preclinical evidence and possible mechanism," *Oxidative Medicine and Cellular Longevity*, vol. 2019, Article ID 2936737, 2019.

[30] B. Srinivasan, A. R. Kolli, M. B. Esch, H. E. Abaci, M. L. Shuler, and J. J. Hickman, "TEER measurement techniques for in vitro barrier model systems," *Journal of Laboratory Automation*, vol. 20, no. 2, pp. 107–126, 2015.

[31] E. Salvador, M. Burek, and C. Y. Forster, "Stretch and/or oxygen glucose deprivation (OGD) in an in vitro traumatic brain injury (TBI) model induces calcium alteration and inflammatory cascade," *Frontiers in Cellular Neuroscience*, vol. 9, p. 323, 2015.

[32] S. Zhang, A. Chen, and X. Chen, "A feedback loop involving microRNA-150 and MYB regulates VEGF expression in brain microvascular endothelial cells after oxygen glucose deprivation," *Frontiers in Physiology*, vol. 12, article 619904, 2021.

[33] M. Campisi, Y. Shin, T. Osaki, C. Hajal, V. Chiono, and R. D. Kamm, "3D self-organized microvascular model of the human blood-brain barrier with endothelial cells, pericytes and astrocytes," *Biomaterials*, vol. 180, pp. 117–129, 2018.

[34] Y. Yamazaki, D. J. Baker, M. Tachibana et al., "Vascular cell senescence contributes to blood-brain barrier breakdown," *Stroke*, vol. 47, no. 4, pp. 1068–1077, 2016.

[35] G. Ndrepepa, "Myeloperoxidase - a bridge linking inflammation and oxidative stress with cardiovascular disease," *Clinica Chimica Acta*, vol. 493, pp. 36–51, 2019.

[36] R. Moretti, M. Giuffré, P. Caruso, S. Gazzin, and C. Tiribelli, "Homocysteine in neurology: a possible contributing factor to small vessel disease," *International Journal of Molecular Sciences*, vol. 22, no. 4, p. 2051, 2021.

[37] S. Di Meo, T. T. Reed, P. Venditti, and V. M. Victor, "Role of ROS and RNS sources in physiological and pathological conditions," *Oxidative Medicine and Cellular Longevity*, vol. 2016, Article ID 1245049, 2016.

[38] T. Nyunt, M. Britton, K. Wanichthanarak et al., "Mitochondrial oxidative stress-induced transcript variants of ATF3 mediate lipotoxic brain microvascular injury," *Free Radical Biology & Medicine*, vol. 143, pp. 25–46, 2019.

[39] S. Mukhopadhyay and D. A. Tulis, "Endocannabinoid regulation of matrix metalloproteinases: implications in ischemic stroke," *Cardiovascular & Hematological Agents in Medicinal Chemistry*, vol. 5, no. 4, pp. 311–318, 2007.

[40] D. P. Wang, K. J. Liu, G. Kasper, Q. Lin, and J. Hai, "Inhibition of SENP3 by URB597 ameliorates neurovascular unit dysfunction in rats with chronic cerebral hypoperfusion," *Biomedicine & Pharmacotherapy*, vol. 91, pp. 872–879, 2017.

[41] Z. Benyó, É. Ruisanchez, M. Leszl-Ishiguro, P. Sándor, and P. Pacher, "Endocannabinoids in cerebrovascular regulation," *American Journal of Physiology. Heart and Circulatory Physiology*, vol. 310, no. 7, pp. H785–H801, 2016.

[42] S. Bátkai, M. Rajesh, P. Mukhopadhyay et al., "Decreased age-related cardiac dysfunction, myocardial nitrative stress, inflammatory gene expression, and apoptosis in mice lacking fatty acid amide hydrolase," *American Journal of Physiology. Heart and Circulatory Physiology*, vol. 293, no. 2, pp. H909–H918, 2007.

[43] T. L. Yen, R. J. Chen, T. Jayakumar et al., "Andrographolide stimulates p38 mitogen-activated protein kinase-nuclear factor erythroid-2-related factor 2-heme oxygenase 1 signaling in primary cerebral endothelial cells for definite protection against ischemic stroke in rats," *Translational Research*, vol. 170, pp. 57–72, 2016.

[44] C. Guccione, M. Oufir, V. Piazzini et al., "Andrographolide-loaded nanoparticles for brain delivery: formulation, characterisation and In Vitro permeability using hCMEC/D3 cell line," *European Journal of Pharmaceutics and Biopharmaceutics*, vol. 119, pp. 253–263, 2017.

[45] T. L. Yen, W. H. Hsu, S. K. H. Huang et al., "A novel bioactivity of andrographolide from Andrographis paniculata on cerebral ischemia/reperfusion-induced brain injury through induction of cerebral endothelial cell apoptosis," *Pharmaceutical Biology*, vol. 51, no. 9, pp. 1150–1157, 2013.

[46] R. K. P. Tripathi, "A perspective review on fatty acid amide hydrolase (FAAH) inhibitors as potential therapeutic agents," *European Journal of Medicinal Chemistry*, vol. 188, article 111953, 2020.

[47] M. S. Brandes and N. E. Gray, "NRF2 as a therapeutic target in neurodegenerative diseases," *ASN Neuro*, vol. 12, 2020.

[48] M. A. Hannan, R. Dash, A. A. M. Sohag, M. N. Haque, and I. S. Moon, "Neuroprotection against oxidative stress: phytochemicals targeting TrkB signaling and the Nrf2-ARE antioxidant system," *Frontiers in Molecular Neuroscience*, vol. 13, p. 116, 2020.

[49] F. Sivandzade, S. Prasad, A. Bhalerao, and L. Cucullo, "NRF2 and NF-κB interplay in cerebrovascular and neurodegenerative disorders: molecular mechanisms and possible therapeutic approaches," *Redox Biology*, vol. 21, article 101059, 2019.

[50] L. Li, X. Zhang, L. Cui et al., "Ursolic acid promotes the neuroprotection by activating Nrf2 pathway after cerebral ischemia in mice," *Brain Research*, vol. 1497, pp. 32–39, 2013.

[51] M. Biernacki, M. Baranowska-Kuczko, G. N. Niklińska, and E. Skrzydlewska, "The FAAH inhibitor URB597 modulates lipid mediators in the brain of rats with spontaneous hypertension," *Biomolecules*, vol. 10, no. 7, p. 1022, 2020.

[52] M. Y. Yang, Q. L. Yu, Y. S. Huang, and G. Yang, "Neuroprotective effects of andrographolide derivative CX-10 in transient focal ischemia in rat: involvement of Nrf2/AE and TLR/NF-κB signaling," *Pharmacological Research*, vol. 144, pp. 227–234, 2019.

[53] B. Chen, Y. Lu, Y. Chen, and J. Cheng, "The role of Nrf2 in oxidative stress-induced endothelial injuries," *The Journal of Endocrinology*, vol. 225, no. 3, pp. R83–R99, 2015.

[54] I. Bellezza, I. Giambanco, A. Minelli, and R. Donato, "Nrf2-Keap1 signaling in oxidative and reductive stress," *Biochimica et Biophysica Acta (BBA)-Molecular Cell Research*, vol. 1865, no. 5, pp. 721–733, 2018.

[55] M. Farina, L. E. Vieira, B. Buttari, E. Profumo, and L. Saso, "The Nrf2 pathway in ischemic stroke: a review," *Molecules*, vol. 26, no. 16, p. 5001, 2021.

Hindawi
Oxidative Medicine and Cellular Longevity
Volume 2022, Article ID 8645714, 23 pages
https://doi.org/10.1155/2022/8645714

Research Article

Thioredoxin-Interacting Protein (TXNIP) Knockdown Protects against Sepsis-Induced Brain Injury and Cognitive Decline in Mice by Suppressing Oxidative Stress and Neuroinflammation

Yu Zhang,[1] **Cheng-Jun Xing**,[1] **Xiao Liu**,[1] **Ya-Hong Li**,[1] **Jing Jia**,[1,2] **Jian-Guo Feng**,[1,2] **Cheng-Jie Yang**,[1,2] **Ye Chen**,[3] **and Jun Zhou**[1,2]

[1]*Department of Anesthesiology, The Affiliated Hospital of Southwest Medical University, Luzhou, China*
[2]*Laboratory of Anesthesiology, Southwest Medical University, Luzhou, China*
[3]*Department of Traditional Chinese Medicine, The Affiliated Hospital of Southwest Medical University, Luzhou, China*

Correspondence should be addressed to Ye Chen; chenye0117@swmu.edu.cn and Jun Zhou; scjunzhou@gmail.com

Received 19 December 2021; Revised 17 April 2022; Accepted 23 April 2022; Published 5 May 2022

Academic Editor: Luzia Kalyne Almeida Moreira Leal

Sepsis-associated encephalopathy (SAE) is linked to increased morbidity and mortality rates in patients with sepsis. Increased cytokine production and neuronal apoptosis are implicated in the pathogenesis of the SAE. Neuroinflammation plays a major role in sepsis-induced brain injury. Thioredoxin-interacting protein (TXNIP), an inhibitor of thioredoxin, is associated with oxidative stress and inflammation. However, whether the TXNIP is involved in the sepsis-induced brain injury and the underlying mechanism is yet to be elucidated. Therefore, the present study was aimed at elucidating the effects of TXNIP knockdown on sepsis-induced brain injury and cognitive decline in mice. Lipopolysaccharide (LPS) was injected intraperitoneally to induce sepsis brain injury in mice. The virus-carrying control or TXNIP shRNA was injected into the lateral ventricle of the brain 4 weeks before the LPS treatment. The histological changes in the hippocampal tissues, encephaledema, and cognitive function were detected, respectively. Also, the 7-day survival rate was recorded. Furthermore, the alterations in microglial activity, oxidative response, proinflammatory factors, apoptosis, protein levels (TXNIP and NLRP3 inflammasome), and apoptosis were examined in the hippocampal tissues. The results demonstrated that the TXNIP and NLRP3 inflammasome expression levels were increased at 6, 12, and 24 h post-LPS injection. TXNIP knockdown dramatically ameliorated the 7-day survival rate, cognitive decline, brain damage, neuronal apoptosis, and the brain water content, inhibited the activation of microglia, downregulated the NLRP3/caspase-1 signaling pathway, and reduced the oxidative stress and the neuroinflammatory cytokine levels at 24 h post-LPS injection. These results suggested a crucial effect of TXNIP knockdown on the mechanism of brain injury and cognitive decline in sepsis mice via suppressing oxidative stress and neuroinflammation. Thus, TXNIP might be a potential therapeutic target for SAE patients.

1. Introduction

Sepsis is a life-threatening complication of severe infection, leading to tissue damage, multiple organ failure, and death if it is not treated promptly [1–3]. Among the multiple organs affected, brain damage occurs early in severe sepsis and promotes the development of other signs and symptoms. Brain damage is manifested by a series of neurological dysfunctions, such as delirium, coma, seizures, and focal neurological symptoms, causing sepsis-associated encephalopathy (SAE) [4–9]. According to previous reports, SAE occurs in about 70% of patients with sepsis, causing poor outcomes in the intensive care unit (ICU) [7, 9, 10]. The SAE is related to increased mortality of patients with sepsis [11, 12]. In addition, the SAE may cause permanent cognitive dysfunction, increase the susceptibility of the brain to

neurodegenerative diseases, and increase the risk of developing dementia [13]. However, the mechanism of brain damage caused by sepsis is yet inconclusive. Currently, there is a lack of specific drugs for SAE treatment. Treating infection, organ failure, and metabolic disorders while avoiding the use of neurotoxic drugs is adopted for managing sepsis [8, 14, 15]. Thus, exploration of the mechanism of SAE will develop specific new therapeutic strategies.

Neuroinflammation and oxidative stress are manifested in various neurological diseases [16–18]. As one of the pattern recognition receptors, the nucleotide-binding oligomerization domain-like receptor protein 3 (NLRP3) inflammasome is a supramolecular complex composed of NLRP3, apoptosis-associated speck-like protein (ASC), and caspase-1, which are indispensable for the body's innate immunity against microbial infection [19]. The complex is enriched in immune cells, including macrophages and microglia, and participates in the progress of inflammatory response. The NLRP3 inflammasome functions via caspase-1 zymogen activation, causing the proteolytic activation of proinflammatory cytokines, IL-1β and IL-18. A previous study using a mouse model showed that the NLRP3/caspase-1 pathway is involved in SAE. Moreover, the application of the NLRP3 inhibitor MCC950 effectuated NLRP3-mediated neuronal pyrolysis and proinflammatory cytokines [20]. However, the mechanism underlying the NLRP3 activation has not yet been elucidated.

The thioredoxin (TRX) system is widely present in the body and functions as a critical antioxidant. TRX is the main member of the TRX system and eliminates reactive oxygen species (ROS) by reducing the thiols [21, 22]. Thioredoxin-interacting protein (TXNIP) is a 46 kDa protein that binds to TRX, inhibits the antioxidant effect of TRX, and controls the cellular redox state [23, 24]. TXNIP plays a critical role in cerebrovascular and neurodegenerative diseases, such as subarachnoid hemorrhage and Alzheimer's disease [23, 25]. However, no study has been reported on whether TXNIP is involved in septic brain injuries.

In recent years, the cause-and-effect correlation between oxidative stress and the inflammatory response has gained increasing attention. Oxidative stress and inflammatory response are closely related to the pathogenesis of SAE. Oxidative stress can aggravate proinflammatory cytokine expression. Recent studies have shown that the TXNIP binds to NLRP3 and activates the NLRP3 inflammasome under excessive oxidative stress [24, 26]. Subsequently, the effect of TXNIP on the NLRP3 inflammasome has been observed in animal models, such as renal ischemia-reperfusion injury and myocardial ischemia-reperfusion injury models [27, 28]. Thus, it could be deemed that TXNIP is the modulator between oxidative stress and inflammation. However, specific research on the role of the TXNIP/NLRP3 signaling pathway in septic brain injury is yet lacking.

Consequently, the present study was aimed at evaluating the effects of TXNIP knockdown on sepsis-induced brain injury and cognitive impairment and the related molecular mechanism. Herein, we proposed that TXNIP knockdown ameliorates brain injury and cognitive decline after sepsis by regulating oxidative stress and neuroinflammation.

2. Materials and Methods

2.1. Animals. The current study protocol was approved by the Animal Care Committee of the Southwest Medical University, Luzhou, China (approval number: 20180306042). All procedures were performed following the National Institutes of Health guidelines for the use of experimental animals. A total of 518 male C57BL/6 mice (6–8 weeks), weighing 18–22 g, were purchased from Chengdu Dossy Experimental Animals Co., Ltd., China. The animals were housed in cages in a temperature-controlled room (22 ± 2°C) with an alternating 12 h light/dark cycle and acclimated for a week before the study.

2.2. Experimental Design. In the current study, all mice were randomly assigned to the following three experiments (Figure 1).

2.2.1. Experiment 1. To evaluate the injury and endogenous TXNIP, NLRP3, and cleaved caspase-1 temporal levels in the hippocampus of septic mice, 104 surviving animals were randomly divided into four groups ($n = 26$/group): negative control (NC) and 6, 12, and 24 h after lipopolysaccharide (LPS) treatment. The mice in the sepsis groups were injected intraperitoneally with 15 mg/kg LPS (Sigma-Aldrich, St. Louis, MO, USA), while the NC group was injected with an equivalent volume of normal saline. Western blotting, hematoxylin-eosin (HE) staining, enzyme-linked immunosorbent assay (ELISA), and Iba1 immunofluorescence staining were conducted at the corresponding time points after the LPS injection.

2.2.2. Experiment 2. To screen the most effective interference fragment of TXNIP, 60 surviving mice were randomly divided into five groups ($n = 12$/group): NC, LPS, LPS+control shRNA, LPS+TXNIP $shRNA_1$, and LPS+TXNIP $shRNA_2$. A 5 μL virus-carrying control shRNA, TXNIP $shRNA_1$, or TXNIP $shRNA_2$ was injected into the lateral cerebral ventricle in the LPS+control shRNA, LPS+TXNIP $shRNA_1$, and LPS+TXNIP $shRNA_2$ groups, respectively. The shRNA sequences are listed in the following: TXNIP $shRNA_1$ (5′-GCAAACAGACTTTGGACTACTCGAGT AGTCC-AAAGTCTGTTTGC-3′) and TXNIP $shRNA_2$ (5′ -GCTGGATAGACCTAAACATCT- CGAGATGTTTA GGTCTATCCAGC-3′). The control shRNA sequences are as follows: 5′-CCTAAGGTTAAGTCGCCCTCGCTCGA GCGAGGGCGACTTAACC-TTAGG-3′. After 4 weeks, a sepsis model was established by intraperitoneal injection of 15 mg/kg LPS or the same volume of normal saline. Western blotting and quantitative real-time polymerase chain reaction (qRT-PCR) were performed 24 h post-LPS injection.

2.2.3. Experiment 3. To observe the effect of TXNIP knockdown on the injury and NLRP3/caspase-1 pathway in the hippocampus of septic mice, 280 enrolled mice were randomly divided into four groups ($n = 70$/group): NC, LPS, LPS+control shRNA, and LPS+TXNIP shRNA. A volume of 5 μL adeno-associated virus (AAV) vectors containing control shRNA or TXNIP $shRNA_1$ was injected into the

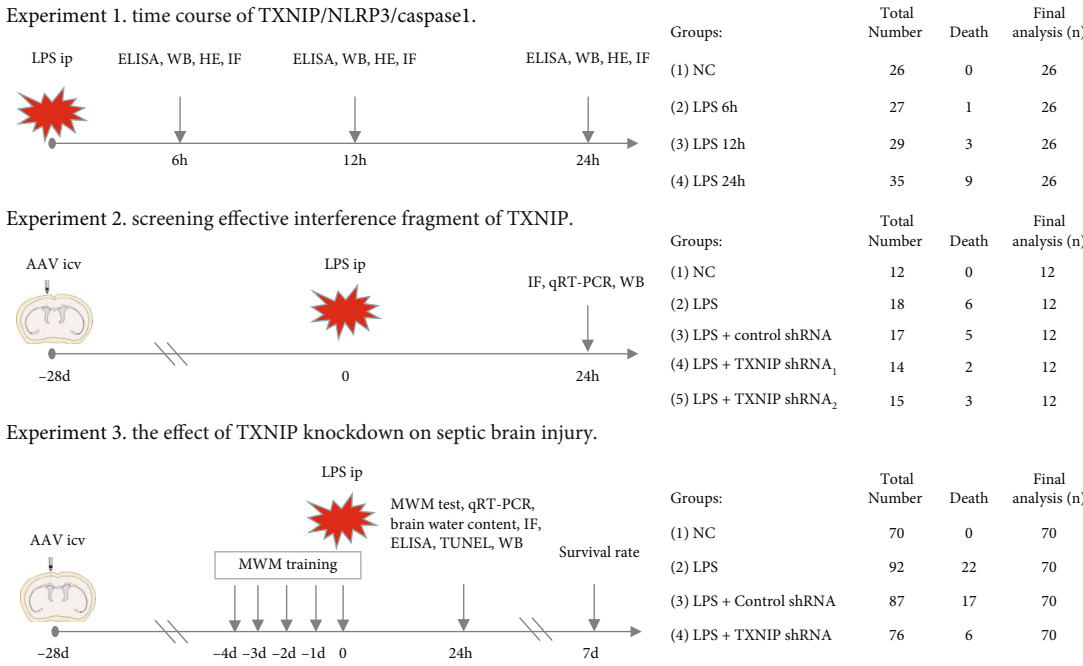

Figure 1: Experimental design and animal groups. AAV: adeno-associated virus; LPS: lipopolysaccharide; ip: intraperitoneal injection; icv: lateral cerebral ventricle; TXNIP: thioredoxin-interacting protein; NLRP3: nucleotide-binding oligomerization domain-like receptor protein 3; MWM: Morris water maze; HE: hematoxylin-eosin staining; WB: Western blotting; IF: immunofluorescence; qRT-PCR: quantitative real-time polymerase chain reaction; TUNEL: terminal deoxynucleotidyl transferase dUTP nick end labeling; ELISA: enzyme-linked immunosorbent assay.

lateral ventricle of the brain in the LPS+control shRNA or LPS+TXNIP shRNA group, respectively. After 4 weeks, a sepsis model was established by the intraperitoneal injection of 15 mg/kg LPS or the equivalent volume of normal saline. For the survival study, 20 mice from each group were selected randomly to observe the survival rate for 7 days. In addition, on the 4th day (-4 d) before modeling, 10 mice from each group were selected randomly for the water maze experiment. Subsequently, another 40 mice were sacrificed 24 h after modeling for the brain water content, Western blotting, qRT-PCR, enzyme-linked immunosorbent assay (ELISA), hematoxylin-eosin (HE) staining, Iba1 immunofluorescence staining, and terminal deoxynucleotidyl transferase dUTP nick end-labeling (TUNEL) staining.

2.3. Sepsis Model. Animals in the LPS group received an intraperitoneal injection (ip) of LPS (15 mg/kg) isolated from *Escherichia coli* O111:B4 and diluted in sterile normal saline, while the NC group received an equal volume of normal saline. Since LPS induced a high mortality rate, mice that died during the experiment (except for the survival study) were excluded and relevant mice were supplemented as previously described [29–31].

2.4. Specimen Preparation. At the corresponding time after the LPS injection, mice were sacrificed under anesthesia and the blood was collected from eyes for the ELISA test. The whole brains were removed immediately and postfixed for 24 h. The sections were then prepared for HE staining, immunohistochemical staining, and the TUNEL assay. Moreover, the hippocampal CA1 region was rapidly microdissected from both sides of the hippocampal fissure by sharp dissection on ice, frozen in liquid nitrogen, and stored at -80°C for subsequent testing as previously described [32, 33].

2.5. AAV Injection. The AAV carried the enhanced green fluorescent protein (*EGFP*) gene. The AAV injection was administered on day 28 before the LPS or normal saline injection, as described previously [34]. Briefly, the AAV vectors (AAV-control shRNA, AAV-TXNIP $shRNA_1$, and AAV-TXNIP $shRNA_2$) were constructed by Yunzhou Biosciences Co., Ltd. (Guangzhou, China). Before exposing the skull, the mice were anesthetized with pentobarbital sodium using a stereotaxic apparatus (RWD, Shenzhen, China). A volume of 5 μL AAV vectors was injected stereotaxically into the bilateral ventricles (AP -0.3 mm; ML ±1.0 mm; DV 3.0 mm) at a rate of 0.5 μL/min. The needle was kept in place for 5 min and screwed out slowly. The skin incision was sutured, and the mice were housed in a single cage after the recovery from anesthesia.

2.6. 7-Day Survival Rate. The survival of mice in each group was recorded daily after modeling, and the observation was continued for 7 days.

2.7. Morris Water Maze (MWM) Test. The function of spatial learning and memory for mice was assessed using the MWM test. The maze (Shanghai XinRuan Information Technology Co. Ltd., Shanghai, China) consisted of a round tank (height 50 cm and diameter 120 cm), a platform (diameter 10 cm), and a camera analysis system [35]. The mice

were trained for four trials per day for 5 consecutive days (-4 d to 0 d) before modeling. In every trial, the mice were placed on a different start quadrant and allowed to find a platform submerged 1 cm below the water surface within a maximum time of 60 s, and the escape latency was recorded. Animals that failed to locate the platform within 60 s were manually guided to the platform. On the fifth day (0 d) after MWM training, the mice were injected LPS or saline intraperitoneally. The water maze test was performed on the sixth day; namely, at 24 hours after modeling (24 h), the mice were placed into the water facing the pool wall to navigate freely in the water for 60 s, and the escape latency and the swimming speed were recorded. Then, the platform was withdrawn, and the mice were allowed to navigate freely in the water again for 60 s. During the trial, the percentage of retention time in the target quadrant and the times of crossing the former platform were recorded as we previously described [30, 35, 36].

2.8. Brain Water Content Measurement. The brain water content was estimated by the wet-to-dry brain weight ratio, as described previously [36]. Briefly, the whole brains were harvested under deep anesthesia and immediately weighed to obtain the wet weight. Then, the brain tissues were dried at 65°C for 48 h to obtain the dry weight. Brain water content = (wet weight − dry weight)/wet weight × 100%.

2.9. HE Staining. The whole brain tissues were fixed in 4% paraformaldehyde, embedded in paraffin, and cut into 3 μm thick hippocampus coronal sections. The tissue sections were stained with HE and observed under a light microscope (Olympus, Tokyo, Japan) by two experienced pathologists blinded to the study. The number of normal neurons per square millimeter (cells/mm^2) in 6 brain sections of each mouse was calculated according to the size of the CA1 subregion in four randomly selected high-magnification fields (×400) of each section and averaged as we previously described [36].

2.10. TUNEL Staining. Fixed brain tissue was dehydrated by sucrose gradient solutions, and frozen sections were collected after the optimal cutting temperature (OCT) medium embedding. The apoptosis of neural cells in the hippocampus was detected by the TUNEL method, following the manufacturer's instructions (Roche, Basel, Switzerland). The TUNEL reagents of terminal deoxynucleotidyl transferase (TdT) enzyme reaction solution and tetramethylrhodamine (TMR) labeling solution at a ratio of 1 : 9 were added to the sections for 1 h. The nuclei were stained with 4′,6-diamidino-2-phenylindole (DAPI) (Solarbio, Beijing, China) for 5 min. The stained tissue sections were observed under a fluorescence microscope (Olympus), and the images were captured. The TUNEL-positive cell percentage (%) was calculated as follows: TUNEL-positive cells/total cells × 100% [36].

2.11. Immunofluorescence Staining. The protein expression of ionized calcium binding adaptor molecule 1 (Iba1) reflecting the activation of microglia was detected by the immunofluorescence method [36]. Briefly, fixed brain tissue was dehydrated by sucrose gradient solutions, and the frozen sections were stained after OCT medium embedding. Subsequently, the tissue sections were fixed in paraformaldehyde for 30 min, permeabilized with 0.2% Triton X-100 for 15 min, blocked in 1% bovine serum albumin for 30 min, and incubated with primary antibody rabbit anti-Iba1 (1 : 100, Cell Signaling Technology (CST), Danvers, MA, USA) at 4°C overnight. After washing, the sections were incubated with the corresponding FITC-labeled or Cy3-labeled secondary antibody (Kangwei Century Biotechnology Co., Ltd., Beijing, China) in the dark at 37°C for 60 min. Finally, the tissue sections were incubated for 5 min with DAPI before examining the protein levels under a fluorescence microscope. For quantification, the HE mean number of Iba1-positive cells in hippocampal CA1 area was calculated. Activated microglia were calculated as the percentage of cells with shorter, stubbier processes, namely, activated microglia% = (the number of activated microglia/total number of Iba1-positive cells) × 100 [36].

2.12. qRT-PCR. Total RNA was extracted from the hippocampal tissues using an RNAsimple total RNA kit (Tiangen, Beijing, China), following the manufacturer's protocol. The isolated RNA was reverse transcribed into cDNA using the ReverTra Ace qPCR RT Master Mix (Toyobo Co., Ltd., Osaka, Japan), according to the manufacturer's protocol. Then, the cDNA was amplified using SuperReal PreMix Plus (SYBR Green) (Tiangen, Beijing, China) on a real-time PCR system (Roche). The amplification parameters were as follows: 95°C for 15 min, followed by 5 cycles of 95°C for 10 s and 60°C for 32 s. β-Actin was used as an internal reference for the quantification of the TXNIP gene expression level. The normalized mRNA expression level in the control group (target mRNA/β-actin value) was utilized to calculate the fold changes of the mRNA levels in the other groups. The primer sequences are as follows: TXNIP (forward: 5′-ATACTCCTTGCTGATCTACG-3′, reverse: 5′-TGGGGT ATCTGGG-ATGTTTA-3′) and β-actin (forward: 5′-TTTGCAGCTCCTTCGTTGC-3′, reverse: 5′-TCGTCA TCCATGGCGAACT-3′).

2.13. ROS, MDA, GSH-Px, and SOD Level Measurement. Supernatants from hippocampal tissues were obtained, and specific kits (Nanjing Jiancheng Biotechnology Research Institute, Nanjing, China) were used to measure the ROS and MDA levels and GSH-Px and SOD activities, according to the manufacturer's instructions and previous studies [37, 38].

2.14. ELISA. The hippocampal tissue homogenates were prepared, and supernatants were collected by centrifugation of the lysates at 12000 rpm, 4°C for 15 min. The TNF-α, IL-6, IL-1β, and IL-18 levels were estimated in the hippocampal tissues using the ELISA kits (Meimian, Wuhan, China), following the manufacturer's instructions and as described previously [37, 39].

2.15. Western Blotting Analysis. The hippocampal tissue was excised and placed on ice for 30 min before lysis, followed by

ultracentrifugation at 4°C. The protein concentration of the supernatant was measured by using the BCA kit (Beyotime, Shanghai, China). An equivalent of 25 μg protein was separated by sodium dodecyl sulfate-polyacrylamide gel electrophoresis (SDS-PAGE), transferred to a polyvinylidene fluoride membrane (Amersham Biosciences, NJ, USA), or a nitrocellulose membrane (Beyotime), blocked with 5% skimmed milk for 2 h, and probed with the following primary antibodies at 4°C overnight: anti-TXNIP (1 : 1000, CST), anti-NLRP3 (1 : 1000, CST), anti-caspase-1 (1 : 200, Santa Cruz Biotech, Santa Cruz, CA, USA), anti-Bcl-2 (1 : 1000, Abcam, Cambridge, MA, USA), anti-Bax (1 : 1000, Proteintech, China), anti-cleaved caspase-3 (1 : 500, Proteintech), and anti-β-actin (1 : 5000, Proteintech). Subsequently, the membrane was incubated with the horseradish peroxidase-labeled goat anti-rabbit or goat anti-mouse secondary antibody (1 : 1000, Solarbio) at 37°C for 1 h. Finally, the membrane was exposed to enhanced chemiluminescence, and the immunoreactive bands were quantitated using the ImageJ software (version 1.31; National Institutes of Health, Bethesda, MD, USA) [30].

2.16. Statistical Analysis. GraphPad Prism 8.3 statistical software (GraphPad Software, San Diego, CA, USA) was used for all statistical analyses. The data were expressed as the mean and standard error of the mean (mean ± SEM). One-way analysis of variance (ANOVA) and Tukey's post hoc test were used for comparisons. For the training phase of the MWM test, the escape latency over time was analyzed by two-way repeated measures ANOVA [36]. Kaplan-Meier survival curves were analyzed using the log-rank test. $P < 0.05$ indicated statistically significant difference.

3. Results

3.1. Effects of LPS on Brain Injury in Mice. The HE staining showed that the cone cells in the hippocampal CA1 area in the NC group were arranged in an orderly manner and evenly distributed with obvious nucleoli, while in the LPS group, the cells were arranged disorderly and were morphologically irregular, the cytoplasm was deeply stained, and the nuclei were constricted (Figure 2(a)). Compared to the NC group, the number of normal pyramidal cells in the hippocampal CA1 area in the LPS group was reduced and further minimized in the LPS 24 h group ($P < 0.01$) (Figure 2(b)).

3.2. Changes in the Inflammatory Cytokine Levels in the Serum and Hippocampus. As presented in Figure 3, compared to the NC group, the levels of TNF-α, IL-6, IL-1β, and IL-18 in the serum (Figures 3(a)–3(d)) and hippocampus (Figures 3(e)–3(h)) were increased significantly in the LPS 6 h, LPS 12 h, and LPS 24 h groups and reached the peak in the LPS 24 h group ($P < 0.05$ or $P < 0.01$).

3.3. Effects of LPS on Microglial Activation in the Hippocampus of Mice. The microglia cell was small, and the synapses were slender and scattered in the NC group. Compared to the NC group, a significantly increased number of Iba1-positive cells and the percentage of activated microglia indicated by enlarged cell bodies and shortened synapse were found in the hippocampal CA1 area after the LPS injection, especially in the LPS 24 h group (Figures 4(a)–4(c)).

3.4. Effects of LPS on the Expression of TXNIP and NLRP3 Inflammasome. The Western blot results showed (Figure 5) that the expression level of TXNIP, NLRP3, procaspase-1, and cleaved caspase-1 in the hippocampus in the LPS group was significantly increased compared to that in the NC group at 6, 12, and 24 h after LPS injection ($P < 0.05$ or $P < 0.01$). These results suggested that LPS could cause the activation of the TXNIP-NLRP3 signaling pathway.

3.5. AAV-TXNIP shRNA Inhibited the Expression of TXNIP in the Hippocampus. As shown in Figure 6(a), no fluorescence was observed in the NC and LPS groups. However, bright green fluorescence was observed in the hippocampus of each group of mice transfected with the AVV, indicating that the AAV successfully transfected the hippocampus and expressed the green fluorescent protein.

The qRT-PCR and Western blot results (Figures 6(b)–6(d)) showed that the hippocampal TXNIP mRNA and protein expression levels in the LPS and LPS+control shRNA groups were significantly upregulated compared to those in the NC group ($P < 0.01$). Compared to the LPS+control shRNA group, the TXNIP mRNA and protein levels in the LPS+TXNIP shRNA$_1$ and LPS+TXNIP shRNA$_2$ groups were significantly downregulated ($P < 0.01$).

3.6. TXNIP Knockdown Improved the 7-Day Survival Rate and Cognitive Dysfunction. As shown in Figure 7(a), the 7-day survival rate was 100% in the NC group. However, the 7-day survival rate in the LPS group and the LPS+control shRNA group was significantly lower than that in the NC group ($P < 0.01$). Conversely, the 7-day survival rate in the LPS+TXNIP shRNA group was significantly higher than that in the LPS+control shRNA group ($P < 0.05$).

Figures 7(b)–7(g) showed that the escape latency in each group was gradually shortened over the training time before modeling, and no statistically significant difference was detected among the groups ($P > 0.05$). However, the escape latency was prolonged, and the percentage of time in the target quadrant and the times crossing the platform were significantly reduced ($P < 0.01$) in the LPS and LPS+control shRNA groups compared to the NC group. Furthermore, compared to the LPS+control shRNA group, the mice in the LPS+TXNIP shRNA group showed a shorter escape latency and increased time in the target quadrant and times crossing the platform ($P < 0.05$ or $P < 0.01$). However, no significant difference was observed in the average swimming speed of the mice among groups ($P > 0.05$).

3.7. TXNIP Knockdown Attenuated Pathological Damage and Edema in the Brain Tissues. The results of HE staining (Figure 8(a)) showed a regular morphology of the hippocampal CA1 region in the NC group. The morphologically normal pyramidal cells with clear nuclei and nucleoli were observed. However, many injured neurons, characterized by the shrunken appearance and dark staining, were observed after LPS injection.

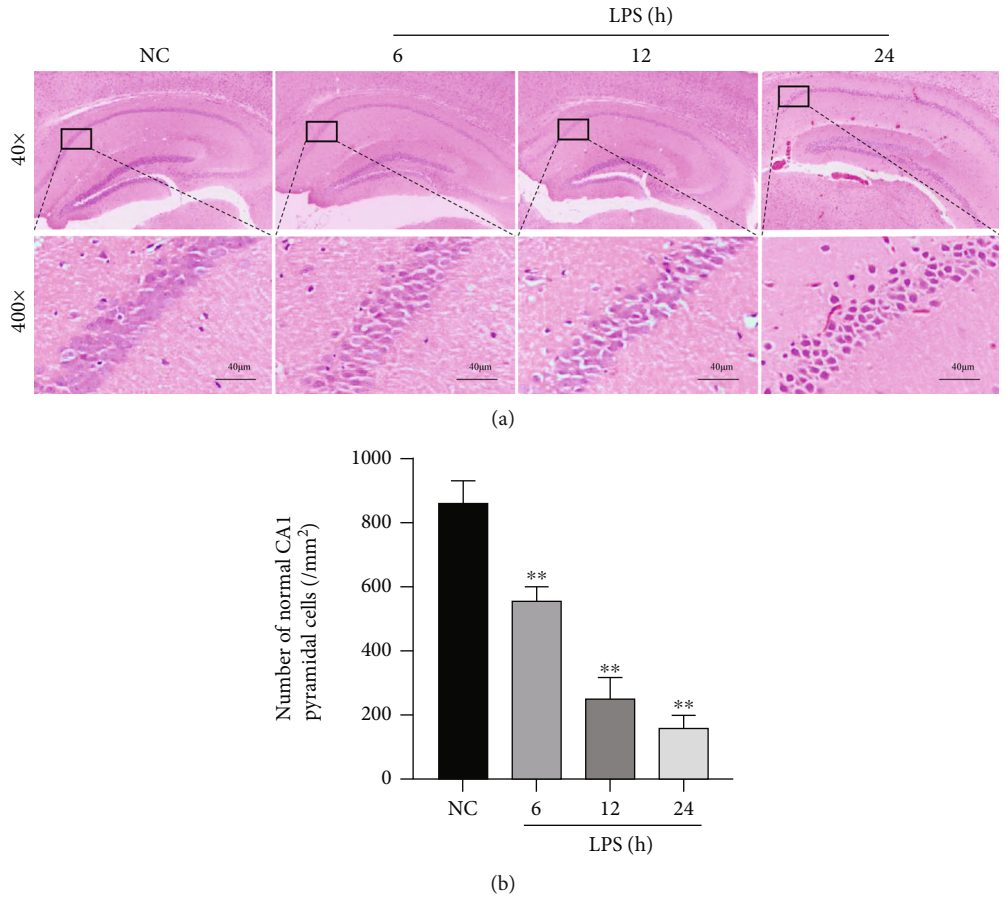

Figure 2: LPS caused histological injury to the hippocampus. (a) HE staining of the hippocampal CA1 region (×400) (scale bar = 40 μm). (b) Statistics of the normal pyramidal cells in the hippocampal CA1 area. The data are presented as the mean ± SEM. $^{**}P < 0.01$ *vs.* NC group ($n = 8$).

Moreover, the mice in the LPS and LPS+TXNIP shRNA groups had significantly fewer normal neurons in the hippocampal CA1 area and higher brain water content in the whole brain tissues than those in the NC group at 24 h after LPS injection ($P < 0.01$). Compared to the animals in the LPS+control shRNA, normal neurons in the hippocampus were increased, and the brain edema was reduced significantly after TXNIP knockdown ($P < 0.05$ or $P < 0.01$) (Figures 8(b) and 8(c)), suggesting that TXNIP knockdown could reduce the brain damage in septic mice.

3.8. TXNIP Knockdown Reduced the Hippocampal Neuronal Apoptosis. The neuronal apoptosis in the hippocampal CA1 region of the brain was evaluated by the TUNEL method. No obvious apoptotic cells were found in the NC group, but those in the LPS and the LPS+control shRNA groups increased significantly ($P < 0.01$). These changes were alleviated by TXNIP knockdown and manifested as a decreased number of TUNEL-positive cells ($P < 0.01$) (Figures 9(a) and 9(c)).

The results of Western blot (Figure 9(b)) showed increased protein levels of the cleaved caspase-3 and Bax in the LPS and the LPS+control shRNA groups compared to the NC group ($P < 0.01$) but decreased levels in the LPS+TXNIP shRNA group compared to the LPS group ($P < 0.05$). On the other hand, the protein level of Bcl-2 was significantly lower in the LPS and LPS+control groups compared to the NC group ($P < 0.01$), but it increased in the LPS+TXNIP shRNA group compared to the LPS+control group ($P < 0.01$) (Figures 9(d)–9(f)).

3.9. TXNIP Knockdown Inhibited the Microglial Activation in the Hippocampus. To better understand the effect of TXNIP knockdown on the activation of microglia after sepsis, double immunofluorescence staining was performed with Iba1 and DAPI (Figure 10). Iba1 protein in the microglia was fluorescently labeled in the hippocampus of each group at 24 h after LPS injection. The microglia cells were small, and the synapses were slender and scattered in the cortex in the NC group. The number of Iba1-positive cells and the percentage of activated microglia were observed in the LPS and LPS+control shRNA groups accompanied by enlarged cell bodies and shortened synapses that accumulated in the hippocampus ($P < 0.01$). However, the number of Iba1-positive cells and the percentage of activated microglia in the hippocampus were significantly inhibited after TXNIP knockdown ($P < 0.01$).

3.10. TXNIP Knockdown Improved ROS, MDA, GSH-Px, and SOD Levels in the Hippocampus. Hippocampal ROS, MDA,

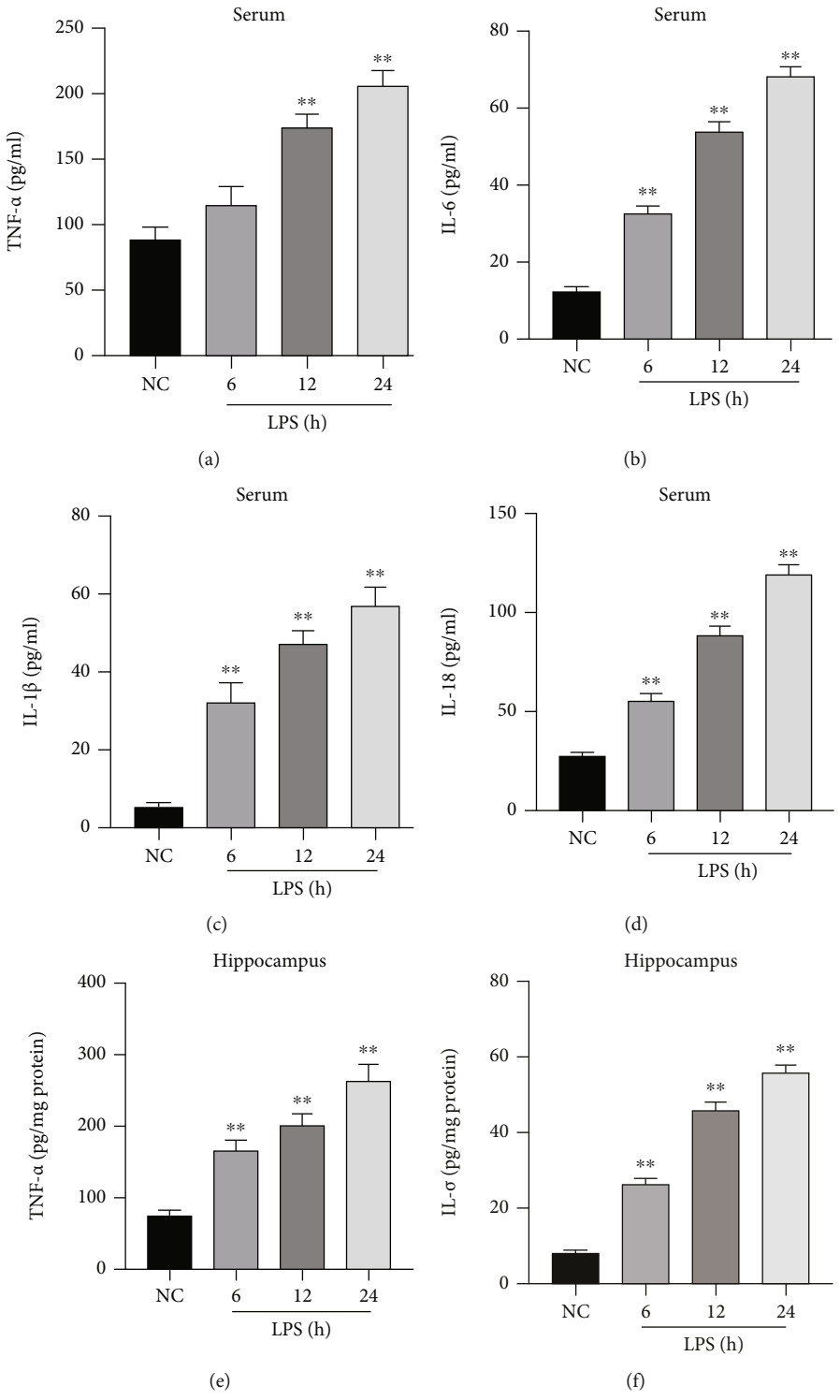

Figure 3: Continued.

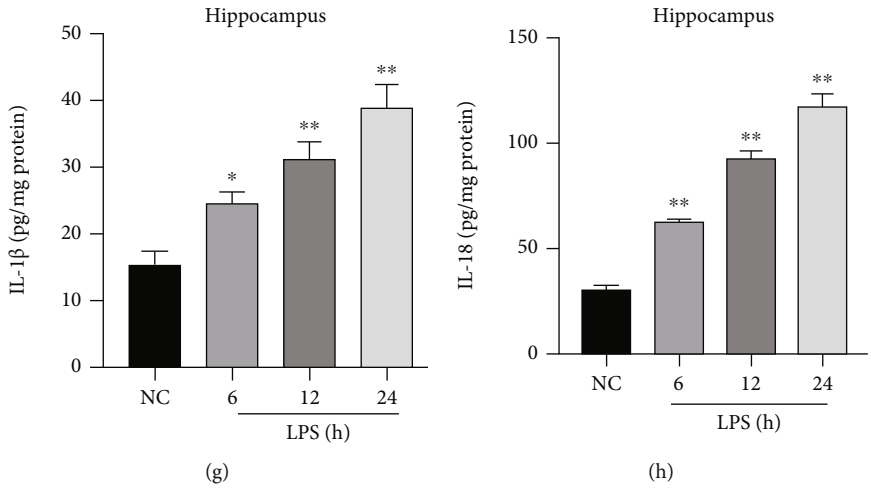

(g) (h)

Figure 3: Changes in the inflammatory factors in the serum and hippocampus. (a–d) The levels of TNF-α, IL-6, IL-1β, and IL-18 in the serum, respectively. (e–h) The levels of TNF-α, IL-6, IL-1β, and IL-18 in the hippocampus, respectively. The values are presented as mean ± SEM. $^{*}P < 0.05$, $^{**}P < 0.01$ *vs.* NC group ($n = 6$).

GSH-Px, and SOD levels are excellent indexes reflecting lipid peroxidation and the antioxidant ability of tissues. As shown in Figure 11, the levels of ROS (Figure 11(a)) and MDA (Figure 11(b)) were significantly higher ($P < 0.01$), while GSH-Px (Figure 11(c)) and SOD (Figure 11(d)) activities were markedly lower ($P < 0.01$) in the LPS group compared to the NC group. In addition, ROS and MDA levels were significantly lower ($P < 0.01$), and GSH-Px and SOD activities were markedly higher ($P < 0.01$) in the LPS+TXNIP shRNA group compared to the LPS+control shRNA group.

3.11. TXNIP Knockdown Reduced the Levels of Inflammatory Factors. As presented in Figure 12, the levels of TNF-α, IL-6, IL-1β, and IL-18 were significantly increased in the LPS and LPS+control shRNA groups compared to the NC group ($P < 0.01$), while the levels of inflammatory factors were reduced in the LPS+TXNIP shRNA group compared to the LPS+control shRNA group ($P < 0.01$).

3.12. TXNIP Knockdown Inhibited the NLRP3/Caspase-1 Signaling Pathway. As presented in Figure 13, compared to the NC group, the expressions of TXNIP, NLRP3, procaspase-1, and cleaved caspase-1 were significantly upregulated in the LPS and LPS+control shRNA groups ($P < 0.01$). Compared to the LPS+control shRNA group, the levels of these indicators were significantly downregulated in the LPS+TXNIP shRNA group ($P < 0.01$), indicating that TXNIP knockdown significantly inhibits the NLRP3/caspase-1 signaling pathway.

4. Discussion

The current study found the following. (1) The TXNIP and NLRP3 inflammasome expression levels were increased in the hippocampal CA1 region of the brain at 6, 12, and 24 h after LPS injection, especially at 24 h. (2) TXNIP knockdown significantly improved the 7-day survival rate, reduced the brain water content and brain injury, and improved the cognitive dysfunction of sepsis brain injury mice. (3) TXNIP knockdown inhibited the activation of microglia, downregulated the NLRP3/caspase-1 signaling pathway, and reduced the oxidative stress and the neuroinflammatory cytokine levels at 24 h post-LPS injection. (4) TXNIP knockdown significantly inhibited the hippocampal neuronal apoptosis and downregulated the expression of apoptosis-associated proteins cleaved caspase-3 and Bax, but upregulated the antiapoptotic protein Bcl-2. These results indicated that the TXNIP knockdown attenuated brain injury and cognitive decline in septic mice by suppressing oxidative stress and neuroinflammation.

Sepsis is a common complication of uncontrolled infection following severe trauma and other stress states, leading to shock, and is the main cause of ICU hospitalization and deaths worldwide [1, 2, 40, 41]. SAE is a diffuse brain dysfunction that occurs secondary to sepsis without overt central nervous system infection with the clinical manifestations of delirium, coma, seizures, and focal nervous system signs. A prospective autopsy study showed that ischemic lesions are found in the brains of all patients with SAE [10]. These ischemic lesions are mainly located in the brain areas that reduce the cerebral blood flow [2, 42]. The hippocampal CA1 region is extremely vulnerable to ischemia, hypoxia, and other harmful stimuli [43]. It plays a crucial role in learning and memory, and its destruction and dysfunction have been linked to cognitive deficits [30, 36, 44]. Therefore, combining those factors, the CA1 region was selected in the study rather than CA2, CA3, or dentate gyrus regions.

Lipopolysaccharide plays a significant role in Gram-negative bacterial infection and disease pathogenesis and has been widely used in the establishment of sepsis animal models [45]. The mice are remarkably less sensitive to the toxic or lethal effects of LPS. Thus, the dose of LPS, which leads to death in approximately half of mice (i.e., the LD50 dose) is about 1-25 mg/kg [46]. Interestingly, our preliminary experiments also showed that 7-day survival rates of mice gradually

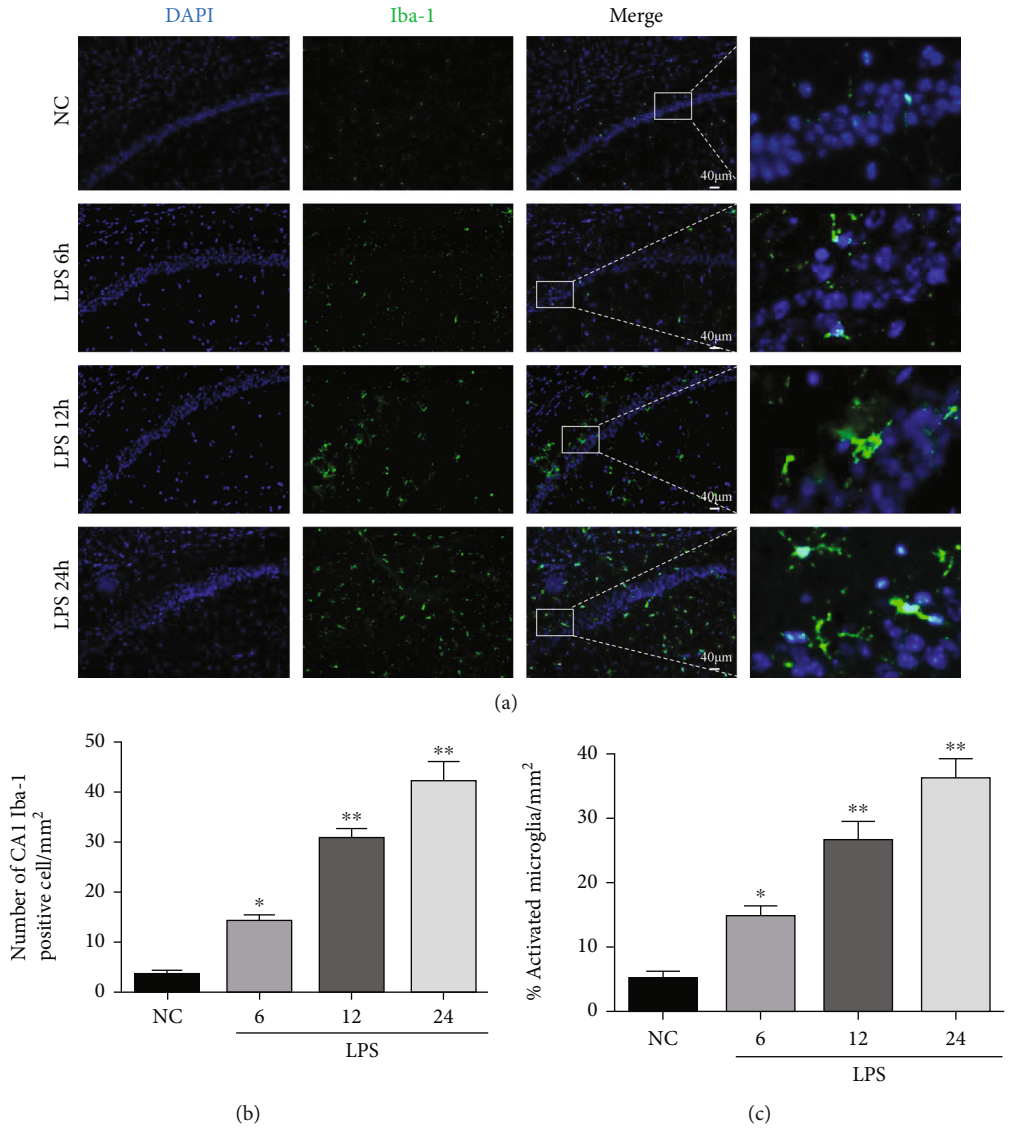

FIGURE 4: Changes in Iba1-positive cells in the hippocampal CA1 region after LPS injection. (a) Immunofluorescence of the microglia in the hippocampal CA1 region (×100) (scale bar = 40 μm). Nuclei were labeled with blue fluorescence (DAPI), and Iba1 was labeled with green fluorescence. (b, c) Quantitative analysis of Iba1-positive cells and activated microglia in the hippocampal CA1 region. The data are presented as the mean ± SEM. $^{*}P < 0.05$, $^{**}P < 0.01$ *vs.* NC group ($n = 6$).

decreased with the different doses of LPS (5, 7.5, 15, or 20 mg/kg). LPS at 20 mg/kg caused total death in mice within 7 days, while 5 and 7.5 mg/kg did not cause appropriate septic brain damage (data not shown). Therefore, combining the above factors, we chose the dose of 15 mg/kg in the study based on our preliminary experiments and previous studies [47–49]. Previous studies have shown that the levels of proinflammatory cytokines, TNF-α, IL-1β, and IL-6, began to rise in 2-4 h after the intravenous or intraperitoneal injection of LPS, and these changes continued for several hours up to 24 h [45, 50]. In the present study, the mice manifested the sepsis symptoms such as upside-down hair, loose stools, hunched back, shortness of breath, and white viscous material around the eyes after the intraperitoneal injection of LPS at a dose of 15 mg/kg, and the 7-day survival rate was decreased significantly, while the expression levels of the TNF-α, IL-6, IL-1β, and IL-18 in the serum and hippocampus of mice after LPS injection were increased significantly. The cell arrangement in the hippocampus was disordered, the cytoplasm was deeply stained, and the nucleus was constricted. Moreover, the number of normal cone cells in the hippocampus decreased with prolonged injection time. These results indicated that septic brain damage could be induced in mice by an intraperitoneal injection of 15 mg/kg of LPS. It is reported that most damage of the brain might be caused around 6 to 48 h after sepsis, including gut origin sepsis [36, 51, 52]. The number of morphologically normal pyramidal cells with clear nuclei and nucleoli in the hippocampal CA1 region was counted according to many previous studies [36, 51]. However, damaged neurons with abnormal appearing condensed, pyknotic, and shrunken nuclei were not counted. Therefore, the results showed that LPS might reduce the number of morphologically

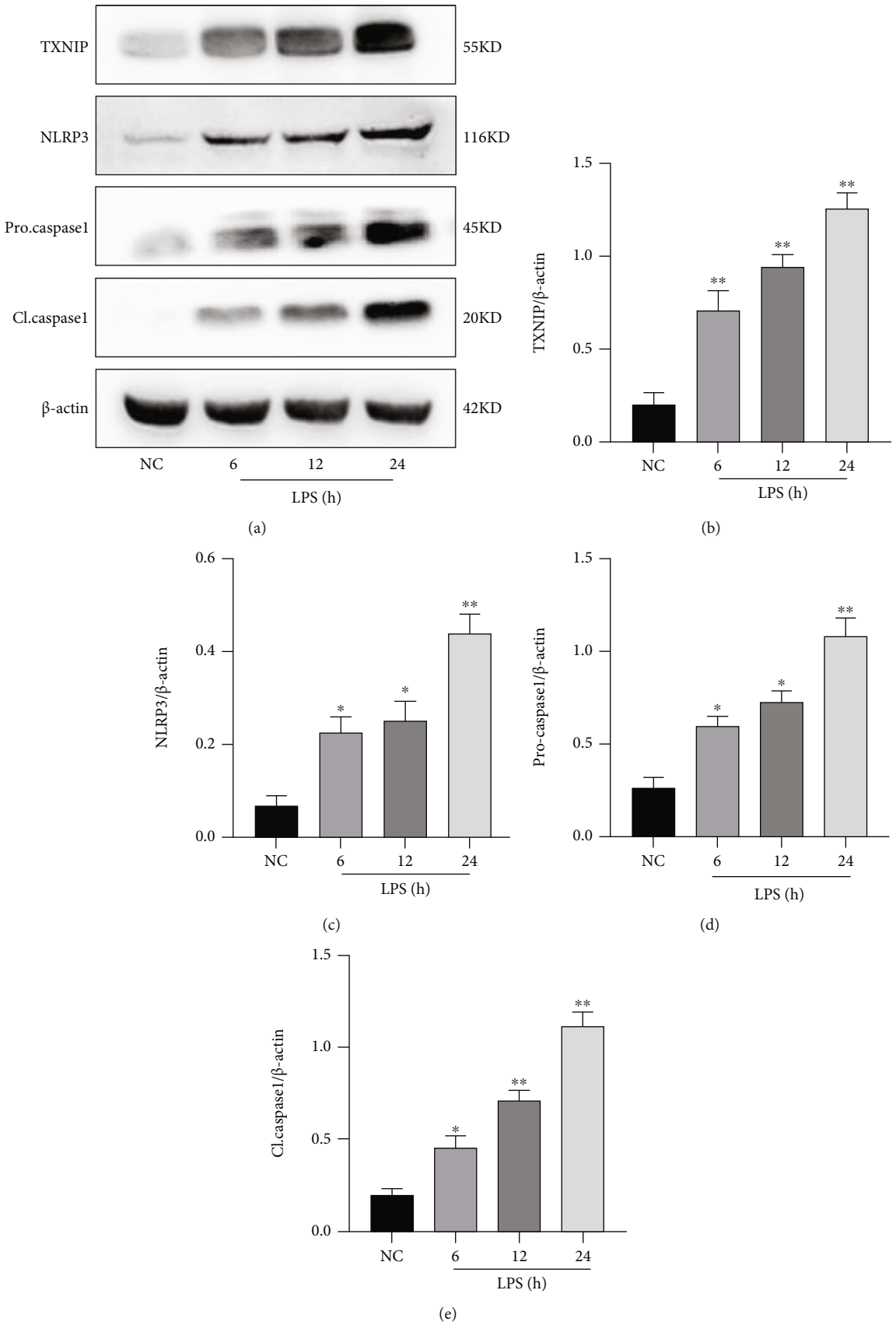

Figure 5: Expression of the TXNIP-NLRP3 signaling pathway in the hippocampus. (a) Bands of the TXNIP, NLRP3, procaspase-1, and cleaved caspase-1. (b–e) Quantification of the expression levels of TXNIP, NLRP3, procaspase-1, and cleaved caspase-1. The data are presented as mean ± SEM. $^{*}P < 0.05$, $^{**}P < 0.01$ *vs*. NC group ($n = 6$).

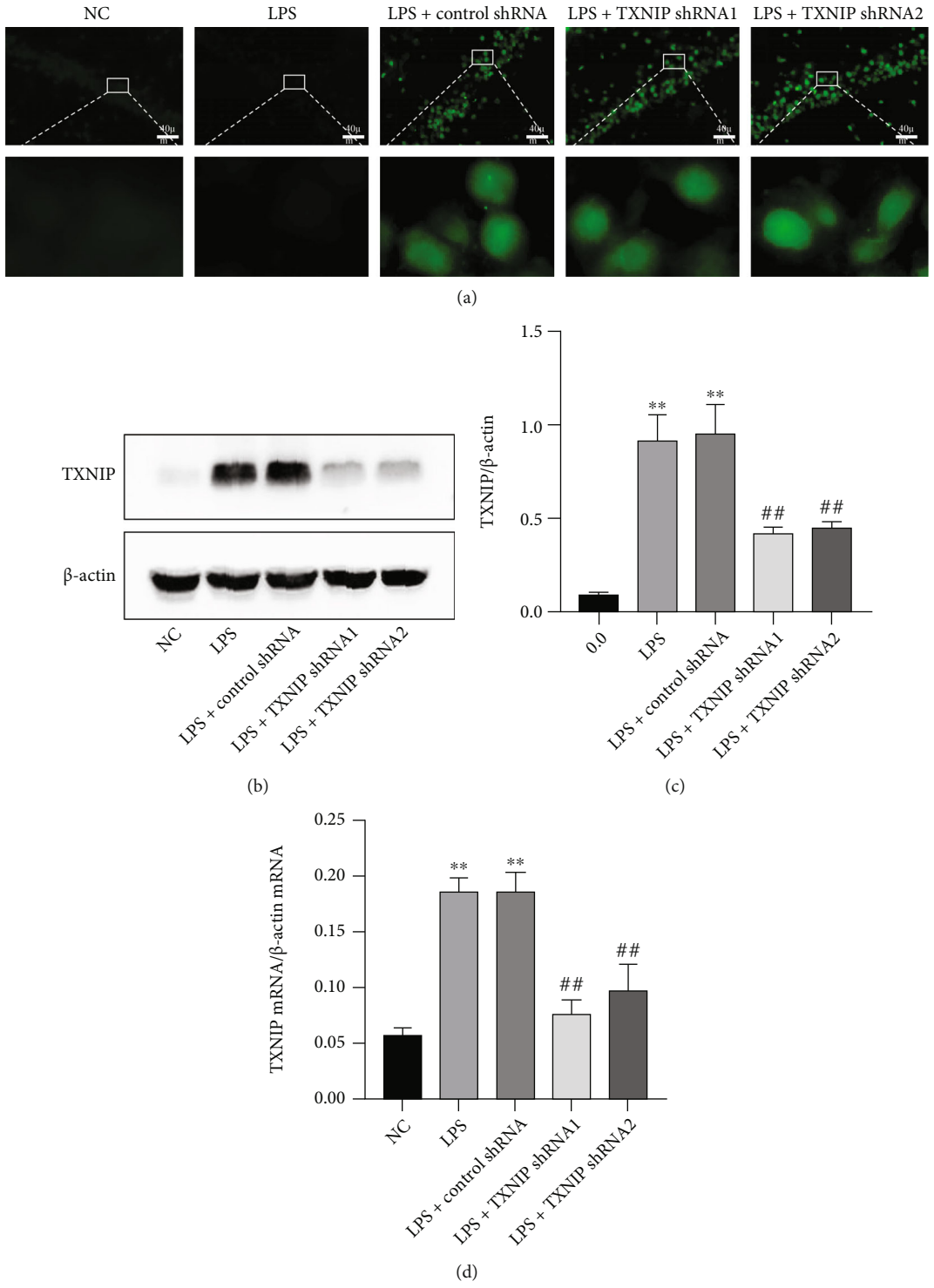

Figure 6: Effect of AAV-TXNIP shRNA on the expression of TXNIP. After transfection of TXNIP shRNA with the AAV carrier, the expression of TXNIP was detected in the hippocampus. (a) The AAV expresses EGFP (green) in the hippocampus (×400) (scale bar = 40 μm). (b, c) Representative Western blot and quantitative analysis of TXNIP. (d) qRT-PCR results of *TXNIP* mRNA. $^{**}P < 0.01$ *vs*. NC group, $^{\#\#}P < 0.01$ *vs*. LPS+control shRNA group ($n = 6$).

normal pyramidal cells but not the total number of pyramidal cells (including cells with abnormal morphology) in the CA1 area within 24 hours and even 6 hours after sepsis. Since apoptotic cells cannot be identified well by hematoxylin-eosin staining, therefore, TUNEL staining was further performed. The results also showed that apoptotic cells in the CA1 area increased after LPS injection. This phenomenon is also consistent with many previous studies [30, 36, 53, 54].

The NLRP3 inflammasome is composed of NLRP3, ASC, and caspase-1 zymogen that are crucial components

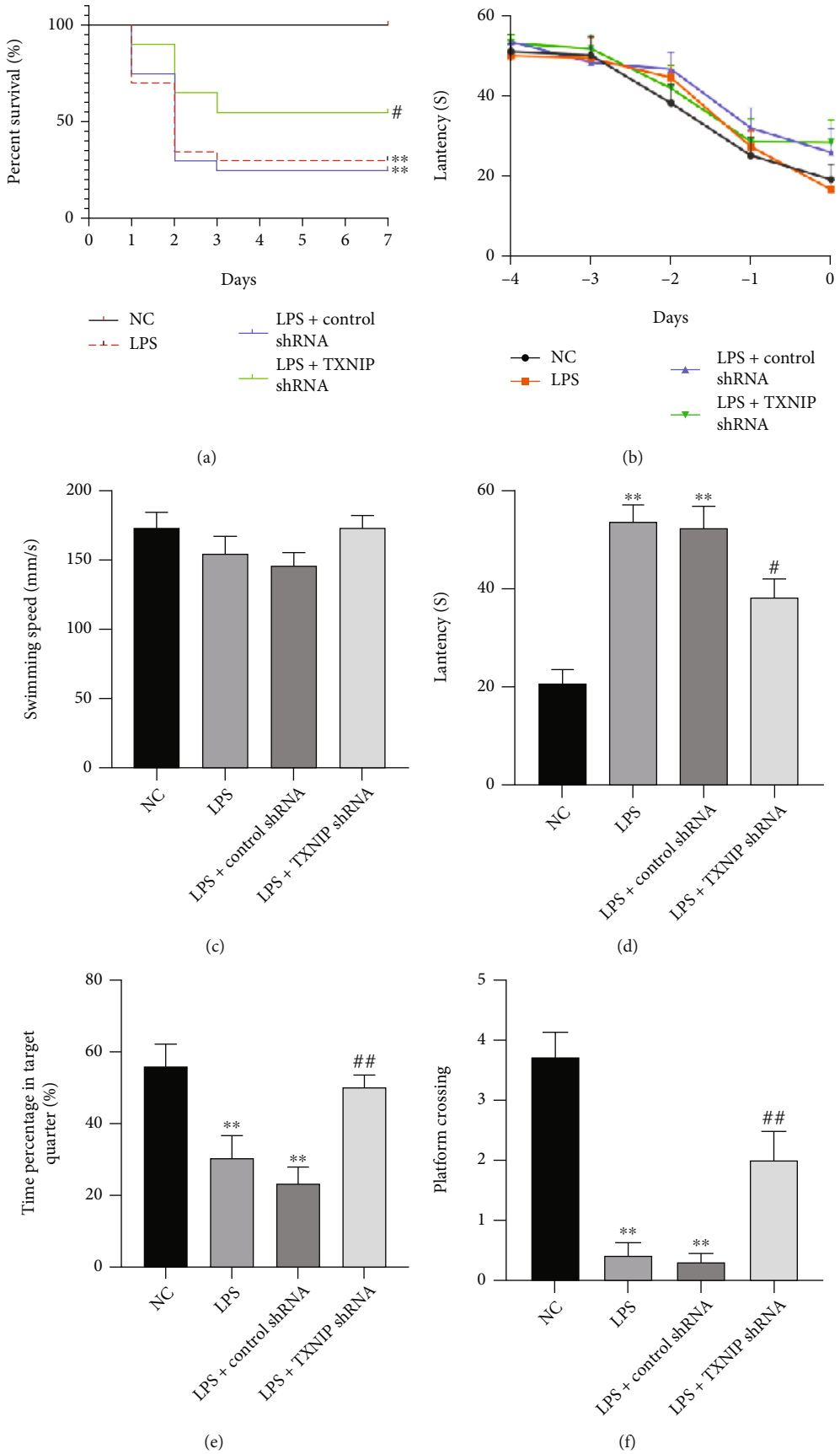

Figure 7: Continued.

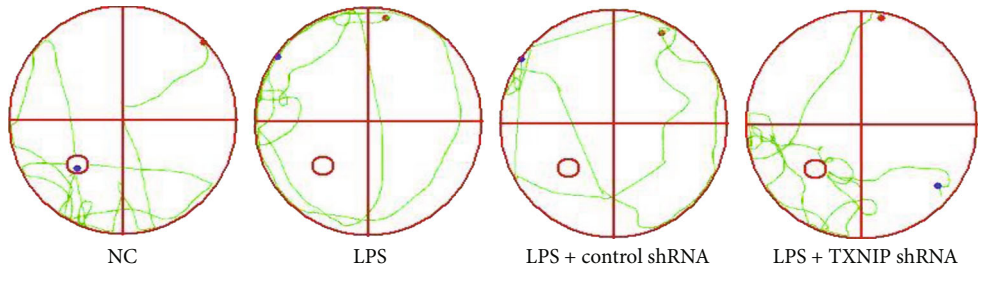

(g)

Figure 7: Effect of TXNIP knockdown on 7-day survival rate and cognitive function. (a) The Kaplan-Meier survival curve ($n = 20$). Cognitive function was assessed by the Morris water maze test. (b) The latency of each group before modeling (-4 d to 0 d). (c–g) The swimming speed, the latency of each group on the sixth day, percentage of stay time in the target quadrant, times of crossing the platform, and representative swim traces of each group in the space exploration experiment. The data are presented as mean ± SEM. $^{**}P < 0.01$ *vs.* NC group, $^{\#\#}P < 0.01$, $^{\#}P < 0.05$ *vs.* LPS+control shRNA ($n = 10$).

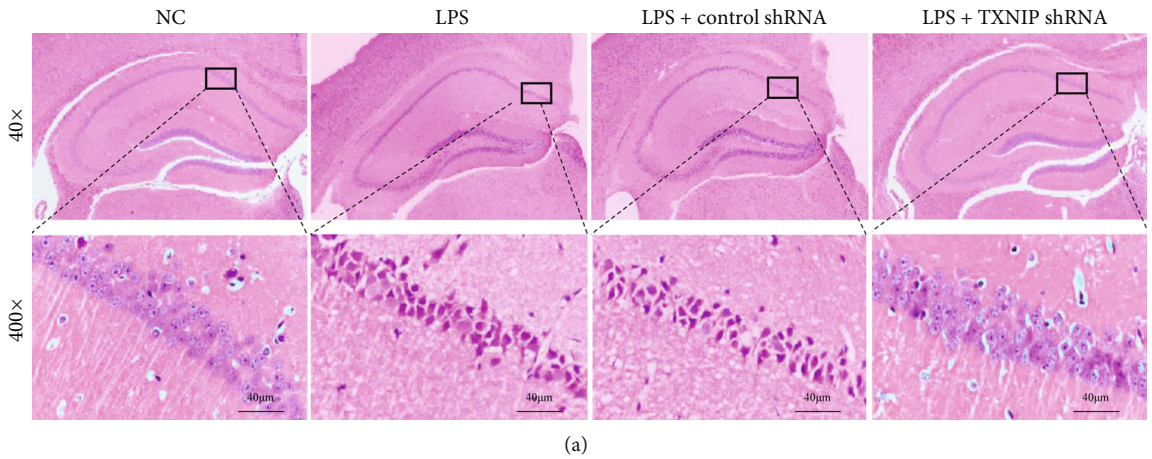

(a)

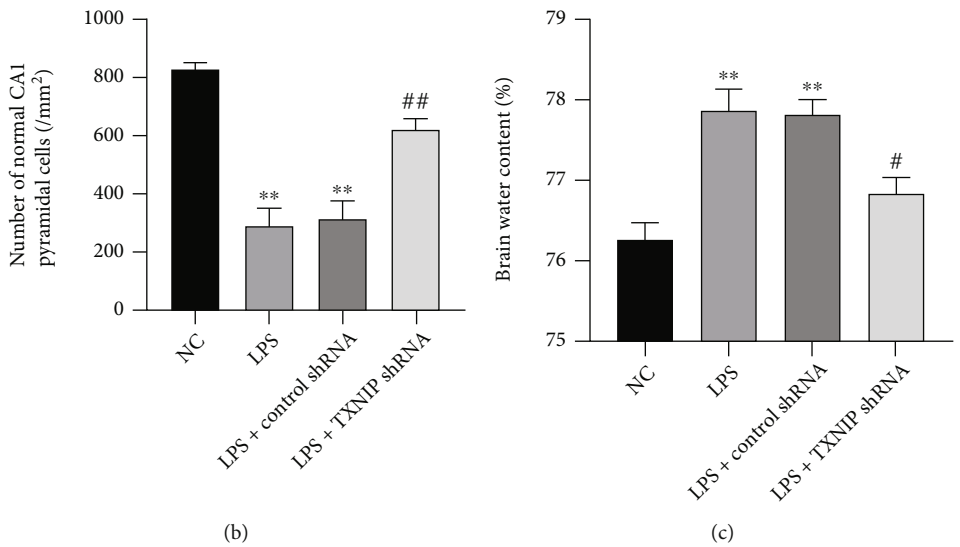

(b) (c)

Figure 8: Pathological changes and encephaledema in the brain tissues. (a) HE staining in the hippocampal CA1 region (×400, scale bar = 40 μm). (b) Statistics of the normal pyramidal cells in the hippocampal CA1 area. (c) The brain water content. The data are presented as the mean ± SEM. $^{**}P < 0.01$ *vs.* NC group; $^{\#}P < 0.05$, $^{\#\#}P < 0.01$ *vs.* LPS+control shRNA group ($n = 8$).

of the body's innate immune system. After activation, NLRP3 recruits ASC and caspase-1 zymogen and promotes the maturation and release of the inflammatory cytokines: IL-1β and IL-18 [19, 55]. Therefore, the inhibition of NLRP3 inflammasome activity has been suggested as a strategy for the treatment of neurological diseases [19]. The NLRP3 inflammasome promotes inflammation and apoptosis and is involved in the pathogenesis of SAE [51]. The hippocampus-

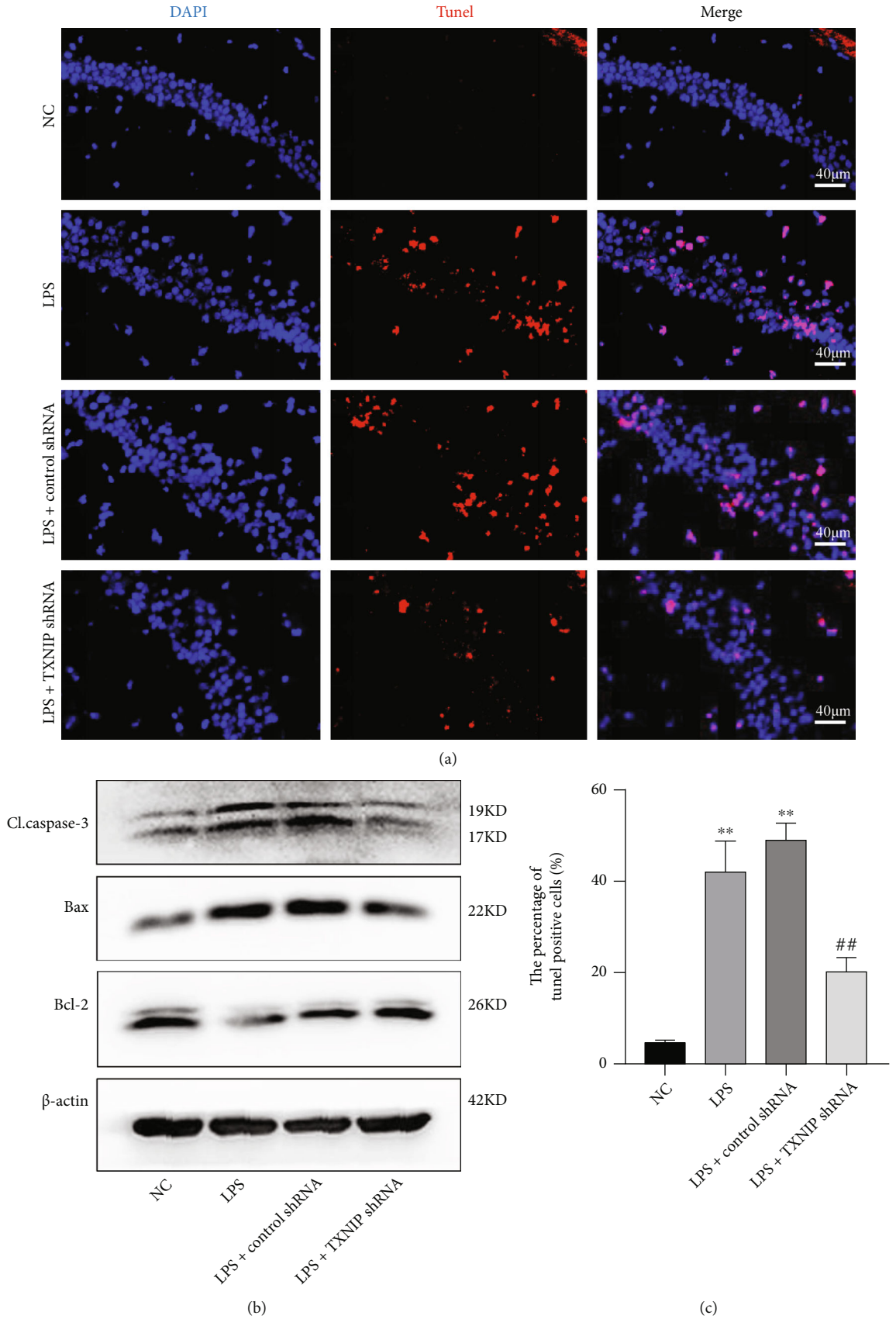

Figure 9: Continued.

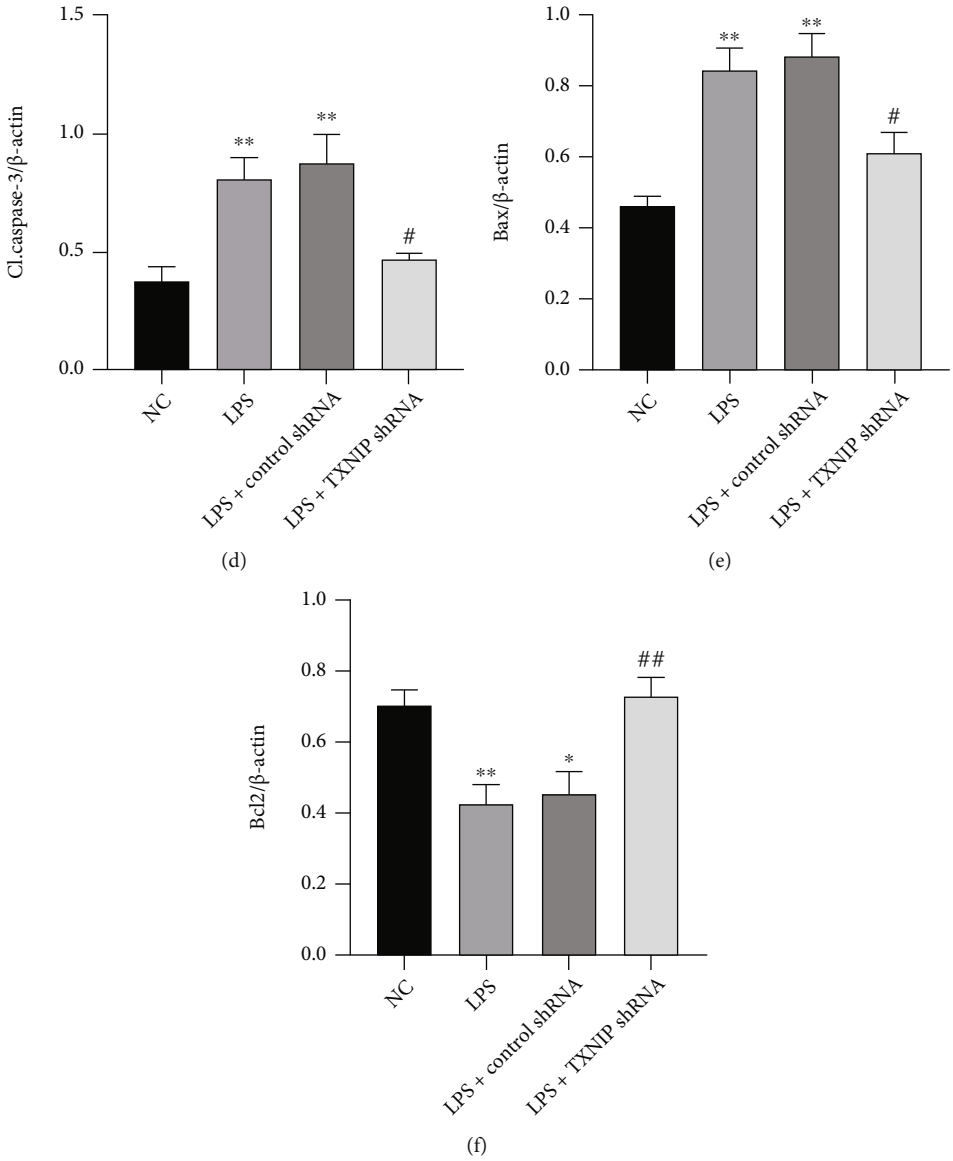

Figure 9: Neuronal apoptosis and expression of the apoptosis-related proteins in hippocampal CA1 of mice. (a) TUNEL (red) staining in the hippocampal CA1 area (×400) (scale bar = 40 μm). (b) The bands of Bcl-2, Bax, and cleaved caspase-3. (c) Percentage of TUNEL-positive cells in the hippocampus. (d–f) Relative quantification of cleaved caspase-3, Bax, and Bcl-2. Data are presented as mean ± SEM. $^{*}P < 0.05$, $^{**}P < 0.01$ *vs*. NC group; $^{\#}P < 0.05$, $^{\#\#}P < 0.01$ *vs*. LPS+control shRNA group (n = 6-8).

dependent memory impairment induced by the cecal perforation (CLP) was accompanied by increased levels of NLRP3, caspase-1, and proinflammatory cytokines. The application of the NLRP3-specific inhibitor MCC950 improved cognitive deficits and reduced the NLRP3/caspase-1 pathway-induced neuronal pyrolysis in a mouse model of SAE [20]. A recent study also showed that the caspase-1 inhibition dramatically downregulated the pyroptosis, reduced the release of the inflammatory cytokines, protected the ultrastructure of the brain, and preserved the cognitive functions in the CLP-induced experimental sepsis [56]. In the current study, Western blot results showed that hippocampal NLRP3, procaspase-1, and cleaved caspase-1 were upregulated in the sepsis brain injury mice. Furthermore, we discovered that the expression of TXNIP in the hippocampus of septic mice also increased markedly. This increase occurred before the upregulation of NLRP3, procaspase-1, and cleaved caspase-1 expression levels. Therefore, we speculated that the TXNIP/NLRP3/caspase-1 pathway might mediate the LPS-induced septic brain damage.

In recent years, gene transfection technology has been widely used in various cell experiments and animal studies [34, 57]. In this study, the adeno-associated virus (AAV) vectors containing different interference fragments were injected into the lateral ventricle of the brain. Furthermore, virus was delivered at concentrations of 1.0×10^{11}, 1.0×10^{12}, and 1.0×10^{13} viral particles per mL in our preliminary

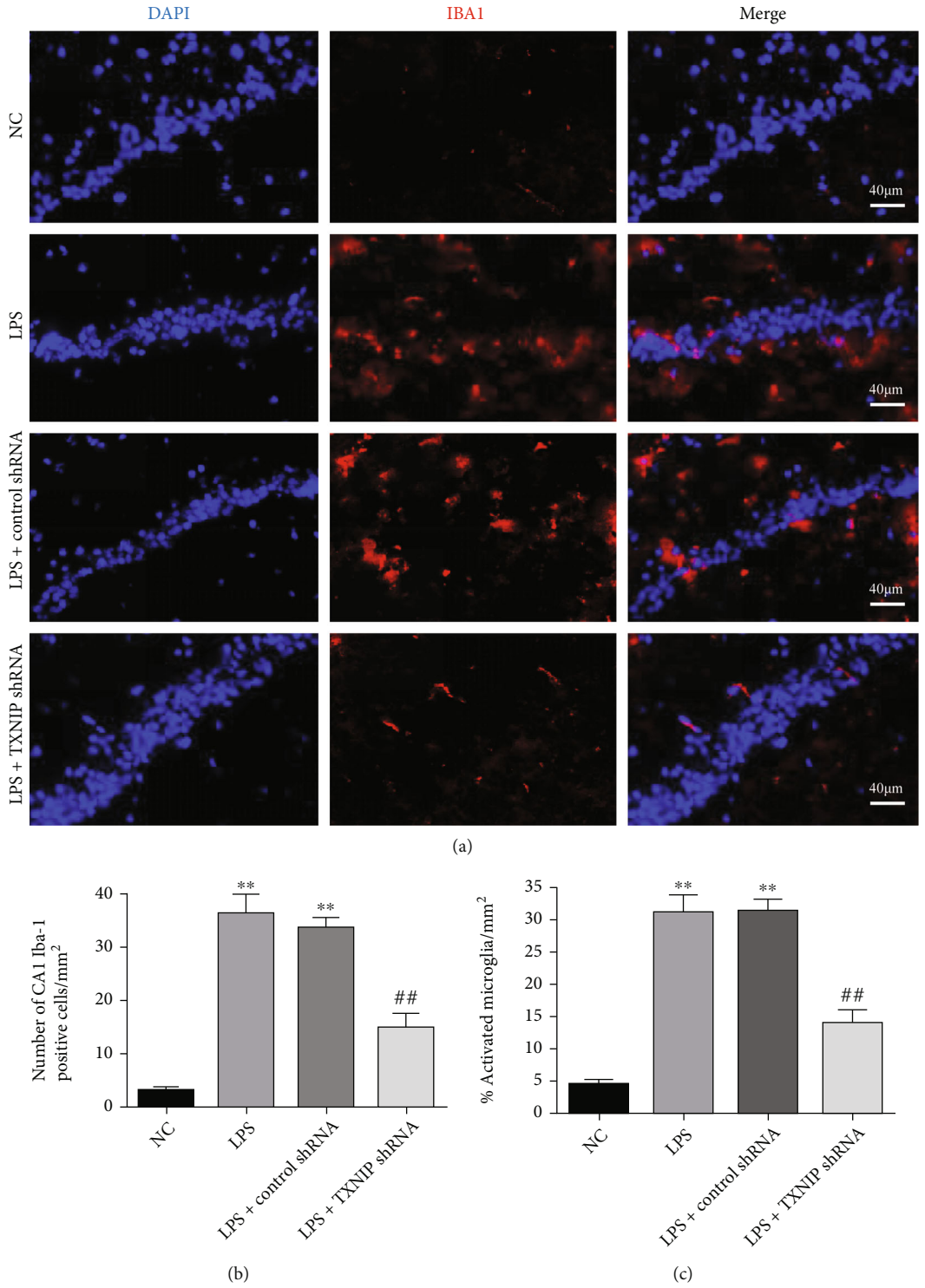

Figure 10: Effects of TXNIP knockdown on microglial activation. (a) Iba1 (red) immunofluorescence in the hippocampus (×400) (scale bar = 40 μm). Nuclei were labeled with blue fluorescence (DAPI); Iba1 was labeled with red fluorescence. (b, c) Quantitative analysis of Iba1-positive cells and activated microglia in the hippocampus. $^{**}P < 0.01$ *vs.* NC group; $^{\#\#}P < 0.01$ *vs.* LPS+control shRNA group ($n = 8$).

experiments. After 4 weeks, the EGFP expressed by the AAV was observed in the hippocampus of the brain, indicating that AAV (1.0×10^{13} viral particles per mL) successfully infected the hippocampus. Importantly, the TXNIP mRNA and protein levels in the hippocampus were significantly reduced in the LPS+TXNIP $shRNA_1$ and LPS+TXNIP $shRNA_2$

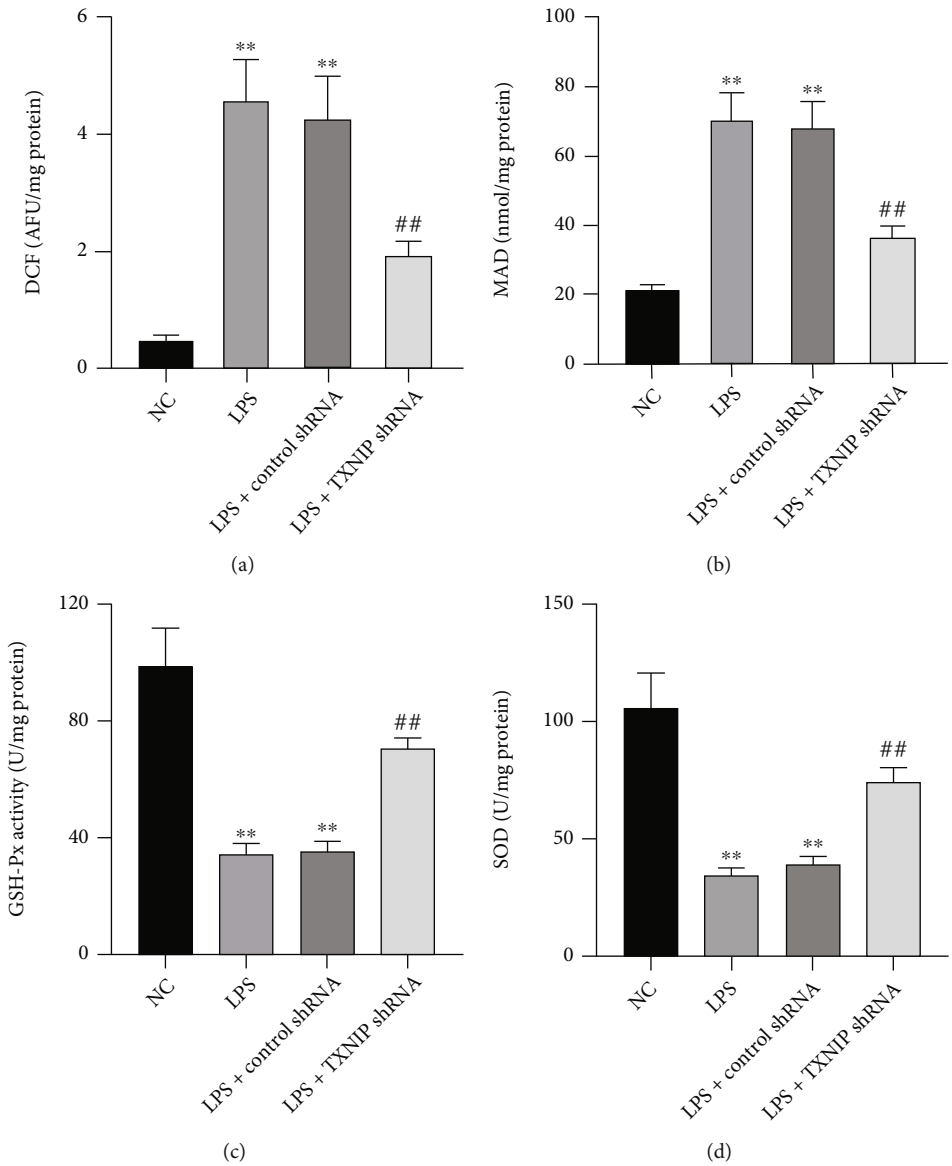

Figure 11: Effects of TXNIP knockdown on ROS, MDA, GSH-Px, and SOD levels. TXNIP knockdown significantly reduced the ROS and MDA levels and improved GSH-Px and SOD activities (a–d). The data are expressed as mean ± SEM. $^{**}P < 0.01$ *vs*. NC group; $^{\#\#}P < 0.01$ *vs*. LPS+control shRNA group ($n = 8$).

groups, although TXNIP shRNA$_1$ had the most obvious inhibitory effect. However, the control shRNA transfected with AAV as a vector did not affect the expression level of TXNIP. The behavioral pathological and inflammatory factors of the mice in the LPS+control shRNA group did not differ from those in the LPS group without virus injection, indicating that the AAV does not cause brain damage, and the regulatory effect of the shRNA transfected with the AAV on sepsis mice was mainly due to the transfection of various shRNAs. Unfortunately, it is difficult to make sure which one, the TXNIP gene or the whole compound, is exerting the role of neuroprotection in brain injury. We conjectured that reducing the gene of TXNIP might have potential protective effect, not the whole compound (TXNIP shRNA) in the present experiment based on previous studies [58, 59].

A strong link has been established between oxidative stress and inflammation [24]. TXNIP has been considered an endogenous negative regulator in the TRX system with a pivotal role in central system diseases, such as stroke, subarachnoid hemorrhage, and Alzheimer's disease [23, 25]. Ezetimibe reduces oxidative stress and neuroinflammation by activating the AMPK/Nrf2/TXNIP signaling pathway in rats with middle cerebral artery occlusion [60]. TXNIP shRNA was used to knock down TXNIP in experiment 3. Subsequently, TXNIP knockdown significantly improved the 7-day survival rate in sepsis mice, reduced brain edema and hippocampal pathological damage, and improved cognitive dysfunction. Sepsis is a systemic inflammatory response syndrome, often accompanied by the release of a large number of inflammatory cytokines, such as TNF-α and IL-6, in the central and peripheral nervous systems

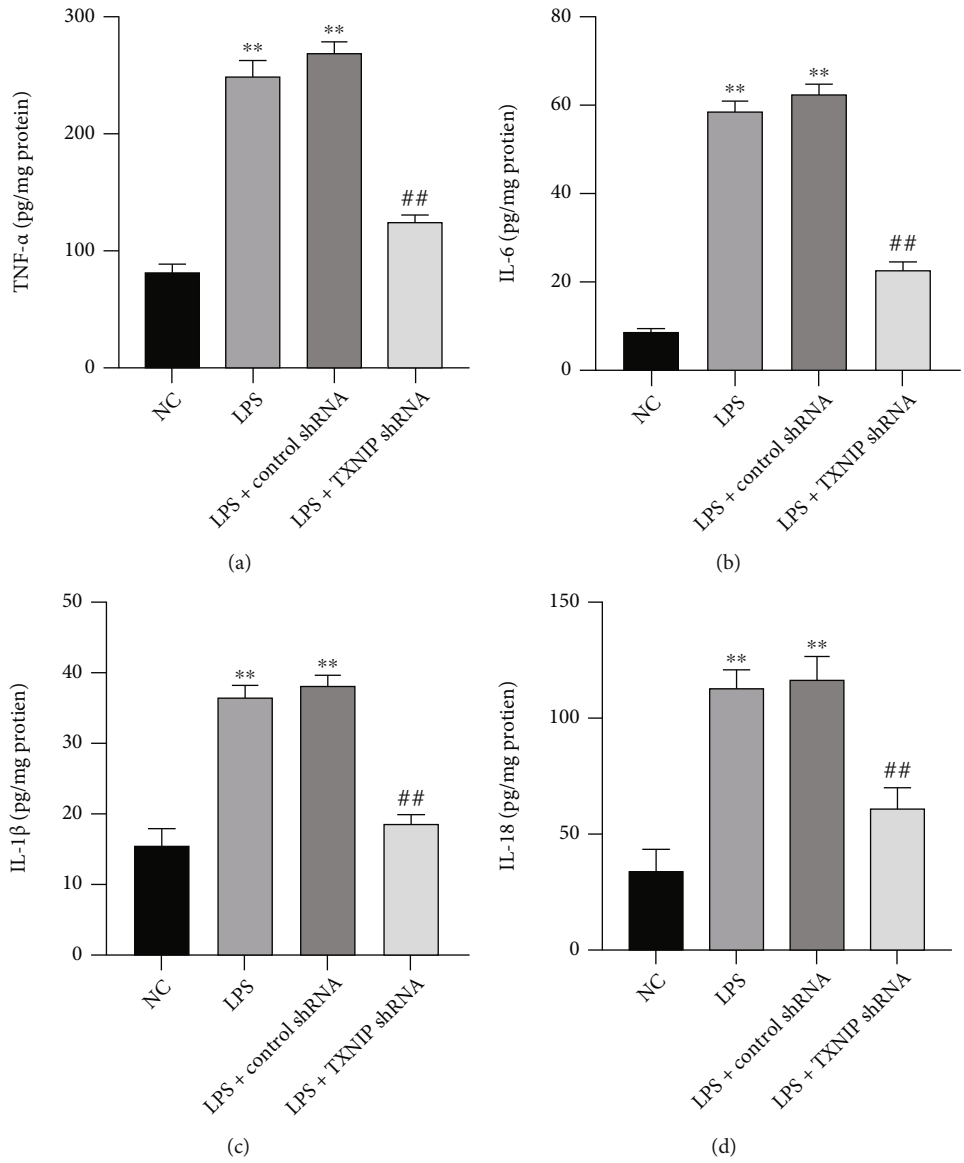

Figure 12: Changes in the inflammatory factors in the hippocampus. (a–d) The levels of TNF-α, IL-6, IL-1β, and IL-18 in the hippocampus, respectively. The values are presented as mean ± SEM. $^{**}P < 0.01$ *vs.* NC group; $^{\#\#}P < 0.01$ *vs.* LPS+control shRNA group ($n = 10$).

[7]. In this study, the release of proinflammatory cytokines, such as TNF-α, IL-6, IL-1β, and IL-18, was inhibited after TXNIP knockdown.

Oxidative stress also plays a key role in septic brain injury. The level of free radicals increases sharply during sepsis, accompanied by decreased activities of antioxidant enzymes. The MDA levels could reflect the severity of peroxidation in the body, while GSH-Px and SOD are crucial antioxidant factors [37, 38]. In the present study, ROS and MDA levels were increased evidently, while GSH-Px and SOD levels were decreased significantly as a consequence of decompensated activation of oxidative stress. TXNIP knockdown improved the alterations of oxidative stress. These findings demonstrated that TXNIP knockdown inhibits inflammatory responses, scavenges toxic free radicals, and regulates the activities of antioxidant enzymes, thereby exerting antioxidant effects. We also observed that the apoptotic rate of the hippocampal neurons in the TXNIP knockdown group was significantly lower than that of the sepsis mice without TXNIP knockdown. These results suggested that TXNIP is partially involved in the pathogenesis of sepsis brain injury.

The effect of the NLRP3 inflammasome on sepsis brain injury has been preliminarily studied in the CLP-induced mouse model, but the role of its regulatory protein TXNIP in the sepsis brain injury and the effects on the NLRP3 inflammasome remain unknown [20]. The microglia are the resident immune cells of the central nervous system and play a critical role in neuroinflammation [36]. In the central nervous system, NLRP3 is mainly expressed in microglia [39]. The maturation and release of IL-1β and IL-18 indicate NLRP3 inflammasome activation. The present study showed that TXNIP knockdown significantly inhibited hippocampal microglia activation in the sepsis mice, while the NLRP3 and cleaved caspase-1 protein

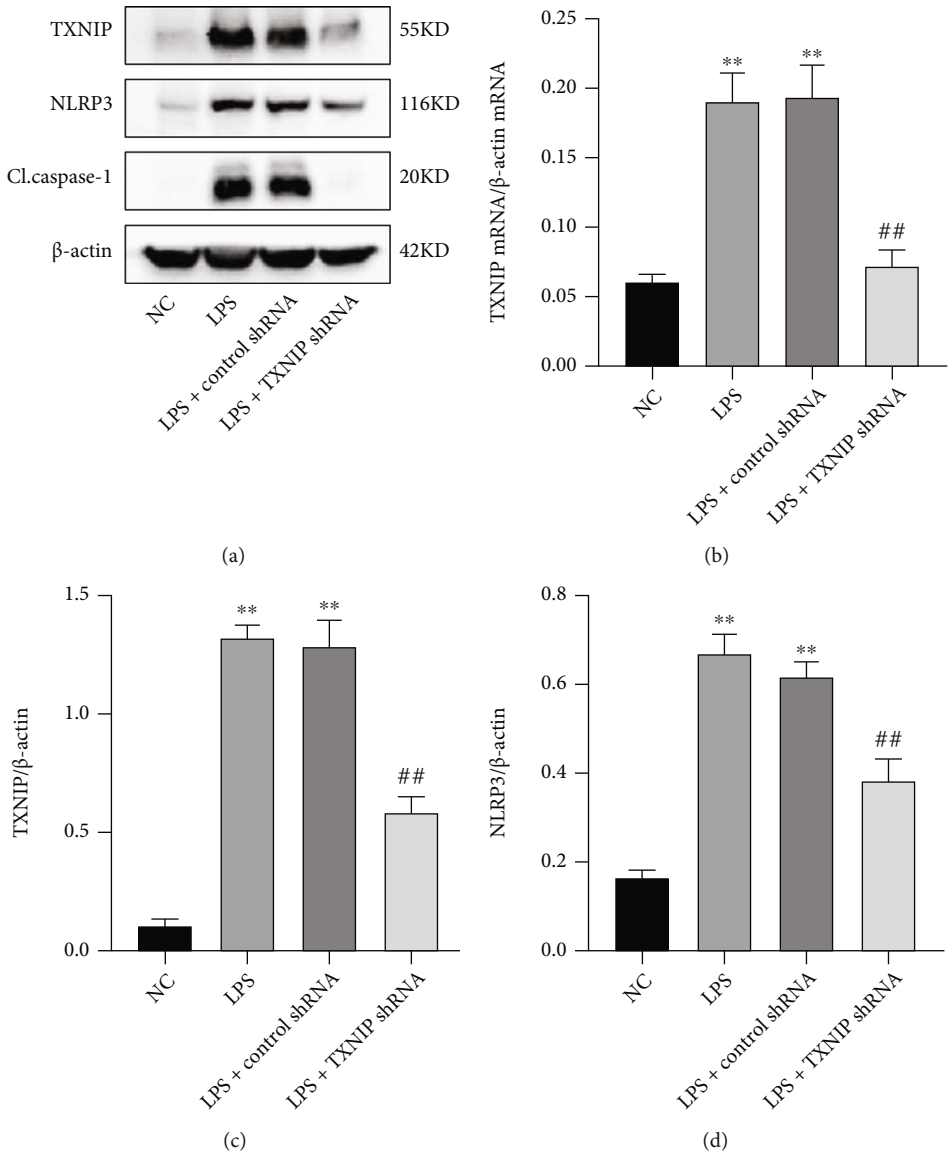

Figure 13: Continued.

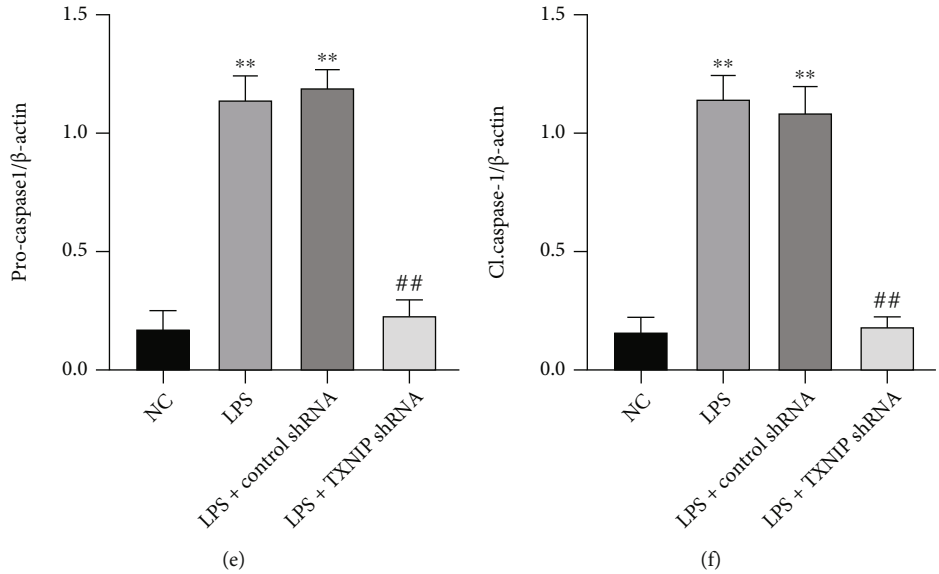

Figure 13: Expression of the TXNIP-NLRP3 signaling pathway in the hippocampus. (a) Bands of TXNIP, NLRP3, procaspase-1, and cleaved caspase-1 in the hippocampus. (b) qRT-PCR results of TXNIP mRNA. (c–f) Quantification of the TXNIP, NLRP3, procaspase-1, and cleaved caspase-1 levels in the hippocampus normalized to β-actin. The values are presented as mean ± SEM. $^{**}P < 0.01$ *vs.* NC group; $^{\#\#}P < 0.01$ *vs.* LPS+control shRNA group ($n = 6$).

expression levels and the inflammatory factors, IL-1β and IL-18, were significantly reduced in the hippocampus. The proapoptotic protein Bax and the antiapoptotic protein Bcl-2 mainly affect the release of the mitochondrial cytochrome C, thereby activating or inhibiting caspase-3 [61]. We also observed that TXNIP knockdown upregulated the level of Bcl-2 and downregulated the cleaved caspase-3 and Bax levels in the hippocampus of sepsis mice, thereby inhibiting neuronal apoptosis. Consistent with the previous study [62], caspase-1 catalyzed by the activated NLRP3 inflammasome promotes the release of IL-1β and IL-18 to regulate inflammation and apoptosis and the production of caspase-3.

Nevertheless, the present study has some limitations. Firstly, this study only evaluated the effect of TXNIP knockdown on brain damage, and hence, it is necessary to further evaluate the effect of TXNIP overexpression on brain damage in sepsis mice. Secondly, this study only explored the related mechanisms of the neuroprotective effect of TXNIP on sepsis mice with respect to oxidative stress and inflammatory response, while efficiency and other mechanisms need further study. Thirdly, the main goal/emphasis of the present study was to demonstrate the effects of TXNIP knockdown on sepsis-mediated brain injury and cognitive decline of animal through a new experiment and to investigate the possible mechanisms related to suppressing oxidative stress and neuroinflammation; we did not thoroughly investigate its dosage and some correlation. If this study might draw a conclusion that TXNIP had some diagnostic potential, its dosage should be studied. That is a tremendous work, and we will design other new experiments to address this question in the future. Finally, the clinical application of this study needs to be elucidated further.

5. Conclusion

In conclusion, the present study demonstrated that the TXNIP knockdown ameliorated sepsis-induced brain injury and cognitive decline by preventing oxidative stress and neuroinflammation in mice. Therefore, TXNIP might be a potential therapeutic target in SAE patients.

Data Availability

The data used to support the findings of this study are included within the article and are available from the corresponding author upon request.

Conflicts of Interest

The authors declare that they have no conflicts of interest.

Authors' Contributions

Yu Zhang, Cheng-Jun Xing, and Xiao Liu contributed equally to this study. Ye Chen and Jun Zhou conceived and designed the experiments. Yu Zhang, Cheng-Jun Xing, and Xiao Liu performed the experiments. Ya-Hong Li and Cheng-Jie Yang analyzed the data. Jing Jia and Jian-Guo Feng contributed the reagents/materials/analysis tools. Jun Zhou wrote the paper. All authors read and approved the manuscript.

Acknowledgments

This study was supported by grants from the National Natural Science Foundation of China (Nos. 81873930 and

81301055) partly by grants from the Department of Science and Technology of Sichuan Province (No. 20YYJC2019) and Talent Development Project of the Affiliated Hospital of Southwest Medical University (No. 20063). We would like to thank Dr. Sunil Saroj for the critical reading and language revision of this manuscript.

References

[1] M. Singer, C. S. Deutschman, C. W. Seymour et al., "The Third International Consensus Definitions for Sepsis and Septic Shock (Sepsis-3)," *Journal of the American Medical Association*, vol. 315, no. 8, pp. 801–810, 2016.

[2] M. Cecconi, L. Evans, M. Levy, and A. Rhodes, "Sepsis and septic shock," *Lancet*, vol. 392, no. 10141, pp. 75–87, 2018.

[3] B. Zheng, H. Yang, J. Zhang et al., "Lidocaine alleviates sepsis-induced acute lung injury in mice by suppressing tissue factor and matrix metalloproteinase-2/9," *Oxidative Medicine and Cellular Longevity*, vol. 2021, Article ID 3827501, 13 pages, 2021.

[4] J. Xie, Z. Z. Zhao, P. Li et al., "Senkyunolide I protects against sepsis-associated encephalopathy by attenuating sleep deprivation in a murine model of cecal ligation and puncture," *Oxidative Medicine and Cellular Longevity*, vol. 2021, Article ID 6647258, 11 pages, 2021.

[5] A. Mazeraud, F. A. Bozza, and T. Sharshar, "Sepsis-associated encephalopathy is septic," *American Journal of Respiratory and Critical Care Medicine*, vol. 197, no. 6, pp. 698-699, 2018.

[6] C. Ren, R. Q. Yao, H. Zhang, Y. W. Feng, and Y. M. Yao, "Sepsis-associated encephalopathy: a vicious cycle of immunosuppression," *Journal of Neuroinflammation*, vol. 17, no. 1, pp. 1–15, 2020.

[7] T. E. Gofton and G. B. Young, "Sepsis-associated encephalopathy," *Nature Reviews. Neurology*, vol. 8, no. 10, pp. 557–566, 2012.

[8] S. C. Tauber, M. Djukic, J. Gossner, H. Eiffert, W. Brück, and R. Nau, "Sepsis-associated encephalopathy and septic encephalitis: an update," *Expert Review of Anti-Infective Therapy*, vol. 19, no. 2, pp. 215–231, 2021.

[9] A. Mazeraud, C. Righy, E. Bouchereau, S. Benghanem, F. A. Bozza, and T. Sharshar, "Septic-associated encephalopathy: a comprehensive review," *Neurotherapeutics*, vol. 17, no. 2, pp. 392–403, 2020.

[10] L. A. Eidelman, D. Putterman, C. Putterman, and C. L. Sprung, "The spectrum of septic encephalopathy," *Journal of the American Medical Association*, vol. 275, no. 6, pp. 470–473, 1996.

[11] C. N. Widmann and M. T. Heneka, "Long-term cerebral consequences of sepsis," *Lancet Neurology*, vol. 13, no. 6, pp. 630–636, 2014.

[12] M. Ebersoldt, T. Sharshar, and D. Annane, "Sepsis-associated delirium," *Intensive Care Medicine*, vol. 33, no. 6, pp. 941–950, 2007.

[13] S. R. Guttikonda, L. Sikkema, J. Tchieu et al., "Fully defined human pluripotent stem cell-derived microglia and tri-culture system model C3 production in Alzheimer's disease," *Nature Neuroscience*, vol. 24, no. 3, pp. 343–354, 2021.

[14] B. Haileselassie, A. U. Joshi, P. S. Minhas, R. Mukherjee, K. I. Andreasson, and D. Mochly-Rosen, "Mitochondrial dysfunction mediated through dynamin-related protein 1 (Drp1) propagates impairment in blood brain barrier in septic encephalopathy," *Journal of Neuroinflammation*, vol. 17, no. 1, pp. 1–11, 2020.

[15] A. M. Klawonn, M. Fritz, S. Castany et al., "Microglial activation elicits a negative affective state through prostaglandin-mediated modulation of striatal neurons," *Immunity*, vol. 54, no. 2, pp. 225–34.e6, 2021.

[16] Y. Liu, H. Li, Y. Li, M. Yang, X. Wang, and Y. Peng, "Velvet antler methanol extracts ameliorate Parkinson's disease by inhibiting oxidative stress and neuroinflammation: from C. elegans to mice," *Oxidative Medicine and Cellular Longevity*, vol. 2021, Article ID 8864395, 13 pages, 2021.

[17] S. Chen, J. Peng, P. Sherchan et al., "TREM2 activation attenuates neuroinflammation and neuronal apoptosis via PI3K/Akt pathway after intracerebral hemorrhage in mice," *Journal of Neuroinflammation*, vol. 17, no. 1, pp. 1–16, 2020.

[18] M. Sendler, C. van den Brandt, J. Glaubitz et al., "NLRP3 inflammasome regulates development of systemic inflammatory response and compensatory anti-inflammatory response syndromes in mice with acute pancreatitis," *Gastroenterology*, vol. 158, no. 1, pp. 253–69.e14, 2020.

[19] K. V. Swanson, M. Deng, and J. P. Ting, "The NLRP3 inflammasome: molecular activation and regulation to therapeutics," *Nature Reviews. Immunology*, vol. 19, no. 8, pp. 477–489, 2019.

[20] Q. Fu, J. Wu, X. Y. Zhou et al., "NLRP3/caspase-1 pathway-induced pyroptosis mediated cognitive deficits in a mouse model of sepsis-associated encephalopathy," *Inflammation*, vol. 42, no. 1, pp. 306–318, 2019.

[21] X. Ren, L. Zou, X. Zhang et al., "Redox signaling mediated by thioredoxin and glutathione systems in the central nervous system," *Antioxidants & Redox Signaling*, vol. 27, no. 13, pp. 989–1010, 2017.

[22] J. Lu and A. Holmgren, "The thioredoxin antioxidant system," *Free Radical Biology & Medicine*, vol. 66, pp. 75–87, 2014.

[23] S. Nasoohi, S. Ismael, and T. Ishrat, "Thioredoxin-interacting protein (TXNIP) in cerebrovascular and neurodegenerative diseases: regulation and implication," *Molecular Neurobiology*, vol. 55, no. 10, pp. 7900–7920, 2018.

[24] R. Zhou, A. Tardivel, B. Thorens, I. Choi, and J. Tschopp, "Thioredoxin-interacting protein links oxidative stress to inflammasome activation," *Nature Immunology*, vol. 11, no. 2, pp. 136–140, 2010.

[25] Q. Zhao, X. Che, H. Zhang et al., "Thioredoxin-interacting protein links endoplasmic reticulum stress to inflammatory brain injury and apoptosis after subarachnoid haemorrhage," *Journal of Neuroinflammation*, vol. 14, no. 1, pp. 1–15, 2017.

[26] T. S. Anthonymuthu, N. Kim-Campbell, and H. Bayır, "Oxidative lipidomics: applications in critical care," *Current Opinion in Critical Care*, vol. 23, no. 4, pp. 251–256, 2017.

[27] Y. Wen, Y. R. Liu, T. T. Tang et al., "mROS-TXNIP axis activates NLRP3 inflammasome to mediate renal injury during ischemic AKI," *The International Journal of Biochemistry & Cell Biology*, vol. 98, pp. 43–53, 2018.

[28] Y. Liu, K. Lian, L. Zhang et al., "TXNIP mediates NLRP3 inflammasome activation in cardiac microvascular endothelial cells as a novel mechanism in myocardial ischemia/reperfusion injury," *Basic Research in Cardiology*, vol. 109, no. 5, pp. 1–14, 2014.

[29] Y. Wu, J. Pang, J. Peng et al., "Apolipoprotein E deficiency aggravates neuronal injury by enhancing neuroinflammation via the JNK/c-Jun pathway in the early phase of experimental subarachnoid hemorrhage in mice," *Oxidative Medicine and*

Cellular Longevity, vol. 2019, Article ID 3832648, 15 pages, 2019.

[30] B. Yang, L. Y. Zhang, Y. Chen et al., "Melatonin alleviates intestinal injury, neuroinflammation and cognitive dysfunction caused by intestinal ischemia/reperfusion," *International Immunopharmacology*, vol. 85, article 106596, 2020.

[31] A. E. Atici, S. Arabacı Tamer, H. N. Levent et al., "Neuropeptide W attenuates oxidative multi-organ injury in rats induced with intra-abdominal sepsis," *Inflammation*, vol. 45, no. 1, pp. 279–296, 2022.

[32] B. Han, Q. Wang, G. Cui, X. Shen, and Z. Zhu, "Post-treatment of Bax-inhibiting peptide reduces neuronal death and behavioral deficits following global cerebral ischemia," *Neurochemistry International*, vol. 58, no. 2, pp. 224–233, 2011.

[33] C. H. Cho, H. R. Byun, T. Jover-Mengual et al., "Gadd45b acts as neuroprotective effector in global ischemia-induced neuronal death," *International Neurourology Journal*, vol. 23, Suppl 1, pp. S11–S21, 2019.

[34] D. A. Amado, J. M. Rieders, F. Diatta et al., "AAV-mediated progranulin delivery to a mouse model of progranulin deficiency causes T cell-mediated toxicity," *Molecular Therapy*, vol. 27, no. 2, pp. 465–478, 2019.

[35] Y. Chen, Y. Lei, L. Q. Mo et al., "Electroacupuncture pretreatment with different waveforms prevents brain injury in rats subjected to cecal ligation and puncture via inhibiting microglial activation, and attenuating inflammation, oxidative stress and apoptosis," *Brain Research Bulletin*, vol. 127, pp. 248–259, 2016.

[36] J. Zhou, W. Q. Huang, C. Li et al., "Intestinal ischemia/reperfusion enhances microglial activation and induces cerebral injury and memory dysfunction in rats," *Critical Care Medicine*, vol. 40, no. 8, pp. 2438–2448, 2012.

[37] X. Fan, J. Du, M. H. Wang et al., "Irisin contributes to the hepatoprotection of dexmedetomidine during intestinal ischemia/reperfusion," *Oxidative Medicine And Cellular Longevity*, vol. 2019, Article ID 7857082, 15 pages, 2019.

[38] J. Du, X. Fan, B. Yang, Y. Chen, K. X. Liu, and J. Zhou, "Irisin pretreatment ameliorates intestinal ischemia/reperfusion injury in mice through activation of the Nrf2 pathway," *International Immunopharmacology*, vol. 73, pp. 225–235, 2019.

[39] Y. Zhang, S. L. Tan, J. Du et al., "Dexmedetomidine alleviates neuroinflammation, restores sleep disorders and neurobehavioral abnormalities in rats with minimal hepatic encephalopathy," *International Immunopharmacology*, vol. 96, article 107795, 2021.

[40] H. C. Prescott and D. C. Angus, "Enhancing recovery from sepsis: a review," *JAMA*, vol. 319, no. 1, pp. 62–75, 2018.

[41] C. Lelubre and J. L. Vincent, "Mechanisms and treatment of organ failure in sepsis," *Nature Reviews. Nephrology*, vol. 14, no. 7, pp. 417–427, 2018.

[42] T. Sharshar, D. Annane, G. L. de la Grandmaison, J. P. Brouland, N. S. Hopkinson, and G. Françoise, "The neuropathology of septic shock," *Brain Pathology*, vol. 14, no. 1, pp. 21–33, 2004.

[43] C. J. McBain, S. F. Traynelis, and R. Dingledine, "Regional variation of extracellular space in the hippocampus," *Science*, vol. 249, no. 4969, pp. 674–677, 1990.

[44] D. E. Pellegrini-Giampietro, R. S. Zukin, M. V. Bennett, S. Cho, and W. A. Pulsinelli, "Switch in glutamate receptor subunit gene expression in CA1 subfield of hippocampus following global ischemia in rats," *Proceedings of the National Academy of Sciences of the United States of America*, vol. 89, no. 21, pp. 10499–10503, 1992.

[45] J. J. Yan, J. S. Jung, J. E. Lee et al., "Therapeutic effects of lysophosphatidylcholine in experimental sepsis," *Nature Medicine*, vol. 10, no. 2, pp. 161–167, 2004.

[46] M. P. Fink, "Animal models of sepsis," *Virulence*, vol. 5, no. 1, pp. 143–153, 2014.

[47] S. Wei, Z. Xiao, J. Huang, Z. Peng, B. Zhang, and W. Li, "Disulfiram inhibits oxidative stress and NLRP3 inflammasome activation to prevent LPS-induced cardiac injury," *International Immunopharmacology*, vol. 105, article 108545, 2022.

[48] K. E. Henry, A. M. Chaney, V. L. Nagle et al., "Demarcation of sepsis-induced peripheral and central acidosis with pH (low) insertion cycle peptide," *Journal of Nuclear Medicine*, vol. 61, no. 9, pp. 1361–1368, 2020.

[49] D. Coquerel, R. Neviere, E. Delile et al., "Gene deletion of protein tyrosine phosphatase 1B protects against sepsis-induced cardiovascular dysfunction and mortality," *Arteriosclerosis, Thrombosis, and Vascular Biology*, vol. 34, no. 5, pp. 1032–1044, 2014.

[50] T. Honda, Q. He, F. Wang, and A. N. Redington, "Acute and chronic remote ischemic conditioning attenuate septic cardiomyopathy, improve cardiac output, protect systemic organs, and improve mortality in a lipopolysaccharide-induced sepsis model," *Basic Research in Cardiology*, vol. 114, no. 3, pp. 1–11, 2019.

[51] W. Zhu, F. S. Cao, J. Feng et al., "NLRP3 inflammasome activation contributes to long-term behavioral alterations in mice injected with lipopolysaccharide," *Neuroscience*, vol. 343, pp. 77–84, 2017.

[52] H. Z. Toklu, M. K. Uysal, L. Kabasakal, S. Sirvanci, F. Ercan, and M. Kaya, "The effects of riluzole on neurological, brain biochemical, and histological changes in early and late term of sepsis in rats," *The Journal of Surgical Research*, vol. 152, no. 2, pp. 238–248, 2009.

[53] A. Shao, H. Wu, Y. Hong et al., "Hydrogen-rich saline attenuated subarachnoid hemorrhage-induced early brain injury in rats by suppressing inflammatory response: possible involvement of NF-κB pathway and NLRP3 inflammasome," *Molecular Neurobiology*, vol. 53, no. 5, pp. 3462–3476, 2016.

[54] B. Dehqanizadeh, Z. F. Mohammadi, A. H. T. Kalani, and S. J. Mirghani, "Effect of early exercise on inflammatory parameters and apoptosis in CA1 area of the hippocampus following cerebral ischemia-reperfusion in rats," *Brain Research Bulletin*, vol. 182, pp. 102–110, 2022.

[55] L. Franchi, T. Eigenbrod, R. Muñoz-Planillo, and G. Nuñez, "The inflammasome: a caspase-1-activation platform that regulates immune responses and disease pathogenesis," *Nature Immunology*, vol. 10, no. 3, pp. 241–247, 2009.

[56] X. E. Xu, L. Liu, Y. C. Wang et al., "Caspase-1 inhibitor exerts brain-protective effects against sepsis-associated encephalopathy and cognitive impairments in a mouse model of sepsis," *Brain, Behavior, and Immunity*, vol. 80, pp. 859–870, 2019.

[57] D. Wang, P. W. Tai, and G. Gao, "Adeno-associated virus vector as a platform for gene therapy delivery," *Nature Reviews. Drug Discovery*, vol. 18, no. 5, pp. 358–378, 2019.

[58] L. Xu, X. Lin, M. Guan, Y. Zeng, and Y. Liu, "Verapamil attenuated prediabetic neuropathy in high-fat diet-fed mice through inhibiting TXNIP-mediated apoptosis and inflammation," *Oxidative Medicine and Cellular Longevity*, vol. 2019, Article ID 1896041, 14 pages, 2019.

[59] L. Perrone, T. S. Devi, K. I. Hosoya, T. Terasaki, and L. P. Singh, "Inhibition of TXNIP expression in vivo blocks early pathologies of diabetic retinopathy," *Cell Death & Disease*, vol. 1, no. 8, article e65, 2010.

[60] J. Yu, W. N. Wang, N. Matei et al., "Ezetimibe attenuates oxidative stress and neuroinflammation via the AMPK/Nrf2/TXNIP pathway after MCAO in rats," *Oxidative Medicine and Cellular Longevity*, vol. 2020, Article ID 4717258, 14 pages, 2020.

[61] K. G. Wolter, Y. T. Hsu, C. L. Smith, A. Nechushtan, X. G. Xi, and R. J. Youle, "Movement of Bax from the cytosol to mitochondria during apoptosis," *The Journal of Cell Biology*, vol. 139, no. 5, pp. 1281–1292, 1997.

[62] M. S. Lee, H. Kwon, E. Y. Lee et al., "Shiga toxins activate the NLRP3 inflammasome pathway to promote both production of the proinflammatory cytokine interleukin-1β and apoptotic cell death," *Infection and Immunity*, vol. 84, no. 1, pp. 172–186, 2016.

Hindawi
Oxidative Medicine and Cellular Longevity
Volume 2022, Article ID 6304087, 14 pages
https://doi.org/10.1155/2022/6304087

Research Article

Antineuroinflammatory Effect of *Amburana cearensis* and Its Molecules Coumarin and Amburoside A by Inhibiting the MAPK Signaling Pathway in LPS-Activated BV-2 Microglial Cells

Ana Bruna de Araújo,[1] **Francisco Vinícius Clemente Serra Azul**,[1] **Francisca Raysse Mesquita Silva**,[1] **Talysson Silva de Almeida**,[1] **João Victor Nunes Oliveira**,[1] **Antônia Torres Ávila Pimenta**,[1] **Antônio Marcos Esmeraldo Bezerra**,[1] **Nuno J. Machado**,[1,2] **and Luzia Kalyne Almeida Moreira Leal**[1]

[1]*Centro de Estudos Farmacêuticos e Cosméticos (CEFAC), Departamento de Farmácia, Faculdade de Farmácia, Odontologia e Enfermagem, Universidade Federal do Ceará, Fortaleza, CE, Brazil*
[2]*Programa de Pós-Graduação em Ciências da Saúde, Universidade Federal do Ceará, Sobral, CE, Brazil*

Correspondence should be addressed to Nuno J. Machado; nuno.machado.br@gmail.com
and Luzia Kalyne Almeida Moreira Leal; kalyne@ufc.br

Received 10 February 2022; Accepted 21 March 2022; Published 28 April 2022

Academic Editor: Abdur Rauf

Microglia plays an important role in the neuroinflammatory response, identified as one of the major factors in the development and progression of neurodegenerative diseases. *Amburana cearensis* and its bioactive compounds, including coumarin (CM), vanillic acid (VA), and amburoside A (AMB), exert antioxidant, anti-inflammatory, and neuroprotective activities, on 6-OHDA-induced neurotoxicity in rat mesencephalic cells determined by our group. The present study investigated the anti-inflammatory effect of the dry extract from *A. cearensis* (DEAC), CM, AMB, and VA on lipopolysaccharide- (LPS-) stimulated microglial cells and elucidated the possible molecular mechanism of action. The DEAC was characterized by HPLC-PDA (chemical markers: CM, AMB, and VA). The BV-2 microglial cell line was pretreated with increasing concentrations of DEAC, CM, AMB, or VA in the presence or absence of LPS to evaluate the toxicity and anti-inflammatory activity. The cytotoxicity of DEAC, CM, AMB, or VA on BV-2 cells was evaluated by the MTT test, the free radical scavenging activity of test drugs was investigated, and the nitric oxide (NO) production was determined using the Griess reagent, while cytokine levels were measured by ELISA. The expressions of toll-like receptor 4 (TLR-4), nuclear factor kappa B (NF-κB), MAPK members (JNK and ERK1/2), and iNOS were determined through Western blot analysis. DEAC, CM, AMB, or VA (5-100 μg/mL) did not induce any detectable cytotoxicity in BV-2 cells. All test drugs (100 μg/mL) showed free radical scavenging activity (hydroxyl and superoxide radicals); however, only DEAC, CM, and AMB (5-100 μg/mL) significantly reduced NO production. DEAC (100 μg/mL), as well as CM (50 and 100 μg/mL) and AMB (25 μg/mL), reduced at least 50% of NO produced and markedly decrease the production of TNF-α and IL-6 but they did not significantly affect IL-10 levels. Only DEAC (100 μg/mL) and AMB (25 μg/mL) reduced the expression of iNOS, and they did not affect arginase activity. DEAC (100 μg/mL) suppressed the activation of the MAPKs JNK and ERK1/2 in LPS-activated BV-2 cells but it did not suppress the expression of TLR-4 nor the phosphorylation of NF-κB. In conclusion, DEAC, CM, and AMB exerted anti-inflammatory activity in LPS-activated microglial cells as observed by the reduction in the production of inflammatory mediators and the expression of iNOS. We identified the MAPK signaling pathway as a probable mechanism of action to the anti-inflammatory effects observed.

1. Introduction

There is increasing evidence of the important role of neuroinflammation in the pathogenesis of several neurodegenerative diseases, including Alzheimer's disease and Parkinson's disease [1–3]. The neuroinflammatory process includes a variety of events marked by the accumulation of various proinflammatory mediators, such as tumor necrosis factor alpha (TNF-α), interleukin 1β (IL-1β), interleukin 6 (IL-6), prostaglandins, nitric oxide (NO) (generated by inducible nitric oxide synthase (iNOS) and reactive oxygen species (ROS)). Microglia and astrocytes are the innate immune cells primarily involved in these proinflammatory mechanisms which cause damage to neuronal networks. In parallel, under physiological conditions, these cells have a protective function in preserving the homeostasis of the central nervous system (CNS) by secreting anti-inflammatory mediators and neurotrophic factors, such as transforming growth factor-β, interleukin 10 (IL-10), and arginase-1 [3, 4]. Thus, controlling microglial activation or modulating its phenotypes in response to damage-associated stimuli may be a promising strategy in the development of a therapy for neuroinflammatory diseases.

Microglial cells can be activated by various endogenous and environmental stimuli such as IFN-γ (interferon-gamma), glutamate, arachidonate, and lipopolysaccharide (LPS). LPS is found on the outer membrane of Gram-negative bacteria, acting as an endotoxin that binds to specific receptors, and it has been widely used to study inflammation due to its reproducible action and easy handling [5]. LPS induces activation of the toll-like receptor 4 (TLR-4) which activates nuclear factor kappa B (NF-κB) and mitogen-activated protein kinases (MAPKs) that play critical roles in the production of inflammatory mediators [6, 7].

Due to a deficit in therapeutical options, herbal products have been the focus of several studies for the treatment or prevention of neurodegenerative diseases [8, 9]. *Amburana cearensis* A. C. Smith (Fabaceae), a plant native to the Brazilian semiarid region, has been extensively studied by our group that determined its chemical profile and pharmacological properties [10–13]. Other previous studies developed by our group [10, 14–18] allowed us to determine the anti-inflammatory and antioxidant activities of the extract of *A. cearensis* (wild or cultivated) and/or its chemical constituents, such as coumarin (CM), amburoside A (AMB, phenol glucoside), and vanillic acid (VA, phenol acid). Outside the brain, they exert anti-inflammatory activity mainly by inhibiting the accumulation and activation of polymorphonuclear cells and the production of cytokines and ROS. Additionally, in rat mesencephalic cell cultures exposed to 6-hydroxydopamine (6-OHDA), Leal and colleagues [15] showed that AMB reduced the damage caused by this neurotoxin through the inhibition of the increase in lipidic peroxidation and production of nitrite. These data suggest that this phenol glucoside, among the main chemical constituents of *A. cearensis*, could provide benefits as a therapeutic agent in neurodegenerative diseases such as Parkinson's disease. Therefore, the present study was designed to evaluate the anti-inflammatory effects of a standardized dry extract of *A. cearensis* and its chemical constituents (CM, AMB, and VA) in LPS-stimulated microglial cells. Moreover, it is aimed at contributing to the elucidation of the mechanisms of action involved by evaluating the role of the signaling pathways of TLR-4, NF-κB, and MAPKs.

2. Materials and Methods

2.1. Preparation and Chemical Characterization of Dried Extract from Amburana cearensis Extract (DEAC). To achieve a sustainable alternative for economic utilization of *A. cearensis*, in the last years, our research group became focused also on *A. cearensis* cultivated plant which has chemical and biological properties similar to the wild variety [16]. Seeds of *A. cearensis* were collected at the Quixeramobim region, Ceará State, Brazil, and voucher specimen (n° 52618) was deposited in the herbarium Prisco Bezerra, Department of Biology, Federal University of Ceará. *A. cearensis* seeds were cultivated, and seven months later, the plant was harvested from the garden beds, dried, and ground. The extraction was carried out by maceration for 24 h with ethanol as previously determined by our laboratory [17]. The drying process of the ethanol extract was performed at room temperature using a mini spray-dryer model LM MSD 1.0 (Labmaq do Brazil Ltda, Ribeirão Preto, SP, Brazil). The colloidal silicon dioxide was used as drying carrier (30% of the solid residues) with a feed flow of 1 L/h, inlet temperature of 100°C, and airflow of 40 L/min.

2.2. HPLC-PDA Analysis. Dried extract of *A. cearensis* (DEAC) was analyzed by high-performance liquid chromatography–photodiode array (HPLC-PDA) (Waters) according to the method developed previously by our laboratory [10]. The analysis of the three chemical markers (coumarin (CM), amburoside A (AMB), and vanillic acid (VA)) was performed through their calibration curves, obtained by injection of external standards. The analysis of DEAC was performed in a C18 reverse phase column (4.6 mm × 250 mm) at a temperature of 45°C. The mobile phase was composed of acetonitrile (A), 0.01% phosphoric acid (B), and n-propanol (C), flow of 1 mL per minute. Detection was performed in a PDA detector using the wavelengths of 219 nm, 277 nm, and 220 nm for the determination of VA, CM, and AMB, respectively. The HPLC-PDA analysis of the DEAC allowed the identification and quantification of vanillic acid, amburoside, and coumarin.

2.3. Chemicals and Antibodies. The amburoside A (AMB) was isolated from *A. cearensis* according to the methodology described previously by our group [18]. Vanillic acid (VA), coumarin (CM), *N*-(1-Naphthyl) ethylenediamine dihydrochloride (NEED), 3-(4,5-dimethylthiazol-2-yl)-2,5-diphenyltetrazolium bromide (MTT), dimethyl sulfoxide (DMSO), bovine serum albumin (BSA), 2-thiobarbituric acid (TBA), nitrotetrazolium blue chloride (NBT), hypoxanthine (HPX) and xanthine oxidase (XOD), phosphoric acid (H_3PO_4), ferric chloride ($FeCl_3$), hydrogen peroxide (H_2O_2), and L-ascorbic acid (vitamin C) were obtained commercially from Sigma-Aldrich, USA. Sulfanilamide and ethylenediaminetetraacetic acid tetrasodium salt dehydrate

(EDTA) were purchased from Dinâmica Química Contemporânea, Brazil. Trichloroacetic acid (TCA) was acquired from Êxodo Científica, Brazil.

Fetal bovine serum (FBS) and cell culture medium RPMI-1640 were purchased from Gibco, USA. Murine microglial (BV-2) cells were acquired from Banco de Células do Rio de Janeiro, Brazil.

The antibodies anti-NF-κB, p-NF-κB, JNK, p-JNK, and p-ERK were obtained from Cell Signaling Technologies. TLR-4 antibody was obtained from Invitrogen, Carlsbad, CA, USA. Anti-iNOS, ERK, β-actin antibodies, and secondary antibodies (anti-rabbit and anti-mouse) were obtained from Abcam Cambridge, UK. ELISA kits for TNF-α, IL-6, IL-10, and IL-1β were purchased from BD Bioscience Pharmingen, San Diego, CA, USA.

2.4. Cell Culture Conditions. The murine BV-2 cells were maintained in RPMI-1640 medium supplemented with 10% fetal bovine serum. The cells were grown to 70-80% confluency and incubated at 37°C in an atmosphere of 5% CO_2.

2.5. Cell Viability Assay. Before conducting the anti-inflammatory activity test of the DEAC and its chemical constituents, we performed the cytotoxicity test first in BV-2 cells. The MTT test evaluated BV-2 cells' viability using the method previously described by Mosmann [19]. The cells (1×10^5 cells/mL) were plated in 96-well plates and treated with DEAC, CM, VA, or AMB (5, 10, 25, 50, and 100 μg/mL) and 0.1% dimethyl sulfoxide (DMSO, Sigma-Aldrich, USA) (drug vehicle) for 24 h. After the incubation period, the salt 3-(4,5-dimethyl-2-thiazolyl)-2,5-diphenyl-2H-tetrazolium bromide (MTT) solution (0.5 mg/mL final concentration) was added into the plate, then incubated for 90 minutes at 37°C. At last, the cells were centrifuged at 200 g for 10 minutes, the supernatant discarded, and the formazan crystals dissolved in DMSO. The absorbance of each well was recorded at 570 nm by using a plate reader (Bio-Tek, Winooski, VT, USA).

2.6. NO Measurement. The concentration of nitrite in LPS-induced BV-2 cells was determined by the Griess assay [20]. The cells (1×10^6 cells/mL) were plated in 96-well plates and incubated with DEAC, CM, VA, or AMB (5, 10, 25, 50, and 100 μg/mL) and 0.1% DMSO (drug vehicle), and 1 h later, LPS (0.5 μg/mL) was added. After 24 h, Griess reagent (1% sulfanilamide in 5% phosphoric acid and 0.1% *N*-(1-Naphthyl) ethylenediamine dihydrochloride (NEED) in distilled water, 1 : 1) was added to cell medium at room temperature, and 15 minutes later, absorbance at 540 nm was measured on a plate reader. The concentrations of NO were calculated from the standard curve generated by known concentrations of sodium nitrite.

2.7. Measurement of Hydroxyl Radical. The hydroxyl radical was measured using the deoxyribose method according to Zhao and colleagues [21] with modifications. Ascorbic acid (1 mM), EDTA (1 mM), H_2O_2 (10 mM), $FeCl_3$ (1 mM), and deoxyribose (DOR) (36 mM) were added to a reaction tube with DEAC (100 μg/mL), CM (100 μg/mL), VA (100 μg/mL), AMB (100 μg/mL), or 0.1% DMSO (drug vehicle) in 25 mM phosphate buffer (pH 7.4) and incubated for 1 h at 37°C. TCA 10% and TBA 1% (prepared in NaOH 50 mM) were added, and the solution was heated in a water bath at 85°C for 15 minutes. Absorbance at 532 nm was measured.

2.8. Assay for Superoxide Radical Scavenging Activity. Superoxide generation was measured by a slight modification of the previous method described by Hodgson and Fridovich [22] using the hypoxanthine/xanthine oxidase (Sigma-Aldrich, USA) system. Nitrotetrazolium blue chloride (NBT), hypoxanthine (HPX), and xanthine oxidase (XOD) solutions were prepared in Tris buffer. DEAC, CM, VA, or AMB at 100 μg/mL, or 0.1% DMSO, were added to the reaction solution containing 0.05 M Tris buffer, 5×10^{-3} M HPX, and 10^{-3} M NBT. Then, 1.67 μg/mL XOD was added, except in the negative control. The absorbance was measured at 560 nm every minute for 21 min.

2.9. Enzyme-Linked Immunosorbent Assay (ELISA). BV-2 cells were pretreated with DEAC (100 μg/mL), AMB (25 μg/mL), CM (50 and 100 μg/mL), or 0.1% DMSO (drug vehicle) for 1 h, then stimulated with LPS (0.5 μg/mL) for 24 h. The levels of TNF-α, IL-6, IL-1β, and IL-10 in the culture supernatant were quantified using commercially available ELISA kits (BD Bioscience Pharmingen, San Diego, CA, USA) according to the manufacturer's protocol. The absorbance at 450 nm was measured using a microplate reader.

2.10. Western Blot Analysis. BV-2 microglial cells (1×10^6 cells/mL) were pretreated with DEAC (100 μg/mL), CM (50, 100 μg/mL), AMB (25 μg/mL), or 0.1% DMSO (drug vehicle) for 1 h. LPS (0.5 μg/mL) was added, and the cells were incubated for 1 h or 24 h. The cells were harvested, and adherent cells were resuspended in ice-cold phosphate-buffered saline (PBS). Cellular proteins were extracted by incubating with radioimmunoprecipitation assay buffer (RIPA) containing protease inhibitor cocktail (1 : 20), phenylmethylsulfonyl fluoride (1 : 50), and phosphatase inhibitor cocktail set III (1 : 20). The cell lysate was centrifuged at 12500 × g for 10 min at 4°C, and the supernatant was kept as the protein extract. Protein concentration was determined with a BCA kit using bovine serum albumin (BSA) as standard, and the protein concentration of all samples was normalized with *Laemmli* buffer. Equal amounts of protein (30 μg) from each sample were subjected to 7.5-10% SDS-PAGE and transferred to PVDF membranes. After blocking at room temperature with 5% nonfat dry milk or 5% BSA for 1 h, the blocked membranes were incubated for 18 h with primary antibodies against p-NF-κB 1 : 1000 (#3033S), NF-κB 1 : 2000 (#6956S), p-ERK1/2 1 : 1000 (#9101S), ERK1/2 1 : 1000 (ab36991), p-JNK 1 : 1000 (#9255S), JNK 1 : 2000 (#9252S), iNOS 1 : 1000 (ab178945), TLR-4 1 : 200 (482300), and β-actin 1 : 5000 (ab8226) at 4°C. After washing three times with TBS-T (10 mM Tris-HCl (pH 7.6), 150 mM NaCl, 0.1% Tween 20), the membranes were incubated with the secondary antibody for 2 h at room temperature. Protein bands were visualized using enhanced chemiluminescence reagent (Bio-Rad, USA) in an imaging

system (ChemiDoc MP, Bio-Rad, USA) [23], and the protein levels were analyzed using the ImageLab 6 software (Bio-Rad, USA) and normalized with β-actin or total proteins.

2.11. Analysis of Arginase Activity. Arginase activity was evaluated according to the method described by Corraliza et al. [24]. BV-2 cells (1×10^6 cells/mL) were pretreated with DEAC or CM (100 μg/mL) or 0.1% DMSO (drug vehicle), for 1 h before the addition of LPS (0.5 μg/mL), or vehicle. After 24 h, cells were lysed with buffer containing 0.1% Triton X-100. The enzyme was activated by heating the plates for 10 minutes at 55°C, using enzyme activation buffer (10 mM $MnCl_2$, 25 mM Tris-HCl). The hydrolysis of L-arginine (25 μL, 0.5 M, pH 9.7) was induced through the incubation of lysate (50 μL) with 25 μL of L-arginine (Sigma-Aldrich, USA) 0.5 M (pH 9.7) during 60 min at 37°C. The reaction was stopped with 400 μL of buffer containing $H_2SO_4/H_3PO_4/H_2O$ (1/3/7, *v*/*v*/*v*). After the addition of α-isonitrosopropiophenone (25 μL, 9%) and heating for 30 minutes at 95°C, the concentration of urea (final product of the reaction) was determined by spectrophotometric analysis (540 nm). The concentrations of urea were interpolated from the linear equation obtained from the standard curve generated by known concentrations of urea (1.5 to 300 μg/mL).

2.12. Statistical Analysis. Statistical analyses were performed using the GraphPad Prism 6.01 software (GraphPad Software, Inc.), and all results were expressed in ± SEM (standard error of mean). Differences were evaluated by one-way ANOVA or two-way ANOVA with Bonferroni's post hoc test or one-sample *t*-test. Statistical significance was considered when $p < 0.05$.

3. Results

3.1. Standardized DEAC and Its Active Compounds Are Not Toxic to BV-2 Microglial Cells. The dried extract of *A. cearensis* (DEAC) was characterized by HPLC-PDA as shown in Figure 1(a). The HPLC analysis allowed to detect and quantify three compounds (mg/g of dried extract): vanillic acid (2.70 ± 0.01 mg/g), amburoside A (30.40 ± 0.01 mg/g), and coumarin (70.07 ± 0.01 mg/g). To first evaluate the effect of DEAC and its chemical constituents on cell viability by MTT test, we pretreated BV-2 microglial cells with increasing concentrations of test drugs. As shown in Figure 1(b), the treatment of cells with DEAC, CM, AMB, or VA (5, 10, 25, 50, and 100 μg/mL) did not significantly affect the viability of cells when compared to the control group (100% of viability) (see Figure 1).

3.2. DEAC, CM, and AMB Reduce NO Production in LPS-Stimulated Microglial Cells. Microglia plays a central role in neuroinflammation being responsible for the synthesis and release of a wide array of chemical mediators including cytokines such as TNF-α, IL-1β, IL-6, ROS, and NO. First, we investigated the effect of DEAC and its active principles (AMB, CM, and VA) on nitrite production of LPS-stimulated microglial cells. The addition of DEAC or its chemical constituents in increasing concentrations did not alter the basal levels of NO in BV-2 cells (data not shown). LPS increased NO release by approximately 13x (Figure 2) in microglial cells when compared to the untreated group (control group). This effect was significantly reduced by the pretreatment of cells with noncytotoxic concentrations of DEAC, AMB, or CM, reaching maximal reduction at 100 μg/mL (nitrite: 6.1 ± 1.0 μM, 4.4 ± 1.4 μM, and 7.0 ± 1.5 μM, respectively). The LPS-only groups released nitrite at the following concentrations: 13.0 ± 1.4 μM, 16.7 ± 0.2 μM, and 23.6 ± 2.8 μM, respectively. AMB in particular showed a significant reduction in the NO production from 25 μg/mL. The pretreatment of the BV-2 cells with VA did not significantly interfere in the NO production induced by LPS.

3.3. DEAC, CM, and AMB Regulate Cytokine Production in LPS-Stimulated Microglial Cells. Considering the results obtained in the Griess assay, we chose the lowest anti-inflammatory concentration for each drug (DEAC, AMB, and CM) to evaluate their effects on the production of proinflammatory and anti-inflammatory cytokines (Figures 3(a)–3(i)). The addition of LPS for 24 h induced a significant increase in the TNF-α, IL-6, and IL-1β levels while IL-10 levels (anti-inflammatory cytokine) were reduced when compared to the untreated group. Pretreatment of cells with DEAC, AMB, or CM for 1 h before the addition of LPS significantly reduced the concentration of proinflammatory cytokines. On the other hand, the reduction of IL-10 induced by LPS on BV-2 cells was not significantly affected by the tested drugs, although DEAC and AMB increased its concentration by approximately 20.6% and 62.7%, respectively, compared to the LPS group.

3.4. DEAC, CM, AMB, and VA Have Free Radical Scavenging Activity: Hydroxyl Radical and Superoxide Anion. An excessive amount of ROS produced by activated microglial cells can lead to cell damage and apoptosis. We investigated the possible oxygen free radical scavenging activity of DEAC and its active principles. DEAC, CM, VA, and AMB showed effective anion superoxide and hydroxyl radical scavenging activity (Figure 4). Superoxide anion scavenging activity of AMB (100 μg/mL) was found to be 77.0 ± 12.3%, an effect comparable to gallic acid used as a reference compound (81.4 ± 7.1%). DEAC, CM, and VA exhibited scavenging activity of 55.2 ± 10.8%, 33.3 ± 3.3%, and 43.0 ± 4.0%, respectively. The scavenging effect of DEAC and its active principles on the hydroxyl radical decreased in the order of DEAC > VA > AMB > CM.

3.5. Effect of DEAC, AMB, and CM in LPS-Induced iNOS Expression in BV-2 Cells by Western Blot. Following the study, we investigated whether the suppression of NO production by DEAC, AMB, or CM was related to the expression of its synthase, iNOS. LPS induced a significant increase in the density of iNOS, but this effect was significantly reduced by the pretreatment with DEAC (100 μg/mL) or AMB (25 μg/mL) (Figure 5). On the other hand, the treatment of BV-2 cells with CM did not affect iNOS

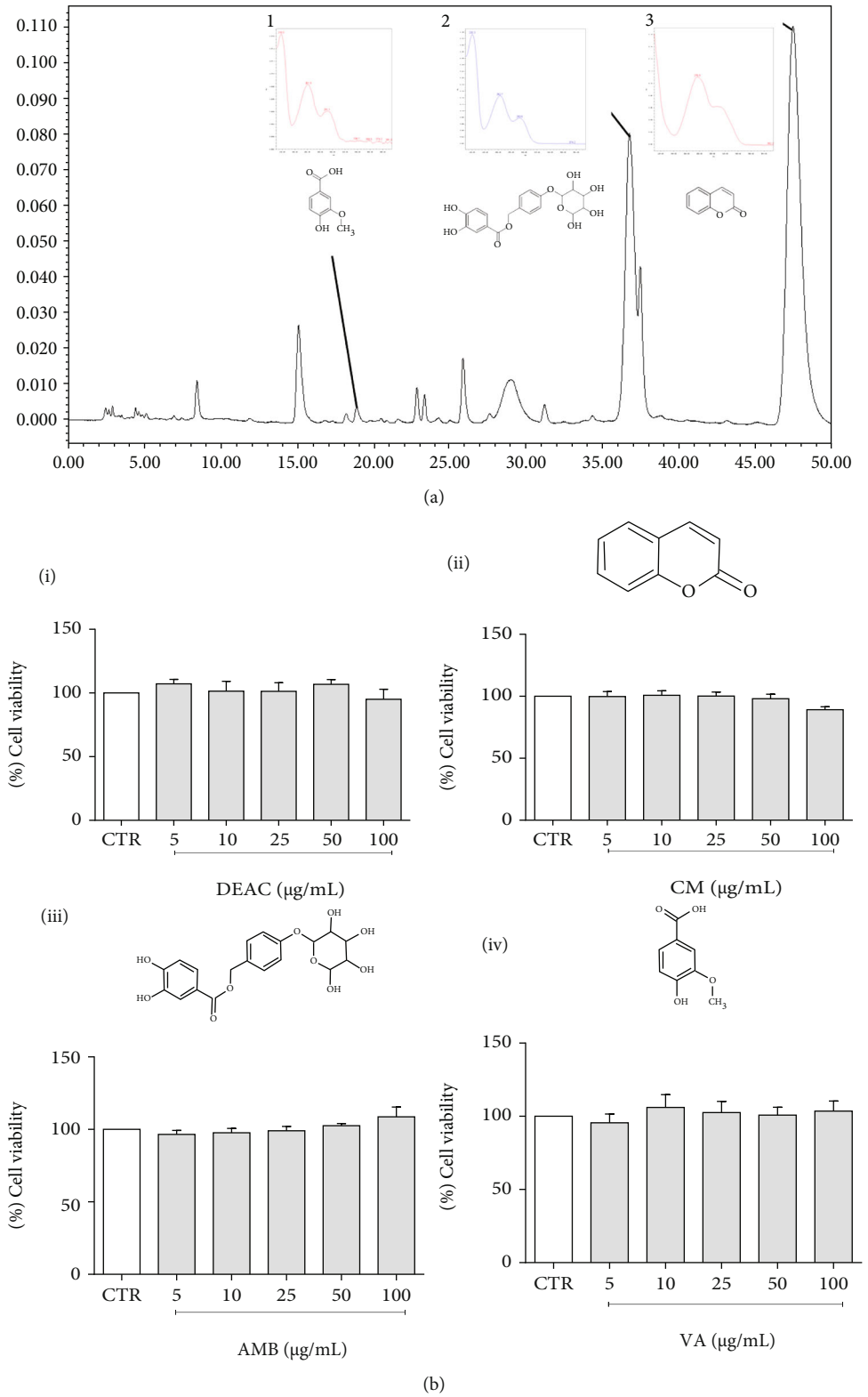

Figure 1: Chromatographic profile of dry extract from *A. cearensis* (DEAC) and identification of three compounds (a). Effect of DEAC (i), CM (ii), AMB (iii), and VA (iv) (5-100 μg/mL) in BV-2 cell viability measured through the MTT assay. Data are shown as percentage of controls (CTR; 0.1% DMSO). Results are expressed as the mean ± SEM. ANOVA test followed by the Bonferroni posttest, $n = 4$/group.

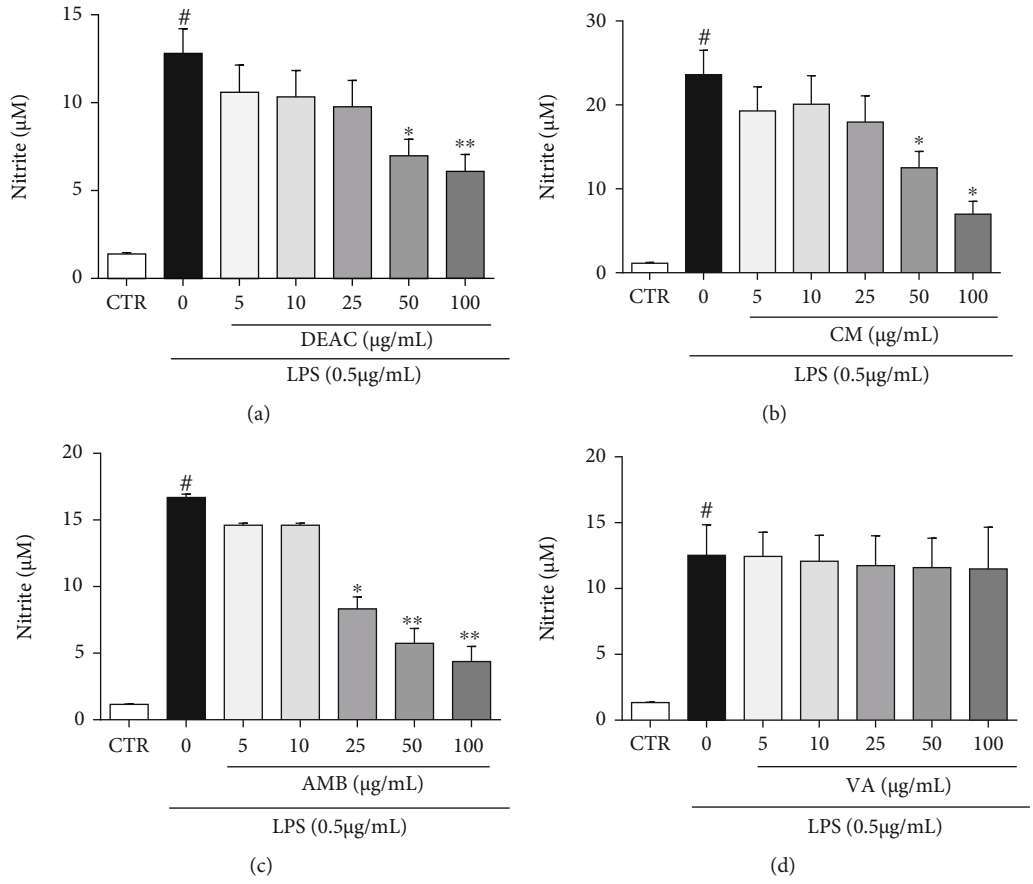

Figure 2: Effect of DEAC (a), CM (b), AMB (c), and VA (d) (5-100 μg/mL) in LPS-induced nitrite production. BV-2 cells were pretreated with the drugs for 1 h and incubated with or without LPS (0.5 μg/mL) for 24 h. All values are expressed as mean ± SEM of concentration of nitrite. One-way ANOVA was used followed by the Bonferroni posttest. $^{\#}$vs. control group (DMSO 0.1%) ($p < 0.05$), $^{*}p < 0.05$; $^{**}p < 0.01$ vs. LPS group, $n = 4$/group.

expression. In the absence of LPS, DEAC and its active principles did not change the expression of iNOS.

3.6. DEAC and CM Did Not Prevent the Reduction of Arginase Activity Induced by LPS in BV-2 Cells. The addition of LPS (0.5 μg/mL) to BV-2 cells significantly reduced arginase activity, measured by the concentration of urea (50.5 ± 7.7 μg/mL) when compared to the nontreated group (87.2 ± 11.6 μg/mL). In the absence of LPS, only CM (100 μg/mL: 10.3 ± 0.6 μg/mL), but not DEAC (100 μg/mL: 93.0 ± 12.0 μg/mL), significantly reduced the concentration of urea. None of DEAC or CM was able to prevent the reduction of arginase activity when compared to the LPS group (LPS 0.5 μg/mL), although the DEAC (100 μg/mL: 58.2 ± 3.0 μg/mL) showed a tendency to increase arginase activity by approximately 15.4%.

3.7. Effects of DEAC in LPS-Induced TLR-4/NF-κB/ERK1/2 and JNK Pathways. LPS induces an inflammatory response by interacting with the TLR-4 receptor. We first investigated the effect of DEAC on the expression of this receptor in BV-2 cells, followed by the analysis of the phosphorylation of its downstream signaling proteins (NF-κB and MAPKs). Western blotting results showed that the LPS exposure significantly increased the expression of TLR-4 in BV-2 cells when compared to the control group (not the treated group). However, DEAC pretreatment did not significantly prevent this increase (Figure 6(a)). As shown in Figures 6(b) and 6(c), LPS stimulation resulted in the phosphorylation of ERK1/2 and JNK, and DEAC pretreatment significantly decreased the phosphorylation of both MAPKs. Phosphorylation of NF-κB was not changed by DEAC (Figure 6(d)).

4. Discussion

Evidence suggests that exacerbated neuroinflammation response in the central nervous system is decisively related to degenerative processes in several neurological diseases, including multiple sclerosis, Alzheimer's disease, and Parkinson's disease. Moreover, the literature has shown that microglial activation has a key role in the progression of those diseases [25–27]. Therefore, regulating neuroinflammation is a therapeutic goal. The present work sought to investigate the effects of standardized dried extract of *A. cearensis* (DEAC) and its chemical constituents (CM, AMB, and VA) in LPS-induced inflammation in microglial

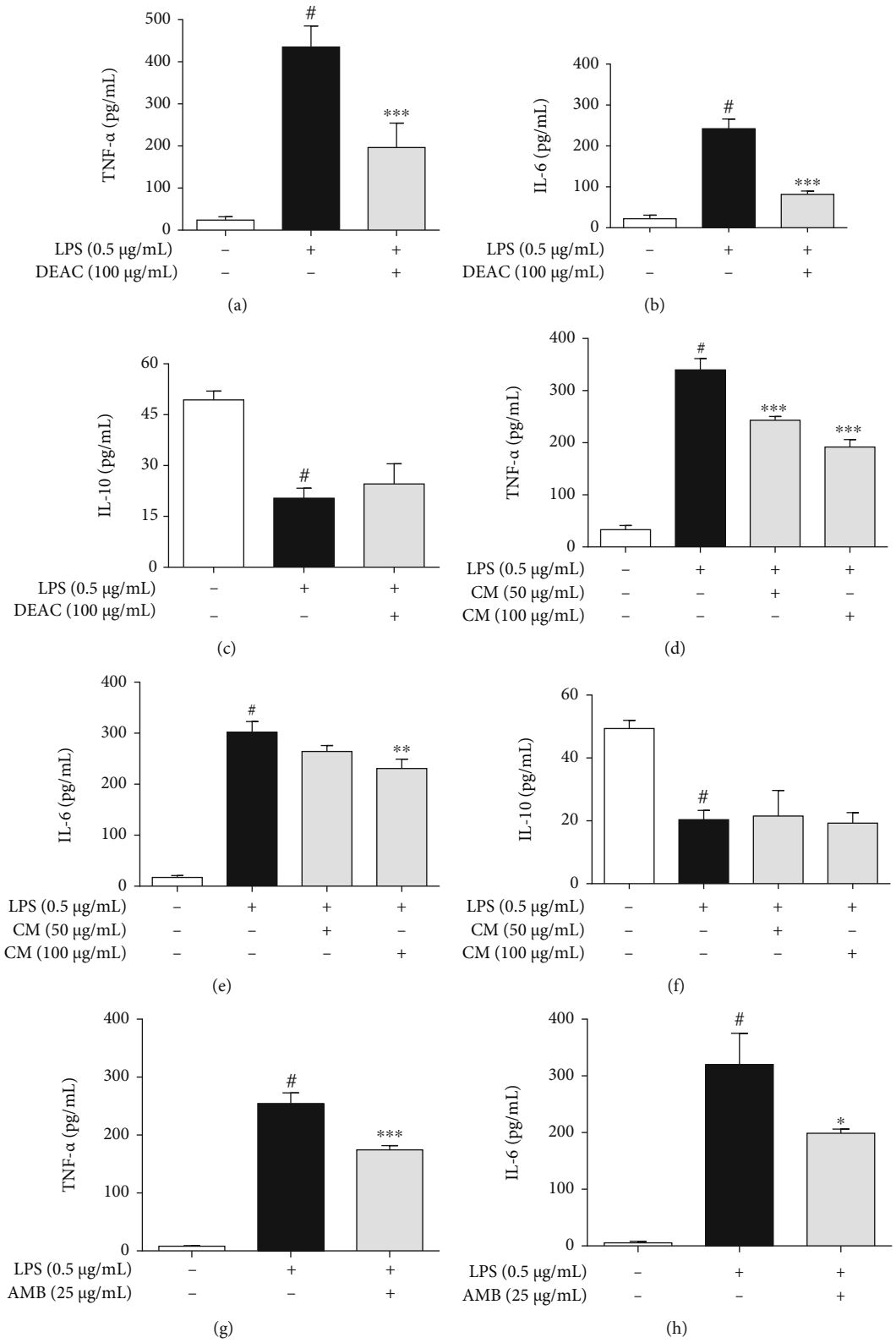

Figure 3: Continued.

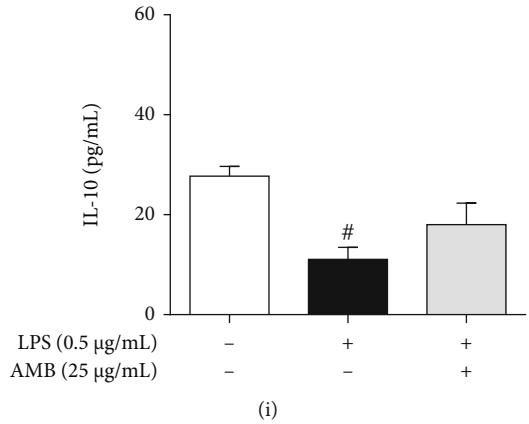

Figure 3: Effects of DEAC, CM, and AMB on inflammatory cytokine release in LPS-stimulated BV-2 cells. Cells were pretreated with DEAC (100 μg/mL), CM (50 and 100 μg/mL), and AMB (25 μg/mL) for 1 h and activated with LPS (0.5 μg/mL) for additional 24 h. The results are expressed as mean ± SEM. For statistical analysis, one-way ANOVA was used followed by the Bonferroni posttest. $^{\#}p < 0.05$ vs. negative control (0.1% DMSO, drug vehicle); $^{*}p < 0.05$, $^{**}p < 0.01$, $^{***}p < 0.001$ vs. LPS group, $n = 4$/group.

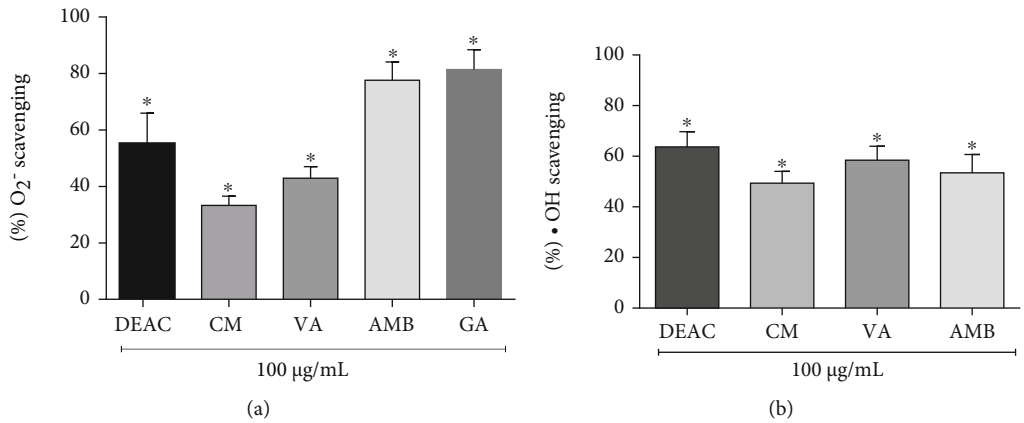

Figure 4: Antioxidant activity assay of DEAC, CM, VA, and AMB (100 μg/mL). Scavenging effect on (a) superoxide anion and (b) hydroxyl radical. For statistical analysis, a one-sample t-test was used, * vs. 100%.

cells. When activated, these cells release several inflammatory and potentially neurotoxic mediators, including proteases, excitatory amino acids, cytokines, ROS, and reactive nitrogen species (RNS). Lipopolysaccharide, a bacterial endotoxin, is extensively used as an inflammatory stimulus for microglial activation [28]. This experimental model has been a useful tool to understand the role of neuroinflammation in the progression of neurological diseases. The production of inflammatory mediators after stimulation with LPS is the result of a sequence of reactions that begins at the binding of LPS to cell membrane receptors which activate a cascade of intracellular signaling pathways, resulting in the release of several mediators, including nitric oxide (NO). DEAC and its compounds, except VA, decreased nitrite production, elevated by the exposure to LPS, without significantly affecting cell viability, as assessed by the MTT test. Additionally, the plant extract and all chemical constituents evaluated (CM, AMB, and VA) showed antioxidant activity, acting as scavengers of hydroxyl and superoxide anion radicals. These results are consistent with previous studies developed by our laboratory which showed the anti-inflammatory and antioxidant effect of AMB and isokaempferide (flavonol) from *A. cearensis* in mesencephalic cells of rats exposed to the neurotoxin 6-hydroxydopamine (6-OHDA), human neutrophils, and/or CCl4-induced hepatotoxicity in rats [11, 18, 29].

Nitric oxide is associated with both beneficial and deleterious effects in humans. In the central nervous system (CNS), the iNOS upregulation and the accumulation of NO exacerbate the neuroinflammatory microenvironment, which contributes to neuronal cell death. The toxicity of NO is enhanced when it is combined with superoxide anion, generating peroxynitrite anion [30]. Decomposition of peroxynitrite results in the formation of some highly reactive species such as hydroxyl radicals [31]. Previous studies [32, 33] showed that higher hydroxyl radical levels and lower superoxide dismutase activity, an oxidoreductase responsible to dismutate the superoxide anion, seem to contribute to the onset and progression of neurodegenerative diseases, such as Parkinson's disease and Alzheimer's disease. Therefore, the

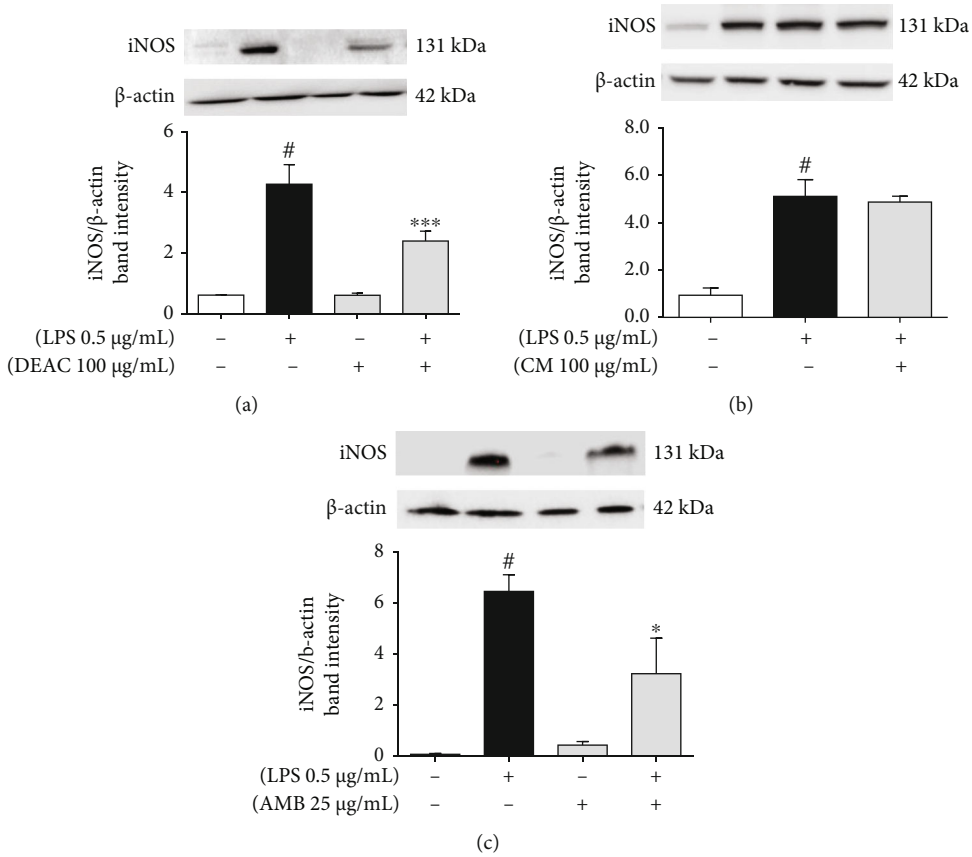

Figure 5: Effects of DEAC (a), CM (b), and AMB (c) on iNOS expression in LPS-stimulated BV-2 cells. Cells were pretreated with DEAC (100 μg/mL), CM (50 and 100 μg/mL), or AMB (25 μg/mL) for 1 h and incubated with LPS (0.5 μg/mL) for additional 24 h. Two-way ANOVA in graphs (a) and (c), and one-way ANOVA for graph (b), followed by Bonferroni posttest. $^{\#}p < 0.05$ vs. negative control (0.1% DMSO, drug vehicle), $^{**}p < 0.01$; $^{***}p < 0.001$ vs. LPS group, $n = 4$/group.

reduction of nitrite concentration and the scavenging activity of hydroxyl and superoxide anion radicals exerted by DEAC and its active compounds suggest that DEAC's anti-inflammatory effects reduce the accumulation of reactive oxygen and nitrogen species (ROS/RNS) which play a major role in neuroinflammation-induced neuronal death [34]. Corroborating these data, Yeo et al. [35], describing the anti-inflammatory activity of a *Piper sarmentosum* extract in microglial cells, showed that the inhibition of NO production by the plant extract was associated with its free radical scavenging property.

Apart from NO, proinflammatory cytokines such as IL-1β, IL-6, and TNF-α are triggers of the inflammatory response and contribute to maintaining the high microglial activity that sustains the development of chronic inflammatory diseases [25]. These pathologies can be controlled by reducing the proinflammatory response and/or improving natural anti-inflammatory mechanisms. Thus, our study also investigated the effect of DEAC, CM, or AMB on the level of inflammatory and anti-inflammatory cytokines in LPS-stimulated BV-2 cells. Importantly, DEAC, CM, and AMB inhibited LPS-induced release of proinflammatory cytokines (TNF-α and IL-6), but we did not observe significant effects on the IL-10 (anti-inflammatory cytokine) reduction caused by LPS. Collectively, these data suggest that DEAC and its active principles CM and AMB may protect against neuronal death considering that IL-1β and TNF-α act synergistically as neurotoxic agents mediated at least in part by NO [36]. This hypothesis is corroborated by previous studies [15] where we described the anti-inflammatory and antioxidant activities of AMB from *A. cearensis* in mesencephalic cells of rats exposed to neurotoxin 6-OHDA.

NO synthesis can be limited by arginine availability and/or on the level of iNOS protein expression. During the NO synthesis, arginase-1 (expressed in microglial cells) competes with iNOS for L-arginine [37, 38]. Therefore, we investigated the effect of DEAC and its compounds on iNOS expression and arginase catalytic activity in LPS-stimulated BV-2 cells. We observed that LPS induced an increase in iNOS expression in BV-2 microglial cells, and pretreatment with DEAC or AMB decreased the expression of this enzyme. Meanwhile, the addition of CM in BV-2 cells did not affect the iNOS expression, and none of the test drugs improved the arginase activity when compared to the LPS-only group. Taken together, these results demonstrate that the inhibition of NO production by the extract of *A. cearensis* and AMB in microglial cells is related, at least in part, to their ability to reduce iNOS expression in microglial cells. Additional

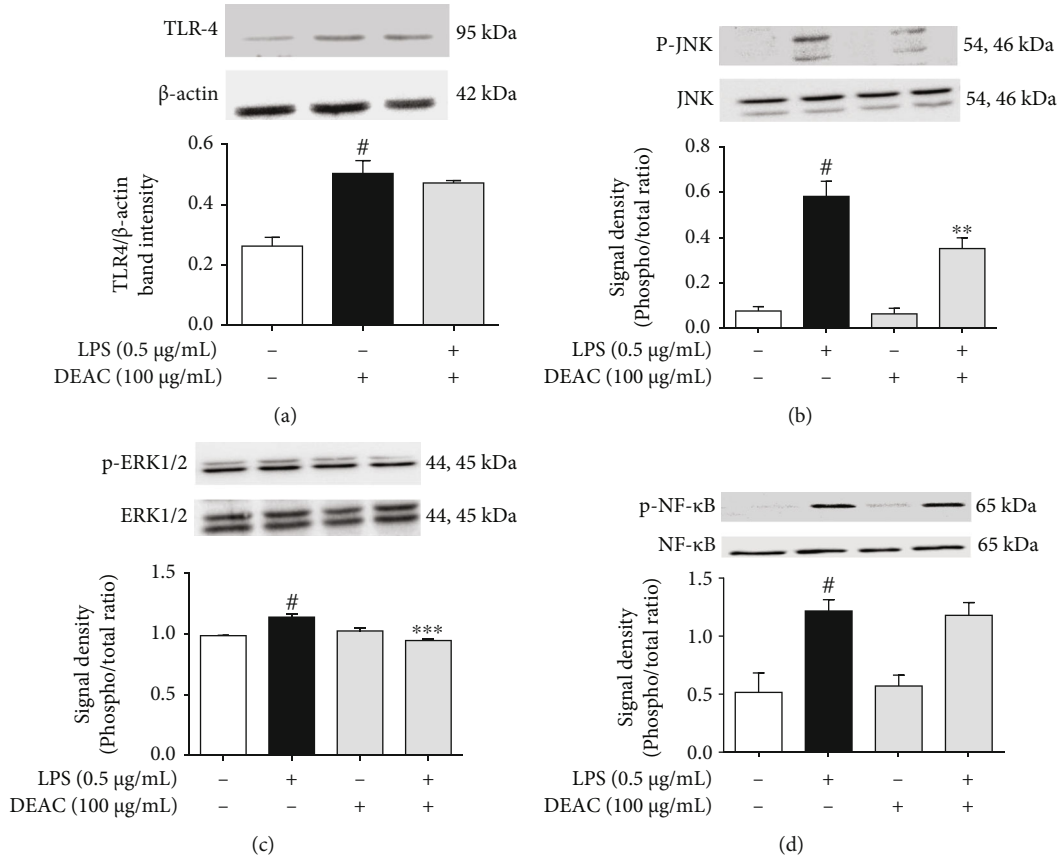

Figure 6: Effects of DEAC on TLR-4, p-NF-κB, p-JNK, and p-ERK1/2 expression in LPS-stimulated BV-2 cells. Cells were pretreated with DEAC (100 μg/mL) for 1 h and incubated with LPS (0.5 μg/mL) for 1 more hour. The results are expressed as mean ± SEM. For statistical analysis, one-way ANOVA (a), two-way ANOVA (b–d), followed by Bonferroni posttest. $^{\#}p < 0.05$ vs. negative control (0.1% DMSO, drug vehicle), $^{**}p < 0.01$; $^{***}p < 0.001$ vs. LPS group, $n = 4$/group.

studies are necessary to describe how CM reduced the nitrite production in LPS-stimulated BV-2 cells without affecting iNOS expression. We hypothesize that it may act as an iNOS inhibitor.

The anti-inflammatory and antioxidant activities of DEAC described in the present study in microglial cells are corroborated by a previous study by Pereira et al. [13] which described the neuroprotective effect of an *A. cearensis* seed extract against neural damage induced by glutamate in cerebellar cells, which was associated to glial and neuronal preservation, and antioxidant activity. As DEAC's main bioactive markers CM and AMB showed a promising anti-inflammatory effect, we then further described the mechanisms underlying DEAC-mediated attenuation of inflammation in BV-2 cells. There are several published works describing *A. cearensis* or its active principles' anti-inflammatory or antioxidant activities [10, 11, 15, 17, 29, 39–41]. However, these studies are mainly confined to just showing their effects without further investigating the molecular mechanism underlying them. Therefore, the present study investigated the role of TLR-4, NF-κB, and MAPK signaling pathways in the anti-inflammatory effect of DEAC in LPS-stimulated BV-2 cells. The binding of TLR-4 on the cell membrane by LPS in BV-2 cells activates various signaling cascades, including NF-κB pathway via the MyD88–IRAK–TRAF6–TAK1 signaling complex leading to the activation of IκB kinase complex (IKK). Activation of IKK includes the phosphorylation of NF-κB which leads to its translocation to the nucleus. As a transcription factor, NF-κB stimulates the synthesis of proinflammatory mediators including NO, IL-6, and TNF-α and the secretion of ROS. In addition to NF-κB, LPS is a potent activator of the MAPK signaling pathways, which in turn modulate the activation of several transcription factors, including activator protein-1 (AP-1), STAT-1, and NF-κB. AP-1 upregulates cytokine expression playing a key role in neuroinflammation [42–45]. In the present study, we found that DEAC treatment significantly inhibited LPS-stimulated phosphorylation of two MAP kinase pathways (JNK and ERK1/2) in microglial cells. However, DEAC did not interfere in the increased expression of TLR-4 or phosphorylation of NF-κB induced by LPS (Figure 7).

Evidence demonstrates that excessive production of inflammatory mediators acts as inductors of MAPKs which in turn amplify and prolongs the inflammation process [45]. This vicious cycle leads to neuronal damage and death

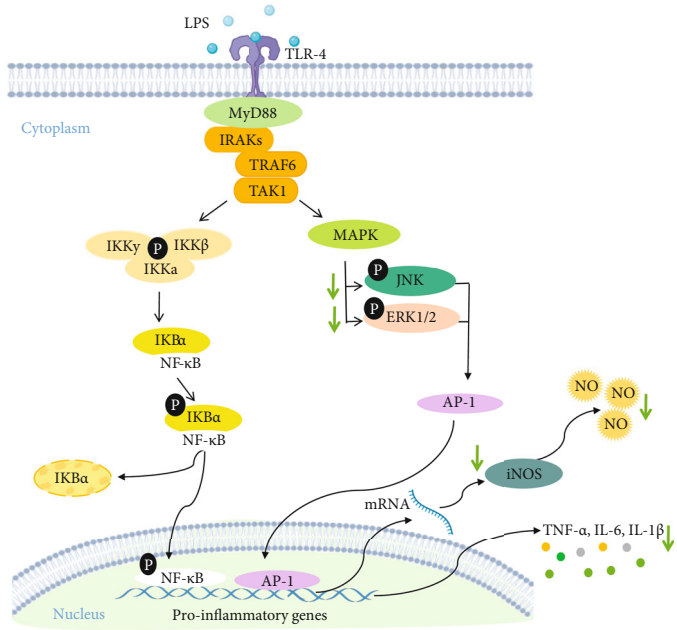

Figure 7: Proposed signaling mechanism for the effects of DEAC and chemical constituents (CM and AMB) in LPS-induced neuroinflammation in BV-2 cells. Activation of toll-like receptor 4 (TLR-4) with LPS leads to activation of the NF-κB and MAPK pathways. The IKK complex phosphorylates IkBα, which leads to the degradation of IkBα and subsequent nuclear translocation of NF-κB. At the same time, the MAPK pathway (JNK and ERK1/2) regulates the transcription of inflammatory mediators through the activation of the transcription factor AP-1. Activation of NF-κB and AP-1 results in the expression of iNOS and the production of proinflammatory mediators. DEAC disrupts LPS-induced neuroinflammatory pathways, decreasing JNK and ERK1/2 signaling. DEAC and chemical constituents decrease the expression of iNOS, as well as the production of inflammatory mediators (NO and cytokines). IKK: IκB kinase complex; IκBα: kappa B inhibitor; P: phosphate; NF-κB: nuclear kappa factor B; MAPK: mitogen-activated protein kinase; ERK: extracellular signal regulatory kinase; AP-1: activator protein 1.

which is a hallmark of neurodegenerative diseases, such as Alzheimer's disease (AD) and Parkinson's disease (PD) [45]. Both JNK and ERK promote the phosphorylation of amyloid precursor protein that, when cleaved by β- and γ-secretases, yields the neurotoxic β-amyloid peptide which plays a key role in AD. In addition, studies demonstrated that TNF-α, a classical factor secreted from activated microglia, can induce a significant increase in the α-SNC secretion (a marker of PD) from both differentiated PC12 and SHSY5Y cells [35, 42]. Therefore, the inhibition of MAPK pathways by DEAC indicates that it may be a promising anti-inflammatory drug, useful for the treatment of neurodegenerative disorders.

The anti-inflammatory effect of DEAC is associated at least in part with the presence of AMB and CM in the plant extract, but the pharmacological importance of other chemical constituents from *A. cearensis* cannot be excluded. Moreover, the present work studied the effects of different drugs in an isolated microglial cell line; therefore, the anti-inflammatory activity observed may not fully represent an in vivo effect in reducing neuroinflammation. Because of this, future trials should be carried out using experimental animal models of neurodegenerative diseases to evaluate the effect of DEAC, AMB, and CM, investigating the anti-inflammatory, antioxidant, and consequent neuroprotective potential. The in vivo study will allow to know if these drugs have limitations associated to bioavailability and how they act in living system with complex interplay between the different cell types at different time points in the progression of neuroinflammatory diseases.

5. Conclusion

Taken together, our results demonstrate that DEAC and its active principles (AMB and CM) (100 μg/mL) have free radical scavenging activity and inhibit the production of NO (up to 100 μg/mL). At their concentrations that reduced at least 50% of NO production, they also reduced the release of the proinflammatory cytokines TNF-α and IL-6 as well as the expression of iNOS in LPS-stimulated BV-2 microglial cells (DEAC at 100 μg/mL, CM at 50 and 100 μg/mL, and AMB at 25 μg/mL). These effects were not related to cytotoxicity and seem to occur through inhibition JNK and ERK1/2 MAPK pathways (DEAC at 100 μg/mL). These data provide an experimental basis that the standardized dry extract of *A. cearensis* (cultivated species), CM, and AMB presents therapeutic potential for the treatment of inflammatory diseases where microglial activation plays a key role, such as neurodegenerative diseases.

Abbreviations

6-OHDA: 6-Hydroxydopamine
AD: Alzheimer's disease
AMB: Amburoside A
AP-1: Activator protein-1
BSA: Bovine serum albumin
CNS: Central nervous system
CM: Coumarin
DEAC: Dry extract from *Amburana cearensis*
DMSO: Dimethyl sulfoxide
EDTA: Ethylenediaminetetraacetic acid tetrasodium salt dihydrate
ERK: Extracellular signal-regulated kinase
FBS: Fetal bovine serum
$FeCl_3$: Ferric chloride
H_2O_2: Hydrogen peroxide
H_3PO_4: Phosphoric acid
HPLC-PDA: High-performance liquid chromatography–photodiode array
HPX: Hypoxanthine
IFN-γ: Interferon-gamma
IKK: IkB kinase complex
IL: Interleukin
iNOS: Inducible nitric oxide synthase
JNK: C-Jun N-terminal kinase
L-Ascorbic acid: Vitamin C
LPS: Lipopolysaccharide
MAPKs: Mitogen-activated protein kinases
MTT: 3-(4,5-Dimethylthiazol-2-yl)-2,5-diphenyltetrazolium bromide
NBT: Nitrotetrazolium blue chloride
NEED: N-(1-Naphthyl)ethylenediamine dihydrochloride
NF-κB: Nuclear factor kappa B
NO: Nitric oxide
PBS: Phosphate-buffered saline
PD: Parkinson's disease
RIPA: Radioimmunoprecipitation assay buffer
RNS: Reactive nitrogen species
ROS: Reactive oxygen species
SDS: Sodium dodecyl sulfate
TBA: 2-Thiobarbituric acid
TCA: Trichloroacetic acid
TLR-4: Toll-like receptor 4
TNF-α: Tumor necrosis factor alpha
VA: Vanillic acid
XOD: Xanthine oxidase.

Data Availability

The data used to support the findings of this study are included within the article.

Conflicts of Interest

The authors declare that they have no conflict of interest.

Acknowledgments

L.K.A.M. Leal acknowledges the Brazilian National Research Council (CNPq) for their research fellowships (316948/2021-7). This work was supported by the Coordination for the Improvement of Higher Education Personnel (CAPES), the Research Foundation of the State of Ceara (FUNCAP), and CNPq.

References

[1] F. Leng and P. Edison, "Neuroinflammation and microglial activation in Alzheimer disease: where do we go from here?," *Nature Reviews Neurology*, vol. 17, no. 3, pp. 157–172, 2021.

[2] R. M. Ransohoff, "How neuroinflammation contributes to neurodegeneration," *Science*, vol. 353, no. 6301, pp. 777–783, 2016.

[3] Z. Yu, L. Tang, L. Chen, J. Li, W. Wu, and C. Hu, "Capillarisin suppresses lipopolysaccharide-induced inflammatory mediators in BV2 microglial cells by suppressing TLR4-mediated NF-κB and MAPKs signaling pathway," *Neurochemical Research*, vol. 40, no. 6, pp. 1095–1101, 2015.

[4] S.-C. Ho, K.-S. Chang, and P.-W. Chang, "Inhibition of neuroinflammation by cinnamon and its main components," *Food Chemistry*, vol. 138, no. 4, pp. 2275–2282, 2013.

[5] L. Heinbockel, G. Weindl, G. Martinez-de-Tejada et al., "Inhibition of lipopolysaccharide- and lipoprotein-induced inflammation by antitoxin peptide Pep19-2.5," *Frontiers in Immunology*, vol. 9, pp. 1–6, 2018.

[6] W. Abate, A. A. Alghaithy, J. Parton, K. P. Jones, and S. K. Jackson, "Surfactant lipids regulate LPS-induced interleukin-8 production in A549 lung epithelial cells by inhibiting translocation of TLR4 into lipid raft domains," *Journal of Lipid Research*, vol. 51, no. 2, pp. 334–344, 2010.

[7] X. Zhu, J. S. Owen, M. D. Wilson et al., "Macrophage ABCA1 reduces MyD88-dependent Toll-like receptor trafficking to lipid rafts by reduction of lipid raft cholesterol[S]," *Journal of Lipid Research*, vol. 51, no. 11, pp. 3196–3206, 2010.

[8] H. G. Kim, G. Park, Y. Piao et al., "Effects of the root bark of Paeonia suffruticosa on mitochondria-mediated neuroprotection in an MPTP-induced model of Parkinson's disease," *Food and Chemical Toxicology*, vol. 65, pp. 293–300, 2014.

[9] N. S. Mohd Sairazi and K. N. S. Sirajudeen, "Natural products and their bioactive compounds: neuroprotective potentials against neurodegenerative diseases," *Evidence-based Complementary and Alternative Medicine*, vol. 2020, 7 pages, 2020.

[10] H. H. D. S. Amaral, "Extrato seco padronizado de Amburana cearensis cultivada e constituintes químicos modulam a inflamação em um novo modelo de asma exacerbada em camundongos BALB/C e a resposta neutrofílica in vitro," *Universidade Federal do Ceará*, 2017.

[11] L. K. A. M. Leal, K. M. Canuto, K. C. da Silva Costa et al., "Effects of amburoside a and isokaempferide, polyphenols from amburana cearensis, on rodent inflammatory processes and myeloperoxidase activity in human neutrophils," *Basic and Clinical Pharmacology and Toxicology*, vol. 104, no. 3, pp. 198–205, 2009.

[12] J. H. C. E. Silva, R. S. Ferreira, E. P. Pereira et al., "Amburana cearensis: pharmacological and neuroprotective effects of its compounds," *Molecules*, vol. 25, no. 15, pp. 3316–3394, 2020.

[13] É. P. Lima Pereira, C. Santos Souza, J. Amparo et al., "Amburana cearensis seed extract protects brain mitochondria from oxidative stress and cerebellar cells from excitotoxicity induced by glutamate," *Journal of Ethnopharmacology*, vol. 209, pp. 157–166, 2017.

[14] E. C. Pereira, D. L. Lucetti, J. M. Barbosa-Filho et al., "Coumarin effects on amino acid levels in mice prefrontal cortex and hippocampus," *Neuroscience Letters*, vol. 454, no. 2, pp. 139–142, 2009.

[15] L. K. A. M. Leal, H. V. N. Júnior, G. M. A. Cunha et al., "Amburoside A, a glucoside from Amburana cearensis, protects mesencephalic cells against 6-hydroxydopamine-induced neurotoxicity," *Neuroscience Letters*, vol. 388, no. 2, pp. 86–90, 2005.

[16] L. K. A. M. Leal, T. M. Pierdoná, J. G. S. Góes et al., "A comparative chemical and pharmacological study of standardized extracts and vanillic acid from wild and cultivated Amburana cearensis A.C. Smith," *Phytomedicine*, vol. 18, no. 2-3, pp. 230–233, 2011.

[17] N. R. Lima, "Desenvolvimento farmacêutico e avaliação farmacológica do extrato padronizado (CLAE-DAD) e constituintes químicos de Amburana cearensis (cumaru) cultivado," *Universidade Federal do Ceará*, 2013.

[18] K. M. Canuto, E. R. Silveira, and A. M. E. Bezerra, "Estudo fitoquímico de espécimens cultivados de cumaru (Amburana cearensis A. C. Smith)," *Quimica Nova*, vol. 33, no. 3, pp. 662–666, 2010.

[19] T. Mosmann, "Rapid colorimetric assay for cellular growth and survival: application to proliferation and cytotoxicity assays," *Journal of Immunological Methods*, vol. 65, no. 1-2, pp. 55–63, 1983.

[20] L. C. Green, D. A. Wagner, J. Glogowski, P. L. Skipper, J. S. Wishnok, and S. R. Tannenbaum, "Analysis of nitrate, nitrite, and [^{15}N]nitrate in biological fluids," *Analytical Biochemistry*, vol. 126, no. 1, pp. 131–138, 1982.

[21] H. Zhao, J. Dong, J. Lu et al., "Effects of extraction solvent mixtures on antioxidant activity evaluation and their extraction capacity and selectivity for free phenolic compounds in barley (Hordeum vulgare L.)," *Journal of Agricultural and Food Chemistry*, vol. 54, no. 19, pp. 7277–7286, 2006.

[22] E. K. Hodgson and I. Fridovich, "The accumulation of superoxide radical during the aerobic action of xanthine oxidase A requiem for H_2O_4," *Biochimica et Biophysica Acta*, vol. 430, no. 1, pp. 182–188, 1976.

[23] Z. Zhao, L. Tao, A. Liu et al., "NF-κB is a key modulator in the signaling pathway of Borrelia burgdorferi BmpA-induced inflammatory chemokines in murine microglia BV2 cells," *Molecular Medicine Reports*, vol. 17, no. 4, pp. 4953–4958, 2018.

[24] I. M. Corraliza, M. L. Campo, G. Soler, and M. Modolell, "Determination of arginase activity in macrophages: a micromethod," *Journal of Immunological Methods*, vol. 174, no. 1–2, pp. 231–235, 1994.

[25] S. Bachiller, I. Jiménez-Ferrer, A. Paulus et al., "Microglia in neurological diseases: a road map to brain-disease dependent-inflammatory response," *Frontiers in Cellular Neuroscience*, vol. 12, pp. 1–17, 2018.

[26] H. S. Kwon and S.-H. Koh, "Neuroinflammation in neurodegenerative disorders: the roles of microglia and astrocytes," *Translational Neurodegeneration*, vol. 9, no. 1, p. 42, 2020.

[27] L. Muzio, A. Viotti, and G. Martino, "Microglia in neuroinflammation and neurodegeneration: from understanding to therapy," *Frontiers in Neuroscience*, vol. 15, 2021.

[28] S. Lively and L. C. Schlichter, "Microglia responses to pro-inflammatory stimuli (LPS, IFNγ+TNFα) and reprogramming by resolving cytokines (IL-4, IL-10)," *Frontiers in Cellular Neuroscience*, vol. 12, p. 215, 2018.

[29] L. K. A. M. Leal, F. Fonseca, F. Pereira et al., "Protective effects of amburoside A, a phenol glucoside from Amburana cearensis, against CCl 4-induced hepatotoxicity in rats," *Planta Medica*, vol. 74, no. 5, pp. 497–502, 2008.

[30] H. L. Hsieh and C. M. Yang, "Role of redox signaling in neuroinflammation and neurodegenerative diseases," *Bio Med Research International*, vol. 2013, 2013.

[31] S. Tharmalingam, A. Alhasawi, V. P. Appanna, J. Lemire, and V. D. Appanna, "Reactive nitrogen species (RNS)-resistant microbes: adaptation and medical implications," *Biological Chemistry*, vol. 398, no. 11, pp. 1193–1208, 2017.

[32] E. Kienzl, K. Jellinger, H. Stachelberger, and W. Linert, "Iron as catalyst for oxidative stress in the pathogenesis of Parkinson's disease?," *Life Sciences*, vol. 65, no. 18–19, pp. 1973–1976, 1999.

[33] F. Collin, "Chemical basis of reactive oxygen species reactivity and involvement in neurodegenerative diseases," *International Journal of Molecular Sciences*, vol. 20, no. 10, 2019.

[34] J. E. Yuste, E. Tarragon, C. M. Campuzano, and F. Ros-Bernal, "Implications of glial nitric oxide in neurodegenerative diseases," *Frontiers in Cellular Neuroscience*, vol. 9, pp. 1–13, 2015.

[35] E. T. Y. Yeo, K. W. L. Wong, M. L. See, K. Y. Wong, S. Y. Gan, and E. W. L. Chan, "Piper sarmentosum Roxb. confers neuroprotection on beta-amyloid (Aβ)-induced microglia-mediated neuroinflammation and attenuates tau hyperphosphorylation in SH-SY5Y cells," *Journal of Ethnopharmacology*, vol. 217, pp. 187–194, 2018.

[36] C. C. Chao, S. X. Hu, L. Ehrlich, and P. K. Peterson, "Interleukin-1 and tumor necrosis factor-α synergistically mediate neurotoxicity: involvement of nitric oxide and of n-methyl-d-aspartate receptors," *Brain Behavior and Immunity*, vol. 9, no. 4, pp. 355–365, 1995.

[37] M. Rath, I. Müller, P. Kropf, E. I. Closs, and M. Munder, "Metabolism via arginase or nitric oxide synthase: two competing arginine pathways in macrophages," *Frontiers in Immunology*, vol. 5, pp. 1–11, 2014.

[38] C. D. Mills, L. L. Lenz, and K. Ley, "Macrophages at the fork in the road to health or disease," *Frontiers in Immunology*, vol. 6, pp. 1–7, 2015.

[39] L. K. A. M. Leal, M. Nechio, E. R. Silveira et al., "Anti-inflammatory and smooth muscle relaxant activities of the hydroalcoholic extract and chemical constituents from Amburana cearensis A. C. Smith," *Phytotherapy research : PTR*, vol. 17, no. 4, pp. 335–340, 2003.

[40] Z. Balion, K. Ramanauskienė, A. Jekabsone, and D. Majienė, "The role of mitochondria in brain cell protection from ischaemia by differently prepared propolis extracts," *Antioxidants*, vol. 9, no. 12, pp. 1–20, 2020.

[41] P. de Araújo Rodrigues, S. M. de Morais, J. F. Pereira et al., "Neuroprotective effects of proanthocyanidins of grape seed extracts against oxidative stress and apoptosis induced by 6-hydroxydopamine in PC12 cells," *Conjecturas*, vol. 21, no. 2, pp. 68–86, 2021.

[42] T. Ahmed, A. Zulfiqar, S. Arguelles et al., "Map kinase signaling as therapeutic target for neurodegeneration," *Pharmacological Research*, vol. 160, 2020.

[43] C. J. Wei, Y. L. Li, Z. L. Zhu et al., "Inhibition of activator protein 1 attenuates neuroinflammation and brain injury after experimental intracerebral hemorrhage," *CNS Neuroscience and Therapeutics*, vol. 25, no. 10, pp. 1182–1188, 2019.

[44] M. Rahimifard, F. Maqbool, S. Moeini-Nodeh et al., "Targeting the TLR4 signaling pathway by polyphenols: a novel therapeutic strategy for neuroinflammation," *Ageing Research Reviews*, vol. 36, pp. 11–19, 2017.

[45] C. R. A. Batista, G. F. Gomes, E. Candelario-Jalil, B. L. Fiebich, and A. C. P. de Oliveira, "Lipopolysaccharide-induced neuroinflammation as a bridge to understand neurodegeneration," *International Journal of Molecular Sciences*, vol. 20, no. 9, p. 2293, 2019.

Hindawi
Oxidative Medicine and Cellular Longevity
Volume 2022, Article ID 4943965, 10 pages
https://doi.org/10.1155/2022/4943965

Research Article

Evaluation of Antiarthritic and Antinociceptive Effects of Cedrol in a Rat Model of Arthritis

Fatemeh Forouzanfar,[1,2] **Ali Mohammad Pourbagher-Shahri**,[3] **and Hamed Ghazavi**[1,2]

[1]*Neuroscience Research Center, Mashhad University of Medical Sciences, Mashhad, Iran*
[2]*Department of Neuroscience, Faculty of Medicine, Mashhad University of Medical Sciences, Mashhad, Iran*
[3]*Medical Toxicology Research Center, Faculty of Medicine, Mashhad University of Medical Sciences, Mashhad, Iran*

Correspondence should be addressed to Fatemeh Forouzanfar; forouzanfarff@gmail.com

Received 7 December 2021; Revised 11 February 2022; Accepted 9 April 2022; Published 25 April 2022

Academic Editor: Francisco Rios

Pharmacological studies revealed that cedrol, a natural sesquiterpene, has antioxidant, anti-inflammatory, and analgesic properties. This study is aimed at evaluating the potential antiarthritic activity of cedrol in a rat experimental model of arthritis induced by using complete Freund's adjuvant (CFA). Arthritis was induced in Wistar rats by CFA (0.1 ml) injection. Cedrol (10 and 20 mg/kg) and indomethacin (5 mg/kg) were orally administered from day one and continued for 21 days. The antiarthritic activity was assessed through mechanical allodynia and thermal hyperalgesia responses, paw edema assessment, and arthritis scores. Serum TNF-α and IL-1β levels were measured for the evaluation of inflammation. Furthermore, serum oxidative stress markers, including malondialdehyde (MDA) and thiol levels, as well as superoxide dismutase (SOD) and glutathione peroxidase (GPx) activities, were also assessed. Oral administration of cedrol and indomethacin significantly decreased paw edema and arthritis score. Besides, cedrol and indomethacin significantly decreased pain responses. In the serum of the CFA group, TNF-α, IL-1β, and MDA were higher, while thiol and SOD and GPx were lower than the control group. Treatment by cedrol and indomethacin corrected the biochemical parameters in the serum. In this study, cedrol offers potential antiarthritic properties through its anti-inflammatory and antioxidant effects.

1. Introduction

Rheumatoid arthritis (RA) is a chronic systemic inflammatory disease described by multijoint inflammation, pain, and destruction of cartilage and bone [1, 2]. The disease may progress to a severe disability with negative consequences on the quality of life and increased mortality rate [3]. Autoimmunity and chronic inflammation are activated by an imbalance between pro- and anti-inflammatory cytokines, resulting in joint damage in RA [4]. Although nonsteroidal anti-inflammatory drugs effectively reduce symptoms, they do not prevent the disease from progressing and do not protect the tissue or joint against erosion. Also, they have severe side effects or cardiovascular complications; growing interest in herbal remedies in RA patients indicates the need to find new agents from herbal medicines [5]. Indeed, safe and effective agents for the treatment of RA are urgently required. Natural plant compounds are suggested to prevent or treat RA [6]. Terpenes, also known as terpenoids, are the largest and most diverse group of natural products. They are classified according to the number of isoprene units to mono, di, tri, tetra, and sesquiterpenes [7]. Sesquiterpenes (C15) are composed of 3 units of isoprenoid, which are secondary metabolites produced mostly in plants [8]. Recent studies showed that sesquiterpenes have various therapeutic effects, such as being effective in pain management [9], protection against stroke [10], and RA [11]. Cedrol, a natural sesquiterpene, is known to carry many pharmacological effects, including antioxidant [12], anti-inflammatory [13], antibacterial [14], analgesic [12], sedative [15], hair growth inducer [16], platelet-activating factor (PAF) antagonist [17], and antitumor effects [18]. The present investigation

is aimed at evaluating the potential antiarthritic effect of cedrol on complete Freund's adjuvant- (CFA-) induced experimental arthritis in rats.

2. Chemicals

Ketamine and xylazine were bought from Alfasan Pharmaceutical Co. (Woerden, Netherlands). Pyrogallol, 2-thiobarbituric acid (TBA), CFA, dimethyl sulfoxide (DMSO), potassium chloride, hydrochloric acid (HCl), trichloroacetic acid (TCA), cedrol, and ethylenediaminetetraacetic acid (EDTA) were purchased from Sigma-Aldrich (Sigma-Aldrich, St. Louis, MO).

3. Animals

Adult male rats weighing between 180 and 220 g were provided by the animal facility of the medical school, Mashhad University of Medical Sciences (MUMS), Mashhad, Iran. Animals were kept at 22-25°C with food and water ad libitum with a natural dark and light (12: 12 h) cycle. All experiments were conducted according to the care and use of Laboratory Animals and Animal Ethics Guidelines of MUMS.

4. Induction of Arthritis and Treatment Protocol

Arthritis was induced on day 0 by a 0.1 ml subcutaneous injection of CFA into the right hind footpad of the rat. Rats were randomly divided into five experimental groups.

(i) *Group I*. For the control group, rats were administered with 0.1 ml normal saline instead of CFA in the right hind paw

(ii) *Group II*. For the CFA group, rats were administered with 0.1 ml CFA

(iii) *Group III*. For the positive control group, rats were administered with indomethacin (5 mg/kg, p.o.) daily for 21 days after the CFA injection

(iv) *Group IV*. For the drug-treated group, rats were administered with cedrol (10 mg/kg, p.o.) daily for 21 days after the CFA injection

(v) *Group V*. For the drug-treated group, rats were administered with cedrol (20 mg/kg, p.o.) daily for 21 days after the CFA injection

4.1. Drug Administration. All drugs/vehicles were precisely administered by oral gavage. Cedrol dissolved in saline containing 1% DMSO. All measurements were performed blinded, and the investigator did not know what treatment each rat received.

Nociceptive behavioral examines, paw volume evaluation, and arthritis score were examined on days 0, 7, 14, and 21. The hind footpad's paw thickness (right) was measured in each rat using a caliper.

4.2. Arthritis Score. The severity of arthritis was assessed as follows [1]: 0 = no change, 1 = mild erythema or swelling of the digits, 2 = moderate swelling and erythema, 3 = severe swelling and erythema involving the ankle, and 4 = ankylosis and inability to bend the ankle.

4.3. Thermal Hyperalgesia. The hot plate was used to assess thermal hyperalgesia. In this test, rats were individually placed on a hot plate maintained at 55°C. The latency to the first sign of paw licking or jump response to avoid the heat nociception was taken as an index of the pain threshold; the cut-off time was set at 10 s to prevent any injury to the tissues of the paws [1].

4.4. Mechanical Allodynia. Animals were placed on an elevated box (30 × 30 × 30 cm) with a metal wire floor, and an ascending series of von Frey filaments (Bioseb) were applied in ascending style to the plantar surface. The cut-off threshold was set at 60 g to prevent tissue damage. Each filament was tested five times. A positive response is if the animal responded to at least three withdrawals out of five consecutive trials. That gram force was considered as the paw withdrawal threshold [19].

4.5. Biochemical Assays. The serum interleukin 1 β (IL-1β) and tumor necrosis factor α (TNF-α) levels were detected using a commercial ELISA kit (Karmania Pars Gene Company, Kerman, Iran). The levels of malondialdehyde (MDA), as the final product of the lipid peroxidation process, superoxide dismutase (SOD) activity, and thiol concentration in serum, were assessed based on the methods reported by previous publication [20]. Glutathione peroxidase (GPX) activity was detected using a commercial ELISA GPX assay kit (ZellBio, German).

4.6. Statistical Analysis. GraphPad Prism (version 6.0) was used for analyzing the data. All data were shown as mean ± SEM. Behavioral parameters were measured by two-way analysis of variance (ANOVA) followed by Bonferroni's test. Biochemical parameters were measured by one-way ANOVA followed by Tukey's test. p values lower than 0.05 were statistically significant.

5. Results

5.1. Effect of Cedrol on the Arthritis Score in CFA-Induced Arthritic Rats. As shown in Figure 1, the arthritis score in all groups on day 0 was 0. The arthritis score in the cedrol (10 mg/kg) group was lower than that detected in the CFA group on day 21 ($p < 0.05$). The arthritis score in the cedrol (20 mg/kg) group was lower than that detected in the CFA group on days 7, 14, and 21 ($p < 0.05$, $p < 0.001$, and $p < 0.001$, respectively). A significant decrease in arthritic index was recorded in the indomethacin group compared to the CFA group on days 7, 14, and 21 ($p < 0.05$, $p < 0.01$, and $p < 0.001$, respectively).

5.2. Effect of Cedrol on Paw Volume in CFA-Induced Arthritic Rats. As shown in Figure 2, there was no significant difference in paw volume between groups on day 0. The paw

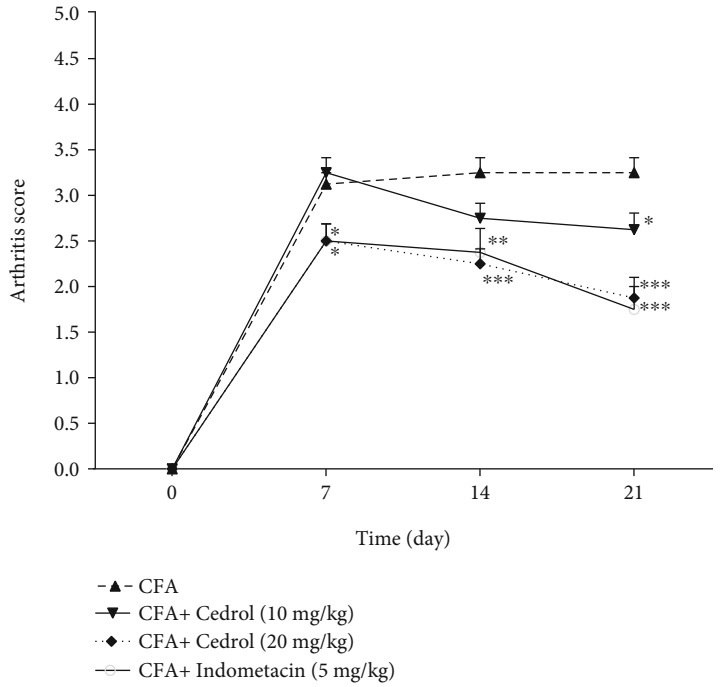

Figure 1: Effects of cedrol on arthritis score. Values are mean ± SEM, $n = 8$ in each group. $^{*}p < 0.05$, $^{**}p < 0.01$, and $^{***}p < 0.001$ vs. CFA group.

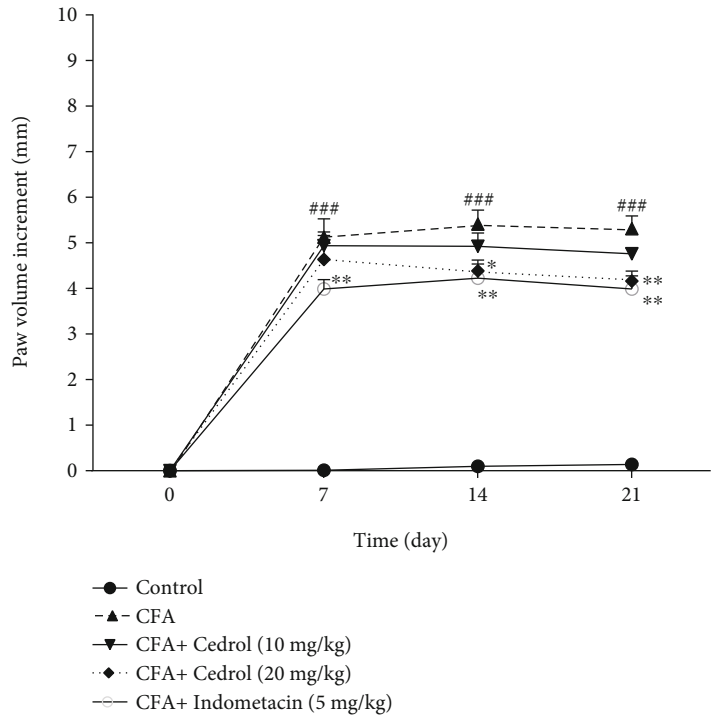

Figure 2: Effects of cedrol on paw volume. Values are mean ± SEM, $n = 8$ in each group. $^{*}p < 0.05$ and $^{**}p < 0.01$ vs. CFA group. $\#\#\#p < 0.001$ vs. control group.

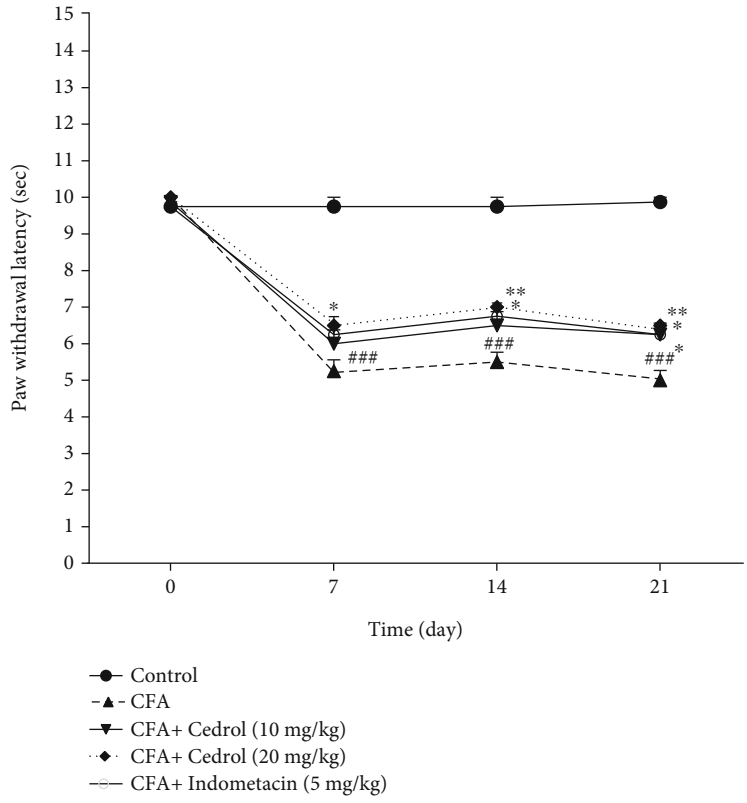

Figure 3: Effect of cedrol on paw withdrawal latency (s). Values are mean ± SEM. $n = 8$ in each group. $^{*}p < 0.05$ and $^{**}p < 0.01$ vs. CFA group. $\#\#\#p < 0.001$ vs. control group.

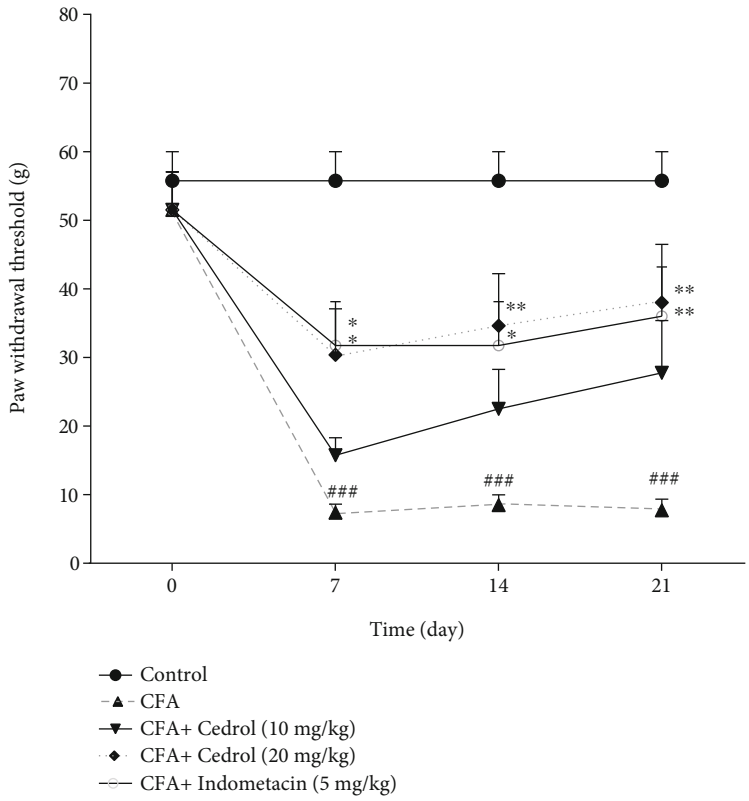

Figure 4: Effect of cedrol on paw withdrawal threshold (g). Values are mean ± SEM. $n = 8$ in each group. $^{*}p < 0.05$ and $^{**}p < 0.01$ vs. CFA group. $\#\#\#p < 0.001$ vs. control group.

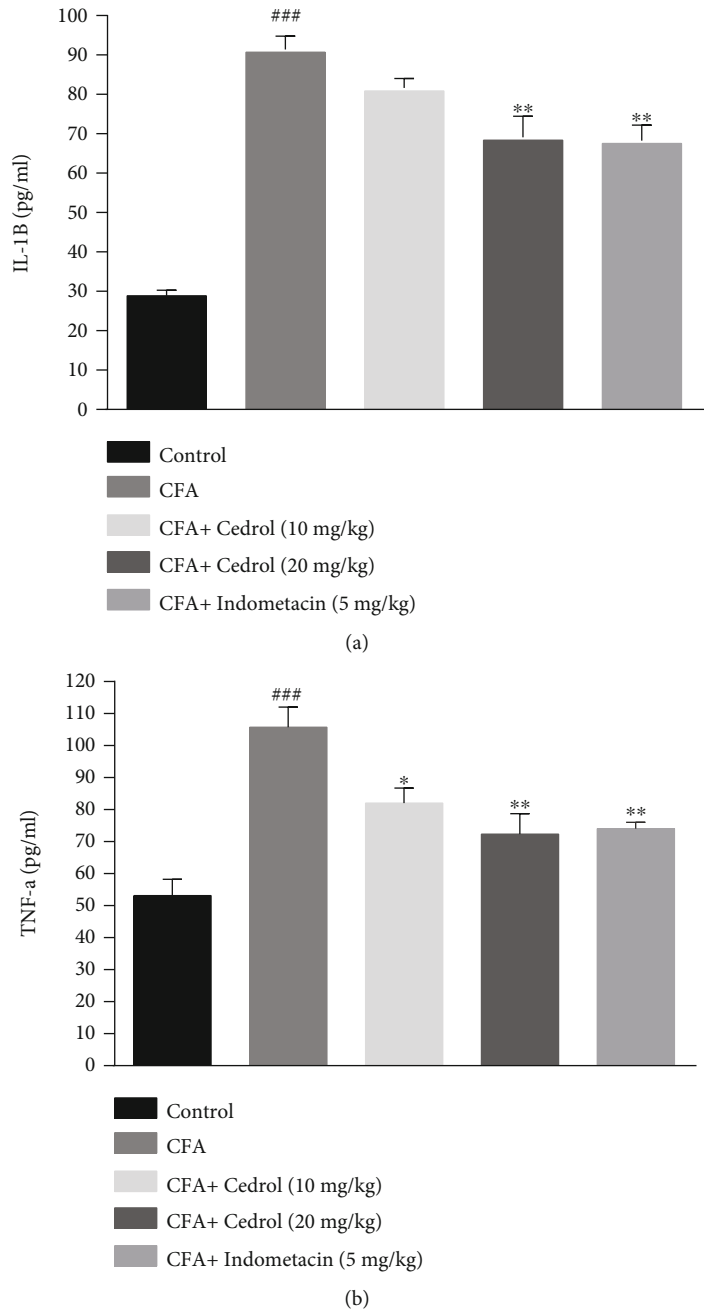

Figure 5: Effect of cedrol on (a) IL-1β and (b) TNF-α concentration. Values are mean ± SEM. $n = 6$ in each group. $^{*}p < 0.05$ and $^{**}p < 0.01$ vs. CFA group. $^{\#\#\#}p < 0.001$ vs. control group.

volume in the CFA group significantly increased on days 7, 14, and 21 compared to the control group ($p < 0.001$). The paw volume in the indomethacin (5 mg/kg) group was lower than that detected in the CFA group on day 7 ($p < 0.01$). The paw volume in the cedrol (20 mg/kg) group and indomethacin (5 mg/kg) group was lower than that detected in the CFA group on day 14 ($p < 0.05$ and $p < 0.01$, respectively). Over time, the paw volume decreased further in the treatment groups; the paw volume in the cedrol (20 mg/kg) and indomethacin (5 mg/kg) group was lower than that detected in the CFA group on day 21 ($p < 0.01$).

5.3. Effect of Cedrol on Thermal Hyperalgesia in CFA-Induced Arthritic Rats. The CFA-injected rats showed a significant decrease in thermal hyperalgesia threshold on day 7, continuing until day 21 compared to the control group ($p < 0.001$). However, highest dose of cedrol (20 mg/kg) attenuated CFA-induced thermal hyperalgesia on days 7, 14, and 21 compared to the CFA-control group ($p < 0.05$, $p < 0.01$, and $p < 0.01$, respectively). Indomethacin (5 mg/kg) attenuated CFA-induced thermal hyperalgesia on days 14 and 21 compared to the CFA-control group ($p < 0.05$). 10 mg/kg cedrol treatment also led to a significant

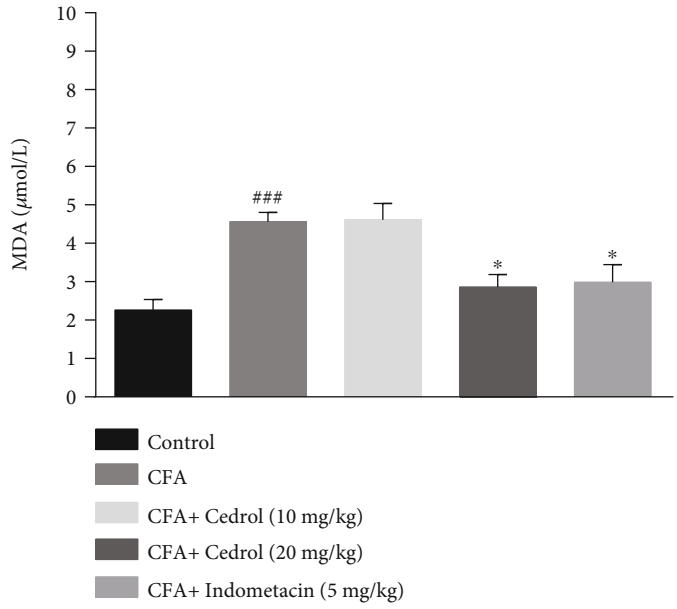

(a)

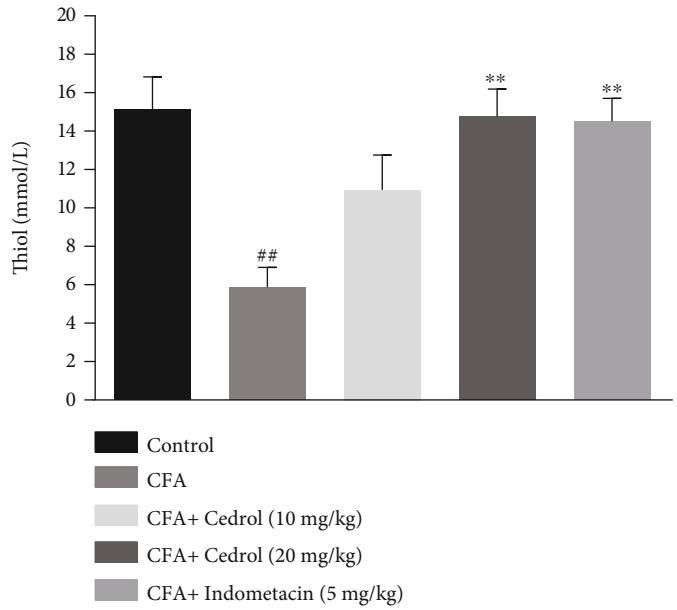

(b)

Figure 6: Continued.

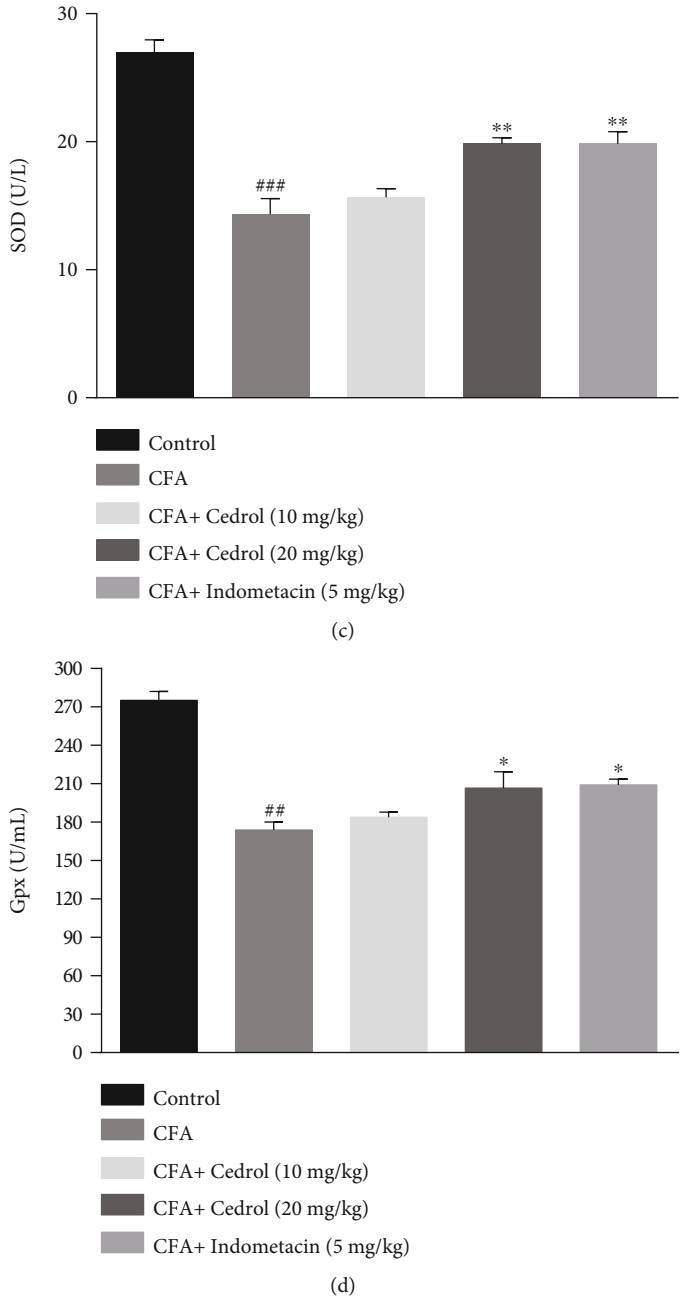

Figure 6: Effect of cedrol on (a) MDA concentration, (b) thiol concentration, (c) SOD activity, and (d) Gpx activity. Values are mean ± SEM . $n = 6$ in each group. $^{*}p < 0.05$ and $^{**}p < 0.01$ vs. CFA group. $\#\#p < 0.001$ and $\#\#\#p < 0.001$ vs. control group.

improvement on day 21 (increased paw withdrawal latency) compared to the CFA-control group ($p < 0.05$) (Figure 3).

5.4. Effect of Cedrol on Mechanical Allodynia in CFA-Induced Arthritic Rats. CFA-injected rats showed a significant reduction in paw withdrawal mechanical threshold (mechanical allodynia) on days 7, 14, and 21 as compared with the nonarthritic control group, which continued to worsen till the end of the experiment ($p < 0.001$). However, treatment with cedrol (10 mg/kg) did not significantly differ from CFA-treated rats. Cedrol (20 mg/kg) showed a statistically significant enhancement in paw withdrawal threshold in CFA-induced arthritic rats on days 7, 14, and 21 compared to the CFA-control group ($p < 0.05$, $p < 0.01$, and $p < 0.01$, respectively). Similarly, indomethacin (5 mg/kg) also significantly augmented the paw withdrawal threshold in the CFA group on days 7, 14, and 21 compared to the CFA-control group ($p < 0.05$, $p < 0.05$, and $p < 0.01$, respectively) (Figure 4).

5.5. Effect of Cedrol on the Serum Levels of IL-1β and TNF-α in CFA-Induced Arthritic Rats. The IL-1β level was significantly higher ($p < 0.001$) in the CFA group compared to the control group. The treatment with indomethacin was effective in decreasing IL-1β level in serum of CFA-induced

rats compared to the CFA-control group ($p < 0.01$), besides the treatment with cedrol (20 mg/kg) reduced IL-1β level in serum of CFA-induced rats compared to the CFA-control group ($p < 0.01$) (Figure 5(a)).

As displayed in Figure 5(b), administration of CFA significantly increased the serum TNF-α level ($p < 0.001$) in the arthritic (CFA group) compared to the control group. The treatment with indomethacin was effective to decrease TNF-α level in serum of CFA-induced rats ($p < 0.01$ versus CFA group), besides the treatment with cedrol (10 and 20 mg/kg) reduced TNF-α level in serum of CFA-induced rats compared to the CFA group ($p < 0.05$ and $p < 0.01$, respectively).

5.6. Effect of Cedrol on the Oxidative Stress in CFA-Induced Arthritic Rats. MDA level was significantly higher ($p < 0.001$) in the arthritic (CFA group) compared to the control group. The treatment with indomethacin was effective in decreasing MDA level in serum of CFA-induced rats compared to the CFA group ($p < 0.05$), besides the treatment with cedrol (20 mg/kg) reduced MDA level in serum of CFA-induced rats compared to the CFA-control group ($p < 0.05$) (Figure 6(a)).

As shown in Figure 6(b), administration of CFA markedly decreased serum levels of thiol as compared to the control group ($p < 0.01$). The treatment with cedrol (20 mg/kg) and indomethacin significantly increased thiol level in serum of CFA-induced rats compared to the CFA-control group ($p < 0.01$).

SOD activity was significantly lower ($p < 0.001$) in the arthritic (CFA group) compared to the control group. In the treatment groups (cedrol (20 mg/kg) and indomethacin), SOD activity elevated significantly compared to the CFA group ($p < 0.01$) (Figure 6(c)).

Gpx activity was significantly lower ($p < 0.01$) in the arthritic (CFA group) compared to the control group. The treatment with indomethacin was effective to increase Gpx activity in serum of CFA-induced rats compared to the CFA-control group ($p < 0.05$), besides the treatment with cedrol (20 mg/kg) increased Gpx activity in serum of CFA-induced rats compared to the CFA group ($p < 0.05$) (Figure 6(d)).

6. Discussion

The CFA-induced experimental model of arthritis is known to have numerous human RA features, such as robust hypersensitivity to mechanical and heat stimuli, polyarticular inflammation, and deterioration of the joint structures. This model is widely used to study RA's pathogenesis and assess potential therapeutic targets useful for the treatment of RA [1, 21, 22]. Following intraplantar injection of CFA, the mycobacterial constituents in the CFA cause T-lymphocytes to provoke a robust immune response in the rat paws. The T-lymphocytes interact with dendritic cells, monocytes, and macrophages to produce the major proinflammatory cytokine participating in the pathogenesis of RA, including TNF-α, IL-1β, and IL-6 in the synovial membrane [23–26]. The interaction between these proinflammatory mediators causes synovial inflammation and cartilage/bone destruction [27]. It has been revealed that TNF-α blockade reduces the symptoms of RA [28]. The inflammatory cytokines IL-1β and TNF-α are the therapeutic targets in RA treatment strategies [29, 30].

On the other hand, arthritis can cause chronic inflammatory pain. Moreover, chronic inflammatory pain is modeled via CFA attributed to provoke inflammatory cytokines, which sensitizes nociceptive neurons and reduces the pain threshold [31]. Previous studies have highlighted that sesquiterpenes show anti-inflammatory, antioxidant [32], and analgesic properties [33]. Consequently, in the present study, the potential protective properties of cedrol were examined against CFA-induced arthritis in rats. According to the present study, cedrol improved the nociception behaviors of the rats exposed to CFA. Anti-inflammatory and antioxidant effects also accompanied it. Cedrol reduced the paw's thickness by inhibiting the release of inflammatory mediators (IL-1B and TNF-α), indicating its anti-inflammatory potential in CFA-induced arthritis. As a non-steroidal anti-inflammatory drug, indomethacin inhibits the production of prostaglandins by inhibiting the activity of cyclooxygenase [34]. In this study, indomethacin reduced the thickness of the paw and exerted antinociceptive behaviors. Besides, indomethacin reduced serum levels of TNF-α and IL-1β as well. Antioxidant therapy has thus represented an effective treatment for oxidative stress/inflammation-related diseases. Oxidative stress occurs due to an imbalance between prooxidants and antioxidants and consequent excessive production of reactive oxygen species (ROS) [35]. Several defense systems, including enzymatic (SOD and GPx) and nonenzymatic antioxidants (GSH), have been involved in the cells preventing uncontrolled ROS. Indeed, these antioxidants' impairments have been reported in active RA patients [36]. ROS production inside the joints has an essential role in arthritis pathogenesis since oxidants by direct action or indirect activation of latent collagenases degrade matrix ingredients [37]. Besides, ROS are positively linked with the severity of RA [38]. ROS participate in the signaling of inflammation. Mitochondrial ROS stimulate proinflammatory cytokine production, IL-1B, IL-6, and TNF-α.

On the other hand, the inflammation process also causes oxidative stress as host immune cells, like neutrophils, also known as polymorphonuclear neutrophils, release large amounts of ROS via the NADPH oxidase enzyme pathway [38]. In the current study, cedrol or indomethacin showed antioxidant properties, as it decreased the MDA levels while antioxidant molecules (thiol, SOD, and GPx) increased. These results are in accordance with the previous study reported that administration of cedrol (20 and 40 mg/kg, i.p.) once a day for 14 days postchronic constriction injury model of neuropathic pain attenuated nociception pain behaviors in rats by inhibition of inflammatory response and reduction of oxidative stress markers [12]. Another study showed cedrol reduced collagen-induced arthritis in mice and modulates the inflammatory response in lipopolysaccharide-mediated fibroblast-like synoviocytes [39]. Treatment with Budlein A, a sesquiterpene lactone from *Viguiera robusta*, showed anti-inflammatory and

analgesic effects in antigen-induced arthritis in mice [40]. Arthritis score and swelling of the paw are indexes to access the antiarthritic action of numerous medicines [5], and these indexes were used to evaluate the effect of cedrol in this study. The cedrol groups noteworthy attenuated paw thickness and arthritis scores. In the current investigation, cedrol modified different parameters of arthritis in rats, including arthritic score, paw volume, nociception behaviors, oxidative stress markers, and inflammation. Thus, cedrol may be effective as a long-term antiarthritis agent to overcome the distressing manifestation of RA.

In conclusion, we conclude that cedrol exhibits antiarthritic properties presumably through inhibition of oxidative stress and inflammation. Overall, these results provided supportive evidence for the therapeutic potential of cedrol in RA treatment.

Data Availability

The dataset that supports the results and findings of this research is available from the corresponding author upon request.

Conflicts of Interest

The authors declare that they have no conflicts of interest.

Authors' Contributions

Fatemeh Forouzanfar, and Hamed Ghazavi, have participated in writing the article. Ali Mohammad Pourbagher-Shahri and Fatemeh Forouzanfar performed the experiments. Fatemeh Forouzanfar was the supervisor on the project and prepared the final draft of the paper.

Acknowledgments

This work was supported by grants from the Vice Chancellery for Research and Technology, Mashhad University of Medical Sciences (MUMS), Mashhad, Iran (981095).

References

[1] A. Kumar, N. Dhaliwal, J. Dhaliwal, R. N. Dharavath, and K. Chopra, "Astaxanthin attenuates oxidative stress and inflammatory responses in complete Freund-adjuvant-induced arthritis in rats," *Pharmacological Reports*, vol. 72, no. 1, pp. 104–114, 2020.

[2] C. Nasuti, D. Fedeli, L. Bordoni et al., "Anti-inflammatory, anti-arthritic and anti-nociceptive activities of Nigella sativa oil in a rat model of arthritis," *Antioxidants*, vol. 8, no. 9, p. 342, 2019.

[3] H. J. Mahdi, N. A. K. Khan, M. Z. B. Asmawi, R. Mahmud, A. Vikneswaran, and L. Murugaiyah, "*In vivo* anti-arthritic and anti-nociceptive effects of ethanol extract of *Moringa oleifera* leaves on complete Freund's adjuvant (CFA)-induced arthritis in rats," *Integrative medicine research*, vol. 7, no. 1, pp. 85–94, 2018.

[4] I. B. McInnes and G. Schett, "Cytokines in the pathogenesis of rheumatoid arthritis," *Nature Reviews Immunology*, vol. 7, no. 6, pp. 429–442, 2007.

[5] Z. Tong, L. Cheng, J. Song et al., "Therapeutic effects of Caesalpinia minax Hance on complete Freund's adjuvant (CFA)-induced arthritis and the anti-inflammatory activity of cassane diterpenes as main active components," *Journal of Ethnopharmacology*, vol. 226, pp. 90–96, 2018.

[6] B. N. Lindler, K. E. Long, N. A. Taylor, and W. Lei, "Use of herbal medications for treatment of osteoarthritis and rheumatoid arthritis," *Medicine*, vol. 7, no. 11, p. 67, 2020.

[7] D. Cox-Georgian, N. Ramadoss, C. Dona, and C. Basu, *Therapeutic and Medicinal Uses of Terpenes*, Springer, Medicinal Plants, 2019.

[8] H. Bártíková, V. Hanusova, L. Skalova, M. Ambroz, and I. Bousova, "Antioxidant, pro-oxidant and other biological activities of sesquiterpenes," *Current topics in medicinal chemistry*, vol. 14, no. 22, pp. 2478–2494, 2014.

[9] D. S. Aguilar-Ávila, M. E. Flores-Soto, C. Tapia-Vázquez, O. A. Pastor-Zarandona, R. I. López-Roa, and J. M. Viveros-Paredes, "β-Caryophyllene, a natural sesquiterpene, attenuates neuropathic pain and depressive-like behavior in experimental diabetic mice," *Journal of medicinal food*, vol. 22, no. 5, pp. 460–468, 2019.

[10] H. Yousefi-Manesh, A. R. Dehpour, S. Shirooie et al., "Isofuranodiene, a natural sesquiterpene isolated from wild celery (*Smyrnium olusatrum* L.), protects rats against acute ischemic stroke," *Pharmaceuticals*, vol. 14, no. 4, p. 344, 2021.

[11] S. Gao, Q. Wang, X.-H. Tian et al., "Total sesquiterpene lactones prepared from *Inula helenium* L. has potentials in prevention and therapy of rheumatoid arthritis," *Journal of Ethnopharmacology*, vol. 196, pp. 39–46, 2017.

[12] M. H. Sakhaee, S. A. H. Sayyadi, N. Sakhaee et al., "Cedrol protects against chronic constriction injury-induced neuropathic pain through inhibiting oxidative stress and inflammation," *Metabolic Brain Disease*, vol. 35, no. 7, pp. 1119–1126, 2020.

[13] I. Jantan, I. Rafi, and J. Jalil, "Platelet-activating factor (PAF) receptor-binding antagonist activity of Malaysian medicinal plants," *Phytomedicine*, vol. 12, no. 1-2, pp. 88–92, 2005.

[14] I. Oh, W.-Y. Yang, J. Park et al., "In vitro Na+/K+-ATPase inhibitory activity and antimicrobial activity of sesquiterpenes isolated from Thujopsis dolabrata," *Archives of pharmacal research*, vol. 34, no. 12, pp. 2141–2147, 2011.

[15] D. Kagawa, H. Jokura, R. Ochiai, I. Tokimitsu, and H. Tsubone, "The sedative effects and mechanism of action of cedrol inhalation with behavioral pharmacological evaluation," *Planta Medica*, vol. 69, no. 7, pp. 637–641, 2003.

[16] Y. Zhang, L. Han, S.-S. Chen, J. Guan, F.-Z. Qu, and Y.-Q. Zhao, "Hair growth promoting activity of cedrol isolated from the leaves of Platycladus orientalis," *Biomedicine & Pharmacotherapy*, vol. 83, pp. 641–647, 2016.

[17] H. O. Yang, D.-Y. Suh, and B. H. Han, "Isolation and characterization of platelet-activating factor receptor binding antagonists from Biota orientalis," *Planta Medica*, vol. 61, no. 1, pp. 37–40, 1995.

[18] M. Loizzo, R. Tundis, F. Menichini, A. Saab, G. Statti, and F. Menichini, "Antiproliferative effects of essential oils and their major constituents in human renal adenocarcinoma and amelanotic melanoma cells," *Cell Proliferation*, vol. 41, no. 6, pp. 1002–1012, 2008.

[19] F. Forouzanfar, H. Hosseinzadeh, M. B. Khorrami, S. Asgharzade, and H. Rakhshandeh, "Attenuating effect of Portulaca oleracea extract on chronic constriction injury

induced neuropathic pain in rats: an evidence of anti-oxidative and anti-inflammatory effects," *CNS & Neurological Disorders-Drug Targets (Formerly Current Drug Targets-CNS & Neurological Disorders)*, vol. 18, no. 4, pp. 342–349, 2019.

[20] M. B. Khorrami, H. R. Sadeghnia, A. Pasdar et al., "Antioxidant and toxicity studies of biosynthesized cerium oxide nanoparticles in rats," *International Journal of Nanomedicine*, vol. 14, pp. 2915–2926, 2019.

[21] A. Bendele, "Animal models of rheumatoid arthritis," *Journal of Musculoskeletal & Neuronal Interactions*, vol. 1, no. 4, pp. 377–385, 2001.

[22] R. Lal, J. Dhaliwal, N. Dhaliwal, R. N. Dharavath, and K. Chopra, "Activation of the Nrf2/HO-1 signaling pathway by dimethyl fumarate ameliorates complete Freund's adjuvant-induced arthritis in rats," *European Journal of Pharmacology*, vol. 899, article 174044, 2021.

[23] F.-L. Voon, M. R. Sulaiman, M. N. Akhtar et al., "Cardamonin (2′, 4′-dihydroxy-6′-methoxychalcone) isolated from *Boesenbergia rotunda* (L.) Mansf. inhibits CFA-induced rheumatoid arthritis in rats," *European journal of pharmacology*, vol. 794, pp. 127–134, 2017.

[24] C. N. Tran, S. K. Lundy, and D. A. Fox, "Synovial biology and T cells in rheumatoid arthritis," *Pathophysiology*, vol. 12, no. 3, pp. 183–189, 2005.

[25] L. Magyari, D. Varszegi, E. Kovesdi et al., "Interleukins and interleukin receptors in rheumatoid arthritis: research, diagnostics and clinical implications," *World Journal of Orthopedics*, vol. 5, no. 4, pp. 516–536, 2014.

[26] F. Qin, H. Zhang, A. Liu et al., "Analgesic effect of *Zanthoxylum nitidum* extract in inflammatory pain models through targeting of ERK and NF-κB signaling," *Frontiers in pharmacology*, vol. 10, p. 359, 2019.

[27] P. He, Y. Hu, C. Huang et al., "N-Butanol extract of *Gastrodia elata* suppresses inflammatory responses in lipopolysaccharide-stimulated macrophages and complete Freund's adjuvant-(CFA-) induced arthritis rats via inhibition of MAPK signaling pathway," *Evidence-Based Complementary and Alternative Medicine*, vol. 2020, Article ID 1658618, 11 pages, 2020.

[28] D. Mewar and A. G. Wilson, "Treatment of rheumatoid arthritis with tumour necrosis factor inhibitors," *British journal of pharmacology*, vol. 162, no. 4, pp. 785–791, 2011.

[29] Y. Zhuang, S. Lyn, Y. Lv et al., "Pharmacokinetics and safety of golimumab in healthy Chinese subjects following a single subcutaneous administration in a randomized phase I trial," *Clinical drug investigation*, vol. 33, no. 11, pp. 795–800, 2013.

[30] S. Nikfar, P. Saiyarsarai, B. M. Tigabu, and M. Abdollahi, "Efficacy and safety of interleukin-1 antagonists in rheumatoid arthritis: a systematic review and meta-analysis," *Rheumatology international*, vol. 38, no. 8, pp. 1363–1383, 2018.

[31] T. Liu and B. Su, "*Styphnolobium japonicum* (L.) Schott flower extract alleviates oxidative stress and inflammatory factors in the adjuvant-induced arthritis rat model," *Research*, vol. 14, pp. 2907–2919, 2021.

[32] S. S. Dahham, Y. M. Tabana, M. A. Iqbal et al., "The anticancer, antioxidant and antimicrobial properties of the sesquiterpene β-caryophyllene from the essential oil of Aquilaria crassna," *Molecules*, vol. 20, no. 7, pp. 11808–11829, 2015.

[33] M. J. Chavan, P. S. Wakte, and D. B. Shinde, "Analgesic and anti-inflammatory activities of the sesquiterpene fraction from *Annona reticulata* L. bark," *Natural product research*, vol. 26, no. 16, pp. 1515–1518, 2012.

[34] S. Nalamachu and R. Wortmann, "Role of indomethacin in acute pain and inflammation management: a review of the literature," *Postgraduate Medicine*, vol. 126, no. 4, pp. 92–97, 2014.

[35] R. R. Mititelu, R. Pădureanu, M. Băcănoiu et al., "Inflammatory and oxidative stress markers—mirror tools in rheumatoid arthritis," *Biomedicine*, vol. 8, no. 5, p. 125, 2020.

[36] C. M. Quiñonez-Flores, S. A. González-Chávez, N. D. Del Rio, and C. Pacheco-Tena, "Oxidative stress relevance in the pathogenesis of the rheumatoid arthritis: a systematic review," *BioMed research international*, vol. 2016, Article ID 6097417, 14 pages, 2016.

[37] P. Vasanthi, G. Nalini, and G. Rajasekhar, "Status of oxidative stress in rheumatoid arthritis," *International journal of rheumatic diseases*, vol. 12, no. 1, pp. 29–33, 2009.

[38] A. García-Sánchez, A. G. Miranda-Díaz, and E. G. Cardona-Muñoz, "The role of oxidative stress in physiopathology and pharmacological treatment with pro- and antioxidant properties in chronic diseases," *Oxidative Medicine and Cellular Longevity*, vol. 2020, Article ID 2082145, 16 pages, 2020.

[39] X. Chen, J. Shen, J.-m. Zhao et al., "Cedrol attenuates collagen-induced arthritis in mice and modulates the inflammatory response in LPS-mediated fibroblast-like synoviocytes," *Food & Function*, vol. 11, no. 5, pp. 4752–4764, 2020.

[40] A. C. Zarpelon, V. Fattori, F. O. Souto et al., "The sesquiterpene lactone, budlein A, inhibits antigen-induced arthritis in mice: role of NF-κB and cytokines," *Inflammation*, vol. 40, no. 6, pp. 2020–2032, 2017.

Hindawi
Oxidative Medicine and Cellular Longevity
Volume 2022, Article ID 8438528, 18 pages
https://doi.org/10.1155/2022/8438528

Research Article

Glycyrrhizin Attenuates Hypoxic-Ischemic Brain Damage by Inhibiting Ferroptosis and Neuroinflammation in Neonatal Rats via the HMGB1/GPX4 Pathway

Kaiyi Zhu,[1] Xing Zhu,[1] Shiqi Liu,[1] Jie Yu,[1] Songwei Wu,[1] and Mingyan Hei[1,2]

[1]*Department of Neonatology, Neonatal Center, Beijing Children's Hospital, Capital Medical University, National Center for Children's Health, Beijing 100045, China*
[2]*Key Laboratory of Major Diseases in Children, Ministry of Education, Beijing 100045, China*

Correspondence should be addressed to Mingyan Hei; heimingyan@bch.com.cn

Received 8 December 2021; Revised 20 February 2022; Accepted 7 March 2022; Published 7 April 2022

Academic Editor: Silvânia Maria Mendes Vasconcelos

With unknown etiology and limited treatment options, neonatal hypoxic-ischemic brain damage (HIBD) remains a major cause of mortality in newborns. Ferroptosis, a recently discovered type of cell death triggered by lipid peroxidation, is closely associated with HIBD. High-mobility group box 1 (HMGB1), a molecule associated with inflammation damage, can induce neuronal death in HIBD. However, it remains unknown whether HMGB1 contributes to neuronal ferroptosis in patients with HIBD. Herein, glycyrrhizin (GL), an HMGB1 inhibitor, was used to investigate the relationship between ferroptosis and HMGB1. RAS-selective lethal 3(RSL3), a ferroptosis agonist, was administered to further confirm the changes in the signaling pathway between HMGB1 and ferroptosis. Western blot analysis revealed that GL markedly suppressed the expression of HMGB1 and increased the level of GPX4 in the context of HIBD. We observed changes in neuronal ultrastructure via transmission electron microscopy to further confirm the occurrence of ferroptosis. Real-time PCR indicated that GL inhibited the expression of ferroptosis-related genes and inflammatory factors. Immunofluorescence and immunohistochemistry staining confirmed GL inhibition of neuronal damage and ferroptosis in HIBD associated with GPX4 and ROS. GL not only inhibited ferroptosis induced by RSL3 and oxygen-glucose deprivation in vitro but also inhibited ferroptosis induced by HIBD in vivo. More importantly, GL may improve oxidative stress imbalance and mitochondrial damage, alleviate the downstream production of inflammatory factors, and ultimately reduce ferroptosis and damage to cortical neurons following HIBD via the HMGB1/GPX4 pathway. In conclusion, we showed for the first time that GL could suppress the occurrence of neuronal ferroptosis and reduce neuronal loss in HIBD via the HMGB1/GPX4 pathway. These findings highlight the potential of HMGB1 signaling antagonists to treat neuronal damage by suppressing ferroptosis, provide new and unique insights into GL as a neuroprotective agent, and suggest new prevention and treatment strategies for HIBD.

1. Introduction

Neonatal hypoxic-ischemic brain damage (HIBD) remains a major cause of mortality in newborns during the perinatal period [1, 2]. Survivors exhibit an increased incidence of severe and permanent neurological sequelae, including cerebral palsy, cognitive impairment, learning impairment, developmental delay, and epilepsy; these sequelae compromise the quality of life of HIBD children and impose an immense economic and psychological burden on families and society [1–3]. To date, hypothermia is the only recognized therapy for newborns with moderate to severe HIBD; however, this treatment has limited efficacy [2, 4]. The exact pathogenesis of HIBD is a complex process that is not fully understood; it includes oxidative stress, mitochondrial damage, and inflammation, eventually leading to progressive neuronal death [4, 5].

Ferroptosis is a recently discovered, caspase-independent type of cell death that is triggered by lipid peroxidation and is genetically distinct from other types of cell death [6, 7].

Table 1: Primer sets used for qPCR.

	Forward primer (5′-3′)	Reverse primer (5′-3′)
ATP5G3	GACTAGGACTGGAGAGGGCT	ATACCAGCACCAGAACCAGC
PTGS2	CTTCGGGAGCACAACAGAGT	TTCAGAGGCAATGCGGTTCT
IREB2	GGGAATTCTTGGGTGGGGAG	AACAAACTTTCCAGCCACGC
CS	GCTACAGAAGGAAGTCGGCA	CCCGAGTTGAGTGTGTTCCA
RPL8	GCAAGCCTTCCACTATCCGA	CAATGAGACCCACTTTGCGC
TNF-α	GCATGATCCGAGATGTGGAACTGG	CGCCACGAGCAGGAATGAGAAG
IL-6	AGGAGTGGCTAAGGACCAAGACC	TGCCGAGTAGACCTCATAGTGACC
IL-1β	ATCTCACAGCATCTCGACAAG	CACACTAGCAGGTCGTCATCC
β-Actin	CACGATGGAGGGGCCGGACTCATC	TAAAGACCTCTATGCCAACACAGT

The occurrence of ferroptosis is independent of the mediators of apoptosis (caspase-3), necroptosis (RIP1 or RIP3), and pyroptosis (caspase-1 or caspase-11) [8]. Cell death by ferroptosis is caused by factors such as iron toxicity, glutathione (GSH) depletion, glutathione peroxidase 4 (GPX4) impairment, formation of excessive lipid peroxides and reactive oxygen species (ROS), and mitochondrial damage [9, 10]. The induction of ferroptosis through GSH deficiency is related to decreased GPX4 activity, resulting in the accumulation of membrane lipid peroxides and lethal ROS [11–13]. Ferroptosis is distinguished morphologically by mitochondrial shrinkage and is regulated by a number of genes, including ATP synthase F0 complex subunit C3 (ATP5G3), prostaglandin-endoperoxide synthase 2 (PTGS2), citrate synthase (CS), iron response element binding protein 2 (IREB2), and ribosomal protein L8 (RPL8) [8, 14, 15]. In addition, ferroptosis can potently induce inflammation through the release of proinflammatory molecules such as tumor necrosis factor- (TNF-) α, interleukin- (IL-) 1β, and IL-6 [15, 16]. Ferroptosis can be triggered by specific inducers, including erastin and RAS-selective lethal 3 (RSL3), and can be specifically inhibited by ferrostatin-1 and liproxstatin-1 [8, 17]. At present, there is accumulating evidence that ferroptosis plays a very important role in central nervous system (CNS) diseases, including intracerebral hemorrhage, traumatic brain injury and even HIBD, and inhibiting ferroptosis can prevent neuronal death in some CNS diseases [7, 18–20]. However, the clinical development of ferroptosis inhibitors for the treatment of brain diseases is limited because they have difficulty crossing the blood–brain barrier [18, 21]. Thus, there is a need to elucidate the underlying mechanisms of ferroptosis in HIBD and investigate potential antiferroptosis drugs to prevent and treat HIBD.

Glycyrrhizin (GL) is a natural glycosyl triterpenoid product and is recognized as an inhibitor of high-mobility group box 1 (HMGB1) [22]. HMGB1 is a ubiquitous transcription factor that is involved in the maintenance of nucleosome structure, chromatin remodeling, and the regulation of DNA recombination and repair [23–25]. Numerous studies have shown that HMGB1 is released from damaged cells and exhibits cytokine activity that contributes to the pathogenesis of numerous CNS diseases, including HIBD [24]. Our early studies showed that HMGB1 was upregulated in both the cerebral cortex and serum in HIBD and that GL decreased the ipsilateral infarct size and the degree of cerebral edema [26]. Recent studies have shown that ferroptosis mediates HMGB1 release and subsequent inflammation in an acute pancreatitis model [6]. It is still unclear, however, whether the inhibition of HMGB1 can ameliorate inflammation and brain damage in HIBD by inhibiting ferroptosis.

In the present study, GL, the main extract from the root of *Glycyrrhiza*, was used to investigate whether HMGB1 inhibition alleviates brain damage related to ferroptosis in vivo and in vitro. In addition, RSL3, an agonist of ferroptosis, was administered to further confirm the relationship between GL and ferroptosis and the corresponding changes in signaling pathways. The aim of this study may reveal a novel function of GL in ferroptosis in a rat model and identify a possible therapeutic strategy that could be translated from bench to bedside for HIBD and possibly even other ferroptosis-related diseases.

2. Materials and Methods

2.1. HIBD Animal Model and Drug Administration. Male and female neonatal Sprague–Dawley rats on postpartum day 7 (P7) were provided by SPF Biotechnology (Beijing, China). A neonatal rat HIBD model was established based on a previously described method [27]. In short, each animal was anesthetized with isoflurane (4% for induction, 2% for maintenance), the skin was incised, and the left common carotid artery was exposed. This artery was ligated with a 5-0 suture and cut, and the skin was sutured closed. Next, the pups recovered for 1 h with their mother. Subsequently, the pups were placed in a hypoxia chamber (8% O_2+92% N_2 mixture) for 2 h. After 2 h of hypoxia, the animals were placed back with their dam. The rat pups were randomly divided into 4 groups: (1) in the control (Con) group, the common carotid artery was merely exposed and separated from the left common carotid artery; (2) in the hypoxia-ischemia (HI) group, the pups underwent cerebral HIBD; (3) in the HI + glycyrrhizin (HI + GL) group, the pups received GL (20 mg/kg, Selleck, USA) injections intraperitoneally at 0 h, 24 h, and 48 h after HIBD; and (4) in the HI + GL+ RSL3 group, the rats in the HI + GL group received RSL3 (5 mg/kg, Selleck, USA) treatment at the same time. The rats were euthanized at P10 for subsequent analysis.

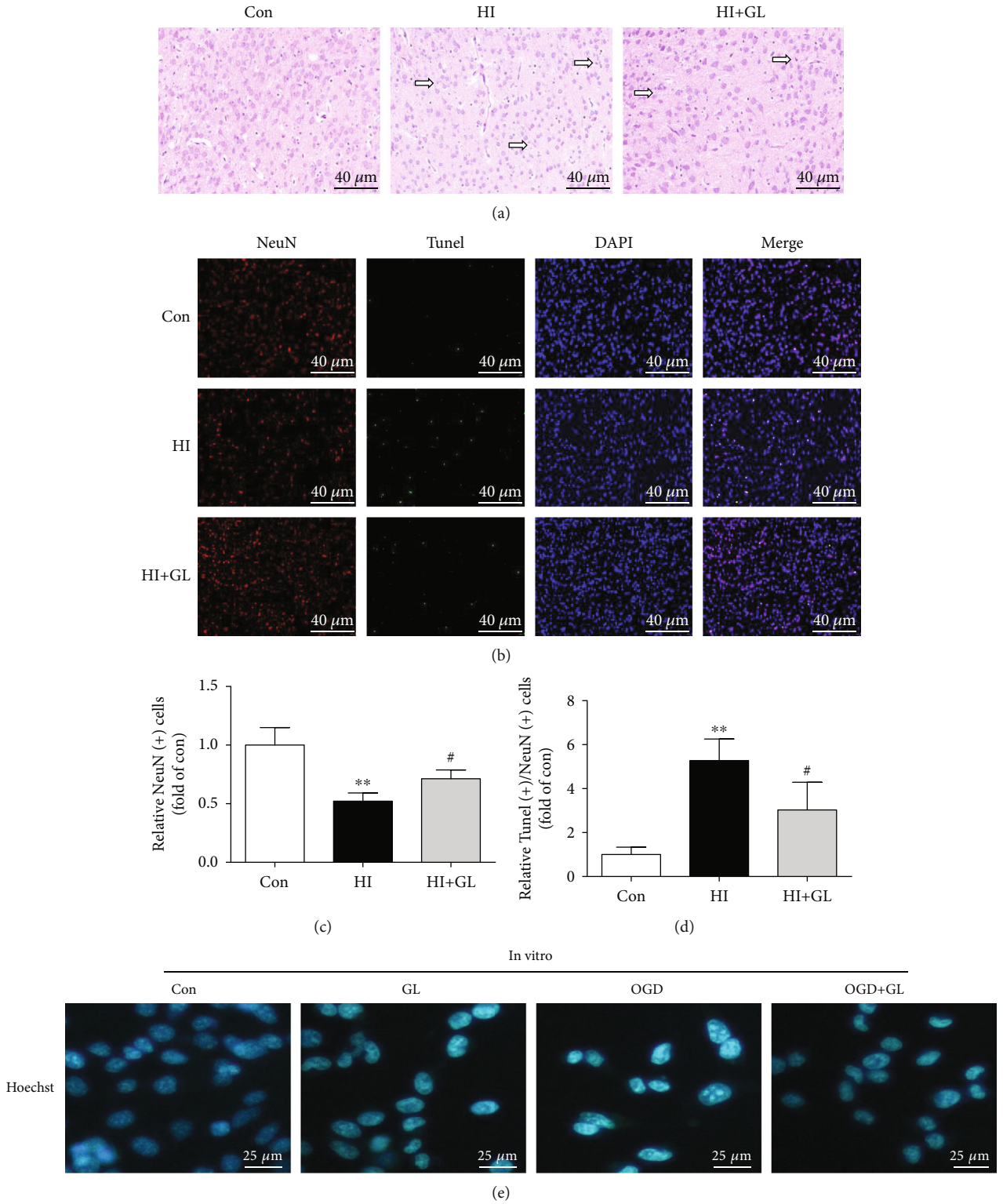

Figure 1: Continued.

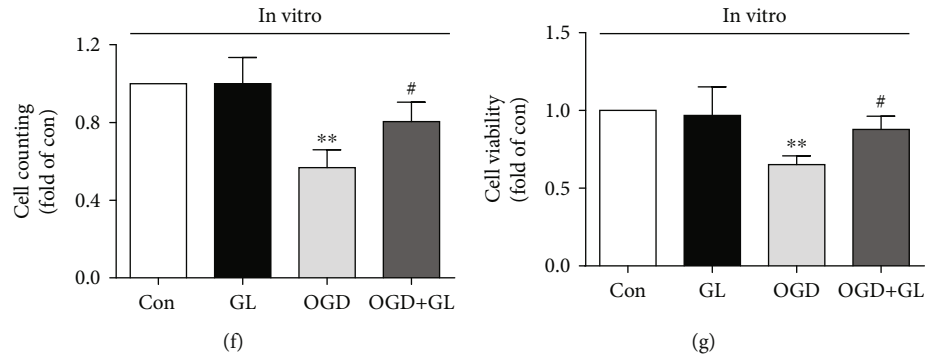

Figure 1: Glycyrrhizin improves cortical neuronal loss after HIBD and OGD. (a) HE-stained coronal sections from each group. The arrow indicates shrunken neuronal nuclei and sparse neurons. (b) Immunofluorescence labeling of TUNEL and NeuN in the cerebral cortex 72 h after HI ($n = 6$). (c) The statistical analysis of NeuN (+) cell counts ($n = 6$). (d) Statistical analysis of TUNEL (+)/NeuN (+) cell counts ($n = 6$). (e) Representative immunofluorescence of nuclear staining in primary cortical neurons. (f, g) Cell counting and cell viability in vitro ($n = 4$). $^{**}P < 0.01$ vs. the Con group; $\#P < 0.05$ vs. the HI group or OGD group.

2.2. Primary Cortical Neuron Culture and Treatment. Rat pups at P1 were decapitated, the brains were collected, and the meninges were removed. The brain tissue was fragmented, digested with trypsin, and filtered with a 50 mm sterile nylon filter. Cortical neurons for differentiation and treatment were cultured in Dulbecco's Modified Eagle's Medium (DMEM; HyClone, Logan, Utah, USA) supplemented with 100 U/mL penicillin and 100 mg/mL streptomycin and 10% fetal bovine serum (FBS, HyClone, USA). To establish an oxygen-glucose deprivation (OGD) model, the cells were cultured in a glucose-free Earle's balanced salt solution with 100 U/mL penicillin and 100 mg/mL streptomycin and incubated under an atmosphere of 5% CO_2 and 1% O_2 for 3 h at 37°C in a tri-gas incubator (HERA cell VIOS 160i, Thermo, USA).

To detect the effect of GL on OGD-treated cells, the cells were divided into the following groups: (1) Con group: the cells were cultured with untreated medium in a normal incubator, (2) GL group: the conditions were the same as in the Con group except for the addition of GL (55 μM), (3) OGD group: the cells were subjected to OGD, and (4) OGD + GL group: GL was added to the wells 2 h before the cells were incubated under OGD conditions. To investigate the function of GL on RSL3-induced ferroptosis, the cells were divided into four groups: (1) the Con group, (2) the GL group, (3) the RSL3 group, in which the cells were treated with RSL3 (0.1 μM) for 12 h under normal conditions, and (4) the RSL3 + GL group, in which the cells were treated with GL for 2 h and subsequently cultured in medium with RSL3. To further verify the relationship between GL and ferroptosis, the cells were grouped as follows: (1) the Con group, (2) the OGD group, (3) the OGD + GL group, and (4) the OGD + RSL3 + GL group, in which the cells were cultured for 9 h with RSL3 and GL and then subjected to OGD treatment. In the Con and OGD group, an equal volume of DMSO was administered.

For the in vitro procedure, RSL3 was dissolved in 1% dimethyl sulfoxide (DMSO) at a concentration of 100 μM for storage and further diluted in medium to the required concentration of 0.1 μM; GL was dissolved in 1% dimethyl DMSO at a concentration of 55 mm for storage and further diluted in medium to the required concentration of 55 μM.

2.3. Cell Viability Assay. An MTT assay was used to evaluate cell viability in vitro. The cell density of the groups was adjusted prior to the cell viability assay, and cells were seeded in 24-well plates at a density of 2×10^4 cells/well. The cells were cultivated for 4 h in medium containing 3-(4,5-dimethylthiazol-2-yl)-2,5-diphenyltetrazolium bromide (0.5 mg/mL) at the indicated time points. The supernatant was aspirated, the cells were suspended in DMSO, and the optical density (OD) was quantified at 490 nm. The cell viability was calculated after quantifying the absorbances in the MTT assay using the following formula: cell viability (%) = OD of treated group/OD of control group × 100.

2.4. Oxidative Stress Analysis. The activity of various oxidative stress indicators, including malondialdehyde (MDA), catalase (CAT), GSH, superoxide dismutase (SOD), Mn-SOD, and Cu/Zn-SOD, in the cortex of the left hemisphere was measured according to the respective reagent manufacturers' protocol and previously described methods [21].

2.5. Determination of ROS Levels. The cells were stained with 10 μM dihydroethidium (DHE), an ROS probe, for 30 min in a dark humidified chamber. After being quickly washed with PBS, the cells were imaged using a fluorescence microscope and analyzed via NIH ImageJ software.

2.6. Hematoxylin and Eosin (HE) Staining and Immunofluorescence Staining. HE staining and immunofluorescence staining were performed according to a method that we have previously described [28]. For HE staining, the brain tissues were cut into coronal sections. Then, the sections were fixed, rinsed, and stained with hematoxylin and eosin, after which they were imaged with a light microscope.

For immunofluorescence staining, coronal sections of brain tissues were washed, blocked, and subsequently incubated overnight with rabbit anti-NeuN (1 : 200 dilution, ab177487, Abcam, USA) or mouse anti-IL-1β (1 : 100; sc-

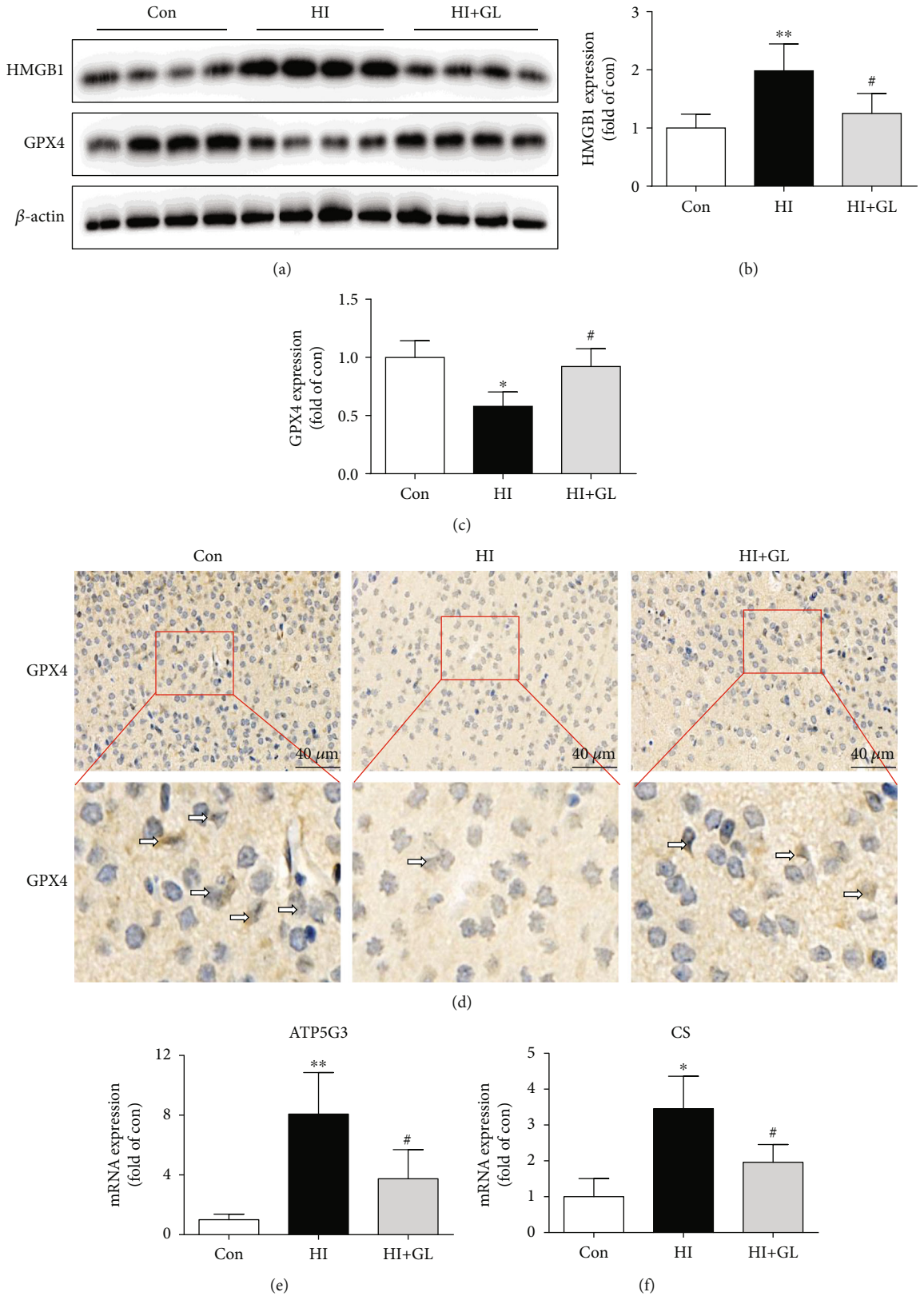

Figure 2: Continued.

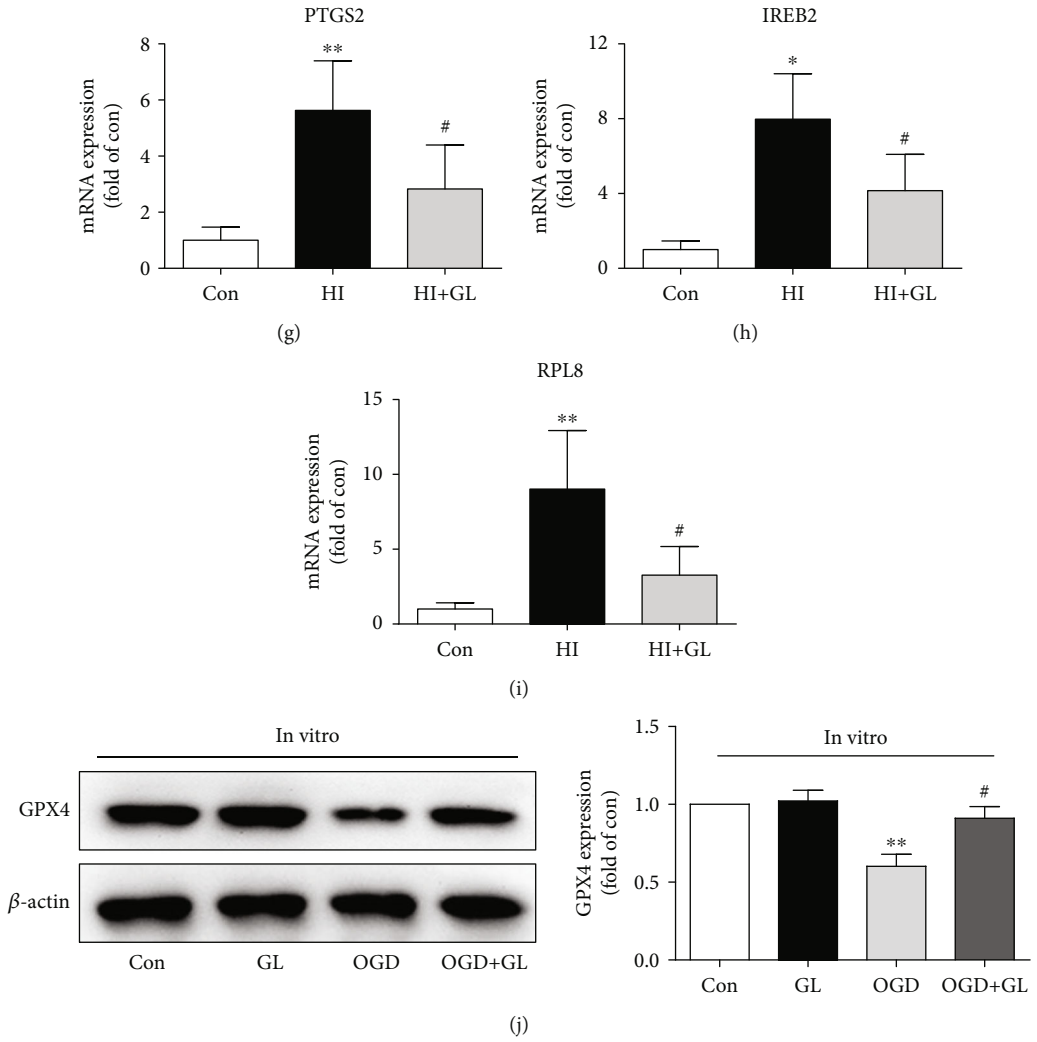

Figure 2: Glycyrrhizin inhibits HI-induced neuronal ferroptosis. (a)–(c) Western blots and average data for HMGB1 and GPX4 in the injured cortex at 72 h after HI ($n = 5$). (d) Representative immunohistochemical images of the GPX4 expression in the cerebral cortex. The arrows indicate GPX4+ cells. (e)–(i) Ferroptosis-related genes, including ATP5G3, CS, PTGS2, IREB2, and RPL8, were analyzed by qPCR ($n = 5$). (j) Western blots and the average data for GPX4 in vitro ($n = 3$). $^{*}P < 0.05$, $^{**}P < 0.01$ vs. the Con group; $\#P < 0.05$ vs. the HI group or OGD group.

32294, Santa Cruz Biotechnology, USA). The following day, the sections were incubated with secondary antibodies and stained with a commercial TUNEL staining kit (Apo Alert DNA Fragmentation Assay kit; Clontech, BD Biosciences, Palo Alto, CA, USA) and diamidino-2-phenylindole (DAPI, 1 : 1000, C1002, Beyotime). The purpose of TUNEL staining is to show apoptotic cells, and the purpose of NeuN staining is to display neurons.

2.7. Reverse Transcription Real-Time Quantitative Polymerase Chain Reaction (RT–qPCR). Total RNA from the injured cortex was isolated using a TRIzol kit (Invitrogen, Thermo Fisher Scientific, USA). RNA (2 μg) was reverse transcribed to complementary DNA (cDNA) using the Reverse Transcription System (Invitrogen, Thermo Fisher Scientific) in accordance with the manufacturer's protocol. RT–PCR was carried out in a 20 μL reaction system containing cDNA SYBR Green Master Mix (TaKaRa, Japan) and specific primers according to the manufacturer's instructions. The primers were designed for ATP5G3, PTGS2, CS, IREB2, and RPL8; the sequences of these primer pairs are listed in Table 1.

2.8. Transmission Electron Microscopy (TEM). Rat brain tissues (2 × 2 mm) from the cortex of the lesioned side were fixed in phosphate-buffered glutaraldehyde (2.5%) and osmium tetroxide (1%), sliced into 50 nm-thick sections, stained with uranium acetate and lead citrate, and finally imaged with a transmission electron microscope (Hitachi HT7700, Japan).

2.9. Western Blot Analysis. The frozen cortex tissue and cell samples were washed twice with ice-cold phosphate buffered saline (PBS) and were completely lysed in ice-cold lysis buffer containing phenylmethanesulfonyl fluoride and phosphatase and protease inhibitors. The total cell lysates were

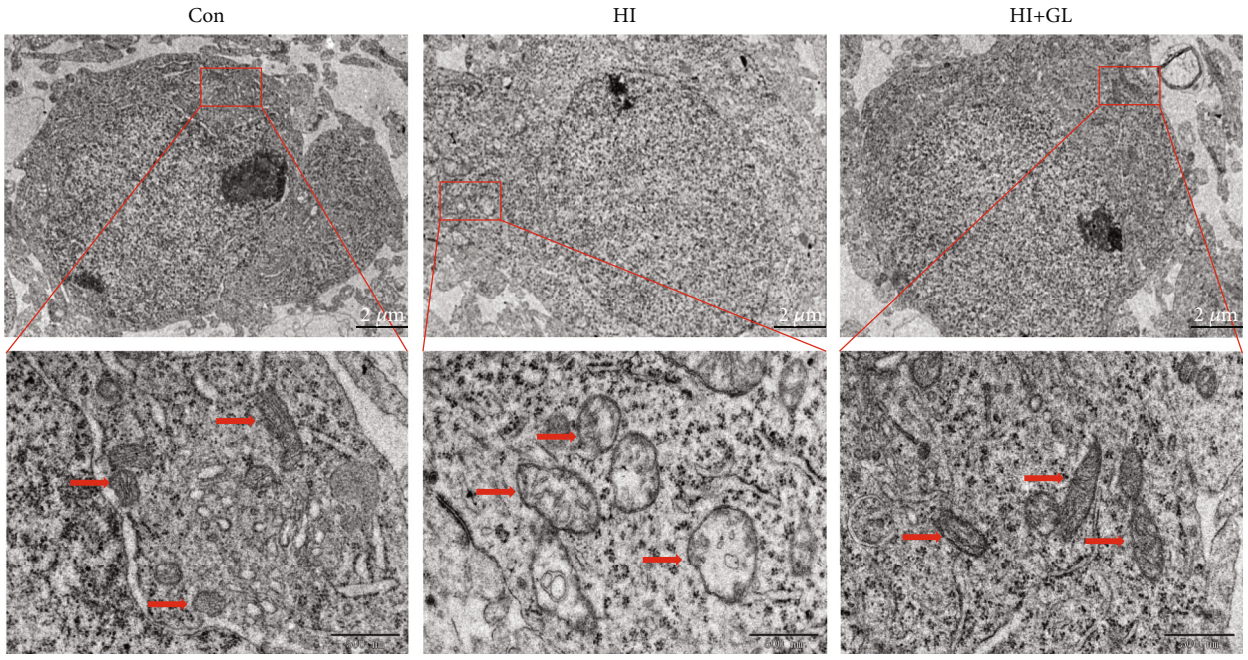

(a)

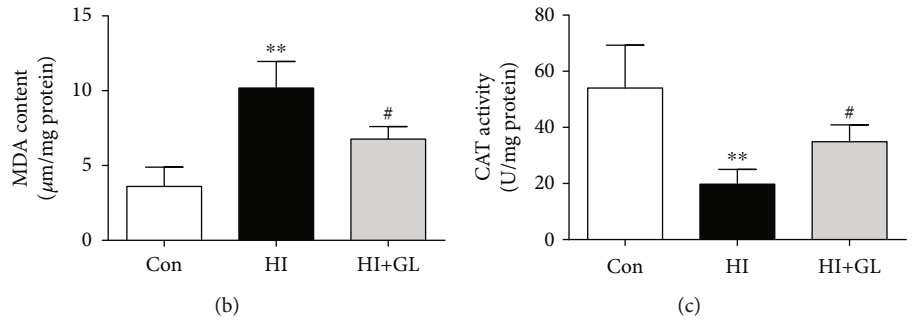

(b)

(c)

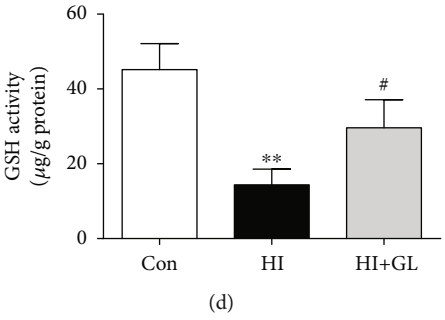

(d)

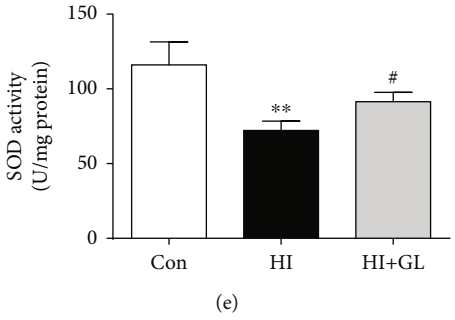

(e)

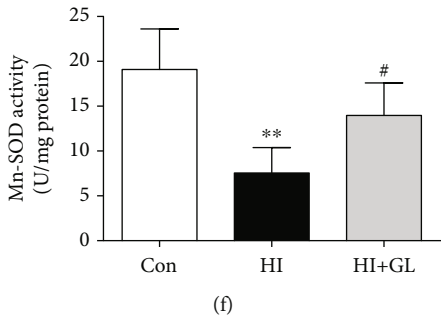

(f)

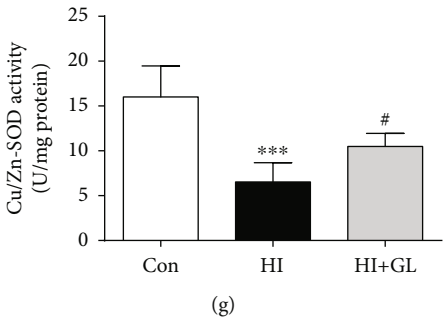

(g)

Figure 3: Continued.

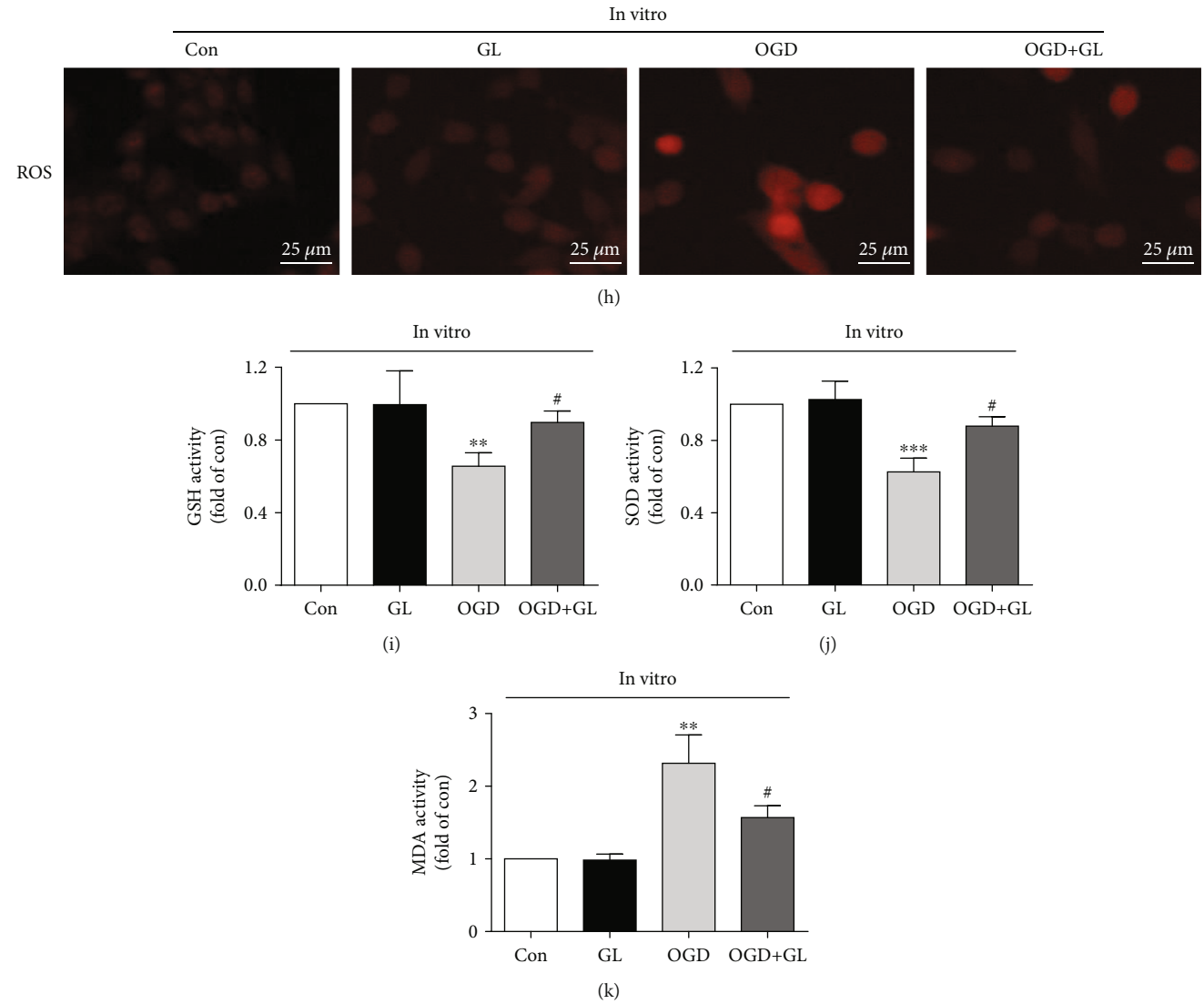

Figure 3: Glycyrrhizin ameliorates HIBD-induced mitochondrial injury and oxidative stress. (a) Representative TEM images of neurons and mitochondria in neurons in the injured cortex. (b)–(g) The level of MDA and the activity levels of CAT, GSH, SOD Mn-SOD, and Cu/Zn-SOD in different groups ($n = 6$). (h) Representative images of DHE (red) staining in cortical neuronal cells. (i)–(k) The levels of GSH, SOD, and MDA in vitro ($n = 4$). $^{**}P < 0.01$, $^{***}P < 0.001$ vs. the Con group; $\#P < 0.05$ vs. the HI group or OGD group.

centrifuged at 12,000 rpm for 20 min at 4°C. Afterward, the supernatant was collected to determine the quantity of protein in the samples with a Pierce BCA Protein Assay Kit. Equal amounts of proteins (10-20 mg) were isolated from the left cortex or primary cortical neurons, separated by SDS–PAGE (12%), and then electrotransferred onto polyvinylidene fluoride (PVDF) membranes. The membranes were blocked, incubated with rabbit anti-HMGB1 (1 : 1000, ab18256, Abcam, USA) and rabbit anti-GPX4 (1 : 1000; ab125066; Abcam, USA), washed, and incubated with secondary antibodies. The proteins were visualized by enhanced chemiluminescence (Pierce, Rockford, IL, USA, #32106) and quantified with NIH ImageJ software.

2.10. Statistical Analysis. Student's *t*-test was used to analyze the difference between two groups, and one-way ANOVA followed by multiple pairwise comparisons with the Bonferroni correction was used to evaluate the differences among more than two groups. A P value <0.05 was defined as statistically significant.

3. Results

3.1. Glycyrrhizin Reduced Cortical Neuronal Loss after HIBD. First, at P10, we observed left cortex neuronal morphology by HE staining. Compared with the Con group, the HI group had sparse, disarranged neurons with shrunken nuclei, and these effects were reduced in the HI + GL group (Figure 1(a)). NeuN immunofluorescence labeling in conjunction with TUNEL staining was performed on neurons to detect neuronal damage (Figures 1(b)–1(d)). In the HI group, the number of NeuN-immunopositive cells in the cortex decreased significantly compared with the Con group, but the number of TUNEL/NeuN-double-positive cells

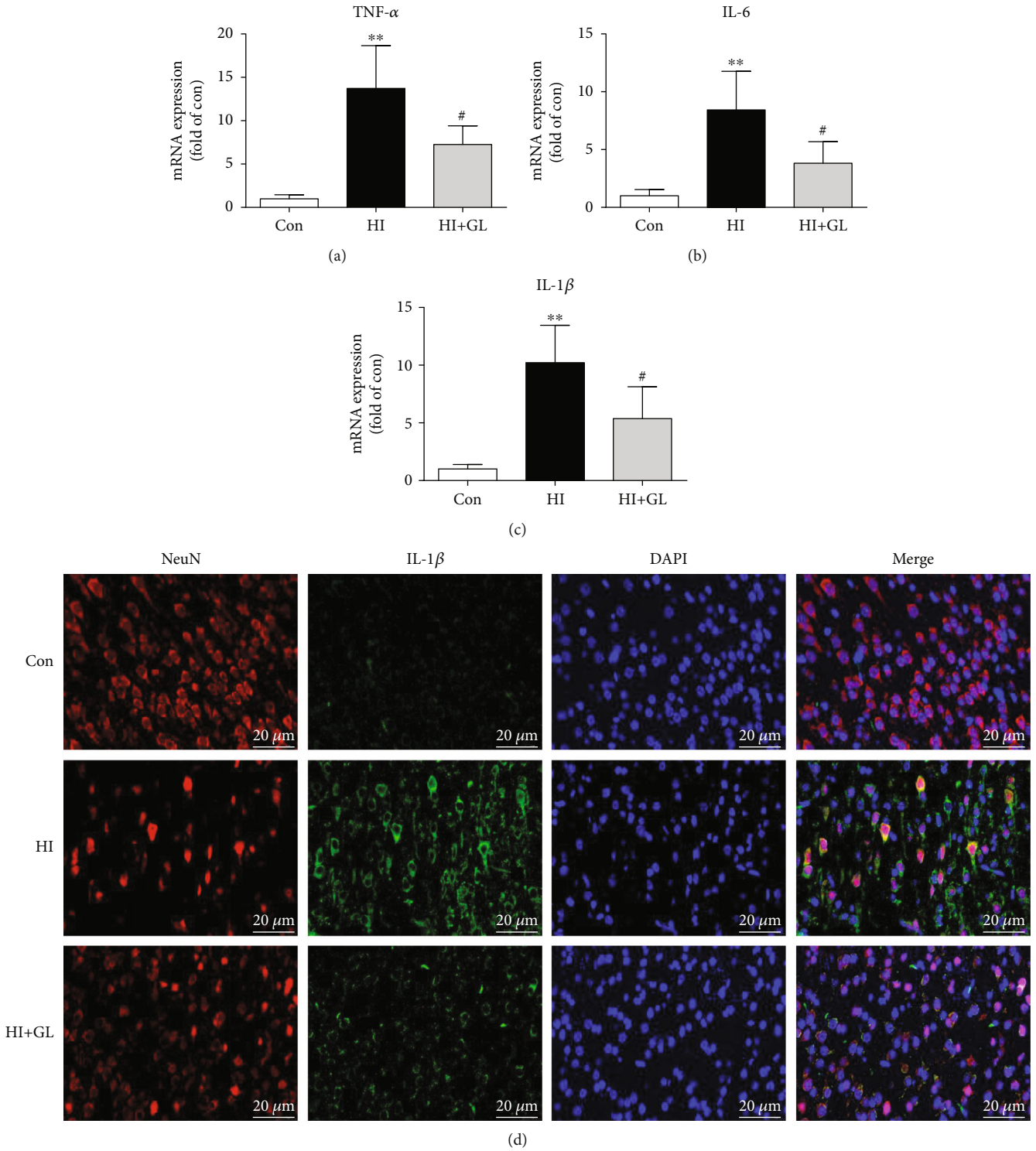

FIGURE 4: Inhibiting HMGB1 alleviates the activation of neuroinflammation. (a)-(c) The proinflammatory cytokines in the injured cortex at 72 h after HI, including TNF-α, IL-6, and IL-1β, were analyzed by qPCR ($n = 5$). (d) Representative immunofluorescence images of the IL-1β expression in cortical neurons. $^{**}P < 0.01$ vs. the Con group; $^{\#}P < 0.05$ vs. the HI group.

increased significantly (Figures 1(b)–1(d)). Treatment with GL after HI induction increased the number of NeuN-positive neurons and reduced the number of TUNEL/NeuN-double-positive cells in the cortex area (Figures 1(b)–1(d)).

To further assess whether GL contributed to the cortical neuron damage induced by OGD at the cellular level in vitro, we assessed the number and viability of cortical neuron. Nuclear staining showed that the number of nuclei decreased in the OGD group and could be rescued in the

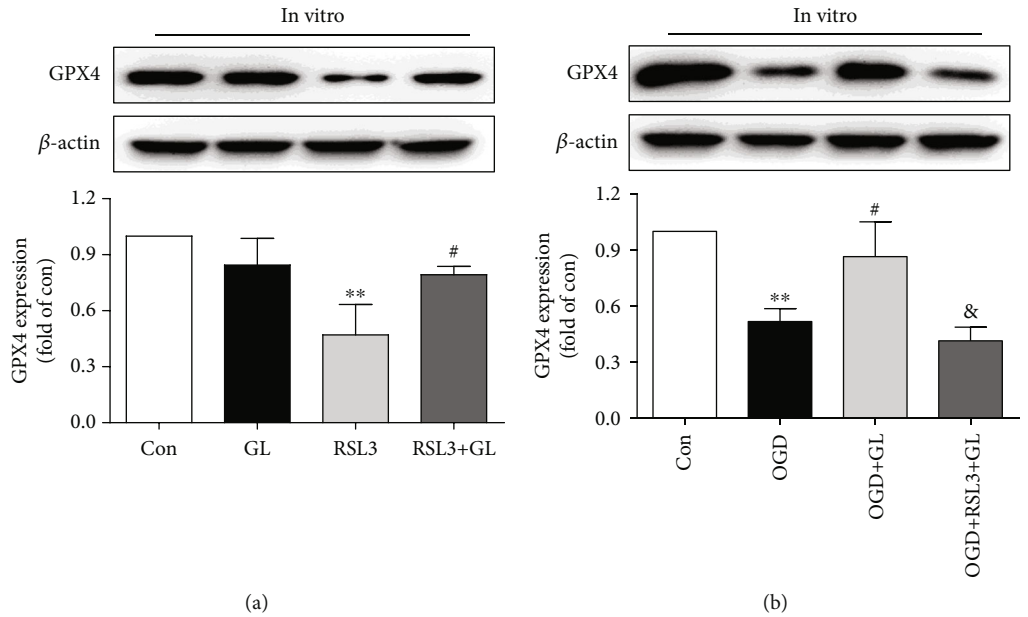

(a) (b)

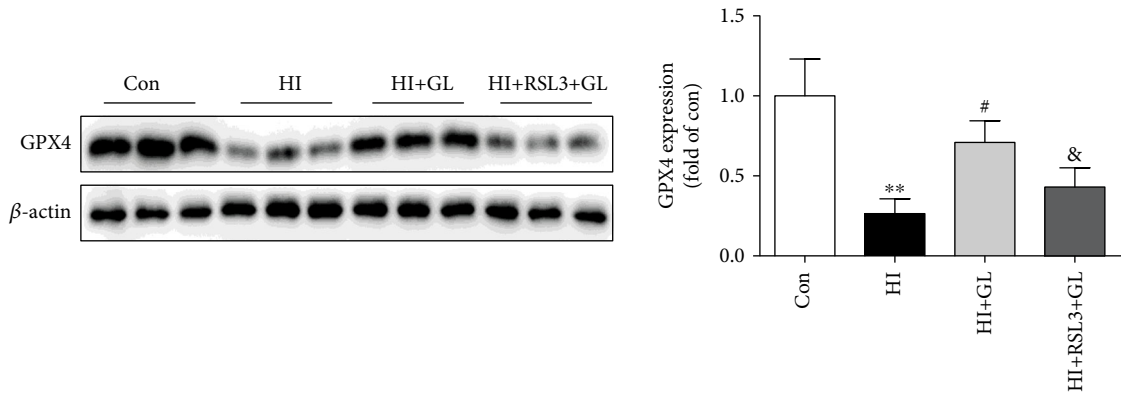

(c)

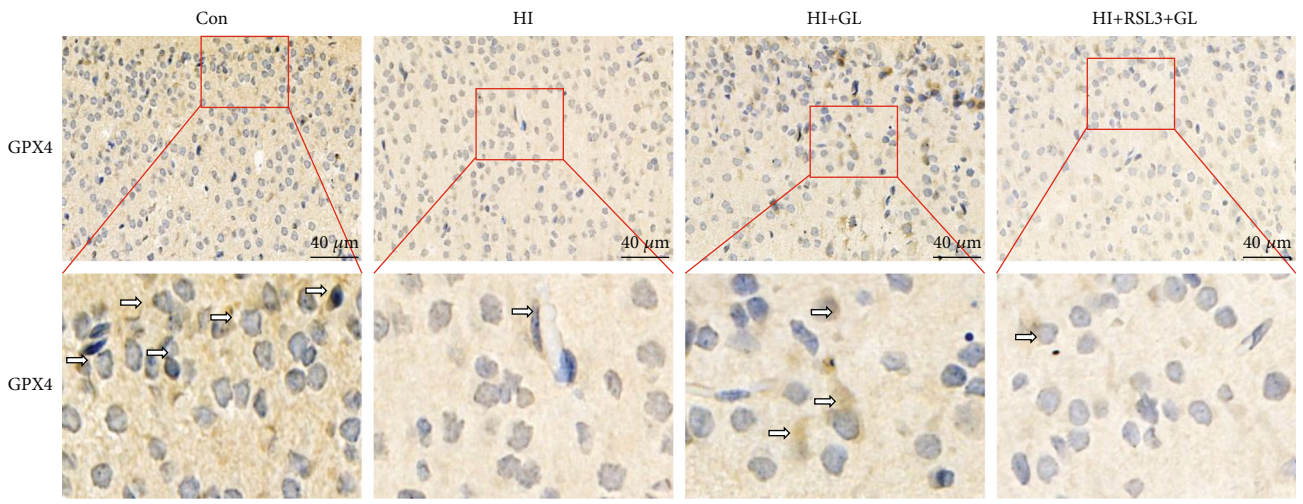

(d)

Figure 5: Continued.

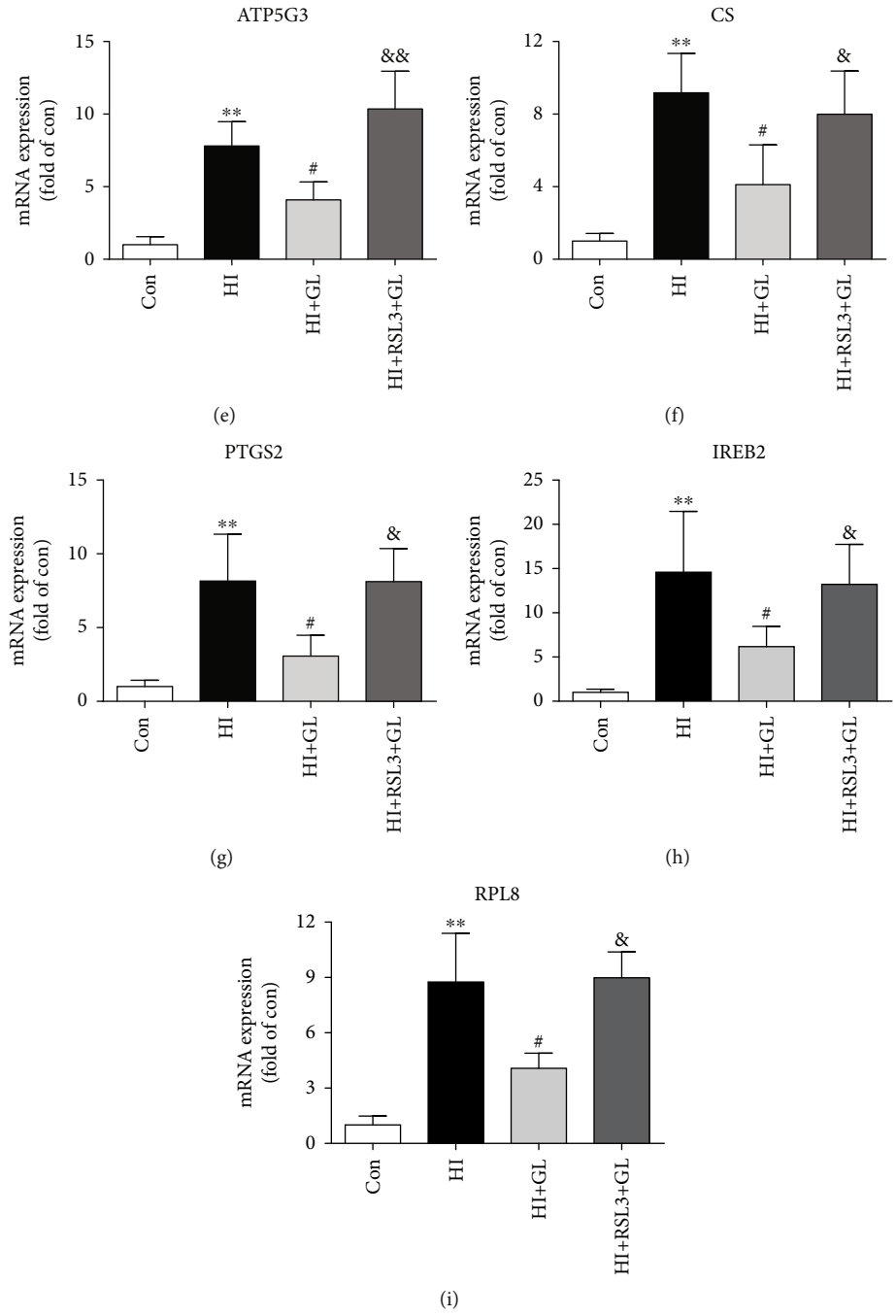

Figure 5: GPX4 inhibition with RSL3 blocked the glycyrrhizin-induced improvement in neuronal ferroptosis following HIBD. (a, b) Western blots and the average data for GPX4 in vitro ($n = 3$). (c) Representative Western blots and the average data of GPX4 in the different in vivo experiments ($n = 6$). (d) Representative immunohistochemical images of the GPX4 expression in the injured cortex at 72 h after HI. (e)–(i) Ferroptosis-related genes, including ATP5G3, CS, PTGS2, IREB2, and RPL8, were analyzed by qPCR ($n = 6$). $^{**}P < 0.01$ vs. the Con group; $\#P < 0.05$ vs. the HI, RSL3 or OGD group; $\&P < 0.05$, $\&\&P < 0.01$ vs. the HI + GL or OGD + GL group.

OGD + GL group (Figure 1(e)). Similar protective effects of GL on OGD-induced cell damage were observed in terms of cell counts and cell viability (Figures 1(f) and 1(g)). These results suggest that inhibiting HMGB1 mitigates cortical neuronal damage after HIBD and OGD.

3.2. HMGB1 Depletion Rescued HI-Induced Neuronal Ferroptosis. To determine whether GL could protect against neuronal damage after HIBD by inhibiting ferroptosis, we next assessed the protein levels of GPX4 and the mRNA levels of ferroptosis-related genes. Western blot analysis revealed that GL markedly suppressed the elevated expression of HMGB1 in HIBD (Figures 2(a) and 2(b)). However, the GPX4 protein expression was significantly reduced following HIBD and restored in the HI + GL group (Figures 2(a) and 2(c)). Similarly, immunohistochemistry

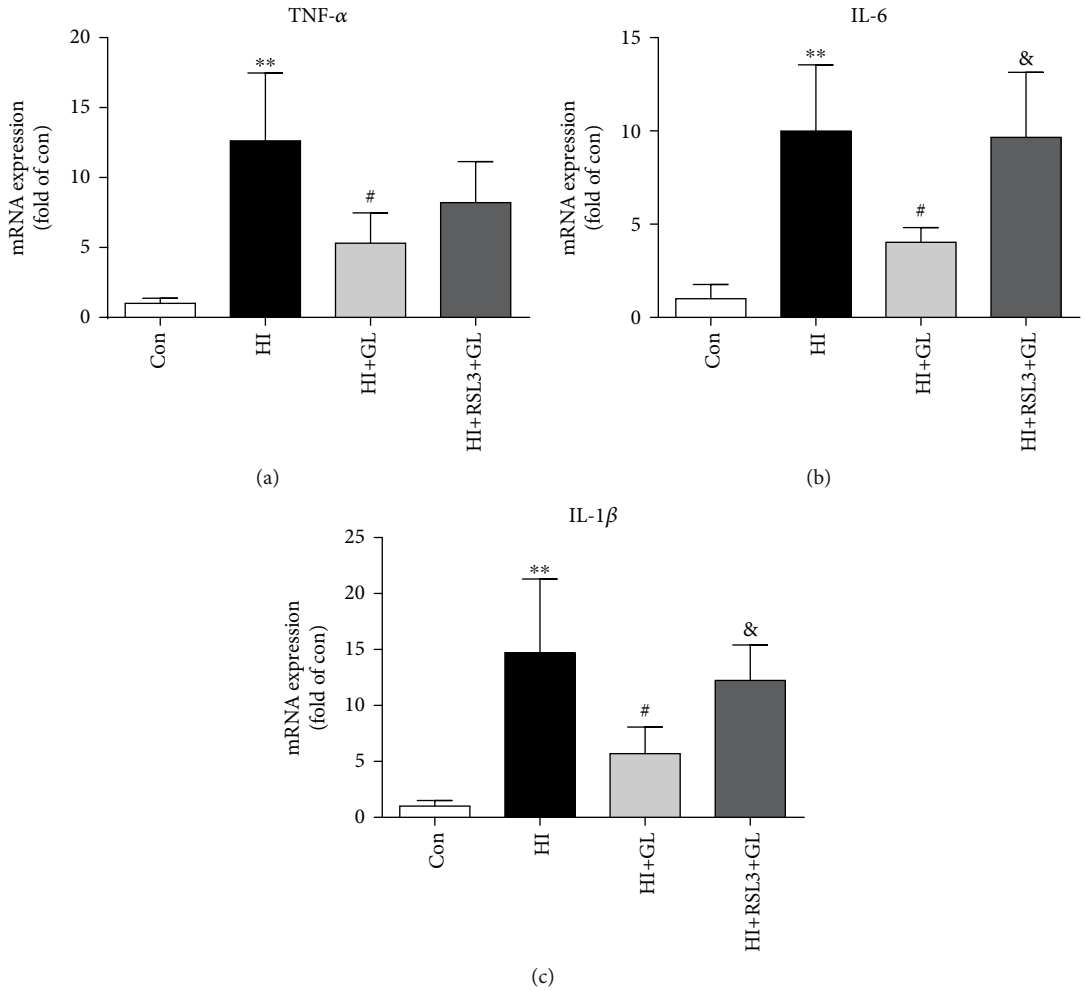

Figure 6: Continued.

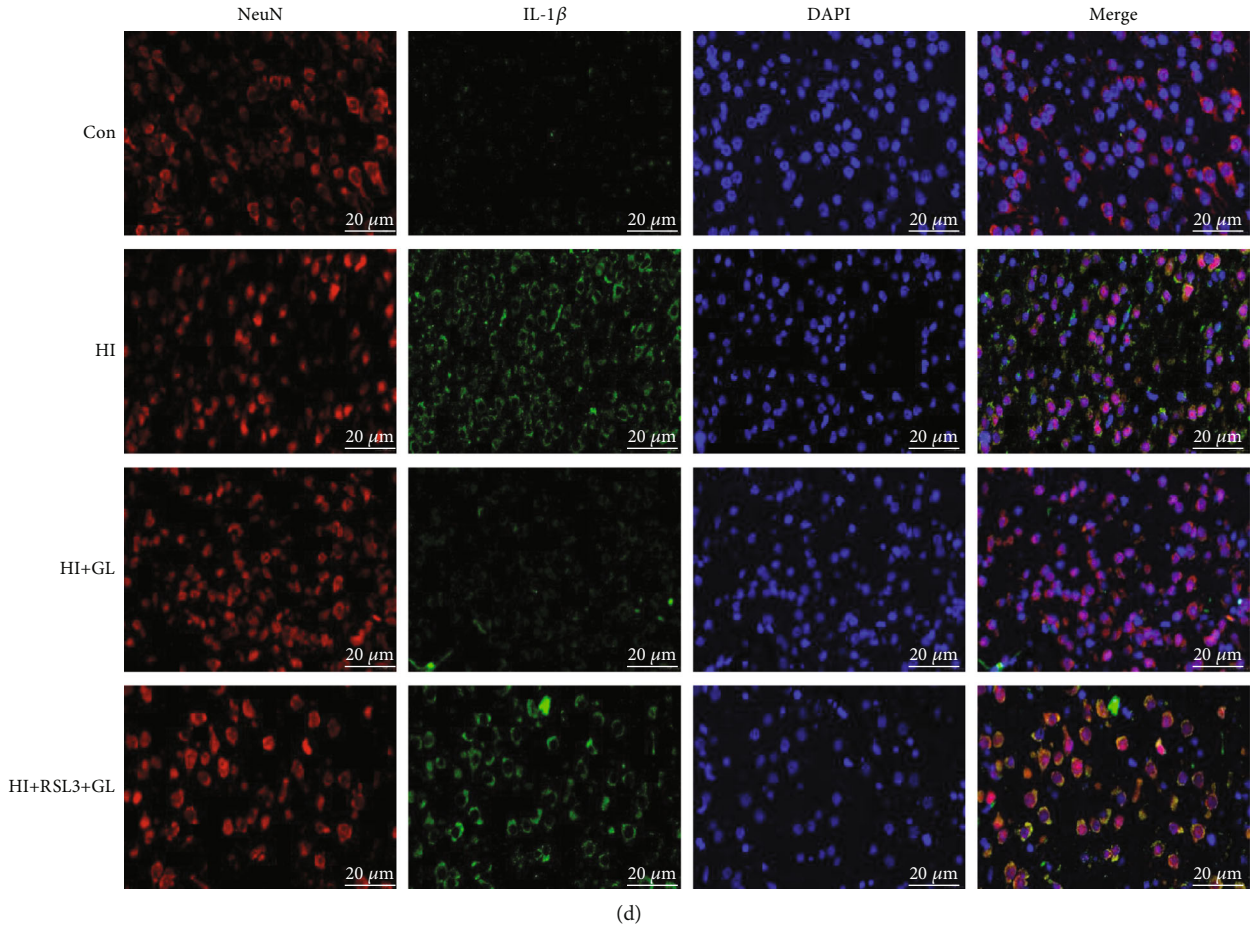

(d)

Figure 6: RSL3 hinders glycyrrhizin in ameliorating the activation of neuroinflammation. (a)–(c) The expression of TNF-α, IL-6, and IL-1β was analyzed by qPCR ($n = 6$). (d) Representative immunofluorescence images of IL-1β and NeuN staining. $^{**}P < 0.01$ vs. the Con group; #$P < 0.05$ vs. the HI group; &$P < 0.05$ vs. the HI + GL group.

verified that GPX4 protein levels were depleted in the HI group and increased following GL injection (Figure 2(d)). The mRNA levels of ferroptosis-related genes, including ATP5G3, CS, PTGS2, IREB2, and RPL8, were increased significantly in the HI group compared with the Con group and markedly reduced compared with the HI + GL group (Figures 2(e)–2(i)). GPX4 protein levels were decreased in the OGD group and improved following GL treatment in vitro (Figure 2(j)). These results show that GL can inhibit not only the expression of HMGB1 but also the occurrence of neuronal ferroptosis in HIBD.

3.3. Glycyrrhizin Ameliorated Mitochondrial Injury and Oxidative Stress Levels in the Cortex following HIBD. To further confirm the occurrence of ferroptosis, we observed the changes in neuronal ultrastructure via TEM. In contrast to the normal mitochondria in the Con group, morphologically abnormal mitochondria were observed in the HI group; these abnormalities were closely associated with ferroptosis, including smaller mitochondria, the disappearance of mitochondrial cristae, mitochondrial swelling, and mitochondrial vacuoles (Figure 3(a)). However, in the HI + GL group, the number of abnormal mitochondria was significantly reduced, and the morphology of abnormal mitochondria was improved (Figure 3(a)). To investigate whether GL protects against neuronal ferroptosis by adjusting the redox balance, the abundance of oxidants and antioxidants was measured in rat cortical tissue. The increase in the MDA level in the HI group was markedly inhibited in the HI + GL group (Figure 3(b)), indicating that tissue oxidative lipid damage was reduced. The activity levels of antioxidative enzymes, including CAT, GSH, SOD, Mn-SOD, and Cu/Zn-SOD, were reduced in the HI group in comparison with the Con group, and these changes were significantly reversed in the HI + GL group (Figures 3(c)–3(g)). Additionally, we measured ROS levels in vitro using DHE. Interestingly, the increase in red fluorescence in the OGD group was clearly mitigated in the OGD + GL group (Figure 3(h)). Furthermore, the results of GSH, SOD, and MDA detection in vitro were similar to the results in vivo (Figures 3(i)–3(k)). Therefore, it is concluded that mitochondrial damage and redox imbalance induced by HIBD or OGD can be rescued with GL; these mechanisms might play a key role in the therapeutic effects of GL on HIBD-induced neuronal ferroptosis.

3.4. Glycyrrhizin Prevents Neuroinflammation after HIBD. To further test the role of GL in HIBD, the relevant

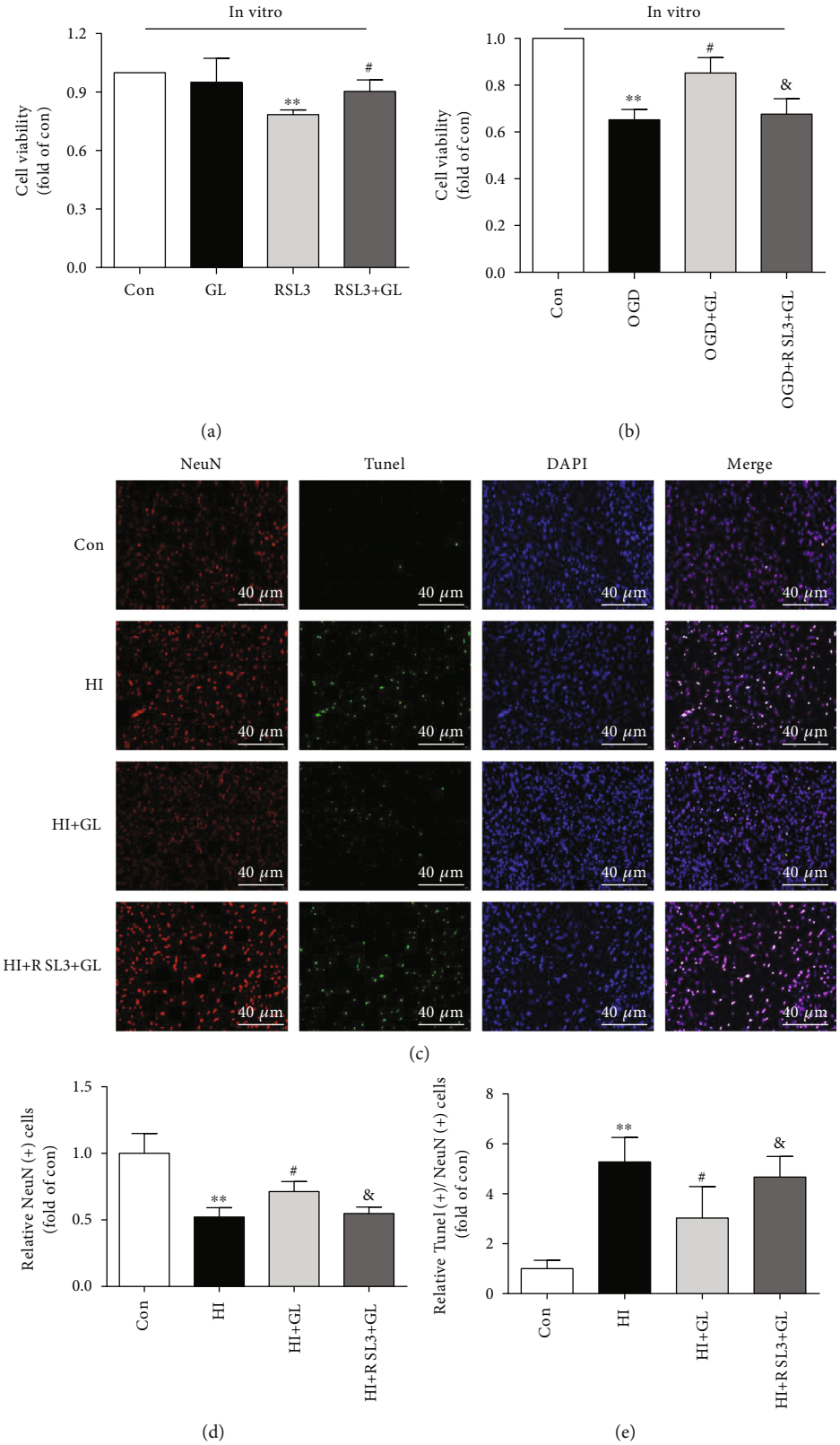

FIGURE 7: HIBD-induced cortical neuronal loss can be alleviated by glycyrrhizin via the GPX4 axis. (a) The cell death induced by RSL3 was evaluated using the MTT assay ($n = 4$). (b) GL increased the viability of cortical neurons subjected to OGD ($n = 4$). (c) Representative immunofluorescent images of TUNEL and NeuN staining in the injured cortex at 72 h after HI ($n = 6$). (d) The statistical analysis of NeuN (+) cell counts ($n = 6$). (e) The average data for TUNEL (+)/NeuN (+) cell counts ($n = 6$). $^{**}P < 0.01$ vs. the Con group; $\#P < 0.05$ vs. the HI, RSL3 or OGD group; $\&P < 0.05$ vs. the HI + GL or OGD + GL group.

inflammatory factors TNF-α, IL-6, and IL-1β were detected by qRT–PCR. The results indicated that the levels of TNF-α, IL-6, and IL-1β were significantly increased at 72 h following HIBD in the injured cortex, which was obviously suppressed by GL treatment (Figures 4(a)–4(c)). Furthermore, the immunofluorescence of the IL-1β expression in injured cortical neurons further suggested that there was a significant decrease in the expression of IL-1β in the HI + GL group compared with the HI group (Figure 4(d)).

3.5. Glycyrrhizin Improves Neuronal Ferroptosis through the GPX4 Axis. To further verify that GL reduces HIBD-induced neuronal damage by inhibiting neuronal ferroptosis, RSL3, a ferroptosis inducer and an inactivator of GPX4, was used in the in vivo and in vitro experiments. Interestingly, we found that RSL3-induced downregulation of GPX4 in vitro could be rescued by GL in the RSL3 + GL group (Figure 5(a)). Furthermore, OGD-induced GPX4 inhibition was improved in the OGD + GL group, and this improvement was attenuated by RSL3 in the OGD + GL + RSL3 group (Figure 5(b)). In vivo, we found that GL treatment restored the GPX4 level to normal after HIBD, while treatment with RSL3 reversed this effect (Figure 5(c)). Consistently, compared with the HI + GL group, the expression of GPX4 in immunohistochemistry of the injured cortex was suppressed by RSL3 in the HI + GL + RSL3 group (Figure 5(d)). Additionally, the RT–qPCR results revealed that compared with the HI + GL group, the mRNA levels of ATP5G3, CS, PTGS2, IREB2, and RPL8 were significantly increased in the HI + GL + RSL3 group (Figures 5(e)–5(i)). These findings suggest that inhibiting HMGB1 alleviates neuronal ferroptosis via the GPX4 signaling pathway.

3.6. RSL3 Impedes GL to Ameliorate Neuroinflammation in HIBD. Subsequently, we test whether GL exerts a protective effect by suppressing ferroptosis-induced inflammation. There was no significant difference in TNF-α levels between the HI + GL group and the HI + GL + RSL3 group (Figure 6(a)). Compared with the HI + GL group, however, the HI + GL + RSL3 group had a significant increase in the levels of IL-6 and IL-1β in the injured cortex (Figures 6(b) and 6(c)). Moreover, the ferroptosis-related inflammatory product IL-1β was also indicated by the immunofluorescence results, which showed that IL-1β was more highly expressed in the cortical neurons of the HI + GL + RSL3 group than in those of the HI + GL group (Figure 6(d)).

3.7. Glycyrrhizin Improves Cortical Neuronal Loss Related to Ferroptosis through the GPX4 Axis. To further investigate the protective effect of GL on OGD-induced cell death via ferroptosis, we assessed cell viability by MTT in vitro. First, RSL3 significantly reduced cell viability in vitro, and GL ameliorated RSL3-induced cytotoxicity (Figure 7(a)). Furthermore, GL treatment improved cell viability following OGD, while treatment with RSL3 reversed this effect (Figure 5(b)). In addition, TUNEL staining and immunohistochemical neuronal staining were jointly performed to further verify that GL rescued HIBD-induced neuronal damage through ferroptosis related to the GPX4 axis (Figure 7(c)). The number of NeuN-immunopositive cells in the cortex was significantly decreased in the HI + GL + RSL3 group compared with the HI + GL group (Figures 7(c) and 7(d)). However, there were more TUNEL/NeuN-double-positive cells in the HI + GL + RSL3 group than in the HI + GL group (Figures 7(c) and 7(e)). Therefore, these results indicate that GL downregulates the level of neuronal ferroptosis by promoting the GPX4 expression, and that this effect of GL can improve cortical neuronal loss in HIBD and OGD.

4. Discussion

With limited treatment options, HIBD remains an imposing clinical problem and is particularly closely related to the quality of life of newborns [29]. Previous studies have demonstrated that the exhaustion of brain cell energy production, oxidative stress injury, mitochondrial damage, and inflammation leads to the occurrence and development of cell damage in HIBD [26, 29–31]. However, the specific mechanism of neuronal damage in HIBD is unclear.

HMGB1, a damage-associated molecule, can stimulate and amplify inflammatory responses and ultimately induce the loss of neurons in HIBD [30]. In previous studies, HMGB1 was released from cells beginning 6 h after HI; this molecule is considered a sensitive marker of HIBD in neonates [24]. Recent studies have shown that HMGB1 inhibition can reduce infarct size and ameliorate neurobehavioral impairments in neonatal HIBD, suggesting that GL can be used as a neuroprotective agent for the treatment of HIBD [26, 30]. In our study, we further observed that inhibiting HMGB1 with GL could significantly reduce the amount of neuronal death and ameliorate cortical neuronal loss in HIBD by suppressing ferroptosis.

Ferroptosis is a recently discovered form of necrotic cell death that is characterized by the iron-dependent accumulation of ROS [32]. Dysregulation of ferroptosis is closely associated with various diseases, including cancer, ischemia–reperfusion injury, Parkinson's disease, stroke, and neurodegeneration [32, 33]. Our recent research has also shown an intimate link between HIBD and ferroptosis [15]. The characteristics of ferroptosis are iron-dependent ROS accumulation, inflammation, and mitochondria-dependent damage within the cell, which are also the underlying pathogeneses of HIBD [4, 5, 20, 34, 35]. In the current study, we investigated the effect of GL on oxidative stress levels, mitochondrial damage, and neuroinflammation in HIBD. The results indicated that these injuries, including increased MDA levels; decreased CAT, GSH, SOD, Mn-SOD, and Cu/Zn-SOD levels; increased expression of ferroptosis-related genes, including ATP5G3, CS, PTGS2, IREB2, and RPL8; and induced mitochondrial damage and neuroinflammation in the HIBD rat model, could be alleviated by GL administration; these effects were accompanied by a decrease in neuronal ferroptosis. These findings further show that GL may play a neuroprotective role in HIBD as a ferroptosis inhibitor.

Ferroptosis inhibitors, including ferrostatin-1 and liproxstatin-1, have been demonstrated to have a protective

effect in the transient middle cerebral artery occlusion model of ischemic stroke in mice and rats and in intracerebral hemorrhage in mice [18, 21]. Owing to the difficulty of delivering these two ferroptosis inhibitors across the blood–brain barrier, their clinical applications to CNS diseases are limited [18, 21]. GL, a major constituent of licorice root, has been demonstrated to pass through the blood–brain barrier and exert a neuroprotective effect when administered by intraperitoneal injection [22]. The protective effect of GL against mitochondrial injury and oxidative stress has also been confirmed in pathological conditions [36]. GL may be associated with the improvement of mitochondrial electron transfer chain activity, transmembrane potential, and decreased aconitase activity in the tricarboxylic acid cycle, which, in turn, decreases the formation of ROS and results in the improvement of mitochondrial function [36–38]. The present study demonstrated that GL not only inhibited ferroptosis induced by RSL3 and OGD in vitro but also inhibited ferroptosis induced by HIBD in vivo. More importantly, GL may improve oxidative stress imbalance and mitochondrial damage, alleviate their downstream inflammatory factors, and ultimately reduce ferroptosis and damage to cortical neurons following HIBD by regulating the expression of HMGB1 and GPX4. Therefore, these findings provide conclusive evidence that GL may inhibit RSL3- and HIBD-induced ferroptosis and reveal the potential of GL to treat diseases that are characterized by ferroptosis, including HIBD.

To date, research has shown that ferroptosis can be controlled by GPX4 and radical-trapping antioxidants [39]. GPX4 is an essential regulator that scavenges lipid peroxides under oxidative stress [40]. Reduced GSH is exploited by the antioxidant enzyme GPX4 to convert phospholipid hydroperoxides to lipid alcohols [33]. Inactivation of GPX4 promotes excessive lipid peroxide formation and results in mitochondrial damage, which plays an important role in the occurrence of ferroptosis [9, 41]. RSL3 drives ferroptosis by binding and inactivating GPX4 [42]. To elucidate the function and mechanism of HMGB1 and ferroptosis, we further analyzed the effects of RSL3 and GL on the activation of GPX4 and neuronal damage. We found that the expression of GPX4 was increased by GL in HIBD; however, this effect did not occur in the presence of RSL3 in rats subjected to HI. Furthermore, GPX4 inhibition using RSL3 eliminated GL-mediated amelioration of neuronal damage, improvement of neuronal ferroptosis, and reduction of neuroinflammation in HIBD rats. Taken together, these findings further demonstrate that GL improves neuronal loss, ameliorates mitochondrial damage, and reduces neuroinflammation following HIBD by inhibiting neuronal ferroptosis through the HMGB1/GPX4 pathway.

One limitation of our study is that we showed only the connection between HMGB1 and neuronal ferroptosis; the other modes of neuronal death, including apoptosis, autophagy, and pyroptosis, were not examined here. Another possible limitation is that this experiment focused on the acute phase of HIBD (72 h) and did not observe the long-term effect. GL is considered an HMGB1 inhibitor and can also inhibit superoxide, NO, and ONOO- production, helping to reduce HMGB1 and confer neuroprotection in ischemic brain injury [43]. Our research confirmed that GL can suppress MDA levels and increase the levels of CAT, GSH, SOD, Mn-SOD, and Cu/Zn-SOD, which implies that the neuroprotective effects of GL in reducing ferroptosis could also be attributable to its antioxidant activity in HIBD. Therefore, the antioxidant activity and inhibition of HMGB1 are both involved in the suppression of ferroptosis by GL in HIBD. The functions of antioxidant activity and HMGB1 inhibition may simultaneously exist. However, in this study, we did not further investigate whether antioxidant activity or HMGB1 inhibition plays a more important role in the regulation of ferroptosis by GL in HIBD. Finally, this study merely indicated the effect of HMGB1 inhibition on neuronal ferroptosis by pharmacological approaches and perspectives and did not explore the deeper mechanisms apart from the GPX4 signaling pathway. Therefore, these limitations need to be further addressed in subsequent research.

5. Conclusion

In summary, we indicated for the first time that GL could suppress the occurrence of neuronal ferroptosis, inhibit oxidative stress, reduce mitochondrial damage, and ameliorate neuroinflammation in HIBD via the HMGB1/GPX4 pathway. Collectively, these findings highlight the potential of HMGB1 signaling antagonists to treat neuronal damage by suppressing ferroptosis, provide new and unique insights into GL as a neuroprotective agent and a ferroptosis inhibitor, and suggest new prevention and treatment strategies for diseases featuring ferroptosis, especially HIBD.

Data Availability

The data that support the findings of this study are available from the corresponding author upon reasonable request.

Ethical Approval

All experimental procedures and protocols were reviewed and approved by the Animal Investigation Ethics Committee of Capital Medical University, Beijing, and were performed in accordance with the Guidelines for the Chinese Experimental Animal Administration Legislation.

Conflicts of Interest

The authors declare no competing interests.

Acknowledgments

We are truly grateful to all the members of the MOH Key Laboratory of Geriatrics for their technical support and valuable suggestions for the study. This work was supported by grants from the Natural Scientific Foundation of Beijing (7192061) and Newborn Young Doctors Scientific Research Fund (Z-2019-41-2101-04).

References

[1] W.-d. Luo, J. W. Min, W. X. Huang et al., "Vitexin reduces epilepsy after hypoxic ischemia in the neonatal brain via inhibition of NKCC1," *Journal of Neuroinflammation*, vol. 15, no. 1, p. 186, 2018.

[2] X.-B. Lan, Q. Wang, J.-M. Yang et al., "Neuroprotective effect of vanillin on hypoxic-ischemic brain damage in neonatal rats," *Biomedicine & Pharmacotherapy*, vol. 118, article 109196, 2019.

[3] C. Dai, Y. Liu, and Z. Dong, "Tanshinone I alleviates motor and cognitive impairments via suppressing oxidative stress in the neonatal rats after hypoxic-ischemic brain damage," *Molecular Brain*, vol. 10, no. 1, p. 52, 2017.

[4] J.-J. Zhu, B.-Y. Yu, X.-K. Huang et al., "Neferine protects against hypoxic-ischemic brain damage in neonatal rats by suppressing NLRP3-mediated inflammasome activation," *Oxidative Medicine and Cellular Longevity*, vol. 2021, Article ID 6654954, 19 pages, 2021.

[5] W. Wei, M. Lu, X.-B. Lan et al., "Neuroprotective effects of oxymatrine on PI3K/Akt/mTOR pathway after hypoxic-ischemic brain damage in neonatal rats," *Frontiers in Pharmacology*, vol. 12, article 642415, 2021.

[6] Y. Liu, Y. Wang, J. Liu, R. Kang, and D. Tang, "The circadian clock protects against ferroptosis-induced sterile inflammation," *Biochemical and Biophysical Research Communications*, vol. 525, no. 3, pp. 620–625, 2020.

[7] I. Alim, J. T. Caulfield, Y. Chen et al., "Selenium drives a transcriptional adaptive program to block ferroptosis and treat stroke," *Cell*, vol. 177, no. 5, pp. 1262–1279.e25, 2019.

[8] B. S. Xie, Y. Q. Wang, Y. Lin et al., "Inhibition of ferroptosis attenuates tissue damage and improves long-term outcomes after traumatic brain injury in mice," *CNS Neuroscience & Therapeutics*, vol. 25, no. 4, pp. 465–475, 2019.

[9] A. Jelinek, L. Heyder, M. Daude et al., "Mitochondrial rescue prevents glutathione peroxidase-dependent ferroptosis," *Free Radical Biology and Medicine*, vol. 117, pp. 45–57, 2018.

[10] Z. Wang, Y. Ding, X. Wang et al., "Pseudolaric acid B triggers ferroptosis in glioma cells via activation of Nox4 and inhibition of xCT," *Cancer Letters*, vol. 428, pp. 21–33, 2018.

[11] S. Doll, B. Proneth, Y. Y. Tyurina et al., "ACSL4 dictates ferroptosis sensitivity by shaping cellular lipid composition," *Nature Chemical Biology*, vol. 13, no. 1, pp. 91–98, 2017.

[12] X. Guan, X. Li, X. Yang et al., "The neuroprotective effects of carvacrol on ischemia/reperfusion-induced hippocampal neuronal impairment by ferroptosis mitigation," *Life Sciences*, vol. 235, article 116795, 2019.

[13] B. Lan, J. W. Ge, S. W. Cheng et al., "Extract of Naotaifang, a compound Chinese herbal medicine, protects neuron ferroptosis induced by acute cerebral ischemia in rats," *Journal of Integrative Medicine*, vol. 18, no. 4, pp. 344–350, 2020.

[14] S. J. Dixon, K. M. Lemberg, M. R. Lamprecht et al., "Ferroptosis: an iron-dependent form of nonapoptotic cell death," *Cell*, vol. 149, no. 5, pp. 1060–1072, 2012.

[15] K. Zhu, X. Zhu, S. Sun et al., "Inhibition of TLR4 prevents hippocampal hypoxic-ischemic injury by regulating ferroptosis in neonatal rats," *Experimental Neurology*, vol. 345, article 113828, 2021.

[16] Y. Sun, P. Chen, B. Zhai et al., "The emerging role of ferroptosis in inflammation," *Biomedicine & Pharmacotherapy = Biomedecine & pharmacotherapie*, vol. 127, no. 110108, p. 110108, 2020.

[17] H. Imai, M. Matsuoka, T. Kumagai, T. Sakamoto, and T. Koumura, "Lipid peroxidation-dependent cell death regulated by GPx4 and ferroptosis," *Current Topics in Microbiology and Immunology*, vol. 403, pp. 143–170, 2017.

[18] Q. Li, X. Han, X. Lan et al., "Inhibition of neuronal ferroptosis protects hemorrhagic brain," *JCI Insight*, vol. 2, no. 7, article e90777, 2017.

[19] E. M. Kenny, E. Fidan, Q. Yang et al., "Ferroptosis contributes to neuronal death and functional outcome after traumatic brain injury," *Neurologic Critical Care*, vol. 47, no. 3, pp. 410–418, 2019.

[20] Z. Gou, X. Su, X. Hu et al., "Melatonin improves hypoxic-ischemic brain damage through the Akt/Nrf2/Gpx4 signaling pathway," *Brain Research Bulletin*, vol. 163, pp. 40–48, 2020.

[21] Q. Z. Tuo, P. Lei, K. A. Jackman et al., "Tau-mediated iron export prevents ferroptotic damage after ischemic stroke," *Molecular Psychiatry*, vol. 22, no. 11, pp. 1520–1530, 2017.

[22] S. W. Mu, Y. Dang, Y. C. Fan et al., "Effect of HMGB1 and RAGE on brain injury and the protective mechanism of glycyrrhizin in intracranial-sinus occlusion followed by mechanical thrombectomy recanalization," *International Journal of Molecular Medicine*, vol. 44, no. 3, pp. 813–822, 2019.

[23] F. Ye, W. Chai, M. Xie et al., "HMGB1 regulates erastin-induced ferroptosis via RAS-JNK/p38 signaling in HL-60/NRAS^{Q61L} cells," *American Journal of Cancer Research*, vol. 9, no. 4, pp. 730–739, 2019.

[24] X. Chen, J. Zhang, B. Kim et al., "High-mobility group box-1 translocation and release after hypoxic ischemic brain injury in neonatal rats," *Experimental Neurology*, vol. 311, pp. 1–14, 2019.

[25] L. Yang, F. Wang, L. Yang et al., "HMGB1 a-box reverses brain edema and deterioration of neurological function in a traumatic brain injury mouse model," *Cellular Physiology and Biochemistry*, vol. 46, no. 6, pp. 2532–2542, 2018.

[26] Y. Sun, M. Hei, Z. Fang, Z. Tang, B. Wang, and N. Hu, "High-mobility group box 1 contributes to cerebral cortex injury in a neonatal hypoxic-ischemic rat model by regulating the phenotypic polarization of microglia," *Frontiers in Cellular Neuroscience*, vol. 13, p. 506, 2019.

[27] J. E. Rice, R. C. Vannucci, and J. B. Brierley, "The influence of immaturity on hypoxic-ischemic brain damage in the rat," *Annals of Neurology*, vol. 9, no. 2, pp. 131–141, 1981.

[28] Z. Tang, S. Cheng, Y. Sun et al., "Early TLR4 inhibition reduces hippocampal injury at puberty in a rat model of neonatal hypoxic-ischemic brain damage via regulation of neuroimmunity and synaptic plasticity," *Experimental Neurology*, vol. 321, article 113039, 2019.

[29] Y. Cao, H. Liu, J. Zhang, and Y. Dong, "Circular RNA cZNF292 silence alleviates OGD/R-induced injury through up-regulation of miR-22 in rat neural stem cells (NSCs)," *Artificial Cells, Nanomedicine, and Biotechnology*, vol. 48, no. 1, pp. 594–601, 2020.

[30] K. Le, S. Wu, E. Chibaatar, A. I. Ali, and Y. Guo, "Alarmin HMGB1 plays a detrimental role in hippocampal dysfunction caused by hypoxia-ischemia insult in neonatal mice: evidence from the application of the HMGB1 inhibitor glycyrrhizin," *ACS Chemical Neuroscience*, vol. 11, no. 6, pp. 979–993, 2020.

[31] W. Jiang, M. Guo, M. Gong et al., "Vitamin a bio-modulates apoptosis via the mitochondrial pathway after hypoxic-

ischemic brain damage," *Molecular Brain*, vol. 11, no. 1, p. 14, 2018.

[32] Y. Li, D. Feng, Z. Wang et al., "Ischemia-induced ACSL4 activation contributes to ferroptosis-mediated tissue injury in intestinal ischemia/reperfusion," *Cell Death and Differentiation*, vol. 26, no. 11, pp. 2284–2299, 2019.

[33] H. Lee, F. Zandkarimi, Y. Zhang et al., "Energy-stress-mediated AMPK activation inhibits ferroptosis," *Nature Cell Biology*, vol. 22, no. 2, pp. 225–234, 2020.

[34] E. Park and S. W. Chung, "ROS-mediated autophagy increases intracellular iron levels and ferroptosis by ferritin and transferrin receptor regulation," *Cell Death and Disease*, vol. 10, no. 11, p. 822, 2019.

[35] S. Wei, T. Qiu, X. Yao et al., "Arsenic induces pancreatic dysfunction and ferroptosis via mitochondrial ROS- autophagy-lysosomal pathway," *Journal of Hazardous Materials*, vol. 384, article 121390, 2020.

[36] R. Sil and A. S. Chakraborti, "Oxidative inactivation of liver mitochondria in high fructose diet-induced metabolic syndrome in rats: effect of glycyrrhizin treatment," *Phytotherapy Research : PTR*, vol. 30, no. 9, pp. 1503–1512, 2016.

[37] W. Li, Y. Li, X. Jiang, X. Li, and Z. Yu, "Compound ammonium glycyrrhizin protects hepatocytes from injury induced by lipopolysaccharide/florfenicol through a mitochondrial pathway," *Molecules*, vol. 23, no. 9, p. 2378, 2018.

[38] Q. Tang, Y. Cao, W. Xiong et al., "Glycyrrhizic acid exerts protective effects against hypoxia/reoxygenation-induced human coronary artery endothelial cell damage by regulating mitochondria," *Experimental and Therapeutic Medicine*, vol. 20, no. 1, pp. 335–342, 2020.

[39] S. Doll, F. P. Freitas, R. Shah et al., "FSP1 is a glutathione-independent ferroptosis suppressor," *Nature*, vol. 575, no. 7784, pp. 693–698, 2019.

[40] X. Chen, S. Xu, C. Zhao, and B. Liu, "Role of TLR4/NADPH oxidase 4 pathway in promoting cell death through autophagy and ferroptosis during heart failure," *Biochemical and Biophysical Research Communications*, vol. 516, no. 1, pp. 37–43, 2019.

[41] S. Tsurusaki, Y. Tsuchiya, T. Koumura et al., "Hepatic ferroptosis plays an important role as the trigger for initiating inflammation in nonalcoholic steatohepatitis," *Cell Death and Disease*, vol. 10, no. 6, 2019.

[42] X. Sui, R. Zhang, S. Liu et al., "RSL3 drives ferroptosis through GPX4 inactivation and ROS production in colorectal cancer," *Frontiers in Pharmacology*, vol. 9, p. 1371, 2018.

[43] H. Chen, B. Guan, B. Wang et al., "Glycyrrhizin prevents hemorrhagic transformation and improves neurological outcome in ischemic stroke with delayed thrombolysis through targeting peroxynitrite-mediated HMGB1 signaling," *Translational Stroke Research*, vol. 11, no. 5, pp. 967–982, 2020.

Hindawi
Oxidative Medicine and Cellular Longevity
Volume 2022, Article ID 7907814, 17 pages
https://doi.org/10.1155/2022/7907814

Research Article

The Polysaccharides from the Aerial Parts of *Bupleurum chinense* DC Attenuate Epilepsy-Like Behavior through Oxidative Stress Signaling Pathways

Xiaomao Li, Yan Liu, Siyi Wang, Yikai Jiang, Adnan Mohammed Algradi, Yuanyuan Zhou, Wei Guan, Juan Pan, Haixue Kuang, and Bingyou Yang

Key Laboratory of Basic and Application Research of Beiyao (Heilongjiang University of Chinese Medicine), Ministry of Education, Heilongjiang University of Chinese Medicine, 24 Heping Road, Xiangfang District, Harbin 150040, China

Correspondence should be addressed to Haixue Kuang; hxkuang@yahoo.com and Bingyou Yang; ybywater@163.com

Xiaomao Li and Yan Liu contributed equally to this work.

Received 15 February 2022; Revised 8 March 2022; Accepted 24 March 2022; Published 7 April 2022

Academic Editor: Silvânia Maria Mendes Vasconcelos

Bupleurum chinense DC. is a traditional Chinese medicine with a long medicinal history and is often used as the main ingredient in prescription drugs for epilepsy. The aerial parts of *B. chinense* DC. have similar efficacy and composition to *B. chinense* DC. Therefore, we speculated that the aerial parts of *B. chinense* DC. could be used in the treatment of epilepsy. Polysaccharides from the aerial parts of *B. chinense* DC. were selected to explore their therapeutic effects on epilepsy and their potential mechanism of action. The study is aimed at clarifying the antiepileptic effects of the polysaccharides from the aerial parts of *B. chinense* DC. and their potential underlying mechanisms. The chemical profile of the aerial parts of *B. chinense* DC. polysaccharides (ABP) was characterized by FT-IR spectrum and HPLC chromatogram. To determine the therapeutic effects of ABPs on epilepsy, we established a kainic acid- (KA-) induced rat model of epilepsy, and through H&E staining, Nissl staining, immunohistochemistry, biochemical analysis, ELISA, and Western blot analysis, we explored the mechanisms underlying the therapeutic effects of ABPs on epilepsy. The monosaccharide content of ABP included galacturonic acid (45.19%), galactose (36.63%), arabinose rhamnose (12.13%), and mannose (6.05%). Moreover, the average molecular weight of ABP was 1.38×10^3 kDa. ABP could improve hippocampal injuries and neuronal function in the KA-induced epilepsy rat model. ABP significantly inhibited oxidative stress in the hippocampus of KA-induced rats. More importantly, ABP could regulate TREM2 activation in the PI3K/Akt/GSK-3β pathway to inhibit neuronal apoptosis, including increasing the expression of superoxide dismutase and lactate dehydrogenase and decreasing the expression of malondialdehyde. The current study defined the potential role of ABP in inhibiting the development of epilepsy, indicating that ABP could upregulate TREM2 to alleviate neuronal apoptosis, by activating the PI3K/Akt/GSK-3β pathway and oxidative stress in epilepsy.

1. Introduction

Epilepsy is one of the most common neurological diseases. Currently, there are approximately 50 million people with epilepsy worldwide, accounting for 1% of the total number of patients with any disease worldwide [1]. The prevalence of epilepsy in China is approximately 7%, with 300,000-400,000 new patients diagnosed every year. In the treatment of epilepsy, the prescribed drugs show a poor treatment effect in approximately 30% of patients, which leads to refractory epilepsy [2]. Repeated and long-term seizures tend to lead to the activation of inflammatory factors, calcium homeostasis and increased free radical generation, and selective brain damage of neurons in the hippocampus, including neuronal necrosis and apoptosis [3]. The brain is one of the most sensitive organs to oxidative stress. As it mostly obtains energy through the aerobic metabolism of the mitochondrial respiratory chain, it produces a large number of free radicals. The brain

is rich in unsaturated fatty acids and has a weak antioxidant capacity, which makes it very vulnerable to oxidative stress injury [4]. The high sensitivity of the brain to oxidative stress injury suggests that oxidative stress plays an important role in the pathophysiology of epilepsy. In recent years, many molecular biology and genetic studies have attempted to clarify the relationship between oxidative stress and epilepsy.

Polysaccharides are biopolymers that are usually the main bioactive component of traditional Chinese medicine and the affective component of dietary supplements. Recent studies have shown that polysaccharides have important antioxidative, antitumor, anti-inflammatory, and antifatigue effects and play a relevant role in immune regulation [5–9]. At present, many natural polysaccharides are considered safe and effective therapeutic agents for epilepsy because they are nontoxic [10]. Thus, these polysaccharides have attracted considerable interest in the development of nontoxic natural foods and drugs. *Bupleurum chinense* DC. is a traditional Chinese medicine with a long medicinal history and extensive clinical application because of its antiepileptic and sedative-hypnotic effects [10]. Its main active ingredients are polysaccharides and saponins. The aerial part of *Bupleurum chinense* DC. was rich in resources, and its composition and pharmacological action were similar to that of *Bupleurum chinense* DC. [11]. The *B. chinense* DC. polysaccharides showed a strong oxidation capacity and possessed promising hepatoprotective effects against GalN-induced liver damage, which might be mediated through augmentation of antioxidant defenses [12]. So, the aerial part of *Bupleurum chinense* DC. polysaccharides also might possess the oxidation capacity. And, the preliminary study of our group showed that the extracts from the aerial parts of *B. chinense* DC. had a good therapeutic effect on epilepsy through behavioral evaluation [13]. However, the effects of the polysaccharides from the aerial parts of *B. chinense* DC. on epilepsy have rarely been reported. Therefore, in this study, we aimed to explore the potential mechanisms of the polysaccharides from the aerial parts of *B. chinense* DC. for the treatment of epilepsy by inhibiting oxidative stress.

2. Materials and Methods

2.1. Plant Materials and Reagents. The aerial parts of *B. chinense* DC. were collected in Daqing, Heilongjiang Province, China, in 2017 and identified as *B. chinense* DC. by Professor Rui-feng Fan from the Heilongjiang University of Chinese Medicine. The aerial parts were kept in the laboratory of Chinese Medicine Chemistry of the Heilongjiang University of Chinese Medicine (specimen number 20170910). Kainic acid (KA) was obtained from Sigma-Aldrich (Shanghai, China), a sodium valproate oral solution was obtained from Sanofi (Hangzhou, China), and Dian Xian Ning tablets were purchased from Kunming Chinese Medicine Factory Co., Ltd. (Kunming, China). All other analytical reagents were purchased from Sigma-Aldrich.

2.2. Animals. Four-to-six-week-old male Sprague-Dawley (SD) rats ($n = 70$) weighing 180-200 g were purchased from Liaoning Changsheng Biotechnology Co., Ltd. (SCXK (Liao) 2020-0001). The experimental animals were raised under standardized conditions at 20°C-23°C and with a humidity of 50%-60%. All experiments were approved by the Animal Experiment Committee of the Heilongjiang University of Chinese Medicine (20201230001).

2.3. ABP Extraction. The weight of the aerial parts of *B. chinense* DC. was 1.0 kg. The petroleum ether extract was degreased three times for 12 h each, and the residue of the volatilized dry petroleum ether was heated three times during reflux extraction with distilled water at 100°C for 3 h each. The extract was then combined, filtered, and concentrated to 1/4 of the original volume, and then, anhydrous ethanol was added to adjust the volume to obtain an ethanol volume fraction of 70%. After centrifugation at 4,000 × g for 8 min, the precipitate was collected to obtain the crude polysaccharides from the above-ground aerial parts of *B. chinense* DC. The protein in the crude polysaccharide was removed using the Sevag reagent (chloroform : n – butanol = 4 : 1, V/V) and repeated four times. The supernatant was collected and dialyzed with distilled water using a 3500 Da dialysis bag for 72 h. ABP was obtained after freeze-drying.

2.4. Characterisation of the ABP. 5 mg of the ABP was placed in an agate mortar, an appropriate amount of dry KBr powder was added, ground, and mixed, and the infrared spectrum was determined after tablet pressing, using a scanning range of 4,000-400 cm^{-1} [14–16]. The monosaccharide composition of the ABP was assessed using reverse-phase HPLC, as described previously [17, 18]. We dissolved 10 mg of ABP samples in 2 mL of 2 M trifluoroacetic acid. The monosaccharides from hydrolyzed ABP were analyzed using Sugar-Pak TM1 chromatographic column (6.5 × 300 mm) by using HPLC.

2.5. Experimental Design. After anesthetizing 60 rats, their lateral ventricle was stereo-positioned, and a custom-made microinjection tube was used to lower a 3.8 mm needle into the right lateral ventricle to inject a uniform injection volume of 3 μL of a KA solution at a concentration of 0.5 μg/μL (50 rats) or to inject 3 μL of normal saline (10 rats). After the injection, the needle was retained for 5 min to establish a KA-induced epilepsy rat model [19]. Drug administration was initiated the day after successful model establishment.

Ten unoperated male SD rats as the control group (CON). 10 male SD rats inject normal saline as the sham-operated group (Sham). 50 male SD rats with epilepsy were randomly divided into five groups with 10 rats in each group: model group (MOD), western medicine positive drug group (sodium valproate oral solution (VPA), 180 mg/kg b.w., po., 28 days), traditional Chinese medicine positive drug group (Dianxianning tablets (DXN), 500 mg/kg b.w., po., 28 days), ABP high-dose group (ABPH, 200 mg/kg b.w., po., 28 days), and ABP low-dose group (ABPL, 50 mg/kg b.w., po., 28 days). And CON, sham, and MOD groups were given the same amount of normal saline (po., 28 days).

2.6. Behavioural Assessment. Epileptic seizures were observed and recorded in rats after the cerebral injection of KA. The epileptic seizure grade was assessed according to the Racine grading criteria: grade 0: no reaction, no seizure, and no

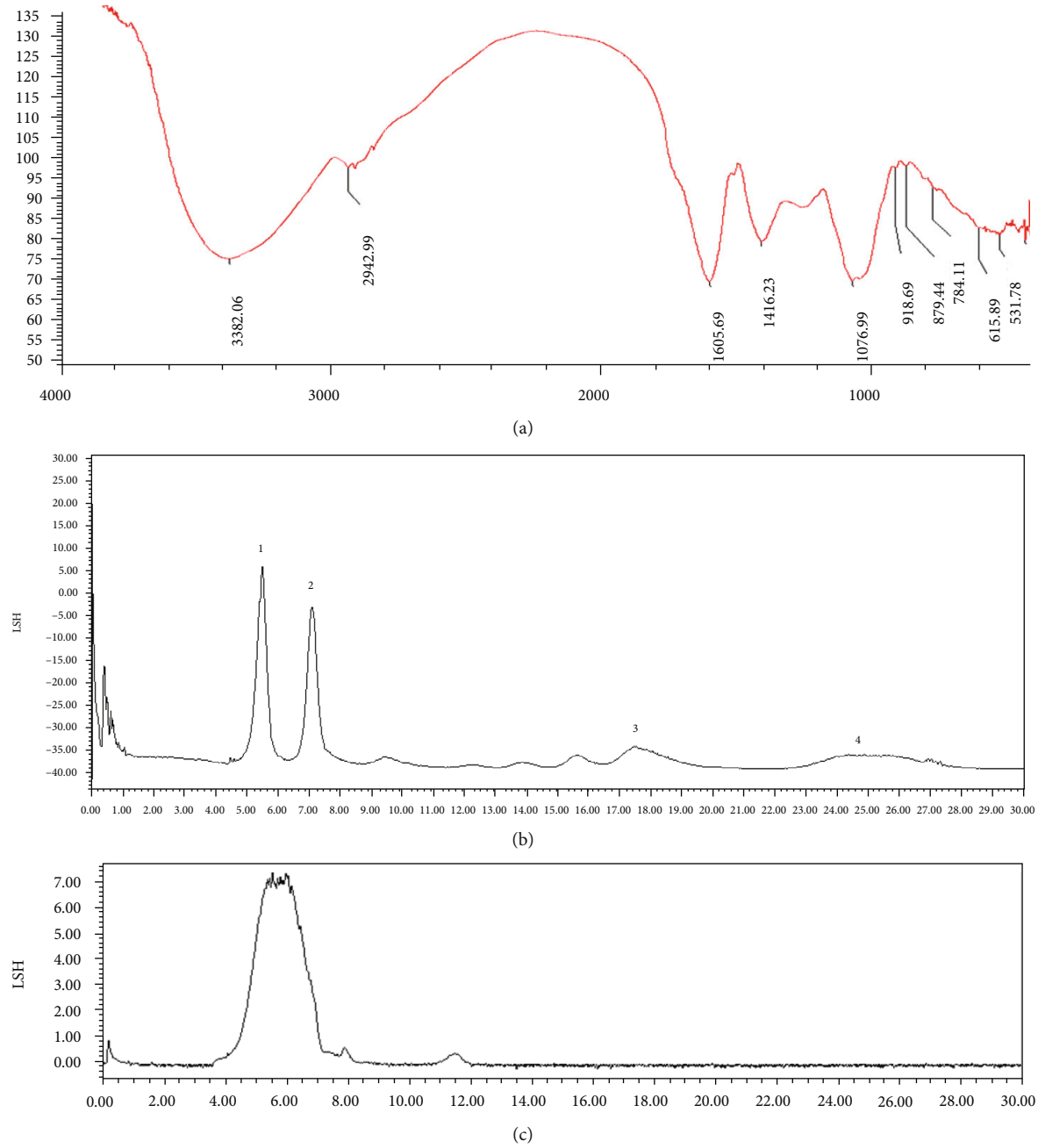

Figure 1: The characterization of ABP. (a) The infrared spectrum of the ABP. (b) Monosaccharide composition of ABP on HPLC. (c) The average molecular weight of ABP.

difference in behavioral performance from that of normal rats; grade I: facial clonus, including blinking, whisker shaking, rhythmical chewing, and wet dog head shaking; grade II: grade I and rhythmic nodding or shaking of the head; grade III: grade II and paroxysmal clonus of forelimb; grade IV: grade III and hind limb standing; grade V: grade IV, ankylosis, and spasm of both hind limbs, falling backward or sideways, losing balance, and violent convulsions of the limbs [20].

2.7. Haematoxylin and Eosin Staining. The rats were anesthetized via abdominal injection of 1% pentobarbital sodium (50 mg/kg), intubated through the ascending aorta, irrigated with normal saline, infused with 500 mL of 4% paraformaldehyde, and immersed in 4% paraformaldehyde after brain extraction for 4-6 h. Each brain was immersed in a 30% sucrose solution, and a frozen slicer was used to cut 30 mm-thick slices in the coronal position. These slices were then attached to the glass-bearing slices, defatted in water, soaked with hematoxylin for 10 min, and washed briefly with water. They were then differentiated under a microscope with a 1% hydrochloric acid-alcohol solution, rinsed with water for 30 min, soaked with eosin for 5 min, dehydrated to make them transparent, and sealed [21]. The CA1 and CA3 regions of the hippocampus were selected for observation.

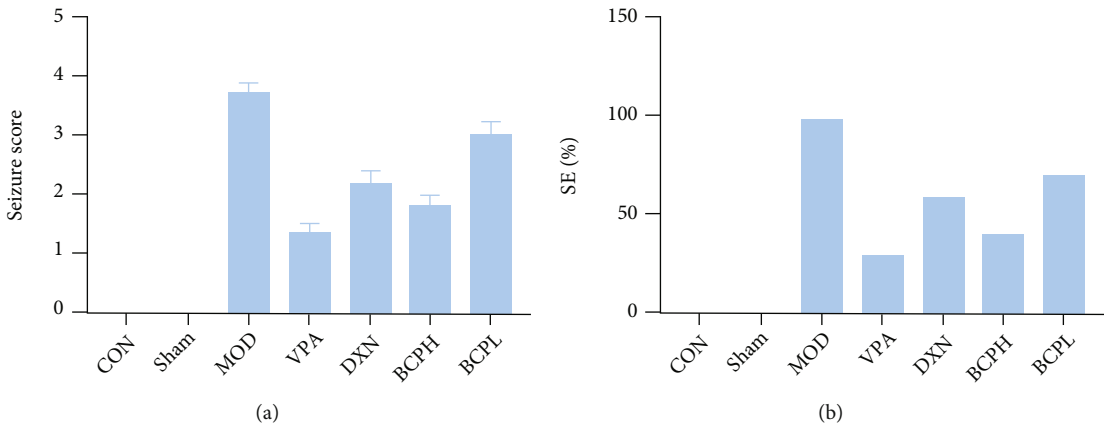

Figure 2: Antiepileptic effects of ABP on KA-induced rats. (a) Seizure core of epilepsy rats after treatment; (b) SE% of epilepsy rats after treatment. Compared with CON and sham groups, the difference was significant ($^{\#}P < 0.05$); compared with the MOD group, the difference was significant ($^{*}P < 0.05$).

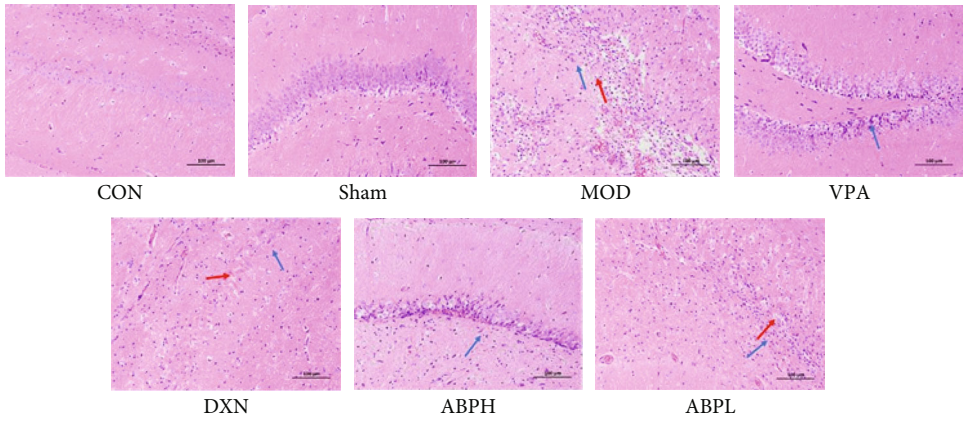

Figure 3: The HE staining of KA-induced rats with treatment.

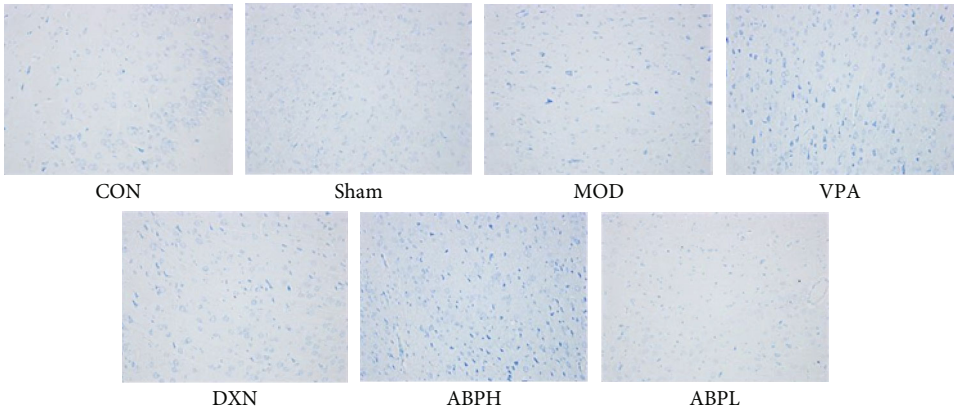

Figure 4: The Nissl staining of KA-induced rats with treatment.

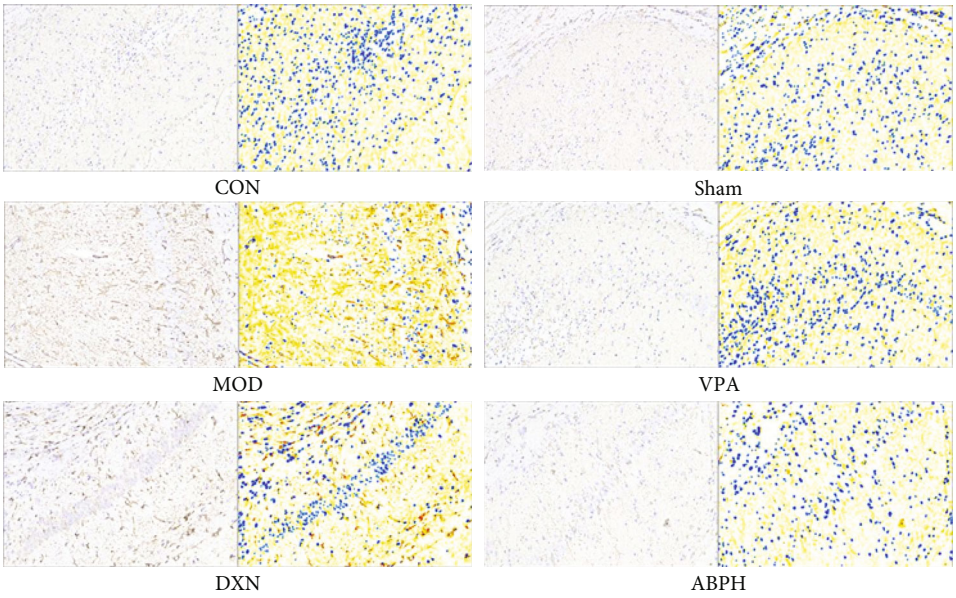

Figure 5: GFAP positive cell expression of KA-induced rats with treatment.

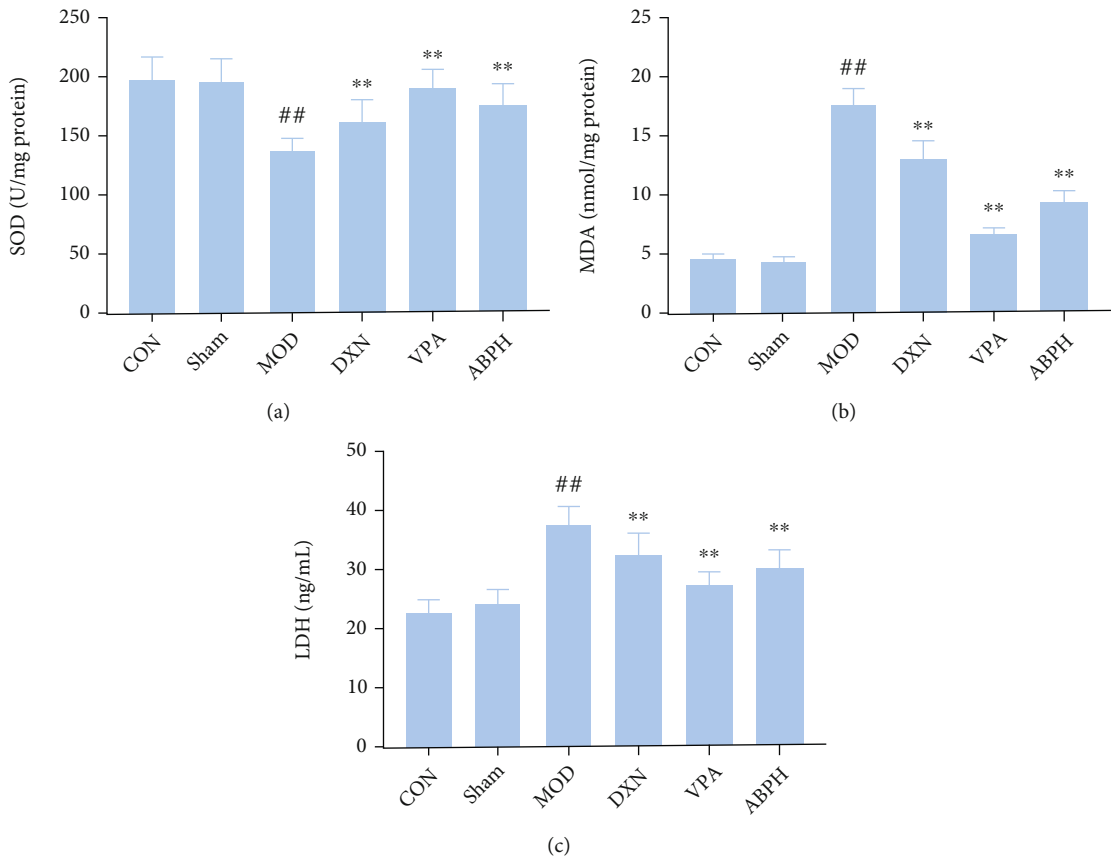

Figure 6: The oxidative stress index levels of KA-induced rats with treatment. (a) The content of SOD in KA-induced epilepsy rats with treatment; (b) the content of MDA in KA-induced epilepsy rats with treatment; (c) the content of LDH in KA-induced epilepsy rats with treatment. Compared with CON and sham groups, the difference was significant ($^{\#}P < 0.05$); Compared with the MOD group, the difference was significant ($^{*}P < 0.05$).

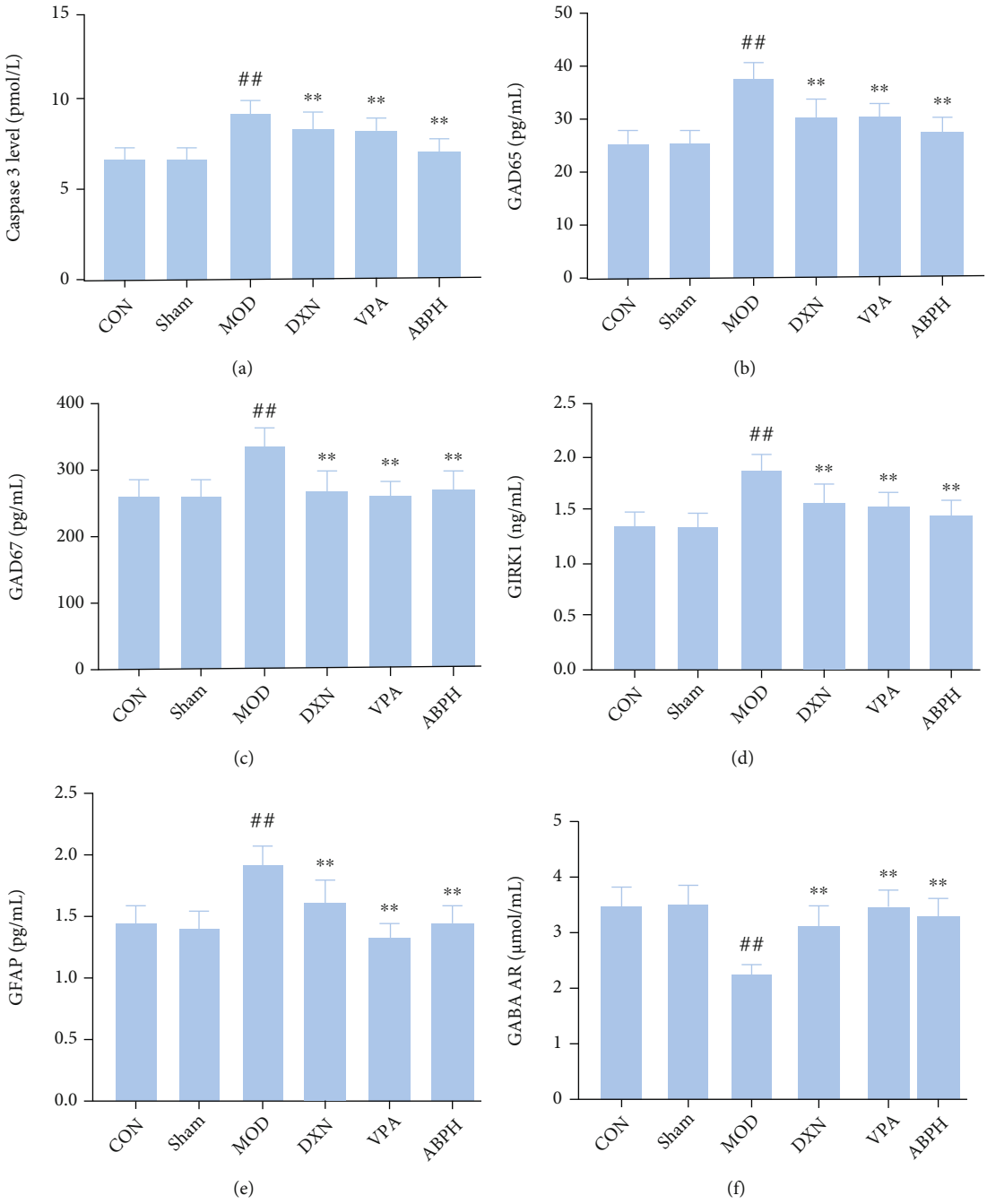

Figure 7: Continued.

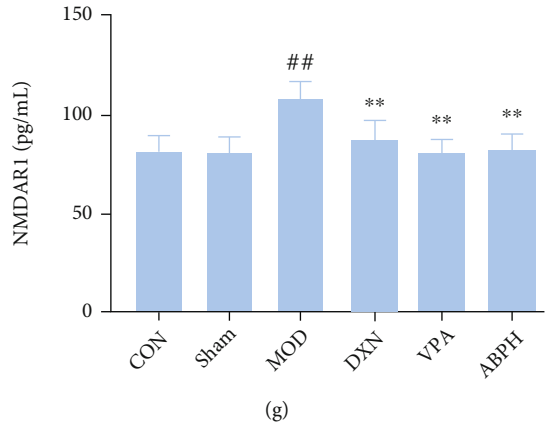

Figure 7: The apoptotic factors and neurotransmitters levels of KA-induced rats with treatment. (a) The content of caspase 3 in KA-induced epilepsy rats with treatment; (b) the content of GAD65 in KA-induced epilepsy rats with treatment; (c) the content of GAD67 in KA-induced epilepsy rats with treatment; (d) the content of GIRK 1 in KA-induced epilepsy rats with treatment; (e) the content of GFAP in KA-induced epilepsy rats with treatment; (f) the content of GABA AR in KA-induced epilepsy rats with treatment; (g) the content of NMDAR 1 in KA-induced epilepsy rats with treatment. Compared with CON and sham groups, the difference was significant ($^{\#}P < 0.05$); compared with the MOD group, the difference was significant ($^{*}P < 0.05$).

2.8. Nissl Staining. The brain sections were degreased with dimethyl benzene and an alcohol gradient, soaked in distilled water for 5 min, soaked with 1% toluidine blue at 60°C for 40 min, rinsed with distilled water for 5 min, differentiated with 95% alcohol for 1 min, dehydrated with anhydrous alcohol to make them transparent, and sealed. The CA1 and CA3 regions of the hippocampus were then observed under a light microscope (Nikon Eclipse Ci-L, Japan, magnification, ×200) [22].

2.9. Immunohistochemistry. Brain slices were immersed in 0.1 M phosphate buffer saline (PBS) containing 0.5% Triton X-100 for 60 min and a 0.6% H_2O_2 ethanol saline solution (50% ethanol and 0.9% sodium chloride) for 45 min. Normal sheep serum was added to them, followed by incubation for 60 min. The residual serum was poured out without washing the slices, and these were dripped with rabbit-derived glial fibrillary acidic protein polyclonal antibody (Abclonal, Wuhan, China, 1 : 500) and incubated at 4°C for 36-48 h. Biotinylated secondary antibody (sheep anti-rabbit) was added to the slices dropwise, and these were incubated at 25°C for 2 h. Streptavidin labeled with horseradish enzyme was added dropwise, followed by incubation at room temperature for 2 h. Between each step, the slices were washed three times with 0.01 M PBS for 10 min each. The sections were then stained with 3, 3′-diaminobenzidine tetrahydrochloride, counterstained with hematoxylin, dehydrated to make them transparent, and sealed. The positive expression of the hippocampus CA1 and CA3 regions were observed under a microscope, and the f positive expression was calculated using Image J 18.0 (200x magnification).

2.10. Biochemical Analysis. Total protein was extracted from the fresh hippocampal tissues of the experimental rats of each group. The malondialdehyde (MDA) content and the superoxide dismutase (SOD) and lactate dehydrogenase (LDH) activities were determined using UV spectrophotometry according to the manufacturer's instructions for each test kit (Nanjing Jiancheng Bioengineering Institute, Nanjing, China). The expression of Caspase 3, COX2, TLR4, HMBG1, NMDAR 1, GABA AR, GAD65, GAD67, and GAFP was determined using specific methods, according to the instructions of the corresponding ELISA kits (Shanghai Enzyme-linked Biotechnology Co., Ltd.).

2.11. Western Blot Analysis. Total protein was extracted from the fresh hippocampal tissues of the rats of each group. The total protein of 20 μg of each sample was separated using polyacrylamide gel electrophoresis, which was then transferred onto a polyvinyl difluoride membrane. After sealing, the protein was incubated with primary antibodies against Bax, Bcl-2, caspase 3, TREM2, PI3K, p-Akt, Akt, and GSK-3β (1 : 1000, Abclonal, Wuhan, China) at 4°C overnight. The ECL reagent was added, followed by incubation at room temperature for 1 h with an appropriate dilution of the corresponding HRP-labelled secondary antibody (Abclonal). GAPDH (1 : 1000, Abclonal) was used as an internal reference. The expression level results were compared with those of each control group, which was used as the standard, and with the results of other groups.

2.12. Cell Culture. The highly differentiated PC12 rat pheochromocytoma cells (Cell Bank of Chinese Academy of Sciences, Shanghai) were cultured in RPMI 1640 containing 10% fetal bovine serum and placed in a 5% CO_2 incubator at 37°C for routine passage. The confluent cells (70%-80% confluency) were digested using trypsin and washed with PBS, and a single-cell suspension was prepared, which was then used to inoculate 96-well plates at a density of 5000 cells/well. After 24 h of culture, the cells were randomly divided into six groups after cell adherence: (1) control group: normal culture; (2) model group: RPMI 1640 with H_2O_2 (500 μM) for 4 h, and then replaced with RPMI 1640

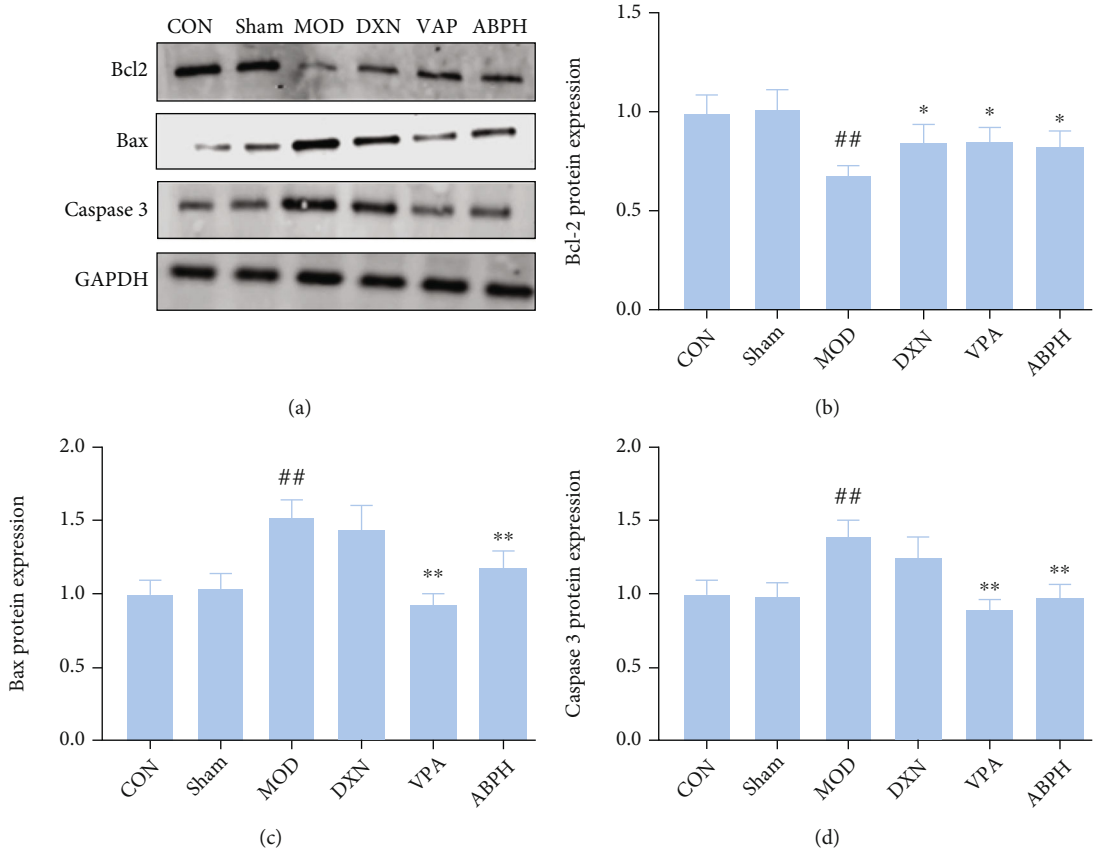

FIGURE 8: The regulation apoptotic pathway of KA-induced rats with treatment. (a) Western blotting in KA-induced epilepsy rats with treatment; (b) the expression of Bcl2 in KA-induced epilepsy rats with treatment; (c) the expression of Bax in KA-induced epilepsy rats with treatment; (d) the expression of caspase 3 in KA-induced epilepsy rats with treatment.

containing 10% fetal bovine serum for 24 h; (3) VPA group: RPMI 1640 containing valproic acid sodium (1 mM), which was replaced after 4 h with 500 μM H_2O_2; (4) ABP groups: RPMI 1640 for 4 h, which was then replaced with RPMI 1640 containing ABP at different concentrations (20, 40, and 80 μg/mL).

2.13. Cell Viability Assay. After treatment, the culture medium was removed, the cells were washed with PBS, and 100 μL of RPMI 1640 and 10 μL of a CCK8 solution were added to each well. After a slight shock, the cells were incubated at 37°C for 1 h. Then, the absorbance of each well was measured at 450 nm, and the relative cell viability was calculated.

2.14. Apoptosis Assays Using Flow Cytometry Analysis. Confluent PC12 cells were used to inoculate 6-well plates at a density of 1×10^6 cells/well and then divided into groups for posttreatment. Then, the cells were gently scraped and washed twice with PBS. A total of 1×10^5 cells were collected from each group, and the supernatant was discarded after 4°C 1000 r/min centrifugation 15 min. Next, 195 μL of an Annexin V-FITC staining solution and 5 μL of a PI staining solution were added, and the cells were incubated in a 37°C incubator for 20 min without light after a slight shock. The cells were washed once with PBS and resuspended. Fluorescence detection was performed using flow cytometry.

2.15. Statistical Analysis. Statistical analyses were conducted using SPSS 17 (SPSS Inc., Chicago, IL, USA). All data are presented as the mean ± standard error (SEM). Statistical significance was analyzed using two-way analysis of variance (ANOVA), and multiple comparisons between groups were made using the Tukey test. Statistical significance was set at $P < 0.05$.

3. Results

3.1. The Characterisation of ABP. As shown in Figure 1(a), there is a wide and smooth strong absorption peak near 3,400 cm^{-1} (3,382.05 cm^{-1}), which is the O-H stretching vibration peak, and the absorption was caused by the intramolecular and intermolecular O-H stretching vibration of sugar. A very weak characteristic absorption peak was observed at 2942.99 cm^{-1}, namely, the absorption peak corresponding to the C-H stretching vibration [22, 23]. The absorption peaks in these areas are characteristic absorption peaks of sugars. The absorption peak at approximately 1,615 cm^{-1} (1,605.69 cm^{-1}) is the stretching vibration peak of C=O, and the weak absorption peak at

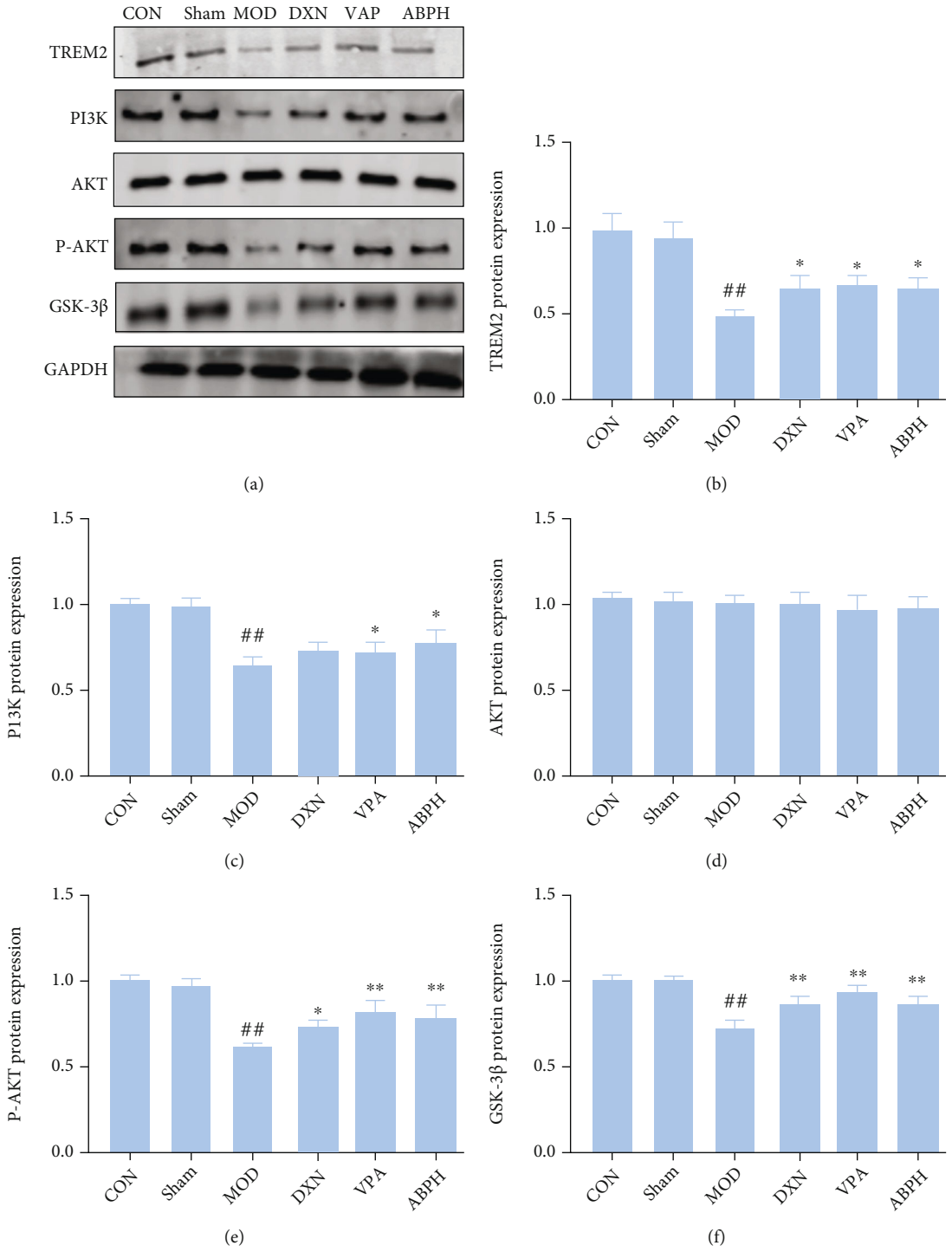

Figure 9: The regulation of oxidative stress pathways of KA-induced rats with treatment. (a) Western blotting in KA-induced epilepsy rats with treatment; (b) the expression of TREM 2 in KA-induced epilepsy rats with treatment; (c) the expression of PI3K in KA-induced epilepsy rats with treatment; (d) the expression of AKT in KA-induced epilepsy rats with treatment; (e) the expression of P-AKT in KA-induced epilepsy rats with treatment; (f) the expression of GSK-3β in KA-induced epilepsy rats with treatment.

1420 cm^{-1} (1416.23 cm^{-1}) is the in-plane bending vibration peak of C-H [24]. There are two furanose absorption peaks in the 1100-1010 cm^{-1} range, which indicate that ABP contained furanose. However, a weak characteristic absorption peak was observed around 890 cm^{-1}, confirming the presence of β-glycosidic bonds linking the sugar residues [25].

The monosaccharide composition of the ABP was analyzed using HPLC after hydrolysis, and the ABP contained

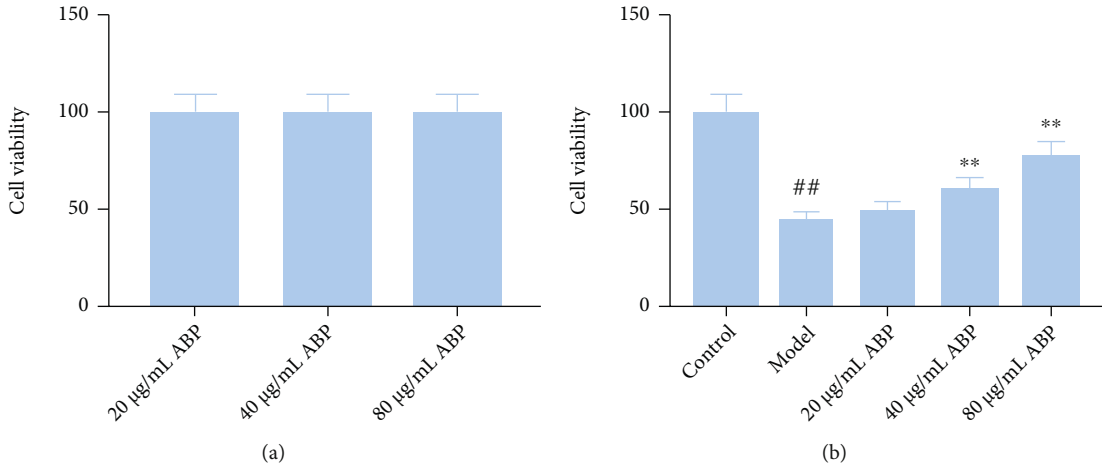

FIGURE 10: The effect of ABP on PC12 cells induced by H_2O_2. (a) The cell viability of different doses of BEO; (b) the effect of different doses of BEO on hippocampal neuron model of epilepsy. Compared with the control group, the difference was significant ($^{\#}P < 0.05$); compared with the model group, the difference was significant ($^{*}P < 0.05$).

galacturonic acid (45.19%), galactose (36.63%), arabinose rhamnose (12.13%), and mannose (6.05%) (Figure 1(b)). Furthermore, the average molecular weight of ABP was 1.38×10^3 kDa (Figure 1(c)).

3.2. Antiepileptic Effects of ABP on the KA-Induced Rat Model of Epilepsy. The rats in the sham group had no specific behavior or seizures after the injection of normal saline into their hippocampus. After the KA injection, the rats in the MOD group had seizures of varying degrees, with an incidence of 100%, and 80% of the rats showed simultaneous rhythmic convulsions of the limbs (grade IV or above). The epileptic seizure degree and the behavioral score of rats in the ABPH group were significantly lower than those of the rats in the MOD group ($P < 0.05$) (Figure 2).

3.3. Histological and Immunohistochemical Analyses. The neurons in the CON and sham groups were neatly arranged, with clear cell outlines, abundant cytoplasm, basophilic, and had around and centered nucleus and clear nucleoli. In the MOD group, the neuron boundaries were not clear, the cell body was wrinkled, cells had a reduced volume, having lost the typical polygon shape, and became round or triangular, the cytoplasm was vacuolated or concentrated and dark, the nucleus was concentrated and deeply stained, and no nucleoli could be observed. The voids around the neurons increased, and there were more holes left after the disappearance of the neurons. The degree of degeneration and necrosis of the hippocampal neurons and the number of neurons affected by these in the VPA and ABPH groups were lower than those in the MOD group. Neuronal injury was improved, and the pyramidal cell nucleus hyperchromatism, fragmentation, or dissolution was reduced in the VPA and ABPH groups, but no significant improvement was observed in the ABPL group (Figures 3 and 4).

Three sections from each animal were randomly selected to observe the number of GFAP-positive cells in the hippocampus. The results showed that the number of GFAP-positive cells in the hippocampus of the MOD group rats was significantly higher than that of the CON and sham group rats ($P < 0.01$). The number of GFAP-positive cells of the positive drug and ABPH groups was significantly lower than that of the MOD group ($P < 0.01$), while there was no significant difference between the CON and sham groups regarding this parameter, as shown in Figure 5.

3.4. Oxidative Stress Index Analysis. Compared with those in the CON and sham groups, the content of MDA and the activity of LDH in the MOD group were significantly higher, while the activity of SOD was significantly lower ($P < 0.01$). Compared with those in the MOD group, the activity of SOD was significantly higher and the content of MDA and the activity of LDH were significantly lower in the ABPH group ($P < 0.01$), as shown in Figure 6.

3.5. Neurotransmitter Content Analysis. The effects of ABP on the neurotransmitter content of the KA-induced rats were explored. As shown in Figure 7, the caspase 3, GAD65, GAD67, GIRK1, GFAP, and NMDAR1 contents were significantly higher ($P < 0\,01$) in the MOD group rats than in the CON group rats, while GABA AR content was significantly lower ($P < 0.01$). Interestingly, the caspase 3, GAD65, GAD67, GIRK1, GFAP, and NMDAR1 contents were significantly lower, and GABA AR content was significantly higher in the ABPH group rats than in the MOD group rats ($P < 0\,01$).

3.6. Regulation of the Oxidative Stress Pathways in KA-Induced Rats. As shown in Figure 8, KA decreased the expression of Bcl-2 and increased the expression of Bax and caspase 3 ($P < 0\,01$). Moreover, ABPH could improve the KA-induced neuronal apoptosis, increased the expression of Bcl-2, and decreased the expression of Bax and caspase 3 ($P < 0\,01$).

The expression of TREM2, PI3K, P-Akt, and GSK3β was significantly lower in the epilepsy group rats than in the

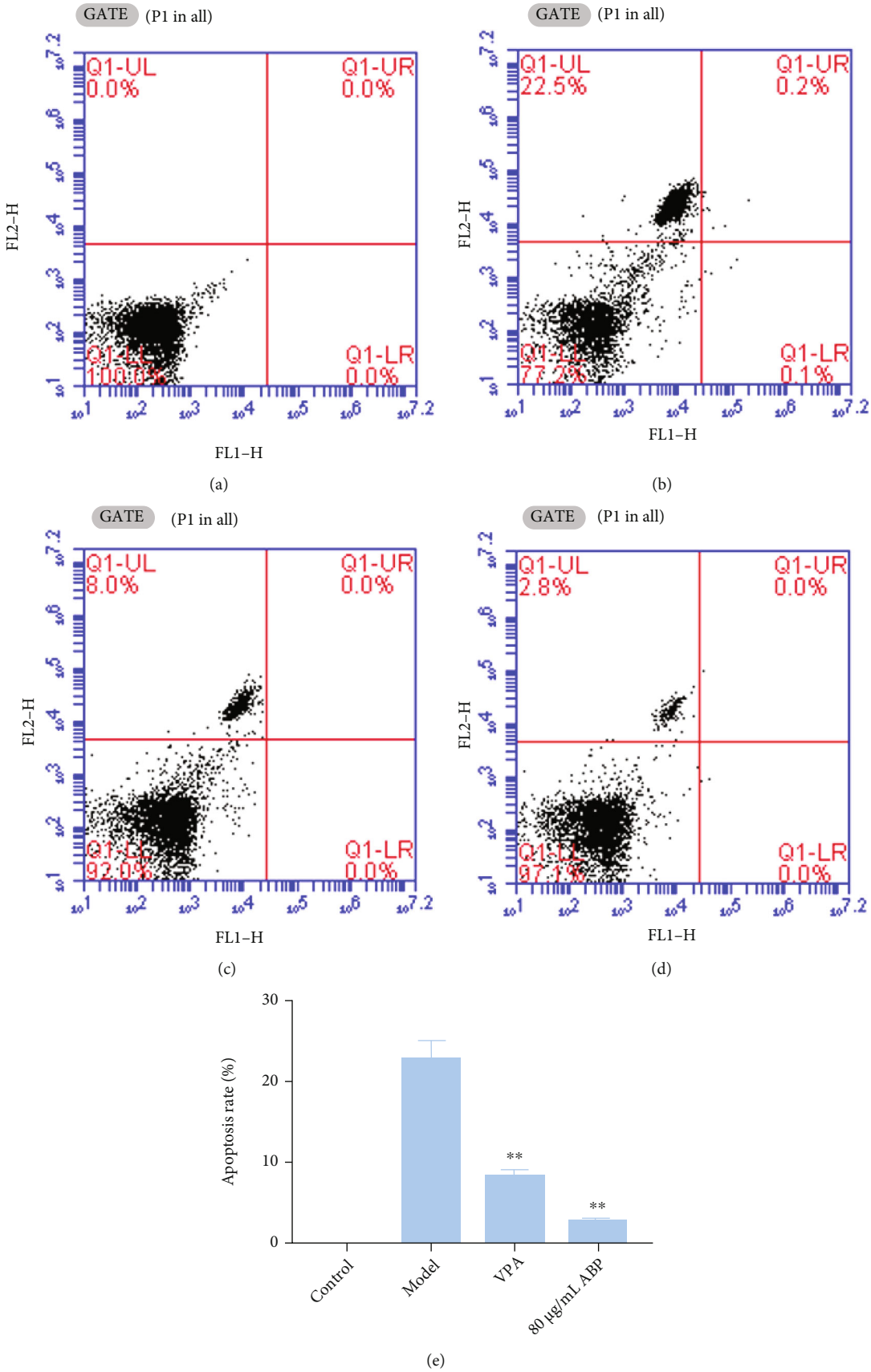

Figure 11: The antiapoptosis effect of ABP on PC12 cells induced by H_2O_2. Compared with the model group, the difference was significant ($^*P < 0.05$).

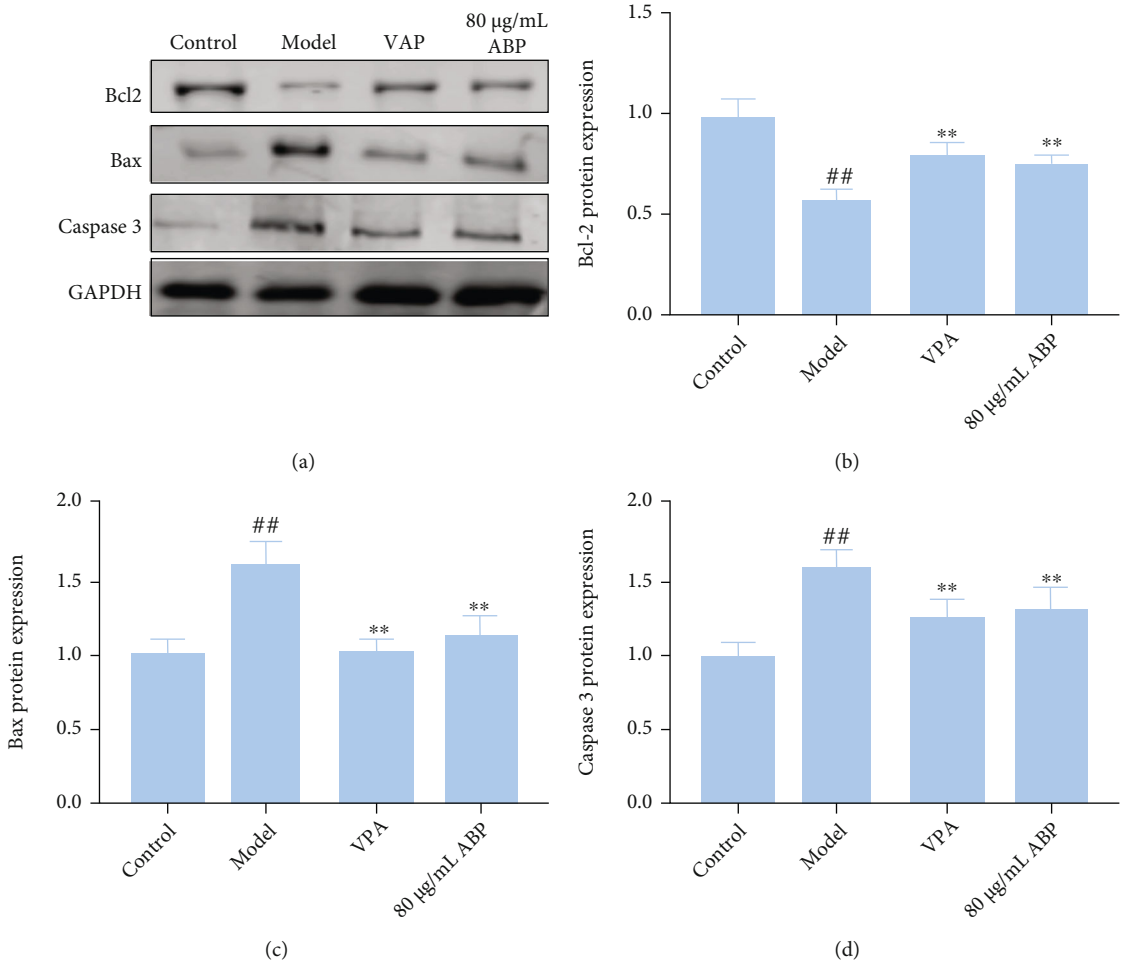

Figure 12: The regulation apoptotic pathway of H_2O_2-induced PC12 cells with treatment. (a) Western blotting in H_2O_2-induced PC12 cells with treatment; (b) the expression of Bcl2 in H_2O_2-induced PC12 cells with treatment; (c) the expression of Bax in H_2O_2-induced PC12 cells with treatment; (d) the expression of caspase 3 in H_2O_2-induced PC12 cells with treatment.

CON and sham group rats, and there was no significant change in Akt expression. Compared with the MOD group, ABPH could decrease the expressions of TREM2, PI3K, P-Akt, and GSK3β. Thus, we hypothesized that ABP might activate the PI3K/Akt/GSK-3β pathway by regulating TREM2, as shown in Figure 9.

3.7. Effect of ABP on PC12 Cells Induced by H_2O_2. The viability of the model group cells was significantly lower than that of the control group cells ($P < 0.01$). The viability of the ABP group cells was higher than that of the model group cells, and the increase in cell viability was more obvious with the increase in ABP concentration ($P < 0.01$) (Figure 10). At the same time, the flow cytometry results also confirmed that ABP could reduce the apoptosis caused by oxidative stress, as shown in Figure 11.

3.8. Regulation of the Oxidative Stress Pathways in H_2O_2-Induced PC12 Cells. As shown in Figures 12 and 13, the levels of caspase-3 and Bax proteins in the model cells were upregulated, whereas the expression levels of Bcl-2, PI3K, p-Akt, and GSK-3β were downregulated, compared with those in the control cells ($P < 0\,01$). The caspase-3 and Bax protein levels were significantly lower in all the ABP-treated (80 μg/mL) cells than in the model cells, whereas the Bcl-2, PI3K, p-Akt, and GSK-3β ($P < 0\,05$) levels increased following treatment with 80 μg/mL ABP.

4. Discussion

Epilepsy is a common chronic neurological disease whose pathogenesis is not completely clarified, and it often requires long-term antiepileptic drug treatment; the treatment of refractory epilepsy is also very difficult. In recent years, there has been increasing evidence of a close link between epileptic seizures and oxidative stress [26]. Polysaccharides from traditional Chinese medicine have attracted extensive attention because of their unique antioxidant ability [12, 27]. In this study, the antiepileptic effects of the ABP were studied (Figures 2–5).

Microinjection of KA in the hippocampus of rats could cause the death of neurons in hippocampal CA1 and CA3 regions [28, 29], dentate gyrus, and other brain regions.

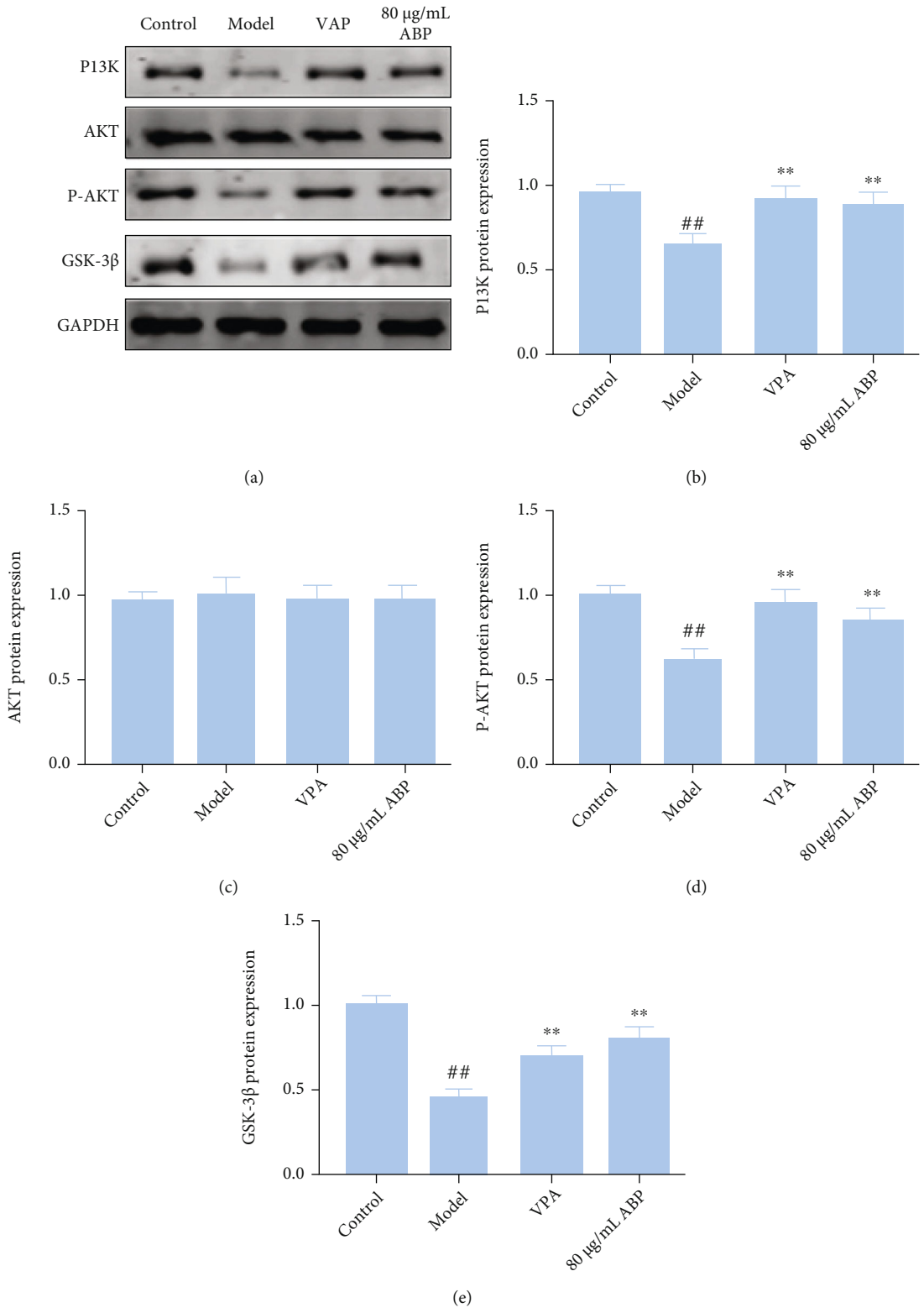

FIGURE 13: The regulation of oxidative stress pathway of H_2O_2-induced PC12 cells with treatment. (a) Western blotting in H_2O_2-induced PC12 cells with treatment; (b) the expression of PI3K in H_2O_2-induced PC12 cells with treatment; (c) the expression of AKT in H_2O_2-induced PC12 cells with treatment; (d) the expression of P-AKT in H_2O_2-induced PC12 cells with treatment; (f) the expression of GSK-3β in H_2O_2-induced PC12 cells with treatment. Compared with the control group, the difference was significant ($^{\#}P < 0.05$); Compared with the model group, the difference was significant ($^{*}P < 0.05$).

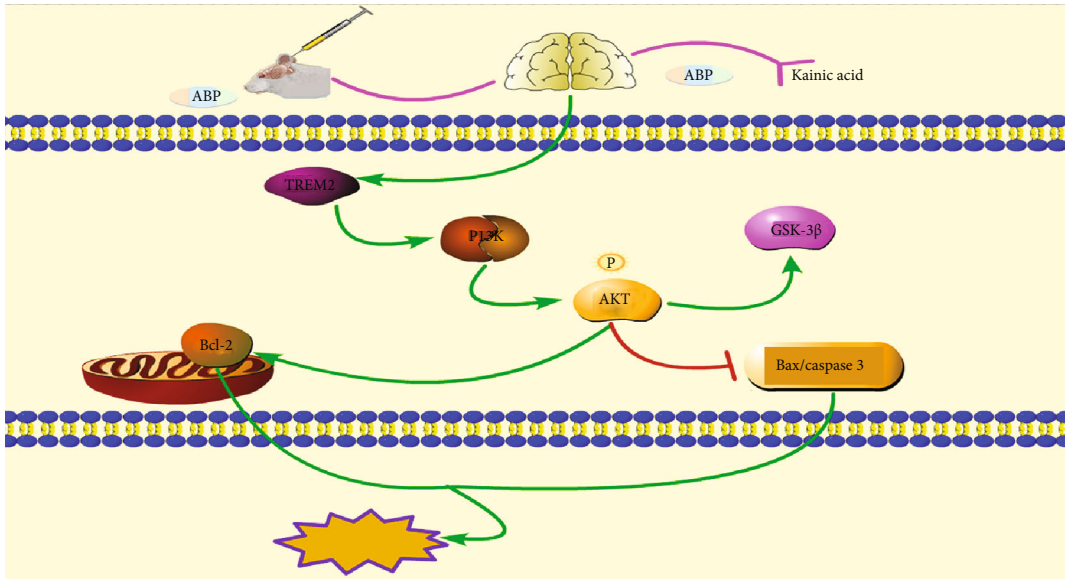

Figure 14: The therapeutic mechanism of ABP treats KA-induced epilepsy.

Pyramidal cells in the hippocampal CA3 region synapse with mossy fibers and receive excitatory afferents from mossy fibers. Due to the loss of pyramidal cells and mossy cells in the CA3 region, mossy fibers lose their postsynaptic targeting cell connections, resulting in the sprouted mossy fibers to the granulosa cell layer and molecular layer. It could form new excitatory synaptic connections with itself or other granulosa cells, enhance excitatory synaptic transmission of glutamate, and destroy the excitatory and inhibitory balance in the hippocampus, thus causing seizures [30, 31]. Through the analysis of pathology and neurotransmitters, it was found that ABP could improve the neuronal injury in CA1 and CA3 areas and neurotransmitter abnormalities in the hippocampal (Figures 3–5 and 7). And we found that oxidative stress was also an important cause of hippocampal injury [26, 32]. Therefore, the effects of oxidative stress indexes on epileptic rats and ABP on oxidative stress indexes were investigated in the follow-up study.

Free radicals are related to the pathogenesis of many nervous system diseases, such as epilepsy, cerebral ischemia-reperfusion injury, Alzheimer's disease, and Parkinson's disease [26, 32]. SOD can block the chain reaction of free radicals by catalyzing the disproportionation of superoxide anion free radicals to protect cells from oxidative damage. MDA, which is a metabolite produced by the reaction of free radicals with unsaturated fatty acids, is often used to indirectly reflect the changes in free radical metabolism and the degree of cell damage. The determination of the SOD levels is often combined with the determination of the MDA levels to reflect the severity of the free radical attack on cells and the ability to scavenge the oxygen free radicals [33]. In our study, ABP reduced the MDA content and enhanced the activity of SOD in a KA-induced epilepsy rat model (Figure 6). It was speculated that ABP could scavenge hydroxyl radicals and inhibit spontaneous or hydroxyl radical-induced lipid peroxidation. LDH is an important oxidoreductase in the body. Changes in the LDH content could reflect tissue damage to a certain extent. This is a sensitive biochemical index that reflects cell activity and function [34], and its release can be used as a cell damage marker. Through pharmacodynamics and pathological evaluation, we could find that the efficacy of the high dose of ABP significantly decreased epileptic scores and SE% and also improved neuronal damage in hippocampal tissue, but the low doses had no significant effect. And by reviewing the literature [35, 36], our selection is consistent with the report, so only the high dose of ABP was selected for the oxidative stress index detection. In our study, ABPH reduced the MDA content, enhanced the activity of SOD, and increased LDH release in a KA-induced epilepsy rat model (Figure 6). It was speculated that ABP could scavenge hydroxyl radicals and inhibit spontaneous or hydroxyl radical-induced lipid peroxidation.

The apoptosis of neurons after the KA-induced epileptic seizures was observed in the rats throughout the whole process, and the apoptosis of the CA3 region in rats was also obvious. Caspase-3 is a key protein in the apoptosis pathway, and programmed cell death could be caused by the action of cytokines in the Bcl-2 family of proteins, which are important regulatory factors of the mitochondrial pathway. Bcl-2 and Bax are two genes in the Bcl-2 family that are closely related to apoptosis [37]. They are a pair of apoptosis regulatory genes that are functionally opposite to each other and the protein product they express. Bcl-2 protein can inhibit the apoptosis of cells, while Bax protein promotes apoptosis and antagonizes the function of Bcl-2 [38]. As a soluble protein, Bax is mainly located in the cytoplasm or the skeleton of cells. When apoptosis is induced by injury factors, Bax is rapidly transferred to the mitochondria and binds to Bcl-2; the resulting dimer can induce apoptosis. In both rat

and cell models, we observed that ABP might improve apoptosis by regulating the expression of caspase 3 and Bcl-2/Bax (Figures 4 and 8).

The excitatory glutamate toxicity increases in the hippocampal tissue during seizures. A large number of oxygen free radicals can promote hippocampal nerve cell apoptosis and even necrosis, and activating the PI3K/Akt signaling pathway can substantially inhibit hippocampal nerve cell apoptosis [39]. In this study, we speculated that ABP activates the PI3K/Akt signaling pathway, which is involved in the apoptosis of hippocampal neurons. The PI3K/Akt signaling pathway is important for maintaining cell apoptosis and growth by regulating the downstream apoptotic proteins and cyclins (Figures 3, 11, and 13). Akt is a target kinase that is downstream of PI3K. When stimulated by intracellular signals, PI3K activates PIP3 production, phosphorylates Akt, and triggers a cascade reaction, thereby regulating cell apoptosis [40]. GSK-3β is a subtype of GSK-3, which can phosphorylate multiple transcription factors and proteins and plays an important role in initiating apoptosis [41]. The PI3K/Akt signaling pathway has the most apparent effect on GSK-3β [40]. This experiment showed that the levels of the PI3K/P-Akt protein complex and the downstream molecule GSK-3β were lower in the MOD group than in the CON group and that ABP modulated the abnormal levels of these proteins. These results suggest that ABP regulates the PI3K/Akt/GSK-3β pathway to suppress neuronal apoptosis and are consistent with the cell experiment results (Figures 9 and 13).

Recently, a study has shown that the expression of TREM2 is downregulated in an epileptic hippocampal neuron model, which could repair the damaged central nervous system tissue and further decrease the phagocytosis of apoptotic neurons via the NF-κB pathway [39, 40, 42]. Therefore, we studied the regulation of TREM2 expression in epilepsy via the PI3K/Akt pathway in an epileptic rat model. Importantly, our results show that TREM2 can activate the PI3K/Akt signaling pathway, inhibit the apoptosis and injury of hippocampal neurons, and reduce oxidative stress. In summary, ABP upregulated the expression of TREM2 to suppress the expression of the apoptosis-related proteins Bax and caspase 3, increase the Bcl-2 expression, and activate the PI3K/Akt pathway, which possibly holds therapeutic implications for inhibiting neuronal apoptosis.

At present, this study is limited to the unknown structure of the polysaccharides from the aerial part of *Bupleurum chinense* DC.. Some further characterizations such as sugar linkages and anomeric configuration are highly desirable. Since all properties particularly the biological properties of polysaccharides are controlled by the molecular structure, the detail of structure is essential. Therefore, we will further study the polysaccharide structure of the aerial part of *Bupleurum chinense* DC., to reveal the correlation between the polysaccharide structure and its mechanism of epilepsy.

5. Conclusions

Polysaccharides from the aerial parts of *B. chinense* DC have an average molecular weight of 1.38×10^3 kDa and are composed of galacturonic acid, galactose, arabinose rhamnose, and mannose. In the present study, we evaluated the antiepileptic effects of ABP on KA-induced epileptic rats, the protective effects of ABP against H_2O_2-induced injury in PC12 cells, and the underlying molecular mechanisms. ABP exerted remarkable antiepileptic effects and protective effects against oxidative damage through upregulating TREM2 expression and alleviating hippocampal neuronal injury and oxidative stress. ABP also inhibited oxidative stress by activating the PI3K/Akt/GSK-3β pathway (Figure 14). The present study provides insights into the use of the polysaccharides from *B. chinense* DC aerial parts for treating epilepsy.

Abbreviations

ABP: Polysaccharide from the aerial parts of *Bupleurum chinense* DC.
ELISA: Enzyme-linked immunosorbent assay
HE: Haematoxylin-eosin
GAD: Glutamic acid decarboxylase
GIRK: G protein gated inwardly rectifying K channels
DAB: 3,3′-diaminobenzidine tetrahydrochloride
b. w.: Body weight
TFA: Trifluoroacetic acid
SD: Sprague-Dawley
KA: Kainic acid
HPLC: High-performance liquid chromatography
GABA: γ-Aminobutyric acid type A
GFAP: Glial fibrillary acidic protein
NMDAR: N-methyl-D-aspartic acid receptor
KBr: Potassium bromide
p. o.: Oral
TCM: Traditional Chinese medicine.

Data Availability

The data used to support the findings of this study are included in the article. Further data or information required are available from the corresponding author upon request.

Conflicts of Interest

The authors declare that they have no known competing financial interests or personal relationships that could have appeared to influence the work reported in this paper.

Authors' Contributions

Contributions of Xiaomao Li and Yan Liu were equal. Xiaomao Li designed the experiment, completed the experiment, and wrote the first draft; Yan Liu designed the experiments and revised the manuscript. Siyi Wang is responsible for data validation and Yikai Jiang for supervision; Adnan Mohammed Algradi polished the language of the manuscript; Yuanyuan Zhou, Wei Guan, and Juan Pan are assigned for the investigation; Haixue Kuang verified the data; Bingyou Yang provided funding and checked the data. Xiaomao Li and Yan Liu have contributed equally to this work.

Acknowledgments

This study was financially supported by the National Natural Science Foundation of China (81973440) and Heilongjiang Touyan Innovation Team Program.

References

[1] T. A. Milligan, "Epilepsy: a clinical overview," *The American Journal of Medicine*, vol. 134, no. 7, pp. 840–847, 2021.

[2] R. S. Fisher, C. Acevedo, A. Arzimanoglou et al., "ILAE official report: a practical clinical definition of epilepsy," *Epilepsia*, vol. 55, no. 4, pp. 475–482, 2014.

[3] C. Helmstaedter and J. A. Witt, "Epilepsy and cognition - a bidirectional relationship?," *Seizure*, vol. 49, pp. 83–89, 2017.

[4] S. L. Moshe, E. Perucca, and P. Ryvlin, "Epilepsy: new advances," *Lancet*, vol. 385, no. 9971, pp. 884–898, 2015.

[5] F. X. Wang, W. Wang, X. B. Niu, Y. L. Huang, and J. Zhang, "Isolation and structural characterization of a second polysaccharide from bulbs of Lanzhou lily," *Applied Biochemistry and Biotechnology*, vol. 186, no. 3, pp. 535–546, 2018.

[6] B. G. Goo, G. Baek, D. J. Choi et al., "Characterization of a renewable extracellular polysaccharide from defatted microalgae _Dunaliella tertiolecta_," *Bioresource Technology*, vol. 129, pp. 343–350, 2013.

[7] K. B. Jeddou, F. Chaari, S. Maktouf, O. Nouri-Ellouz, C. B. Helbert, and R. E. Ghorbel, "Structural, functional, and antioxidant properties of water-soluble polysaccharides from potatoes peels," *Food Chemistry*, vol. 205, pp. 97–105, 2016.

[8] D. L. Komura, E. R. Carbonero, A. H. P. Gracher et al., "Structure of Agaricus spp. fucogalactans and their anti-inflammatory and antinociceptive properties," *Bioresource Technology*, vol. 101, no. 15, pp. 6192–6199, 2010.

[9] Z. Y. Zhu, M. Meng, H. Sun, Y. Li, N. Yu, and Y. M. Zhang, "Structural analysis and immunostimulatory activity of glycopeptides from Paecilomyces sinensis," *Food & Function*, vol. 7, no. 3, pp. 1593–1600, 2016.

[10] Y. Xu, F. Cai, Z. Yu et al., "Optimisation of pressurised water extraction of polysaccharides from blackcurrant and its antioxidant activity," *Food Chemistry*, vol. 194, pp. 650–658, 2016.

[11] Z. Y. Xiao, Y. Liu, Y. P. Sun, Y. Liu, and H. X. Kuang, "A new alkaloid from the aerial parts of Bupleurum chinense DC.," *Chemistry & Biodiversity*, vol. 17, no. 3, article e1900697, 2020.

[12] Z. Wei, L. Junjie, Y. Shuqiang, L.-Y. Zhang, and K.-F. Dou, "Antioxidant activity and hepatoprotective effect of a polysaccharide from Bei Chaihu (Bupleurum chinense DC)," *Carbohydrate Polymers*, vol. 89, no. 2, pp. 448–452, 2012.

[13] B. Y. Yang, Y. Liu, and H. X. Kuang, "Antiepileptic effect of different extracts of aerial part of Bupleurum chinense DC," 2019, Patent.

[14] J. L. Brunelle and R. Green, "Coomassie blue staining," *Methods in Enzymology*, vol. 541, pp. 166-167, 2014.

[15] A. Albalasmeh, A. Berhe, and T. A. Ghezzehei, "A new method for rapid determination of carbohydrate and total carbon concentrations using UV spectrophotometry," *Carbohydrate Polymers*, vol. 97, no. 2, pp. 253–261, 2013.

[16] B. Suárez, Á. L. Álvarez, Y. D. García, G. Barrio, A. P. Lobo, and F. Parra, "Phenolic profiles, antioxidant activity and in vitro antiviral properties of apple pomace," *Food Chemistry*, vol. 120, no. 1, pp. 339–342, 2010.

[17] J. D. Ding, X. H. Zhang, X. C. Yao, Y. W. Huang, and C. W. Lin, "Determination of sisal pectin content by carbazole colorimetric method," *Food Research and Development*, vol. 31, pp. 138–140, 2010.

[18] S. Wang, J. Xu, C. Wang et al., "Paeoniae radix alba_ polysaccharides obtained via optimized extraction treat experimental autoimmune hepatitis effectively," *International Journal of Biological Macromolecules*, vol. 164, pp. 1554–1564, 2020.

[19] H. Li, T. Kang, B. Qi et al., "Neuroprotective effects of ginseng protein on PI3K/Akt signaling pathway in the hippocampus of D-galactose/$AlCl_3$ inducing rats model of Alzheimer's disease," *Journal of Ethnopharmacology*, vol. 179, pp. 162–169, 2016.

[20] J. A. Gorter, E. A. van Vliet, E. Aronica et al., "Potential new antiepileptogenic targets indicated by microarray analysis in a rat model for temporal lobe epilepsy," *The Journal of Neuroscience*, vol. 26, no. 43, pp. 11083–11110, 2006.

[21] D. H. Liu, E. Agbo, S. H. Zhang, and J. L. Zhu, "Anticonvulsant and neuroprotective effects of paeonol in epileptic rats," *Neurochemical Research*, vol. 44, no. 11, pp. 2556–2565, 2019.

[22] Y. Wang, Y. Tian, J. Shao et al., "Macrophage immunomodulatory activity of the polysaccharide isolated from _Collybia radicata mushroom," *International Journal of Biological Macromolecules*, vol. 108, pp. 300–306, 2018.

[23] R. Z. Chen, H. P. Li, S. Z. Li, C. G. Jin, and J. Lu, "Extraction optimization, preliminary characterization and immunological activity of polysaccharides from figs," *International Journal of Biological Macromolecules*, vol. 72, pp. 185–194, 2015.

[24] J. Y. Yin, B. C. L. Chan, H. Yu et al., "Separation, structure characterization, conformation and immunomodulating effect of a hyperbranched heteroglycan from Radix Astragali," *Carbohydrate Polymers*, vol. 87, no. 1, pp. 667–675, 2012.

[25] J. Bengzon, P. Mohapel, C. T. Ekdahl, and O. Lindvall, "Neuronal apoptosis after brief and prolonged seizures," *Progress in Brain Research*, vol. 135, pp. 111–119, 2002.

[26] M. N. Patel, "Oxidative Stress, mitochondrial dysfunction, and epilepsy," *Free Radical Research*, vol. 36, no. 11, pp. 1139–1146, 2002.

[27] M. Monirsadat, A. M. Reza, and K. Leila, "Antioxidant, antiradical, and antimicrobial activities of polysaccharides obtained by microwave-assisted extraction method: a review," *Carbohydrate Polymers*, vol. 229, article 115421, 2020.

[28] S. R. Parathath, S. Parathath, and S. E. Tsirka, "Nitric oxide mediates neurodegeneration and breakdown of the blood-brain barrier in tPA-dependent excitotoxic injury in mice," *Journal of Cell Science*, vol. 119, no. 2, pp. 339–349, 2006.

[29] X. Zhang, S. S. Cui, A. E. Wallace et al., "Relations between brain pathology and temporal lobe epilepsy," *The Journal of Neuroscience*, vol. 22, no. 14, pp. 6052–6061, 2002.

[30] H. E. Scharfman, "The CA3 "backprojection" to the dentate gyrus," *Progress in Brain Research*, vol. 163, pp. 627–637, 2007.

[31] P. A. Williams, J. P. Wuarin, P. Dou, D. J. Ferraro, and F. E. Dudek, "Reassessment of the effects of cycloheximide on mossy fiber sprouting and epileptogenesis in the pilocarpine model of temporal lobe epilepsy," *Journal of Neurophysiology*, vol. 88, no. 4, pp. 2075–2087, 2002.

[32] U. Yiş, E. Seçkin, S. Hız Kurul, F. Kuralay, and E. Dirik, "Effects of epilepsy and valproic acid on oxidant status in children with idiopathic epilepsy," *Epilepsy Research*, vol. 84, no. 2-3, pp. 232–237, 2009.

[33] J. Li, L. N. Wang, H. L. Xiao, X. Li, and J. J. Yang, "Effect of electroacupuncture intervention on levels of SOD, GSH, GSH-Px, MDA, and apoptosis of dopaminergic neurons in substantia Nigra in rats with Parkinson's disease," *Zhen Ci Yan Jiu*, vol. 39, no. 3, pp. 185–191, 2014.

[34] G. Liu, H. Guo, C. Guo, S. J. Zhao, D. S. Gong, and Y. B. Zhao, "Involvement of IRE1α signaling in the hippocampus in patients with mesial temporal lobe epilepsy," *Brain Research Bulletin*, vol. 84, no. 1, pp. 94–102, 2011.

[35] N. Farnaz, B. Rafie, and R. Homa, "2-Deoxyglucose protects hippocampal neurons against kainate-induced temporal lobe epilepsy by modulating monocyte-derived macrophages (mo-MΦ) and progranulin production in the hippocampus," *Neuropeptides*, vol. 76, article 101932, 2019.

[36] X. Zhu, O. Jiankun Liu, O. Chen et al., "Neuroprotective and anti-inflammatory effects of isoliquiritigenin in kainic acid-induced epileptic rats via the TLR4/MYD88 signaling pathway," *Inflammopharmacology*, vol. 27, no. 6, pp. 1143–1153, 2019.

[37] Z. Rupniewska and A. Bojarska-Junak, "Apoptosis: mitochondrial membrane permeabilization and the role played by Bcl-2 family proteins," *Postępy Higieny i Medycyny Doświadczalnej*, vol. 58, pp. 538–547, 2004.

[38] G. Liu, T. Wang, T. Wang, J. Song, and Z. Zhou, "Effects of apoptosis related proteins caspase-3, Bax and Bcl-2 on cerebral ischemia rats," *Biomed Rep.*, vol. 1, no. 6, pp. 861–867, 2013.

[39] X. Yuan, N. Xie, Y. Lin et al., "Role of PI3K/Akt in diazoxide preconditioning against rat hippocampal neuronal death in pilocarpine-induced seizures," *Brain Research*, vol. 1383, pp. 135–140, 2011.

[40] S. Li, L. Zhang, X. Yu, S. Zhang, G. Zhang, and P. Ding, "Neuroprotective effect of electric conduction treatment on hippocampus cell apoptosis in KA induced acute temporal lobe epileptic rats," *Brain Stimulation*, vol. 9, no. 6, pp. 933–939, 2016.

[41] R. Wu, X. Li, P. Xu et al., "TREM2 protects against cerebral ischemia/reperfusion injury," *Molecular Brain*, vol. 10, no. 1, p. 20, 2017.

[42] G. Kleinberger, Y. Yamanishi, M. Suarez-Calvet et al., "TREM2 mutations implicated in neurodegeneration impair cell surface transport and phagocytosis," *Science Translational Medicine*, vol. 6, no. 243, pp. 243–286, 2014.

Hindawi
Oxidative Medicine and Cellular Longevity
Volume 2021, Article ID 5005136, 13 pages
https://doi.org/10.1155/2021/5005136

Review Article

Ferroptosis Mediated by Lipid Reactive Oxygen Species: A Possible Causal Link of Neuroinflammation to Neurological Disorders

Ying Cheng,[1] Yiting Song,[1] Huan Chen,[1] Qianqian Li,[2] Yuan Gao,[1] Guanchao Lu,[3] and Chengliang Luo[1]

[1]*Department of Forensic Medicine, School of Basic Medicine and Biological Sciences, Soochow University, Suzhou 215123, China*
[2]*School of Forensic Medicine, Wannan Medical College, Wuhu 241002, China*
[3]*Department of Neurology, Fuping County Hospital, Weinan 711700, China*

Correspondence should be addressed to Yuan Gao; gaoyuansz@suda.edu.cn, Guanchao Lu; luyishisanxian@163.com, and Chengliang Luo; clluo@suda.edu.cn

Received 26 August 2021; Accepted 13 October 2021; Published 23 October 2021

Academic Editor: Francisco Rios

Increasing evidence indicates a possible causal link between neuroinflammation and neurological disorders, including Alzheimer's disease (AD), Parkinson's disease (PD), Huntington's disease (HD), and stroke. A putative mechanism underlying such a link can be explained by ferroptosis. Current studies have shown that disturbances of iron homeostasis, glutamate excitatory toxicity, lipid reactive oxygen species (ROS), and other manifestations related to ferroptosis can be detected in several neurological disorders caused by neuroinflammation. To date, compelling evidence indicates that damage-associated molecular pattern (DAMP) molecules (e.g., ROS) produced in the process of ferroptosis activate glial cells by activating neuroimmune pathways and then produce a series of inflammatory factors which contribute to neurological disorders. Our review article provides a current view of the involvement of ferroptosis or ROS in the pathological process of neuroinflammation, the effects of neuroinflammation mediated by ferroptosis in neurological disorders, a better understanding of the mechanisms underlying ferroptosis participates in neuroinflammation, and the potential treatments for neurological disorders. In addition, further research on the mechanisms of ferroptosis as well as the link between ferroptosis and neuroinflammation will help provide new targets for treatment.

1. Introduction

In 2003, Dolma et al. discovered that camptothecin (CPT) and a new compound erastin could selectively kill tumor cells that expressed RasV12 protein, but their lethal mechanisms are different. Cell death induced by CPT showed changes in nuclear morphology, deoxyribonucleic acid (DNA) fragmentation, and caspase activation, which could be inhibited by caspase inhibitors. However, cell death induced by erastin was different from what had been seen before [1]. Therefore, erastin may have induced a new type of cell death. Later, Yang and Stockwell and Yagoda et al. showed that this mode of cell death could be inhibited by iron-chelating agents, and increased ROS appeared in cells [2, 3]. Dixon et al. officially named this mode of cell death ferroptosis, an iron-dependent and nonapoptotic form of cell death characterized by intracellular accumulation of ROS. Through electron microscopy, it can be observed that the mitochondria of cells with ferroptosis are significantly shrunken with an increased membrane density [4].

Neuroinflammation is a complex process attributing to the interactions of glial cells and peripheral immune cells in the central nervous system (CNS). The activation of glial cells and peripheral lymphocytes releases inflammatory factors that cause damage to the nervous system. Current studies have shown that disturbances of iron homeostasis, lipid ROS accumulation, and other manifestations related to ferroptosis can be detected in some neurological disorders

caused by neuroinflammation [5–10], indicating that ferroptosis may play a tremendous role in the occurrence and development of neurological disorders, including Alzheimer's disease (AD), Parkinson's disease (PD), Huntington's disease (HD), and stroke. Therefore, we give a current view on the relationship between ferroptosis and neuroinflammation in neurological disorders, including the putative pathway for ferroptosis that participates in neuroinflammation and the potential treatments for neurological disorders.

2. The Pathway of Ferroptosis

As a new type of cell death, ferroptosis is iron-dependent and induced by intracellular lipid peroxidation accumulation. The occurrence of ferroptosis is caused by the imbalance between the production and degradation of lipid ROS in cells. Here, we summarize the main mechanisms involved in the process of ferroptosis such as accumulation of lipid ROS, inhibition of system Xc^-, glutathione peroxidase 4 (GPX4) enzyme activity, and iron metabolism disorder (Figure 1).

2.1. Ferroptosis Mediated by Lipid Reactive Oxygen Species. Apart from the iron-mediated ROS produced by the Fenton reaction, there are plentiful potential sources of ROS in the cell. Among them, one pivotal generator of intracellular ROS is NADPH oxidases (NOX) which is a family of seven transmembrane proteins which transfer electrons across biological membranes, including five monooxidases (NOX1-5) and two dual oxidases (Duox1-2) [11, 12]. When oxygen accepts an electron, the product of the electron transfer reaction is superoxide. The biological function of NOX enzymes is therefore the generation of ROS, including hydroperoxides (H_2O_2) [13], which contributes to Fenton reaction. Members of the NOX family have been shown to promote ferroptotic cancer cell death [14–16]. The NOX inhibitor could prevent erastin-induced ferroptotic death [4], whereas NOX activation sensitizes ferroptosis [15]. Mitochondria are another main source of intracellular oxidant production. Electrons are often lost during the transfer of electron transport chain complexes in oxidative phosphorylation of mitochondria. ROS are generated after electrons binding with molecular oxygen, eventually leading to oxidative stress.

As transmembrane channels, voltage-dependent anion channels (VDACs) transport ions and metabolites [17]. Yagoda et al. found that erastin could act on VDACs. With the help of RNA interference (RNAi) technology, it was found that cells with lower expression of VDAC2 or VDAC3 were tolerant to ferroptosis induced by erastin. Furthermore, erastin can also lead to changes in mitochondrial outer membrane permeability. Consequently, Yagoda et al. believed that the interference of VDACs may conduce to mitochondrial dysfunction and ROS release [3].

In addition to NADPH oxidases and mitochondria, extra sources of ROS include plentiful enzymes such as cyclooxygenases (COX), lipoxygenases (LOX), xanthine oxidase (XO), and monoamine oxidase (MAO) which produce ROS because of their enzyme function [18]. Studies have expounded that the polyunsaturated fatty acid (PUFA) chain of membrane lipids can form lipid ROS by reacting with ROS [4]. PUFAs can undergo enzymatic or nonenzymatic oxidation reactions to form lipid H_2O_2, which can combine with iron to produce toxic lipid free radicals, causing cell damage. These free radicals can transfer protons adjacent to PUFAs, initiating a new round of lipid oxidation reactions and further transmitting oxidative damage, which directly triggers ferroptosis. Lysophosphatidylcholine acyltransferase 3 (LPCAT3) and acyl-CoA synthetase long-chain family member 4 (ACSL4), two genes related to lipid metabolism, can induce lipid peroxidation. Hence, the suppression of ACSL4 and LPCAT3 may play a fundamental role in inhibiting ferroptosis [19]. Interestingly, Gao et al. found that autophagy may engender ferroptosis by regulating intracellular iron homeostasis and the generation of ROS [20]. Park and Chung also observed that ferroptosis inducer (erastin) enhanced intracellular lipid peroxidation and ROS in wild-type cells, but not in autophagy defective cells, which indicated that autophagy may induce ferroptosis by increasing lipid peroxidation [21]. What is more, Ma's group demonstrated that iron-mediated ROS generation can induce autophagy [22]. This complex cycle continuously induces ferroptosis and the production of lipid ROS, causing cell damage.

2.2. Inducing Ferroptosis by Suppressing System Xc^-. System Xc^-, a heterodimer composed of SLC7A11 and SLC3A2 subunits, is an amino acid antiporter widely distributed in the phospholipid bilayer and also well known as an important antioxidant component. System Xc^- balances excess hydrogen peroxide and peroxides by regulating the synthesis of glutathione (GSH) through the import and export of cysteine and glutamate [23]. Yang and Stockwell found that the decrease of GSH leads to the decrease in the activity of GPXs, which plays a crucial role in inhibiting the generation of lipid ROS [2], and glutathione is also an essential cofactor that contributes as the main substrate of GPX4 [24]. Pharmacologically, several system Xc^- inhibitors have been reported such as erastin, blocking the absorption of cystine, which induces ROS accumulation and ferroptosis [25]. The mRNA and protein expression levels of SLC7A11 were significantly decreased after the upregulation of P53 gene expression, thus confirming that SLC7A11 is a new target of the P53 gene [26].

2.3. Inducing Ferroptosis by Suppressing GPX4. There are many members of the GPXs family, including GPX1~GPX8. GPX4 converts reduced glutathione (GSH) to oxidized glutathione (GSSH) and reduces cellular lipid hydroperoxides (L-OOH) to corresponding alcohols [27, 28]. Research has already reported that cells with downregulated GPX4 expression were more sensitive to malnutrition, whereas upregulated GPX4 expression inhibited ferroptosis [2], indicating that GPX4 plays an important role in ferroptosis. In addition, current studies founded that an official ferroptosis inducer (RSL3) and some other compounds, such as DPI7 and DPI10, can directly inhibit GPX4 and reduce the antioxidant capacity of cells. Moreover, the mevalonate pathway which targets GPX4 by regulating the maturation of

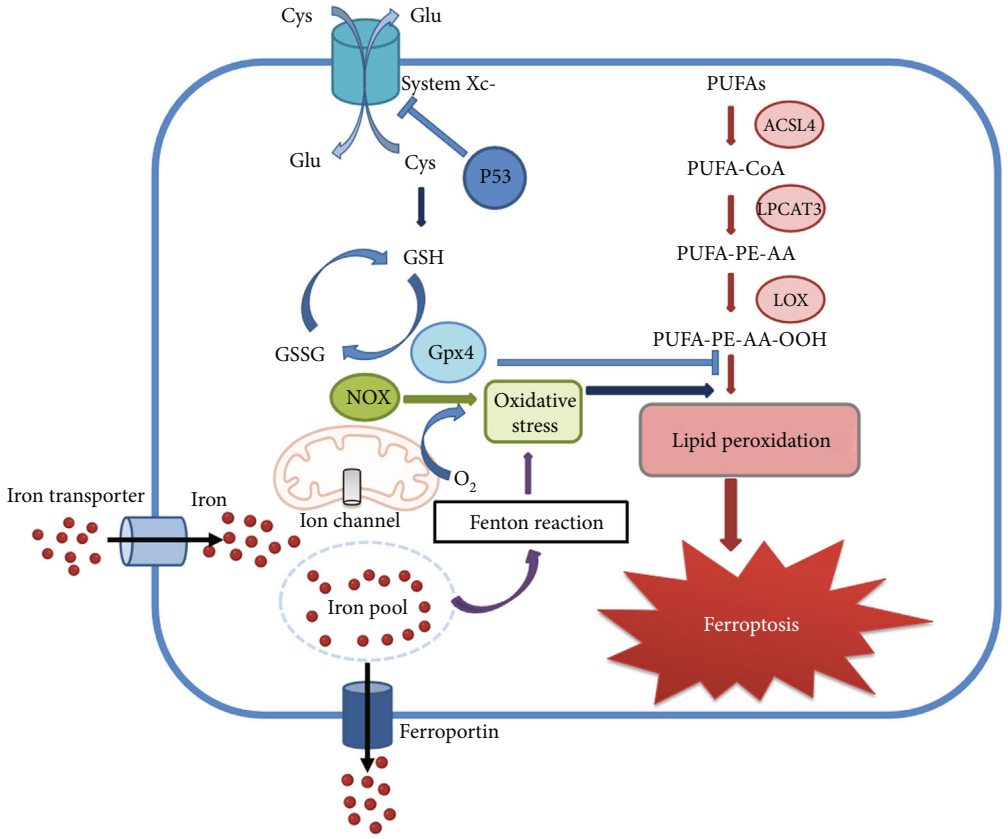

Figure 1: Mechanism pathways of ferroptosis.

selenocysteine tRNA gives rise to ferroptosis [29]. Selenocysteine is one of the amino acids in the active center of GPX4, and the insertion of selenocysteine into GPX4 requires a special transporter—selenocysteine tRNA [30]. Maturation of selenocysteine tRNA depends on the transfer of isopentenyl groups from isopentenyl pyrophosphate (IPP) to the precursor of selenocysteine tRNA by isopentenyl transferase [31]. In consequence, the mevalonate pathway can affect the synthesis of selenocysteine tRNA by downregulating IPP and further interfere with the activity of GPX4, resulting in ferroptosis.

2.4. Ferroptosis Mediated by Iron Metabolism Disorder. Free iron ions in serum are always transported together with transferrin. The Tf-Fe^{3+} complex binds to the transferrin receptor 1 (TfR1) on the cell membrane and enters the cell through endocytosis, forming a stable endosome. Fe^{3+} in the cells was reduced to Fe^{2+} by the six-transmembrane epithelial antigen of the prostate 3 (STEAP3). Fe^{2+} was transported from the nucleus to the unstable cytosol mediated by divalent metal transporter 1 (DMT1). The excessive free iron ions are stored in ferritin or transferred to the outside of the cell by ferroportin (Fpn) to maintain intracellular iron homeostasis [32]. Our recent study expounded that ferritin-knockout mice are less resistant to ferroptosis [33]. Excess iron can directly catalyze the production of lipid ROS through the Fenton reaction that brings about the continuous accumulation of intracellular lipid ROS and ferroptosis [34]. In addition, non-transferrin-bound iron (NTBI) can be transferred into the cell by ZIP14 and ZIP8 (SLC39A14 and SLC39A8) [35, 36]. Cascades underpinning imbalance of iron metabolism could be active drivers of neuropathology in major neurological disorders.

3. The Involvement of Ferroptosis in the Pathological Process of Neuroinflammation

Given that ferroptosis has been discovered to promote pathological processes in neurological disorders, many researchers sought to gain insight into mechanisms of ferroptosis that participates in neuroinflammation to neurological disorders. Summarily, DAMP molecules, produced in the process of ferroptosis, activate glial cells by activating neuroimmune pathways. Activated glial cells produce a series of inflammatory factors which contribute to neuronal damage and a series of neurological disorders (Figure 2).

3.1. Activation of NF-κB Pathway by ROS. In the pathogenesis of ferroptosis, a key point is the deficiency of GPX4, which leads to the accumulation of lipid ROS and further bringing about ferroptosis [29, 37]. GPX4 utilizes GSH as a cofactor to remove lipid peroxidation from the membrane. GPX4 reduces the complex hydroperoxide including phosphatidyl hydroperoxide and cholesterol hydroperoxide to the corresponding alcohol to maintain the redox balance and avoid harmful oxidative stress damage. ROS and

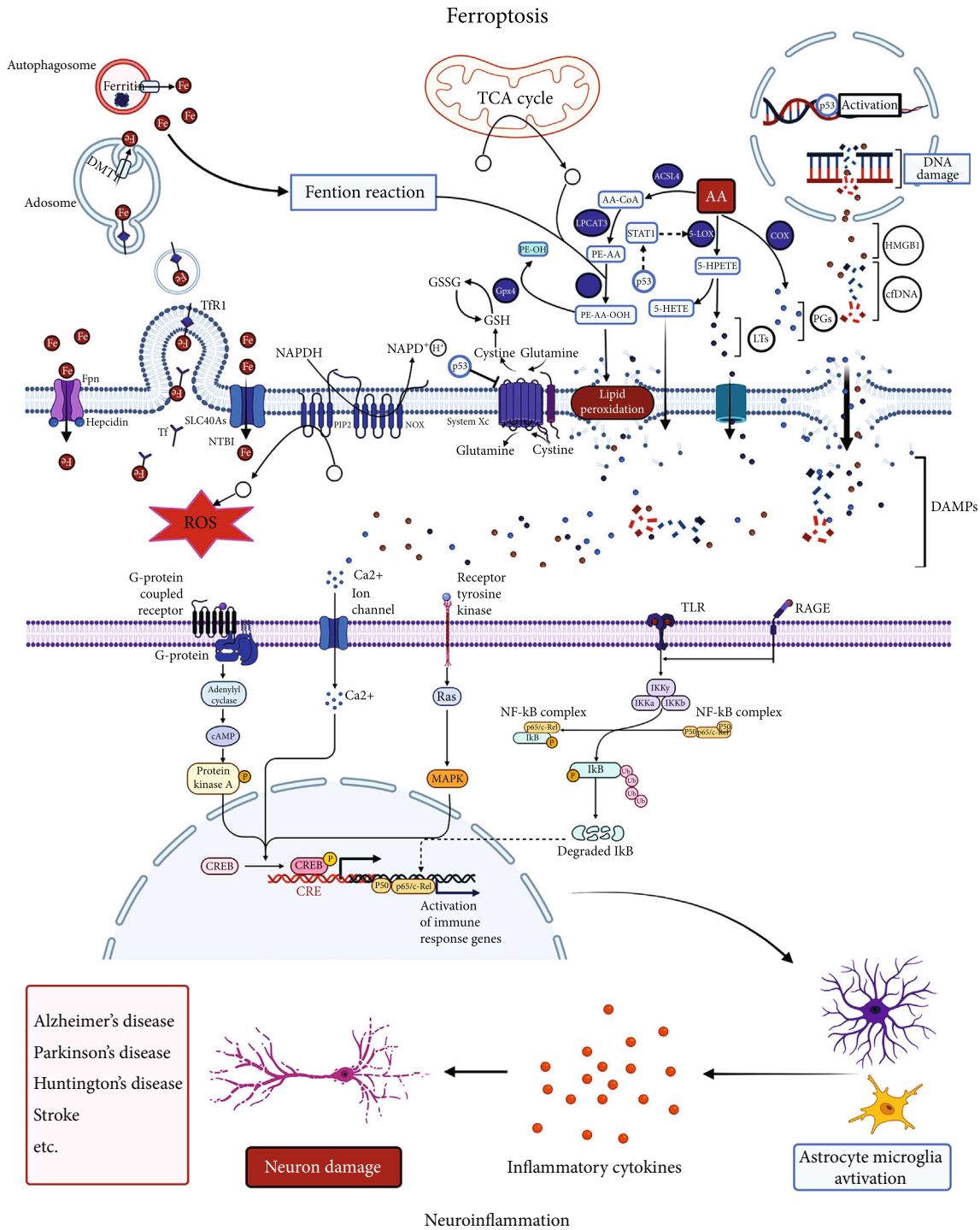

Figure 2: Putative pathway for ferroptosis participates in neuroinflammation to neurological disorders. Damage-associated molecular pattern (DAMP) molecules (e.g., ROS, cfDNA, HMGB1, ITs, and PGs) produced in the process of ferroptosis activate glial cells by activating neuroimmune pathways. Activated glial cells produce a series of inflammatory factors which contribute to neuronal damage and a series of neurological disorders, such as Alzheimer's disease, Parkinson's disease, Huntington's disease, and stroke.

oxidative stress are common features associated with inflammation [38]. ROS can activate the nuclear factor kappa B (NF-κB) transcription factor system, which is a key player in inflammation-related cancers. The core components of the NF-κB pathway are mainly the inhibitory IκB protein, the IκB kinase (IKK) complex, and the transcription factor NF-κB itself. External stimuli trigger IKK, initiating the phosphorylation, ubiquitination, and degradation of IκB protein. The released dimer of NF-κB is further activated by various posttranslational modifications and is transferred to the nucleus to bind to specific DNA sequences, promoting the transcription of target genes. Studies have shown that

ROS, especially H_2O_2, can activate IKK in certain cell types [39]. ROS promotes IKKγ/NEMO dimerization which is the subunit of IKK by promoting the formation of disulfide bonds between Cys54 and Cys347, resulting in the activation of IKK and the initiation of the NF-κB pathway. Additionally, ROS regulation of the upstream NF-κB activation pathway is also reflected in selective IκBα phosphorylation [40]. IκBα is usually phosphorylated at Ser32 and Ser36, but H_2O_2 causes ubiquitination and degradation of IκBα by influencing the phosphorylation of IκBα at Tyr42 or other tyrosine residues. The released dimer of NF-κB migrates to the nucleus, where it binds to the κB site on the DNA sequence and promotes the transcription of target genes. Therefore, GPX4 plays a significant role in the elimination of peroxides, reducing the accumulation of ROS and inhibiting the activation of NF-κB. NF-κB is a nuclear transcription factor closely related to inflammation [41], which is expressed in almost all cell tissues, such as microglia, neurons, and astrocytes. It regulates multiple functional target genes and participates in a variety of biological processes such as immune response, inflammatory response, apoptosis, and tumorigenesis. Microglia are one of the most important immune cells in the CNS and play a vital role in both normal brain development and neuroinflammatory diseases. The NF-κB signaling pathway of the glial also plays a critical role in inflammatory responses in the nervous system. Chronic activation of NF-κB can induce transcription of various neuroinflammatory genes [42] and promote the secretion of inflammatory cytokines, such as TNF-α, IL-6, IL-1β, nitric oxide, adhesion molecules, and neurotoxins, inducing neuronal apoptosis. Accumulated ROS during the ferroptosis process in the brain leads to the activation of the NF-κB pathway in glial cells and the occurrence of neuroinflammation.

3.2. Neuroinflammatory Damage Caused by Lipid Peroxidation. In the complex mechanism of ferroptosis, another hallmark lipid peroxidation must be mentioned. Researches have shown that lipids not only form lipid peroxides to interfere with the structures of membrane and functions of membrane proteins but also induce intracellular signal transduction and stimulate other pathways leading to cell death [4, 43]. Many studies have illustrated that lipid may play a vital role in inflammation, immunity, metabolism, and various biofilms. Excessive ROS such as H_2O_2 and hydroxyl radical (·OH), as well as reactive nitrogen species (RNS) such as NO· and ONOO-, may give rise to oxidative stress [44], oxidizing biological macromolecules such as lipids, DNA, or proteins. The ·OH is the most dynamic and dangerous reactive oxygen radical, which is formed by H_2O_2 in the presence of metal ions. Hydroxyl radicals play a key role in lipid peroxidation, which oxidizes lipids containing carbon-carbon double bonds, especially PUFAs. In PUFAs, the C=C units are separated by a single-bonded C atom, and the hydrogen atoms (diallyl hydrogens) attached to these C atoms (bis-allylic hydrogens) are vulnerable to hydroxyl radical. Therefore, PUFA such as arachidonic acid (AA) is highly oxidized fatty acid. The peroxides of PUFAs and their final production—reactive aldehydes like 4-hydroxynonaldehyde (4-HNE)—lead to carbonylation of proteins, which is associated with atherosclerosis, neurodegenerative diseases, and other diseases [45]. Oxidation of PUFAs can be carried out by nonenzymatic or enzymatic means. Lipoxygenases are ferric enzymes that catalyze the oxygenation of PUFAs to produce fatty acid hydroperoxides. According to the research, the cascade reaction of arachidonic acid involves enzymes related to lipid peroxidation metabolism [46]. The oxidation cascade of AA first releases the polyunsaturated fatty acid AA from the N-2 position of the membrane phospholipid by phosphatase A2 (PLA2). AA produces bioactive eicosanoids (prostaglandins, leukotrienes, and epoxy-fatty acids) using enzymes related to lipid peroxidase (COX, LOX, and cytochrome P450 enzymes). Under physiological conditions, COX-2 plays a role in regulating cerebral vascular and synaptic plasticity in the nervous system. Under pathological conditions, the metabolism of AA mediated by COX to produce prostaglandin was also enhanced in a rat model of focal cerebral ischemia [47]. Prostaglandins, a class of carotenoids, are reported to be a key factor in ischemic and excitotoxic nerve injury. Overexpression of COX-2 during lipid peroxidation mediates neurotoxicity through prostaglandin E2 (PGE2). If the toxic stimulation persists, it may also lead to secondary neuroinflammation damage of the CNS. Experimental studies support that the application of COX-2 inhibitors reduces the level of proinflammatory cytokines such as IL-1β and TNF-α [48, 49]. Drug suppression or gene knockout of 15-LOX also leads to reduced production of IL-1 and TNF-α [50, 51].

3.3. DAMPs Inducing Neuroinflammation. Iron disturbance is a basic element of ferroptosis. Excess iron from hemoglobin and the periphery can be transported through a series of ion channels and transporters, including divalent metal transporter 1 (DMT1), transferrin receptor 1 (TfR1), and ferroportin (Fpn). Fe^{2+} directly catalyzes the generation of lipid ROS through the Fenton reaction, resulting in the continuous accumulation of intracellular lipid ROS and causing ferroptosis. It was founded that excess Fe^{2+} transported from the microglia resulted in iron metabolism disorder [34]. In the CNS, glial cells not only continuously monitor the dynamic balance of the internal environment but also act as immune cells, resisting endogenous and exogenous pathogenic stimuli [52]. Immune cells recognize pathogens primarily by pattern recognition receptors (PRRs), which include pathogen-associated molecular patterns (PAMPs) and damage-associated molecular patterns (DAMPs). The main form of PRRs is the Toll-like receptor (TLR) family, which is not only abundant in immune cells but also expressed in CNS glial cells. The danger signal DAMP is an endogenous molecule encoded directly by endogenous genes of the host. It can be released immediately under certain conditions of tissue damage, without the need for protein synthesis. DAMPs from ferroptosis cells and proinflammatory cytokines provide prefeedback signals that reinforce the programmed death of more cells [53]. Severe cycles of death can lead to barrier dysfunction, with inflammation spreading throughout the body, which may

eventually bring about extensive multiorgan failure. DAMPs, hemoglobin, erythrocyte, and iron are produced during ferroptosis [54], which can be recognized by PRRs, namely, TLRs in glial cells. Both microglia and astrocytes are activated and secrete inflammatory cytokines such as IFN-α, IFN-β, IL-1β, IL-6, IL-10, IL-12, IL-18, and TNF-α, as well as ROS and chemokines, participating in neuroinflammation caused by an infection in the nervous system [55–57]. In the TLR family, the TLR3 signal induces the strongest proinflammatory polarization response, which is characterized by the secretion of high levels of IL-12, TNF-α, IL-6, CXCL10, IL-10, and IFN-β [58]. In acute infectious or noninfectious CNS diseases caused by ferroptosis of nerve cells, activated TLR signals in glial cells are involved in neuronal injury under the action of endogenous and exogenous pathogens or the release of products from cell damage. In AD, amyloid, S100 protein, and high mobility group box-1 (HMGB1) are secondary key factors following primary neuritis, further exacerbating the production of proinflammatory cytokines. HMGB1 belongs to the Ia DAMP category, which can be perceived by PRRs on several cells. Class Ia DAMPs signal danger to surrounding PRR-carrying cells, such as phagocytes, triggers sterile inflammation [59].

3.4. Ferroptosis Mediated by P53 Gene Inducing Neuroinflammation. P53 gene, as a tumor suppressor gene that mediates the inhibition, senescence, and apoptosis of cell cycle, plays an important role in tumorigenesis and development. Recently, acetylated defective P53 mutants have been found to promote ferroptosis [60]. Jiang et al. discovered that the activity of H1299 cells with P53 gene silenced did not change when they were treated with ROS [61]. However, treated with ROS after the P53 gene was activated, 90% of the H1299 cells died, indicating that the activation of P53 reduced the antioxidant capacity of these cells. Studies have demonstrated that the P53 gene mainly affects the synthesis of GSH by inhibiting system Xc^- [32]. In addition, P53 can promote ferroptosis by enhancing the expression of spermine N1-acetyltransferase 1 (SAT1), which acetylates spermine and is an important rate-limiting enzyme in polyamine catabolism. The abnormal metabolism of polyamine and aberrant SAT1 expression is associated with a variety of pathological conditions, including neurological disorders and cancer [62, 63]. The activity of SAT1 will increase in a variety of stress reactions, including oxidative stress and inflammatory stimuli. The activation of SAT1 may lead to lipid peroxidation and ferroptosis induced by ROS, resulting in neuroinflammatory damage. Previous studies have also observed that overexpression of SAT1 leads to rapid depletion of spermine in cells, ultimately giving rise to significant growth inhibition and mitochondrial apoptosis [64]. The induction of SAT1 was related to the expression level of 15-LOX, and pharmacological inhibition of 15-LOX by PD146176 attenuated SAT1-mediated ferroptosis [65]. Moreover, 15-LOX, together with COX-2 which is overexpressed during ferroptosis, is also involved in the metabolic process of arachidonic acid, producing prostaglandins, peroxides, ROS, and other substances to induce inflammatory injury of the nervous system [66].

4. The Effects of Neuroinflammation Mediated by Ferroptosis in Neurological Disorders

Neuroinflammation of the CNS is an extremely complex process. In the initial stage, glial cells act as immune cells, performing defensive reactions in response to traumatic stimuli. Mediated by ATP, microglia are activated to produce proinflammatory cytokines [67, 68]. Local damage of the CNS may affect other brain regions far away from the damage site through Ca^{2+} waves [69]. Lipid ROS dysregulation can also destroy physiological calcium signals [70]. During the progressive stage of neuroinflammation, the inflammatory microenvironment may induce glial cells to transform into different phenotypes and regulate inflammation through cell feedback and cell-to-cell communication mechanisms, resulting in the proinflammatory and anti-inflammatory reactions of neuroinflammation. Besides, ferroptotic neurons themselves also could release proinflammatory DAMPs, which then triggered the innate immune system in brain tissues [54]. In the prognostic stage of neuroinflammation, glial cells are subjected to endogenous changes such as persistent stimulation, aging, or gene defects under severe pathological conditions, which will lead to chronic neuroinflammation of the CNS and degeneration of neurons. Chronic neuroinflammation is one of the most important mechanisms in the pathogenesis of neurodegenerative diseases. Physiologically, iron, as an important redox metal, produces ATP in the cellular metabolism of the CNS, which supplies energy for cell metabolism in physiological processes. However, when iron metabolism is disrupted, the nerve system is vulnerable to damage caused by excess iron and oxidative stress. Recently, studies supported that iron metabolism disorders, glutamate excitatory toxicity, lipid ROS accumulation, and other characteristics related to ferroptosis can be detected in some neurological disorders. Accumulated evidence demonstrates that ferroptosis participates in the neuroinflammatory pathological process. Ferroptosis inhibitors have also been found to improve the prognosis of neurological disorders. Therefore, further investigation into the mechanism of ferroptosis involved in the neuroinflammatory process will be valuable to the treatment and improvement of neurological disorders. The effects of neuroinflammation mediated by ferroptosis in several characteristic neurological disorders are described below.

4.1. Alzheimer's Disease (AD). Among the classical properties of AD, the amyloid cascade theory is an important study to explain the pathogenesis of AD. Amyloid β-protein (Aβ) accumulation is also considered to be an initial event in the pathogenesis of AD. Another feature of AD is intracellular neurofibrillary tangles (NFT) due to hyperphosphorylation of Tau protein. Under physiological conditions, tau protein stabilizes microtubules and regulates axon transport. Pathological changes will make tau separate from microtubules, resulting in synaptic loss and neuronal dysfunction. What is more, the neurocognitive decline is associated with synaptic reduction and neurotransmitter oxidation, which could

be attributed to oxidative stress, mainly the increase of ROS and intracellular and extracellular hydrogen peroxide [71, 72]. There has been early evidence of an association between iron accumulation in the cerebral cortex and the development of AD [73, 74]. Svobodová et al. proved that free iron and ferritin accumulated after amyloid plaque formation in the cerebral cortex of β-amyloid precursor protein (APP)/-presenilin 1 (PS1) transgenic mouse model [75]; iron deposition is involved in the formation of Aβ plaque and the misfolding process of NFT. Inhibition of lipid peroxidation and ferroptosis mediated by ACSL4 and ACSL4 special protein 1 (SP1) mimicked the beneficial effects of aldehyde dehydrogenase (ALDH2) overexpression in APP/PS1-mutant mice [76]. APP is a type 1 transmembrane protein; the proteolytic cleavage of which forms the Aβ is associated with the pathogenesis of AD. In the presence of free iron, Aβ plaques are effectively involved in ROS production, leading to increased lipid peroxidation, protein oxidation, and DNA damage [77]. Proteolysis cleavage in APP occurs through enzyme complexes including α-secretase or β-secretase and γ-secretase. Tsatsanis et al. showed that APP promotes the iron efflux of neurons by stabilizing the expression of ferroportin on the cell surface [78]. The proteolytic cleavage of APP under the action of β-secretase leads to the accumulation of iron in the neuron cells, resulting in the generation of Aβ. Hambright et al. found in a mouse model with a condition deletion in neurons of the forebrain of GPX4 that GPX4-deficient mice have significant learning and memory dysfunction, which is related to markers of ferroptosis, such as increased lipid peroxidation and neuroinflammation [79]. Furthermore, treatment with liproxstatin-1, a ferroptosis inhibitor, ameliorated neuronal death and memory impairment induced by Aβ [80]. In addition, enzymes involved in lipid peroxidation, such as COX-2, LOX, and cytochrome P450 enzymes, metabolize AA into substances such as prostaglandins, leukotrienes, and epoxide fatty acids. COX-2 mediates neurotoxicity through PGE2 produced from AA, which is an important member of DAMPs. If the toxic stimulation persists, it may also conduce secondary neuroinflammation damage in the CNS. More and more evidence indicates that the amyloid cascade theory alone may not be convinced to explain the pathogenesis of AD. Therefore, researchers attempt to explore the relationship with other pathological mechanisms. The increased levels of inflammatory markers in the brain of AD patients and the discovery of AD risk genes related to innate immune function suggest that neuroinflammation may play a significant role in the pathogenesis of AD [81–85]. A hallmark of neuroinflammation is the production of proinflammatory cytokines, and the innate immune cells involved in the process of neuroinflammation are mainly microglia and astrocytes. Capillary endothelial cells and permeable blood cells also participate in neuroinflammation, especially when the blood-brain barrier (BBB) is subjected to biochemical or mechanical damage [86, 87]. Astrocytes respond to pathological injury through reactive gliosis, and inflammatory injury induces A1 astrocyte phenotype through the NF-κB pathway, expressing inflammatory mediators. Microglia recognize pathogens, cell debris, or abnormal proteins through TLR and induce microglia cell response [82], internalizing and degrading pathogenic substances through pinocytosis. The process usually disappears once the pathogen or irritant is eliminated. Nonetheless, the function of microglia in the brain of the elderly is impaired. In the case of severe pathological conditions or continuous stimulation by pathogens, the glia is always in the activated state and secreting inflammatory factors, leading to neuroinflammatory damage [88]. Furthermore, crosstalk between glial cells and neurons can also be observed in AD. Aβ activates NF-κB in astrocytes, resulting in an increased release of complement C3, which acts on the C3a receptors of microglia and neurons, and the secretion of IL-1α in activated microglia induces the production of A1 astrocytes. In the inflammatory environment of AD, glial crosstalk may form positive feedback, leading to nervous system disorders and self-amplifying inflammatory responses. Evidence from genome-wide association studies also supports the initiating role of neuroinflammation in AD, and mutations in microglia or innate immune genes are associated with an increased incidence of AD in the population [84]. The influence of neuroinflammation on AD has also been confirmed in clinical imaging studies, and the activation of microglia in AD patients is negatively correlated with the structural integrity or functional activity of the brain [89]. Preclinical studies correspondingly support clinical imaging observations that microglia activated by Aβ produce neurotoxic cytokines that lead to neuronal dysfunction [90]. Several current studies have proved that ferroptosis and neuroinflammation play a fundamental role in the pathogenesis and progression of AD, and glial cells are the core of neuroinflammation. Regulating the occurrence of lipid peroxidation and ferroptosis in neurons has important therapeutic significance for neurodegenerative diseases. Meanwhile, targeting glial cells as a breakthrough for drug treatment of AD also has a certain prospect.

4.2. Parkinson's Disease (PD). The typical pathological feature of Parkinson's disease is the degeneration of dopaminergic neurons in the substantia nigra, which is linked with the systematic and progressive accumulation of iron in the substantia nigra, leading to the consumption of dopamine in the striatum. Meanwhile, Lewy bodies also appear in the cells, with α-synuclein aggregation as the main component. Studies have shown that the accumulated α-synuclein is accountable for the generation of ROS followed by lipid peroxidation in an iron-dependent manner, leading to cell death [70]. The increase of iron in the substantia nigra and globus pallidus in PD patients has also been observed by magnetic resonance imaging (MRI), which is closely related to the duration of disease, neurodegeneration, and the severity of sports injuries [6, 91]. The study indicated that treatment with deferiprone, an iron chelator, substantially reduced unstable iron and biological damage in oxidatively stressed cells, which improve motor function. In addition, studies have shown that the related mechanisms of neuroinflammation, such as activation of microglia, the proliferation of astrocytes, and other peripheral immune cells, may contribute to the impairment of dopaminergic neurons in the

substantia nigra. Some cellular and molecular responses related to neuroinflammation may induce harmful events such as oxidative stress and apoptosis mediated by cytokine receptors, eventually leading to dopamine cell death [92]. In 1988, McGeer et al. found activated microglia in the substantia nigra of the nervous system in an autopsy study of patients with Parkinson's disease [93]. Bertrand and colleagues reported that there is mild microglial activation in the locus blue in patients with Parkinson's disease [94]. These are important neuropathological features of Parkinson's disease. Activated microglia produce voluminous oxygen-derived and nitrogen-derived products, among which NO and O^{2-} can combine to form a highly reactive nitrogen species peroxynitrite (ONOO-), which can cause oxidative damage to various proteins. Another important neuropathological feature of the substantia nigra in Parkinson's disease is astrocyte response. Astrocytes may protect the nervous system by eliminating reactive oxygen species in the nervous system through GPX4 or secreting glial cell-derived neurotrophic factor (GDNF). The deficiency or decreased activity of GPX4 may cause ROS accumulation, lipid peroxidation, or activation of the NF-κB pathway to produce inflammatory mediators, resulting in inflammatory damage to the nervous system. There may be few astrocytes around vulnerable neurons in patients with PD, and a limited astrocyte environment may be a susceptibility factor for the disease [95]. Mogi et al. showed increased concentrations of TNF-α, TGF-α, TGF-β1, and IL-1β in the striatum of patients with Parkinson's disease. TNF-α, IL-1β, and IFN-γ were also detected in the patient's substantia nigra [96]. In addition, dopaminergic neurons express receptors for these cytokines, which combine with the cytokines to cause neurotoxicity. These inflammatory cytokines, such as TNF-α, IL-1β, and IFN-γ, can induce the expression of nitric oxide synthase (iNOS) or COX-2. LOX and COX are important metabolic enzymes in lipid peroxidation, resulting in the metabolism of arachidonic acid into prostaglandin, leukotriene, and other substances. COX-2 mediates neurotoxicity through PGE2, resulting in inflammatory damage to the nervous system. Concentrations of other enzymes involved in neuroinflammation mediated by oxidative stress are also increased in PD. Biofluid studies also support the role of neuroinflammatory processes in Parkinson's disease, with elevated levels of IL-2, IL-6, and TNF-α in the serum of patients with PD. Regardless of the original nerve conduction in PD, prevention or inhibition of ferroptosis in the nervous system, as well as the inflammatory immune response of glial cells, is important to prevent the progression of the disease.

4.3. Huntington's Disease (HD). A study demonstrated that a larger concentration of iron in neurons was observed in a mouse HD model compared to the wild-type model, suggesting that iron accumulation may be involved in neurodegeneration in HD patients. When excessive Fe^{2+} is generated intracellularly, the production of lipid ROS can be directly catalyzed by the Fenton reaction, resulting in the continuous accumulation of lipid ROS and eventually causing cell ferroptosis [34]. Hence, the overexpression of antioxidant genes in HD can be explained as an adaptive response to ROS imbalance. Ferritin is identified as an iron storage protein with antioxidant activity. Previous research reported the accumulation of ferritin in microglia of R6/2 mice appeared to be a protective mechanism to counteract iron accumulation [9]. Mitochondria are the main source of ROS in cells. During the transfer of electron transport chain complexes in oxidative phosphorylation, electrons are often lost, and ROS are generated after electron binding with molecular oxygen, ultimately, leading to oxidative stress. Furthermore, mutated Huntington's protein (mHTT) in HD is expressed in both neurons and glial cells, which can bring about the production of free radicals in the CNS, eventually triggering oxidative stress [97]. The accumulation of reactive microglia and astrocytes can be observed in the brain of HD patients. Upregulated expression of IL-6, IL-8, and tumor necrosis factor (TNF) in cerebrospinal fluid indicates immune activation. Under the condition of the injury, astrocytes magnify the inflammatory process, remove cell debris, and repair the damaged tissue. Astrocytes that express mHTT were found to be functionally deficient, with low expression of glutamate transporters and inhibited glutamate uptake, resulting in striatal neurons being affected by extracellular glutamate and exhibiting the neuronal glutamate excitability associated with ferroptosis observed in HD. In addition, astrocytes expressing mHTT have been shown to reduce the availability of the inflammatory C-C chemokine ligand 5 (CCL5) to neurons [98]. On the one hand, the mHTT reduced the transcription of CCL5 in astrocytes in an NF-κB-dependent manner. On the other hand, it prevents astrocytes from secreting the CCL5 protein; the loss of which may adversely affect neuronal function [99, 100]. The death of neurons and protein aggregates caused by various oxidative stresses, known as DAMPs, can be recognized by PRRs, namely, Toll-like receptors (TLRs) in glial cells, resulting in activation of both microglia and astrocytes and the secretion of inflammatory cytokines, which may cause aseptic encephalitis in HD. Neuroinflammation is an important component of the pathogenesis of HD, and the expression of mutant Huntington protein alters specific processes of glial response, such as cell signaling, cytokine release, and migration. Changes in microglia and astrocyte function may result in a chronic pathogenic inflammatory response that leads to the death of other neurons, leading to more neuroinflammation.

4.4. Stroke. Stroke has an extremely high incidence, mortality, and disability, which can be classified into two major categories: hemorrhagic and ischemic stroke according to the original cause of occurrence [101]. Ischemic stroke is caused by the stenosis or occlusion of carotid and vertebral arteries and insufficient blood supply to the brain, resulting in the depletion of oxygen and nutrients, causing a cascade reaction leading to oxidative stress and mitochondrial damage [102]. Researches have indicated that ferroptosis is strongly associated with ischemic stroke. In 2014, Ahmad et al. found that in a mouse model of ischemic stroke, the content of GSH significantly decreased while the content of lipid ROS increased. The imbalance between ROS and antioxidant

defense results in oxidative stress, lipid peroxidation, and eventually neuronal damage [103]. Tuo et al. also reported in their research that ferroptosis caused neuronal degeneration after ischemic stroke, and the use of ferroptosis inhibitors such as ferrostatin-1 or liproxstatin-1 exerted the neuroprotection in a mouse ischemic model [104]. Studies have shown that selenium ions can enhance the expression of GPX4 and inhibit ferroptosis by activating transcription factors TFAP2c and Sp1 [105]. The addition of GPX4 in a mouse model of ischemic stroke exerted an effect on the improvement of behavioral defects to some extent. After ischemic stroke, microglia are activated and change morphologically and phenotypically. As the innate immune cells in the CNS, microglia play a key role in the removal of foreign bodies, cell debris, and the production of cytokines. Studies have revealed that the release of cytokines can destroy the blood-brain barrier [102], leading to the aggregation of various inflammatory cells such as macrophages, natural killer cells, and glial cells to the ischemic site to produce inflammatory responses. Interestingly, activated microglia play a dual role in ischemic stroke. On the one hand, microglia cause inflammatory damage to nerve tissue by secreting proinflammatory cytokines, and on the other hand, they also secrete anti-inflammatory factors to play a neuroprotective role [106, 107]. Pharmacological reduction of 15-LOX expression exerted to neuroprotection and improved behavioral recovery in a stroke model [108]. Jin et al. demonstrated that the consumption of microglia by PLX3397, a dual colony-stimulating factor-1 inhibitor, could aggravate cerebral infarction and neurological defects, and the failure of microglia could also exaggerate the expression of inflammatory mediators in the nervous system [109]. Different subsets of microglia may play diverse roles after ischemic stroke in the brain, striking a balance between proinflammatory and anti-inflammatory. Astrocytes, like microglia, also play essential immune functions in the CNS. Under normal physiological conditions, astrocytes take glutamate from extracellular sources. Nonetheless, in severe pathological conditions, such as ischemic stroke, the expression of glutamate transporter EAAT2 in astrocytes is defective, which prevents astrocytes from absorbing excessive extracellular glutamate, giving rise to impaired glutamate excitability of neurons. After ischemic stroke, astrocytes are stimulated by cytokines from neurons and glial cells to generate IL-1β, IL-6, and TNF-α, which stimulate and exacerbate the inflammatory response.

5. Conclusion and Expectation

There are a series of complex biochemical reactions during ferroptosis pathology including lipid ROS accumulation, glutamate transport inhibition, and iron metabolism disorder, which promote neuroinflammation and oxidative stress response and then aggravate the CNS damage. Activated microglia, reactive astrocytes, invading T cells, and overproduction of inflammatory mediators constitute the neuroinflammatory response. In the initial stage, acute inflammatory responses that happen in CNS trauma may play a protective role, limiting the severity of the injury and enhancing neuronal repair. If the acute inflammation does not subside sufficiently, it will turn into chronic inflammation and is difficult to control. In this case, glial cells tend to aggravate oxidative stress on neurons. Although neuroinflammation is not necessary during the initial stage of neurological disorders, a persistent inflammatory response can cause the exacerbation of diseases. Voluminous studies have confirmed that ferroptosis is closely related to AD, PD, HD, stroke, and other neurological disorders. Although the characteristics and pathogenesis of ferroptosis, as well as the pathological mechanism of ferroptosis's involvement in neuroinflammation, have been initially understood, there are still many problems to be solved in this field. For instance, what are the similarities and differences in the molecular mechanisms of ferroptosis in the context of different neurological disorders? The use of inhibitors of ferroptosis in experimental animal models can improve the severity of the diseases, but whether drugs targeting ferroptosis can play a role in the clinical treatment of chronic neuroinflammatory diseases still needs a lot of clinical verification. Further researches on ferroptosis will help us to deeply comprehend the pathogenesis of neurological disorders and provide a theoretical basis and transformation strategies for the clinical prevention and treatment of neurological disorders.

Conflicts of Interest

The authors declare that there are no conflicts of interest regarding the publication of this paper.

Authors' Contributions

Ying Cheng and Yiting Song contributed equally to this work.

Acknowledgments

This study was financially supported by the National Natural Science Foundation of China (No. 81971163 and No. 82101972), the Suzhou Municipal Science and Technology Bureau (SYS2019027), a project funded by the Priority Academic Program Development of Jiangsu Higher Education Institutions (PAPD), the outstanding young backbone teacher of the "Blue Project" in Jiangsu Province (to Chengliang Luo), the National Training Program of Innovation and Entrepreneurship for Undergraduate (202110285046Z), and the Key Project of Science Foundation of Wannan Medical College (WK2020Z05).

References

[1] S. Dolma, S. L. Lessnick, W. C. Hahn, and B. R. Stockwell, "Identification of genotype-selective antitumor agents using synthetic lethal chemical screening in engineered human tumor cells," *Cancer Cell*, vol. 3, no. 3, pp. 285–296, 2003.

[2] W. S. Yang and B. R. Stockwell, "Synthetic lethal screening identifies compounds activating iron-dependent, nonapoptotic cell death in oncogenic-RAS-harboring cancer cells," *Chemistry & Biology*, vol. 15, no. 3, pp. 234–245, 2008.

[3] N. Yagoda, M. von Rechenberg, E. Zaganjor et al., "RAS-RAF-MEK-dependent oxidative cell death involving voltage-dependent anion channels," *Nature*, vol. 447, no. 7146, pp. 865–869, 2007.

[4] S. J. Dixon, K. M. Lemberg, M. R. Lamprecht et al., "Ferroptosis: an iron-dependent form of nonapoptotic cell death," *Cell*, vol. 149, no. 5, pp. 1060–1072, 2012.

[5] Y. Mi, X. Gao, H. Xu, Y. Cui, Y. Zhang, and X. Gou, "The emerging roles of ferroptosis in Huntington's disease," *NeuroMolecular Medicine*, vol. 21, no. 2, pp. 110–119, 2019.

[6] M. Rossi, H. Ruottinen, S. Soimakallio, I. Elovaara, and P. Dastidar, "Clinical MRI for iron detection in Parkinson's disease," *Clinical Imaging*, vol. 37, no. 4, pp. 631–636, 2013.

[7] J. Wu, J.-J. Yang, Y. Cao et al., "Iron overload contributes to general anaesthesia-induced neurotoxicity and cognitive deficits," *Journal of Neuroinflammation*, vol. 17, no. 1, p. 110, 2020.

[8] S. Ayton, Y. Wang, I. Diouf et al., "Brain iron is associated with accelerated cognitive decline in people with Alzheimer pathology," *Molecular Psychiatry*, vol. 25, no. 11, pp. 2932–2941, 2020.

[9] D. A. Simmons, M. Casale, B. Alcon, N. Pham, N. Narayan, and G. Lynch, "Ferritin accumulation in dystrophic microglia is an early event in the development of Huntington's disease," *Glia*, vol. 55, no. 10, pp. 1074–1084, 2007.

[10] J.-X. Ren, X. Sun, X.-L. Yan, Z. N. Guo, and Y. Yang, "Ferroptosis in neurological diseases," *Frontiers in Cellular Neuroscience*, vol. 14, p. 218, 2020.

[11] K. Wingler, J. J. R. Hermans, P. Schiffers, A. L. Moens, M. Paul, and H. H. H. W. Schmidt, "NOX1, 2, 4, 5: counting out oxidative stress," *British Journal of Pharmacology*, vol. 164, no. 3, pp. 866–883, 2011.

[12] R.-N. Zhang, Q. Pan, R.-D. Zheng et al., "Genome-wide analysis of DNA methylation in human peripheral leukocytes identifies potential biomarkers of nonalcoholic fatty liver disease," *International Journal of Molecular Medicine*, vol. 42, no. 1, pp. 443–452, 2018.

[13] K. Bedard and K.-H. Krause, "The NOX family of ROS-generating NADPH oxidases: physiology and pathophysiology," *Physiological Reviews*, vol. 87, no. 1, pp. 245–313, 2007.

[14] Y. Xie, S. Zhu, X. Song et al., "The Tumor Suppressor p53 Limits Ferroptosis by Blocking DPP4 Activity," *Cell Reports*, vol. 20, no. 7, pp. 1692–1704, 2017.

[15] W.-H. Yang, Z. Huang, J. Wu, C. K. Ding, S. K. Murphy, and J. T. Chi, "A TAZ-ANGPTL4-NOX2 axis regulates ferroptotic cell death and chemoresistance in epithelial ovarian cancer," *Molecular Cancer Research*, vol. 18, no. 1, pp. 79–90, 2020.

[16] W.-H. Yang, C.-K. C. Ding, T. Sun et al., "The Hippo pathway effector TAZ regulates ferroptosis in renal cell carcinoma," *Cell Reports*, vol. 28, no. 10, pp. 2501–2508.e4, 2019.

[17] M. Skonieczna, A. Cieslar-Pobuda, Y. Saenko et al., "The impact of DIDS-induced inhibition of voltage-dependent anion channels (VDAC) on cellular response of lymphoblastoid cells to ionizing radiation," *Medicinal Chemistry*, vol. 13, no. 5, pp. 477–483, 2017.

[18] T. Finkel, "Signal transduction by reactive oxygen species," *The Journal of Cell Biology*, vol. 194, no. 1, pp. 7–15, 2011.

[19] Y. Xie, W. Hou, X. Song et al., "Ferroptosis: process and function," *Cell Death and Differentiation*, vol. 23, no. 3, pp. 369–379, 2016.

[20] M. Gao, P. Monian, Q. Pan, W. Zhang, J. Xiang, and X. Jiang, "Ferroptosis is an autophagic cell death process," *Cell Research*, vol. 26, no. 9, pp. 1021–1032, 2016.

[21] E. Park and S. W. Chung, "ROS-mediated autophagy increases intracellular iron levels and ferroptosis by ferritin and transferrin receptor regulation," *Cell Death & Disease*, vol. 10, no. 11, p. 822, 2019.

[22] S. Ma, R. F. Dielschneider, E. S. Henson et al., "Ferroptosis and autophagy induced cell death occur independently after siramesine and lapatinib treatment in breast cancer cells," *PLoS One*, vol. 12, no. 8, article e0182921, 2017.

[23] C.-H. Lin, P.-P. Lin, C.-Y. Lin et al., "Decreased mRNA expression for the two subunits of system x_c^-, *SLC3A2* and *SLC7A11* , in WBC in patients with schizophrenia: Evidence in support of the hypo- glutamatergic hypothesis of schizophrenia," *Journal of Psychiatric Research*, vol. 72, pp. 58–63, 2016.

[24] M. Maiorino, M. Conrad, and F. Ursini, "GPx4, lipid peroxidation, and cell death: discoveries, rediscoveries, and open issues," *Antioxidants & Redox Signaling*, vol. 29, no. 1, pp. 61–74, 2018.

[25] Y. Zhang, H. Tan, J. D. Daniels et al., "Imidazole ketone erastin induces ferroptosis and slows tumor growth in a mouse lymphoma model," *Cell Chemical Biology*, vol. 26, no. 5, pp. 623–633.e9, 2019.

[26] L. Jiang, N. Kon, T. Li et al., "Ferroptosis as a p53-mediated activity during tumour suppression," *Nature*, vol. 520, no. 7545, pp. 57–62, 2015.

[27] A. Tarangelo, L. Magtanong, K. T. Bieging-Rolett et al., "P53 suppresses metabolic stress-induced ferroptosis in cancer cells," *Cell Reports*, vol. 22, no. 3, pp. 569–575, 2018.

[28] J. P. Thomas, P. G. Geiger, M. Maiorino, F. Ursini, and A. W. Girotti, "Enzymatic reduction of phospholipid and cholesterol hydroperoxides in artificial bilayers and lipoproteins," *Biochimica et Biophysica Acta*, vol. 1045, no. 3, pp. 252–260, 1990.

[29] W. S. Yang, R. SriRamaratnam, M. E. Welsch et al., "Regulation of ferroptotic cancer cell death by GPX4," *Cell*, vol. 156, no. 1–2, pp. 317–331, 2014.

[30] "Characterization of mammalian selenoproteomes - PubMed," August 2021, https://pubmed.ncbi.nlm.nih.gov/12775843/.

[31] G. J. Warner, M. J. Berry, M. E. Moustafa, B. A. Carlson, D. L. Hatfield, and J. R. Faust, "Inhibition of Selenoprotein Synthesis by Selenocysteine $tRNA^{[Ser]Sec}$ Lacking Isopentenyladenosine," *The Journal of Biological Chemistry*, vol. 275, no. 36, pp. 28110–28119, 2000.

[32] D. J. R. Lane, A. M. Merlot, M. L.-H. Huang et al., "Cellular iron uptake, trafficking and metabolism: key molecules and mechanisms and their roles in disease," *Biochimica et Biophysica Acta (BBA) - Molecular Cell Research*, vol. 1853, no. 5, pp. 1130–1144, 2015.

[33] T. Rui, H. Wang, Q. Li et al., "Deletion of ferritin H in neurons counteracts the protective effect of melatonin against traumatic brain injury-induced ferroptosis," *Journal of Pineal Research*, vol. 70, no. 2, article e12704, 2021.

[34] A. R. Bogdan, M. Miyazawa, K. Hashimoto, and Y. Tsuji, "Regulators of iron homeostasis: new players in metabolism, cell death, and disease," *Trends in Biochemical Sciences*, vol. 41, no. 3, pp. 274–286, 2016.

[35] Y. Yu, L. Jiang, H. Wang et al., "Hepatic transferrin plays a role in systemic iron homeostasis and liver ferroptosis," *Blood*, vol. 136, no. 6, pp. 726–739, 2020.

[36] J. Yin, N. Hu, L. Yi et al., "Identification of ferroptosis biomarker in AHH-1 lymphocytes associated with low dose radiation," *Health Physics*, vol. 120, no. 5, pp. 541–551, 2021.

[37] H. Zhu, A. Santo, Z. Jia, and Y. Robert Li, "GPx4 in bacterial infection and polymicrobial sepsis: involvement of ferroptosis and pyroptosis," *Reactive Oxygen Species*, vol. 7, no. 21, pp. 154–160, 2019.

[38] H. Mao, Y. Zhao, H. Li, and L. Lei, "Ferroptosis as an emerging target in inflammatory diseases," *Progress in Biophysics and Molecular Biology*, vol. 155, pp. 20–28, 2020.

[39] M. Herscovitch, W. Comb, T. Ennis et al., "Intermolecular disulfide bond formation in the NEMO dimer requires Cys54 and Cys347," *Biochemical and Biophysical Research Communications*, vol. 367, no. 1, pp. 103–108, 2008.

[40] "Crosstalk of reactive oxygen species and NF-κB signaling - PubMed," August 2021, https://pubmed.ncbi.nlm.nih.gov/21187859/.

[41] S. S. Singh, S. N. Rai, H. Birla, W. Zahra, A. S. Rathore, and S. P. Singh, "NF-κB-mediated neuroinflammation in Parkinson's disease and potential therapeutic effect of polyphenols," *Neurotoxicity Research*, vol. 37, no. 3, pp. 491–507, 2020.

[42] C. Wang, W. Yuan, A. Hu et al., "Dexmedetomidine alleviated sepsis-induced myocardial ferroptosis and septic heart injury," *Molecular Medicine Reports*, vol. 22, no. 1, pp. 175–184, 2020.

[43] W. S. Yang, K. J. Kim, M. M. Gaschler, M. Patel, M. S. Shchepinov, and B. R. Stockwell, "Peroxidation of polyunsaturated fatty acids by lipoxygenases drives ferroptosis," *Proceedings of the National Academy of Sciences of the United States of America*, vol. 113, no. 34, pp. E4966–E4975, 2016.

[44] F. Ito, Y. Sono, and T. Ito, "Measurement and clinical significance of lipid peroxidation as a biomarker of oxidative stress: oxidative stress in diabetes, atherosclerosis, and chronic inflammation," *Antioxidants*, vol. 8, no. 3, p. 72, 2019.

[45] K. S. Fritz and D. R. Petersen, "An overview of the chemistry and biology of reactive aldehydes," *Free Radical Biology & Medicine*, vol. 59, pp. 85–91, 2013.

[46] "Arachidonic acid metabolism in brain physiology and pathology: lessons from genetically altered mouse models - PubMed," August 2021, https://pubmed.ncbi.nlm.nih.gov/17403135/.

[47] S. Nogawa, F. Zhang, M. E. Ross, and C. Iadecola, "Cyclo-oxygenase-2 gene expression in neurons contributes to ischemic brain damage," *The Journal of Neuroscience*, vol. 17, no. 8, pp. 2746–2755, 1997.

[48] Y.-G. Park, S.-K. Kang, S.-H. Noh et al., "PGE_2 induces IL-1β gene expression in mouse osteoblasts through a cAMP-PKA signaling pathway," *International Immunopharmacology*, vol. 4, no. 6, pp. 779–789, 2004.

[49] "Cyclooxygenase-2 regulates NLRP3 inflammasome-derived IL-1β production - PubMed," August 2021, https://pubmed.ncbi.nlm.nih.gov/25294243/.

[50] "Involvement of 15-lipoxygenase in the inflammatory arthritis - PubMed," August 2021, https://pubmed.ncbi.nlm.nih.gov/22573549/.

[51] C. Abrial, S. Grassin-Delyle, H. Salvator, M. Brollo, E. Naline, and P. Devillier, "15-Lipoxygenases regulate the production of chemokines in human lung macrophages," *British Journal of Pharmacology*, vol. 172, no. 17, pp. 4319–4330, 2015.

[52] Q. Yang and J. Zhou, "Neuroinflammation in the central nervous system: symphony of glial cells," *Glia*, vol. 67, no. 6, pp. 1017–1035, 2019.

[53] E. H. Kim, S.-W. Wong, and J. Martinez, "Programmed necrosis and disease: we interrupt your regular programming to bring you necroinflammation," *Cell Death & Differentiation*, vol. 26, no. 1, pp. 25–40, 2019.

[54] B. Proneth and M. Conrad, "Ferroptosis and necroinflammation, a yet poorly explored link," *Cell Death & Differentiation*, vol. 26, no. 1, pp. 14–24, 2019.

[55] G. W. Konat, T. Kielian, and I. Marriott, "The role of Toll-like receptors in CNS response to microbial challenge," *Journal of Neurochemistry*, vol. 99, no. 1, pp. 1–12, 2006.

[56] S. Lehnardt, "Innate immunity and neuroinflammation in the CNS: the role of microglia in Toll-like receptor-mediated neuronal injury," *Glia*, vol. 58, no. 3, pp. 253–263, 2009.

[57] J. Minkiewicz, J. P. de Rivero Vaccari, and R. W. Keane, "Human astrocytes express a novel NLRP2 inflammasome: the NLRP2 inflammasome activated by ATP," *Glia*, vol. 61, no. 7, pp. 1113–1121, 2013.

[58] C. S. Jack, N. Arbour, J. Manusow et al., "TLR signaling tailors innate immune responses in human microglia and astrocytes," *Journal of Immunology*, vol. 175, no. 7, pp. 4320–4330, 2005.

[59] M. Sarhan, W. G. Land, W. Tonnus, C. P. Hugo, and A. Linkermann, "Origin and consequences of necroinflammation," *Physiological Reviews*, vol. 98, no. 2, pp. 727–780, 2018.

[60] J. Li, F. Cao, H. Yin et al., "Ferroptosis: past, present and future," *Cell Death & Disease*, vol. 11, no. 2, p. 88, 2020.

[61] L. Jiang, J. H. Hickman, S.-J. Wang, and W. Gu, "Dynamic roles of p53-mediated metabolic activities in ROS-induced stress responses," *Cell Cycle*, vol. 14, no. 18, pp. 2881–2885, 2015.

[62] R. Kang, G. Kroemer, and D. Tang, "The tumor suppressor protein p53 and the ferroptosis network," *Free Radical Biology & Medicine*, vol. 133, pp. 162–168, 2019.

[63] T. Thomas and T. J. Thomas, "Polyamine metabolism and cancer," *Journal of Cellular and Molecular Medicine*, vol. 7, no. 2, pp. 113–126, 2003.

[64] S. Mandal, A. Mandal, and M. H. Park, "Depletion of the polyamines spermidine and spermine by overexpression of spermidine/spermine N^1-acetyltransferase 1 (SAT1) leads to mitochondria-mediated apoptosis in mammalian cells," *The Biochemical Journal*, vol. 468, no. 3, pp. 435–447, 2015.

[65] Y. Ou, S.-J. Wang, D. Li, B. Chu, and W. Gu, "Activation of SAT1 engages polyamine metabolism with p53-mediated ferroptotic responses," *Proceedings of the National Academy of Sciences of the United States of America*, vol. 113, no. 44, pp. E6806–E6812, 2016.

[66] R. U. Macías-Rodríguez, M. E. Inzaugarat, A. Ruiz-Margáin, L. J. Nelson, C. Trautwein, and F. J. Cubero, "Reclassifying hepatic cell death during liver damage: ferroptosis—a novel form of non-apoptotic cell death?," *International Journal of Molecular Sciences*, vol. 21, no. 5, article 1651, 2020.

[67] A. Franceschini, M. Capece, P. Chiozzi et al., "The P2X7 receptor directly interacts with the NLRP3 inflammasome scaffold protein," *The FASEB Journal*, vol. 29, no. 6, pp. 2450–2461, 2015.

[68] A. Gustin, M. Kirchmeyer, E. Koncina et al., "NLRP3 inflammasome is expressed and functional in mouse brain

microglia but not in astrocytes," *PLoS One*, vol. 10, no. 6, article e0130624, 2015.

[69] C. Agulhon, M.-Y. Sun, T. Murphy, T. Myers, K. Lauderdale, and T. A. Fiacco, "Calcium signaling and gliotransmission in normal vs. reactive astrocytes," *Frontiers in Pharmacology*, vol. 3, p. 139, 2012.

[70] P. R. Angelova, M. L. Choi, A. V. Berezhnov et al., "Alpha synuclein aggregation drives ferroptosis: an interplay of iron, calcium and lipid peroxidation," *Cell Death & Differentiation*, vol. 27, no. 10, pp. 2781–2796, 2020.

[71] M. A. Smith, G. Perry, and W. A. Pryor, "Causes and consequences of oxidative stress in Alzheimer's disease1, 2," *Free Radical Biology & Medicine*, vol. 32, no. 11, p. 1049, 2002.

[72] W. R. Markesbery and J. M. Carney, "Oxidative alterations in Alzheimer's disease," *Brain Pathology*, vol. 9, no. 1, pp. 133–146, 1999.

[73] B. Hallgren and P. Sourander, "The non-haemin iron in the cerebral cortex in Alzheimer's disease," *Journal of Neurochemistry*, vol. 5, pp. 307–310, 1960.

[74] D. J. Dedman, A. Treffry, J. M. Candy et al., "Iron and aluminium in relation to brain ferritin in normal individuals and Alzheimer's-disease and chronic renal-dialysis patients," *The Biochemical Journal*, vol. 287, no. 2, pp. 509–514, 1992.

[75] H. Svobodová, D. Kosnáč, Z. Balázsiová et al., "Elevated age-related cortical iron, ferritin and amyloid plaques in APP(swe)/PS1(deltaE9) transgenic mouse model of Alzheimer's disease," *Physiological Research*, vol. 68, Suppl 4, pp. S445–S451, 2019.

[76] Z.-Y. Zhu, Y.-D. Liu, Y. Gong et al., "Mitochondrial aldehyde dehydrogenase (ALDH2) rescues cardiac contractile dysfunction in an APP/PS1 murine model of Alzheimer's disease via inhibition of ACSL4-dependent ferroptosis," *Acta Pharmacol Sin*, 2021.

[77] D. G. Smith, R. Cappai, and K. J. Barnham, "The redox chemistry of the Alzheimer's disease amyloid beta peptide," *Biochimica et Biophysica Acta*, vol. 1768, no. 8, pp. 1976–1990, 2007.

[78] A. Tsatsanis, B. X. Wong, A. P. Gunn et al., "Amyloidogenic processing of Alzheimer's disease β-amyloid precursor protein induces cellular iron retention," *Molecular Psychiatry*, vol. 25, no. 9, pp. 1958–1966, 2020.

[79] W. S. Hambright, R. S. Fonseca, L. Chen, R. Na, and Q. Ran, "Ablation of ferroptosis regulator glutathione peroxidase 4 in forebrain neurons promotes cognitive impairment and neurodegeneration," *Redox Biology*, vol. 12, pp. 8–17, 2017.

[80] W.-D. Bao, P. Pang, X.-T. Zhou et al., "Loss of ferroportin induces memory impairment by promoting ferroptosis in Alzheimer's disease," *Cell Death & Differentiation*, vol. 28, no. 5, pp. 1548–1562, 2021.

[81] V. Calsolaro and P. Edison, "Neuroinflammation in Alzheimer's disease: current evidence and future directions," *Alzheimers Dement*, vol. 12, no. 6, pp. 719–732, 2016.

[82] M. T. Heneka, M. J. Carson, J. El Khoury et al., "Neuroinflammation in Alzheimer's disease," *The Lancet Neurology*, vol. 14, no. 4, pp. 388–405, 2015.

[83] M. Obulesu and M. Jhansilakshmi, "Neuroinflammation in Alzheimer's disease: an understanding of physiology and pathology," *The International Journal of Neuroscience*, vol. 124, no. 4, pp. 227–235, 2014.

[84] T. Jonsson, H. Stefansson, S. Steinberg et al., "Variant of TREM2 associated with the risk of Alzheimer's disease," *The New England Journal of Medicine*, vol. 368, no. 2, pp. 107–116, 2013.

[85] T. T. Rohn, "The Triggering Receptor Expressed on Myeloid Cells 2: "TREM-ming" the Inflammatory Component Associated with Alzheimer's Disease," *Oxidative Medicine and Cellular Longevity*, vol. 2013, Article ID 860959, 8 pages, 2013.

[86] D. J. DiSabato, N. Quan, and J. P. Godbout, "Neuroinflammation: the devil is in the details," *Journal of Neurochemistry*, vol. 139, pp. 136–153, 2016.

[87] M. T. Heneka, M. P. Kummer, and E. Latz, "Innate immune activation in neurodegenerative disease," *Nature Reviews Immunology*, vol. 14, no. 7, pp. 463–477, 2014.

[88] F. Leng and P. Edison, "Neuroinflammation and microglial activation in Alzheimer disease: where do we go from here?," *Nature Reviews Neurology*, vol. 17, no. 3, pp. 157–172, 2021.

[89] G. D. Femminella, S. Ninan, R. Atkinson, Z. Fan, D. J. Brooks, and P. Edison, "Does microglial activation influence hippocampal volume and neuronal function in Alzheimer's disease and Parkinson's disease dementia?," *Journal of Alzheimer's Disease*, vol. 51, no. 4, pp. 1275–1289, 2016.

[90] E. E. Spangenberg and K. N. Green, "Inflammation in Alzheimer's disease: lessons learned from microglia-depletion models," *Brain, Behavior, and Immunity*, vol. 61, pp. 1–11, 2017.

[91] J. M. Graham, M. N. Paley, R. A. Grünewald, N. Hoggard, and P. D. Griffiths, "Brain iron deposition in Parkinson's disease imaged using the PRIME magnetic resonance sequence," *Brain*, vol. 123, no. 12, pp. 2423–2431, 2000.

[92] E. C. Hirsch and S. Hunot, "Neuroinflammation in Parkinson's disease: a target for neuroprotection?," *The Lancet Neurology*, vol. 8, no. 4, pp. 382–397, 2009.

[93] P. L. McGeer, S. Itagaki, B. E. Boyes, and E. G. McGeer, "Reactive microglia are positive for HLA-DR in the substantia nigra of Parkinson's and Alzheimer's disease brains," *Neurology*, vol. 38, no. 8, pp. 1285–1291, 1988.

[94] E. Bertrand, W. Lechowicz, G. M. Szpak, E. Lewandowska, A. Członkowska, and J. Dymecki, "Quantitative study of pathological forms of astroglia in Wilson's disease," *Folia Neuropathologica*, vol. 35, no. 4, pp. 227–232, 1997.

[95] P. Damier, E. C. Hirsch, P. Zhang, Y. Agid, and F. Javoy-Agid, "Glutathione peroxidase, glial cells and Parkinson's disease," *Neuroscience*, vol. 52, no. 1, pp. 1–6, 1993.

[96] M. Mogi, M. Harada, P. Riederer, H. Narabayashi, K. Fujita, and T. Nagatsu, "Tumor necrosis factor-α (TNF-α) increases both in the brain and in the cerebrospinal fluid from parkinsonian patients," *Neuroscience Letters*, vol. 165, no. 1–2, pp. 208–210, 1994.

[97] S. Hands, M. U. Sajjad, M. J. Newton, and A. Wyttenbach, "*In Vitro* and *in Vivo* Aggregation of a Fragment of Huntingtin Protein Directly Causes Free Radical Production," *The Journal of Biological Chemistry*, vol. 286, no. 52, pp. 44512–44520, 2011.

[98] S.-Y. Chou, J.-Y. Weng, H.-L. Lai et al., "Expanded-polyglutamine huntingtin protein suppresses the secretion and production of a chemokine (CCL5/RANTES) by astrocytes," *The Journal of Neuroscience*, vol. 28, no. 13, pp. 3277–3290, 2008.

[99] T. L. Spires, H. E. Grote, S. Garry et al., "Dendritic spine pathology and deficits in experience-dependent dendritic plasticity in R6/1 Huntington's disease transgenic mice,"

The European Journal of Neuroscience, vol. 19, no. 10, pp. 2799–2807, 2004.

[100] M. A. Ariano, C. Cepeda, C. R. Calvert et al., "Striatal potassium channel dysfunction in Huntington's disease transgenic mice," *Journal of Neurophysiology*, vol. 93, no. 5, pp. 2565–2574, 2005.

[101] G. J. Hankey, "Stroke," *The Lancet*, vol. 389, no. 10069, pp. 641–654, 2017.

[102] C. Iadecola and J. Anrather, "The immunology of stroke: from mechanisms to translation," *Nature Medicine*, vol. 17, no. 7, pp. 796–808, 2011.

[103] S. Ahmad, N. M. Elsherbiny, R. Haque et al., "Sesamin attenuates neurotoxicity in mouse model of ischemic brain stroke," *Neurotoxicology*, vol. 45, pp. 100–110, 2014.

[104] Q. Tuo, P. Lei, K. A. Jackman et al., "Tau-mediated iron export prevents ferroptotic damage after ischemic stroke," *Molecular Psychiatry*, vol. 22, no. 11, pp. 1520–1530, 2017.

[105] I. Alim, J. T. Caulfield, Y. Chen et al., "Selenium drives a transcriptional adaptive program to block ferroptosis and treat stroke," *Cell*, vol. 177, no. 5, pp. 1262–1279.e25, 2019.

[106] E. D. Ponomarev, T. Veremeyko, and H. L. Weiner, "MicroRNAs are universal regulators of differentiation, activation, and polarization of microglia and macrophages in normal and diseased CNS," *Glia*, vol. 61, no. 1, pp. 91–103, 2013.

[107] E. Parada, J. Egea, I. Buendia et al., "The microglial α7-acetylcholine nicotinic receptor is a key element in promoting neuroprotection by inducing heme oxygenase-1 via nuclear factor erythroid-2-related factor 2," *Antioxidants & Redox Signaling*, vol. 19, no. 11, pp. 1135–1148, 2013.

[108] S. S. Karuppagounder, L. Alin, Y. Chen et al., "N-Acetylcysteine targets 5 lipoxygenase-derived, toxic lipids and can synergize with prostaglandin E2to inhibit ferroptosis and improve outcomes following hemorrhagic stroke in mice," *Annals of Neurology*, vol. 84, no. 6, pp. 854–872, 2018.

[109] W.-N. Jin, S. X.-Y. Shi, Z. Li, K. Wood, R. J. Gonzales, and Q. Liu, "Depletion of microglia exacerbates postischemic inflammation and brain injury," *Journal of Cerebral Blood Flow and Metabolism*, vol. 37, no. 6, pp. 2224–2236, 2017.